



VNIVERSITAT
DE VALÈNCIA

Phenomenological and cosmological aspects of electroweak models beyond the Standard Model

Tesi Doctoral
Programa de Doctorat en Física

Clara Murgui Galvez

Departament de Física Teòrica
IFIC (Universitat de València - CSIC)

Sota la supervisió de
Antonio Pich Zardoya i Pavel Fileviez Perez

Agost 2020

*Als meus pares
i germans.*

Antonio Pich Zardoya, catedràtic de la Universitat de València, y **Pavel Fileviez Perez**, professor titular a Case Western Reserve University,

certifiquen:

que la present memòria *Phenomenological and cosmological aspects of electroweak models beyond the Standard Model* ha sigut realitzada sota la seua direcció a l'Institut de Física Corpuscular, centre mixte de la Universitat de València i del CSIC, per **Clara Murgui Galvez** i constitueix la seua Tesi per a optar al grau de Doctora en Física.

I perquè així conste, en compliment de la legislació vigent, presenten en el Departament de Física Teòrica de la Universitat de València la referida Tesi Doctoral, i firmen el present certificat.

València, a 11 d'Agost del 2020.

Antonio Pich Zardoya

Pavel Fileviez Perez

Glossary

B	Baryon
BBN	Big Bang Nucleosynthesis
BGL	Boyd-Grinstein-Lebed
ChPT	Chiral Perturbation Theory
CKM	Cabibbo-Kobayashi-Maskawa
CLN	Caprini-Lellouch-Neubert
DD	Direct Detection
DFSZ	Dine-Fischler-Srednicki-Zhitnitsky
DFW	Duerr-Fileviez Perez-Wise
DM	Dark Matter
d.o.f.	degree(s) of freedom
EDM	Electric Dipole Moment
EFT	Effective Field Theory
EW	Electroweak
FF	Form Factor(s)
FOP	Fileviez Perez-Ohmer-Patel
FSR	Final State Radiation
GB	Goldstone Boson
GUT	Grand Unified Theory
HFLAV	Heavy Flavor Averaging Group
HK	Hyper-Kamiokande
HQEFT	Heavy Quark Effective Field Theory
IO	Inverted Ordering
KSVZ	Kim-Shifman-Vainshtein-Zakharov
L	Lepton
LCSR	Light Cone Sum Rules
LH	Left Handed

LNV	Lepton Number Violation
LQ	Lepto-Quark
LQCD	Lattice Quantum Chromodynamics
MOND	MOdified Newtonian Dynamics
MSSM	Minimal Supersymmetric Standard Model
NMR	Nuclear Magnetic Resonance
NO	Normal Ordering
NP	New Physics
PMNS	Pontecorvo-Maki-Nakagawa-Sakata
PQ	Peccei-Quinn
QCD	Quantum Chromodynamics
QED	Quantum Electrodynamics
RF	RadioFrequency
RGE	Running Group Evolution
RH	Right Handed
RHS	Right Hand Side
SK	Super-Kamiokande
SM	Standard Model
SMEFT	Standard Model Effective Field Theory
SQUID	Superconducting Quantum Interference Device
SSB	Spontaneous Symmetry Breaking
UV	Ultraviolet
vev	vacuum expectation value
WC	Wilson Coefficient
WET	Weak Effective Theory
WIMP	Weakly Interacting Massive Particle

Contents

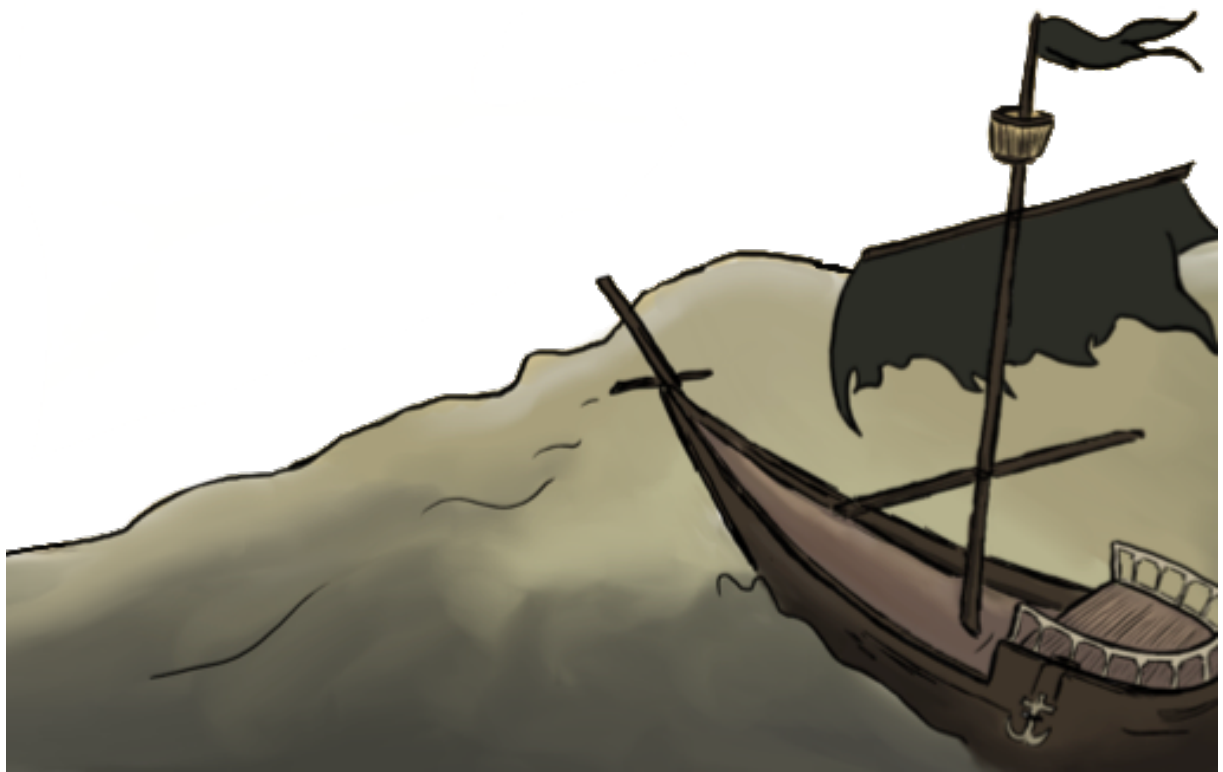
Preface	1
1 Neutrino physics	5
1.1 Nature of neutrinos: Lepton number	9
1.2 Mechanisms for neutrino mass generation $\Delta L = 2$	12
1.2.1 Type-I seesaw mechanism	12
1.2.2 Type-II seesaw mechanism	13
1.2.3 Type-III seesaw mechanism	15
1.2.4 Zee model	16
1.2.5 Colored seesaw	17
2 Dark matter	19
2.1 WIMPs	21
2.1.1 Relic abundance	23
2.1.2 Detecting WIMPs	38
2.2 Axions	51
2.2.1 The $U(1)_A$ anomaly	52
2.2.2 The Strong CP problem	58
2.2.3 The electroweak axion	64
2.2.4 Invisible axion models	67
2.2.5 Misalignment mechanism	71
2.2.6 Direct detection of dark matter axions	73
3 Gauging Baryon and Lepton Numbers	83
3.1 Anomaly cancellation	86
3.2 Gauge theories for Baryon and Lepton numbers	93
3.2.1 Model by Duerr, Fileviez Perez and Wise (DFW)	93
3.2.2 Model by Fileviez Perez, Ohmer and Patel (FOP)	95
3.3 Spontaneous breaking of local B and L symmetries	96

3.4	Experimental lower bound on the NP scale	99
4	Leptophobic Force	103
4.1	Theoretical framework	104
4.1.1	Spontaneous symmetry breaking	104
4.1.2	Kinetic Mixing	108
4.1.3	Towards a simplified model for dark matter	111
4.2	Phenomenological and cosmological bounds for DM	118
4.2.1	Relic density	118
4.2.2	Direct Detection	123
4.2.3	Gamma Lines	126
4.3	LHC phenomenology of $U(1)_B$	134
4.3.1	Leptophobic Gauge Boson at the LHC	134
4.3.2	Exotic Decays of the SM-like Higgs	139
4.3.3	Associated production	143
4.4	Conclusions	147
5	Leptophilic force	149
5.1	Unbroken local $U(1)_{B-L}$: Stueckelberg Scenario	151
5.1.1	Theoretical framework	151
5.1.2	Cosmological bounds	152
5.2	Broken $U(1)_{B-L}$ in 2 units	160
5.2.1	Theoretical framework	160
5.2.2	Cosmological bounds	161
5.2.3	Phenomenological bounds	166
5.2.4	Lepton Number Violation at the LHC	166
5.3	Local $U(1)_L$	171
5.3.1	Theoretical framework	171
5.3.2	Cosmological bounds	173
5.3.3	Phenomenological bounds	176
5.4	Conclusions	178
6	Neutrinos in Grand Unified Theories	179
6.1	Minimal GUT : $SU(5)$ <i>à la</i> Georgi and Glashow	181
6.1.1	Unification constraints	186
6.1.2	Proton decay	189
6.2	Mechanisms for neutrino mass generation in $SU(5)$	195
6.2.1	Type-I seesaw	195
6.2.2	Type-II seesaw	196

6.2.3	Type-III seesaw	197
6.2.4	Colored seesaw	199
6.2.5	Zee mechanism	200
6.3	Minimal realistic $SU(5)$ theories	201
6.3.1	The Zee- $SU(5)$	201
6.3.2	$SU(5)$ with minimal scalars	208
6.4	Conclusions	219
7	Axions in Grand Unified Theories	221
7.1	KSVZ mechanism in $SU(5)$	225
7.1.1	Implementation of the PQ mechanism	228
7.1.2	Predicting the GUT scale	229
7.1.3	Axion mass and phenomenology	235
7.2	DFSZ mechanism in $SU(5)$	239
7.2.1	Predicting the GUT scale	242
7.2.2	Axion mass and phenomenology	245
7.3	Conclusions	249
8	Effective Field Theories for $b \rightarrow c$ transitions	251
8.1	New physics behind the $b \rightarrow c$ anomalies	252
8.1.1	$R_2 \sim (3, 2, 7/6)$ scalar leptoquark	256
8.1.2	$\bar{R}_2 \sim (3, 2, 1/6)$ scalar leptoquark	257
8.1.3	$S_1 \sim (\bar{3}, 1, 1/3)$ scalar leptoquark	258
8.1.4	$S_3 \sim (\bar{3}, 3, 1/3)$ scalar leptoquark	259
8.1.5	$\Phi \sim (1, 2, 1/2)$ second Higgs boson	259
8.1.6	$U_1^\mu \sim (3, 1, 2/3)$ vector leptoquark	260
8.1.7	$U_3^\mu \sim (3, 3, 2/3)$ vector leptoquark	261
8.1.8	$V_2^\mu \sim (\bar{3}, 2, 5/6)$ vector leptoquark	261
8.1.9	$\tilde{V}_2^\mu \sim (\bar{3}, 2, -1/6)$ vector leptoquark	262
8.1.10	$W'^\mu \sim (1, 3, 0)$ vector boson	263
8.1.11	$V^\mu \sim (1, 1, -1)$ vector boson	263
8.2	Leptonic transitions	264
8.3	Semileptonic transitions: The helicity formalism.	266
8.3.1	$B \rightarrow D \tau \bar{\nu}$	272
8.3.2	$B \rightarrow D^* \tau \bar{\nu}$	275
8.4	Hadronic Form Factors	285

9	Global fit to $b \rightarrow c$ transitions	289
9.1	Global fit to $b \rightarrow c$ transitions: SMEFT	293
9.1.1	Fit independent analysis	293
9.1.2	Global Fit	296
9.1.3	Predictions	304
9.1.4	Interpretation of the results	306
9.2	Global fit to $b \rightarrow c$: Including C_{RL}^V	310
9.3	Global fit to $b \rightarrow c$: Including ν_R	313
9.3.1	Fit-independent analysis	314
9.3.2	Global Fit	315
9.3.3	Scenarios involving all possible UV-mediators	318
9.3.4	Predictions	324
9.3.5	Interpretation of the results	328
9.4	Conclusions	329
	Final remarks	333
	Appendices	336
A	Fierz and charge conjugation identities	337
A.1	Fierz identities involving chiral fermions	337
A.2	Charge conjugation identities	337
B	Gamma lines	339
B.1	Cross Sections for the Gamma Lines	339
B.2	Final State Radiation	340
	Bibliography	341
	Resum	379
	Acknowledgments	391





THE NEW Beyond the

Flavour
Anomalies

Chapter 9

Neutrino
Physics

Chapter 5

Chapters 8 & 9

Chapter 1

Chapter 3

The Standard Model
of particle physics

Chapter 2

CS

NEW WORLD

to Standard Model



Chapter 6

Lepton L
Baryon
numbers

$SU(3)_c$

Chapters 4 & 5

Chapter 7

Dark Matter

Preface

“When someone is searching, -said Siddhartha, - then it might easily happen that the only thing his eyes still see is that what he searches for, that he is unable to find anything, to let anything enter his mind, because he always thinks of nothing but the object of his search, because he has a goal, because he is obsessed by the goal. Searching means: having a goal. But finding means: being free, being open, having no goal. You, oh venerable one, are perhaps indeed a searcher, because, striving for your goal, there are many things you don't see, which are directly in front of your eyes.”

— *Siddhartha*. Hermann Hesse.

The Standard Model of particle physics (SM) is the best theory that we have so far to understand the nature. It is a theory that has been built collecting the effort from brilliant physicists who have adapted mathematical concepts and extended the available theoretical framework by the need of accommodating it to the experimental evidence. Although the SM describes with high accuracy most phenomena in nature, there is evidence of physics beyond it, which challenges physicists to seek answers. We will introduce first some of its Achilles heels that, supported by experimental observations, denote that the SM cannot be the ultimate theory and forces us to think beyond it:

- **The origin of neutrino masses and their nature.** Neutrinos are particularly interesting as, in addition to their unexpected tiny mass, which cannot be explained in the context of the SM, they are the only neutral fermions in the SM, allowing them to be their own antiparticles. We will describe their status and introduce the main mechanisms behind their mass generation in Chapter 1, their connection between their nature and lepton number will be discussed in

Chapter 5, while also in that chapter and in Chapter 6 we will study their interplay with other open problems such as dark matter or Grand Unified Theories (GUTs).

- **The nature of dark matter:** Experimental evidence indicates that the universe is filled by some unknown matter, which several candidates could explain. Dark matter (DM) will be introduced in Chapter 2, where two of the most appealing candidates will be presented: weak interacting massive particles and axions.
- **Matter-antimatter asymmetry:** In the early universe equal amount of matter and antimatter should have been created; however, here we are. A tiny portion of matter – about one particle per billion – managed to survive. One of the conditions required for this asymmetry to occur in the evolution of the universe is the violation of baryon number. In Chapter 3 and 4 we will introduce theories where such condition can be satisfied.
- **The flavour B-anomalies:** Recently, hints of lepton flavour universality violation have been reported in B meson decays. Puzzled by their possible origin, in Chapter 9 we perform a global fit to $b \rightarrow c$ transitions including as input the most updated values available. For that, we will adopt a bottom-up approach from an effective field theory point of view, presented in Chapter 8. We will show that, although the fit prefers new scenarios rather than the SM, no preference for a certain type of new physics is found.

Apart from the topics mentioned above, the SM also leaves without a satisfactory explanation several concepts that make them less aesthetic and claim for a better understanding. Among them,

- **The symmetries of the SM:** The three forces in the SM suggest a common origin at high energies. The original GUT proposed by Georgi and Glashow based on $SU(5)$, in spite of its predictive power and beauty, fails to reproduce the correct mass relations among fermions, unification of gauge couplings and massive neutrinos, as will be explained in Chapter 6. In that chapter, as well as in Chapter 7, we present minimal realistic alternatives to the original model and their interplay with other problems of the SM such as neutrino masses (Chapter 6), the existence of DM and the strong CP problem (Chapter 7).

Besides the SM gauge symmetries, there are accidental symmetries such as baryon and lepton numbers, or combinations of both, which could suggest a local symmetry behind them. Those will be discussed in Chapter 3. In there, we will show that, by gauging these symmetries, very appealing connections between neutrino masses and DM appear as well as rich phenomenology regarding DM, which naturally arises in some of these models as a prediction of anomaly cancellation. The fact that the upper bound of these theories is at the multi-TeV scale makes their phenomenology testable at the current or near future stages of colliders (LHC), direct detection (Xenon-IT, Xenon-nT...) or indirect detection (Fermi Lat, HESS, CTA...) DM experiments, as we will show in Chapters 3, 4 and 5. Particularly interesting are, as we will show, theories for local baryon number, motivated by the capability of the LHC to detect their hypothetical leptophobic gauge boson mediator and their consequent low scale phenomenology.

- **The strong CP problem:** Why does Quantum Chromodynamics (QCD) seem to preserve CP? A pseudoscalar field called "axion" is an attractive answer. Axions will be discussed in Chapter 2 and their embedding in GUT theories in Chapter 7, where we will show that, in their context, the mass of the axion can be predicted.

The aforementioned topics, as shown above, might be deeply connected. The aim of this thesis is to explore motivated extensions of the SM connecting the different open problems just presented under the guidance of:

- **Simplicity**, meaning minimal amount of content to explain the maximum number of open issues. Nature may be wayward, but having two potential paths towards an answer, we will bet for the simplest one.
- **Predictivity**, meaning that the elements in the theory are connected in some extend. The less freedom the theory enjoys, the more predictive power it has, therefore becoming more attractive.
- **Testability**, in the sense that their predictions may be falsified by current or near future experiments.

The above define the compass we will take for our journey in beyond the standard model territories, and this thesis is going to be the logbook of that wonderful trip.

1.- Neutrino physics

Neutrino masses are certainly a clear evidence for beyond the Standard Model physics. The SM of particle physics predicts massless neutrinos: no mass term is allowed by the symmetries $SU(3)_c \otimes SU(2)_L \otimes U(1)_Y$ within the matter content of the theory. The later was believed for a long time, reinforced by the experimental evidence of lepton flavour number conservation, until in the late 90s several experiments had reported anomalies in the interaction rates of solar [1] and atmospheric [2] neutrinos. The well-known solar neutrino problem exhibits a mismatch between the expected and observed neutrinos coming from the Sun; although the vast majority of neutrinos emitted by the Sun were supposed to be produced as electron flavour eigenstate neutrinos, only a third of those were observed at the detectors. This apparent contradiction was finally resolved by the Sudbury Neutrino Observatory (SNO) in 2001 [3]. Neutrino oscillations were also reported in other experiments based on reactor and accelerator beam neutrinos [4, 5].

Such phenomenon observed at experiment indicates that the neutrino flavour eigenstates do not correspond to their mass eigenstates, which would be the case if they were massless. In this context, there should be a rotation matrix connecting the mass eigenbasis with the flavour one, since both the charged and neutral lepton mass matrices, in general, cannot be simultaneously diagonalized, as we will briefly show in the following.

Let us assume that a Dirac mass term for the neutrinos is violating the lepton flavour number in the Lagrangian,

$$- \mathcal{L}_Y \supset \bar{e}_L Y_e \frac{v_0}{\sqrt{2}} e_R + \bar{\nu}_L Y_\nu \frac{v_0}{\sqrt{2}} \nu_R + \text{h.c.} \quad (1.1)$$

where $v_0 = 246$ GeV is the vacuum expectation value (vev) of the SM Higgs boson. It is well known that any complex matrix (i.e. flavour Yukawa couplings) can be brought to a positive definite diagonal form by a bi-unitary transformation, particularly the lepton Yukawa terms in the broken phase, as follows:

$$-\mathcal{L}_Y \supset \bar{e}_L V_{eL} M_e^{\text{diag}} V_{eR}^\dagger e_R + \bar{\nu}_L V_{\nu L} M_\nu^{\text{diag}} V_{\nu R}^\dagger \nu_R + \text{h.c.} \quad (1.2)$$

By redefining the leptons in the following way $e_{L,R} \rightarrow V_{eL,R} e_{L,R}$ and $\nu_{L,R} \rightarrow V_{\nu L,R} \nu_{L,R}$, the mass matrices in Lagrangian are brought to a diagonal form, so that our fields are now physical states. This rotation, however, analogously to the quark sector, induces a mixing term in the charged leptonic current from the $i\bar{\ell}_L D_\mu \gamma^\mu \ell_L$ kinetic term:

$$\mathcal{L} \supset -\frac{g}{\sqrt{2}} \bar{e}_L W_\mu^- \gamma^\mu \nu_L \rightarrow -\frac{g}{\sqrt{2}} \bar{e}_L W_\mu^- \gamma^\mu \underbrace{V_{eL}^\dagger V_{\nu L}}_{U_{\text{PMNS}}} \nu_L. \quad (1.3)$$

where g refers to the $SU(2)_L$ gauge coupling. Therefore, choosing the basis such that the charged lepton flavour states are diagonal, we can absorb the rotation matrices in the neutrino transformation in the matrix U_{PMNS} , the Pontecorvo-Maki-Nakagawa-Sakata (PMNS) matrix, as Eq. 1.3 shows. This matrix is the analogous to the Cabibbo-Kobayashi-Maskawa (CKM) mixing matrix, V_{CKM} , in the quark sector; it connects the mass and flavour eigenstates of the neutrinos and it is responsible for the neutrino oscillations:

$$\begin{pmatrix} \nu_{eL} \\ \nu_{\mu L} \\ \nu_{\tau L} \end{pmatrix} = U_{\text{PMNS}} \begin{pmatrix} \nu_{1L} \\ \nu_{2L} \\ \nu_{3L} \end{pmatrix}, \quad \text{where} \quad U_{\text{PMNS}} \equiv \begin{pmatrix} U_{e1} & U_{e2} & U_{e3} \\ U_{\mu 1} & U_{\mu 2} & U_{\mu 3} \\ U_{\tau 1} & U_{\tau 2} & U_{\tau 3} \end{pmatrix}. \quad (1.4)$$

Taking into account that the matrix is unitary, it can be expressed as

$$U_{\text{PMNS}} = e^{iH}, \quad \text{where} \quad H^\dagger = H. \quad (1.5)$$

On the other hand, any matrix can be decomposed in a symmetric (S) and antisymmetric (A) part as follows: $H = S + A$. Then, because of the hermitian nature of H , $S = S^*$ and $A = -A^*$. Now, taking into account the number of degrees

of freedom (d.o.f.), illustrated in the diagram below, we obtain:

$$\left[S = \left(\begin{array}{c} \text{[Diagram: Blue triangle pointing down-left, red triangle pointing up-right]} \end{array} \right) \left\{ \frac{N^2 - N}{2} + N \right\} - (2N - 1) \Rightarrow N_{\text{Im}} = \frac{(N - 1)(N - 2)}{2} \right.$$

$$\left[A = \left(\begin{array}{c} \text{[Diagram: Red triangle pointing down-left]} \end{array} \right) \left\{ \frac{N^2 - N}{2} \right\} \Rightarrow N_{\text{Re}} = \frac{N(N - 1)}{2} \right. \quad (1.6)$$

where the $2N - 1$ account for the d.o.f. we can rotate away by using the freedom of the lepton global phases. Therefore, for $N = 3$ (three families of neutrinos) we can parametrize the U_{PMNS} matrix with $N_{\text{Re}} = 3$ real (Euler) angles and $N_{\text{Im}} = 1$ complex (CP) phase that can lead to CP violation:

$$U_{\text{PMNS}} = \begin{pmatrix} 1 & 0 & 0 \\ 0 & c_{23} & s_{23} \\ 0 & -s_{23} & c_{23} \end{pmatrix} \begin{pmatrix} c_{13} & 0 & e^{-i\delta} \\ 0 & 1 & 0 \\ -s_{13} e^{i\delta} & 0 & c_{13} \end{pmatrix} \begin{pmatrix} c_{12} & s_{12} & 0 \\ s_{12} & c_{12} & 0 \\ 0 & 0 & 1 \end{pmatrix}. \quad (1.7)$$

Note that, if neutrinos are Majorana (discussed in Sec. 1.1), a global phase redefinition does not leave the Majorana mass term invariant so that two extra CP violating phases should be taken into account in this case.¹ The fact that $U_{\text{PMNS}} \neq \mathbb{I}$ implies that the flavour states will evolve as a linear combination of mass eigenstates over time. The later allows us to talk about the conversion probability between flavour states, which quantum mechanics tells us that is given by,

$$P(\nu_a \rightarrow \nu_b) = -4 \sum_{i < j} \text{Re}[U_{ai}^* U_{bi} U_{aj} U_{bj}^*] \sin^2 \Delta_{ij} + 2 \sum_{i < j} \text{Im}[U_{ai}^* U_{bi} U_{aj} U_{bj}^*] \sin 2\Delta_{ij}, \quad (1.8)$$

where $\Delta_{ij} = (m_i^2 - m_j^2)L/4E_\nu$, being L the distance at which the neutrino interacts along its direction of flight, and E_ν its energy. From Eq. 1.8, the reader can conclude that the existence of neutrino oscillations implies the existence of at least two non-degenerate massive neutrinos. From the experimental data on neutrino oscillations one can extract the absolute value of the mass differences between the three neutrino mass eigenstates.

¹These Majorana phases, however, do not enter in the neutrino oscillations. They only enter in processes where lepton number is violated in two units.

$\Delta m_{21}^2 [10^{-5} \text{ eV}^2]$		$\Delta m_{3\ell}^2 [10^{-3} \text{ eV}^2]$		$\sin^2 \theta_{12}/10^{-1}$	
NO and IO		NO	IO	NO	IO
$7.42^{+0.21}_{-0.20}$		$2.517^{+0.026}_{-0.028}$	-2.498 ± 0.028	3.04 ± 0.12	$3.04^{+0.13}_{-0.12}$
$\sin^2 \theta_{23}/10^{-1}$		$\sin^2 \theta_3/10^{-2}$		$\delta[^\circ]$	
NO	IO	NO	IO	NO	IO
$5.73^{+0.16}_{-0.20}$	$5.75^{+0.16}_{-0.19}$	$2.238^{+0.063}_{-0.062}$	$2.219^{+0.062}_{-0.063}$	197^{+27}_{-24}	282^{+26}_{-30}

Table 1.1: Best fit parameters at $\pm 1\sigma$ for the neutrino parameters given by the recent global analysis from Ref. [8], where $\ell = 1$ for NO and $\ell = 2$ for IO (see main text).

However, notice that Eq. 1.8 does not allow us to predict their absolute mass scale from neutrino oscillation data, although other experiments set an upper bound for the scale of neutrino masses [6],

$$m_\beta < 1.1 \text{ eV at } 90\% \text{ C.L.}, \quad \text{where} \quad m_\beta^2 \equiv \sum_j^3 |U_{ej}|^2 m_j^2, \quad (1.9)$$

which is suggested to be even stronger by cosmological probes [7],

$$\sum_i m_{\nu_i} < 0.12 \text{ eV}. \quad (1.10)$$

Nevertheless, the later bound depends on the combination of data adopted and could be weakened depending on the data set considered in the fit. Such ambiguity in the sign of $|\Delta m_{ij}|^2$ gives rise to two possible non-equivalent hierarchies: normal ordering (NO), $m_1 < m_2 < m_3$, and inverted ordering (IO), $m_1 > m_2 > m_3$.² We show in Table 1.1 the results on the neutrino parameters from the most recent global fit analysis in Ref. [8]³

After this brief introduction on neutrino physics we are aware that, although the observation of neutrino oscillations clearly brings out the incompleteness of the SM, the neutrino mass hierarchy, the reason why the neutrino masses is more than one million times smaller than the mass of the electron, their mass values, together with the key question whether they are Dirac or Majorana particles are still shrouded in mystery.

²Global fit results on the parameters describing neutrino physics show a preference for the normal hierarchy, mildly below 3σ [8] when only data from oscillation experiments is taken into account. When also including cosmological input, such preference increases up to 3.3σ [9].

³See also Ref. [9] for an alternative fit with similar results.

1.1 Nature of neutrinos: Lepton number

One can distinguish three reasons why the neutrinos are massless in the SM, or in other words, why $B-L$ is an exact symmetry:

- (a) there is no right-handed (RH) lepton field allowing for a Yukawa interaction with the $SU(2)_L$ lepton doublet,
- (b) there is only one scalar in the theory: the SM Higgs is a $SU(2)_L$ doublet with hypercharge $1/2$,
- (c) when referring strictly speaking to the SM we assume a renormalizable theory, i.e. only dimension 4 interactions are considered in the Lagrangian.

Therefore, the SM matter content and gauge symmetries do not allow for a mass term in a renormalizable Lagrangian. However, we have discussed that neutrinos must have mass to account for the experimental hints on lepton flavour oscillations. Hence, we should expect either (a), (b) or (c) to be incorrect.

Let us start by assuming (a) is false and that the SM contains a RH neutrino, $\nu_R \sim (1, 1, 0)$. If so, the SM gauge symmetry group allows for the following interaction in the Yukawa Lagrangian,

$$- \mathcal{L}_Y \supset Y_\nu \ell_L i \sigma_2 H^* \nu_R + \text{h.c.}, \quad (1.11)$$

so that neutrinos will get mass through the Higgs mechanism as well as the rest of the charged fermions in the SM. Their mass is connected to the electroweak (EW) scale via the EW spontaneous symmetry breaking (SSB) as follows,

$$M_\nu^D = Y_\nu \frac{v_0}{\sqrt{2}}. \quad (1.12)$$

Therefore, we would need a Yukawa of order $Y_\nu \sim \mathcal{O}(10^{-12})$ in order to achieve the proper mass scale for the neutrinos, fixed by Eq. 1.9, which is absurdly six orders of magnitude smaller than the electron. This brings us to the puzzling question: *Why neutrinos are so light?*

At this point, some comments are in order. In the physics community, it is common to hear complaints about the smallness of the Y_ν in the case neutrinos are Dirac particles. This issue is typically (and wrongly) called a *fine tuning problem*. It should be therefore stressed that having a small Yukawa coupling is totally natural in the sense that this parameter is protected by the chiral symmetry, as well as are the rest of Yukawa couplings in the Lagrangian. Furthermore, by *fine tuning* we usually refer to tuned cancellations between two (or more) terms, which is transversal to our scenario. Said that, it is fair to also stress that such strong hierarchy between the Yukawa couplings of the neutrinos and the charged leptons is also present in the quark sector, where there are 5 orders of magnitude between the Yukawa couplings of the up and top quarks. Hence, there is nothing wrong about neutrinos being Dirac particles, although aiming to understand from a theoretical point of view such hierarchy among the fermion masses, Majorana neutrinos would be appreciated since, as we will see in the following, they can provide a nice justification for that.

Neutrinos are unquestionably Dirac particles if lepton number is conserved but, as we will learn in Chapter 3, lepton number is just an accidental symmetry in the SM renormalizable Lagrangian, in general not guaranteed anymore when new fields are considered, so that nothing prevents the Lagrangian from having the following bare mass term,

$$- \mathcal{L} \supset \frac{1}{2} \nu_R^T C M_R \nu_R + \text{h.c.}, \quad (1.13)$$

allowed by gauge symmetries and Lorentz invariance. Notice that the above interaction violates lepton number in two units! In this case, one can introduce the following 4-component field,

$$\Psi_N = \nu_R + (\nu_R)^c, \quad (1.14)$$

so that neutrinos are their own antiparticles ($(\Psi_N)^c = \Psi_N$), i.e. they are Majorana particles. Actually, there is no specific need for having RH neutrinos in the theory to account for neutrino masses. Let us look closer to option (c). As commented in the Preface, we know that the SM cannot be the ultimate theory for nature. If we think of it as a part of (up to dimension-4) an effective field theory (EFT), we expect the lowest dimensional operator to dominate the effect of new physics (NP), in this case dimension 5 operators. Curiously, it turns out that by taking into account the symmetries and

particle content of the SM, there is only one possible dimension 5 operator that can be written down: the so-called Weinberg operator [10],

$$\mathcal{L} = \mathcal{L}_{\text{SM}}^{\text{d}=4} + \frac{C^{(5)}}{\Lambda} \mathcal{O}^{(5)} + \sum_{n=6}^{\infty} \frac{C^{(n)}}{\Lambda^{n-4}} \mathcal{O}^{(n)} \quad \text{where} \quad \mathcal{O}^{(5)} = (\bar{\ell}_L^c i \sigma_2 H^*) (H^T i \sigma_2 \ell_L), \quad (1.15)$$

which, after SSB, leads to a Majorana mass term for the left-handed (LH) neutrino. That mass is naturally suppressed by the scale of NP, in that case, the scale where lepton number is violated in two units ($\Delta L = 2$). Indeed, the scenario of a RH neutrino commented above is naturally included in this approach when the ν_R is integrated out! There are two possible topologies that can lead to the Weinberg operator at the renormalizable level,⁴

$$\text{Topology I:} \quad \left\{ \begin{array}{l} H \otimes H \sim \underbrace{(1, 1, 1)}_{\delta^+} \oplus \underbrace{(1, 3, 1)}_{\Delta: \text{Type-II}} \\ \ell \otimes \ell \sim (1, 1, -1) \oplus (1, 3, -1) \end{array} \right. \quad (1.16)$$

$$\text{Topology II:} \quad \ell \otimes H \sim \underbrace{(1, 1, 0)}_{\nu_R: \text{Type-I}} \oplus \underbrace{(1, 3, 0)}_{\Sigma: \text{Type-III}} \quad (1.17)$$

Those lead to the three possible realizations at tree level of the Weinberg operator, as represented in Fig. 1.1. In contrast with the tree-level case, there are several realizations of

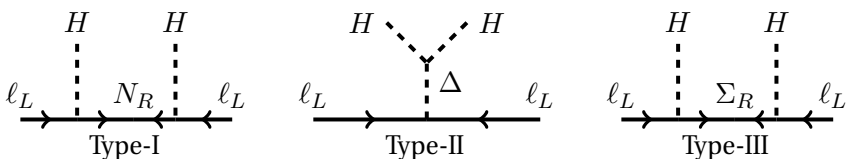


Figure 1.1: Seesaw mechanisms: tree-level realizations of the Weinberg operator. *Figure adapted from Ref. [11].*

the Weinberg operator at the quantum level. We will focus on two of them at the 1-loop level for convenience: the Zee model and the colored seesaw. The following section

⁴Note that, at the renormalizable level, $\nu_R \sim (1, 1, 0)$ (Type-I) and $\Sigma_R \sim (1, 3, 0)$ (Type-III) imply that assumption (a) is incorrect, while $\Delta \sim (1, 3, 1)$ (Type-II) implies that the false statement is (b).

is devoted to discuss the above mechanisms for neutrino masses. We note that these realizations are usually referred as *seesaw* mechanisms because of their resemblance with a seesaw regarding the mass suppression effect: the heavier the NP scale, the smaller the neutrino masses. In Fig. 1.2 we illustrate such analogy.

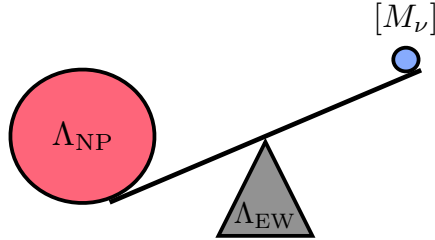


Figure 1.2: Illustration of the seesaw mechanism: The heavier the NP scale, the more it pushes the neutrino masses to be small. The EW scale acts as a fixed support.

1.2 Mechanisms for neutrino mass generation $\Delta L = 2$

First, we will discuss the three seesaw mechanisms based on the three possible tree-level realizations at the renormalizable level of the Weinberg operator and, then, we will discuss two simple possibilities to generate neutrino masses at the 1-loop level.

1.2.1 Type-I seesaw mechanism

The Type-I seesaw [12–16] mechanism is maybe one of the simplest mechanisms for neutrino mass generation, since it only requires the addition of a SM singlet $\nu_R \sim (1, 1, 0)$ to the matter content of the SM. The relevant Lagrangian in this context is given by,

$$-\mathcal{L}^{\text{Type-I}} \supset \bar{\ell}_L Y_\nu i \sigma_2 H^* \nu_R + \frac{1}{2} \overline{(\nu_R)^c} M_R \nu_R + \text{h.c.}, \quad (1.18)$$

where Y_ν and M_R are $3 \times n$ matrices, being n the number of RH neutrinos that we include in the theory. We will assume that $n \geq 2$ because at least two non-degenerated neutrinos are needed to account for neutrino oscillations, as previously commented. Once the theory undergoes SSB, the neutrino mass terms can be identified from the

above Lagrangian as follows,

$$-\mathcal{L}^{\text{Type-I}} \supset \frac{1}{2} \begin{pmatrix} \overline{\nu_L} & \overline{(\nu_R)^c} \end{pmatrix} \begin{pmatrix} 0 & M_D \\ M_D^T & M_R \end{pmatrix} \begin{pmatrix} (\nu_L)^c \\ \nu_R \end{pmatrix} + \text{h.c.}, \quad (1.19)$$

where $M_D = Y_\nu v_0/\sqrt{2}$ is the Dirac mass acquired through the Higgs mechanism, and we have used the properties on the charge conjugated fields listed in Appendix A. If $[M_R] \gg [M_D]$,⁵ the diagonalization of Eq. 1.19 by blocks gives us,

$$M_\nu = -M_D M_R^{-1} M_D^T + \mathcal{O}([M_D]^3/[M_R]^2) \quad \text{and} \quad M_N \sim M_R, \quad (1.20)$$

where ν and N are the physical neutrino states. One can easily recognize from the above expression the analogy with a playground seesaw. Assuming an order one Yukawa $Y_\nu \sim \mathcal{O}(1)$, a Majorana mass of $M_R \sim \mathcal{O}(10^{14})$ GeV would be needed to generate the observed neutrino mass scale (see Eq. 1.9). Such upper bound is commonly called *canonical seesaw scale*. Sadly, if this is the case and our theory sponsors a high scale seesaw (order one Yukawa coupling) it will be barely possible to falsify.

1.2.2 Type-II seesaw mechanism

According to the topologies in Eqs. 1.16 and 1.17, for implementing the Type-II seesaw [16–19] a triplet under $SU(2)_L$ with hypercharge 1, i.e. $\Delta \sim (1, 3, 1)$, is needed:

$$\Delta \equiv \frac{\sigma^i}{\sqrt{2}} \Delta_i = \begin{pmatrix} \Delta^+/\sqrt{2} & \Delta^{++} \\ \Delta^0 & -\Delta^+/\sqrt{2} \end{pmatrix}. \quad (1.21)$$

In this case, the relevant interactions for generating neutrino masses are given by

$$-\mathcal{L}^{\text{Type-II}} \supset (\ell_L^T C i \sigma_2 Y_\Delta \Delta \ell_L + \text{h.c.}) + M_\Delta^2 \text{Tr}\{\Delta^\dagger \Delta\} + (\mu H^\dagger \Delta i \sigma_2 H^* + \text{h.c.}), \quad (1.22)$$

where we do not include here the full scalar Lagrangian but only the relevant terms for understanding the mechanism. Note that in the first Yukawa term we could choose the lepton charge of Δ to be -2 , so that, if $\mu = 0$, lepton number would be a good global

⁵In the following, we will refer to the mass scale of the matrix A as $[A]$.

symmetry of the full Lagrangian. However, if $M_\Delta^2 < 0$, Δ gets a vev and lepton number would be spontaneously broken, leading to the Majoron predicted by the Goldstone theorem. The later possibility is ruled out as it is the original Gelmini-Roncadelli model [20]. Let us consider $\mu \neq 0$ instead, which breaks explicitly lepton number in the Lagrangian from Eq. 1.22. In this context, even if $M_\Delta^2 > 0$, the spontaneous breaking of the EW symmetry triggered by the SM Higgs induces the scalar triplet to get a vev , i.e., $\langle \Delta \rangle = v_\Delta / \sqrt{2}$. Therefore, via the Yukawa interaction in Eq. 1.22, neutrinos get the following Dirac mass:

$$M_\nu = \sqrt{2} Y_\Delta v_\Delta. \quad (1.23)$$

What can we infer from v_Δ ? The triplet Δ carries EW quantum numbers so that its vev enters in the EW gauge boson masses in the following way:

$$M_W^2 = \frac{g^2}{2} (v_0^2 + 2v_\Delta^2), \quad \text{and} \quad M_Z^2 = \frac{g^2}{2 \cos^2 \theta_W} (v_0^2 + 4v_\Delta^2). \quad (1.24)$$

Because of the current constraints on the ρ parameter [21],

$$\rho \equiv \frac{M_W^2}{M_Z^2 \cos^2 \theta_W} = \frac{1 + 2v_\Delta^2/v_0^2}{1 + 4v_\Delta^2/v_0^2} < 1.00038_{-0.0004}^{+0.00020}, \quad (1.25)$$

we know that $v_\Delta \ll v_0$; particularly, $v_\Delta \lesssim 5$ GeV. In this limit, and also assuming $M_\Delta \gg v_0$,⁶ the minimum conditions of the scalar potential imply,

$$v_\Delta \sim \mu \frac{v_0^2}{M_\Delta^2}, \quad (1.26)$$

where we can recognize again the seesaw mechanism: the larger the mass of the triplet, the smaller the neutrino mass, since the vev of the SM Higgs is fixed. Notice that μ , although being a dimensionful parameter, is protected by the global lepton number as commented before and parametrizes the strength of lepton number violation. Therefore, we should expect the mass of the neutrinos to be proportional to μ . In this scenario,

⁶This is a good assumption since collider bounds for the charged scalars do not allow their mass to be below the EW scale. Furthermore, the bare mass for Δ is not protected by any symmetry and, in principle, is sensitive to any UV correction.

very striking phenomenology could be produced if the triplet mass scale is relatively light; see Refs. [22–25] for a detailed study.

1.2.3 Type-III seesaw mechanism

The Type-III seesaw mechanism [26–30] works analogously to the Type-I seesaw but instead of a singlet, the Weinberg operator is obtained by integrating out a real fermion triplet $\Sigma_R \sim (1, 3, 0)$, defined as:

$$\Sigma_R \equiv \frac{\sigma^i}{\sqrt{2}} \Sigma_{iR} = \begin{pmatrix} \Sigma^0/\sqrt{2} & \Sigma^+ \\ \Sigma^- & -\Sigma^0/\sqrt{2} \end{pmatrix}_R. \quad (1.27)$$

The relevant Lagrangian in this context reads as,

$$- \mathcal{L}^{\text{Type-III}} \supset \left(\overline{\ell}_L \sqrt{2} Y_\Sigma \Sigma_R i\sigma_2 H^* + \text{h.c.} \right) + \text{Tr} \{ \Sigma_R^T C M_R \Sigma_R \}. \quad (1.28)$$

After SSB, the mass matrix for the neutral fields is equivalent to the mass matrix from the Type-I seesaw in Eq. 1.19 where now $M_D = Y_\Sigma v_0/\sqrt{2}$,

$$- \mathcal{L}^{\text{Type-III}} \supset \frac{1}{2} \left(\overline{\nu}_L \quad \overline{(\Sigma_R^0)^c} \right) \begin{pmatrix} 0 & M_D \\ M_D^T & M_R \end{pmatrix} \begin{pmatrix} (\nu_L)^c \\ \Sigma_R^0 \end{pmatrix} + \text{h.c.}, \quad (1.29)$$

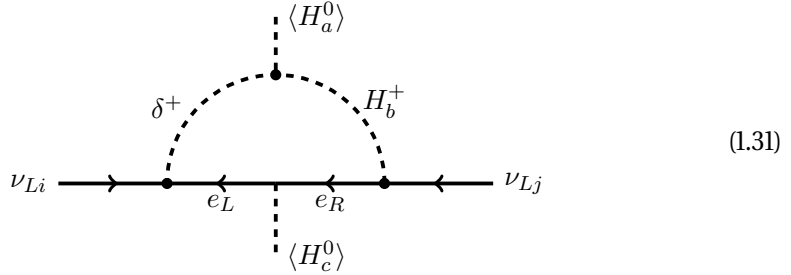
so are the masses of the physical fields:

$$M_\nu^{ij} = \frac{1}{2} Y_\Sigma^i M_R^{-1} Y_\Sigma^j v_0^2. \quad (1.30)$$

Again, a $[M_R] \sim \mathcal{O}(10^{14-15})$ GeV if $Y_\Sigma \sim \mathcal{O}(1)$ (or equivalently a tiny Y_Σ if M_R is light) would be needed to reproduce the proper mass scale. In Eq. 1.30 the flavour indices are written explicitly for the reader to note that, in the context of a single copy of Σ_R , the Yukawa Y_Σ^i is just a vector in the flavour space, so that the rank of the neutrino mass matrix in Eq. 1.30 is only 1. We need to add, as in the Type-I seesaw, at least two copies of Σ_R in order to achieve realistic neutrino masses. In this scenario, however, due to the extra presence of the charged fields Σ^\pm , the phenomenology is much richer. See Refs. [31–33] for studies on the testability of this mechanism at the LHC.

1.2.4 Zee model

The Zee model is a 1-loop mechanism to generate neutrino masses, proposed by A. Zee in Ref. [34]. A mass term can be achieved by adding a charged $SU(2)_L$ singlet, $\delta^+ \sim (1, 1, 1)$ and a second Higgs doublet, $H_2 \sim (1, 2, 1/2)$, so that the loop responsible for a neutrino mass term closes as follows:



The relevant interactions for this mechanism are given by

$$-\mathcal{L}_{\text{Zee}} = \lambda \ell_L^T C i \sigma_2 \ell_L \delta^+ + \bar{\ell}_L Y_c H_c e_R + \mu H_a^\dagger i \sigma_2 H_b^* \delta^+ + \text{h.c.}, \quad (1.32)$$

where Y_c are the Yukawa matrices for the two Higgses present in the theory $H_c = (H_c^+, H_c^0)^T$, being $a, b, c = 1$ or 2 and $a \neq b$ in the above expression. The coupling λ is an antisymmetric 3×3 matrix in the flavor space. Here, the global $B-L$ symmetry is broken due to the simultaneous presence of the interaction proportional to λ and the scalar term proportional to μ , i.e. only in the presence of a second Higgs doublet the lepton number is violated in two units, as desired. The above Lagrangian defines the interaction vertices in Diagram 1.31. Note that we have three charged scalars and two neutral ones with mass matrices that, as defined in Eq. 1.32, are not diagonal. By rotating the charged fields in the $SU(2)_L$ doublets an amount of $\tan \beta = v_1/v_2$,

$$H_1^\pm = \cos \beta H^\pm + \sin \beta G^\pm \quad \text{and} \quad H_2^\pm = -\sin \beta H^\pm + \cos \beta G^\pm. \quad (1.33)$$

the charged Higgses above, together with the neutral Higgses, are diagonalized. Here, $v_1/\sqrt{2}$ and $v_2/\sqrt{2}$ are the vacuum expectation values of the neutral Higgses H_1^0 and H_2^0 , respectively, satisfying the relation $v_1^2 + v_2^2 = v_0^2$, and the G^\pm are the Goldstone bosons eaten up by the W^\pm bosons. Furthermore, the charged Goldstones G^\pm decouple

from δ^+ after such rotation. However, the charged Higgses $H_{1,2}^\pm$ are not physical yet; there is a remaining mixing with the δ^+ in the Lagrangian. These charged fields are brought to their mass eigenbasis by a rotation with angle θ_+ ,

$$\delta^\pm = \cos\theta_+ h_1^\pm + \sin\theta_+ h_2^\pm \quad \text{and} \quad H^\pm = -\sin\theta_+ h_1^\pm + \cos\theta_+ h_2^\pm, \quad (1.34)$$

where, in the above equation, θ_+ is proportional to the μ parameter. Finally, in the broken phase we can compute the Majorana mass term generated by the loop in Diag. 1.31:

$$M_\nu = \frac{1}{8\pi^2} \left(\lambda M_e (Y_1^\dagger \cos\beta - Y_2^\dagger \sin\beta) + (Y_1^* \cos\beta - Y_2^* \sin\beta) M_e^T \lambda^T \right) \sin 2\theta_+ \text{Log} \left(\frac{m_{h_2^+}^2}{m_{h_1^+}^2} \right), \quad (1.35)$$

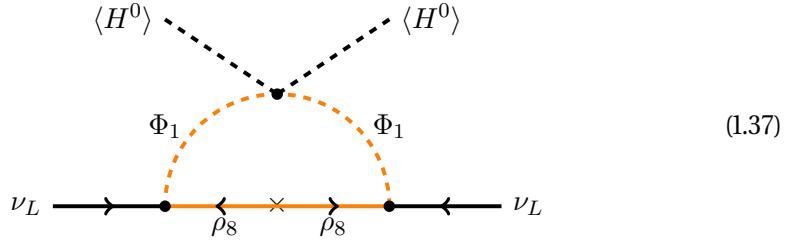
where M_e is the mass matrix for the charged leptons. We note that the neutrino masses are proportional to the μ through θ_+ , as expected since μ quantifies the lepton number violation. Then, when μ is small one can naturally have small neutrino masses and this parameter is protected by the symmetry. Notice that when we assume the Zee-Wolfenstein model [34,35], where only one of the Higgs doublets couples to leptons, the resulting mass matrix has zero diagonal entries. This particular scenario is ruled out by experiment [36,37]. However, in the general Zee model for neutrino masses one has enough freedom to reproduce the values for neutrino mixings and masses. See for example Ref. [38] for a study of the Zee mechanism.

1.2.5 Colored seesaw

The colored seesaw generates neutrino masses via a loop carrying color inside. It was proposed by P. Fileviez Perez and M. Wise in Ref. [39]. Its implementation requires a colored fermion octet, singlet under the EW quantum numbers, $\rho_8 \sim (8, 1, 0)$, together with the Manohar-Wise field $\Phi_1 \sim (8, 2, 1/2)$, which is a second Higgs doublet carrying color. These fields, following the interactions written below,

$$-\mathcal{L}_{\text{colored}} \supset \lambda \ell_L^T C i\sigma_2 \Phi_1 \rho_8 + M_{\rho_8} \text{Tr}\{\rho_8^T C \rho_8\} + \mu \text{Tr}\{\Phi_1^\dagger H\}^2 + \text{h.c.} \quad (1.36)$$

allow for the loop shown in Diagram 1.37, which breaks lepton number in two units.



The neutrino mass matrix is obtained by computing the loop in Diagram 1.37:

$$M_{\nu}^{ij} = \lambda^i \lambda^j \frac{\mu}{16\pi^2} v^2 4M_{\rho_8} \left(\frac{M_{\Phi_1}^2 - M_{\rho_8}^2 + M_{\rho_8}^2 \ln(M_{\rho_8}^2/M_{\Phi_1}^2)}{(M_{\Phi_1}^2 - M_{\rho_8}^2)^2} \right). \quad (1.38)$$

In order to generate more than one massive neutrino, at least two copies of either Φ_1 or ρ_8 are needed to break the degeneracy and raise the rank of the neutrino mass matrix, which otherwise would be 1 since the Yukawa coupling λ in Eq. 1.36 would be just a vector in the flavour space in that case.

We have presented some of the most relevant mechanisms for neutrino mass generation and discussed their main features. In their context, neutrinos are Majorana fermions and $\Delta L = 2$. The tree-level seesaw mechanisms usually require either a heavy NP scale (high-scale seesaw) or a tiny Yukawa coupling as the Dirac case (low-scale seesaw). The 1-loop mechanisms, however, enjoy a natural loop suppression that allows for a less dramatical hierarchy in either the couplings or the mass scales in the particle content of the theory. On the other hand, if lepton number is conserved or broken in a unit different and greater than 2, no Majorana term is allowed by symmetries, and neutrinos are Dirac particles,⁷ as shown below schematically:

$$\Delta L = 2 \quad \leftrightarrow \quad \text{Majorana neutrinos}$$

$$\Delta L > 2 \quad \leftrightarrow \quad \text{Dirac neutrinos}$$

Therefore, there is a strong connection between the conservation or violation of the lepton number and the nature of neutrinos, and consequently, their mass generation.

⁷Notice that we require $\Delta L > 2$ to avoid a Majorana mass term at the radiative level generated by non-renormalizable operators.

2.- Dark matter

Part of the chapter based on the work done in 1901.10483.

There is evidence of dark matter (DM) in the universe, as sustained by the following tokens:

- Galactic rotation curves, which provided the first robust clue for DM. In the stars, which are basically collisionless objects, the motion of matter around them is dictated by their gravitational interactions. At distances extending beyond the galactic center of the star, Newton's law tells us that the dependence of the circular velocity on the distance with respect to the center scales as $v(r) = \sqrt{GM/r}$. However, as observed in the 70s by Vera Rubin et al. [40],¹ and was further studied and confirmed [43–45], the rotation curves flatten out at these distances, implying the existence of some *missing* mass. The later evidences either that the Newton's law is not correct and should be modified, i.e. MODified Newtonian Dynamics (MOND)², or that $M(r) \propto r$ rather than being constant, i.e. there exists a *dark* component concentrated in the halos of massive objects such as stars. See left panel from Fig. 2.4 for an illustration of this phenomenon.
- Measurements provided by the cosmic microwave background (CMB) anisotropies allow to determine the DM component in the universe by measuring the angular scale and heights of the peaks of the power spectrum of temperature fluctuations

¹J. Oort in 1932 [41] and F. Zwicky in 1933 [42] were the pioneers in noticing a discrepancy between the luminous matter and the rotation velocities around the Sun and in the galaxy cluster Coma, respectively, although their observations did not have a significant impact in the scientific community at that time.

²Recently, Ref. [46] pointed out that MOND-like force struggles to simultaneously explain both the rotational velocity and vertical motion of nearby stars in the Milky Way.

in the CMB. The CMB fit could also be explained by MOND, [47, 48] although the quality is notably worse than assuming DM instead. From the anisotropies we can infer that 85% of the matter density conforming the universe is dark, and that, according to *Planck 2018*, the relic abundance of cold DM is $\Omega h^2 = 0.120 \pm 0.001$ [7].

- Weak lensing, clustering, galactic dynamics (e.g. Bullet cluster), are alternative evidences pointing towards the existence of DM.

At the moment, we ignore which kind of matter is filling about a quarter of our universe, although we are aware from the above hints that it should interact gravitationally. This leave us with 70 orders of magnitude in viable mass range for seeking a candidate of DM, as Fig. 2.1 shows. In the first part of this chapter, we will discuss weak interacting

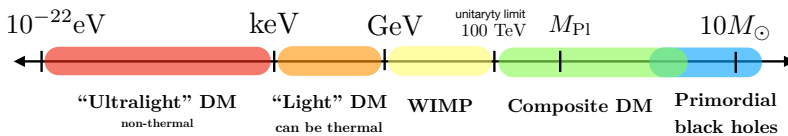


Figure 2.1: Classification of the DM candidates according to their mass scale (not to scale). In this chapter we will focus on WIMPs (GeV - 100 TeV scale) and axions (ultra-light non-thermal bosonic DM). Below $\mathcal{O}(\text{eV})$ only scalar DM is considered. *Image adapted from Ref. [49].*

massive particles (WIMPs) as DM candidates. Cosmological observations suggest that for scalar DM, $M_{\text{scalar}} \gtrsim 10^{-22} \text{ eV}$ [50], while for fermionic DM, $M_{\text{ferm}} \gtrsim 0.7 \text{ keV}$ [51]. Note that, since no new mediator has been noticed so far below the Z boson, the mass of a cold neutral fermion candidate has to be above a few GeVs, which is known as the Lee-Weinberg limit [52], otherwise such candidate would overclose the universe. There is also an upper bound on the WIMP DM mass range, called unitarity bound, which comes from the fact that each partial wave cross-section is limited from above [53].

WIMPs are familiar in the sense that we know how to describe their interactions and we have a well-defined framework to deal with them. Besides, the matter content of the SM may have to be enlarged anyway to account for other of its Achilles' heels, so that WIMPs could be the missing piece of the puzzle, the cornerstone of an improved version

of the SM. In the second part of this chapter, we will propose axions as DM candidates. These particles, apart from being able to generate the observed relic abundance in the universe, also offer an elegant answer to the strong CP problem, which will be introduced along the chapter.

2.1 WIMPs

Let us assume that, apart from the matter we are aware of, our universe is composed of a more extended particle content. These hypothetical unknown particles, if exist, are expected to be (a) electrically neutral, (b) stable or with a lifetime longer than the age of the universe, (c) massive and *cold* in the structure formation era of the universe, (d) weakly interacting, otherwise we would have already noticed their interaction with other SM particles. WIMPs are assumed to be produced in the thermal bath in the early universe. Their evolution until today is expected to travel through different steps: For temperatures above their mass, they are supposed to be in thermal equilibrium with the rest of matter [Fig. 2.2 (a)]. The abundance of such species in equilibrium is maintained by annihilation into ordinary particles and viceversa. However, as the temperature of the universe cools below the DM mass, the WIMP pair creation process is kinematically suppressed so that the equilibrium abundance falls exponentially and the number density of WIMPs departs from that of the thermal bath [Fig. 2.2 (b)]. At some point, the annihilation rate is overcome by the expansion rate of the universe $H(T)$, which also depends on the temperature, i.e. WIMPs do not find partners for their pair annihilation within a Hubble time [Fig. 2.2 (c)]. At lower temperatures, the number density of DM is only diluted by the expansion of the universe, so that the number density per comoving volume is kept constant. In this way, a relic cosmological abundance is generated which could account for the observed cosmological abundance today. It is straightforward to see that the interaction cross-section of WIMPs with the SM content is a key element for determining the current abundance of DM in the universe. Surprisingly, the naive contribution of a WIMP at the TeV scale successfully matches the order of the observed abundance of DM in the universe nowadays. This is known as the *WIMP miracle* and it makes a strong argument for WIMPs as DM candidates. The existence of an interaction rate of the WIMPs with matter also opens a

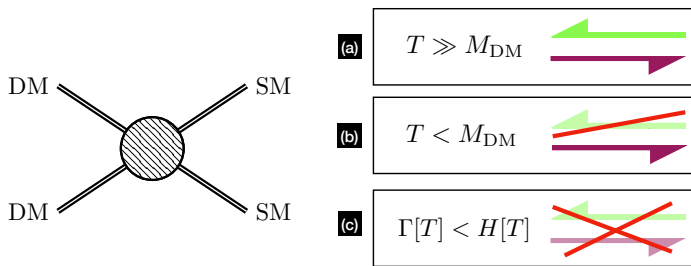


Figure 2.2: Evolution of the WIMP DM as the universe cools down.

wide range of attractive ways towards searching for the WIMPs experimentally. Although their interactions might be very weak, there is a small probability that the WIMP DM trapped in our galaxy collides with nuclei. Direct Detection (DD) experiments search for signals of recoiled nuclei as a consequence of a potential interaction with WIMPs through elastic scattering. WIMP DM could also be detected indirectly in cosmic rays, since WIMPs are expected to be gravitationally accumulated in massive astrophysical objects and the annihilation rate is proportional to the square of the WIMP DM density. Last but not least, WIMPs might leave a track at colliders: even if no visible signatures are produced at the detectors, one can look for missing transverse momentum in the colliding events. See Fig. 2.3 for an illustration of the different pathways to detect WIMP DM according to how it interacts with ordinary matter. Furthermore, it should be

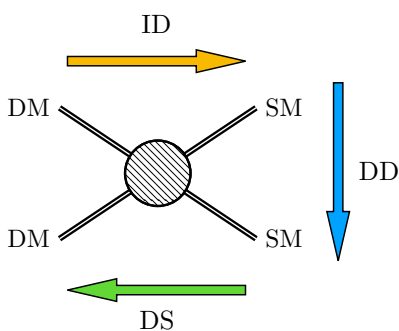


Figure 2.3: WIMP DM searches: direct searches at colliders (DS) -green arrow-, direct detection (DD) by looking at the recoiled nuclei due to elastic scattering -blue arrow-, and indirect detection (ID) by looking for signatures at the cosmic rays -yellow arrow-.

stressed that this kind of particles are naturally predicted in many theories for physics beyond the SM and that the well defined framework of quantum field theory allows us to compute, in a simple way, their relic density. This list of possibilities makes a strong

case for WIMPs, becoming perhaps the most appealing possibility among the long list of DM candidates, and motivates the different experiments to keep looking for their signatures.

2.1.1 Relic abundance

The evolution of the WIMPs abundance in the universe is described by the Boltzmann equation, as it determines the evolution of the phase-space density $f(x, p, t)$ of a given particle species,

$$L[f] = C[f], \quad (2.1)$$

where L is the Liouville operator, which gives the net rate of change in time of the particle space density. In the context of a spatially homogeneous and isotropic universe, it reads as

$$L[f] \equiv \frac{\partial f}{\partial t} - H \frac{|p|^2}{E} \frac{\partial f}{\partial E}, \quad (2.2)$$

where the second term represents the dilution originated by the expansion of the universe. Here, the Hubble parameter $H(T)$ in the radiation-dominated era is given by

$$H(T) \equiv \frac{\dot{a}}{a} = \sqrt{\frac{8\pi G_N \rho(T)}{3}}, \quad (2.3)$$

where G_N is the Newton constant of gravitation, a is the scale factor of the universe, and ρ is the energy density of relativistic species, defined as

$$\rho(T) = \frac{\pi^2}{30} g_{\text{eff}}(T) T^4. \quad (2.4)$$

Here, the effective relativistic d.o.f. g_{eff} (see Sec. 2.1.1.1 for more details) are given by

$$g_{\text{eff}}(T) = \sum_{i=\text{bosons}} g_i \left(\frac{T_i}{T}\right)^4 + \frac{7}{8} \sum_{i=\text{fermions}} g_i \left(\frac{T_i}{T}\right)^4, \quad (2.5)$$

where g_i counts the spin states for all particles and antiparticles, with an additional factor $7/8$ for fermions due to the relative difference in Fermi and Bose statistics, being $g_\gamma = 2$, for instance. We refer the reader to Ref. [54] for a pedagogic introduction to

cosmology in the Early Universe. On the other hand, in the right-hand side (RHS) of Eq. 2.1, we have the collision operator, which parametrizes the number of particles per phase-space volume that are gained or lost per unit time under collision with other particles. In order to describe the evolution of the WIMP DM number density, which in thermal equilibrium is defined as

$$n_{\text{DM}} = \int dn_{\text{DM}} = \int f(E, T) \frac{g d^3p}{(2\pi)^3}, \quad (2.6)$$

we will make use of the Boltzmann equation in Eq. 2.1. The previous equation assumes that the g internal (spin) d.o.f. follow the same distribution $f(E, T)$, which is the known Fermi-Dirac or Bose-Einstein distribution. For temperatures above the DM mass, those distributions can be fairly approximated by

$$f(E, T) = \frac{1}{e^{(E-\mu)/T} + \eta}, \quad (2.7)$$

with $\eta = 0$, i.e. a Maxwell-Boltzmann distribution.³ Here μ refers to the chemical potential of the species. By integrating Eq. 2.1 over the particle momenta and summing over the spin d.o.f., we get

$$\dot{n}_{\text{DM}} + 3H(T) n_{\text{DM}} = -\langle\sigma v\rangle (n_{\text{DM}1} n_{\text{DM}2} - n_{\text{DM}1}^{\text{EQ}} n_{\text{DM}2}^{\text{EQ}}), \quad (2.8)$$

where, for the collision operator, an annihilation of a pair of particles into another pair has been assumed. The first term in brackets accounts for the depletion of WIMPs due to annihilation, while the second term describes the creation of WIMPs from the inverse reaction. Notice that the collision term is characterized by the thermal averaged WIMP DM pair annihilation cross-section, $\langle\sigma v\rangle$, and the square of its number density, which comes from the WIMP pair annihilation and production. Besides the assumptions we already adopted, one should further assume that the DM candidate remains in kinetic equilibrium after decoupling and that the initial chemical potential of the species considered is negligible ($\mu = 0$) to obtain Eq. 2.8. When the particle named under label 2 is the antiparticle of the particle labeled by 1, the density of the species is

³In Eq. 2.7, $\eta = 1$ for Fermi-Dirac and $\eta = -1$ for Bose-Einstein distributions.

$n_{\text{DM}} = n_{\text{DM}1} + n_{\text{DM}2}$. Since we are assuming that the chemical potential is negligible, then $n_{\text{DM}1} = n_{\text{DM}2}$, and therefore

$$\dot{n}_{\text{DM}} + 3H(T) n_{\text{DM}} = -\frac{1}{2} \langle \sigma v \rangle (n_{\text{DM}}^2 - (n_{\text{DM}}^{\text{EQ}})^2). \quad (2.9)$$

The above equation describes the evolution of Dirac particles. However, if particles 1 and 2 are identical, then

$$\dot{n}_{\text{DM}} + 3H(T) n_{\text{DM}} = -\langle \sigma v \rangle (n_{\text{DM}}^2 - (n_{\text{DM}}^{\text{EQ}})^2). \quad (2.10)$$

with an extra factor of 2 in the RHS of the equation, contrary to the naive expectation. Hereinafter, we will consider a Majorana WIMP DM candidate for convenience. Let us write the above expression in a more compact way by introducing the number of particles normalized to the total entropy density of the universe, $Y \equiv n/s$. Since the total entropy per comoving volume is constant,

$$sa^3 = \text{constant} \quad \Rightarrow \quad \dot{s}a^3 + 3sa^2\dot{a} = 0 \quad \Rightarrow \quad \dot{s} = -3Hs, \quad (2.11)$$

i.e. s is also diluted by the expansion of the universe. Therefore, Eq. 2.10 can be rewritten in terms of Y as,

$$\dot{Y} = -s \langle \sigma v \rangle (Y^2 - Y_{\text{EQ}}^2). \quad (2.12)$$

Taking into account the relation between temperature and time, and introducing now the variable $x = M_{\text{DM}}/T$, where T is the photon temperature, we can write Eq. 2.12 as

$$\frac{dY}{dx} = \frac{1}{3H} \frac{ds}{dx} \langle \sigma v \rangle (Y^2 - Y_{\text{EQ}}^2). \quad (2.13)$$

The entropy density, which is given as a function of the effective d.o.f. $h_{\text{eff}}(T)$, is defined as

$$s = h_{\text{eff}}(T) \frac{2\pi^2}{45} T^3, \quad (2.14)$$

where (see Sec. 2.1.1.1 for more details)

$$h_{\text{eff}}(T) = \sum_{i=\text{bosons}} g_i \left(\frac{T_i}{T} \right)^3 + \frac{7}{8} \sum_{i=\text{fermions}} g_i \left(\frac{T_i}{T} \right)^3. \quad (2.15)$$

Computing the derivative of the energy density with respect to variable x ,

$$\begin{aligned} \frac{ds}{dx} &= \frac{ds}{dT} \frac{dT}{dx} = -3h_{\text{eff}}(T) \frac{2\pi^2}{45} T^2 \frac{m}{x^2} \left(1 + \frac{1}{3} \frac{T}{h_{\text{eff}}} \frac{dh_{\text{eff}}}{dT} \right) \\ &= -3 \frac{s}{x} \left(1 + \frac{1}{3} \frac{T}{h_{\text{eff}}} \frac{dh_{\text{eff}}}{dT} \right), \end{aligned} \quad (2.16)$$

the evolution equation for WIMPs in Eq. 2.13 can be simplified as

$$\begin{aligned} \frac{dY}{dx} &= -\frac{s}{Hx} \langle \sigma v \rangle (Y^2 - Y_{\text{EQ}}^2) \left(1 + \frac{1}{3} \frac{T}{h_{\text{eff}}} \frac{dh_{\text{eff}}}{dT} \right) \\ \Rightarrow \frac{x}{Y_{\text{EQ}}} \frac{dY}{dx} &= -n_{\text{DM}}^{\text{EQ}} \langle \sigma v \rangle \left(\frac{Y^2}{Y_{\text{EQ}}^2} - 1 \right) \left(1 + \frac{1}{3} \frac{T}{h_{\text{eff}}} \frac{dh_{\text{eff}}}{dT} \right) / H, \end{aligned} \quad (2.17)$$

where in the last row $Y_{\text{EQ}} \equiv n_{\text{DM}}^{\text{EQ}}/s$. By defining Γ as the probability of annihilation per unit time for a WIMP, i.e. $\Gamma \equiv n_{\text{DM}}^{\text{EQ}} \langle \sigma v \rangle$, the Boltzmann equation reads as

$$\frac{x}{Y_{\text{EQ}}} \frac{dY}{dx} = -\frac{\Gamma}{H} \left[\left(\frac{Y}{Y_{\text{EQ}}} \right)^2 - 1 \right] \left(1 + \frac{1}{3} \frac{T}{h_{\text{eff}}} \frac{dh_{\text{eff}}}{dT} \right). \quad (2.18)$$

As commented earlier, for $x > 1$, the WIMP pair production suffers from kinematical suppression and the decoupling from the thermal bath begins. As a consequence, the ratio $Y/Y_{\text{EQ}} > 1$. The factor Γ/H controls the effectiveness of annihilations. When $H \gg \Gamma$, the annihilation freezes out and Y becomes constant, i.e. it *freezes in*: the species ceases to annihilate, it falls from equilibrium and a cosmological relic abundance $Y(x \geq x_f) = Y_{\text{EQ}}(x_f)$ remains as a consequence. See the right panel from Fig. 2.4 for an illustration. The temperature at which the decoupling occurs, usually called freeze-out temperature T_f , or x_f from an equivalent perspective, is determined

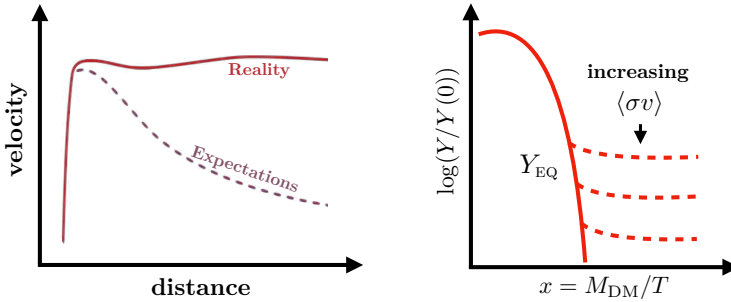


Figure 2.4: In the left panel, the difference between the expected and the observed behaviour of the velocity curve of galaxies is shown. In the right panel, we show naively the typical evolution of the WIMP DM number density in the early universe during the time of freeze-out (*image adapted from Ref. [54]*).

approximately by the condition,

$$H(T_f) = \Gamma(T_f), \quad (2.19)$$

just as we argued before.

2.1.1.1 Effective degrees of freedom and N_{eff}

New light states with non-negligible interactions with the SM could be copiously produced at high temperatures in the early universe. During the radiation era, they would contribute to the total energy density of the universe and therefore modify the predictions for the CMB. Therefore, the observation of the CMB with high angular resolution, as well as other indirect methods, such as the measurement of the abundance of light elements in the universe, can impose relevant bounds on the existence of these light states. To see how those new d.o.f. can be constrained, let us have a closer look to the previously introduced effective relativistic degrees of freedom. In the left panel from Fig. 2.5 we show the calculation done in Ref. [55] for the effective d.o.f. of the energy density, $g_{\text{eff}}(T)$, and the entropy density, $h_{\text{eff}}(T)$ introduced in Eq. 2.5 and 2.15 from the last subsection, respectively. We will assume all species have a common temperature for most of the history of the universe, so that both $h_{\text{eff}}(T)$ and $g_{\text{eff}}(T)$

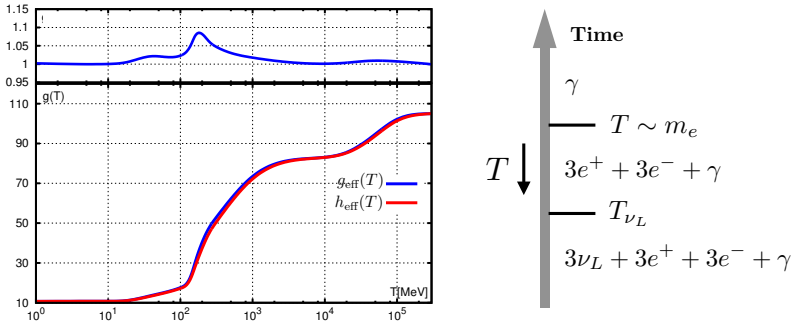


Figure 2.5: On the left panel, the effective d.o.f. of the energy density, $g_{\text{eff}}(T)$, and the entropy density, $h_{\text{eff}}(T)$, extracted from Ref. [55]. On the right panel, relativistic particles contributing to the thermal bath according to the temperature of the universe.

will be approximated by the quantity $g(T)$. Considering also the hypothetical presence of new d.o.f., it would be given by

$$g(T) = g_{\text{SM}}(T) + \sum_{\substack{i=\text{new} \\ \text{bosons}}} g_i + \frac{7}{8} \sum_{\substack{i=\text{new} \\ \text{fermions}}} g_i. \quad (2.20)$$

The validity of such approximation for most of the temperatures is also reflected in the left panel of Fig. 2.5, taken from Ref [55].⁴

Light species in a theory could be, for instance, RH neutrinos ν_R , as we will see later in Chapter 5. In the scenarios in which the RH neutrinos are coupled to a new gauge boson, they could thermalize and contribute to the energy density as follows,

$$\begin{aligned} \rho &= \rho_\gamma + \rho_{\nu_L} + \rho_{\nu_R} \\ &= \rho_\gamma \left(1 + 3 \times \frac{7}{8} \left(\frac{T_{\nu_L}}{T_\gamma} \right)^4 + N_{\nu_R} \times \frac{7}{8} \left(\frac{T_{\nu_R}}{T_\gamma} \right)^4 \right) \\ &= \rho_\gamma \left(1 + \frac{7}{8} \left(\frac{T_{\nu_L}}{T_\gamma} \right)^4 (N_{\text{eff}}^{\text{SM}} + \Delta N_{\text{eff}}) \right), \end{aligned} \quad (2.21)$$

⁴We note that in the calculation of $g_{\text{SM}}(T)$ one needs to take into account the QCD phase transition, i.e. the threshold between quarks and hadrons as d.o.f. This transition can be computed via lattice QCD, as the authors of Ref [55] did.

where ΔN_{eff} encodes any departure from the contribution of the LH neutrinos, and reads as

$$\Delta N_{\text{eff}} = N_{\nu_R} \left(\frac{T_{\nu_R}}{T_{\nu_L}} \right)^4 = N_{\nu_R} \left(\frac{g(T_{\nu_L}^{\text{dec}})}{g(T_{\nu_R}^{\text{dec}})} \right)^{\frac{4}{3}}. \quad (2.22)$$

In the above expression, N_{ν_R} refers to the number of relativistic RH neutrinos. In the last equality we have used the conservation of comoving entropy in the plasma, which also allows us to compute the T_{ν_L}/T_γ temperature by considering the entropy injection to the plasma caused by the electron - positron annihilation. According to the change in number of relativistic d.o.f., shown in the right panel of Fig. 2.5, comparing the entropy per comoving volume before and after the electron - positron annihilation, i.e. below temperatures $T \sim m_e$,

$$S^{\text{before } e^+e^-} = S^{\text{after } e^+e^-} \quad \Rightarrow \quad \frac{T_{\nu_L}}{T_\gamma} = \left(\frac{4}{11} \right)^{\frac{1}{3}}. \quad (2.23)$$

For the active neutrinos we have $T_{\nu_L}^{\text{dec}} \approx 2.3$ MeV [56] and $g(T_{\nu_L}^{\text{dec}}) = 43/4$ (see right panel from Fig. 2.5). For the prediction in the SM we will take the recent result $N_{\text{eff}}^{\text{SM}} = 3.045$ [57].⁵

In order to predict the shift in the effective number of neutrino species, ΔN_{eff} , one needs to estimate the temperature at which the RH neutrinos decouple from the plasma. The latter occurs when the interaction rate drops below the expansion rate of the Universe, according to the decoupling condition from Eq. 2.19,

$$\Gamma(T_{\nu_R}^{\text{dec}}) = H(T_{\nu_R}^{\text{dec}}), \quad (2.24)$$

where the Hubble expansion parameter, defined in Eq. 2.3, in this case particularizes to

$$H(T) = \sqrt{\frac{8\pi G_N \rho(T)}{3}} = \sqrt{\frac{4\pi^3 G_N}{45} \left(g(T) + 3 \times \frac{7}{8} \times g_{\nu_R} \right)} T^2, \quad (2.25)$$

⁵The slightly departure from $N_{\text{eff}}^{\text{SM}} = 3$ can be understood by the fact that, for instance, neutrino decoupling is not fully complete when the electron - positron annihilate, and that there are finite temperature QED corrections that should be considered, among other issues.

where $g_{\nu_R} = 2$ is the number of spin states of the RH neutrinos. On the other hand, we assume that the neutrinos remain in thermal equilibrium with the SM via the following interaction rate:

$$\begin{aligned}\Gamma_{\nu_R}(T) &= n_{\nu_R}(T) \langle \sigma(\bar{\nu}_R \nu_R \rightarrow \bar{f} f) v \rangle \\ &= \frac{g_{\nu_R}^2}{n_{\nu_R}(T)} \int \frac{d^3 \vec{p}}{(2\pi)^3} f_{\nu_R}(p) \int \frac{d^3 \vec{k}}{(2\pi)^3} f_{\nu_R}(k) \sigma_f(s) v,\end{aligned}\quad (2.26)$$

where the Fermi-Dirac distribution has been used to determine the number density of particles in a fermion gas at the thermal equilibrium. According to Eq. 2.7, f_{ν_R} is given by,

$$f_{\nu_R}(k) = (e^{(k-\mu)/T} + 1)^{-1}, \quad (2.27)$$

where the chemical potential μ can be ignored since the particles in the gas are relativistic, $s = 2pk(1 - \cos\theta)$ where p and k are the momenta of the interacting relativistic particles and θ is the angle between them. For a massless RH neutrino,

$$n_{\nu_R}(T) \equiv g_{\nu_R} \int \frac{d^3 \vec{k}}{(2\pi)^3} f_{\nu_R}(k) = \frac{3}{2\pi^2} \xi(3) T^3. \quad (2.28)$$

The measurement of the effective number of neutrino species can be used to constrain theories that have additional light particles that interact with the SM, see for example Refs. [58–68], including RH neutrinos coupled to a Z' and light thermal DM candidates. Axion-like particles that thermalize in the early Universe can also contribute to the value of N_{eff} [69–72]. We will use the above results to constrain theories where the lepton number is a local symmetry in Chapter 5.

2.1.1.2 Freeze out temperature

In order to compute the temperature at which the annihilation of our species *freezes out*, first we need to define what do we mean by that. We will adopt the criterium that a certain species decouples from the plasma when its number density departs from the equilibrium by an order of magnitude relative to the value at thermal equilibrium, i.e.

$$\Delta \equiv Y - Y_{\text{EQ}} \stackrel{!}{=} \delta Y_{\text{EQ}}, \quad (2.29)$$

where $\delta \sim \mathcal{O}(1)$ parameter. Eq. 2.29 describes then the freeze-out condition. Since the later is accomplished, we will say that our species has decoupled from the thermal bath and that, consequently, it is not in thermal equilibrium with the rest of particles anymore. As time passes or, in other words, temperature drops, Δ becomes larger (see right panel from Fig. 2.4). It is convenient to express the WIMP evolution equation 2.13 as a function of the *departure* parameter $\Delta = Y - Y_{\text{EQ}}$, i.e.

$$\frac{d\Delta}{dx} = - \left(\frac{45}{\pi} G \right)^{-1/2} \frac{g_*^{1/2} M_{\text{DM}} \langle \sigma v \rangle \Delta (\Delta + 2Y_{\text{EQ}})}{x^2} - \frac{dY_{\text{EQ}}}{dx}, \quad (2.30)$$

where we have encapsulated all the dependence on the relativistic d.o.f. in the parameter $g_*^{1/2}$, defined as

$$g_*^{1/2}(T) \equiv \frac{h_{\text{eff}}(T)}{g_{\text{eff}}^{1/2}(T)} \left(1 + \frac{1}{3} \frac{T}{h_{\text{eff}}(T)} \frac{dh_{\text{eff}}(T)}{dT} \right). \quad (2.31)$$

By assuming that we are at the freeze out regime ($\Delta = \delta Y_{\text{EQ}}$),

$$\frac{dY_{\text{EQ}}}{dx} = - \left(\frac{45}{\pi} G \right)^{-1/2} \frac{g_*^{1/2} M_{\text{DM}} \langle \sigma v \rangle}{x^2} \frac{\delta(\delta + 2)}{\delta + 1} Y_{\text{EQ}}^2. \quad (2.32)$$

Taking into account that the equilibrium density Y_{EQ} is given by

$$Y_{\text{EQ}} = \frac{45 g x^2 K_2(x)}{4\pi^4 h_{\text{eff}}(T)}, \quad (2.33)$$

where $K_2(x)$ is the second kind of the modified Bessel functions, we obtain the left-hand side of Eq. 2.32 by differentiating the above expression with respect to x ,

$$\frac{dY_{\text{EQ}}}{dx} = \frac{45 g}{4\pi^4} \frac{1}{h_{\text{eff}}(T)} \left(\frac{d}{dx} (x^2 K_2(x)) - \frac{x^2 K_2(x)}{h_{\text{eff}}(T)} \frac{dh_{\text{eff}}(T)}{dT} \frac{dT}{dx} \right). \quad (2.34)$$

Now, from the recursion relations of the modified Bessel functions,

$$\frac{d}{dx} (x^n K_n(x)) = -x^n K_{n-1}(x), \quad (2.35)$$

we have

$$\frac{dY_{\text{EQ}}}{dx} = -Y_{\text{EQ}} \left(\frac{K_1(x)}{K_2(x)} - \frac{1}{x} \frac{d \ln h_{\text{eff}}(T)}{d \ln T} \right), \quad (2.36)$$

and hence, plugging the above result in Eq. 2.32, we get

$$\sqrt{\frac{\pi}{45 G}} g_*^{1/2} M_{\text{DM}} \langle \sigma v \rangle \frac{45 g K_2(x)}{4\pi^4 h_{\text{eff}}(T)} \frac{\delta(\delta + 2)}{\delta + 1} = \left(\frac{K_1(x)}{K_2(x)} - \frac{1}{x} \frac{d \ln h_{\text{eff}}(T)}{d \ln T} \right). \quad (2.37)$$

The above equation allows for the determination of the freeze-out temperature of the species under consideration as a function of the choice made for the decoupling condition in Eq. 2.29, i.e the value of δ . Some approximations can be adopted to further simplify Eq. 2.37: (a) One can neglect the variations in the entropy density, and assuming that $g(T) \approx g_{\text{eff}}(T) \approx h_{\text{eff}}(T)$ as we commented in the subsection 2.1.1.1, we can simplify $g_*^{1/2}(T)$ in Eq. 2.31 as follows,

$$g_*^{1/2}(T) \approx g^{1/2}(T), \quad (2.38)$$

where $g(T)$ is defined in Eq. 2.20. (b) one can consider that we are in the non-relativistic limit $x \gg 1$, where the modified Bessel functions asymptotically behave as

$$K_2(x) \sim K_1(x) \sim \left(\frac{\pi}{2x_f} \right)^{1/2} e^{-x_f}.$$

In the context of the above assumptions, the freeze-out temperature reads as

$$x_f = \ln \left[\left(\frac{45}{32\pi^6} \right)^{1/2} \frac{g M_{\text{Pl}} M_{\text{DM}} \langle \sigma v \rangle}{\sqrt{g_{\text{eff}}(T)} x_f} \frac{\delta(\delta + 2)}{\delta + 1} \right]. \quad (2.39)$$

2.1.1.3 Relic density

The relic density is defined as the ratio of the actual density of particles of a certain species and the critical density ρ_c , which is the density corresponding to a flat universe,

$$\Omega = \frac{\rho}{\rho_c} = \frac{M_{\text{DM}} s(T_0) Y(T_0)}{3H^2/8\pi G}, \quad (2.40)$$

where T_0 refers to the temperature of the universe today, i.e. $T_0 = \theta \times 2.7255$ K, and $H = h \times 100$ km Mpc $^{-1}$ s $^{-1}$. Here h and θ parametrize any possible deviation from the chosen values. Unfortunately, there is no closed-form analytic solution to the Boltzmann equation. One should solve numerically Eq. 2.13 to compute the entropy normalized density $Y(T_0)$ at the current temperature, as codes such as MicrOMEGAs [73] facilitate. In this context,

$$\begin{aligned} \Omega h^2 \theta^{-3} &= \left(\frac{2\pi^2}{45}\right) \left(\frac{8\pi G}{3H^2}\right) h_{\text{eff}}(T_0) \frac{(2.7255)^3 \text{ K}^3}{10^4 (\text{Mpc}^{-1} \text{s}^{-1} \text{km})^2} Y(T_0) \\ &\sim 2.7707 \times 10^8 \frac{M_{\text{DM}}}{\text{GeV}} Y(T_0), \end{aligned} \quad (2.41)$$

where $h_{\text{eff}}(T_0) = 3.9387$ (and $T_0 = 2.7255$ K) [74]. However, there are alternatives to deal with Eq. 2.13: analytical approximations can be obtained by exploiting the freeze-out regime of the DM. We can distinguish between two phases, being the threshold at the temperature at which the species decouples from the thermal bath. In this regime, the density of the particles in the plasma drops out exponentially so that it can be neglected in front of the density of the decoupled particles, which travel in a transparent universe and do not feel interactions anymore. Therefore, neglecting Y_{EQ} from Eq. 2.13 and integrating from x_f to $x(T_0) \sim \infty$,

$$\frac{1}{Y_0} = \frac{1}{Y(x_f)} + \left(\frac{45G}{\pi}\right)^{-\frac{1}{2}} M_{\text{DM}} \int_{x_f}^{\infty} \frac{g_{\text{eff}}^{1/2}}{x^2} \langle \sigma v \rangle dx, \quad (2.42)$$

what allowed us to solve analytically the differential equation. Neglecting $1/Y(T_f)$ in front of $1/Y(T_0)$, we end up with

$$Y(T_0) = \left(\frac{45G}{\pi}\right)^{\frac{1}{2}} \left(M_{\text{DM}} \underbrace{\int_{x_f}^{\infty} \frac{g_{\text{eff}}^{1/2}(M_{\text{DM}}/x)}{x^2} \langle \sigma v \rangle dx}_{J(x_f)} \right)^{-1}. \quad (2.43)$$

The $\langle\sigma v\rangle$ is a function of $x = M_{\text{DM}}/T$ and, according to Ref. [75], it can be computed as

$$\langle\sigma v\rangle = \frac{x}{8M_{\text{DM}}^5 K_2^2(x)} \int_{4M_{\text{DM}}^2}^{\infty} \sigma(s - 4M_{\text{DM}}^2) \sqrt{s} K_1\left(\frac{x\sqrt{s}}{M_{\text{DM}}}\right) ds. \quad (2.44)$$

The above equation then shows that the larger the annihilation cross-section of the DM candidate, the smaller the relic abundance, since naively

$$\Omega h^2 \propto \frac{1}{\langle\sigma v\rangle}. \quad (2.45)$$

2.1.1.4 Fermionic DM Annihilation channels

In the previous section we saw that the annihilation cross-section of the DM into the SM content is a key element in determining the DM contribution to the relic abundance, as Eq. 2.44 brings out. Among the different kind of WIMP DM candidates, i.e. fermionic or bosonic DM, we will focus on the former for convenience.⁶ In this section we will classify all tree-level s-channel annihilation diagrams according to their behaviour.⁷ This classification, aside from providing a guide on how the different type of channels contribute to the relic density, will be also useful when studying DM annihilation into gamma lines.

Let us consider the two possible fermionic DM annihilation channels that are expected to appear in extensions of the SM, with the most general kind of vertex, as illustrated in Fig. 2.6. In there, the double line represents either a fermion or a boson SM current.

- **Scalar fermion current:** $\bar{\chi}\chi J_{\text{SM}}/\Lambda^{(2)}$ [•]

For the interaction mediated by a scalar boson, shown in diagram (a), let us focus on the DM current, whose contribution to the amplitude of the interaction can be written as,

$$\bar{\chi}(p_2)\chi(p_1) \rightarrow \bar{v}_r(p_2)u_s(p_1), \quad (2.46)$$

⁶In Chapters 4 and 5 we will study a fermionic DM candidate in the context of motivated extensions of the SM with gauged lepton or / and baryon number.

⁷We refer the reader to Ref. [76] for a complete classification with both bosonic and fermionic DM.

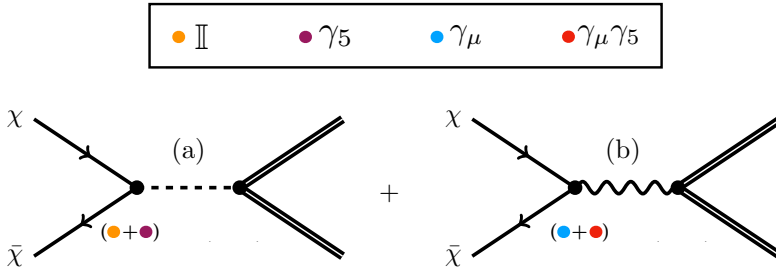


Figure 2.6: Fermionic DM annihilation to a SM current (double line) mediated by a scalar boson (a) and a vector boson (b). The orange, purple, cyan and red represent the scalar, pseudoscalar, vector and axial vertices, respectively.

where u_s (v_r) are four spinors in the chiral representation for a particle (antiparticle) with helicity s (r), and are given by

$$u_s(p) = \begin{pmatrix} \sqrt{p \cdot \sigma} \xi_s \\ \sqrt{p \cdot \bar{\sigma}} \xi_s \end{pmatrix}, \quad \text{and} \quad v_r(p) = \begin{pmatrix} \sqrt{p \cdot \sigma} \eta_r \\ -\sqrt{p \cdot \bar{\sigma}} \eta_r \end{pmatrix}, \quad (2.47)$$

where ξ_s and η_r are two basis of two-component spinors, $\sigma = (\mathbb{I}, \sigma_i)$ and $\bar{\sigma} = (\mathbb{I}, -\sigma_i)$, being σ_i the Pauli matrices. For the square root of a matrix we take the positive root of each eigenvalue. Taking into account that, in the center of mass frame $\vec{p}_1 = -\vec{p}_2$, we have

$$\begin{aligned} \bar{v}_r(p_2) u_s(p_1) &= v_r^\dagger(p_2) \gamma_0 u_s(p_1) \\ &= \left(\eta_r^\dagger \sqrt{p_2 \cdot \sigma} \quad -\eta_r^\dagger \sqrt{p_2 \cdot \bar{\sigma}} \right) \begin{pmatrix} 0 & \mathbb{I} \\ \mathbb{I} & 0 \end{pmatrix} \begin{pmatrix} \sqrt{p_1 \cdot \sigma} \xi_s \\ \sqrt{p_1 \cdot \bar{\sigma}} \xi_s \end{pmatrix} \\ &= \left(\eta_r^\dagger \sqrt{p_1 \cdot \bar{\sigma}} \quad \eta_r^\dagger \sqrt{p_1 \cdot \sigma} \right) \begin{pmatrix} \sqrt{p_1 \cdot \bar{\sigma}} \xi_s \\ \sqrt{p_1 \cdot \sigma} \xi_s \end{pmatrix} \\ &= \eta_r^\dagger (p_1 \cdot \bar{\sigma} - p_1 \cdot \sigma) \xi_s = -2\vec{p}_1 \cdot \vec{\sigma} \eta_r^\dagger \xi_s, \end{aligned} \quad (2.48)$$

where we have used that the gamma matrices in the chiral representation read as

$$\gamma_0 = \begin{pmatrix} 0 & \mathbb{I} \\ \mathbb{I} & 0 \end{pmatrix}, \quad \gamma_i = \begin{pmatrix} 0 & \sigma_i \\ -\sigma_i & 0 \end{pmatrix}, \quad \text{and} \quad \gamma_5 = \begin{pmatrix} -\mathbb{I} & 0 \\ 0 & \mathbb{I} \end{pmatrix}. \quad (2.49)$$

Since $|\vec{p}_1| \propto v_\chi$, in the non-relativistic limit the amplitude for any process where a DM fermion candidate has a scalar coupling to the mediator will be velocity suppressed, regardless on the scalar current to which it annihilates.

• **Pseudoscalar fermion current:** $\bar{\chi}\gamma_5\chi J_{\text{SM}}/\Lambda^{(2)}$ [•]

On the other hand, a pseudo-scalar interaction, also shown in diagram (a), can be expressed as:

$$\begin{aligned}
\bar{v}_r(p_2)\gamma_5 u_s(p_1) &= v_r^\dagger(p_2)\gamma_0\gamma_5 u_s(p_1) \\
&= \left(\eta_r^\dagger\sqrt{p_2\cdot\sigma} \quad -\eta_r^\dagger\sqrt{p_2\cdot\bar{\sigma}} \right) \begin{pmatrix} 0 & \mathbb{I} \\ \mathbb{I} & 0 \end{pmatrix} \begin{pmatrix} -\mathbb{I} & 0 \\ 0 & \mathbb{I} \end{pmatrix} \begin{pmatrix} \sqrt{p_1\cdot\sigma}\xi_s \\ \sqrt{p_1\cdot\bar{\sigma}}\xi_s \end{pmatrix} \\
&= \eta_r^\dagger \begin{pmatrix} \sqrt{p_1\cdot\bar{\sigma}} & -\sqrt{p_1\cdot\sigma} \\ -\sqrt{p_1\cdot\sigma} & \sqrt{p_1\cdot\bar{\sigma}} \end{pmatrix} \begin{pmatrix} \sqrt{p_1\cdot\bar{\sigma}}\xi_s \\ -\sqrt{p_1\cdot\sigma}\xi_s \end{pmatrix} \\
&= \eta_r^\dagger(p_1\cdot\bar{\sigma} + p_1\cdot\sigma)\xi_s = 2E_\chi\eta_r^\dagger\xi_s \sim 2M_{\text{DM}}\eta_r^\dagger\xi_s, \tag{2.50}
\end{aligned}$$

where in the last term the non-relativistic limit has been assumed.

Focusing now on the interaction mediated by a vector boson, the interactions can be vector or/and axial, as diagram (b) shows.

• **Vector fermion current:** $\bar{\chi}\gamma_\mu\chi$ [•]

The vector DM current is given by $\bar{v}_r(\vec{p}_2)\gamma_\mu u_s(\vec{p}_1)$, and we will split the current according to the Lorentz indices. For $\mu = 0$,

$$\bar{v}_r(\vec{p}_2)\gamma_0 u_s(\vec{p}_1) = v_r^\dagger(\vec{p}_2) \underbrace{\gamma_0^2}_{\mathbb{I}} u_s(\vec{p}_1) = v_r^\dagger(-\vec{p}_1)u_s(\vec{p}_1) = 0, \tag{2.51}$$

which is a general result for a vector current, regardless of the speed of the DM.

Now, taking into account $\mu = i$, where $i = 1 \dots 3$, the fermion current gives

$$\begin{aligned}
\bar{v}_r(p_2)\gamma_i u_s(p_1) &= v_r^\dagger(p_2)\gamma_0\gamma_i u_s(p_1) \\
&= \left(\eta_r^\dagger\sqrt{p_2\cdot\sigma} \quad -\eta_r^\dagger\sqrt{p_2\cdot\bar{\sigma}} \right) \begin{pmatrix} 0 & \mathbb{I} \\ \mathbb{I} & 0 \end{pmatrix} \begin{pmatrix} 0 & \sigma_i \\ -\sigma_i & 0 \end{pmatrix} \begin{pmatrix} \sqrt{p_1\cdot\sigma}\xi_s \\ \sqrt{p_1\cdot\bar{\sigma}}\xi_s \end{pmatrix} \\
&= \left(\sqrt{p_1\cdot\bar{\sigma}}\sigma_i\sqrt{p_1\cdot\sigma} + \sqrt{p_1\cdot\sigma}\sigma_i\sqrt{p_1\cdot\bar{\sigma}} \right) \eta_r^\dagger\xi_s \tag{2.52}
\end{aligned}$$

In the non-relativistic limit, $E\sqrt{1 \pm \frac{\vec{p} \cdot \vec{\sigma}}{E}} \sigma_i \sqrt{1 \mp \frac{\vec{p} \cdot \vec{\sigma}}{E}} \sim E\sigma_i + \mathcal{O}(v_\chi^2)$, and hence,

$$\bar{v}_r(\vec{p}_2) \gamma_i u(\vec{p}_1) \sim 2M_{\text{DM}} \eta_r^\dagger \sigma_i \xi_s + \mathcal{O}(v_\chi^2). \quad (2.53)$$

• **Axial fermion current:** $\bar{\chi} \gamma_\mu \gamma_5 \chi$ [•]

For the axial current we have,

$$\begin{aligned} \bar{v}_r(\vec{p}_2) \gamma_\mu \gamma_5 u_s(p_1) &= v_r^\dagger(p_2) \gamma_0^2 \gamma_5 u_s(p_1) \\ &= -(\sqrt{p_1 \cdot \vec{\sigma}} \sqrt{p_1 \cdot \vec{\sigma}} + \sqrt{p_1 \cdot \vec{\sigma}} \sqrt{p_1 \cdot \vec{\sigma}}) \eta_r^\dagger \xi_s \\ &= -2M_{\text{DM}} \eta_r^\dagger \xi_s + \mathcal{O}(v_\chi^2), \end{aligned} \quad (2.54)$$

where we have proceeded as in the previous scenarios and applied in the last row the non-relativistic limit of the DM field. For the axial interaction we do have a contribution in the longitudinal mode and it is not velocity suppressed. However, for the transverse modes $\mu = 1 \dots 3$,

$$\begin{aligned} v_r^\dagger(p_2) \gamma_0 \gamma_i \gamma_5 u_s(p_1) &= \left(\sqrt{p_1 \cdot \vec{\sigma}} \sigma_i \sqrt{p_1 \cdot \vec{\sigma}} - \sqrt{p_1 \cdot \vec{\sigma}} \sigma_i \sqrt{p_1 \cdot \vec{\sigma}} \right) \eta_r^\dagger \xi_s \\ &\sim 0 + \mathcal{O}(v_\chi^2). \end{aligned} \quad (2.55)$$

It is remarkable the opposite behaviour of the vector and axial currents for non-relativistic fields.

Unlike the scalar interactions (diagram a) are independent of the annexed SM current, in the context of vector interactions the annexed current does matter since the gauge boson connects the polarizations from both currents. If the annexed current is fermionic and vectorial, the axial annihilation cross-section is suppressed by the velocity of the DM. No suppression is expected from the rest of combinations. In summary,

\forall external current $\propto v_\chi^2$, $\propto v_\chi^2$, (2.56)

where the vertices follow the code color introduced in Fig. 2.6, and the double line indicates any SM current able to couple to a gauge boson. In Table 2.1 we collect the results obtained so far.

DM / SM bilinear	• $\phi^\dagger \mathbb{I} \phi [\bar{f} \mathbb{I} f]$	• $\phi^\dagger \gamma_5 \phi [\bar{f} \gamma_5 f]$	• $\bar{f} \gamma^\mu f$	• $\bar{f} \gamma^\mu \gamma_5 f$
• $\bar{\chi} \mathbb{I} \chi$	$\langle \sigma v \rangle \sim v_\chi^2 [v_\chi^2]$	$\langle \sigma v \rangle \sim v_\chi^2 [v_\chi^2]$	×	×
• $\bar{\chi} \gamma_5 \chi$	$\langle \sigma v \rangle \sim 1[1]$	$\langle \sigma v \rangle \sim 1[1]$	×	×
• $\bar{\chi} \gamma_\mu \chi$	$\langle \sigma v \rangle \sim 1[\times]$	$\langle \sigma v \rangle \sim 1[\times]$	$\langle \sigma v \rangle \sim 1$	$\langle \sigma v \rangle \sim 1$
• $\bar{\chi} \gamma_\mu \gamma_5 \chi$	$\langle \sigma v \rangle \sim 1[\times]$	$\langle \sigma v \rangle \sim 1[\times]$	$\langle \sigma v \rangle \sim v_\chi^2$	$\langle \sigma v \rangle \sim 1$

Table 2.1: Classification of the annihilation of fermionic DM (χ) into a SM current according to their nature: whether they are or not velocity suppressed. In the first column, the DM bilinears are listed, while the SM bilinears are located in the first row. The symbol \times indicates that the interaction cannot occur.

2.1.2 Detecting WIMPs

The unexpected and striking connection between the observed relic abundance in the universe (cosmology) and the hypothetical abundance that would be produced by a WIMP at the EW scale (particle physics) has encouraged the scientific community to search thoroughly for these candidates. In the last decade, enormous experimental effort has been put on building the devices and working on the techniques needed to catch any possible track of WIMPs. In this section, the main approaches are briefly reviewed.

2.1.2.1 Direct detection

If WIMPs exist, they could be filling the halo of the Milky Way. Consequently, there should be numerous WIMPs crossing the surface of the Earth that could interact to ordinary matter and a non-zero elastic scattering with nuclei would be reasonably expected. Although the rate of the interaction can be very weak, WIMPs could be directly detected by looking at the nuclear recoil generated after the elastic scattering [77].

The rate of events will be given naively by $R \propto n_{\text{DM}} \sigma \langle v \rangle / M_N$, where n_{DM} is the number density of the DM, i.e. $n_{\text{DM}} = \rho_0 / M_{\text{DM}}$, being ρ_0 the local density of WIMPs (near the Earth), $\langle v \rangle$ the average velocity of the WIMP relative to the target, and M_N the nucleus mass.

In reality, we do not know how WIMPs are distributed in our galaxy. However, we can assume that they follow an isotropic isothermal sphere with a given three-dimensional velocity distribution $f(v)$ normalized to the unity. Hence, more accurately,

$$\frac{dR}{dE} = \frac{\rho_0}{M_{\text{DM}} M_N} \int_{v_{\text{min}}}^{v_{\text{max}}} v f(v) \frac{d\sigma(v)}{dE} dv. \quad (2.57)$$

One must integrate over all possible velocities and possible deposited energies to obtain the total rate, i.e.

$$R = \int_{E_T}^{\infty} \frac{dR}{dE} dE. \quad (2.58)$$

Note that, although theoretically the velocity could run up to infinity, in reality it is bounded from above since the DM will escape from the gravitational potential of the galaxy at a certain speed. Regarding the energy range, one should take into account the energy threshold E_T in the detector resolution and the maximum energy that can be deposited, which corresponds to $\theta^* = \pi$ in the following expression

$$E = \frac{|\vec{q}|^2}{2M_N} = \frac{\mu^2 v^2}{M_N} (1 - \cos \theta^*), \quad (2.59)$$

that quantifies the energy transferred to the nucleus, being \vec{q} the momentum transfer, θ^* the scattering angle, and $\mu = M_{\text{DM}} M_N / (M_{\text{DM}} + M_N)$ the reduced mass for the DM-nucleus system. We note that the lower the mass of the DM, the smaller the energy deposited. Detectors cannot be sensitive to an arbitrarily low mass for the WIMP since their resolution is limited. On the other hand, they become less sensitive when higher DM masses are considered because, although the energy deposited in the nuclei is bigger, WIMPs are more diluted (the number density drops linearly with the DM mass) so that the scattering becomes less probable. See Fig. 2.7 for a naive illustration of the detector limits.

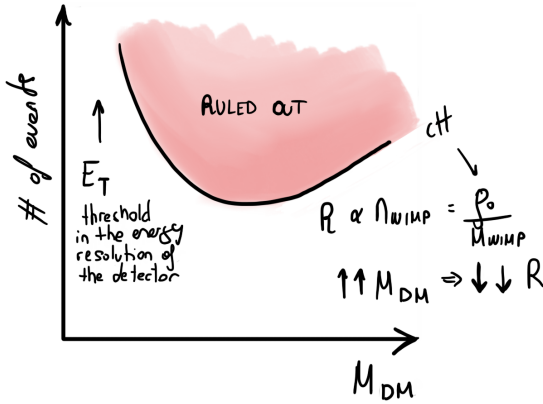


Figure 2.7: Sketch about the sensitivity of DD experiments (logarithmic scale). The red shaded area represents the parameter space that the DD experiments can access. The lower mass regime of the DM candidate suffers from the energy threshold E_T of the detector, below which they are insensitive to the recoil generated by WIMPs-nuclei scattering. On the other hand, the higher the mass of the DM, the smaller the ratio of events since the number of events drops proportionally to the DM mass.

Generally, DD experiments assume that the DM is distributed in an isotropic and isothermal sphere with a Maxwellian velocity distribution. Most of experimental collaborations automatically provide the bounds on the number of events translated to the DM-nuclei cross-section. In that process, they assume that the cross-section is dominated by a velocity independent term. The later will be discussed in more detail in Chapter 4.

Let us focus now on the heart of the elastic scattering: the corresponding cross-section. It will be determined by the concrete theory beyond the SM containing

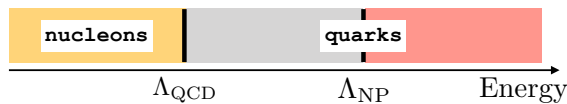


Figure 2.8: Hierarchies of energy scales entering in the EFT approach to DM-nucleon scattering.

the WIMP. In a very generic way, we can consider all possible interactions between the DM candidate and the quarks composing the nucleon from an EFT perspective. There

are two steps that we should mind in the EFT approach, shown in the equation below,

$$\mathcal{L}_{\text{DD}}^q \rightarrow \mathcal{L}_{\text{DD}}^n \rightarrow \mathcal{L}_{\text{DD}}^N, \quad (2.60)$$

according to the energy scales shown in Fig. 2.8. First, we should take into account the microscopic interactions at the quark level ($\mathcal{L}_{\text{DD}}^q$), i.e. DM interacting with quarks. Then, we should consider the interactions at the nucleon level ($\mathcal{L}_{\text{DD}}^n$), by connecting partons and nucleons via the corresponding matrix elements. Finally, the sum of the nucleon-level interactions should be considered in order to obtain the final nucleus-level scattering ($\mathcal{L}_{\text{DD}}^N$). The spin and scalar components of the nucleons must be added coherently. In the last step, the scattering cross-sections can be differentiated in two groups:

- **Spin dependent:** those that involve a γ_5 in the quark current will probe the up, down, and strange contributions to the spin of the nucleus. They add to the nucleus-level operator like

$$\mathcal{O}_N^{\text{SD}} = \left(\frac{\langle S_p \rangle}{J_N} \mathcal{O}_p + \frac{\langle S_n \rangle}{J_N} \mathcal{O}_n \right) \langle J_N \rangle, \quad (2.61)$$

where J_N is the spin of the nucleus, and S_p and S_n are the total spin operators for protons and neutrons in the target nucleus we are considering. In brackets $\langle \dots \rangle$ the corresponding expectation value.

- **Spin independent:** those that involve scalar and vector quark currents in their interactions will not be sensitive to the spin of the nucleus, but to its mass or charge. The nucleon-level interactions add coherently to the nucleus-level operator as follows, where A and Z are the mass and atomic numbers of the nucleon,

$$\mathcal{O}_N^{\text{SI}} = Z\mathcal{O}_p + (A - Z)\mathcal{O}_n. \quad (2.62)$$

The WIMP-nucleus scattering cross-section can be therefore parametrized as

$$\frac{d\sigma}{dE} = \frac{M_N}{2v^2\mu^2} (\sigma_{\text{SI}}(v)F_{\text{SI}}^2(E) + \sigma_{\text{SD}}(v)F_{\text{SD}}^2(E)), \quad (2.63)$$

where $\sigma_{\text{SI}/\text{SD}}$ account for the contribution from the spin independent and spin dependent parts, respectively, and the form factors $F_{\text{SI}}(q)$ and $F_{\text{SD}}(q)$ account for the loss of coherence that the de Broglie wavelength of WIMPs suffers at higher q . In Table 2.2 we show, in a similar manner as we did in Table 2.1 for the annihilation possibilities of the DM, how the different interactions classify under the elastic scattering with nuclei according to their behaviour. We refer the reader to Ref. [76] for a detailed derivation of the results shown in Table 2.2, which can be obtained analogously as we proceeded in the last subsection.

DM / SM bilinear	• $\bar{f} \mathbb{I} f$	• $\bar{f} \gamma_5 f$	• $\bar{f} \gamma^\mu f$	• $\bar{f} \gamma^\mu \gamma_5 f$
• $\bar{\chi} \mathbb{I} \chi$	$\sigma_{\text{SI}} \sim 1$	$\sigma_{\text{SD}} \sim q^2$	×	×
• $\bar{\chi} \gamma_5 \chi$	$\sigma_{\text{SI}} \sim q^2$	$\sigma_{\text{SD}} \sim q^4$	×	×
• $\bar{\chi} \gamma_\mu \chi$	×	×	$\sigma_{\text{SI}} \sim 1$	$\sigma_{\text{SD}} \sim v^2$
• $\bar{\chi} \gamma_\mu \gamma_5 \chi$	×	×	$\sigma_{\text{SI}} \sim v^2$	$\sigma_{\text{SD}} \sim 1$

Table 2.2: Classification of the scattering of fermionic DM with a SM fermion current according to their nature. In the first column, the DM bilinears are listed, while the SM bilinears are located in the first row. *Table adapted from Ref. [76].*

Detectors should count for a very low rate of events: they must be capable to discriminate the background in an extremely precise way, they should be either very large or take very long counting times in order to increase their sensitivity; last but not least, they are expected to enjoy a sophisticated shielding to protect the interesting signals from external noise caused by near events (that is why they are mostly based deep underground) and also its potentially own radiation. Examples of DD experiments are, for instance, LUX [78], DarkSide-50 [79] or PandaX-II [80], and others under construction, for instance, XENON-nT [81]. Nowadays, XENON-IT [82] leads with the strongest available constraints, as Fig. 2.9 shows. In there, current bounds on spin-independent DD cross-section are recopied.⁸ Note that they are already close to the so-called neutrino floor, i.e. the irreducible background from

⁸The spin-dependent bounds are, in general, weaker, because such cross-sections depend on the spin of the nucleon, which are quantities that are still not well determined either theoretically or experimentally, so that there are additional uncertainties involved [85].

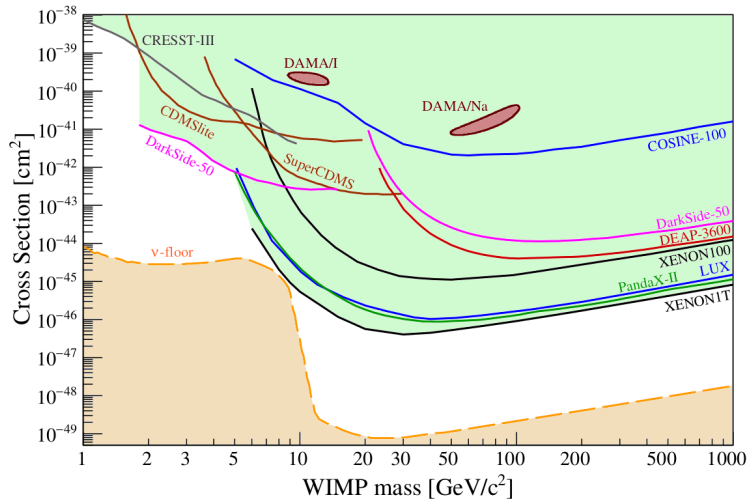


Figure 2.9: Current experimental parameter space for spin-independent WIMP-nucleon cross-sections. Not all published results are shown. The space above the lines is excluded at a 90% confidence level. The dashed line limiting the parameter space from below represents the *neutrino floor* [83] from the irreducible background from coherent neutrino-nucleus scattering. *Image extracted from the recent Ref. [84].*

coherent neutrino-nucleus scattering, below which the DD experiments become neutrino detectors [83]. We close this subsection by referring the reader to the nice review in Ref. [85] about direct detection of DM.

2.1.2.2 Gamma lines

Unfortunately, the current DM direct detection bounds tell us that the experimental sensitivity is close to reach the so-called neutrino floor, making more difficult to detect DM in DD experiments. However, there are indirect ways through which DM could be detected: we can look for its annihilation products. For instance, we can hope to discover gamma lines, very striking and almost background free signals generated by

the DM annihilation into gamma rays, i.e.

$$\text{DM DM} \rightarrow \gamma\gamma, \gamma Z, \gamma h, \quad (2.64)$$

In this section we discuss the predictions for gamma lines from DM annihilation in models where the SM is extended by a new abelian force,

$$SU(3)_c \otimes SU(2)_L \otimes U(1)_Y \otimes U(1)_X.$$

We will assume that the SM fermions are charged under the new force, and that they interact vectorially with the new gauge mediator Z' . The force will be considered abelian for convenience, which could be, for instance, local baryon (B) or lepton (L) number, or linear combinations of them such as $B-L$.

The fact that no signal has been seen in current DM experiments may be reinforcing the idea that DM does not couple directly to the SM fields, i.e. that it lives in a Hidden sector. The definition of Hidden sector encompasses a new set of fields, including a DM candidate, whose connection to the SM sector is defined mainly by a new gauge force:

The observation of gamma lines depends mainly on two factors:

- The annihilation cross-section must be large (and of course non-zero) in order to see a signal at gamma ray telescopes.
- The continuum spectrum generated by other physical processes must be suppressed in order for the gamma line to be distinguishable.

The first condition implies that the theory must be able to predict gamma-lines which are not further suppressed than their already intrinsic 1-loop suppression, while the second condition tells us that the background processes must be weaker than the gamma line, otherwise the signal would be masked by the continuum spectrum of emitted photons as the naive illustration in Fig. 2.10 shows.

According to Diag. 2.64, the gamma line production is a quantum mechanical process where electrically-charged fields are expected to participate. In the center of

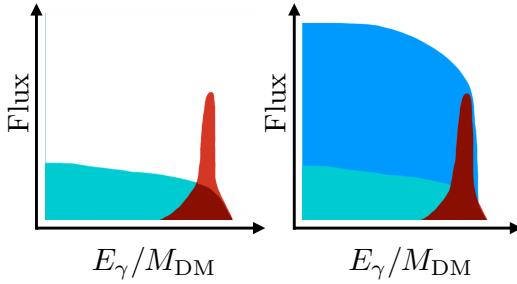


Figure 2.10: In order to detect gamma lines, since they are quantum mechanical processes, we need large cross-sections for the $DM DM \rightarrow \gamma\gamma, \gamma Z, \gamma h$ (left panel), and suppressed FSR processes, otherwise, as the right panel shows, the gamma line will not be distinguished from the continuum. *Figure extracted from Ref. [86].*

mass frame, kinematics tells us that the energy of the gamma lines is given by

$$E_i^\gamma = M_{DM} \left(1 - \frac{M_i^2}{4M_{DM}^2} \right), \quad \text{where } M_i = 0, M_Z, M_h, \quad (2.65)$$

for the $DM DM \rightarrow \gamma\gamma, \gamma Z, \gamma h$ annihilation channels, respectively. Therefore, the observation of a gamma line would allow the determination of the DM mass. However, in a given model, there might be final state radiation (FSR) processes such as

$$DM DM \rightarrow SM SM \gamma, \quad (2.66)$$

where a photon is emitted from one of the SM fermions coming from the DM annihilation. These processes may spoil the visibility of the gamma lines. The maximal energy of the photon in the FSR processes is given by

$$E_{\max}^\gamma = M_{DM} \left(1 - \frac{M_{SM}^2}{M_{DM}^2} \right), \quad (2.67)$$

where M_{SM} is the mass of a SM electrically-charged field. We note that those are, in general, tree level processes and, therefore, they are expected to rise above the gamma lines since the later suffer from loop suppression. Thus, when $M_{DM} \gg M_{SM}$ the visibility of the gamma line is spoiled if the FSR processes are not suppressed because

$E_{\max}^\gamma \approx E_i^\gamma$. Therefore, the relevance of the FSR with respect to the gamma lines will be crucial in determining whether those can be observed or not.

Let us focus in more detail on the spectrum from the gamma lines and the continuum generated by FSR processes. The flux for the gamma lines is given by

$$\frac{d\Phi_\gamma}{dE_\gamma} = \frac{n_\gamma}{8\pi M_{\text{DM}}^2} \frac{d\langle\sigma v_{\text{rel}}\rangle}{dE_\gamma} J_{\text{ann}} \approx \frac{n_\gamma \langle\sigma v_{\text{rel}}\rangle}{8\pi M_{\text{DM}}^2} \frac{dN}{dE_\gamma} J_{\text{ann}}, \quad (2.68)$$

where, in the last equality, the narrow width approximation has been applied. Here, n_γ is a multiplicity factor, $n_\gamma = 2$ ($= 1$) for the $\gamma\gamma$ (γZ) annihilation channel. In order to compute the total flux, we include the cross-sections of both gamma lines and FSR processes. The J -factor, J_{ann} , encodes all astrophysical assumptions made regarding the DM distribution. For the gamma line studies we will present in Chapter 4, we will use the value $J_{\text{ann}} = 13.9 \times 10^{22} \text{ GeV}^2 \text{cm}^{-5}$ [87, 88] for the numerical analysis, which is the J -factor used by Fermi-LAT for the R3 region-of-interest. The spectrum function is given by

$$\frac{dN}{dE_\gamma} = \int_0^\infty dE_0 W_{\text{final}} G(E_\gamma, \xi/\omega, E_0), \quad (2.69)$$

where W_{final} is $W_{\gamma\gamma} = \delta(E_0 - M_{\text{DM}})$ for the annihilation into two photons and

$$W_{\gamma Z} = \frac{1}{\pi} \frac{4M_{\text{DM}}M_Z\Gamma_Z}{(4M_{\text{DM}}^2 - 4M_{\text{DM}}E_0 - M_Z^2)^2 + \Gamma_Z^2 M_Z^2}, \quad (2.70)$$

for the $Z\gamma$ line. Here, we use a Gaussian function to model the detector resolution, $G(E_\gamma, \xi/\omega, E_0)$, which reads as

$$G(E_\gamma, \xi/\omega, E_0) = \frac{1}{\sqrt{2\pi}E_0(\xi/\omega)} e^{-\frac{(E_\gamma - E_0)^2}{2E_0^2(\xi/\omega)^2}}, \quad (2.71)$$

where ξ is the energy resolution and $\omega = 2\sqrt{2\log 2} \approx 2.35$ determines the full width at half maximum, with the standard deviation given by $\sigma_0 = E_0\xi/\omega$.

On the other hand, the DM DM $\rightarrow \gamma \bar{f} f$ processes are described by a three-body phase space, so that the cross-section is given by

$$\frac{d^2 \langle \sigma v_{\text{rel}} \rangle}{dE_\gamma dE_f} = \frac{1}{32\pi^3 s} |\mathcal{M}|_{\text{FSR}}^2 \theta(1 - \cos^2 \theta_{f\gamma}). \quad (2.72)$$

To compute the continuum spectrum of the FSR processes, given by the first equality in Eq. 2.68, one needs to integrate the differential cross-section with respect to the final energy of the photon E_f , whose kinematic range is determined by the condition $\cos^2 \theta_{f\gamma} \leq 1$, i.e.

$$E_f^\pm = M_{\text{DM}} - \frac{E_\gamma}{2} \pm \frac{E_\gamma}{2} \sqrt{1 + \frac{M_f^2}{(E_\gamma - M_{\text{DM}})M_{\text{DM}}}}. \quad (2.73)$$

Whether they can be distinguished from the continuum spectrum will depend on the features of the model, as well as the nature of the DM candidate. Let us first study the different possibilities for the nature of the DM candidate regarding its possibility to predict visible gamma lines:

- **Scalar dark matter.**

In the scenario where the DM is spinless, ϕ , the Higgs portal term $\phi^\dagger \phi H^\dagger H$, where H represents the SM Higgs doublet, is an unavoidable connection to the SM content. Therefore, the annihilation into two SM fermions mediated by a scalar is, in general, not suppressed, nor are the FSR processes in this context. Hence,

$$\left(\begin{array}{c} \text{GL} \\ \text{DM} \text{---} \bullet \text{---} \bullet \text{---} \text{DM} \\ \text{DM} \text{---} \bullet \text{---} \bullet \text{---} \text{DM} \\ \text{---} \gamma \\ \text{---} \gamma, Z, h \end{array} \right) \propto \frac{1}{(16\pi)^2} \left(\begin{array}{c} \text{FSR} \\ \text{DM} \text{---} \bullet \text{---} \bullet \text{---} \text{DM} \\ \text{DM} \text{---} \bullet \text{---} \bullet \text{---} \text{DM} \\ \text{---} f \\ \text{---} \gamma \\ \text{---} \bar{f} \end{array} \right),$$

Since the FSR processes are tree level amplitudes whereas the gamma lines occur at the quantum level, the visibility of the gamma line is, in general, spoiled. In the

case the mediator between the DM and the SM sector is a gauge force, the DM annihilation into a couple of SM fermions is also velocity suppressed because the coupling of the gauge boson with the DM is proportional to the DM momentum. Consequently, the annihilation into gamma lines is also velocity suppressed.

Hence, in the simplest DM scenario with scalar DM, it is impossible to distinguish the gamma lines from the continuum spectrum. For the study of gamma lines in scalar DM models see Refs. [89–92].

- **Fermionic dark matter.** In the context of a fermionic DM candidate, in general, the Higgses present in the theory can mediate these processes, but these contributions are not relevant for the study of gamma-lines because they are both velocity and loop suppressed and, therefore, neglectable (see discussion in Sec. 2.1.1.4). In the following, we will only consider the cases mediated by the new vector boson. Focusing on the annihilation mediated by a gauge boson, let us distinguish between the Dirac and the Majorana nature of the DM candidate.

For a **Dirac DM** candidate (Ψ), the FSR processes, $\bar{\Psi}\Psi \rightarrow \bar{f}f\gamma$, are not suppressed and, generally, the gamma lines generated by the DM annihilation cannot be distinguished from the continuum spectrum. See Refs. [93,94] for the predictions of gamma lines in models for Dirac DM.

For a **Majorana DM** candidate, however, one has the peculiarity that it couples to the gauge boson solely in an axial way. In this case, the squared amplitude of the FSR process reads as

$$|\mathcal{M}|_{\text{FSR}}^2 = \frac{M_f^2}{M_{Z'}^2} A + v^2 B + \mathcal{O}(v^4), \quad (2.74)$$

which tells us that the contribution from the FSR processes is suppressed either by the mass of the Z' or the velocity of the DM candidate. The later is a consequence of the axial-vector suppression of the interaction in the non-relativistic limit of the DM (see Subsec. 2.1.1.4). See Appendix B for the explicit form of the coefficients A and B in the above equation.

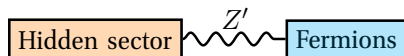
If the theory allows, on the other hand, for non-suppressed amplitudes relevant for the gamma lines we could hope to observe them since, in this case, they could be distinguished from the continuum spectrum. For the study of the gamma lines in models with a Majorana DM candidate see Refs. [95–99].

See also Refs. [100,101] for the study of gamma lines in other DM models.

Taking into account the two conditions that should be satisfied in order to observe gamma lines, let us figure out which are the ingredients that a certain theory should enjoy in order to predict visible gamma lines. For that we will assume a general Lagrangian with the relevant interactions for our discussion,

$$\mathcal{L} \supset g' \bar{\chi} \gamma^\mu \gamma_5 \chi Z'_\mu + g' \bar{f} (n_V^f \gamma^\mu + n_A^f \gamma^\mu \gamma_5) f Z'_\mu + \bar{f} \gamma^\mu (g_V^f + g_A^f \gamma_5) f Z_\mu, \quad (2.75)$$

where g' is the gauge coupling associated to the new force, and f are the electrically-charged fermions participating in the loop from Diag. 2.64. The couplings $n_{V/A}^f$ refer to the interactions between the new mediator and any electrically-charged fermion, f , of the theory; whereas the couplings $g_{V/A}^f$ parametrize how these fermions interact with the SM Z boson. The subindex V and A refer to the vector and axial interactions of the gauge boson with fermions, respectively. Note that we are assuming a theory where the connection between the DM candidate and the rest of the fermions occurs through the mediator of the new force Z' , as the following diagram illustrates:



(2.76)

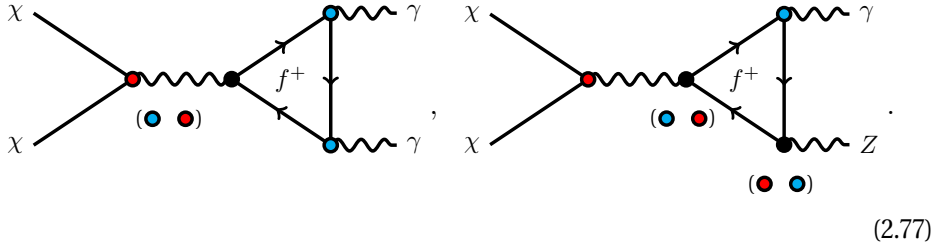
Regarding the possible amplitudes relevant for the gamma lines:⁹

- **DM DM** $\rightarrow \gamma\gamma$

Quantum Electrodynamics (QED) is a vector force: electrically-charged fields couple vectorially as indicated in the left diagram in Diag. 2.77. Since charge conjugation is a symmetry of QED, amplitudes with an odd number of vector currents will be zero. Therefore, we will only expect a non-zero gamma line if

⁹The complete analytical expressions for the cross-sections are relegated to Appendix B.

there are electrically-charged fields that couples axially to the new gauge mediator in the matter sector.



- **DM DM $\rightarrow \gamma Z$**

In this case, the Z boson admits both vector and axial couplings to charged fermions. Charge conjugation tells us that the only combinations allowed are the ones shown in the right diagram from Diag. 2.77, where an even number of vector currents participate, i.e. combinations of $n_V^f g_A^f$ or $n_A^f g_V^f$. Looking in more detail at the analytic expression for the cross-section,

$$\sigma(\chi\chi \rightarrow \gamma Z) \propto \left| \sum_f N_c^f Q_f (n_V^f g_A^f + n_A^f g_V^f (2M_f^2 C_0^Z + 1)) \right|^2, \quad (2.78)$$

we find that the contribution of the vector coupling does not depend on the fermion mass, while the axial contribution does. Notice that the amplitude containing the n_V^f term is proportional to

$$\mathcal{A} \propto \sum_f N_c^f Q_f n_V^f g_A^f, \quad (2.79)$$

which is zero for any well defined theory (ensured by anomaly cancellation, see Chapter 3 for more details). Therefore, only the axial coupling n_A^f will contribute to the amplitude.

- **DM DM $\rightarrow \gamma h$**

In this case, symmetries tell us again that the vector coupling n_V^f is the only non-zero contribution. However, the effective vertex is vectorial and, therefore, from what we discussed in the Subsec. 2.1.1.4 (see Tab. 2.1), is velocity suppressed.

Above we have shown that there are certain conditions under which we can have striking predictions of non-suppressed gamma lines for Majorana DM candidates in the context of gauge theories. We note that, on the other hand, the DM-nucleon elastic scattering is also velocity suppressed. Therefore, direct searches will be, in general, suppressed and close or below the neutrino floor limit. In Table 2.3, we collect the different combinations of couplings which can lead to non-zero contributions to gamma lines.

Gamma Lines	$\gamma\gamma$	$Z\gamma$	$h\gamma$
Couplings	n_A^f	$n_V^f g_A^f, n_A^f \cdot g_V^f$	n_V^f

Table 2.3: Combination of couplings which generates a non-zero effective vertex relevant for the different gamma lines.

We would like to emphasize that, for any vector mediator connecting the fermionic dark sector with the fermions of the theory, only the theories that accommodate fermions that couple axially to the new gauge boson will be relevant for detection of gamma lines, as summarized in Table 2.3. This result has dramatic consequences for anomaly free theories such as $U(1)_{B-L}$ or $U(1)_{B-3L_i}$ (with the addition of 3 RH neutrinos), or $U(1)_{L_i-L_j}$, in which the mediator only couples vectorially to the fermions of the theory and, therefore, no relevant gamma line for indirect searches is expected in their context.

2.2 Axions

Axions are pseudoscalar particles highly non-thermally produced that can play the role of DM. They are the pseudo-Nambu Goldstone bosons (GBs) of a global abelian group, whose symmetry is respected at the classical level but it is broken at the quantum level by the chiral color anomaly. Axions were proposed at the end of the 70s as an elegant solution to the so-called Strong CP problem. In this chapter, we describe the aforementioned topics following a historical introduction: we will first introduce the strong CP problem, whose heart is the $U(1)_A$ anomaly. Then, we introduce the Peccei-Quinn symmetry as a solution to it, and the axion as its consequence, followed by a brief review on the types of models where the Peccei-Quinn mechanism can be

implemented. At the end, we will explain how axions can play the role of a DM candidate and different experimental approaches to detect them.

2.2.1 The $U(1)_A$ anomaly

Axions arise as a solution to the strong CP problem, which is originated by the chiral $U(1)_A$ anomaly, where A refers to *axial*. Let us start from the heart of the strong CP problem, which is deeply related to the well-known $U(1)$ problem [102–104]. In the massless limit of quarks, the QCD Lagrangian with three flavours (u,d,s) enjoys the following global symmetries: $U(3)_L \otimes U(3)_R \equiv SU(3)_L \otimes SU(3)_R \otimes U(1)_B \otimes U(1)_A$, where the vector $U(1)_B$ can be identified with the accidental baryon number (see Chapter 3). When the quarks condensate, i.e. $\langle \bar{q}q \rangle \neq 0$, the axial symmetries are broken and, according to the Goldstone Theorem, $8 + 1$ GBs are expected. Actually, they are pseudo-GBs since the axial symmetries were already slightly broken explicitly by the quark masses at the level of the Lagrangian. Experimentally, an octet of light pseudoscalars was found, confirming the theoretical expectations. However, the ninth pseudo-GB, η' has quite larger mass than the octet, manifesting a conflict between theory and experiment. The solution to this apparent contradiction, known as the $U(1)$ problem, relies on the fact that $U(1)_A$ has never been a good symmetry of the Lagrangian, although classically it totally fakes it. In order to understand why $U(1)_A$ is anomalous, we will draw on the path integral formalism, following the method introduced by Kazuo Fujikawa at the end of the 70s [105,106].

Let us assume without loss of generality a single generation of Dirac fermions $\Psi = \Psi_L + \Psi_R$. For a general complex Yukawa coupling, the following interaction in the Yukawa Lagrangian generates the mass for a given fermion in the broken phase,

$$\mathcal{L} \supset i\bar{\Psi}\partial_\mu\gamma^\mu\Psi - \bar{\Psi}Me^{i\theta_Y}\Psi, \quad (2.80)$$

where M is a real parameter that defines the mass of the fermion and the angle θ_Y encodes the imaginary phase of the Yukawa coupling. Such phase violates CP; however, it can be easily absorbed by a redefinition of the fields performing the following chiral rotation:

$$\Psi \xrightarrow{U(1)_A} e^{i\alpha\gamma_5}\Psi, \quad \text{so that} \quad \bar{\Psi} \xrightarrow{U(1)_A} \bar{\Psi}e^{i\alpha\gamma_5}. \quad (2.81)$$

By taking $\alpha = \theta_Y/2$, the Yukawa complex phase θ_Y can be removed from the Yukawa classical Lagrangian in Eq. 2.80 so that one expects the strong interactions to preserve CP. Indeed, this is what has been observed experimentally so far and if the above was true for all kind of gauge theories, probably the axions would had never been born. However, as we will show in the following, the $U(1)_A$ symmetry is not respected at the quantum level and an extra term in the Lagrangian is induced when performing such transformation. Let us assume an infinitesimal local chiral rotation parametrized by $\alpha(x)$, so that the Lagrangian in Eq. 2.80 transforms as,

$$\mathcal{L} \xrightarrow{U(1)_A} \mathcal{L} - \partial_\mu \alpha \bar{\Psi} \gamma^\mu \gamma_5 \Psi - 2i\alpha M e^{i\theta_Y} \bar{\Psi} \gamma_5 \Psi + \mathcal{O}(\alpha^2). \quad (2.82)$$

Integrating by parts, one can rewrite the variation of the Lagrangian as follows,

$$\delta \mathcal{L} = \alpha \partial_\mu J_A^\mu - 2i\alpha M e^{i\theta_Y} \bar{\Psi} \gamma_5 \Psi + \partial_\mu (\alpha \bar{\Psi} \gamma^\mu \gamma_5 \Psi) + \mathcal{O}(\alpha^2), \quad (2.83)$$

where $J_A \equiv \bar{\Psi} \gamma^\mu \gamma_5 \Psi$, and the last term is a total derivative which, in principle, we would not expect that contributes to the variation of the action. From the above it seems that in the limit of massless fermions, i.e. $M \rightarrow 0$, the axial current is conserved: the $U(1)_A$ symmetry would be a good symmetry of the classical action and, therefore, one would naturally expect $\partial_\mu J_A^\mu = 0$. Let us see what happens at the quantum level.

All physical things we may aim to measure are correlation functions, which are generated by taking derivatives with respect the sources of the following functional, called the generating functional,

$$\mathcal{Z} = \int \mathcal{D}\bar{\Psi} \mathcal{D}\Psi \mathcal{D}A_\mu e^{iS+i \int \mathcal{L}_{\text{sources}}}, \quad (2.84)$$

where we have considered also the possibility that the fermions Ψ are charged under some gauge force mediated by A_μ . The key point here is that an axial transformation, unlike the vector one, does not leave the measure invariant; the Jacobian transforms in a non-trivial way. To see that, let us start expanding the fermion fields in the spinor basis:

$$\Psi = \sum_n a_n \phi_n, \quad \text{and} \quad \bar{\Psi} = \sum_n \phi_n^\dagger \bar{b}_n, \quad (2.85)$$

where a_n and \bar{b}_n are Grassmann variables and carry the anticommuting behaviour of the fermions. The spinors ϕ_n and ϕ_n^\dagger are the eigenfunctions of the hermitian operator $(i\mathcal{D})$:

$$(i\mathcal{D})\phi_n = \lambda_n\phi_n, \quad \text{and} \quad \phi_n^\dagger(i\mathcal{D}) = \lambda_n\phi_n^\dagger. \quad (2.86)$$

Hence, by the spectral theorem, these eigenfunctions are orthogonal, i.e.

$$\phi_n(x)^\dagger\phi_m(y) = \delta_{nm}\delta(x-y). \quad (2.87)$$

Using the orthogonality condition and the fact that a and b are anticommuting c -numbers, one can easily show that

$$\mathcal{D}\bar{\Psi}\mathcal{D}\Psi = \prod \prod \left(\sum_k da_k db_k \right) = \prod_n da_n \prod_m db_m. \quad (2.88)$$

To find how the measure transforms, we should focus on the basis coefficients. By applying the chiral transformation to a fermionic field we have

$$\Psi' = e^{i\alpha\gamma_5}\Psi = \sum_n e^{i\alpha\gamma_5}\phi_n a_n \equiv \sum_m a'_m \phi_m. \quad (2.89)$$

Therefore, the coefficient a'_m , because of the orthonormality conditions in Eq. 2.87, corresponds to the projection of the Ψ' onto ϕ_m ,

$$a'_m \equiv \phi_m^\dagger \Psi' = \sum_n \phi_m^\dagger e^{i\alpha\gamma_5} \phi_n a_n \equiv \sum_n C_{mn} a_n, \quad (2.90)$$

where the integration and spinor dependence on x has been implicitly assumed. Now, due to the properties of Grassmann variables, we know that

$$da'_n = \frac{\partial}{\partial a'_n} = \sum_m \frac{\partial}{\partial a_m} \frac{\partial a_m}{\partial a'_n} = \sum_m \frac{\partial a_m}{\partial a'_n} da_m, \quad (2.91)$$

where the Chain's rule has been applied and, in the last equality, the Grassmann identity $d\theta = \partial/\partial\theta$ has been used again. Coming back to our measure in Eq. 2.88, it therefore

transforms as

$$\begin{aligned} \mathcal{D}\bar{\Psi}'\mathcal{D}\Psi' &= \prod_n da'_n \prod_m db'_m = \left(\prod_n \sum_i \left(\frac{\partial a_i}{\partial a'_n} \right) da_i \right) \left(\prod_m \sum_j \left(\frac{\partial b_j}{\partial b'_m} \right) db_j \right) \\ &= (\det C)^{-2} \prod_n da_n \prod_m da_m = (\det C)^{-2} \mathcal{D}\bar{\Psi}'\mathcal{D}\Psi. \end{aligned} \quad (2.92)$$

The last equality in Eq. 2.92 may be seen clearer in the following way: Given a Grassmann variable that transforms as $\theta' = A\theta$, we have that

$$\begin{aligned} \int d^n\theta f(\theta') &= \int d^n\theta f(A\theta) = \int d^n\theta a_{1\dots n} A_{1i_1} \dots A_{ni_n} \epsilon_{i_1\dots i_n} \\ &= \det A \int d^n\theta a_{1\dots n} = \det A \int d^n\theta f(\theta) = \det A \int d^n\theta' f(\theta'), \end{aligned}$$

where $\epsilon_{i_1\dots i_n}$ is the n-dimensional total antisymmetric tensor, the definition of the determinant has been used and a dummy index redefinition has been performed. Therefore, from the above identity it is straightforward to infer that $\int d^n\theta = \det A \int d^n\theta'$, and the same applies to our basis coefficients:

$$\prod_n a'_n \prod_m b'_m = (\text{Det } C)^{-2} \prod_n a_n \prod_m b_m. \quad (2.93)$$

Thus, we know how the measure transforms, and just to write it in a more convenient way in the path integral let us use the following identity:

$$(\text{Det } C)^{-1} = e^{-\log(\text{Det } C)} = e^{-\log(\prod_i \lambda_i)} = e^{-\sum_i \log(\lambda_i)} = e^{-\text{Tr}\{\log C\}}, \quad (2.94)$$

where we have used the fact that the determinant and the trace of a matrix are invariant. Plugging in the definition of C given in Eq. 2.90,

$$(\text{Det } C)^{-2} = \exp \left[-2i \int dx^4 \alpha \sum_n \phi_n^\dagger(x) \gamma_5 \phi_n(x) \right]. \quad (2.95)$$

In the case of Weyl spinors, $\Psi_L \xrightarrow{U(1)^A} e^{-i\alpha}\Psi_L$ and $\bar{\Psi}_L \xrightarrow{U(1)^A} \bar{\Psi}_L e^{i\alpha}$, we can expand them as

$$\Psi_L = \sum a_n \Phi_{Ln}, \quad \text{and} \quad \bar{\Psi}_L = \sum \Phi_{Rn}^\dagger \bar{b}_n. \quad (2.96)$$

Note that, in their context,

$$D\bar{\Psi}_L D\Psi_L = (\text{Det } C_L)^{-1}(\text{Det } C_R)^{-1} D\bar{\Psi}'_L D\Psi_L = (\text{Det } C)^{-1} D\bar{\Psi}'_L D\Psi_L, \quad (2.97)$$

since

$$(\text{Det } C_L)(\text{Det } C_R) = \exp \left[i \int d^4 x \alpha \sum_n \left(-\phi_{nL}^\dagger \phi_{nL} + \phi_{nR}^\dagger \phi_{nR} \right) \right] = \text{Det } C. \quad (2.98)$$

The exponents of Eqs 2.95 and 2.98 are ill-defined due to the infinite sum in the spinor space. We introduce a cut-off Λ such that

$$\begin{aligned} \lim_{\Lambda \rightarrow \infty} \sum_n \bar{\phi}_n(x) \gamma_5 e^{-\lambda_n/\Lambda} \phi_n(x) &= \lim_{\Lambda \rightarrow \infty} \sum_n \bar{\phi}_n(x) \gamma_5 e^{-(i\mathcal{D})^2/\Lambda} \phi_n(x) \\ &= \lim_{\substack{\Lambda \rightarrow \infty \\ x \rightarrow y}} \text{Tr} \left\{ \gamma_5 e^{-(i\mathcal{D})^2/\Lambda} \right\} \delta(x - y), \end{aligned} \quad (2.99)$$

where in the first equality the Dirac equation has been used and, in the second one, we have applied the orthogonality conditions of the spinorial basis. Notice that the trace of γ_5 is zero, so it is like we are ‘‘summing zero infinite times’’. Now, let us focus on the operator $(i\mathcal{D})^2 = -D_\mu D_\nu \gamma^\mu \gamma^\nu$. By symmetrizing it, we have

$$(i\mathcal{D})^2 = -\frac{\{D_\mu, D_\nu\}}{2} \frac{\{\gamma_\mu, \gamma_\nu\}}{2} - \frac{[D_\mu, D_\nu]}{2} \frac{[\gamma_\mu, \gamma_\nu]}{2} = D^2 + g_S \frac{\sigma^{\mu\nu}}{2} G_{\mu\nu}^a T_a^R, \quad (2.100)$$

where we have used that the product of a symmetric tensor with an antisymmetric one is zero and the definition of the field strength tensor $G_{\mu\nu} \equiv i[D_\mu, D_\nu]/g_S$ and $2\sigma_{\mu\nu} \equiv i[\gamma^\mu, \gamma^\nu]$. Here, T_a^R are the generators in the representation R of the fermion

Ψ . Taking this into account, we have

$$\begin{aligned}
 \text{Eq. 2.99} &= \lim_{\substack{\Lambda \rightarrow \infty \\ x \rightarrow y}} \text{Tr} \left\{ \gamma_5 \exp \left[- \left(D^2 + \frac{g_S}{2} \sigma \cdot G \right) / \Lambda^2 \right] \right\} \delta(x - y) \\
 &= \lim_{\substack{\Lambda \rightarrow \infty \\ x \rightarrow y}} \int \frac{d^4 k}{(2\pi)^4} \text{Tr} \left\{ \gamma_5 \exp \left[- \left(D^2 + \frac{g_S}{2} \sigma \cdot G \right) / \Lambda^2 \right] \right\} e^{ik(x-y)} \quad (2.101) \\
 &= \lim_{\Lambda \rightarrow \infty} \text{Tr} \left\{ \gamma_5 \exp \left[- \frac{g_S}{2\Lambda^2} \sigma \cdot G \right] \right\} \int \frac{d^4 k}{(2\pi)^4} e^{k^2/\Lambda^2}.
 \end{aligned}$$

Let us focus first on the trace. By expanding the exponential, the first surviving contribution is the quadratic term in $\sigma \cdot G$:

$$\text{Tr} \left\{ \gamma_5 \exp \left[- \frac{g_S}{2\Lambda^2} \sigma \cdot G / \Lambda^2 \right] \right\} = \frac{1}{2!} \frac{g_S^2}{4\Lambda^4} \text{Tr} \{ \gamma_5 (\sigma \cdot G)^2 \} + \mathcal{O}(\Lambda^{-6}).$$

On the other hand, the integral over momentum is divergent. However, we can use the Heat Kernel regularisation and perform a Wick rotation $k_0 \rightarrow ik_0^E$. In the Euclidean, the integral can be easily solved:

$$\int \frac{d^4 k_E}{(2\pi^2)^4} e^{-k_E^2/\Lambda^2} = \frac{i\Lambda^4}{16\pi^2}. \quad (2.102)$$

Taking the limit $\Lambda \rightarrow \infty$, only the term $\mathcal{O}(\Lambda^{-4})$ in the trace expansion survives:

$$\begin{aligned}
 &\lim_{\Lambda \rightarrow \infty} \left(\frac{g_S^2}{8\Lambda^4} \text{Tr} \{ \gamma_5 (\sigma \cdot G)^2 \} + \mathcal{O}(\Lambda^{-6}) \right) \frac{i\Lambda^4}{16\pi^2} \\
 &= i \frac{g_S^2}{128\pi^2} \text{Tr} \{ \gamma_5 (\sigma \cdot G)^2 \} = - \frac{g_S^2}{16\pi^2} \underbrace{\frac{1}{2} \epsilon^{\alpha\beta\mu\nu} G_{\alpha\beta}^a G_{\mu\nu}^b}_{G_{\mu\nu}^a \tilde{G}_a^{\mu\nu}} \underbrace{\text{Tr} \{ T_a^R, T_b^R \}}_{T_R}, \quad (2.103)
 \end{aligned}$$

where T_R refers to the Dynkin index of the representation. Here we have used that $G_a^{\alpha\beta}$ and $\sigma^{\alpha\beta}$ are antisymmetric (extra factor of 4) and that $\text{Tr} \{ \gamma_5 \gamma_\mu \gamma_\nu \gamma_\alpha \gamma_\beta \} = -4i\epsilon_{\mu\nu\alpha\beta}$. Therefore, by plugging the above result into Eq. 2.95, and using Eq. 2.92, we finally obtain how the measure transforms

$$\mathcal{D}\bar{\Psi}\mathcal{D}\Psi \rightarrow \mathcal{D}\bar{\Psi}\mathcal{D}\Psi \exp \left[i \frac{g_S^2 T_R}{8\pi^2} \int d^4 x \alpha G_{\mu\nu}^a \tilde{G}_a^{\mu\nu} \right], \quad (2.104)$$

and hence, we know how the generating functional transforms too,

$$\mathcal{Z} \rightarrow \mathcal{Z} \left[\mathbb{I} + \alpha \left(i \delta S + i \delta \mathcal{L}_{\text{sources}} + \int \frac{g_S^2 T_R}{8\pi^2} G_{\mu\nu}^a \tilde{G}_a^{\mu\nu} \right) + \mathcal{O}(\alpha^2) \right]. \quad (2.105)$$

Taking into account how the Lagrangian transforms under an axial transformation (see Eq. 2.83), we automatically get the variation of the classical action δS appearing in the above equation. Finally, the Ward Takahashi identities tell us how anomalous the $U(1)_A$ transformation is:

$$[\delta/\delta\alpha(x)]\mathcal{Z}|_{\alpha=0} = 0 \Rightarrow \partial_\mu J_A^\mu = 2M e^{i\theta_Y} \bar{\Psi} \gamma_5 \Psi - \frac{g_S^2 T_R}{8\pi^2} G_{\mu\nu}^a \tilde{G}_a^{\mu\nu}. \quad (2.106)$$

In the anomaly factor there is an extra factor of 1/2 when the $U(1)_A$ acts on chiral fields. In the above derivation, we have assumed that Ψ is charged under $SU(3)_c$ for convenience, but it can be straightforwardly generalized to any other $SU(N)$. Notice that, from Eq. 2.106 we can infer that even in the context of massless fermions, although at the classical level a chiral transformation is a good symmetry, it is broken at the quantum level by the anomaly factor. Therefore, if we choose $\alpha = \theta_Y/2$ to get rid of the CP phase in the Lagrangian, we will end up with an extra anomalous term proportional to $\theta_Y/2$. Curiously, this unexpected anomalous factor can be rewritten as a total derivative term. This will be shown in the following subsection, where we will discuss whether it is harmless or not.

2.2.2 The Strong CP problem

In the previous subsection, we just realized that redefining the colored fields by a chiral rotation induces an extra term in the Lagrangian proportional to the parameter quantifying the axial transformation (see Eq. 2.106). Particularly, when absorbing the θ_Y in the Lagrangian from Eq. 2.80 by a $q \rightarrow e^{i\theta_Y \gamma_5/2} q$ transformation,¹⁰ the following term is generated due to the anomalous behaviour of $U(1)_A$ at the quantum level:

$$\mathcal{L} \supset \theta_Y \frac{g_S^2}{32\pi^2} G_{\mu\nu}^a \tilde{G}_a^{\mu\nu}. \quad (2.107)$$

¹⁰We have particularized to quarks since we will focus in the color anomaly henceforth.

where $\tilde{G}_{\mu\nu} = \epsilon_{\mu\nu\alpha\beta} G^{\alpha\beta}/2 = (\lambda_a/2)\tilde{G}_{\mu\nu}^a$. In reality, apart from a possible complex phase in the Yukawa interactions, there is another source of CP violation in the Lagrangian, allowed by the SM gauge symmetry group,

$$\mathcal{L} \supset \theta_{\text{QCD}} \frac{g_S^2}{32\pi^2} G_{\mu\nu}^a \tilde{G}_a^{\mu\nu}, \quad (2.108)$$

where θ_{QCD} is a dimensionless parameter. The above term was for a long time forgotten. The reason is that such interaction, as well as that in Eq. 2.107, can be written as a total derivative of the following current,

$$K_\mu = \epsilon_{\mu\nu\rho\sigma} A_a^\nu \left(G^{\rho\sigma a} - \frac{g_S}{3} f^{abc} A_b^\rho A_c^\sigma \right), \quad (2.109)$$

known as the Chern-Simons current and it is well known that, when gauge fields behave properly and go quickly enough to zero (in order to get finite energies), a boundary term does not contribute to the action, nor to the equations of motion, so that one would not expect θ_{QCD} to have any physical effect. The latter holds for an abelian gauge theory, but non-abelian theories allow for gauge field configurations called pure-gauges that are equivalent to the null-field configuration, so that one would expect those to be removed from the functional integral by the well-known gauge-fixing procedure. However, the redundant configurations are those that can be joined by a continuous gauge transformation to configurations that are already counted. Pure gauges are connected to the null-field configuration by gauge transformations that cannot be smoothly deformed into each other without leaving the pure gauge, so that they should be taken into account and will then lead to physical effects. Such non-continuous gauge transformations exist in non-abelian gauge theories as a consequence of their non-trivial and unexpectedly rich vacuum structure. The different equivalent classes of pure gauge configurations, representing different vacua, are defined and distinguished by its topological charge:

$$n \equiv \frac{g_S^2}{32\pi^2} \int d^4x G_{\mu\nu}^a \tilde{G}_a^{\mu\nu}. \quad (2.110)$$

The configurations that connect by tunneling transitions between vacua of consecutive topological charges, as naively illustrated in the classical picture from Fig. 2.11 with a

red string, are called instantons [107,108], and are responsible for rendering the $\theta_{\text{QCD}}G\tilde{G}$ term physical in the Lagrangian.¹¹ The later is not the only consequence of the existence

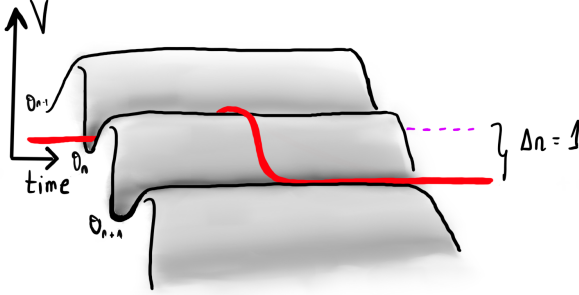


Figure 2.11: Classical analogy to the instanton solutions of QCD.

of instantons; in the last subsection we obtained that a chiral rotation induces a term proportional to $G\tilde{G}$ in the Lagrangian, shown in Eq. 2.107, when a chiral rotation of the quarks is used to remove the Yukawa phase θ_Y from the interactions in Eq. 2.80. Such term is physical too! Those non-perturbative effects of QCD explicitly break $U(1)_A$. The later was first understood by G. t'Hooft [110,111] (see Refs. [112] and [113] for an intuitive interpretation of t'Hooft's more formal language) in 1976. It explains the large mass of η' , and tells us that the CP violating phases in the QCD Lagrangian cannot be removed. Indeed, there is no way to hide those complex phases from both the Yukawa and the topological term simultaneously, because when redefining the chiral color fields, a CP violating phase is induced in the Lagrangian that shifts the topological term, and viceversa, as follows:

$$\mathcal{L}_{\text{CP}}(\theta_Y, \theta_{\text{QCD}}) \leftrightarrow \mathcal{L}_{\text{CP}}(\theta_Y - \alpha, \theta_{\text{QCD}} + N\alpha). \quad (2.111)$$

unless an unexplained tuning occurs between θ_Y and θ_{QCD} contributions. Here N is defined, taking into account the contribution to the anomaly from the chiral fields

¹¹The reader may be wondering why the analogous $(g^2/32\pi^2)\theta_{\text{EW}}W_{\mu\nu}^a\tilde{W}_a^{\mu\nu}$ term should not be added to the Lagrangian since one would also expect instanton effects in the non-abelian $SU(2)_L$. However, in this case, global baryon $U(1)_B$ and lepton $U(1)_L$ number symmetries render θ_{EW} unphysical, playing exactly the same role as a hypothetical massless quark (it will be explained in the main text). However, $U(1)_B$ and $U(1)_L$ are accidental symmetries, as we will discuss in Chapter 3 of the renormalizable SM Lagrangian that could be broken by higher dimensional operators, so that θ_{EW} would become physical if $B + L$ is violated, as the authors of Ref. [109] realized.

shown in Eq. 2.106, as

$$N = 2 \sum_{\Psi_L} C_{\Psi_L} T_D [R_{\Psi_L}] \times \text{mult}[\Psi_L], \quad (2.112)$$

where the sum runs over the fermions carrying color. Let us group all QCD CP-violating phases together in a total phase $\bar{\theta}$ in the topological term, i.e.

$$\mathcal{L} \supset \bar{\Psi}_L M \Psi_R + \text{h.c.} + \frac{g_S^2}{32\pi^2} \underbrace{(\theta_{\text{QCD}} + \theta_Y)}_{\bar{\theta}} G_{\mu\nu}^a \tilde{G}_a^{\mu\nu}, \quad (2.113)$$

where, in the presence of several quark generations, the Yukawa phase is generalized to $\theta_Y = \text{Arg}[\text{Det } M]$, being M the mass matrix of the quarks.

How does $\bar{\theta}$ contribute to the SM phenomenology? Which are its implications? The most relevant observational consequence of $\bar{\theta}$ are the hadronic electric dipole moments (EDMs), which can only be generated by CP violating processes. In particular, the magnitude of the neutron EDM,

$$\mathcal{L}_{\text{EDM}} = -\frac{d_n}{2} (\bar{\Psi}_n i\gamma_5 \sigma^{\mu\nu} \Psi_n) F_{\mu\nu}, \quad \text{where } d_n = (2.4 \pm 1.0)\bar{\theta} \times 10^{-3} \text{ e fm}, \quad (2.114)$$

is proportional to $\bar{\theta}$, where d_n has been computed with QCD sum rules [114–117]. Classically, an EDM parametrizes how charges are distributed. In particular, the neutron EDM would be expected to be order $\mathcal{O}(1)$ as Fig. 2.12 shows.

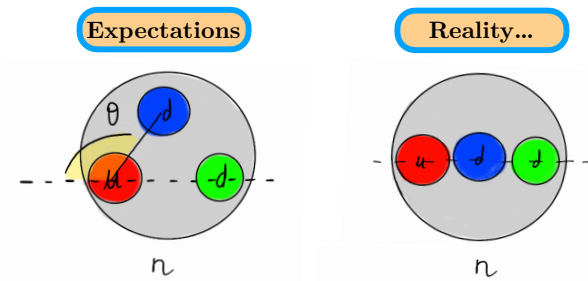


Figure 2.12: Classical picture of the neutron. The angle $\bar{\theta}$ parametrizes the neutron EDM. *Figure adapted from Ref. [118]*

Actually, by computing the scalar potential in Chiral Perturbation Theory (ChPT)¹²,

$$V = -m_\pi^2 f_\pi^2 \sqrt{1 - \frac{4m_u m_d}{(m_u + m_d)^2} \sin^2 \left(\frac{\bar{\theta}}{2} \right)}, \quad (2.115)$$

where m_u , m_d and m_π are the masses of the up, down quarks and the pion, respectively, and f_π the pion decay constant. From the above scalar potential we can see that $\bar{\theta}$ ¹³ also contributes to the masses of the pions, by splitting them in the following way:

$$m_{\pi^0}^2 = a f_\pi \sqrt{m_u^2 + m_d^2 + 2m_u m_d \cos \bar{\theta}}, \quad \text{and} \quad m_{\pi^\pm}^2 = a f_\pi (m_u + m_d), \quad (2.116)$$

which, by experiment, we know that they are pretty similar. This is already giving us a hint on how small $\bar{\theta}$ is. Indeed, experimental bounds on the neutron EDM [21],

$$|d_n|^{\text{exp}} < 0.18 \times 10^{-12} \text{ e fm at 90 \% C.L.} \quad \Rightarrow \quad |\bar{\theta}| \lesssim 7.5 \times 10^{-11}, \quad (2.117)$$

i.e. $\bar{\theta}$ should be extremely small. But, why the neutron EDM is so small? Why does QCD seem to preserve CP? This is the so-called strong CP problem.

The later could be solved, as it was believed at some point before ChPT ruled out this possibility [120], by the existence of a massless quark [111]. Imagine that this was the case and that the up quark was massless. Then, one could redefine it by a chiral transformation such that all CP violating phases contained in the topological term, i.e. $\bar{\theta}$, are swallowed by the rotation, i.e.

$$u \xrightarrow{U(1)_A} e^{i(\bar{\theta}/2)\gamma_5} u, \quad (2.118)$$

so that $\bar{\theta}$ would be unphysical and the problem would be solved! Unfortunately or not, the up-quark is massive. Let us focus on the key point of this trick: in the presence of a massless quark, the $U(1)_A$ symmetry becomes a good symmetry at the classical level while it is broken in the underlying quantum world. If we want to mimic such massless quark, we should look for symmetries that behave as the axial one in the presence of massless fields: a good symmetry at the classical level, broken at the

¹²See Ref. [119] for a nice review on the topic.

¹³The CP violating parameter $\bar{\theta}$ is an angle $\theta \in [0, 2\pi]$ as the potential shows.

quantum level by the chiral anomaly. In the following, we will name symmetries of this kind as Peccei-Quinn symmetries, $U(1)_{\text{PQ}}$. Spontaneous symmetry breaking complicates things indeed, since a chiral symmetry automatically breaks in the presence of massive fermions. However, a broken global symmetry predicts a GB that can be rotated by a chiral transformation such that

$$\mathcal{L} \supset \frac{g_S^2}{32\pi} \left(\bar{\theta} - \frac{a}{f_a} \right) G_{\mu\nu}^a \tilde{G}_a^{\mu\nu} + \mathcal{L}_a^{\text{int}}, \quad (2.119)$$

where f_a is the scale at which the $U(1)_{\text{PQ}}$ is spontaneously broken. In this context, the scalar potential in ChPT modifies as follows

$$V(a) = -m_\pi^2 f_\pi^2 \sqrt{1 - \frac{4m_u m_d}{\sqrt{m_u + m_d}^2} \sin^2 \left(\frac{\bar{\theta} - a/f_a}{2} \right)}, \quad (2.120)$$

such that the minimum of this potential is achieved at $\langle a \rangle = \bar{\theta} f_a$. In other words, the dynamics of QCD itself solves the strong CP problem since the $G\tilde{G}$ is automatically stabilized to zero in the presence of such pseudo-GB,¹⁴ named by F. Wilczek as *the axion*.¹⁵ The $U(1)_{\text{PQ}}$ mechanism, responsible for this success, was proposed by R. Peccei and H. Quinn [121,122], in 1977 inspired by the massless quark scenario. Immediately later, S. Weinberg [123] and F. Wilczek [124] realized that, after such symmetry is spontaneously broken, an axion is born.

By expanding the above potential around the minimum we find that the mass of the axion is given by

$$m_a^2 \sim \frac{m_u m_d}{(m_u + m_d)^2} m_\pi^2 \frac{f_\pi^2}{f_a^2}. \quad (2.121)$$

Note the key feature of the QCD axion: its mass is inversely proportional to the energy scale where it was born.

¹⁴As we will see in the following, the axion is not massless; it takes mass from the QCD potential due to the instantons, as a consequence of the explicitly broken chiral symmetry at the level of the QCD Lagrangian.

¹⁵Rumours affirm that the origin of the name comes from the laundry detergent *Axion*, as an analogy of its cleaning power when washing out the strong CP problem, and because such problem involves *axial* currents.

Before closing this subsection, let us briefly comment on the other interacting terms that arise when rotating the axion from the Yukawa Lagrangian, shown in the following Lagrangian:

$$\mathcal{L}_a^{\text{int}} = -\frac{g_{a\gamma\gamma}}{4} a F_{\mu\nu} \tilde{F}^{\mu\nu} + \sum_f g_{af} (\partial_\mu a) \bar{f} \gamma^\mu \gamma_5 f. \quad (2.122)$$

It contains the axion interaction with photons, generated when the rotated chiral fields have electric charge and parametrized by the coupling $g_{a\gamma\gamma}$, defined below:

$$g_{a\gamma\gamma} = \frac{\alpha_{\text{EM}}}{2\pi f_a} \left(\frac{E}{N} - 1.92(4) \right), \quad (2.123)$$

where the second term in Eq. 2.123 is the contribution arising from non-perturbative effects from the axion coupling to QCD and has been computed at NLO in Ref. [125]. The first term in Eq. (2.123) is given by the anomaly coefficient for the electromagnetic fields, E , analogous to the N (see Eq. 2.112) for the $G\tilde{G}$ term generated by redefining the colored fields. In the Lagrangian from Eq. 2.122 one can also identify the interaction that appears when rotating the fermions because of the local nature of axion, which will lead to axion-nucleon interactions at low energies.

2.2.3 The electroweak axion

In order to implement the Peccei-Quinn (PQ) mechanism, we need a CP-odd physical GB in our scalar potential. In the SM, with one Higgs it is unfortunately not possible since the corresponding CP-odd GB becomes the longitudinal polarization of the Z boson, accounting for its mass. We need an extra GB, i.e. an extra global symmetry to break! Let us add one Higgs doublet more and distribute the PQ charges such that, without loss of generality, one of them interacts only with up-quarks, H_u , and the other one with down-quarks, H_d , in order to cleverly avoid the severe bounds on flavour changing neutral currents. Under the following PQ charge assignment:

$$H_u \rightarrow e^{i\text{PQ}_u} H_u, \quad H_d \rightarrow e^{-i\text{PQ}_d} H_d, \quad d_R \rightarrow e^{i\text{PQ}_d} d_R, \quad \text{and} \quad u_R \rightarrow e^{i\text{PQ}_u} u_R,$$

we can write down the following Yukawa Lagrangian:

$$- \mathcal{L}_{\text{PQ}} \supset \overline{q_L} Y_u i\sigma_2 H_u^* u_R + \overline{q_L} Y_d H_d d_R + \text{h.c.} \quad (2.124)$$

The scalar potential is built upon allowed gauge combinations of the two scalar doublets and the global PQ symmetry,

$$V_{\text{PQ}} = V(|H_u^0|^2, |H_d^0|^2), \quad (2.125)$$

so that two global symmetries are broken when the neutral scalars get a *vev*.¹⁶ *Eccolo!* After SSB, the CP-odd component of the neutral scalars can be written as a linear combination of the two GBs of the theory,

$$H_u^0 \supset \frac{v_u}{\sqrt{2}} e^{ia_u/v_u} = \frac{v_u}{\sqrt{2}} e^{i(q\hat{a}_Z + \text{PQ}_u \hat{a})}, \quad (2.126)$$

$$H_d^0 \supset \frac{v_d}{\sqrt{2}} e^{ia_d/v_d} = \frac{v_d}{\sqrt{2}} e^{i(q\hat{a}_Z + \text{PQ}_d \hat{a})}, \quad (2.127)$$

where \hat{a} and \hat{a}_Z are the phases of the axion and the GB that will be eaten by the Z , respectively. The factor q is the contribution related to the EW quantum numbers and PQ_i parametrizes the presence of the axion in each of the scalar representations. Linearizing the kinetic terms of the CP-odd fields, we have

$$\frac{1}{2} \partial_\mu a_u \partial^\mu a_u = \frac{1}{2} v_u^2 (q^2 \partial_\mu \hat{a}_Z \partial^\mu \hat{a}_Z + 2q \text{PQ}_u \partial_\mu \hat{a}_Z \partial^\mu \hat{a} + \text{PQ}_u^2 \partial_\mu \hat{a} \partial^\mu \hat{a}), \quad (2.128)$$

$$\frac{1}{2} \partial_\mu a_d \partial^\mu a_d = \frac{1}{2} v_d^2 (q^2 \partial_\mu \hat{a}_Z \partial^\mu \hat{a}_Z + 2q \text{PQ}_d \partial_\mu \hat{a}_Z \partial^\mu \hat{a} + \text{PQ}_d^2 \partial_\mu \hat{a} \partial^\mu \hat{a}). \quad (2.129)$$

Orthogonality of the GBs requires the following condition,

$$v_u^2 \text{PQ}_u + v_d^2 \text{PQ}_d = 0, \quad (2.130)$$

¹⁶We should remark that the PQ is not automatic in the two Higgs doublet model Lagrangian. Note that the invariant $H_d^\dagger i\sigma_2 H_u^*$ term and its hermitian conjugate would break the second global symmetry we need if the global $U(1)_{\text{PQ}}$ was not imposed by hand.

whereas the normalization of the kinetic terms of the axion demands that

$$v_u^2 \text{PQ}_u^2 + v_d^2 \text{PQ}_d^2 = n_a^2, \quad (2.131)$$

where n_a is the normalization of the CP-odd phase $\hat{a} = a/n_a$. The conditions in Eqs. 2.130 and 2.131 fix *how much* part of the axion lives in each of the neutral scalars,

$$H_u \supset \frac{v_u}{\sqrt{2}} e^{-i \frac{v_d}{v_u} \frac{a}{v_0}}, \quad \text{and} \quad H_d \supset \frac{v_d}{\sqrt{2}} e^{i \frac{v_u}{v_d} \frac{a}{v_0}}, \quad (2.132)$$

where $v_0 = \sqrt{v_u^2 + v_d^2}$. Substituting the above expressions in the Lagrangian in Eq. 2.124, the reader can see that the axion can be rotated away from the Yukawa interactions by redefining the quarks in the following way:

$$u_{L/R} \rightarrow e^{\pm i \frac{v_d}{v_u} \frac{a}{2v_0}} u_{L/R}, \quad \text{and} \quad d_{L/R} \rightarrow e^{\pm i \frac{v_u}{v_d} \frac{a}{2v_0}} d_{L/R}, \quad (2.133)$$

which, in turn, induces a shift in the topological term proportional to N , according to Eq. 2.112. The color-anomalous factor N is determined by the group theory properties of the quarks we are rotating, i.e.

$$N = \underbrace{3}_{N_f} \times 2 \left(\underbrace{\left(\frac{v_d}{v_u} \times \frac{v_0}{2} \times \frac{1}{2} \right)}_{u_L} + \underbrace{\left(\frac{v_u}{v_d} \times \frac{v_0}{2} \times \frac{1}{2} \right)}_{d_L} \right) \times \underbrace{2}_{L \rightarrow R}. \quad (2.134)$$

In other words, we have transferred the axion from the Yukawa interactions to the topological term (see Eq. 2.111),

$$\mathcal{L}_{\text{PQ}} \supset \frac{\alpha_S}{8\pi} \left(\bar{\theta} + 3 \left(\frac{v_d}{v_u} + \frac{v_u}{v_d} \right) \frac{a}{v_0} \right) G_{\mu\nu}^a \tilde{G}_a^{\mu\nu}. \quad (2.135)$$

Because the PQ symmetry is anomalous, the axion can seep into the $G\tilde{G}$ term and, because of its dynamical nature as a field, is able to wash the strong CP problem out. This beautiful theory proposed by R. Peccei, H. Quinn, S. Weinberg and F. Wilczek (PQWW) [121–124], however, is ruled out because, in this context, the axion is too heavy [126], i.e. the EW scale does not suppress enough the interactions to avoid the

current experimental limit on the branching ratio $\mathcal{B}(K^+ \rightarrow \pi^+ a) \leq 4.5 \times 10^{-11}$ at 90 % C.L. [127]. Yes, it is ruled out because the theory *predicts* the axion mass as a consequence of having the PQ scale f_a linked to a well-defined scale, $v_0 = 246$ GeV. See Fig. 2.13 for an illustration. The theory has launched a prediction and, with that, has been exposed to be falsified. And indeed it has been kicked out by experiment. It should be stressed how powerful a theory of this kind is, and we welcome the reader to mull over this in order to value it.

2.2.4 Invisible axion models

As explained in the last section, the original PQWW model is ruled out because the scale suppressing the interaction between the axion and gluons is not high enough to avoid the experimental bounds. The reason is that the PQ scale is linked to the EW scale since the Higgses containing the axion are charged under the EW force so that their vev s are bounded from their contribution to the gauge boson masses. In order to weaken the axion interactions and be consistent with experiment, we need to decouple the PQ scale, f_a , from the EW scale. That is the role that the invisible axion models play. In this section, we introduce the two kind of mechanisms on which the invisible axion models are based.

2.2.4.1 DFSZ mechanism

In order to decouple the PQ scale from the EW scale, a singlet scalar under the EW gauge symmetry, $S \sim (1, 1, 0)$, must be added. In that context, the vev of the singlet scalar, v_S , is not bounded to the EW gauge boson masses and can be arbitrarily large. Since v_S enters in the PQ scale, one can easily avoid the bounds by suppressing the axion interactions. However, gauge symmetries do not allow a scalar singlet to interact with the SM quarks so that one cannot use the PQ symmetry to rotate away the axion and generate the desired $aG\tilde{G}$ term.

The mechanism proposed by M. Dine, W. Fischler and M. Srednicki in 1981 [128], and one year before by A. Zhitnitsky [129] (although it was overlooked in the literature at that time), consists of the introduction of an extra mediator, a second copy of the Higgs boson *à la* PQWW, that connects indirectly the part of the GB living in the singlet

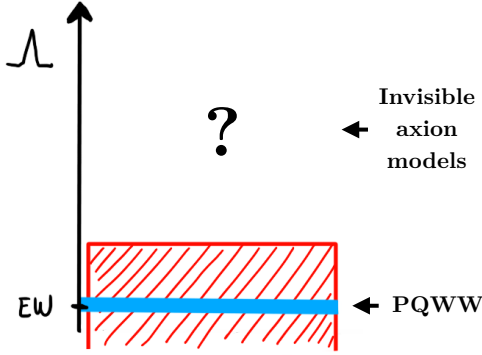


Figure 2.13: In the PQWW model, the mass of the axion is predicted because the PQ scale is connected with the EW scale through the νev of the Higgs doublets where it lives. Unfortunately, the axion is too heavy to satisfy the experimental bounds, represented with a red mesh, and the PQWW model is ruled out. On the other hand, invisible axion models successfully decouple the PQ scale from the EW scale, although now such scale is totally arbitrary and, therefore, the axion mass cannot be predicted in that context unless the axion is embedded in a theory with a well-defined scale.

(suppressed by its arbitrarily large νev) and the quark sector via a mixing term in the scalar potential. The Yukawa Lagrangian relevant for this mechanism is exactly the same as that from the original PQWW model in Eq. 2.124, up to the extra scalar SM singlet in the potential,

$$V_{\text{DFSZ}} = V(|H_u^0|^2, |H_d^0|^2, |S|^2), \quad (2.136)$$

so that there are in total three global symmetries that will be broken once the neutral scalar fields acquire a νev . Then, one expects three GBs in this case, which would not help at all since one would still have the PQWW axion living in the doublets, as before, and a massless CP-odd field living exclusively in the scalar singlet, with no possible interaction with quarks. In order to avoid such dangerous scenario, one has to charge the singlet scalar S under $U(1)_{\text{PQ}}$ such that a mixing term between the three scalars, for instance

$$V_{\text{DFSZ}} \supset -\mu H_u^\dagger H_d S^2 \quad \Rightarrow \quad -\text{PQ}_u + \text{PQ}_d + 2\text{PQ}_S = 0, \quad (2.137)$$

is allowed by the $\mathcal{G}(\text{SM}) \otimes U(1)_{\text{PQ}}$. Note that the existence of this term imposes a constrain on the PQ charges, as shown in the RHS of the above equation. Now, because

of the presence of the mixing term in Eq. 2.137, one of the global symmetries is explicitly broken. The two remaining symmetries give rise to two GBs after SSB: one of them, a combination of the CP-odd fields living in the doublets, will become the longitudinal d.o.f. of the Z boson, and the other GB, a combination of the CP odd fields of all scalars, including the one suppressed by the arbitrarily large scale, will be our axion, as we show in the following. After the SSB of the global symmetries in the scalar potential, the CP-odd component of the neutral scalars can be written as a function of the GBs:

$$H_u^0 \supset \frac{v_u}{\sqrt{2}} e^{ia_u/v_u} = \frac{v_u}{\sqrt{2}} e^{i(q\hat{a}_Z + PQ_u\hat{a})}, \quad (2.138)$$

$$H_d^0 \supset \frac{v_d}{\sqrt{2}} e^{ia_d/v_d} = \frac{v_d}{\sqrt{2}} e^{i(q\hat{a}_Z + PQ_d\hat{a})}, \quad (2.139)$$

$$S^0 \supset \frac{v_S}{\sqrt{2}} e^{ia_S/v_S} = \frac{v_S}{\sqrt{2}} e^{iPQ_S\hat{a}}. \quad (2.140)$$

By following the approach adopted in the previous scenario, the orthogonality and normalization conditions fix how the axion is distributed along the CP-odd phases of the scalars:

$$H_u \supset e^{-2i\frac{v_d^2}{v_0^2}\frac{a}{v_S}}, \quad H_d \supset e^{2i\frac{v_u^2}{v_0^2}\frac{a}{v_S}}, \quad \text{and} \quad S \supset e^{-i\frac{a}{v_S}}. \quad (2.141)$$

where, as before, $v_0 = \sqrt{v_u^2 + v_d^2}$. One can remove the above phases from the Yukawa Lagrangian with the PQ symmetry, by rotating them away with the following redefinition of the quarks:

$$d_{L/R} \rightarrow e^{\pm i\frac{v_d^2}{v_0^2}\frac{a}{v_S}} d_{L/R}, \quad \text{and} \quad u_{L/R} \rightarrow e^{\pm i\frac{v_u^2}{v_0^2}\frac{a}{v_S}}, \quad (2.142)$$

that generates a shift in the $G\tilde{G}$ term, according to Eq. 2.111:

$$\mathcal{L}_{\text{DFSZ}} \supset \frac{\alpha_S}{8\pi} \left(\bar{\theta} + N \frac{a}{v_S} \right) G_{\mu\nu}^a \tilde{G}_a^{\mu\nu}, \quad \text{where} \quad N = 3 \times 2 \left(\underbrace{\frac{1}{2} \times \frac{v_d^2}{v_0^2}}_{u_L} + \underbrace{\frac{1}{2} \frac{v_u^2}{v_0^2}}_{d_L} \right) = 6, \quad (2.143)$$

where Eq. 2.112 has been applied to compute the anomalous factor. In this case, the reader can identify from the topological term that the PQ scale is $f_a = v_S/6$. Note that

the invisible axion models act as a seesaw in the sense that, the larger the v_{ev} of the singlet scalar, the larger the PQ scale and the more suppressed will be the interactions. In this way, as Fig. 2.13 shows, one can easily avoid the experimental bounds but, on the contrary, nothing about the axion mass can be inferred.

2.2.4.2 KSVZ mechanism

Another equivalent implementation of the invisible axion models, proposed by J. Kim [130] and independently by M. Shifman, A. Vainshtein and V. Zakharov [131] in 1979, is to realize the PQ mechanism by the existence of an axion that does not couple to ordinary quarks at tree level. In this case, the SM sector remains untouched: there is only one Higgs doublet, our SM Higgs, interacting with the SM quarks. As the previous mechanism, a scalar SM singlet needs to be introduced in order to decouple the PQ scale from the EW scale, but as argued before, due to the gauge symmetries, this singlet does not interact with the SM quarks so that a $aG\tilde{G}$ term cannot be generated. But, what if the matter content is enlarged by introducing new color fermions whose quantum numbers are such that their interaction with the scalar singlet is allowed? This is the idea of the KSVZ mechanism and its implementation is very straightforward! The scalar potential in this case enjoys two global symmetries for the neutral fields,

$$V_{\text{KSVZ}} = V(|H_{\text{SM}}^0|^2, |S^0|^2), \quad (2.144)$$

that will be spontaneously broken and will consequently generate two GB. In this case, since there is no mixing portal, the axion only lives in the singlet scalar. The new color fermions, that by the symmetries of the Lagrangian are allowed to interact with the singlet, can be used to rotate away the axion from such interaction and directly generate a $G\tilde{G}$ term, according to Eq. 2.111:¹⁷

$$- \mathcal{L}_{\text{KSVZ}} \supset Y_Q \overline{Q}_L Q_R S + \text{h.c.} \xrightarrow{\text{SSB } U(1)_{\text{PQ}}} \mathcal{L}_{\text{KSVZ}} \supset \frac{\alpha_s}{8\pi} \left(\bar{\theta} + N \frac{a}{v_S} G_a^{\mu\nu} \tilde{G}_{\mu\nu}^a \right). \quad (2.145)$$

¹⁷Note that in this case the axion couples directly to the colored fermions, so that no mixing term between scalars is needed. From this perspective, the mechanism is pretty clean.

The PQ scale can be identified as $f_a = v_S/N$, so that one can suppress the axion interactions to taste since v_S is not bounded a priori to any scale. The later saves the theory from being ruled out but makes it loose their appeal.

As we have seen, both the DFSZ and the KSVZ allow to implement the PQ mechanism in a realistic way. However, in contradistinction to its precedent PQWW, in the context of invisible axion models the axion mass cannot be predicted since the vev of the singlet scalar is not linked to any concrete scale, which leave us with a vast range of orders of magnitudes to seek for the axion mass. In Chapter 7, we will show how these invisible axion models can be embedded in a self-consistent theory such that the predictive power of the PQWW is recovered.

2.2.5 Misalignment mechanism

We motivated the axions from their potential to solve two of the SM problems at once: the strong CP problem, already discussed in the previous subsections, and the amount of DM in the universe. Let us see how those curious particles, although having an extremely light mass, can behave as cold DM candidates. In this subsection we describe the misalignment method, proposed by several authors in Refs. [132–134] in 1982, which takes profit of the fact that the axion mass, as well as the expansion rate of the universe, are dynamical parameters which depend on the temperature, or from another perspective, on the time.

By varying the action in a Friedman-Roberston-Walker (FWR) universe, the equation of motion for the axion field at the zero momentum mode reads as

$$\ddot{a} + 3H\dot{a} + \underbrace{m_a^2 a + \mathcal{O}(a^2)}_{V'(a)} = 0, \quad (2.146)$$

where we parametrize the axion field initial value by some angle $a_0 = \bar{\theta}_0 f_a$. We should remind the reader that, as we discussed in the previous sections, the axion mass depends on the temperature; the mass is generated by QCD instanton effects, which are strongly suppressed at temperatures above Λ_{QCD} . In that sense, from $\Lambda_{\text{QCD}} < T < \Lambda_{\text{PQ}}$ axions can be considered massless. In that regime, the QCD dynamics has not set yet

$\bar{\theta} = 0$, so that there is no motivation for any special $\bar{\theta}_0$ and the initial value could take any random value between $[0, 2\pi]$.¹⁸

In the early universe, $H(T) \gg m_a(T)$ so that Eq. 2.146 behaves as an over-damped harmonic oscillator, with $a = f_a \bar{\theta}_0$, as Fig. 2.14 illustrates. As the universe cools down,

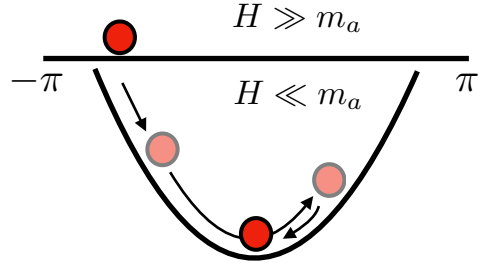


Figure 2.14: Naive illustration of the misalignment mechanism.

at a certain temperature that we will label as *critical*, $H(T_c) \sim m_a$, Eq. 2.146 becomes an under-damped harmonic oscillator instead, whose solution is given by

$$a(t) = A_0 e^{-\frac{3}{2}Ht} \cos(m_a t) \equiv A_0 R(t)^{-3/2} \cos(m_a t), \quad (2.147)$$

where in the last step, the scale factor $R(t) \equiv e^{H(t)}$ has been introduced for simplicity. By ignoring the transition regime between the over- and sub- damped oscillators and matching the solutions from both regimes at T_c , the above equation can be rewritten as

$$a(t) = \bar{\theta}_0 f_a \left(\frac{R(T_c)}{R(t)} \right)^{3/2} \cos(m_a t), \quad (2.148)$$

so that the axion field oscillates coherently. The energy density restored in these oscillations is given by

$$\begin{aligned} \rho_a(t) &= \frac{1}{2} m_a(t) a(t)^2 = \frac{1}{2} m_a(t) \bar{\theta}_0^2 f_a^2 \left(\frac{R(T_c)}{R(t)} \right)^3 \cos^2(m_a t) \\ &= \rho_a(T_c) \frac{m_a(t)}{m_a(T_c)} \left(\frac{R(T_c)}{R(t)} \right)^3. \end{aligned} \quad (2.149)$$

¹⁸In this section, as well as in Chapter 7, we will assume that the PQ scale is broken before inflation takes place, i.e. pre-inflationary scenarios.

The reader might have noticed that once $T < \Lambda_{\text{QCD}}$ and the axion mass settles down, the energy density scales as R^{-3} , so that, in spite of having a tiny mass, axions behave as non-relativistic matter! We note that, whereas the $\rho_a \propto R^{-3}$ dependence only holds in the regime where m_a is constant, the axion number density, i.e. the number of axions per comoving volume, is conserved since $n_a(t) = \rho_a(t)/m_a(t) \sim R^{-3}$.

Assuming that since the axion field began to oscillate there has been no entropy production, we can compute n_a/s at T_c and estimate the contribution of the energy from the axion field oscillations to the relic abundance in the universe, which is roughly given by [118]

$$\Omega h^2 \sim 0.01 \bar{\theta}_0^2 \left(\frac{f_a}{10^{11} \text{ GeV}} \right)^{1.19}. \quad (2.150)$$

Notice that, for an initial misalignment angle of $\bar{\theta}_0 \sim \mathcal{O}(1)$, the PQ scale is expected to be of order $f_{\text{PQ}} \sim \mathcal{O}(10^{12})$ GeV. This would set a lower bound for the PQ scale if we assume that the misalignment mechanism is the only source contributing to the total relic density observed in the universe. Even if this is the case, there is no problem in having a scale larger than 10^{12} GeVs as long as $(f_a/\text{GeV})\bar{\theta}_0^2 \sim 10^{12}$ holds.

2.2.6 Direct detection of dark matter axions

Under the motivation pointed out in the previous sections, many laboratory experiments have been searching axions since their proposal. Colliders were able to rule out the EW axion but, after the invisible axion models appeared as a way out to evade these bounds, the hope to experimentally reach such high scales at accelerators faded out. The situation, however, positively changed when, in 1983, P. Silfvik proposed in Ref. [135] two techniques towards the invisible axion hunt:

- *Helioscopes*: These experiments aim to detect axions produced in the Sun. Examples of helioscopes: the one in Brookhaven [136], in Tokyo [137–139], and CAST at CERN [140].
- *Haloscopes*: These experiments aim to detect axions from the hypothetical DM galactic halo. Examples of haloscopes: that in Brookhaven [141, 142], in Florida U. [143] which later became ADMX, and CARRACK in Japan, among others.

See Refs. [144,145] for nice reviews on axion detecting techniques. In Fig. 2.15, extracted from Ref. [144], we show the current limits imposed by helioscopes, haloscopes and laboratory experiments on the m_a - $g_{a\gamma\gamma}$ plane, being the later defined in Eq. 2.123. Because the $g_{a\gamma\gamma}$ is inversely proportional to the PQ scale, there is a correlation between $g_{a\gamma\gamma}$ and m_a in the QCD-axion models, shown by a yellow band in this figure.¹⁹ Owing

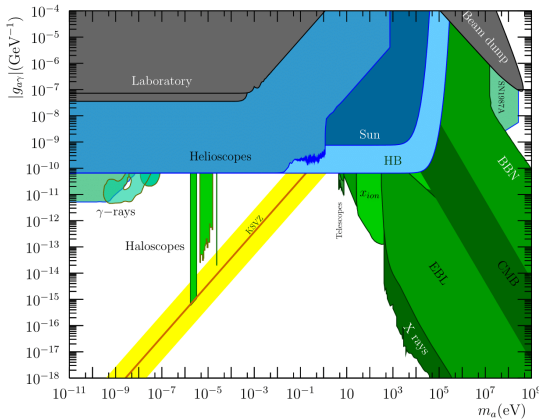


Figure 2.15: Review of experimental constraints in the overall $(g_{a\gamma}, m_a)$ plane. In gray, laboratory axion experiments, in blue bounds from helioscopes, and in green bounds from haloscopes. *Figure extracted from Ref. [144] (updated in 2018).*

to the fact that we will study DM axions in Chapter 7 we will focus on the second technique. Haloscopes exploit the coherence effects driven by the fact that DM axions behave as coherent classical fields to detect them. As we have seen in the previous subsection, DM axions are highly non-relativistic. Therefore, from the dispersion relation for free axion waves, $\omega = \sqrt{|\vec{p}_a|^2 + m_a^2}$, being \vec{p}_a their momentum, the non-relativistic limit can be taken as follows:

$$\omega = m_a \left(1 + \frac{v^2}{2} + \mathcal{O}(v^4) \right) \Rightarrow \frac{\Delta\omega}{\omega} \sim 10^{-6}. \quad (2.151)$$

Such small relative spread in frequency implies that axions are almost monochromatic. Besides, in last subsection we have also estimated the axion number density. Unlike

¹⁹The rest of the parameter space corresponds to the so-called axion-like particles. Those are pseudo-GBs arising from the breaking of global $U(1)$ symmetries that are not related with QCD at all, i.e. do not interact with gluons and their mass is not defined by the QCD instantons. We will not consider axion-like particles since they do not solve the strong CP problem.

²⁰For a recent determination of the velocity dispersion at the Earth's position using N -body simulations see Ref. [146].

WIMPs, which behave like a dilute gas of particles that eventually bump into a detector, axions have a much higher number density. They behave as a Bose condensate since large DM number densities imply macroscopic occupation numbers for each quantum state [54]. Therefore, it is appropriate to treat $a(t)$ as a coherent classical field, which taking into account Eqs. 2.148 and 2.149, can be written as

$$a(t) = \frac{\sqrt{2\rho_a}}{m_a} \sin(m_a t), \quad (2.152)$$

whose amplitude is determined from $\rho_a(T_0) = m_a(T_0)a(T_0)^2/2$ (being T_0 the current temperature in the universe). In most of the experiments, it is common to assume that the contribution from axions to the local energy density is 100%, i.e. $\rho_a \sim \rho_{\text{DM}}$ where $\rho_{\text{DM}} \approx 0.4 \text{ GeV/cm}^3$ [85,147–149] is the local DM energy density. However, we should keep in mind that any signal in reality depends on the product $\rho_{\text{DM}} \tilde{\rho}_a$ rather than ρ_{DM} , being $\tilde{\rho}_a$ the fraction of the total local density comprised by ρ_a .

The coherent oscillations of the DM-axions can be exploited by designing experiments whose signals are enhanced in the presence of a certain axion mass by a resonant effect. Let us take into account the interacting Lagrangian for axions with photons and nucleons that will be the basis for DD experiments,

$$\mathcal{L}_a^{\text{eff}} \supset \boxed{-\frac{g_{a\gamma\gamma}}{4} a F_{\mu\nu} \tilde{F}^{\mu\nu}} + \sum_n g_{aNN} (\partial_\mu a) \bar{\Psi}_n \gamma^\mu \gamma_5 \Psi_n - a F_{\mu\nu} \sum_n \frac{g_{aD}}{2} (i \bar{\Psi}_n \sigma^{\mu\nu} \gamma_5 \Psi_n) \quad (2.153)$$

where we included to the interacting Lagrangian from Eq. 2.122 the dimension 5 term proportional to g_{aD} , responsible for the hadronic EDMs; $g_{a\gamma\gamma}$ parametrizes the axion-photon coupling (see Eq. 2.123), and g_{aNN} parametrizes the coupling to nuclear spins. The later is generated from the transition from g_{af} interaction in Eq. 2.122 at the quark level to the nucleon level. The framed term in red is proportional to $F_{\mu\nu} \tilde{F}^{\mu\nu} \equiv 4(\vec{E} \cdot \vec{B})$. Therefore, in the presence of a magnetic field, an axion can be converted into a photon. Such conversion can be resonantly enhanced by using microwave cavities with a high quality factor Q .

Conventional axion haloscopes consists of a high-Q microwave cavity subjected to a homogeneous external magnetic field B_0 , as such produced in the cavity surrounded by

magnets shown in Fig. 2.16. When the resonant frequency of the cavity ω_c matches the

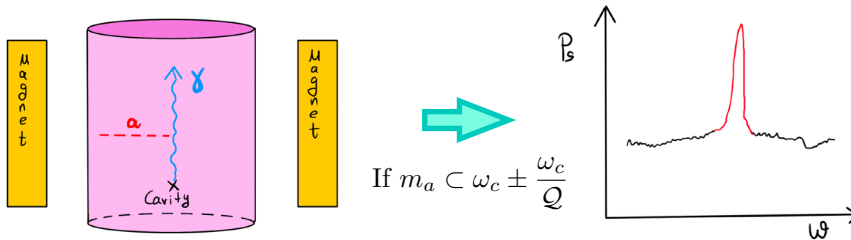


Figure 2.16: Illustration about the methodology of high- Q microwave cavity experiments.

axion mass, the axion-photon conversion experiments an enhancement proportional to the quality factor of the cavity. The signal power P_s in the band $m_a \pm m_a/Q$ is given by

$$P_s \propto \frac{Q}{m_a} g_{a\gamma\gamma}^2 B_0 |G_m|^2 V \rho_a, \quad (2.154)$$

where G_m parametrizes the geometry of the cavity resonant mode (see Ref. [144] for more details) and V quantifies the volume of the cavity. Notice that this kind of experiments based on axion-photon conversion are actually sensitive to the product $g_{a\gamma\gamma} \sqrt{\rho_{\text{DM}} \tilde{\rho}_a}$. On the other hand, the signal of the noise is proportional to m_a , which makes this technique less efficient at heavy axion masses, i.e. high frequencies.

As we just explained, the conventional cavity haloscopes rely on matching the axion mass with the resonant frequency of the cavity. However, going to lower frequencies requires larger cavity volumes. In principle there is hope on building high- Q cavities with large volume but it becomes experimentally challenging to fabricate powerful magnets of large dimensions to surround them, so that low axion masses are difficult to access with such technique. However, what if we decouple the volume of the detector from the axion frequency/mass? That is the brilliant idea on which experiments like ABRACADABRA and CASPER are based. We present them in the two following subsections before closing this chapter.

2.2.6.1 ABRACADABRA

A Broad / Resonant Approach to Cosmic Axion Detection with an Amplifying B-field Ring Apparatus (ABRACADABRA) ²¹ was proposed at MIT, as the name itself suggests, to detect cosmic axions. It exploits the modifications induced by the axion in the Maxwell equations [150,151]. Indeed, the presence of the axion field and its interaction with photons modifies the QED Lagrangian in the following way:

$$\mathcal{L}_{\text{QED}} = -\frac{1}{4}F_{\mu\nu}F^{\mu\nu} - \frac{1}{4}g_{a\gamma\gamma}aF_{\mu\nu}\tilde{F}^{\mu\nu}, \quad (2.155)$$

which leads to the new Maxwell's equations [135] listed below:

$$\begin{aligned} \nabla \cdot \vec{E} &= -g_{a\gamma\gamma}\vec{B} \cdot \nabla a & \vec{\nabla} \cdot \vec{B} &= 0 \\ \nabla \times \vec{E} &= -\frac{\partial \vec{B}}{\partial t} & \vec{\nabla} \times \vec{B} &= \frac{\partial \vec{E}}{\partial t} - g_{a\gamma\gamma} \left(\vec{E} \times \nabla a - \frac{\partial a}{\partial t} \vec{B} \right). \end{aligned} \quad (2.156)$$

Because the local viral velocity of the DM in our galaxy is about $v \sim 10^{-3}$, it will give small gradients $\nabla a \propto v$ so that we can neglect them in the above equations.

In the presence of a static magnetic field, i.e. \vec{B}_0 , and neglecting ∇a , there is no electric field present so that $\partial \vec{E} / \partial t \approx 0$. ²² In this context, the Ampere's law reads

$$\nabla \times \vec{B} = g_{a\gamma\gamma} \frac{\partial a}{\partial t} \vec{B}_0, \quad (2.157)$$

which, under the presence of an oscillating axion field and a static magnetic field as shown in Eq. 2.152 generates an *effective electric current* given by

$$J_a^{\text{eff}} = g_{a\gamma\gamma} \sqrt{2\rho_{\text{DM}}} \cos(m_a t) \vec{B}_0. \quad (2.158)$$

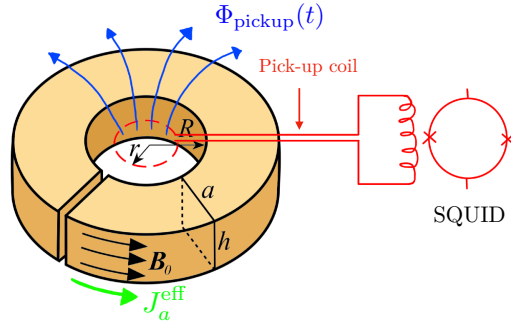
where we have assumed, as ABRACADABRA does, $\tilde{\rho}_a = 1$ (otherwise the obtained bounds of the experiment should be scaled). The above effective current in turn sources a magnetic field oscillating at frequency m_a , perpendicular to \vec{B}_0 , according

²¹Jesse Thaler, one of the members of ABRACADABRA, is a big fan of playing Scrabble.

²²This is known as the Magneto Quasi-Static limit, where either the magnetic induction or the electric displacement current are neglected. At higher axion masses, i.e. higher frequencies, displacement currents could be generated.

to Ampere's law. Therefore, one can hope to test such oscillating flux, proportional to $\sqrt{\rho_{\text{DM}}}$ (assuming $\tilde{\rho}_a \sim 1$) by using a magnetometer. The later is what ABRACADABRA does. The static magnetic field is generated by a superconducting wire wrapping a toroid. The toroidal geometry enjoys the advantage of having the readout region in the center of it, where there is ideally zero static magnetic field. Furthermore, by introducing a small GAP in the toroid, the parasitic capacitance effects that may generate displaced currents can be reduced. The geometry of the experiment is shown in Fig. 2.17. The

Figure 2.17: Geometry of the ABRACADABRA experiment. Image adapted from Ref. [150].



oscillating magnetic flux can be detected with a superconducting pickup loop in the hole of the toroid. For a pickup loop radius smaller than the inner radius of the toroid, the flux is given by

$$\Phi_{\text{pickup}}(t) = g_{a\gamma\gamma} B_{\text{max}} \sqrt{2\rho_{\text{DM}}} \cos(m_a t) V_B, \quad (2.159)$$

where B_{max} is the magnitude of the static field at the inner radius and therefore depends on the geometric factors of the toroid, as well as the effective volume V_B , which quantifies the volume containing the external magnetic field. Note that the magnetic flux is proportional to $g_{a\gamma\gamma}$, which in turn is inversely proportional to the PQ scale, so that an extremely sensitive quantum limited field sensor is required to detect it. ABRACADABRA uses a Super Conducting Quantum Interference Device (SQUID), which is able to reach magnetic sensitivities of $\mathcal{O}(10^{-18})$ T. ABRACADABRA follows two readout approaches on the magnetic flux generated by the hypothetical axion field:

- *Broadband approach:* The magnetometer is untuned. The pickup loop is coupled directly into the SQUID input and all frequencies are acquired at once. This

approach has an enormous advantage: it is able to search all frequencies simultaneously, or at least those not limited by noise.²³ The lower bound on the signal reach of the broadband approach goes as follows,

$$g_{a\gamma\gamma} > [\text{experiment factors}] \left(\frac{m_a}{t} \right)^{1/4} \text{SQUID}_{\text{noise}}, \quad (2.160)$$

where t is the integration time of the axion classical field. Note that the sensitivity to $g_{a\gamma\gamma}$ increases at smaller m_a . On the other hand, the noise of the SQUID scales as $\text{SQUID}_{\text{noise}} \propto 1/m_a$ and dominates below 50 Hz, as the blue line in Fig. 2.18 shows, setting the floor of the experimental reach.

- *Resonant approach:* The magnetometer is tuned. A resonator is inserted into the circuit in order to enhance resonantly the signal before the SQUID noise is introduced. The enhancement of the signal is proportional to the quality factor Q of the resonator. In this case, the sensitivity to the $g_{a\gamma\gamma}$ goes as,

$$g_{a\gamma\gamma} > [\text{experiment factors}] \left(\frac{1}{m_a t} \right)^{1/4}, \quad (2.161)$$

which improves with the time spent on each frequency band and worsens for lower axion masses, since at low frequencies, lower Q factors are required to make sure that the bandwidth matches the interrogation time. The clear disadvantage of this approach relies on the choice of a certain frequency to amplify.

In Fig. 2.18 we show the projected bounds for the ABRACADABRA experiment [150, 151]. A prototype detector ABRACADABRA-10 cm has been launched, following a broadband approach, and the first results appeared in 2018 [152, 153] from the data taken during a month (July-August from that year). In those, a huge amount of noise correlated with the vibration of a plate was found below 10 Hz. Although the reach of the Run-I results is still below the limits from the CAST helioscope, a broad range of frequencies was successfully accessed and, after technical improvements, the ABRACADABRA collaboration plans to reach the projected sensitivities. Note that they

²³At large frequencies / masses the MQS approximation breaks down and displacement currents would screen out the signal.

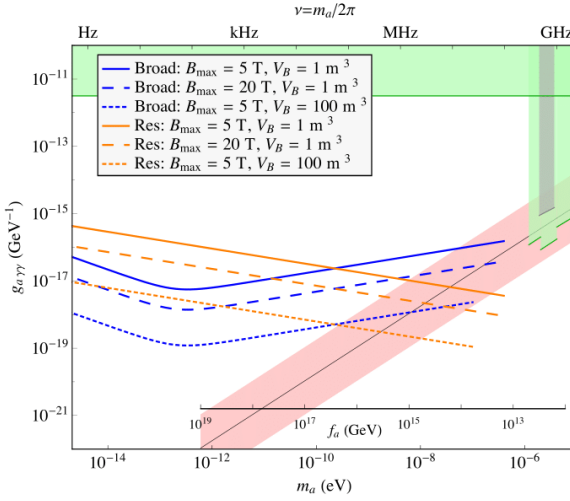


Figure 2.18: Bounds of the ABRACADABRA experiment. In blue (orange) the projected bounds for the broadband (resonant) approaches under some benchmark points for the experimental factors are displayed. The red band shows the QCD axion parameter space. Other projected sensitivities are shown shaded in light green. Published limits from ADMX are shown in gray. *Figure extracted from Ref. [150].*

aim to falsify part of the QCD axion band, including the interesting scale of axions predicted from Grand Unified Theories, which will be addressed in Chapters 6 and 7.

2.2.6.2 CASPEr

Apart from the coupling mediating the electromagnetic interaction between the photon and the axion, $g_{a\gamma\gamma}$, there are two other couplings through which the axion could be accessed. Those are the interaction between the axions and nucleons,

$$\mathcal{L}_a^{\text{eff}} \supset -\frac{g_{a\gamma\gamma}}{4} F_{\mu\nu} \tilde{F}^{\mu\nu} a + \sum_n g_{aN} (\partial_\mu a) \bar{\Psi}_n \gamma^\mu \gamma_5 \Psi_n - a F_{\mu\nu} \sum_n i \frac{g_{aD}}{2} (i \bar{\Psi}_n \sigma^{\mu\nu} \gamma_5 \Psi_n), \quad (2.162)$$

to which the experiment CASPEr is, in principle, sensitive. The Cosmic Axion Spin Precession Experiment aims to detect axion DM by using Nuclear Magnetic Resonance (NMR) techniques [154–156]. The NMR works as follows. In the presence of a magnetic field, \vec{B}_0 , the spin states of a fermion split by an amount of $g_n \mu_N B_0$ as the left panel of Fig. 2.19 shows. In the previous expression g_n is the nuclear Landé factor and μ_N is the nuclear magneton. The spins are polarized in a volume of the sample. Let us consider now a radiofrequency (RF) magnetic field perpendicular to \vec{B}_0 , oscillating at a frequency ω_{RF} . When $\hbar \omega_{\text{RF}} = g_n \mu_N B_0$, a resonant effect allows the RF magnetic field

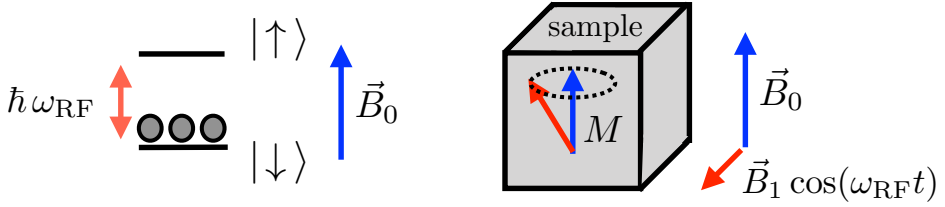


Figure 2.19: Nuclear Magnetic Resonant techniques. On the left panel, the split generated between the spin states by the external magnetic field. When such GAP matches the frequency of the RF magnetic field, a resonant phenomenon occurs. On the right panel, an illustration of the consequences from such resonant effect are shown: the magnetisation of the sample deviates from its initial orientation and precesses.

to flip spins! Under these circumstances, the sample magnetization tilts and precesses, as the right panel of Fig. 2.19 illustrates. A magnetometer located next to the sample could detect the magnetic field created by such precessing magnetization. These NMR techniques are very useful for non-invasive imaging and studying of the molecular structure. Besides, they can be applied to detect DM axions as the CASPER experiment does. CASPER acts as a NMR experiment with no RF magnetic field. Instead, the axion DM is the responsible for flipping the spins.

The CASPER experiment splits in two branches according to the coupling they aim to probe: CASPER electric and CASPER wind. Here, we briefly discuss for convenience the CASPER electric experiment, led by the Boston university group, which aims to measure the EDM coupling g_{aD} . Such term in the Lagrangian from Eq. 2.162, framed in blue, describes at low energies an oscillating nuclear EDM, $\vec{d}_n(t)$, generated by $a(t)$ along the direction of the nuclear spin $\vec{\sigma}_n$:

$$\vec{d}_n(t) = g_{aD} a_0 \cos(m_a t) \vec{\sigma}_n = g_{aD} \frac{\sqrt{2\rho_{\text{DM}}}}{m_a} \cos(m_a t) \vec{\sigma}_n, \quad (2.163)$$

that interacts with an external electric field \vec{E} . Here, we have also assumed that $\tilde{\rho}_a = 1$, as CASPER does. The non-relativistic Hamiltonian that describes such interaction is

given by

$$\mathcal{H}_{\text{EDM}} = -\vec{d}_n(t) \cdot \vec{E} = \vec{\sigma}_n \cdot \underbrace{(g_{aD} a_0 \vec{E} \cos(m_a t))}_{\vec{E}^*(t)}. \quad (2.164)$$

The reader should be reminded that, according to the modified Maxwell equations in 2.156, the presence of an electric field perpendicular to \vec{B}_0 induces a magnetic field that will play the role of the RF magnetic field (B_1 in the right panel of Fig. 2.19). The magnetisation, and consequently the amplitude of the NMR signal, will be proportional to the tilt angle of the spins. The latter depends on the amplitude of the EDM, given by Eq. 2.163. In this context, the magnetization can be written as

$$M \propto n P E^* \frac{g_{aD}}{m_a} \sqrt{2\rho_{\text{DM}}}, \quad (2.165)$$

where n is the spin density, P is the thermal polarization (see Ref. [156]), E^* is the effective electric field present in the sample. For CASPER electric, a ferroelectric crystal is used as a sample, since it enjoys a permanent elastic polarization that creates a strong effective internal electric field \vec{E}^* with which an axion induced EDM can interact.

In Fig. 2.20 the projected bounds for CASPER electric are displayed. Notice that it aims to search a wide range of masses and couplings, and that Phases II and III will be sensitive to the QCD axion band from GUT scales down to the Planck scale, although those still rely on technical improvements. The ultimate sensitivity limit is given by the nuclear spin noise of the sample, marked with a red shaded line in the figure.

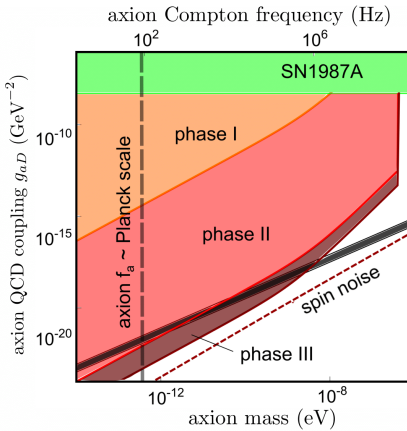


Figure 2.20: Experimental reach of CASPER Electric. The green band is excluded by astrophysical observations. Orange, red, and maroon regions show sensitivity projections in Phase I, II and III, respectively. The fundamental quantum sensitivity limit is given by magnetization noise, shown by the dashed red line. Figure extracted from Ref. [156].

3.- Gauging Baryon and Lepton Numbers

Let us imagine that we are cooking the tasty SM. For that, we add the needed ingredients, i.e. three families of charged leptons, neutrinos and quarks. We follow the known recipe by building the most general Lorentz symmetric structures imposing gauge invariance under $SU(3)_c \otimes SU(2)_L \otimes U(1)_Y$ and, on top of that, we season it by adding the Higgs boson. *Voilà!* We have ended with the well-known Standard Model Lagrangian. However, as any good meal, there might be some features emerging in the final outcome. In this case, surprisingly, some extra symmetries which we did not ask for arise when building it. Since nobody expected them a priori, they are

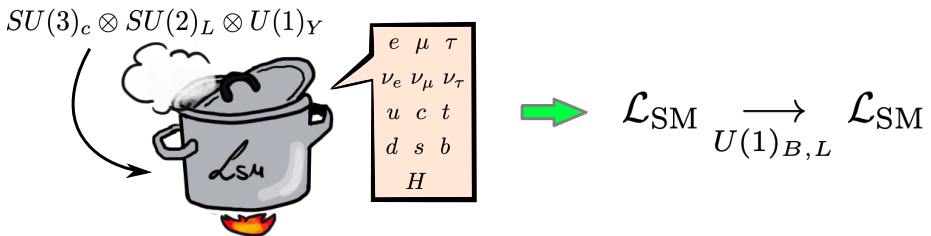


Figure 3.1: Global symmetries such as total baryon and lepton number as well as flavour lepton number and combinations of them emerge unexpectedly from the matter content and symmetries of the SM. They are called *accidental symmetries*.

known as accidental symmetries. Those are total baryon (B) and lepton (L) numbers, and consequently any linear combination of them, as well as lepton flavour number L_i . Particularly, as will be properly addressed in Sec. 3.1, $B-L$, $B - 3L_i$ and $L_i - L_j$ are anomaly free. Leptons in the SM have leptonic charge 1, while quarks have baryonic charge $1/3$, since three of them are needed to give birth to a baryon. Their transformation

under such global symmetries is given by

$$(\ell_L, e_R) \rightarrow e^{in_L}(\ell_L, e_R) \quad \text{and} \quad (q_L, u_R, d_R) \rightarrow e^{in_B}(q_L, u_R, d_R). \quad (3.1)$$

Therefore, in the context of the SM, both lepton and baryon numbers are conserved at the classical level. Notice that at the quantum level, in the SM the $SU(2)_L$ instantons break baryon and lepton number by three units, although such interactions are highly suppressed. However, they are just global symmetries, and we expect them to be broken at some scale, as cosmology suggests.¹ Nowadays, we are aware that the SM cannot be the ultimate theory. For instance, in Chapter 1 we saw that neutrinos are massive and, therefore, lepton flavour number is violated by neutrino oscillations. From the low energy perspective, we should think of the SM as a part of an EFT expansion, i.e. an infinite tower of operators built from the SM material, respecting the SM local symmetries. These higher dimensional operators are generated by the effect of the NP in the UV, and are in turn suppressed by subsequent powers of the NP scale as follows,

$$\mathcal{L} = \mathcal{L}_{\text{SM}} + \frac{1}{\Lambda} \mathcal{O}^{\Delta L=2} + \sum_i \frac{\mathcal{O}_i^{(6)}}{\Lambda^2} + \sum_{n=7}^{\infty} \sum_j \frac{\mathcal{O}_j^{(n)}}{\Lambda^{n-4}}. \quad (3.2)$$

As discussed in Chapter 1, the first and unique dimension five operator in the above expansion is the Weinberg operator, responsible for the Majorana neutrino mass generation. Notice that this interaction violates total lepton number in two units, so that it would be forbidden if lepton number was a good symmetry of the Lagrangian. Beyond the Weinberg operator, higher dimension effective operators violating baryon or lepton number could be present, such as the dimension-6 operator $qqq\ell$ [10].² This particular operator mediates the decay of the proton and, if present, predicts the existence of a *great desert* between the EW and the NP scales of about thirteen orders of magnitude. Such enormous energy gap is needed in order to satisfy the existing experimental bounds on the decay of the proton, which will be later discussed in

¹Violation of baryon number is one of the Sakharov conditions [157] for generating the observed matter-antimatter asymmetry in the universe.

²Those appear in theories like GUTs, where quarks and leptons are forced to live in the same representations and, therefore, the baryon and lepton number are explicitly broken.

Chapter 6. Particularly, for the $p \rightarrow \pi e^+$ channel [158],

$$\tau_p \geq 10^{34} \text{ yr} \quad \Rightarrow \quad \Lambda_B \gtrsim 10^{15} \text{ GeV.} \quad (3.3)$$

In other words, these interactions must be suppressed by a scale at least twelve orders of magnitude larger than the EW scale! This would be very depressing in the sense that no one would ever hope to falsify these theories, being such scale far away from our experimental scope.

At this stage, we may be wondering whether the existence of a *great desert* is really necessary. Indeed, in QFT anything that is not forbidden will eventually happen. Baryon and lepton numbers are merely global symmetries and nothing guarantees those to be respected by non-renormalizable effects. However, the non-observation of neutrinoless double beta decay ($\Delta L = 2$), $\tau_{\beta\beta} > 10^{25}$ years,³ and the decay of the proton ($\Delta B = 1$), $\tau_p > 10^{32} - 10^{34}$ years,⁴ indicates that the total lepton and baryon numbers are very good symmetries in nature. So, what if there is no need to suppress such *dangerous* interactions? What if the reason we have not seen the proton decaying yet is because such process is actually forbidden? On the other hand, we need to understand the breaking of baryon number to account for baryogenesis. What if these baryon and lepton accidental symmetries are the remnant of some unaccounted local gauge symmetry that was broken at a certain scale?

In 1973, A. Pais suggested the possibility to gauge baryon number in Ref. [161]. Although he was the pioneer in presenting such brilliant idea, he did not manage to propose a theory for $U(1)_B$. Other attempts to gauge baryon and lepton numbers were done in Refs. [162–165], being Ref. [166] the first realistic model on local baryon number ever proposed. However, this model and further proposals from Refs. [167, 168] are currently (partially) ruled out by experiment, as we will mention later. The phenomenological study presented in the upcoming Chapters 4 and 5 is based on the theories proposed in Refs. [169,170] and Refs. [171,172], whose content is introduced along this chapter.

³For a review on neutrinoless double beta decay see Ref. [159].

⁴For a review on proton decay in several scenarios for beyond the SM, see Ref. [160].

3.1 Anomaly cancellation

Symmetries of the classical Lagrangian are not always preserved in the full quantum theory, as we already noticed along this thesis. Such anomalies lead to explicit violation of the Ward identities. In the context of global symmetries, the presence of anomalies does not really constitute a problem. However, if these symmetries are local, the violation of the Ward identities breaks the consistency of the theory; in the presence of such anomalous terms, gauge invariance is not further preserved. Therefore, if we aim to gauge the accidental symmetries previously presented, special care must be taken in ensuring that the corresponding local theory is consistent.

We saw in Chapter 2 that chiral currents are dangerous because, although being conserved classically in the limit of massless fermions, they can obtain a non-zero divergence at the one-loop level when coupled to two gauge currents [102,173]. Such anomalous term is known as the chiral anomaly, and we already showed its result in the context of abelian theories (see Eq. 2.106), which must be generalized to non-abelian theories if we are aiming to enlarge the SM gauge group.

The relevant Green functions where the above anomaly appears are the three-point functions involving an axial current,⁵ i.e. $\langle j_\mu^A j_\nu^V j_\rho^V \rangle$. The later arise in the triangle graphs shown below, where the roman letters refer to the generators of the SM gauge group that participates in the current, being X, Y and Z = 1, 2 and 3 for $U(1)_Y$, $SU(2)_L$ and $SU(3)_c$, respectively:

$$\begin{array}{c}
 \begin{array}{c}
 \text{X} \text{---} \gamma_\mu \gamma_5 \text{---} \bullet \\
 \diagup \quad \diagdown \\
 \bullet \quad \bullet \\
 \diagdown \quad \diagup \\
 \gamma_\nu \quad \gamma_\rho \\
 \text{---} \text{Y} \quad \text{---} \text{Z}
 \end{array}
 \quad + \quad
 \begin{array}{c}
 \text{X} \text{---} \gamma_\mu \gamma_5 \text{---} \bullet \\
 \diagdown \quad \diagup \\
 \bullet \quad \bullet \\
 \diagup \quad \diagdown \\
 \gamma_\nu \quad \gamma_\rho \\
 \text{---} \text{Y} \quad \text{---} \text{Z}
 \end{array}
 \quad . \quad (3.4)
 \end{array}$$

These diagrams lead to an anomalous term spoiling the Ward identities proportional to

$$A[X, Y, Z] \equiv \text{Tr}\{T_L^X \{T_L^Y, T_L^Z\}\} - \text{Tr}\{T_R^X \{T_R^Y, T_R^Z\}\}, \quad (3.5)$$

⁵As shown in Eq. 2.106, a two-point correlation function is not enough for generating the anomalous term regarding the Lorentz structure.

to which we will refer as *anomaly factor*. In the above expression, the trace is taken over all fermionic d.o.f. participating in the triangle diagram. The anticommutator arises as a consequence of the two possible momentum routings displayed in Diags. 3.4.

As first proved by Adler and Bardeen [174], gauge anomalies are 1-loop exact:⁶. Furthermore, explicit calculations [175, 176] show that, although they can occur also in box and pentagon one-loop diagrams with an odd number of axial couplings, the contribution to the anomaly is exactly the same as for the one-loop triangle diagram introduced above. Therefore, if we ensure through the symmetry group or particle content of the theory that the coefficient $A[X, Y, Z]$ from Eq. 3.5 vanishes, we can be sure about the consistency of the gauge theory.

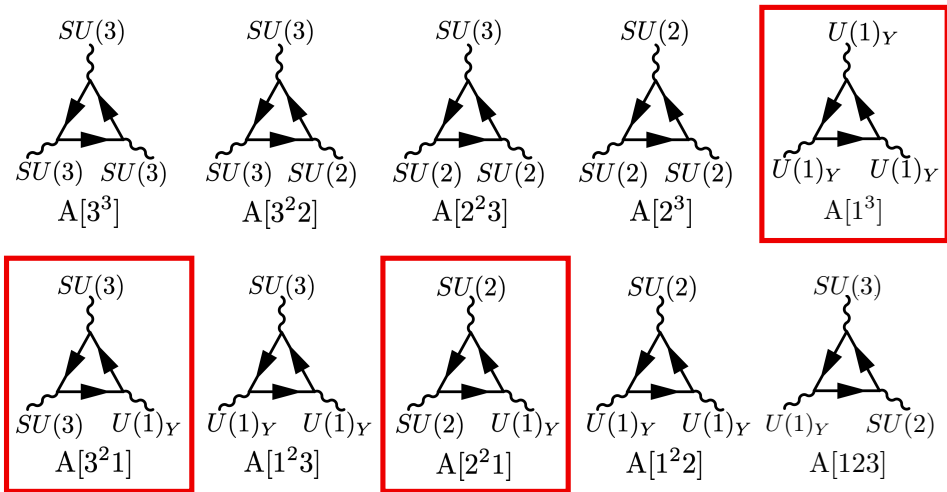


Figure 3.2: Possible gauge anomalies in the context of the SM gauge group. Anomaly cancellation of the red framed diagrams is ensured by the choice of hypercharges and the number of colors in the SM.

In Fig. 3.2, all possible 1-loop triangle combinations among the spin-1 fields in the SM are listed. Fortunately, most of them vanish for symmetry reasons. In addition, one must make sure that the gravitational anomaly vanishes too, i.e. $A[2]$, $A[3]$ and $A[1]$, where the last one is not trivially zero and imposes restrictions among the hypercharges

⁶This is a consequence of the non-renormalization theorem [174]: if the one-loop diagrams are anomaly-free, all higher-order diagrams are anomaly free.

of the SM matter content. The cases where only one generator from a non-abelian gauge group (Pauli matrices and Gell-Mann matrices for $SU(2)_L$ and $SU(3)_c$, respectively) is participating, i.e. $A[2^2 3]$, $A[3^2 2]$, $A[1^2 2]$, $A[2]$, $A[3]$ and $A[1^2 3]$, have a null anomaly factor due to the traceless nature of the $SU(N)$ generators. The triangle diagrams involving pure non-abelian gauge generators are, in the context of the SM, kind of special: the $SU(3)_c$ gauge group manifests solely vector interactions with the SM fermion content so that the contributions from LH and RH quarks exactly cancels, whereas the group $SU(2)_L$ is a pseudo-real group since the fundamental representation behaves as the anti-fundamental one under a gauge transformation. Therefore, in principle the only non-zero anomaly factors could come from the red framed diagrams in Fig. 3.2 and the $A[1]$ from the gravitational anomaly.

Starting from the combination of two $SU(2)_L$ generators and the hypercharge one, we have

$$A[2^2 1] = N_f \sum_{f_L} Y_{f_L} \text{Tr} \left\{ \mathbb{I} \left\{ \frac{\sigma^a}{2}, \frac{\sigma^b}{2} \right\} \right\}, \quad (3.6)$$

where $N_f = 3$ is the number of fermion families. We will make use the following identities about the $SU(N)$ generators,

$$\{T^a, T^b\} = \frac{1}{N} \delta^{ab} \mathbb{I} + d_{abc} T^c, \quad \text{or alternatively,} \quad \text{Tr} \{T^a, T^b\} = T_R \delta^{ab}, \quad (3.7)$$

where d_{abc} ⁷ is a totally symmetric tensor, N is the dimension of the group, and T_R is the Dynkin index of the representation R . Taking into account that the $SU(N)$ generators are traceless, the anomaly factor reads as

$$\begin{aligned} \Rightarrow A[2^2 1] &= N_f \sum_{f_L} Y_{f_L} \delta_{a,b} \text{mul}_{f_L} \frac{1}{N} = N_f \times \frac{\delta_{ab}}{2} \sum_{f_L} Y_{f_L} \text{mul}_{f_L} \\ &= N_f \times \frac{\delta_{ab}}{2} \left(\frac{1}{6} \times N_c + \left(-\frac{1}{2} \right) \right) \stackrel{N_c=3}{=} 0, \end{aligned} \quad (3.8)$$

where N_c the number of colours and mul_{f_L} is the multiplicity of a given LH fermion under the rest of the groups in the tensor product conforming the SM gauge symmetry

⁷The d_{abc} tensor indeed corresponds to the anomaly factor of a *pure* $SU(N)$ diagram for a given fermion f entering in the loop, i.e. $d_{abc} \equiv 2 \text{Tr} \{ \{T^a, T^b\} T^c \} = A_f^{abc} / 2$.

not considered in $A[X,Y,Z]$. It appears as a consequence of summing over all fermionic d.o.f. entering in the diagram.

Similarly, for the rest of the red framed diagrams,

$$A[3^2 1] = N_f \times \frac{\delta_{ab}}{2} \left(\sum_{f_L} Y_{f_L} \text{mul}_{f_L} - \sum_{f_R} Y_{f_R} \text{mul}_{f_R} \right) \propto \left(\frac{1}{6} \times 2 - \frac{2}{3} + \frac{1}{3} \right) = 0, \quad (3.9)$$

$$\begin{aligned} A[1^3] &= N_f \left(\sum_{f_L} Y_{f_L}^3 \text{mul}_{f_L} - \sum_{f_R} Y_{f_R}^3 \text{mul}_{f_R} \right) \\ &= N_f \left(\left(-\frac{1}{2} \right)^3 \times 2 + \left(\frac{1}{6} \right)^3 \times 2 \times N_c + 1^3 - \left(\frac{2}{3} \right)^3 \times N_c + \left(\frac{1}{3} \right)^3 \times N_c \right) \stackrel{N_c=3}{=} 0, \end{aligned} \quad (3.10)$$

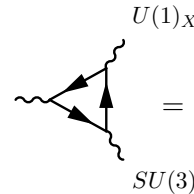
$$\begin{aligned} A[1] &= N_f \left(\sum_{f_L} Y_{f_L} \text{mul}_{f_L} - \sum_{f_R} Y_{f_R} \text{mul}_{f_R} \right) \\ &= N_f \left(-\frac{1}{2} \times 2 + \frac{1}{6} \times 2 \times N_c + 1 - \frac{2}{3} \times N_c + \frac{1}{3} \times N_c \right) \stackrel{N_c=3}{=} 0. \end{aligned} \quad (3.11)$$

Luckily, or rather, *as it could not be otherwise*, the red framed dangerous factors cancel individually, rendering the SM a *safe* and consistent gauge theory.⁸ Nevertheless, when the SM gauge symmetry group is enlarged, nothing guarantees anymore the safeness of the new theory. Particularly, for an extra abelian gauge group, to which we will refer as $U(1)_X$, six extra triangle diagrams arise, which contribute to the anomaly factors as listed below:

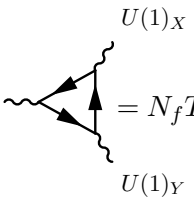
$$\bullet A[2^2 X] \equiv SU(2) \begin{array}{c} \text{---} \\ \diagup \quad \diagdown \\ \text{---} \end{array} \begin{array}{c} U(1)_X \\ \text{---} \\ \diagup \quad \diagdown \\ \text{---} \\ SU(2) \end{array} = N_f \frac{\delta_{ab}}{2} \sum_{f_L} X_{f_L} \text{mul}_{f_L} = N_f \frac{3}{2} \boxed{(3n_B + n_L) \stackrel{!}{=} 0}.$$

⁸Notice that, contrary to the insensitivity of $A[X,Y,Z]$ to the number of families, the consistency of the SM requires $N_c = 3$ colors. Notice also that anomalies in the SM are cancelled because of the particular values of the hypercharges. In other words, anomaly cancellation quantizes the charges of the fermions in the SM!

Here, n_B and n_L represent the charges of the q_L and ℓ_L fields under the new force, respectively. Since in the SM there is only one quark and lepton doublet per family, the anomaly cannot be cancelled unless $n_L = -3n_B$, which is automatically satisfied when the new force is $B-L$ since, in that context, $q_L \sim (3, 2, 1/6, 1/3)$ and $\ell_L \sim (1, 2, -1/2, -1)$. However, for pure lepton or baryon local theories, new fermions in a non-trivial representation of $SU(2)_L$ would be needed. In both cases, the above anomaly factor reads as $A[2^2 B] = A[2^2 L] = 3/2$.

• $A[3^2 X] \equiv$  $= N_f \frac{\delta_{ab}}{2} \left(\sum_{\text{colored } f_L} X_{f_L} \text{mul}_{f_L} - \sum_{\text{colored } f_R} X_{f_R} \text{mul}_{f_R} \right)$
 $= N_f \frac{\delta_{ab}}{2} n_B \left(\sum_{\text{colored } f_L} \text{mul}_{f_L} - \sum_{\text{colored } f_R} \text{mul}_{f_R} \right) = 0.$

In this triangle graph only colored fields contribute. In the last row we have assumed that all quarks are degenerated under the new force. This is, for instance, the case of baryon number, where $n_B = 1/3$. As we can see from above, this anomaly factor is zero for all combinations of baryon (and trivially lepton) number gauge symmetries.

• $A[1^2 X] \equiv$  $= N_f T_R \left(\sum_{f_L} Y_{f_L}^2 X_{f_L} - \sum_{f_R} Y_{f_R}^2 X_{f_R} \right) \propto (3n_B + n_L) \stackrel{!}{=} 0.$

As in the previous case, if all quarks (leptons) are degenerated under the new force, the condition for anomaly cancellation reads $3n_B = -n_L$. Taking into account that $n_B = 1/3$ ($n_L = 1$) for the baryon (lepton) charge of the SM quarks (leptons), one can check that in the context of $U(1)_{B-L}$ the above graph

is anomaly free, while for pure baryon and lepton gauge theories the anomaly factor gives $A[1^2L] = A[1^2B] = -3/2$.

$$\bullet \quad A[X^21] \equiv U(1)_Y \begin{array}{c} U(1)_X \\ \text{---} \nearrow \text{---} \\ \text{---} \searrow \text{---} \\ U(1)_X \end{array} = N_f \left(\sum_{f_L} Y_{f_L} X_{f_L}^2 \text{mul}_{f_L} - \sum_{f_R} Y_{f_R} X_{f_R}^2 \text{mul}_{f_R} \right) = 0.$$

This holds for any new charge common for all leptons or all quarks and would be equivalent to $A[1]$ in the SM applied only to the quark or lepton sector.

$$\bullet \quad A[X^3] \equiv U(1)_X \begin{array}{c} U(1)_X \\ \text{---} \nearrow \text{---} \\ \text{---} \searrow \text{---} \\ U(1)_X \end{array} = N_f \left(\sum_{f_L} X_{f_L}^3 - \sum_{f_R} X_{f_R}^3 \right) = \boxed{3n_L^3 \neq 0}.$$

In the quark sector, the multiplicity of LH d.o.f. matches the fields in the RH sector, so that the anomaly cancellation condition is automatically satisfied when the new charge is common for all quarks. However, in the context of leptons, the matter content in the SM is not symmetric and there is a cubic leptonic charge that does not cancel. This triangle diagram, together with the following one, requires the enlargement of the matter content by a singlet under the SM symmetry group charged as the rest of the leptons, in order not to spoil the rest of anomaly factors. This required d.o.f. $\nu_R \sim (1, 1, 0, n_L)$ can be easily identified as a RH neutrino. Actually, three copies of ν_R are needed for cancellation of the anomalous terms in this diagram and the following one, since $N_f = 3$.

$$\bullet \quad A[X] \equiv U(1)_X \begin{array}{c} g \\ \text{---} \nearrow \text{---} \\ \text{---} \searrow \text{---} \\ g \end{array} = N_f \left(\sum_{f_L} X_{f_L} - \sum_{f_R} X_{f_R} \right) = \boxed{3n_L \neq 0},$$

which also requires the presence of three RH singlets with lepton charge n_L .

The consistency of the theory in the presence of extra gauge symmetries requires cancellation of the gauge anomalies which, in turn, imposes relations among the fermion quantum numbers under the new force and, in most of the cases, predicts the existence of extra matter content. In the context of $B-L$, three RH neutrinos, one per family, are required to render the theory anomaly-free. In that sense, $U(1)_{B-L}$ is strongly connected to neutrino masses, since it is the simplest gauge theory that predicts massive neutrinos. For local baryon and lepton number theories, the matter content must be further enlarged to cancel the extra anomaly factors involving the new mediator, all without spoiling those where the cancellation was already achieved. There are several options for doing that:

- Adding a sequential family where the new quarks have baryonic charge 1 and the new leptons have leptonic charge 3. This option, proposed in Refs. [166,167], is straightforward in the sense that the structure observed in nature is repeated.
- Adding a mirror family. In this case, the new quarks would have baryon number -1 and the leptons, lepton number -3. This option was proposed in Refs. [166,167] too.

Unfortunately, these solutions are in disagreement with collider constraints because the new fermions would get mass from the SM Higgs boson and would change the gluon fusion Higgs production by a factor of 9 [167]. Therefore, both of the above proposals are currently ruled out. Besides, the LHC bounds on the masses of the new fermions are stringent, and the theory suffers from Landau poles for the new Yukawa couplings in the TeV region.

- Adding a fourth generation of vector-like fermions under the SM gauge group, as the authors of Ref. [168] proposed, would avoid Landau poles. In this case, anomaly cancellation requires that the difference between the baryon charges of the new quarks is -1 , whereas the difference of the leptonic charges for the new leptons is -3 . Unfortunately, in this scenario the new charged leptons modify drastically the branching ratio of the Higgs into two photons, reducing it about a factor of 3 [177], so that this proposal is partially ruled out, although the gauged $U(1)_B$ would be still a consistent possibility.

Let us consider instead, following Refs. [169,171], the introduction of new leptons and baryons such that their quantum numbers allow for the simultaneous cancellation of all anomalies listed above and, therefore, define a consistent local theory for baryon or lepton numbers. Looking at the remaining anomalous triangle diagrams in the context of pure $U(1)_B$ or $U(1)_L$, it is straightforward to realize that at least a non-trivial representation of $SU(2)_L$ must be added in order to cancel $A[2^2, X]$. But, of course, adding a non-trivial $SU(2)$ representation implies the addition of more d.o.f. in order to compensate their unavoidable contribution to other triangle diagrams where anomaly cancellation was already satisfied.

3.2 Gauge theories for Baryon and Lepton numbers

Taking into account the comments above, let us specify two simple theories where a minimal set of anomalous (a total of six extra Weyl d.o.f.) is added in order to cancel the $A[2^2 X]$ and $A[1^2 X]$ anomalies (in the case of local lepton number, we are already assuming three generations of ν_R in the matter content so that $A[L]$ and $A[L^3]$ are zero). As we will see, in both cases, a cold DM candidate arises naturally as a prediction of the theory.

3.2.1 Model by Duerr, Fileviez Perez and Wise (DFW)

We could start by adding to the SM the simplest non-trivial $SU(2)_L$ representation: a doublet Ψ_L , charged under the new force. We should keep in mind that this new field will spoil the rest of triangle graphs. Let us add the correspondent chiral partner, a RH doublet Ψ_R , with an opposite $U(1)_X$ charge (otherwise the net contribution to the factor $A[2^2 X]$ would be zero). The extra doublet helps to keep $A[2^3]$ switched off while the choice of charges with flipped signs ensures that $A[X^2 1]$ remains safe. We will also assume, without loss of generality, that the new fields are colorless.⁹ Now, we should care about the anomaly factors where odd powers of the new force contribute, i.e. $A[X]$ and $A[X^3]$, which require the addition of extra d.o.f.. Particularly, inspired by

⁹Alternative solutions with the same number of representations can be found for different color quantum numbers common to the whole new spectra. However, either by cosmological reasons or by making the theory realistic, in these cases the matter content must be further extended. See Ref. [169] for more details.

the SM family structure, we can add $SU(2)_L$ singlets: η_R , η_L , χ_L and χ_R , vector-like under the SM gauge symmetry and charged under $U(1)_Y$ and $U(1)_X$ such that the contribution of the doublet fields in those is cancelled.

The aforementioned fermion content required for anomaly cancellation is listed in Table 3.1, and corresponds to the theory for local baryon and lepton number proposed in Ref. [169], to which we will refer as DFW theory.

Fields	$SU(3)_c$	$SU(2)_L$	$U(1)_Y$	$U(1)_X$
$\Psi_L = (\Psi_L^0, \Psi_L^-)^T$	1	2	-1/2	X_1
$\Psi_R = (\Psi_R^0, \Psi_R^-)^T$	1	2	-1/2	X_2
η_R	1	1	-1	X_1
η_L	1	1	-1	X_2
χ_R	1	1	0	X_1
χ_L	1	1	0	X_2

Table 3.1: Fermionic representations in the DFW model proposed in Ref. [169]. The label $X = B$ or L , where in the last case 3 copies of $\nu_R \sim (1, 1, 0, 1)$ must be also added.

The hypercharges of the new fermions in Table 3.1 should satisfy that

$$Y_\eta^2 + Y_\chi^2 - 2Y_\Psi^2 = \frac{1}{2}, \quad (3.12)$$

imposed by the $A[1^2X]$ factor. In the following, we will stick to the choice $Y_\Psi = -1/2$, $Y_\eta = -1$, and $Y_\chi = 0$ for simplicity. On the other hand, the $A[2^2X]$ require the following relation among the new charges:

$$X_1 - X_2 = -3, \quad (3.13)$$

which is crucial for understanding the relevance of these theories.¹⁰

¹⁰ $A[X]$ and $A[X^3]$ are automatically satisfied regardless of the relation between the baryon / lepton numbers.

The most general Lagrangian under the $\mathcal{G}(\text{SM}) \otimes U(1)_X$ gauge symmetry and the given matter content reads as

$$\mathcal{L} = \mathcal{L}_{\text{SM}} + \mathcal{L}_X, \quad \text{where} \quad \mathcal{L}_X = -\frac{1}{4}B_{\mu\nu}^X B^{\mu\nu,X} - \frac{\sin\epsilon}{2}B_{\mu\nu}B^{\mu\nu,X} + \mathcal{L}_f \quad (3.14)$$

is the kinetic term of the new mediator, being $B_{\mu\nu}^X = \partial_\mu Z'_\nu - \partial_\nu Z'_\mu$ the field strength tensor of the $U(1)_X$ field and ϵ the parameter quantifying the possible kinetic mixing with the hypercharge gauge boson from the SM, which will be discussed in detail in Sec. 4.1.2 from Chapter 4. The interacting Lagrangian reads,

$$\begin{aligned} \mathcal{L}_f^{\text{DFW}} = & i\overline{\chi}_L \not{D}\chi_L + i\overline{\chi}_R \not{D}\chi_R + i\overline{\eta}_L \not{D}\eta_L + i\overline{\eta}_R \not{D}\eta_R + i\overline{\Psi}_L \not{D}\Psi_L + i\overline{\Psi}_R \not{D}\Psi_R \quad (3.15) \\ & -y_1\overline{\Psi}_L H \eta_R - y_2\overline{\Psi}_L i\sigma_2 H^* \chi_R - y_3\overline{\Psi}_R H \eta_L - y_4\overline{\Psi}_R i\sigma_2 H^* \chi_L - Y_\nu \overline{\ell}_L i\sigma_2 H^* \nu_R + \text{h.c.}, \end{aligned}$$

where $D_\mu = \partial_\mu + igW_\mu^a \sigma_a/2 + ig_Y Y B_\mu + ig_X n_X Z'_\mu$, being Y and n_X the $U(1)_Y$ and $U(1)_X$ charges, respectively, of the field on which the covariant derivative acts, and g_Y , g and g_X , and W_μ , B_μ and Z'_μ the strength coupling and the vector bosons of the $SU(2)_L$, $U(1)_Y$ and $U(1)_X$ forces, respectively. The last term in the above Lagrangian should be included when the gauged symmetry is the lepton number.

As Eq. 3.15 manifests, the anomalous are massless fields in this context since no mass term is allowed by the gauge symmetry.

3.2.2 Model by Fileviez Perez, Ohmer and Patel (FOP)

An alternative to the previous procedure towards an anomaly-free $U(1)_{L,B}$ theory is to cancel the contribution of the two $SU(2)_L$ doublets, needed to account for the non-zero $A[2^2 X]$ term, by introducing an extra non-trivial $SU(2)_L$ representation. The adjoint representation does not contribute to the $A[2^3]$ diagram because of its real nature. If chosen hyperchargeless, it does not enter neither in the diagrams involving the $U(1)_Y$ generator. However, it does enter in the $A[2^2 X]$, but the right choice of hypercharges can lead to a simultaneous cancellation of all triangle diagrams within the presence of an extra SM-singlet, charged under the new force. In that sense, this theory, proposed in Ref. [171], is simpler than the one previously introduced regarding the number of representations needed for anomaly cancellation. Furthermore, the baryon

or lepton charges are unambiguously fixed. Note that, as in the previous case, the two different new baryon or lepton charges differ in three units.

Fields	$SU(3)_c$	$SU(2)_L$	$U(1)_Y$	$U(1)_X$
$\Psi_L = (\Psi_L^+, \Psi_L^0)^T$	1	2	1/2	3/2
$\Psi_R = (\Psi_R^+, \Psi_R^0)^T$	1	2	1/2	-3/2
$\Sigma_L = \begin{pmatrix} \Sigma_L^0/\sqrt{2} & \Sigma_L^+ \\ \Sigma_L^- & -\Sigma_L^0/\sqrt{2} \end{pmatrix}$	1	3	0	-3/2
χ_L	1	1	0	-3/2

Table 3.2: Fermionic representations in the model proposed in Ref. [171]. The label $X = B$ or L , where in the last case 3 copies of $\nu_R \sim (1, 1, 0, 1)$ must be also added.

In this context, the Lagrangian corresponds to that given in Eq. 3.14 with now,

$$\begin{aligned} \mathcal{L}_f^{\text{FOP}} = & i\overline{\chi_L}\not{D}\chi_L + i\text{Tr}\{\overline{\Sigma_L}\not{D}\Sigma_L\} + i\overline{\Psi_L}\not{D}\Psi_L + i\overline{\Psi_R}\not{D}\Psi_R \\ & -y_1\overline{\Psi_R}H\chi_L - y_2H^\dagger\Psi_L^T C\chi_L - y_3H^\dagger\Sigma_L^T C\Psi_L - y_4\overline{\Psi_R}\Sigma_L H + \text{h.c.}, \end{aligned} \quad (3.16)$$

where $D_\mu\Sigma_L = \partial_\mu\Sigma_L + ig[W_\mu^a\sigma_a/2, \Sigma_L] - i\frac{3}{2}g_X\Sigma_L$ for the $SU(2)_L$ triplet. We note that here, as in the previous case, the anomalous are massless, what renders the theory unrealistic unless a mechanism for their mass generation is implemented.

3.3 Spontaneous breaking of local B and L symmetries

We now understand how anomaly free theories for baryon and lepton numbers can be promoted to local quantum field theories. In the case of B - L , all extra triangle anomalies are automatically cancelled by adding three copies of a RH neutrino. Since the $\nu_R \sim (1, 1, 0, 1)$ can get a Dirac mass through the Yukawa interaction with the Higgs boson, there is no phenomenological need to break this symmetry. The reader may complain about the existence of a massless neutral gauge boson Z_{BL} in such case; however, it should be stressed the possibility for the B - L generator to acquire mass

through the Stueckelberg mechanism, thus letting the gauge symmetry untouched.¹¹ Although the Stueckelberg mechanism constitutes a successful way out to render abelian anomaly-free theories realistic, this is not the case for pure local baryon and lepton numbers. In contrast with $U(1)_{B-L}$, new fermion fields are required in order to ensure anomaly cancellation in $U(1)_B$ and $U(1)_L$. As we have seen in the previous section, the gauge symmetry does not allow a mass term for these fields in the Lagrangian, whereas a realistic theory requires them to be massive in order to satisfy the experimental constraints. The later can be achieved by adding an extra scalar, singlet under the SM but feeling the new symmetry, which will allow us to understand how baryon and lepton number local symmetries can be spontaneously broken. In both scenarios, the later can be achieved by adding a scalar boson S_X , singlet under the SM gauge group and charged under the new force, where $X = L$ or B . This scalar can acquire a vev via the following scalar potential:

$$V_X = -\mu_X^2 |S_X|^2 + \lambda_X |S_X|^4 + \lambda_{HX} H^\dagger H |S_X|^2. \quad (3.17)$$

The SSB generates a mass term for the anomalous through the following interactions in the Duerr, Fileviez Perez and Wise model,

$$-\mathcal{L}_S^{\text{DFW}} = V_S + \lambda_\Psi \overline{\Psi}_L \Psi_R S_X + \lambda_\eta \overline{\eta}_R \eta_L S_X + \lambda_\chi \overline{\chi}_R \chi_L S_X + \text{h.c.} \quad (3.18)$$

On the other hand, in the Fileviez Perez, Ohmer and Patel proposal, \mathcal{L}_S is given by,

$$-\mathcal{L}_S^{\text{FOP}} = V_S + \lambda_\Psi \overline{\Psi}_L \Psi_R S_X + \lambda_\chi \chi_L^T C \chi_L S_X + \lambda_\Sigma \text{Tr}\{\Sigma_L^T C \Sigma_L\} S_X + \text{h.c.} \quad (3.19)$$

Notice that anomaly cancellation, which constrains the relation among their quantum numbers under the new force, in both cases accomplishes the following relation,

$$|\Delta X| = |X_L^{\text{field}} - X_R^{\text{field}}| = 3 \quad (\text{if Majorana } |2X_L^{\text{field}}| = 3) \quad \Rightarrow \quad S_X \sim (1, 1, 0, 3), \quad (3.20)$$

which fixes the charge of the new scalar boson and, consequently, how lepton and baryon numbers are violated. From the above we can conclude that, in these theories,

¹¹For a review on the Stueckelberg mechanism, see Refs. [178,179].

the baryon or lepton number is broken in three units, curiously in the same amount as in the SM! This is indeed good news for us! By gauging baryon number the gauge symmetry protects the stability of the proton. However, as previously mentioned, there is evidence in the universe that requires the violation of baryon number: the matter-antimatter asymmetry, according to Sakharov's criterium [157]. For $U(1)_B$, we have seen that we are actually forced to spontaneously break the local symmetry in order to generate masses for the enlarged matter sector. Amazingly, the consistency of the theory predicts such breaking to occur in three units! In other words, the dangerous dimension-6 operators with $\Delta B = 1$ remain forbidden and the proton is stable to any order in perturbation theory.¹² The previous statement has a strong consequence: there is no need for a great desert since no suppression is needed, so that in principle the baryon force can be broken at the low scale. On the other hand, the theory allows us to understand the spontaneously breaking of baryon number.

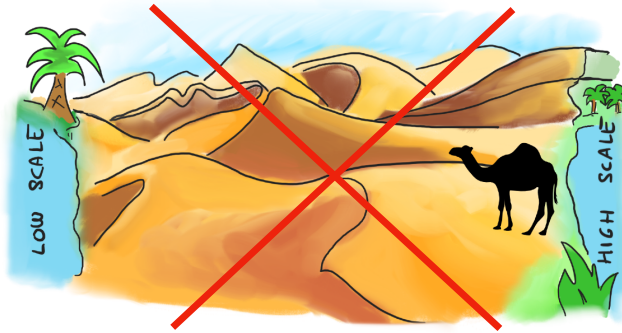


Figure 3.3: The fact that in these simple theories for local $U(1)_B$ the baryon number is broken in three units renders the proton stable so that there is no need to postulate a great desert between the EW and the scale of NP. *Image adapted from Ref. [180].*

Another striking prediction of the spontaneous breaking of $U(1)_{L,B}$ is the existence of a cold DM candidate. The lightest fermion from the new sector is automatically stable, and its stability is a consequence of the baryon or lepton gauge symmetry. When the new force is spontaneously broken, a remnant global symmetry protects the

¹²The reader may wonder about the allowed $\frac{1}{\Lambda_B^{12}} \mathcal{O}^{\Delta B=3}$ operators, that could mediate the decay of the tritium. However, as they are suppressed by twelve powers of the NP scale, $\Lambda_B \sim \Lambda_{EW}$ would still be consistent with the current experimental bounds.

lightest new fermion from decaying; such symmetry is a \mathcal{Z}_2 when Majorana fermions are involved (FOP), while it promotes to a $U(1)_X$ in the presence of Dirac fermions (DFW for $X_1 \neq -X_2$). This is an unexpected and highly appreciated present from these theories, given the need to understand the relic abundance in the universe (see Chapter 2 for more details). It should be emphasized that, in this context, the prediction of a DM candidate is a pure consequence of requiring anomaly cancellation, and that there is no need to impose to the theory any discrete symmetry by hand. Finally, it should be also stressed that in these theories the mass of the DM candidate is determined by the scale of lepton or baryon number violation, and therefore it is connected to the mass of the new mediator. As we will see in the following chapters, this connection has dramatic consequences for such scale.

This class of theories will be discussed in detail in Chapters 4 and 5, being the first chapter devoted the study of local baryon number and the last one, to gauge theories involving the lepton number.

3.4 Experimental lower bound on the NP scale

At this point, the reader might be convinced that these theories could exist in nature being an attractive justification for the existence of the accidental symmetries in the SM, providing an answer to the DM abundance in the universe that the SM cannot satisfy, predicting the stability of the proton and allowing us to understand the origin of dynamical baryon and lepton number violation. In the context of gauged lepton number, they naturally account for neutrino masses too. Despite that, some skepticism may still be reflected under thoughts like *Would be nice if these theories exist, but if they really do, would I notice them?* In the scenario where $B-L$ remains as an unbroken local theory, there are indirect ways to track their unavoidable footprints in the phenomenology, as it will be later discussed in Chapter 5. However, for the broken gauge theories, regardless of the new fermions arising as a consequence of anomaly cancellation, there is a clear representative to look for: a massive gauge boson, Z' , whose mass will define the baryon or lepton number violation scale. Surely, the possibility to notice these theories is closely related to the capacity of our *eyes* (the current set of experiments we dispose) to detect such particle, in other words, to achieve such scale.

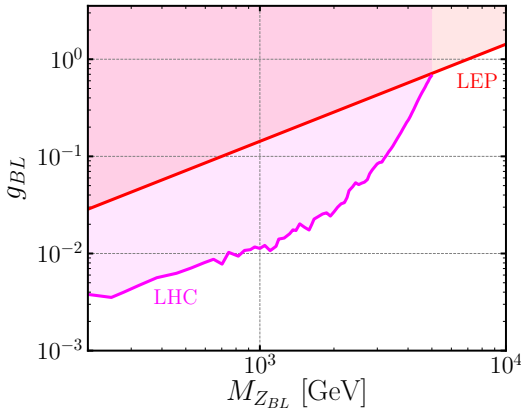


Figure 3.4: Summary of the collider bounds in the $U(1)_{B-L}$ scenario in the $g_{BL}-M_{Z_{BL}}$ plane. The red line corresponds to the bound from LEP [181], while the pink line corresponds to dilepton searches at the LHC with $\sqrt{s} = 13$ TeV and 36.1 fb^{-1} [182]. *Figure extracted from Ref. [183].*

The experimental bounds on an abelian massive gauge boson depend on the nature of its interactions with the SM particles. For a Z' coupling to leptons, there is a pretty strong bound coming from the LEP collider [181] ,

$$\frac{M_{Z_L}}{g_L} \geq 7 \text{ TeV}, \quad (3.21)$$

where g_L refers to the coupling associated to a leptophilic abelian gauge boson Z_L .

This bound relies on the coupling with leptons, and hence, it can also be applied to the gauge coupling g_{BL} and boson Z_{BL} from $U(1)_{B-L}$. Furthermore, dilepton searches at the LHC can also be used to constrain the $U(1)_{B-L}$ scenario; particularly, the result from ATLAS for center-of-mass energy $\sqrt{s} = 13$ TeV and 36.1 fb^{-1} of integrated luminosity [182] is relevant in the region $M_{Z_{BL}} \lesssim 4$ TeV. In Fig. 3.4, the LHC and LEP bounds are shown in the $g_{BL}-M_{Z_{BL}}$ plane. As it can be appreciated, if the gauge coupling is of order one, $g_{BL} \approx 1$, the gauge boson must be heavier than 7-8 TeV.

A different and more hopeful scenario takes place when a leptophobic gauge boson is considered, which would be the case for the generator of $U(1)_B$. When tracking the outcome signals, jets are not as clean as leptons and, therefore, the bounds placed by colliders are weaker for a leptophobic gauge boson. Fig. 3.5 shows a collection of the relevant LHC bounds, placed by both ATLAS and CMS, on a leptophobic gauge boson Z_B which is assumed to interact with the SM quarks according to the following

coupling:

$$-\mathcal{L} \supset \frac{1}{3} g_B \bar{q}_i \gamma_\mu Z_B^\mu q_i, \quad (3.22)$$

where $1/3$ is the baryon charge of any quark q_i in the SM. According to Fig. 3.5, there

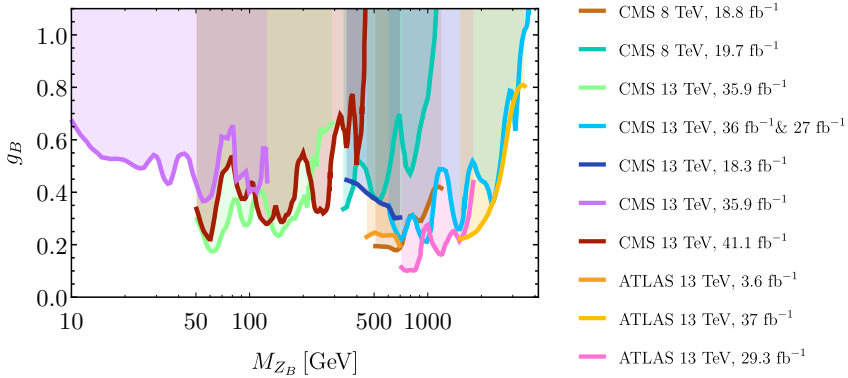


Figure 3.5: Experimental bounds for the leptophobic gauge boson Z_B . Those correspond to the CMS analyses (8 TeV and 18.8 fb^{-1} [184], 8 TeV and 19.7 fb^{-1} [185], 13 TeV and 35.9 fb^{-1} [186,187] and 41.1 fb^{-1} [187], 13 TeV and 36 fb^{-1} & 27 fb^{-1} [188], 13 TeV and 18.3 fb^{-1} [189]), and ATLAS results (13 TeV and 3.6 fb^{-1} and 29.3 fb^{-1} [190]). *Figure adapted from Refs. [191,192].*

is full of room for a light Z_B boson with a *not so-weak* coupling to matter! Indeed, if such light boson exists, the LHC has enough potential to discover it; there is no reason for waiting years and years aiming to see NP in future colliders because we do already have *the tool* to explore in more detail the parameter space where these theories could live. In order to close the chapter with an optimistic feeling, let us highlight here two concrete examples of dijet bounds on a leptophobic gauge boson, collected in Fig. 3.6. The left panel corresponds to the bound placed by ATLAS to a dijet mass distribution for $\sqrt{s} = 13 \text{ TeV}$ and 29.3 fb^{-1} in the range $450 < M_{Z_B} < 1800 \text{ GeV}$ [190], while the right panel shows the statistically combined CMS data from 2016 and 2017 on the limits in the mass vs. coupling plane for $50 < M_{Z_B} < 220 \text{ GeV}$ [187]. As the reader can distinguish from both figures, there is a small excess greater than 2σ around $M_{Z_B} = 1 \text{ TeV}$ (left panel) and a 2.2 standard deviations from the background-only expectation in $M_{Z_B} = 115 \text{ GeV}$ (right panel). The excess in the left panel arises only when the

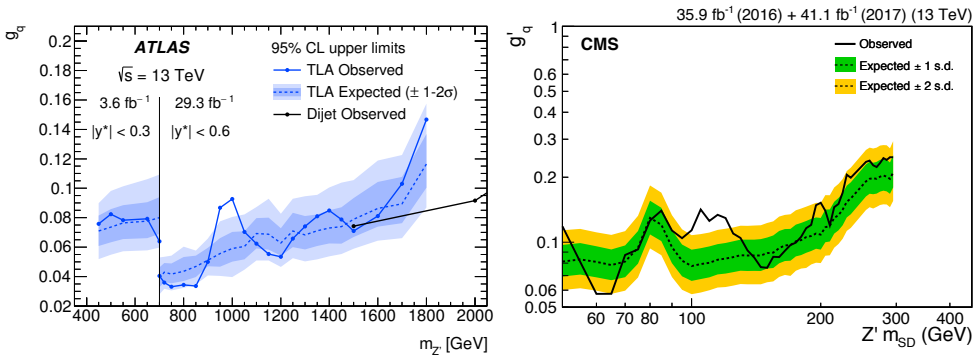


Figure 3.6: Bounds from ATLAS [190] (left panel) and CMS [187] (right panel) on the mass vs. coupling plane. The plots show an excess around 1 TeV in the left panel and at 115 GeV in the right panel.

background estimation takes into account the concrete $U(1)_B$ model while the excess of the right panel, which was a 2.9σ deviation for 2016, was not confirmed with the 2017 data set, where there is a local deviation of 0.5σ . Although they probably disappear with patience and more statistics, these bumps illustrate the capacity of our current detectors to see such class of gauge bosons.

To summarize, experimental bounds on a Z' bring hope to still detect local baryon and lepton number theories at scales close or even below the EW scale. These bounds provide themselves the answer to the skeptical reader *Yes, you can notice them*. And it is not as if these theories were lacking of motivation! They allow one to understand the origin of the accidental symmetries in the SM, they can predict missing pieces of the SM puzzle such as neutrino masses or a so-aimed DM candidate. Let us close this chapter with a spoiler that may increase even more the motivation of the reader: as it will be addressed in Chapters 4 and 5, in the context of the most motivated theories where the lightest neutral anomalon plays the role of a DM candidate, the theory *has to live* at the low scale. Hence, our answer can be rectified to *Yes, you will notice these theories!* And hopefully this chapter itself exposed enough reasons to convince the reader that those are perfect candidates to be under the spotlight of the phenomenological and experimental research.

4.- Leptophobic Force

Chapter based on the work done in 1810.06646, 1904.01017 and 2003.09426.

In Chapter 3, the possibility of promoting the global symmetries baryon and lepton number to local theories was discussed. In here, we will focus solely on the first option. In the SM, the so-called baryon number is an accidental global symmetry at the classical level which is broken at the quantum level by the $SU(2)$ instantons in three units. In theories for physics beyond the SM, there are two possibilities for baryon number violation: 1) Explicit breaking, and 2) Spontaneous Violation. The baryon number is explicitly broken in theories such as the Minimal Supersymmetric SM (MSSM), where one can have the so-called R-parity violating terms, or in Grand Unified Theories, where we have the unification of quarks and leptons in the same representations and the symmetry is broken at the very high scale $M_{\text{GUT}} \geq 10^{15}$ GeV. The only way to understand the spontaneous breaking of baryon number is to think about theories where the baryon number is a local symmetry. Let us summarize here the main features of those, discussed in Chapter 3:

- Simple anomaly free theories based on $U(1)_B$ can be defined, where the consistency of the theory predicts the stability of the proton. In the context of these theories, there is no need to postulate the existence of a great desert between the EW and the NP scales.
- One predicts the existence of a cold DM candidate in this context. It is protected by a remnant global symmetry after SSB and its mass is defined by the scale of the new force.

- The spontaneous breaking of baryon number at the low scale is possible in agreement with all experimental bounds in particle physics and cosmology, without the need of hiding the theory behind a very small gauge coupling.

In this chapter we provide a detailed study of the properties of a leptophobic cold DM candidate based on a local $U(1)_B$ and analyze the strong cosmological implications on this class of gauge theories.

4.1 Theoretical framework

The aim of this section is to build from the common key features of the motivated models for local baryon number a simplified model containing the relevant DM candidate interactions. For that, we should first understand the SSB of baryon number and the nature of the predicted cold DM candidate.

4.1.1 Spontaneous symmetry breaking

In order to generate masses for the fermions composing the new sector, as discussed in Chapter 3, a scalar boson $S_B \sim (1, 1, 0, n_B)$ with baryon charge $n_B = 3$ has to be introduced. It should be reminded that n_B is fixed by anomaly cancellation, which requires the difference between the two different baryon charges of the anomalous to be 3 units, as shown in Eq. 3.13. This relation is a key prediction of the theory; the proton is absolutely stable, and therefore, the symmetry can be broken at the low scale. The spontaneous breaking of $U(1)_B$ (also of the EW gauge group) can be triggered through the following scalar potential, which is composed of the SM scalar potential plus that from Eq. 3.17 with $X = B$:

$$V = -\mu_H^2 H^\dagger H + \lambda_H (H^\dagger H)^2 - \mu_B^2 |S_B|^2 + \lambda_B |S_B|^4 + \lambda_{HB} (H^\dagger H) |S_B|^2. \quad (4.1)$$

Therefore, in the unitary gauge, the scalar bosons read,

$$H = \frac{1}{\sqrt{2}} \begin{pmatrix} 0 \\ h + v_0 \end{pmatrix}, \quad \text{and} \quad S_B = \frac{1}{\sqrt{2}} (s_B + v_B). \quad (4.2)$$

By taking into account that the $vevs$ are non-zero in the zero temperature vacuum of the theory, which is required for the theory to be phenomenologically viable [193], the minimum conditions read as,

$$-\mu_H^2 + \lambda_H v_0^2 + \lambda_{HB} \frac{v_B^2}{2} = 0, \quad \text{and} \quad -\mu_B^2 + \lambda_B v_0^2 + \lambda_{HB} \frac{v_B^2}{2} = 0, \quad (4.3)$$

which lead to the following $vevs$,

$$v_0^2 = 2 \frac{\mu_B^2 \lambda_{HB} - 2\mu_H^2 \lambda_B}{\lambda_{HB}^2 - 4\lambda_B \lambda_H}, \quad \text{and} \quad v_B^2 = 2 \frac{\mu_H^2 \lambda_{HB} - 2\mu_B^2 \lambda_H}{\lambda_{HB}^2 - 4\lambda_B \lambda_H}. \quad (4.4)$$

For this solution to be a minimum, according to the conditions stated by the second partial derivative test,

$$\begin{vmatrix} \frac{\partial^2 V}{\partial \langle H \rangle^2} & \frac{\partial^2 V}{\partial \langle H S_B \rangle^2} \\ \frac{\partial^2 V}{\partial \langle S_B H \rangle^2} & \frac{\partial^2 V}{\partial \langle S_B \rangle^2} \end{vmatrix} \propto \begin{vmatrix} 2\lambda_H & \lambda_{HB} \\ \lambda_{HB} & 2\lambda_B \end{vmatrix} > 0, \quad \text{and} \quad \frac{\partial^2 V}{\partial \langle H \rangle^2} > 0, \quad (4.5)$$

and imposing the potential to be bounded from above, we should require that

$$\lambda_H > 0, \quad \lambda_B > 0, \quad \text{and} \quad \lambda_H \lambda_B - \frac{1}{4} \lambda_{HB}^2 > 0. \quad (4.6)$$

Furthermore, perturbativity of the couplings appearing in Eq. 4.1 further imposes:

$$\lambda_H \leq 4\pi, \quad \lambda_B \leq 4\pi, \quad \text{and} \quad \lambda_{HB} \leq 4\pi. \quad (4.7)$$

After SSB, the mass matrix for the Higgs bosons reads as,

$$\mathcal{M}_0^2 = \begin{pmatrix} h & s_B \end{pmatrix} \begin{pmatrix} v_0^2 \lambda_H & v_0 v_B \lambda_{HB} \\ v_B v_0 \lambda_{HB} & v_B^2 \lambda_B \end{pmatrix} \begin{pmatrix} h \\ s_B \end{pmatrix}, \quad (4.8)$$

which must be diagonalized in order to find the physical states. The latter are given by

$$h_1 = h \cos \theta_B + s_B \sin \theta_B \quad \text{and} \quad h_2 = s_B \cos \theta_B - h \sin \theta_B, \quad (4.9)$$

where the mixing angle, θ_B , is determined from the rotation that brings the mass matrix in Eq. 4.8 to its eigenbasis, defined by

$$\tan 2\theta_B = \frac{\lambda_{HB}v_0v_B}{\lambda_Hv_0^2 - \lambda_Bv_B^2}. \quad (4.10)$$

Collider searches of a new scalar that mixes with the Higgs combined with measurements of Higgs properties provide constraints on the mixing angle [194,195]. In our study, the mass of the second Higgs is above the EW scale, and hence, we take the bound

$$\sin \theta_B \leq 0.3. \quad (4.11)$$

The masses of the physical fields (eigenvalues of Eq. 4.8) are given by

$$\begin{aligned} M_{h_1}^2 &= \lambda_Hv_0^2 + \lambda_Bv_B^2 - (\lambda_Bv_B^2 - \lambda_Hv_0^2) \left(1 + \frac{\lambda_{HB}^2v_0^2v_B^2}{(\lambda_Hv_0^2 - \lambda_Bv_B^2)^2} \right)^{1/2}, \\ M_{h_2}^2 &= \lambda_Hv_0^2 + \lambda_Bv_B^2 + (\lambda_Bv_B^2 - \lambda_Hv_0^2) \left(1 + \frac{\lambda_{HB}^2v_0^2v_B^2}{(\lambda_Hv_0^2 - \lambda_Bv_B^2)^2} \right)^{1/2}, \end{aligned} \quad (4.12)$$

where the expressions listed in Eq. 4.4 were taken into account. The above relations allow us to rewrite the quartic couplings in the scalar potential as a function of the Higgs masses and the mixing angle, as follows:

$$\lambda_H = \frac{1}{4v_0^2} [M_{h_1}^2 + M_{h_2}^2 + (M_{h_1}^2 - M_{h_2}^2) \cos 2\theta_B] < 4\pi, \quad (4.13)$$

$$\lambda_B = \frac{1}{4v_B^2} [M_{h_1}^2 + M_{h_2}^2 + (M_{h_2}^2 - M_{h_1}^2) \cos 2\theta_B] < 4\pi, \quad (4.14)$$

$$\lambda_{HB} = \frac{1}{2v_0v_B} (M_{h_1}^2 - M_{h_2}^2) \sin 2\theta_B < 4\pi, \quad (4.15)$$

where in the last part of the above equations we have imposed the perturbative bounds on the scalar couplings in the Higgs sector (see Eq. 4.7). Taking these constraints into account, together with the conditions to ensure the vacuum stability of the scalar potential stated in Eq. 4.6, restrictions between the masses of the new scalar and the new mediator, M_{h_2} and M_{Z_B} , and the scalar mixing angle θ_B unavoidably appear. On the left panel in Fig. 4.1 the allowed parameter space in the M_{h_2} - M_{Z_B} plane is shown

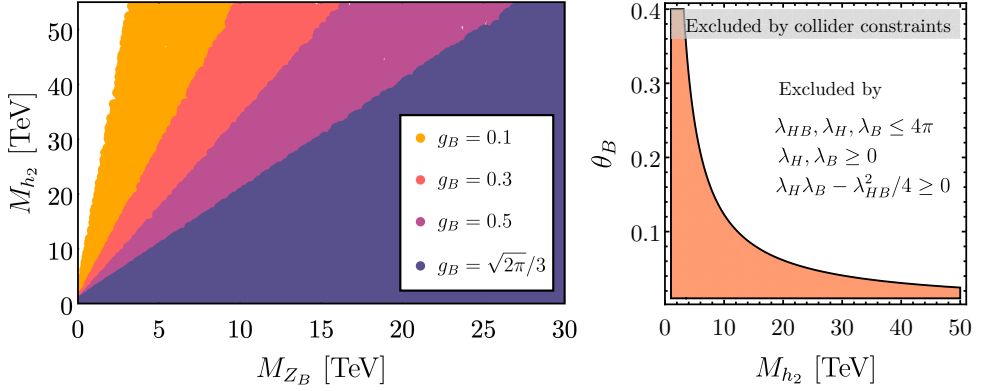


Figure 4.1: On the left panel, parameter space in the M_{h_2} - M_{Z_B} plane allowed by perturbativity bounds, $\lambda_H, \lambda_B, \lambda_{HB} \leq 4\pi$, and the condition from Eq. 4.6. Here, the different colors correspond to the different values for the gauge coupling g_B according to the legend. On the right panel, the available h_2 masses as a function of the scalar mixing angle θ_B are shaded in orange, as a consequence of the condition from Eq. 4.13. In gray, the parameter space ruled out by the phenomenological bound on the scalar mixing angle $\sin \theta_B \leq 0.3$ is displayed.

for different values of the new gauge coupling g_B . As the figure shows, for a given M_{Z_B} , i.e. for a certain baryon violation scale, there is an upper bound for the M_{h_2} , which depends on g_B . Furthermore, Eq. 4.13 allows us to determine the upper bound on the new Higgs mass as a function of the mixing angle θ_B , as the right panel of Fig. 4.1 shows. Remarkably, for the maximum mixing angle allowed, the second Higgs cannot be heavier than 3.5 TeV, regardless of the baryon number breaking scale.

Once the theory undergoes SSB, fermions acquire mass through the Yukawa interactions, and the gauge bosons of the broken symmetries acquire mass from the covariant derivative of the scalars responsible of breaking such symmetries,

$$(D_\mu S_B)^\dagger (D^\mu S_B) \supset -\frac{1}{2} g_B^2 n_B^2 v_B^2 Z_{B\mu} Z_B^\mu, \quad (4.16)$$

where $n_B = 3$ is the charge of the scalar breaking $U(1)_B$. Hence, the mass term of the new gauge boson is given by

$$M_{Z_B} = 3g_B v_B. \quad (4.17)$$

We note that M_{Z_B} defines the scale of baryon number violation. It couples only to quarks and to the new baryons from the theory, i.e. we have a leptophobic gauge boson.

4.1.2 Kinetic Mixing

The simultaneous presence of two or more abelian gauge symmetries allows for a mixing term among their field strength tensors in the Lagrangian. Particularly, in our case we expect kinetic mixing between the $U(1)_Y$ and $U(1)_B$ gauge groups, as we showed in Eq. 3.18 from Chapter 3. This parameter can be constrained by studying the properties of the Z boson in the SM, see e.g. Refs. [196,197]. The most general Lagrangian that can be written under the gauge group $SU(3)_c \otimes SU(2)_L \otimes U(1)_Y \otimes U(1)_B$ involving the neutral gauge bosons of the theory is given by

$$\begin{aligned} \mathcal{L} \supset & -\frac{1}{4}B_{\mu\nu}B^{\mu\nu} - \frac{1}{2}\text{Tr} \{ W_{\mu\nu}W^{\mu\nu} \} - \frac{1}{4}B'_{\mu\nu}B'^{\mu\nu} - \frac{\sin \epsilon}{2}B_{\mu\nu}B'^{\mu\nu} \\ & + \frac{1}{8}(gW_{3\mu} - g_Y B_\mu)(gW_3^\mu - g_Y B^\mu)v_0^2 + \frac{1}{2}\mu_{B'}^2 B'_\mu B'^\mu \\ & - \sum_i \bar{\psi}_i \gamma^\mu [g_Y(Y_L^i P_L + Y_R^i P_R)B_\mu + g_P T^a W_{a\mu}] \psi_i + \frac{g_B}{3} \sum_i \bar{\psi}_i \gamma^\mu \psi_i B'_\mu, \end{aligned} \quad (4.18)$$

where $Y_{L/R}$ are the hypercharges of the LH/RH fields interacting with the hypercharge gauge boson B_μ , $\mu_{B'} = 3g_B v_B$ is the mass term generated after the SSB of $U(1)_B$ and $\sin \epsilon$ parametrizes the kinetic mixing between both Abelian gauge bosons B_μ and B'_μ , being B'_μ the mediator of $U(1)_B$.¹

There are different paths to bring the kinetic terms in the first line of Eq. (4.18) to an orthonormal form via a non-orthogonal transformation. For convenience, we choose a change of basis that does not modify the well-known relation between the neutral SM gauge bosons. The later can be achieved through the following transformation of the B_μ and B'_μ fields:

$$\begin{pmatrix} B_\mu \\ B'_\mu \end{pmatrix} \mapsto \begin{pmatrix} 1 & -\tan \epsilon \\ 0 & \sec \epsilon \end{pmatrix} \begin{pmatrix} B_\mu \\ B'_\mu \end{pmatrix}, \quad (4.19)$$

¹Note that the charge of the SM quarks under the baryon force is $1/3$.

which renders the kinetic Lagrangian for the gauge bosons orthonormalized and leads to the following Lagrangian mass terms

$$\begin{aligned} \mathcal{L} \supset & \frac{1}{8} v_0^2 (g W_{3\mu} - g_Y (B_\mu - \tan \epsilon B'_\mu)) (g W_3^\mu - g_Y (B^\mu - \tan \epsilon B'^\mu)) \\ & + \frac{1}{2} \mu_{B'}^2 \sec^2 \epsilon B'_\mu B'^\mu, \end{aligned} \quad (4.20)$$

with the mass matrix in the neutral gauge boson basis (W_μ^3, B_μ, B'_μ) :

$$M_0^2 = \frac{1}{4} \begin{pmatrix} g^2 v_0^2 & -g_Y g v_0^2 & g_Y g \tan \epsilon v_0^2 \\ -g_Y g v_0^2 & g_Y^2 v_0^2 & -g_Y^2 \tan \epsilon v_0^2 \\ g_Y g \tan \epsilon v_0^2 & -g_Y^2 \tan \epsilon v_0^2 & g_Y^2 \tan^2 \epsilon v_0^2 + 4\mu_{B'}^2 \sec^2 \epsilon \end{pmatrix}. \quad (4.21)$$

Now, by rotating the W_μ^3 and B_μ fields as it is done in the SM,

$$\begin{pmatrix} B_\mu \\ W_{3\mu} \end{pmatrix} = \begin{pmatrix} \cos \theta_W^0 & -\sin \theta_W^0 \\ \sin \theta_W^0 & \cos \theta_W^0 \end{pmatrix} \begin{pmatrix} A_\mu \\ C_\mu \end{pmatrix}, \quad (4.22)$$

where

$$\cos \theta_W^0 \equiv \frac{g}{\sqrt{g_Y^2 + g^2}}, \quad \text{and} \quad \sin \theta_W^0 \equiv \frac{g_Y}{\sqrt{g_Y^2 + g^2}}, \quad (4.23)$$

the photon decouples and we are left with the following mass matrix for the still unphysical neutral gauge bosons C_μ and B'_μ :

$$M_0^2 = \frac{1}{4} \begin{pmatrix} 0 & 0 & 0 \\ 0 & (g_Y^2 + g^2) v_0^2 & \sqrt{g_Y^2 + g^2} g_Y \tan \epsilon v_0^2 \\ 0 & \sqrt{g_Y^2 + g^2} g_Y \tan \epsilon v_0^2 & 4\mu_{B'}^2 \sec^2 \epsilon + g_Y^2 \tan^2 \epsilon v_0^2 \end{pmatrix}. \quad (4.24)$$

The mass matrix in Eq. 4.24 defines ξ ,

$$\begin{aligned} C_\mu &= \cos \xi Z_\mu + \sin \xi Z_{B\mu}, \\ B'_\mu &= -\sin \xi Z_\mu + \cos \xi Z_{B\mu}, \end{aligned} \quad (4.25)$$

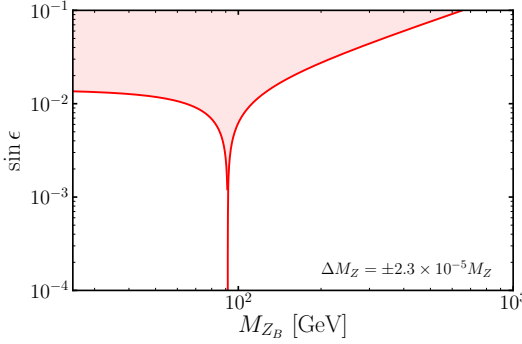


Figure 4.2: Experimental constraint on the kinetic mixing, $\sin \epsilon$, as a function of the Z_B mass. We have used the measurement of the Z boson mass. *Figure extracted from Ref. [192].*

i.e. the angle of the final rotation towards the physical basis, which is given by

$$\tan 2\xi = \frac{2g_Y \sqrt{g_Y^2 + g^2} \tan \epsilon v_0^2}{4\mu_{B'}^2 \sec^2 \epsilon + g_Y^2 \tan^2 \epsilon v_0^2 - (g_Y^2 + g^2)v_0^2}, \quad (4.26)$$

with the following eigenvalues defining their masses:

$$\begin{aligned} M_A^2 &= 0, \\ M_{Z,Z_B}^2 &= \frac{1}{8} (g_Y^2 \sec^2 \epsilon + g^2) v_0^2 + \frac{1}{2} \mu_{B'}^2 \sec^2 \epsilon \\ &\quad \pm \frac{1}{8} \sqrt{(4\mu_{B'}^2 \sec^2 \epsilon + (g_Y^2 \sec^2 \epsilon + g^2)v_0^2)^2 - 16(g_Y^2 + g^2)\mu_{B'}^2 v_0^2 \sec^2 \epsilon}. \end{aligned} \quad (4.27)$$

As expected, in the limit $\epsilon \rightarrow 0$ we recover the original masses in the Lagrangian for Z and Z_B .

We can now apply the high precision measurement of the Z boson mass to constrain the kinetic mixing parameter, $\sin \epsilon$. The mass of the Z boson has been measured to be [198]

$$\frac{\Delta M_Z}{M_Z^{\text{SM}}} = \frac{M_Z - M_Z^{\text{SM}}}{M_Z^{\text{SM}}} \leq \pm 2.3 \times 10^{-5}, \quad (4.28)$$

where the last number is the one standard deviation uncertainty in the experimentally measured Z boson mass and it will constrain the shift induced by the kinetic mixing. In Fig. 4.2 we show this constraint in the M_{Z_B} vs $\sin \epsilon$ plane; as it can be seen, the kinetic mixing is very constrained and has to be very small. Recently, the CMS [199] and

the LHCb [200] collaborations found stronger constraints for this mixing parameter for $M_{Z_B} \leq 200$ GeV by searching for the direct production of a new gauge boson. Given its small impact in the phenomenology, we will neglect the kinetic mixing in the rest of our study.

4.1.3 Towards a simplified model for dark matter

Starting from the model proposed by Duerr, Fileviez, and Wise (DFW) [169], whose Lagrangian, from Eqs. 3.15 and 3.18, can be written as

$$\begin{aligned} \mathcal{L}_{DFW} = & \mathcal{L}_{SM} - \frac{g_B}{3} (\overline{q_L} \gamma_\mu Z_B^\mu q_L + \overline{u_R} \gamma_\mu Z_B^\mu u_R + \overline{d_R} \gamma_\mu Z_B^\mu d_R) \\ & + i\overline{\Psi}_L \not{D} \Psi_L + i\overline{\Psi}_R \not{D} \Psi_R + i\overline{\chi}_L \not{D} \chi_L + i\overline{\chi}_R \not{D} \chi_R + i\overline{\eta}_L \not{D} \eta_L + i\overline{\eta}_R \not{D} \eta_R \\ & + (D_\mu S_B)^\dagger (D^\mu S_B) - V(H, S_B) - (y_1 \overline{\Psi}_L H \eta_R + y_2 \overline{\Psi}_L i\sigma_2 H^* \chi_R + y_3 \overline{\Psi}_R H \eta_L \\ & + y_4 \overline{\Psi}_R i\sigma_2 H^* \chi_L + \lambda_\Psi \overline{\Psi}_R \Psi_L S_B + \lambda_\eta \overline{\eta}_L \eta_R S_B + \lambda_\chi \overline{\chi}_L \chi_R S_B + \text{h.c.}), \end{aligned} \quad (4.29)$$

where \mathcal{L}_{SM} is the Lagrangian of the SM, and $V(H, S_B)$, previously discussed (see Eq. 4.1), contains all the relevant terms for the scalar fields.

As addressed in Chapter 3, anomaly cancellation predicts the existence of new colorless, electrically neutral and charged fermions. After SSB, the mass matrix of the new neutral fermions is given by

$$\mathcal{M}_0 = \begin{pmatrix} \overline{\Psi}_L^0 & \overline{\chi}_L^0 \end{pmatrix} \begin{pmatrix} M_\Psi & M_2 \\ M_4 & M_\chi \end{pmatrix} \begin{pmatrix} \Psi_R^0 \\ \chi_R^0 \end{pmatrix} + \text{h.c.}, \quad (4.30)$$

whose mass terms are listed below,

$$M_\Psi = \frac{\lambda_\Psi v_B}{\sqrt{2}}, \quad M_\chi = \frac{\lambda_\chi v_B}{\sqrt{2}}, \quad M_2 = \frac{y_2 v_0}{\sqrt{2}}, \quad \text{and} \quad M_4 = \frac{y_3 v_0}{\sqrt{2}}. \quad (4.31)$$

For the charged fields, the mass matrix reads as

$$\mathcal{M}_\pm = \begin{pmatrix} \overline{\Psi}_L^\pm & \overline{\eta}_L^\pm \end{pmatrix} \begin{pmatrix} M_\Psi & M_1 \\ M_3 & M_\eta \end{pmatrix} \begin{pmatrix} \Psi_R^\pm \\ \eta_R^\pm \end{pmatrix} + \text{h.c.}, \quad (4.32)$$

where the entries of the mass matrices are given by

$$M_\eta = \lambda_\eta v_B / \sqrt{2}, \quad M_1 = y_1 v_0 / \sqrt{2}, \quad \text{and} \quad M_3 = y_3 v_0 / \sqrt{2}. \quad (4.33)$$

In this theory there are two potential DM candidates: the neutral field living in the doublet representation of $SU(2)_L$, Ψ^0 , and the singlet χ . The pure $SU(2)_L$ DM candidate couples directly to the Z boson and it is excluded by DD constraints (see Appendix B from Ref. [191]). Hence, we will focus on the scenario where the DM candidate is a singlet under the SM gauge group. In this limit, our DM is generally a Dirac fermion ²

$$\chi = \chi_L + \chi_R, \quad (4.34)$$

with mass M_χ defined by the scale of symmetry breaking, i.e. the scale of baryon number violation. We will also assume the limit of the Yukawa couplings y_2 and y_4 being very small because, only in this case, we can avoid large interactions between our DM candidate and the Z gauge boson.

Excluding χ , the rest of the anomalous do not affect the contribution of the DM candidate to the relic abundance because of their heavier masses. Therefore, we will not consider them in the Lagrangian of the simplified model, although we will come back to the electrically-charged anomalous when studying the production of gamma lines, since they play a key role there. A very peculiar feature of this theory, in contrast with most of the simplified models for DM in the literature, is that here both the DM candidate and the new gauge boson get mass from the SSB of the local baryon number. Taking into account Eqs. 4.17 and 4.31, both masses are related as follows:

$$M_\chi = \frac{\lambda_\chi}{3\sqrt{2}g_B} M_{Z_B}. \quad (4.35)$$

It should be stressed that the DM candidate is connected to the SM through a vector and a scalar portal, as Fig. 4.3 schematically shows. The vector portal is mediated by the gauge coupling g_B , while the scalar one is controlled by the degree of mixing between the new and the SM Higgses, given by θ_B . The vector portal occurs through the kinetic

²As long as $X_1 \neq -X_2$.

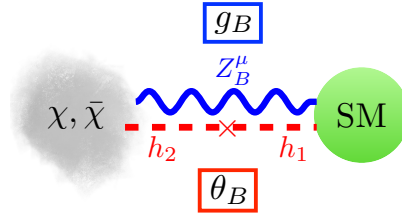


Figure 4.3: DM portal to the SM through the new vector boson and the mixing between the new scalar, responsible of the $U(1)_B$ breaking, and the SM Higgs.

term of the DM candidate:

$$\begin{aligned}
 \mathcal{L}_{\text{DFW}} &\supset i\bar{\chi}_L \not{D} \chi_L + i\bar{\chi}_R \not{D} \chi_R \\
 &= -g_B B_2 \bar{\chi}_L \not{Z}_B \chi_L - g_B B_1 \bar{\chi}_R \not{Z}_B \chi_R \\
 &= -g_B \bar{\chi} \gamma_\mu \left[\frac{B_1 + B_2}{2} \mathbb{I} + \gamma_5 \frac{B_1 - B_2}{2} \right] \chi Z_B^\mu = -\frac{g_B}{2} \bar{\chi} \not{Z}_B (B \mathbb{I} - 3\gamma_5) \chi,
 \end{aligned} \tag{4.36}$$

where $B = B_1 + B_2$ and the anomaly cancellation condition in Eq. 3.13 has been applied.³ We note that, in this case, the DM interacts vectorially and axially with the new mediator, in contrast with the solely vectorial interaction of the Z_B with the SM quarks:

$$\mathcal{L}_{\text{DFW}} \supset i\bar{Q}_L \not{D} Q_L + i\bar{d}_R \not{D} d_R + i\bar{u}_R \not{D} u_R = -\frac{g_B}{3} \bar{q}_i Z_B^\mu \gamma_\mu q_i, \quad \forall q_i \subset \text{SM}. \tag{4.37}$$

The scalar portal opens after SSB, when the DM interacts indirectly with the SM content through the scalar mixing in the broken phase. The term responsible for the DM mass $-\mathcal{L}_{\text{DFW}} \supset \lambda_\chi \bar{\chi}_L \chi_R S_B + \text{h.c.}$ connects both sectors via the mixing, as Fig. 4.3 illustrates. In the broken phase, one can write a simplified Lagrangian where only the relevant interactions for the DM candidate are considered:

$$\mathcal{L}_{\text{DFW}}^{\text{sim}} = -\frac{g_B}{3} \bar{q}_i \not{Z}_B q_i - \frac{g_B}{2} \bar{\chi} \not{Z}_B (B \mathbb{I} - 3\gamma_5) \chi - \left(\frac{\lambda_\chi}{\sqrt{2}} v_B \bar{\chi}_L \chi_R + \frac{\lambda_\chi}{\sqrt{2}} \bar{\chi}_L \chi_R S_B + \text{h.c.} \right). \tag{4.38}$$

³The baryon charges of the new sector in this model are given in Table 3.1 taking $X_i \equiv B_i$.

Taking into account Eq. 4.9, the mass of the DM given in Eq. 4.31 and the mass of the Z_B from Eq. 4.17, the above Lagrangian can be rewritten as

$$\begin{aligned} \mathcal{L}_{\text{DFW}}^{\text{sim}} = & -\frac{g_B}{3}\bar{q}_i Z_B^\mu \gamma_\mu q_i - \frac{g_B}{2}\bar{\chi} Z_B^\mu \gamma_\mu (B\mathbb{I} - 3\gamma_5)\chi + M_\chi \bar{\chi}\chi \\ & + 3g_B \frac{M_\chi}{M_{Z_B}} (\cos\theta_B h_2 + \sin\theta_B h_1) \bar{\chi}\chi. \end{aligned} \quad (4.39)$$

where χ is a Dirac field (see Eq. 4.34). Notice that in total there are six free parameters characterizing this theory:

$$M_\chi, \quad M_{Z_B}, \quad M_{h_2}, \quad \theta_B, \quad B, \quad \text{and} \quad g_B. \quad (4.40)$$

Notice also that in the specific case where $B = 0$, i.e. $B_1 = -B_2$, the baryon charges shown in Table 3.1 are fixed, i.e. $B_1 = -3/2$ and $B_2 = 3/2$. Furthermore, the neutral nature of the DM allows for the following extra Majorana terms in the Lagrangian,

$$\mathcal{L}_{\text{DFW}} \supset -\lambda_{\chi_L} \chi_L^T C \chi_L S_B^* - \lambda_{\chi_R} \chi_R^T C \chi_R S_B + \text{h.c.} \quad (4.41)$$

After diagonalizing the corresponding mass matrix, assuming without loss of generality that $\lambda_{\chi_L} \ll \lambda_{\chi_R}, \lambda_\chi$, we would get a Majorana DM candidate $\chi = \chi_L + (\chi_L)^c$. In this context, we gain the reduction of one d.o.f. (since B is fixed to zero), but we pay the price of a new mixing angle in the χ masses.

On the other hand, let us start with the alternative realistic model for local baryon number proposed by Fileviez, Ohmer and Patel (FOP) [171],

$$\begin{aligned} \mathcal{L}_{\text{FOP}} = & \mathcal{L}_{\text{SM}} - \frac{g_B}{3} (\bar{q}_L \gamma_\mu Z_B^\mu q_L + \bar{u}_R \gamma_\mu Z_B^\mu u_R + \bar{d}_R \gamma_\mu Z_B^\mu d_R) \\ & + (D_\mu S_B)^\dagger (D^\mu S_B) - V(H, S_B) + i\bar{\Psi}_R \not{D} \Psi_R + i\bar{\Psi}_L \not{D} \Psi_L + i\text{Tr}\{\bar{\Sigma}_L \not{D} \Sigma_L\} + i\bar{\chi}_L \not{D} \chi_L \\ & - y_1 \bar{\Psi}_R H \chi_L - y_2 H^\dagger \Psi_L^T C \chi_L - y_3 H^\dagger \Sigma_L^T C \Psi_L - y_4 \bar{\Psi}_R \Sigma_L H - \lambda_\Psi \bar{\Psi}_R \Psi_L S_B^* \\ & - \lambda_\chi \chi_L^T C \chi_L S_B - \lambda_\Sigma \text{Tr}\{\Sigma_L^T C \Sigma_L\} S_B + \text{h.c.}, \end{aligned} \quad (4.42)$$

where $D^\mu \chi_L = \partial^\mu \chi_L - i(3g_B/2)Z_B^\mu \chi_L$ and $D^\mu \Sigma_L = \partial^\mu \Sigma_L + ig[\sigma^a/2W_a^\mu, \Sigma_L] - ig_B \frac{3}{2} Z_B^\mu \Sigma_L$. It is remarkable that this theory only requires four new representations for anomaly cancellation whose baryonic charges are totally fixed. In this case, the DM

candidate is genuinely Majorana,

$$\chi = \chi_L + (\chi_L)^c, \quad (4.43)$$

i.e. $\chi = \chi^c$. The scalar boson needed to break the $U(1)_B$ is exactly the same as in the previous model, $S_B \sim (1, 1, 0, 3)$, so it is the SSB mechanism through the scalar potential. In this context, the anomalous get mass after SSB in the following way:

$$\mathcal{L}_{\text{FOP}} \supset -\frac{1}{2}\bar{\varphi}^T C \mathcal{M}_0 \bar{\varphi}^T - \left(\overline{\Sigma_R^+} \quad \overline{\Psi_R^+} \right) \mathcal{M}_{\pm} \left(\Sigma_L^+ \quad \Psi_L^+ \right)^T + \text{h.c.}, \quad (4.44)$$

where $\bar{\varphi} \equiv \left(\Psi_L^0 \quad (\Psi^{0c})_L \quad \Sigma_L^0 \quad \chi_L \right)$, and the mass matrices are given by

$$\mathcal{M}_0 = \begin{pmatrix} 0 & \frac{1}{\sqrt{2}}\lambda_{\Psi}v_B & -\frac{1}{2}y_3v_0 & \frac{1}{\sqrt{2}}y_2v_0 \\ \frac{1}{\sqrt{2}}\lambda_{\Psi}v_B & 0 & -\frac{1}{2}y_4v_0 & \frac{1}{\sqrt{2}}y_1v_0 \\ -\frac{1}{2}y_3v_0 & -\frac{1}{2}y_4v_0 & \sqrt{2}\lambda_{\Sigma}v_B & 0 \\ \frac{1}{\sqrt{2}}y_2v_0 & \frac{1}{\sqrt{2}}y_1v_0 & 0 & \sqrt{2}\lambda_{\chi}v_B \end{pmatrix}, \quad \text{and} \quad \mathcal{M}_{\pm} = \begin{pmatrix} \sqrt{2}\lambda_{\Sigma}v_B & y_4\frac{v_0}{2} \\ y_3\frac{v_0}{2} & \lambda_{\Psi}\frac{v_B}{\sqrt{2}} \end{pmatrix}. \quad (4.45)$$

In the following we will adopt the limit of very small Yukawa couplings $y_i \rightarrow 0$ under the same motivation from the previous scenario.

Notice that the Majorana mass term in the Lagrangian,

$$\mathcal{L}_{\text{FOP}} \supset -\lambda_{\chi} \chi_L^T C \chi_L S_B + \text{h.c.} = -\lambda_{\chi} \chi_L^T C \chi_L S_B - \lambda_{\chi}^* \chi_L^{\dagger} C^{\dagger} (\chi_L^{\dagger})^T S_B^*, \quad (4.46)$$

can be rewritten, by using $-C(\gamma^{\mu})^T = \gamma^{\mu}C$ (see Appendix A), as

$$\begin{aligned} \mathcal{L}_{\text{FOP}} \supset & -\lambda_{\chi} \left(\chi_L^T C \chi_L S_B + (\chi^c)_L^T C (\chi^c)_L S_B^* \right) \\ & \xrightarrow{SSB} \lambda_{\chi} \left(v_B \chi^T C \chi + h_1 \sin \theta_B \chi^T C \chi + h_2 \cos \theta_B \chi^T C \chi \right) / \sqrt{2}, \end{aligned} \quad (4.47)$$

where χ is the Majorana DM (see Eq. 4.43) and in the last row from Eq. 4.47, we have written that Lagrangian in the broken phase. Now, looking at the kinetic term of the χ_L

field, one can also rewrite it as a function of the 4-component Majorana field as follows,

$$\begin{aligned}
\mathcal{L}_{\text{FOP}} \supset i \bar{\chi}_L \not{D} \chi_L &= -\frac{i}{2} \left(-\bar{\chi} \not{D} P_L \chi + \overline{(\chi^c)} \not{D} P_R \chi^c \right) \\
&= -\frac{i}{2} \left(\bar{\chi} \not{D} \gamma_5 P_L \chi + \overline{(\chi^c)} \not{D} \gamma_5 P_R \chi^c \right) \\
&= -\frac{i}{2} \left(\bar{\chi}_L \not{D} \gamma_5 \chi_L + \overline{(\chi_L)^c} \not{D} \gamma_5 (\chi_L)^c \right) = -\frac{i}{2} \bar{\chi} \not{D} \gamma_5 \chi,
\end{aligned} \tag{4.48}$$

where we have used that $\gamma_5 P_L = -P_L$ and $\gamma_5 P_R = P_R$, and the relation $\overline{\chi^c} \gamma_\mu P_R \chi^c = -\bar{\chi} \gamma_\mu P_L \chi$ (see Appendix A).

Taking into account the relevant d.o.f. for the study of the DM, the Lagrangian of the simplified model can be identified as

$$\mathcal{L}_{\text{FOP}}^{\text{sim}} \supset \frac{3}{4} g_B \bar{\chi} \not{Z}_B \gamma^5 \chi - \frac{g_B}{3} \bar{q} \not{Z}_B q + \frac{M_\chi}{2v_B} (\sin \theta_B h_1 - \cos \theta_B h_2) \bar{\chi} \chi - \frac{1}{2} M_\chi \bar{\chi} \chi, \tag{4.49}$$

in the FOP case, where the DM mass can be read from Eq. 4.47,

$$M_\chi = \sqrt{2} \lambda_\chi v_B. \tag{4.50}$$

It is remarkable that this realization of local baryon number contains only five free parameters this time,

$$M_\chi, \quad M_{Z_B}, \quad M_{h_2}, \quad \theta_B, \quad \text{and} \quad g_B. \tag{4.51}$$

In both DFW and FOP models, $\sin \theta_B \lesssim 0.3$ is bounded by collider constraints as Eq. 4.11 states, and the gauge coupling is bounded by perturbativity as follows,

$$g_B < \frac{\sqrt{2\pi}}{3}, \tag{4.52}$$

which comes from the largest gauge interaction in this theory:

$$(D^\mu S_B)^\dagger (D_\mu S_B) \supset -\frac{9}{2} g_B^2 s_B^2 Z_B^\mu Z_{B\mu}. \tag{4.53}$$

Finally, we should emphasize again the connection between the DM candidate and the leptophobic gauge boson. Because of the perturbative bound on the Yukawa coupling $\lambda_\chi \leq \sqrt{2\pi}$,

$$\frac{M_{Z_B}}{M_\chi} \geq \frac{3g_B}{2\sqrt{\pi}}. \quad (4.54)$$

The above condition has strong implications in the theory because, as we will see, together with the cosmological bound on the relic density and the perturbative bound on the gauge coupling, they impose an upper bound to the scale of baryon number violation at the few-TeV. Having such small number of free parameters to control the theory and knowing how they are related allows us to study in great detail the phenomenology of the DM candidate. We note that the simplified Lagrangian from Eq. 4.49 is also valid for the Majorana limit of the DFW model up to a couple of small differences:

- In this context, the DM candidate has a baryonic charge $n_B^\chi = -3/2$, while in the Majorana limit of the previous scenario $n_B^\chi = 3/2$. This has only a small implication in the annihilation of the DM to quarks: in the DFW model the diagrams interfere destructively while in the FOP model they add constructively.
- Apart from assuming small Yukawa couplings y_1, y_2, y_3 and y_4 to avoid large mixings between the DM candidate and the rest of the anomalous, in the Majorana limit of the DFW model one has to further assume $\lambda_\chi \ll \lambda_{\chi_L} < \lambda_{\chi_R}$ for making use of the simplified Lagrangian in Eq. 4.49.

In the following, we will study the properties of a Majorana DM candidate based on the simplified Lagrangian from Eq. 4.49. This scenario will be compared with the predictions in the Dirac case, being the main difference the freedom in the choice of the total baryon number B . The reasons why we opted for the Majorana nature of the DM, apart from being more minimal in the sense of number of free parameters and representations describing the theory where it is embedded, will become clear when going through the phenomenology of the DM.

4.2 Phenomenological and cosmological bounds for DM

In this section we present a numerical study of the properties of the DM candidate and investigate its viability by contrasting the possible parameter space of the theory based on local baryon number with the existing experimental constraints.

4.2.1 Relic density

As derived in Chapter 2, the contribution to the relic abundance of a certain field is inversely proportional to its annihilation cross-sections. Having a complete theory as starting point, i.e. knowing all the Feynman rules of the model, allows us to investigate in detail the DM annihilation channels of the theory. In this context, the DM can annihilate as follows:

$$\chi\chi \rightarrow Z_B Z_B = \chi\chi \rightarrow Z_B Z_B + \chi\chi \rightarrow Z_B Z_B + \chi\chi \rightarrow Z_B Z_B \quad (4.55)$$

$$\chi\chi \rightarrow q\bar{q} = \chi\chi \rightarrow q\bar{q} + \chi\chi \rightarrow q\bar{q} \quad (4.56)$$

$$\chi\chi \rightarrow h_i h_j = \chi\chi \rightarrow h_i h_j + \chi\chi \rightarrow h_i h_j + \chi\chi \rightarrow h_i h_j \quad (4.57)$$

$$\chi\chi \rightarrow Z_B h_i = \chi\chi \rightarrow Z_B h_i + \chi\chi \rightarrow Z_B h_i + \chi\chi \rightarrow Z_B h_i \quad (4.58)$$

$$\chi\chi \rightarrow W^+ Z = \chi\chi \rightarrow W^- Z \quad (4.59)$$

i.e.

$$\chi\chi \rightarrow \bar{q}q, Z_B Z_B, Z_B h_1, Z_B h_2, h_1 h_1, h_1 h_2, h_2 h_2, WW, ZZ.$$

Notice that the channels $Z_B h_1, h_1 h_1, h_1 h_2, WW$ and ZZ are suppressed by the mixing angle θ_B . The vertices colored in red denote an axial interaction, which is a consequence of having a Majorana DM candidate. See Sec. 2.1.1.4 from Chapter 2 for more details on their implication on velocity suppressed amplitudes.

For the numerical study of the relic abundance we have implemented the model in LanHEP 3.2 [201] and performed the calculation of $\Omega_\chi h^2$ using MicrOMEGAS 5.0.6 [73]. Moreover, we performed an independent calculation in Mathematica.

Besides the cosmological constraint on the measured relic abundance by the Planck satellite $\Omega_\chi h^2 = 0.1197 \pm 0.0022$ [202], there are other bounds that must be taken into account. The Z_B mediator couples directly to quarks and would appear as a resonance in dijet searches at the LHC. In our work, we apply the bounds from CMS and ATLAS, discussed in Section 3.4 from Chapter 3 and present the excluded regions in the upcoming figures in purple bands. These collider bounds, shown in Fig. 3.5 from that chapter, have a strong dependence on the coupling g_B and disappear for $g_B \leq 0.1$. In the upcoming figures, the region shaded in red represents the parameter space ruled out by the perturbative bound on the Yukawa coupling, $\lambda_\chi < \sqrt{2\pi}$. Similarly, in the following figures, the yellow region will show the parameter space ruled out by the perturbative bound on the scalar quartic coupling, $\lambda_B < 4\pi$. In order to proceed with the numerical analysis, the mass of the second Higgs will be fixed to $M_{h_2} = 500$ GeV and the mixing angle to zero, i.e. $\theta_B = 0$.⁴ We also impose the perturbative bound on the gauge coupling previously discussed, $g_B < \sqrt{2\pi}/3$ (see Eq. 4.52).

In Fig. 4.4 we show the allowed parameter space by the cosmological, theoretical and collider bounds for different values of the gauge coupling g_B . In order to develop a better understanding of our results, we show in Fig. 4.5 explicitly which channel from

⁴The choice of zero scalar mixing can be motivated as follows. In the SM, the EW phase transition occurs around $T_{EW} \approx 160$ GeV. For masses above the TeV scale (which is the region preferred after considering LHC bounds), we find the DM freeze-out temperature to be $x_f \approx 26 - 29$. Consequently, for $M_\chi \gtrsim 5$ TeV the freeze-out temperature is above the EW phase transition, and hence, at the time when DM freezes out the Higgs field has zero vacuum expectation value and there is no scalar mixing. It is important to mention that the bounds from the relic density constraint are very similar in the case where one considers a non-zero mixing angle.

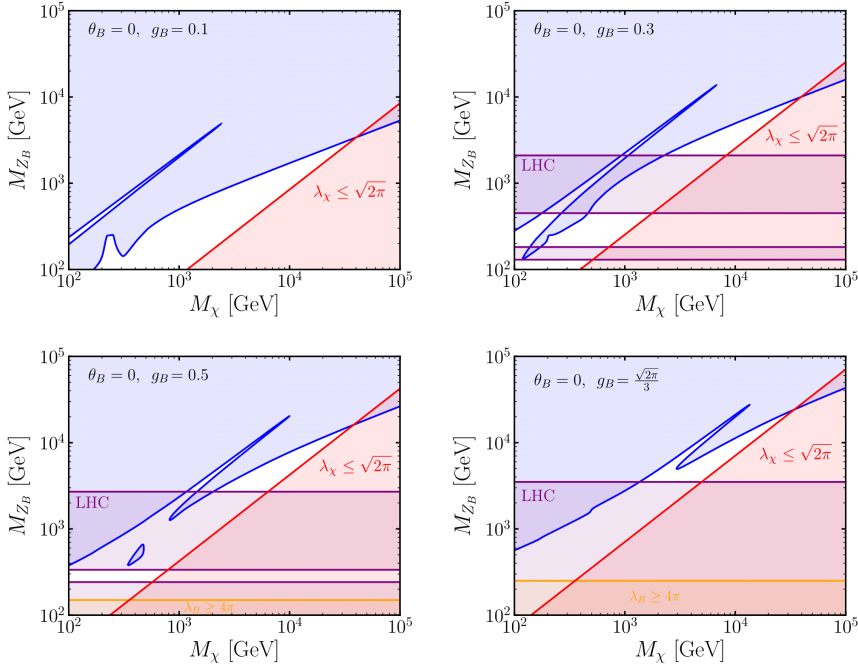


Figure 4.4: Parameter space allowed by the relic density constraint, LHC bounds and perturbative bounds for four different scenarios, $g_B = 0.1$ (top-left), $g_B = 0.3$ (top-right), $g_B = 0.5$ (bottom-left) and $g_B = \sqrt{2\pi}/3$ (bottom-right). We take $M_{h_2} = 500$ GeV and no mixing angle. The region in blue is excluded by $\Omega_\chi h^2 \leq 0.12$ and the region in red (yellow) is excluded by the perturbative bound on the Yukawa coupling λ_χ (scalar coupling λ_B). The horizontal purple bands are excluded by the LHC bounds on the leptophobic gauge boson mass. *Figure extracted from Ref. [203]*

Diagrams 4.55-4.59 dominates the viable parameter space shown in Fig. 4.4. We color each region depending on the dominant annihilation channel; namely, the one that gives the largest contribution to the relic abundance at freeze-out. The region in dark blue corresponds to the area in parameter space where annihilation into quarks is the dominant channel; this happens near the resonance $M_\chi \approx M_{Z_B}/2$, to which we will refer as *resonance region*. The rest of the allowed parameter space, as the shape of these figures show, will be called *plateau*. In there, the region in light blue is where the annihilation into $Z_B Z_B$ is the dominant one. This occurs due to the resonance $\chi\chi \rightarrow h_2^* \rightarrow Z_B Z_B$ when $M_\chi \approx M_{h_2}/2 \approx 250$ GeV. This resonant behavior can be

easily appreciated in the upper left panels in Figs. 4.4 and 4.5. In there, one can see that such resonance is cut close to the diagonal $M_\chi \approx M_{Z_B}$, because the $Z_B Z_B$ channel becomes kinematically closed above. The region in which the $h_2 h_2$ annihilation channel

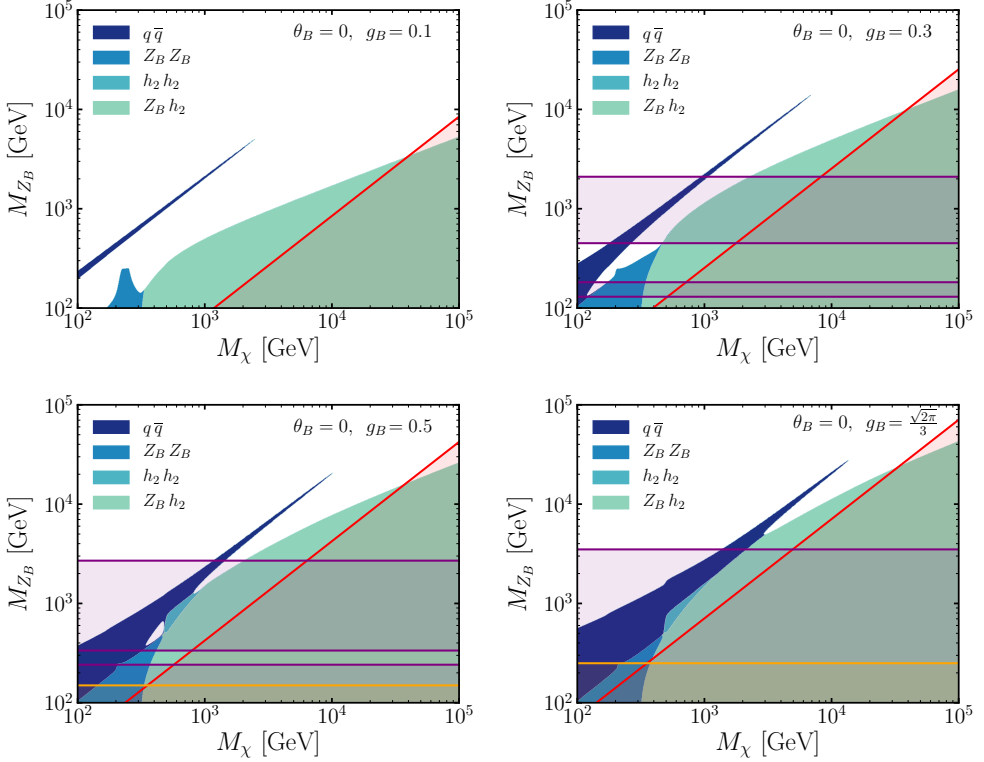


Figure 4.5: Regions in the M_χ versus M_{Z_B} plane that satisfy the relic density constraint $\Omega_\chi h^2 \leq 0.12$, the colors indicate which annihilation channel is the dominant one. We fix $M_{h_2} = 500$ GeV and $\theta_B = 0$. The horizontal purple bands are excluded by dijet searches at the LHC. The region in red (yellow) is excluded by the perturbative bound on the Yukawa coupling λ_χ (scalar quartic coupling λ_B). *Figure extracted from Ref. [203].*

is the dominant one is colored in dark green. The latter is velocity-suppressed since at the freeze-out, $v_{\text{DM}} \approx 0.3$ (see Eq. 2.151); consequently, this channel is dominant only in a small region in the parameter space. Once the $Z_B h_2$ channel becomes kinematically open, it becomes the dominant channel, as illustrated by the region in light green.

As commented at the end of the previous section (see Eq. 4.52), the perturbative limit on the gauge coupling $g_B = \sqrt{2\pi}/3$ is responsible for the existence of an absolute upper bound on the symmetry breaking scale, since it constitutes the scenario where the largest masses for the DM and the Z_B can be achieved in consistency with the cosmological and perturbative bounds on the Yukawa couplings. For $M_{h_2} = 500$ GeV and $\theta_B = 0$, the upper bound is given by

$$M_{Z_B} \leq 28 \text{ TeV}. \quad (4.60)$$

As it can be appreciated, from Figures 4.4 and 4.5, this upper bound on the gauge boson mass, and therefore on the baryon number violation scale, is defined by the annihilation into quarks (resonant region), while the upper bound on the DM mass, $M_\chi \leq 34$ TeV, is determined by the $Z_B h_2$ channel. This bound for M_{Z_B} is an extreme case in the sense that assumes the largest possible gauge coupling; in turn, as these figures show, the lower the gauge coupling the *shorter* the resonant region. On the other hand, as Eq. 4.54 shows, the smaller the gauge coupling, the stronger the bound on the ratio between the M_{Z_B} and M_χ , so that the upper bound on the Z_B given by the *plateau* is lowered too. Hence the theory is expected to live at most around the 20 TeV scale. This striking feature tells us that there is hope to test or rule out this theory in the near future.

The reader may wonder how the results would be affected if the DM candidate was a Dirac field. In that case, one has an extra free parameter in the theory, entering in the cross-section of the annihilation channel $\sigma(\bar{\chi}\chi \rightarrow Z_B Z_B) \propto B^4$. However, we note that the parameter B cannot be arbitrarily large, otherwise the coupling $\mathcal{L} \supset -g_B/2 B \bar{\chi} Z_B^\mu \gamma_\mu \chi$ would spoil perturbativity. Therefore, the behaviour of the parameter space satisfying the relic density bound is analogous to the Majorana case up to some differences: since Dirac DM allows for a vector coupling with the leptophobic gauge boson, the annihilation into quarks do not suffer from velocity suppression. Hence, depending on the B choice, the resonant region could determine the upper bound on the baryon number violating scale, although it will still be around $\mathcal{O}(10)$ TeV. In Fig. 4.6 we show the branching ratio for the different channels in the zero-mixing case with

respect to the total thermal averaged cross-section, assuming $x_f = 24$ in the context of a Dirac (left panel) and Majorana (right panel) DM candidate.

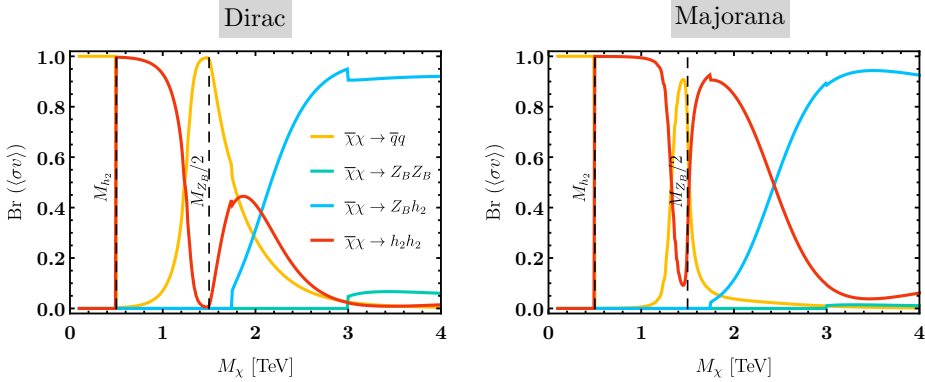


Figure 4.6: Branching ratios for the different DM annihilation channels when the mixing angle between the Higgses is $\theta_B = 0$. For illustration, we use the following values for the input parameters: $M_{Z_B} = 3$ TeV, $M_{h_2} = 1$ TeV, $g_B = 0.5$, $x_f = 24$, and $B = -1$. On the left panel, Dirac DM has been assumed, while in the right panel, the DM is Majorana. *Figure in the left panel extracted from Ref. [191].*

4.2.2 Direct Detection

Our DM candidate can interact with quarks in the nucleon (N) via exchange of either a leptophobic gauge boson or one of the physical scalars through the Higgs mixing, as shown in the diagrams below. In those, the red, blue and green dots represent axial, vector and mixing suppressed vertices, respectively.

$$\begin{array}{ccccc}
 \chi & \text{---} & \text{---} & \chi & \chi & \text{---} & \text{---} & \chi & \chi & \text{---} & \text{---} & \chi \\
 & & \bullet & & & & \bullet & & & & \bullet & \\
 & & | & & & & | & & & & | & \\
 & & Z_B & & + & & h_1 & & + & & h_2 & \\
 & & | & & & & | & & & & | & \\
 N & \text{---} & \bullet & \text{---} & N & N & \text{---} & \bullet & \text{---} & N & N & \text{---} & \bullet & \text{---} & N
 \end{array}
 \tag{4.61}$$

These processes with two different mediators do not interfere with each other so that the spin-independent cross-section between χ and a nucleon can be written as $\sigma_{\chi N}^{\text{TOT}} =$

$\sigma_{\chi N}(Z_B) + \sigma_{\chi N}(h_i)$, where

$$\sigma_{\chi N}^{\text{SI}}(Z_B) = \frac{27}{8\pi} \frac{g_B^4 M_N^2}{M_{Z_B}^4} v^2, \quad (4.62)$$

$$\sigma_{\chi N}^{\text{SI}}(h_i) = \frac{72G_F}{\sqrt{24\pi}} \sin^2 \theta_B \cos^2 \theta_B M_N^4 \frac{g_B^2 M_\chi^2}{M_{Z_B}^2} \left(\frac{1}{M_{h_1}^2} - \frac{1}{M_{h_2}^2} \right)^2 f_N^2, \quad (4.63)$$

v is the DM velocity, M_N refers to the nucleon mass, G_F is the Fermi constant and for the effective Higgs-nucleon-nucleon coupling we take $f_N = 0.3$ [204]. We note that the above expressions are independent of the nucleon matrix elements because protons and neutrons have a definite baryon number. This allows us to obtain clean predictions for the elastic scattering since we do not rely on any non-perturbative calculation.

The axial coupling between χ and Z_B leads to velocity suppression of the interaction mediated by Z_B , which can be factorized out from that cross-section in the following way,

$$\sigma_{\chi N}^{\text{TOT}} = \sigma_{\chi N}(h_i) + \sigma_{\chi N}^0(Z_B)v^2. \quad (4.64)$$

As commented in Chapter 2, DD experiments assume that the leading term in the cross-section is velocity independent, i.e. $\sigma_{\text{SI}} = \sigma_{\text{SI}}^0 + \mathcal{O}(v^2)$. Then, according to Eq. 2.57 from Chapter 2, the differential rate would be given by

$$\frac{dR}{dE} = \frac{\rho_0}{M_\chi M_N} \sigma_{\text{SI}}^0 \underbrace{\int_{v_{\text{min}}}^{v_{\text{max}}} v f(v) dv}_{\bar{v}} < \frac{dR}{dE}^{\text{DDexp}}. \quad (4.65)$$

In order to apply these bounds also to the velocity suppressed cross-section, we should take into account that for the scattering mediated by the Z_B , $\sigma_{\text{SI}} = v^2 \sigma_{\text{SI}}^0$, so that the differential rate in this case reads as,

$$\frac{dR}{dE} = \frac{\rho_0}{M_\chi M_N} \sigma_{\text{SI}}^0 \underbrace{\int_{v_{\text{min}}}^{v_{\text{max}}} v^3 f(v) dv}_{v^3} \quad (4.66)$$

Therefore, we proceed as follows,

$$\sigma_{\chi N}(h_i) + \sigma_{\chi N}^0(Z_B)v_{\text{eff}}^2 \leq \sigma_{\chi N}^{\text{DDexp}}, \quad (4.67)$$

where $\sigma_{\chi N}^{\text{DDexp}}$ is the upper bound on the scattering cross-section given by the DD experiments, and the effective velocity is given by the ratio $\overline{v^3}/\overline{v}$, where the averaged velocity is the velocity of the DM convoluted with a Maxwell-Boltzmann distribution. We find that $v_{\text{eff}} \approx 0.001 c$.

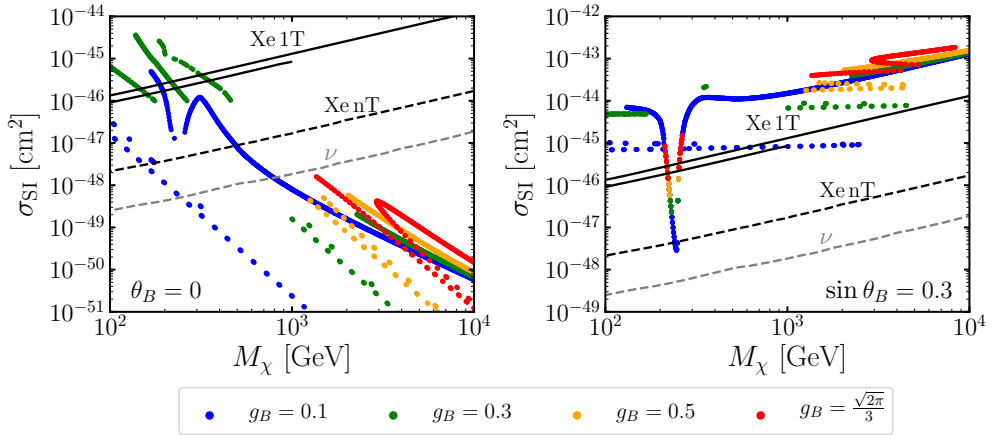


Figure 4.7: Predictions for the DD spin-independent cross-section as a function of the DM mass. In the left (right) panel we present the predictions for $\theta_B = 0$ ($\sin \theta_B = 0.3$). All points agree with the measured relic abundance by the Planck satellite $\Omega_\chi h^2 = 0.1197 \pm 0.0022$ [202] and satisfy constraints from the LHC. The solid black lines show current experimental bounds from Xenon-1T [205,206], the dashed black line shows the projected sensitivity for Xenon-nT [81] and the dashed gray line shows the coherent neutrino scattering limit [83]. *Figure extracted from Ref. [203].*

In Fig. 4.7 we present the predictions for the spin-independent cross-section for different values of g_B . To select the points displayed there we proceed as follows. First, we select those points that give the measured relic abundance of $\Omega_\chi h^2 = 0.1197 \pm 0.0022$. Then, we remove those points that do not satisfy LHC and/or perturbativity bounds. This is the reason behind the discontinuities in the scan shown. The left panel shows the results for $\theta_B = 0$ and, as expected, due to the velocity suppression the points with DM mass above the TeV scale lie below the neutrino floor and will escape detection from future experiments. In contrast, for the maximal mixing allowed, $\sin \theta_B = 0.3$, all the points that saturate the relic density are ruled out by DD bounds except for those that lie close to the h_2 resonance ($M_\chi \approx M_{h_2}/2$). The later is shown in

the right panel in Fig. 4.7. For intermediate values of the mixing angle, the predictions lie in between these two regions, and thus, some of these points will be probed by future DD experiments, such as Xenon-nT [81].

To complete the discussion, let us refer to the predictions for a Dirac DM candidate in the context of the simplified Lagrangian shown in Eq. 4.39, where the spin-independent elastic nucleon-DM cross section is given by

$$\begin{aligned} \sigma_{\chi N}^{\text{SI}} = & \frac{g_B^2 M_N^2 M_\chi^2}{4\pi M_{h_1}^4 M_{h_2}^4 M_{Z_B}^4 v_0^2 (M_\chi + M_N)^2} \\ & \times [2B g_B v_0 M_{h_1}^2 M_{h_2}^2 + 3f_N M_\chi M_N M_{Z_B} \sin(2\theta_B) (M_{h_1}^2 - M_{h_2}^2)]^2. \end{aligned} \quad (4.68)$$

As the above equation reflects, there is no velocity suppression in this case, and therefore one expects the DD bounds to have a stronger impact in the available parameter space, being therefore more damaged than the Majorana case. This is an advantage for considering Majorana rather than Dirac DM.

4.2.3 Gamma Lines

Apart from DD, as discussed in Sec. 2.1.2 from Chapter 2, there are indirect ways to detect DM. In this section, we will discuss the prediction and observation of gamma lines. We will argue that the extra fermions required to make the theory anomaly-free also lead to DM annihilation into photons. Consequently, the photon spectrum will contain features that could be observed in future telescopes.

In order to predict the cross-sections for $\chi\chi \rightarrow \gamma\gamma, \gamma Z, \gamma h_i$,

$$+ \quad (4.69)$$

we need to study the full spectrum of the anomaly-free gauge theories based on $U(1)_B$. These processes are quantum mechanical and can be predicted only after anomaly cancellation is understood, i.e. their predictions are model dependent. Since we have

two beautiful and complete theories behind our DM study, we will now investigate the gamma line predictions in the context of these models: DFW [169] and FOP [171].

Gamma lines are typically suppressed with respect to other processes contributing to the continuum of radiated photons, such as final state radiation (FSR) processes, making it hard to observe them. However, it is possible to have scenarios in which the processes that contribute to the continuum close to the gamma lines are highly suppressed so that they become visible. In Sec. 2.1.2 from Chapter 2 we concluded that in order to distinguish the gamma line from the continuum spectrum, the theory must contain: (a) a Majorana DM candidate, (b) new electrically charged fields with a non-zero axial coupling to the new mediator. Both conditions are satisfied in the context of local baryon gauge theories! Consequently, there is hope to observe the striking phenomenological signal of gamma lines.⁵

4.2.3.1 Predictions for Gamma Lines

The relevant interactions for the DM annihilation into gamma lines are encoded in the following Lagrangian,

$$\mathcal{L} \supset -g_B \bar{f} \left(n_V^f \gamma^\mu + n_A^f \gamma^\mu \gamma^5 \right) f Z_\mu^B - \frac{e}{\sin \theta_W \cos \theta_W} \bar{f} \left(g_V^f \gamma^\mu + g_A^f \gamma^\mu \gamma^5 \right) f Z_\mu, \quad (4.70)$$

where f refers to the electrically-charged fermions entering in the loops from Diagrams 4.69, where the three different possibilities to generate gamma lines are represented. As discussed in Chapter 2, the annihilation channel to $h_i \gamma$ is velocity suppressed, so that we will neglect it in the following. On the other hand, the cross-section for the gamma lines coming from $\chi\chi \rightarrow \gamma\gamma$ and $\chi\chi \rightarrow \gamma Z$ can be large. Those are listed, together with the suppressed $\chi\chi \rightarrow \gamma h_i$, in Appendix B. With this information at hand, let us study the gamma line production in the context of the two simplest models for local baryon number:

- **Model DFW.**

In this context, taking into account that electrically-charged fermions with axial couplings to the Z_B are needed, only the charged anomalous Ψ^- and η^- , defined

⁵This is another argument for considering Majorana DM versus Dirac DM.

as Dirac fields in the broken phase:

$$\Psi^- \equiv \Psi_L^- + \Psi_R^-, \quad \text{and} \quad \eta^- \equiv \eta_L^- + \eta_R^- \quad (4.71)$$

will contribute to the DM annihilation into gamma lines:

$$= \text{Diagram 1} + \text{Diagram 2} \quad (4.72)$$

The relevant Lagrangian in this case is given by

$$\begin{aligned} \mathcal{L}^{\text{DFW}} \supset & e \bar{\Psi}^- \not{A} \Psi^- + e \bar{\eta}^- \not{A} \eta^- + \frac{e}{\tan 2\theta_W} \bar{\Psi}^- \not{Z} \Psi^- \\ & - e \tan \theta_W \bar{\eta}^- \not{Z} \eta^- - \frac{3}{2} g_B \bar{\Psi}^- \not{Z}_B \gamma_5 \Psi^- + \frac{3}{2} g_B \bar{\eta}^- \not{Z}_B \gamma_5 \eta^-, \end{aligned} \quad (4.73)$$

from which one can read the couplings to the Z_B gauge boson: $n_V^{\Psi^-} = 0$, $n_A^{\Psi^-} = 3/2$, $n_V^{\eta^-} = 0$ and $n_A^{\eta^-} = -3/2$, and the couplings to the Z boson: $g_V^{\Psi^-} = -\frac{1}{2}$, $g_A^{\Psi^-} = 0$, $g_V^{\eta^-} = \sin^2 \theta_W$ and $g_A^{\eta^-} = 0$. Note that, in this case, the anomalous only interact with the Z boson vectorially, so that only the vertex combination in Diag. 4.72 survives. In the limit where $y_1 = y_2 = y_3 = y_4 = 0$, the masses for the new electrically-charged fermions, as stated in Eqs. 4.32 and 4.33, read as

$$M_{\Psi^-} = \frac{\lambda_\Psi M_{Z_B}}{3\sqrt{2}g_B}, \quad \text{and} \quad M_{\eta^-} = \frac{\lambda_\eta M_{Z_B}}{3\sqrt{2}g_B}. \quad (4.74)$$

The upper bound on M_{Z_B} derived from relic density constraints defines a global upper bound for the new charged fermion masses since the Yukawa couplings λ_Ψ and λ_η are bounded by perturbativity. Moreover, the perturbative bounds define an upper bound for each mass of the new mediator. Hence, for a given M_{Z_B} and

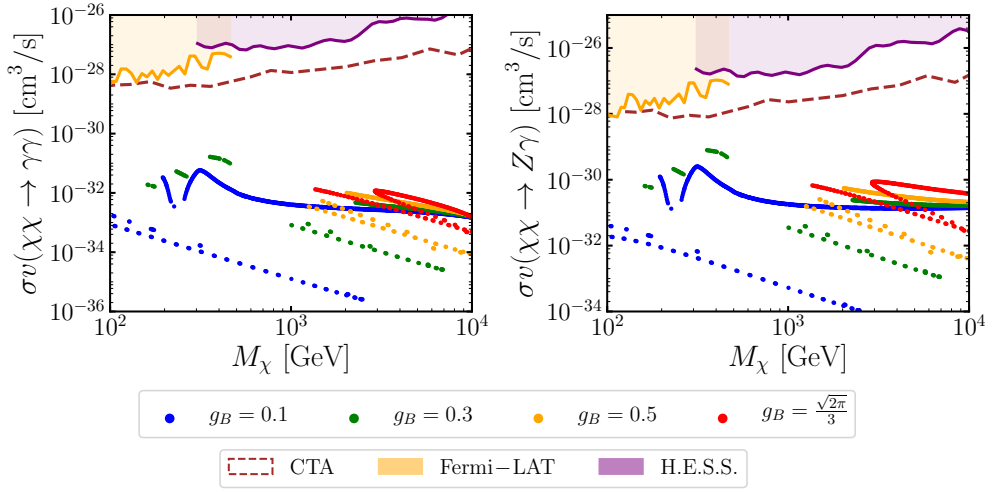


Figure 4.8: Predictions for the DM annihilation into two photons (left panel) and a photon and a Z boson (right panel) in the context of Model DFW. We set $M_{h_2} = 500$ GeV and $\theta_B = 0$. The value of M_{Z_B} is chosen such that every point satisfies $\Omega_\chi h^2 = 0.1197 \pm 0.0022$, different colors correspond to different values of the gauge coupling g_B . All points shown pass LHC and direct detection constraints. The regions colored in yellow are purple show the excluded parameter space by the Fermi-LAT [87, 88] and H.E.S.S. [207], respectively. The dashed brown line shows the projected sensitivity from the CTA collaboration [208]. *Figure extracted from Ref. [203].*

M_χ , the masses of the anomalous are constrained to be in the following range,

$$M_\chi < M_{f^+} \leq \frac{2\sqrt{\pi}}{3g_B} M_{Z_B}, \quad (4.75)$$

where f^+ symbolizes any of the charged new fermions; the lower bound comes from ensuring the stability of the DM candidate whereas the upper bound comes from perturbativity on the Yukawa couplings. We note that the DM candidate and the anomalous satisfy the same perturbative bound.

In Fig. 4.8 we present the predictions for the DM annihilation into gamma lines for different choices of g_B in the context of DFW model for the two relevant annihilation channels. All the points shown saturate the relic abundance, and satisfy collider and DD constraints. From Eqs. (B.2) and (B.4) in Appendix B we

can see that when the charged fermions have the same mass, the cross-section vanishes. We have taken the maximum mass splitting by choosing $M_{\Psi^-} = 1.3M_\chi$ (in order to ensure the stability of the DM candidate), and $M_{\eta^-} = 2\sqrt{\pi}M_{Z_B}/3g_B$, i.e. the largest value allowed by perturbativity. Additionally, for each point we check that Eq. (4.75) is satisfied.

- **Model FOP.**

In this context, the relevant Lagrangian for the gamma lines reads as

$$\begin{aligned} \mathcal{L}^{\text{FOP}} \supset & -e\overline{\Sigma^+}A\Sigma^+ - e\overline{\Psi^+}A\Psi^+ - \frac{e}{\tan\theta_W}\overline{\Sigma^+}\not{Z}\Sigma^+ - \frac{e}{\tan 2\theta_W}\overline{\Psi^+}\not{Z}\Psi^+ \\ & + \frac{3}{2}g_B\overline{\Psi^+}\not{Z}_B\gamma_5\Psi^+ - \frac{3}{2}g_B\overline{\Sigma^+}\not{Z}_B\gamma_5\Sigma^+, \end{aligned} \quad (4.76)$$

where Σ^+ and Ψ^+ correspond to the Dirac fields contributing to DM annihilation into gamma lines, defined as

$$\Sigma^+ \equiv \Sigma_L^+ + (\Sigma_L^-)^c, \quad \text{and} \quad \Psi^+ \equiv \Psi_L^+ + \Psi_R^+, \quad (4.77)$$

$$= \text{Diagram 1} + \text{Diagram 2} \quad (4.78)$$

From the above Lagrangian, one can identify the couplings to the Z_B boson: $n_V^{\Psi^+} = 0$, $n_A^{\Psi^+} = -\frac{3}{2}$, $n_V^{\Sigma^+} = 0$, $n_A^{\Sigma^+} = \frac{3}{2}$, and the couplings to the Z boson: $g_V^{\Psi^+} = \frac{1}{2}$, $g_A^{\Psi^+} = 0$, $g_V^{\Sigma^+} = \cos^2\theta_W$ and $g_A^{\Sigma^+} = 0$. Also in this case the Z boson has a purely vector interaction with the charged anomalous (see Diag. 4.78). In this scenario, in the limit where the couplings $y_1 = y_2 = y_3 = y_4 = 0$ the masses for the new electrically-charged fermions, according to Eq. 4.45, read as

$$M_{\Psi^+} = \frac{\lambda_1 M_{Z_B}}{3\sqrt{2}g_B}, \quad \text{and} \quad M_{\Sigma^+} = \frac{\sqrt{2}\lambda_\Sigma M_{Z_B}}{3g_B}. \quad (4.79)$$

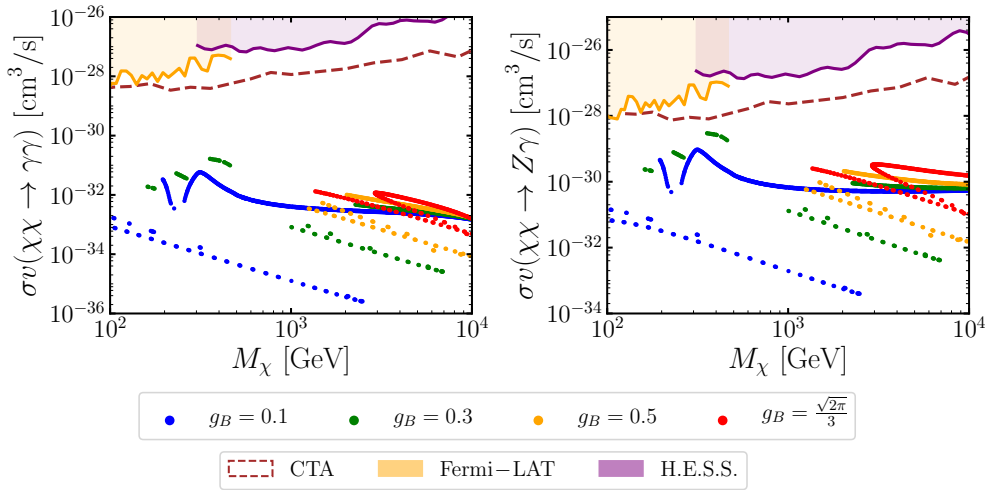


Figure 4.9: Predictions for the DM annihilation into two photons (left panel) and a photon and a Z boson (right panel) in the context of FOP model. We set $M_{h_2} = 500$ GeV and $\theta_B = 0$. The value of M_{Z_B} is chosen such that every point satisfies $\Omega_\chi h^2 = 0.1197 \pm 0.0022$, different colors correspond to different values of the gauge coupling g_B . All points shown pass LHC and direct detection constraints. The regions colored in yellow are purple show the excluded parameter space by the Fermi-LAT [87, 88] and H.E.S.S. [207], respectively. The dashed brown line shows the projected sensitivity from the CTA collaboration [208]. *Figure extracted from Ref. [203].*

In here there is also a global upper bound on the charged fermion masses defined by the upper bound on the M_{Z_B} , the gauge coupling g_B , and the perturbative bounds of the Yukawa couplings. Therefore, as in the previous scenario, the masses of the anomalous must be in the range defined by Eq. (4.75).

In Fig. 4.9 we present our predictions for the DM annihilation into gamma lines for different choices of g_B in the context of FOP model. As in DFW model, the points satisfy $\Omega_\chi h^2 = 0.1197 \pm 0.0022$ and the masses of the anomalous are chosen to maximize the splitting among them: $M_{\Psi^+} = 1.3M_\chi$ (for ensuring the stability of the DM) and $M_{\Sigma^+} = 2\sqrt{\pi}M_{Z_B}/3g_B$.

Regarding the gamma lines, the only difference between both models is the coupling of one of the extra fields to the Z boson. Consequently, for the same choice of masses,

the $\gamma\gamma$ line (left panel from Figs. 4.8 and 4.9) is the same in the context of both models, but there are small differences for the γZ line (right panels from Figs. 4.8 and 4.9). As it can be appreciated, for the DFW model the predictions are slightly weaker than for the FOP model (due to the fact that $\eta^-\eta^-Z$ coupling is suppressed by $\tan^2\theta_W$ with respect to the $\Sigma^+\Sigma^+Z$ coupling, as shown in the Lagrangians from Eqs. 4.76 and 4.73). The signals displayed in Figs. 4.8 and 4.9 are, unfortunately, in a region that remains a few orders of magnitude below from the current experimental sensitivity. However, we would like to remark that these two $U(1)_B$ models are two of the most motivated SM extensions that predict axial interactions between electrically-charged fermions with the new mediator that allow the predictions for the DM annihilation into gamma lines, although being small, to be different from zero. Furthermore, as discussed in Chapter 2, the fact that they predict a Majorana DM is crucial regarding the visibility of the gamma lines. This is because, from Eq. 2.74, one can see that the FSR processes are either velocity or mass (M_q/M_{Z_B}) suppressed in that context. Therefore, in this case, one can hope to distinguish the gamma lines from the continuum spectrum and that future telescopes test or rule out these predictions.

4.2.3.2 Gamma Line Spectra

The prediction for the gamma-ray flux is discussed in Sec. 2.1.2 from Chapter 2. Here we apply it to our results in the context of the DFW and the FOP models for local baryon number.

In the upper panels of Fig. 4.10 we present our results for the differential spectrum of DM annihilation into gamma rays for parameters satisfying the correct relic abundance in Model DFW and different values of the energy resolution $\xi = \{0.01, 0.05, 0.1\}$. As it can be appreciated, the gamma lines can be easily distinguished from the continuum spectrum because the FSR processes are highly suppressed. However, for gamma ray telescopes with energy resolution larger than 5% it is impossible to distinguish the gamma lines between the $\chi\chi \rightarrow \gamma\gamma$ and $\chi\chi \rightarrow \gamma Z$ annihilation channels. In the lower panels of Fig. 4.10 we also show the predictions for the differential spectrum of the DM annihilation into gamma rays for different values saturating the relic abundance in two different scenarios in the context of the FOP model.

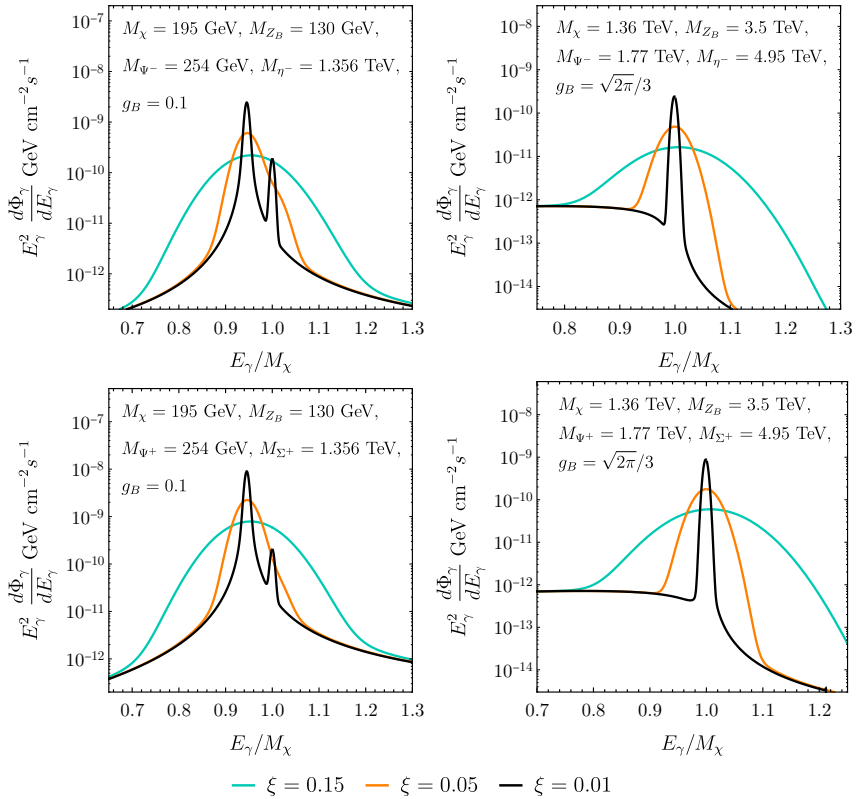


Figure 4.10: Differential spectrum of the DM annihilation into gamma rays for two different scenarios that satisfy $\Omega_\chi h^2 = 0.1197 \pm 0.0022$ [202] in DFW model (upper panels) and FOP model (lower panels). We set $M_{h_2} = 500$ GeV and $\theta_B = 0$. Lines with different colors correspond to different energy resolutions $\xi = \{0.01, 0.05, 0.1\}$. *Figure extracted from Ref. [203].*

4.3 LHC phenomenology of $U(1)_B$

Nowadays, thanks to the great effort of the experimental collaborations at the LHC we know well the properties of the SM Higgs and the existing experimental constraints on its decays and production mechanisms. See for instance Ref. [198] for a detailed discussion. The Higgs boson, however, could open a door to a NP sector. The LHC could discover new decays and/or production channels for the Higgs boson and, combining different searches, we could have access to new interactions and discover new particles with masses below the TeV scale.⁶

In this section, we investigate the effect of the existence of a new interaction with a leptophobic gauge boson in the SM Higgs phenomenology, i.e. possible new decays and production mechanisms. In this case, as discussed in Chapter 3, the leptophobic gauge boson can be light with mass below the EW scale in agreement with all experimental bounds and without the necessity to assume a tiny gauge coupling.

4.3.1 Leptophobic Gauge Boson at the LHC

Let us start presenting the decay rate of the leptophobic mediator in the scenario where it is the lightest particle from the $U(1)_B$ sector. The partial decay width of the leptophobic gauge boson Z_B with mass M_{Z_B} is given by

$$\Gamma(Z_B \rightarrow \bar{q}q) = \frac{g_B^2 M_{Z_B}}{36\pi} \sqrt{1 - \frac{4M_q^2}{M_{Z_B}^2}} \left(1 + \frac{2M_q^2}{M_{Z_B}^2} \right), \quad (4.80)$$

where M_q is the mass of a given quark. In the left panel in Fig. 4.11 we show the decay width of Z_B for different values of the gauge coupling g_B as a function of its mass. In red, we show the regions that are ruled out by the collider bounds shown in Fig. 3.5 in Chapter 3. The decay width of the Z_B allows us to infer which are the permitted values for the decay width of the leptophobic gauge boson. Moreover, with this information of the decay width at hand, we can predict the different cross-sections relevant for different collider searches. In the right panel in Fig. 4.11, we present contours of Γ_{Z_B} in

⁶See Ref. [209] for a report on future studies at the LHC.

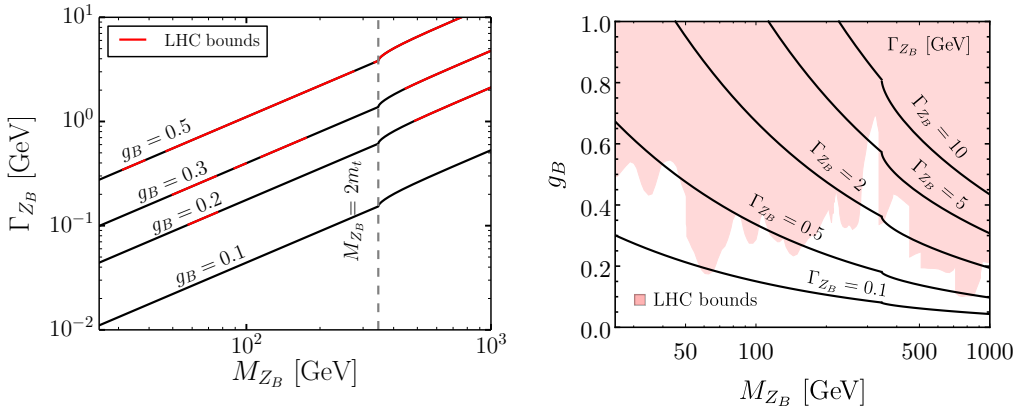


Figure 4.11: *Left panel:* Decay width of the Z_B boson as a function of its mass. The regions highlighted in red are excluded by searches at the LHC. To the right of the dashed vertical line the decay channel $Z_B \rightarrow t\bar{t}$ is open. *Right panel:* Contour lines for the decay width of the Z_B boson in the g_B vs M_{Z_B} plane. *Figure extracted from Ref. [192].*

the g_B - M_{Z_B} plane. From this figure, we conclude that a Γ_{Z_B} of order GeV is already mostly excluded.

As Fig. 3.5 from Chapter 3 shows, there is hope to produce this gauge boson at the LHC with large cross-sections, what makes it possible to study its properties. The hadronic production cross-section reads as

$$\sigma(pp \rightarrow XY)(s) = \int_{\tau_0}^1 d\tau \frac{d\mathcal{L}_{q\bar{q}}^{pp}}{d\tau} \sigma(q\bar{q} \rightarrow XY)(\hat{s}), \quad (4.81)$$

where $\sigma(q\bar{q} \rightarrow XY)(\hat{s})$ corresponds to the partonic cross-section and

$$\frac{d\mathcal{L}_{q\bar{q}}^{pp}}{d\tau} = \int_{\tau}^1 \frac{dx}{x} \left[f_{q/p}(x, \mu) f_{\bar{q}/p}\left(\frac{\tau}{x}, \mu\right) + f_{q/p}\left(\frac{\tau}{x}, \mu\right) f_{\bar{q}/p}(x, \mu) \right]. \quad (4.82)$$

In the above expressions, the parameter $\tau = \hat{s}/s$, where \hat{s} is the partonic center-of-mass energy squared, s is the hadronic center-of-mass energy squared, $\tau_0 = (M_X + M_Y)^2/s$ is the production threshold, and μ is the factorization scale. Let us study the different partonic cross-sections where the Z_B can contribute:

and the coefficients C_V and C_A correspond to the vector and axial couplings of the gauge bosons, respectively, which are given by

$$Z_B Z : C_V = \frac{g}{\cos \theta_W} \left(\frac{1}{2} T_q^3 - Q_q \sin^2 \theta_W \right), \quad C_A = -\frac{g}{2 \cos \theta_W} T_q^3, \quad (4.88)$$

$$Z_B W^\pm : C_V = \frac{g}{2\sqrt{2}}, \quad C_A = -\frac{g}{2\sqrt{2}}, \quad (4.89)$$

$$Z_B Z_B : C_V = \frac{g_B}{3}, \quad C_A = 0. \quad (4.90)$$

- For the process $q\bar{q} \rightarrow Z_B \gamma$, described by diagrams in Eq. 4.85 but replacing the EW bosons by a photon, the averaged squared amplitude is given by,

$$|\overline{\mathcal{M}}(q\bar{q} \rightarrow Z_B \gamma)|^2 = \frac{2 e^2 Q_q^2 g_B^2 [M_{Z_B}^4 - 2M_{Z_B}^2 t + s^2 + 2t(s+t)]}{27 t (M_{Z_B}^2 - s - t)}, \quad (4.91)$$

where Q_q corresponds to the electric charge of the quark. In order to compute the proton-proton cross-section we impose the following cuts on the rapidity and the transverse momentum:

$$|\eta| < 2.5, \quad \text{and} \quad p_T > 150 \text{ GeV}. \quad (4.92)$$

These cuts will be also applied in the channels $pp \rightarrow Z_B q$ and $Z_B g$.

- For the process $q\bar{q} \rightarrow Z_B g$, described by the same feynman graphs as those shown in Eq. 4.85 but replacing the EW bosons by a gluon. We have

$$|\overline{\mathcal{M}}(q\bar{q} \rightarrow Z_B g)|^2 = \frac{8 g_S^2 g_B^2 [M_{Z_B}^4 - 2M_{Z_B}^2 t + s^2 + 2t(s+t)]}{81 t (M_{Z_B}^2 - s - t)}, \quad (4.93)$$

where g_S corresponds to the strong coupling in the SM. In here we also make use of the cuts listed in Eq. 4.92.

- For the process $qg \rightarrow Z_B q$, characterized by the following diagrams,

$$(4.94)$$

the averaged squared amplitude is given by

$$|\overline{\mathcal{M}}(qg \rightarrow Z_B q)|^2 = \frac{g_B^2 g_S^2}{27} \frac{M_{Z_B}^4 - 2M_{Z_B}^2 s + 2s^2 + 2st + t^2}{s(s+t - M_{Z_B}^2)}, \quad (4.95)$$

and we follow the same procedure as the previous processes, using the cuts from Eq. 4.92 to compute the proton-proton cross-section.

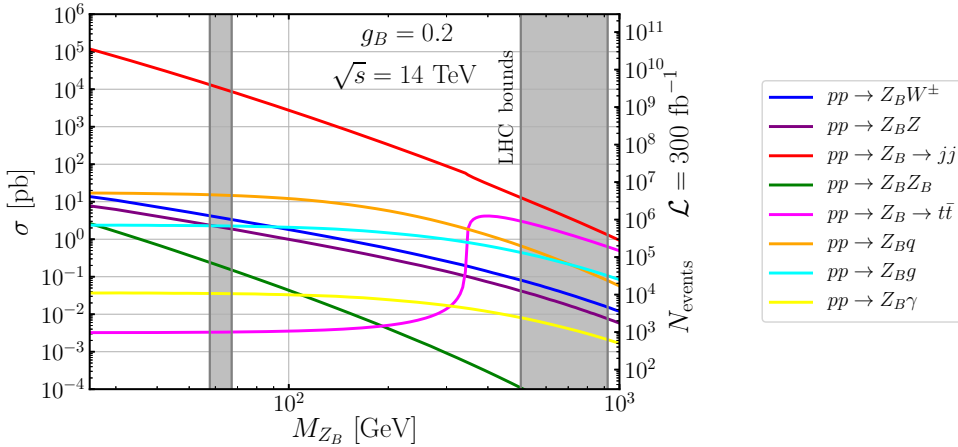


Figure 4.12: Production cross-sections at the LHC for center-of-mass energy of 14 TeV in units of picobarns. We fixed $g_B = 0.2$ for illustration. On the right side of the vertical axis we show the expected number of events assuming 300 fb^{-1} for the integrated luminosity. The regions shaded in gray are excluded by LHC searches for the Z_B boson. *Figure extracted from Ref. [192].*

In Fig. 4.12 we present our results for the production cross-section for different channels that involve at least one Z_B , fixing the gauge coupling to $g_B = 0.2$. These results correspond to the LHC with center-of-mass energy of 14 TeV and the number of events

shown on the right vertical axis corresponds to an integrated luminosity of 300 fb^{-1} . The model has been implemented in `FeynRules 2.0` [210] and the cross-sections obtained using `MadGraph5aMC@NLO - v2.7.0` [211] (at tree-level), we cross-checked our results in a `Mathematica` notebook where we use of the `MSTW2008` [212] set of parton distribution functions. From Fig. 4.12 one can see that the dijet cross-section dominates across the plot, and in the region $M_{Z_B} > 2M_t$ the process $pp \rightarrow Z_B \rightarrow t\bar{t}$ can be large as well. The process $pp \rightarrow Z_B q$ can be significant, since there is a large contribution from the parton distribution function of the gluon in the initial state. We note that the $pp \rightarrow Z_B \gamma$, $Z_B q$ and $Z_B g$ channels are relevant for searches in the low mass regime.

4.3.2 Exotic Decays of the SM-like Higgs

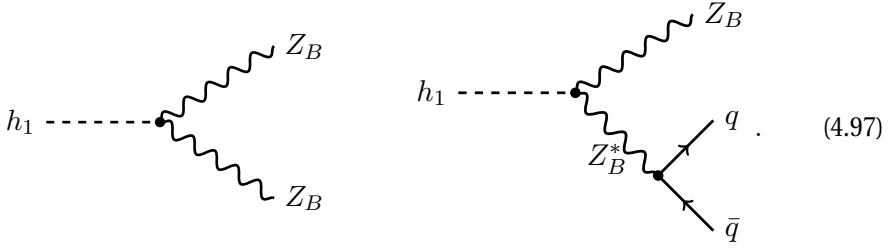
In extensions of the SM with a leptophobic gauge boson [166,168,169,171], its mass generation comes from the vev of a new Higgs boson charged under $U(1)_B$, and hence, the models have two Higgs scalars that can mix with each other, as described in Eq. 4.9. After SSB, the SM-like Higgs (h_1) will have the following coupling to the Z_B :

$$h_1 Z_B^\mu Z_B^\nu : 2i \frac{M_{Z_B}^2}{v_B} g^{\mu\nu} \sin \theta_B, \quad (4.96)$$

where θ_B is the mixing angle in the scalar sector, defined in Eq. 4.10, $M_{Z_B} = n_B g_B v_B$ and n_B is the baryon number of the scalar breaking $U(1)_B$. In the context of the minimal models for local baryon number, i.e. DFW and FOP, $n_B = 3$. Since the leptophobic gauge boson can be light, the SM-like Higgs can have the following decays

$$h_1 \rightarrow Z_B Z_B, Z_B^* Z_B,$$

depending on the Z_B mass.



Notice that the couplings between the SM-like Higgs and SM particles will scale by a factor $\cos \theta_B$. By computing the total Higgs decay width $\Gamma_{h_1} = \cos^2 \theta_B \Gamma_{\text{SM}} + \Gamma_{\text{BSM}}$, where in our case Γ_{BSM} corresponds to the decay into two leptophobic gauge bosons, we can quantify the impact of these novel decays of the SM-like Higgs. In our study we

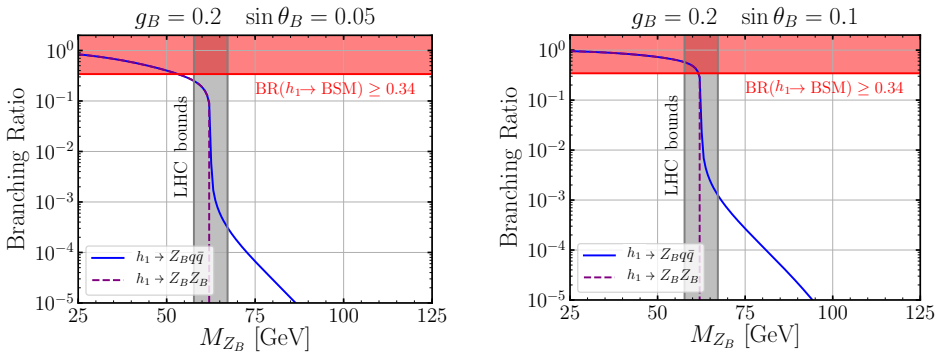


Figure 4.13: Branching ratios for the channels $h_1 \rightarrow Z_B Z_B$ and $h_1 \rightarrow Z_B Z_B^* \rightarrow Z_B q \bar{q}$. The left (right) panel corresponds to $g_B = 0.2$ and $\sin \theta_B = 0.1$ ($\sin \theta_B = 0.05$). The region shaded in red shows the exclusion bounds from the constraint $\text{BR}(h_1 \rightarrow \text{BSM}) < 0.34$. The region shaded in gray corresponds to the exclusion bounds from direct searches for the Z_B boson at the LHC. *Figure extracted from Ref. [192].*

take the bound $\sin \theta_B \leq 0.3$ [195], according to Eq. 4.11. Current LHC measurements of the properties of the SM-like Higgs boson give the following constraint on its branching ratio into BSM particles [213]

$$\text{BR}(h_1 \rightarrow \text{BSM}) < 0.34 \quad \text{at } 95\% \text{ C.L.}, \quad (4.98)$$

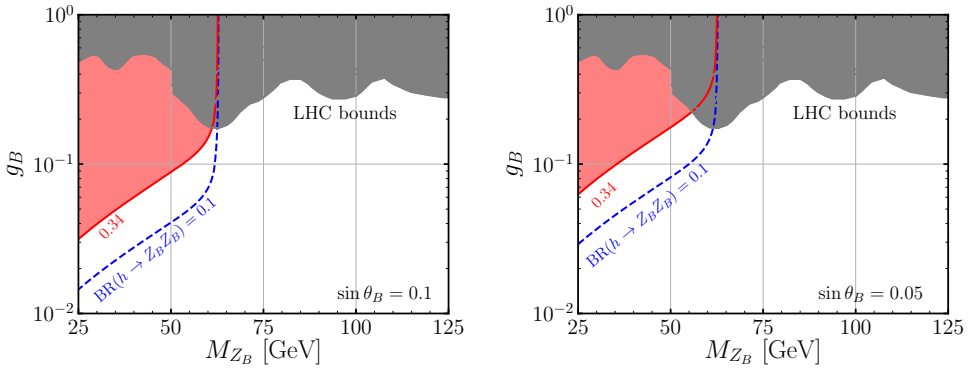


Figure 4.14: Exclusion bounds in the g_B vs M_{Z_B} plane. The region shaded in red shows the exclusion bounds from the constraint on the SM-like Higgs branching ratio $\text{BR}(h \rightarrow Z_B Z_B) < 0.34$, while the blue dashed line corresponds to $\text{BR}(h_1 \rightarrow Z_B Z_B) = 0.1$. The region shaded in gray is excluded by searches for the Z_B at the LHC. The left (right) panel corresponds to $\sin \theta_B = 0.1$ ($\sin \theta_B = 0.05$). *Figure extracted from Ref. [192].*

which is obtained assuming the production of the Higgs in the SM. Therefore, we scale the bound by the ratio between the production cross-section for the Higgs in the SM with the one in this model, which is given by $\text{BR}(h_1 \rightarrow \text{BSM}) < 0.34 \times (\sigma_{h_1}^{\text{SM}} / \sigma_{h_1}) = 0.34 / \cos^2 \theta_B$. The width for the new two-body decays, $h_1 \rightarrow Z_B Z_B$, of the SM Higgs boson is

$$\Gamma(h_1 \rightarrow Z_B Z_B) = \frac{G_B M_{h_1}^3 \sin^2 \theta_B}{16\sqrt{2}\pi} \sqrt{1 - 4x} (1 - 4x + 12x^2), \quad (4.99)$$

with $x = M_{Z_B}^2 / M_{h_1}^2$ and $G_B = 1 / (\sqrt{2} v_B^2)$.

The three-body decay, $h_1 \rightarrow Z_B(p_1) q(p_2) \bar{q}(p_3)$, is given by

$$\Gamma(h_1 \rightarrow Z_B q \bar{q}) = \frac{1}{(2\pi)^3} \frac{1}{32 M_{h_1}^3} \int_{p_{12}^{\min}}^{p_{12}^{\max}} dp_{12} \int_{p_{23}^{\min}}^{p_{23}^{\max}} dp_{23} |\bar{A}(h_1 \rightarrow \bar{q} q Z_B)|^2 \quad (4.100)$$

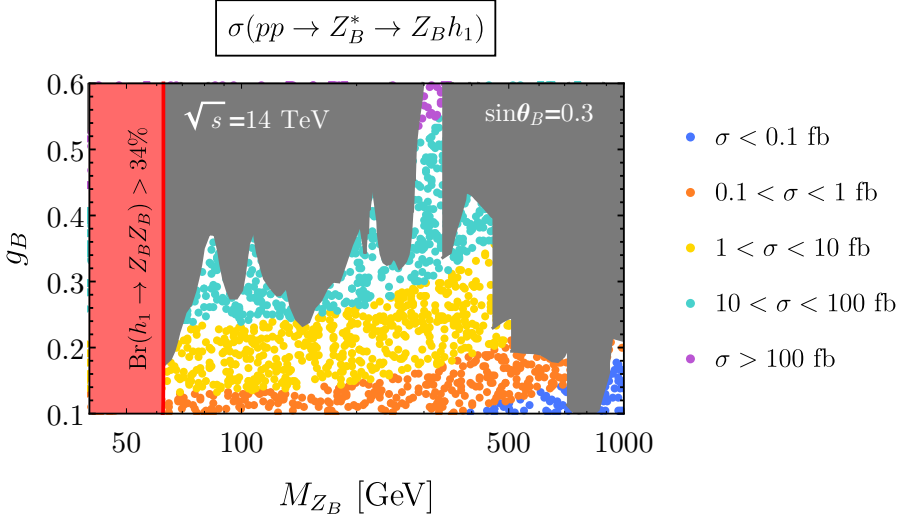


Figure 4.15: Predictions for the associated production cross-section $pp \rightarrow Z_B^* \rightarrow Z_B h_1$ at the LHC with center-of-mass energy of 14 TeV. The gray region is excluded by the LHC bounds, while the red region is excluded by the bound on the branching ratio of the new Higgs decays. The scalar mixing angle is fixed to $\sin \theta_B = 0.3$ for this plot. *Figure extracted from Ref. [192].*

Neglecting the quark masses we have that

$$\begin{aligned}
 p_{12}^{\min} &= M_{Z_B}^2, & p_{12}^{\max} &= M_{h_1}^2, \\
 p_{23}^{\min} &= 0, & p_{23}^{\max} &= \frac{1}{p_{12}}(p_{12} - M_{Z_B}^2)(M_{h_1}^2 - p_{12}),
 \end{aligned} \tag{4.101}$$

where $p_{ij} = (p_i + p_j)^2$ and the spin-averaged squared amplitude is given by

$$\begin{aligned}
 |\overline{A}(h_1 \rightarrow \bar{q}q Z_B)|^2 &= \frac{8 g_B^2}{3 v_B^2} \frac{M_{Z_B}^4 \sin^2 \theta_B}{\left((p_{23} - M_{Z_B}^2)^2 + M_{Z_B}^2 \Gamma_{Z_B}^2 \right)} \\
 &\times \left(p_{23} + \frac{(p_{12} - M_{Z_B}^2)(M_{h_1}^2 - p_{12} - p_{23})}{M_{Z_B}^2} \right). \tag{4.102}
 \end{aligned}$$

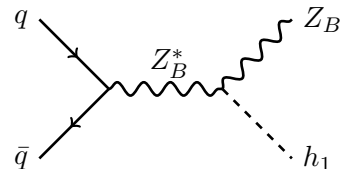
In Fig. 4.13 we present the results obtained for the branching ratios for the decay channels $h_1 \rightarrow Z_B Z_B$ and $h_1 \rightarrow Z_B q \bar{q}$ of the SM Higgs. The latter includes both, the on-shell and the off-shell contribution from the Z_B . In the region with $M_{Z_B} \leq M_{h_1}/2 \approx 62.5$ GeV the channel $h_1 \rightarrow Z_B Z_B$ becomes the dominant decay channel and the Higgs decay width can become of order GeV. In this region, the bound on $\text{BR}(h_1 \rightarrow \text{BSM}) < 0.34$ gives a strong constraint shown by the area shaded in red. The gray band in this figure corresponds to the exclusion bounds from direct searches for the Z_B boson at the LHC discussed in the last section of Chapter 3.

On the other hand, when $M_{Z_B} \geq M_{h_1}/2$ the two-body decay is kinematically closed and the three-body decay gives a much smaller contribution to the Higgs width. In this regime, experiments can search for the associated Higgs Z_B production to probe the existence of these interactions, as we discuss in the following section.

The experimental bound on the branching ratio of Higgs decays to BSM particles can be translated to the g_B vs M_{Z_B} plane. Nevertheless, we note that this bound also depends on the scalar mixing. In Fig. 4.14 we present our results for two different mixing angles. For $\sin \theta_B = 0.1$ this constraint is strong in the region $M_{Z_B} \leq M_{h_1}/2$ and excludes $g_B \gtrsim 0.03$ for $M_{Z_B} = 25$ GeV. In order to relax this bound one needs to go to very small mixing angles, $\sin \theta_B < 0.05$, as shown in the right panel. It is important to emphasize that the SM-like Higgs can have a large branching ratio into two leptophobic gauge bosons in agreement with all current experimental bounds.

4.3.3 Associated production

In the previous section we discussed the possible new Higgs decays due to the existence of a leptophobic gauge boson. In the scenarios where these Higgs decays are not allowed or highly suppressed, one can study the associated production:

$$pp \rightarrow Z_B^* \rightarrow Z_B h_1, \quad (4.103)$$


to test the existence of the new h_1 - Z_B - Z_B interaction. The cross-section at the partonic level is given by

$$\sigma(\bar{q}q \rightarrow Z_B^* \rightarrow Z_B h_1)(\hat{s}) = \frac{g_B^4 \sin^2 \theta_B \left[\hat{s}^2 - 2\hat{s}(M_{Z_B}^2 + M_{h_1}^2) + (M_{Z_B}^2 - M_{h_1}^2)^2 \right]^{1/2}}{144\pi\hat{s}^2 \left[(\hat{s} - M_{Z_B}^2)^2 + M_{Z_B}^2 \Gamma_{Z_B}^2 \right]} \times \left[\hat{s}^2 + 2\hat{s}(5M_{Z_B}^2 - M_{h_1}^2) + (M_{Z_B}^2 - M_{h_1}^2)^2 \right], \quad (4.104)$$

In Fig. 4.15 we show the numerical predictions for the associated production $pp \rightarrow Z_B^* \rightarrow Z_B h_1$ in the g_B - M_{Z_B} plane, in the maximal mixing scenario where $\sin \theta_B = 0.3$ and with center-of-mass energy of $\sqrt{s} = 14$ TeV. The region shaded in red is excluded by the experimental bound on the branching ratio of the SM Higgs into BSM particles discussed in the previous section. The different colored dotted regions correspond to the predictions in different ranges: $\sigma < 0.1$ fb (blue dots), $0.1 \text{ fb} < \sigma < 1$ fb (orange dots), $1 \text{ fb} < \sigma < 10$ fb (yellow dots), $10 \text{ fb} < \sigma < 100$ fb (cyan dots), and $\sigma > 100$ fb (purple dots). The production cross-section can easily be in the tens of femtobarns which is not too far from the $pp \rightarrow Zh_1$ cross-section of 990.33 fb in the SM [214]. The region shaded in gray is excluded by the collider bounds discussed in Fig. 3.5 from Chapter 3. The associated cross-section is proportional to $\sin^2 \theta_B$. Therefore, although in Fig. 4.15 we show only the predictions for $\sin \theta_B = 0.3$, one can easily find the predictions for other mixing angles by properly scaling them. It is important to mention that the associated production can be significant due to the fact that the gauge coupling can be large and the mass of the leptophobic gauge boson can be below the EW scale.

Knowing the possible h_1 and Z_B decays we can show the predictions for the number of events at the LHC for the following channels:

$$\gamma\gamma t\bar{t}, \gamma\gamma b\bar{b}, \gamma\gamma jj, b\bar{b}b\bar{b}, b\bar{b}t\bar{t}, \text{ and } b\bar{b}jj.$$

The number of events for each of these channels is given by

$$N_{\text{events}}(x\bar{x}y\bar{y}) = \mathcal{L} \times \sigma(pp \rightarrow Z_B^* \rightarrow Z_B h_1) \times \text{BR}(h_1 \rightarrow x\bar{x}) \times \text{BR}(Z_B \rightarrow y\bar{y}). \quad (4.105)$$

In Fig. 4.16 we show the predictions for the expected number of events assuming that the integrated luminosity is $\mathcal{L} = 3000 \text{ fb}^{-1}$ as planned for the High-Luminosity LHC [215], and using the maximal allowed value for the mixing angle $\sin \theta_B = 0.3$. The gray regions in Fig. 4.16 are excluded by the collider bounds discussed in Fig. 3.5 from Chapter 3, while the regions in red are excluded by the experimental bound on the branching ratio of SM Higgs exotic decays.

The $Z h_1$ associated production has been measured at ATLAS [216] and CMS [217], and a similar technique can be used to make the reconstruction of the processes in Fig. 4.16. However, in our case the Z_B decays only to quarks and then the QCD background is more challenging. For example, the largest number of events is for the channel: $pp \rightarrow Z_B h_1 \rightarrow jj\bar{b}b$. In this case two b jets should have an invariant mass around the Higgs mass of 125 GeV. Furthermore, the large p_T of the Higgs or the gauge boson can help to discriminate the signal with respect to the background [218].

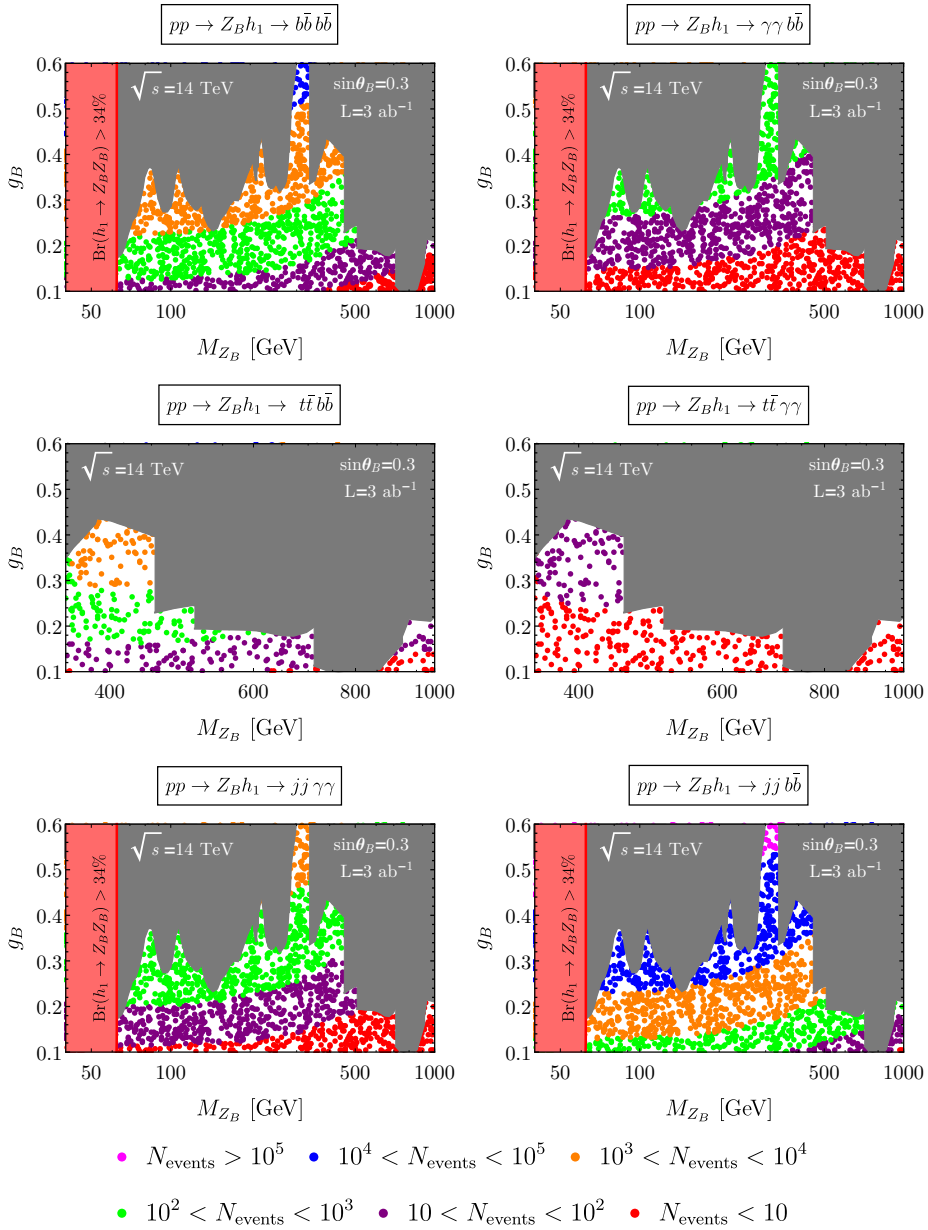


Figure 4.16: Predictions for the number of events at the LHC with center-of-mass energy of 14 TeV assuming that the integrated luminosity is $\mathcal{L} = 3000$ fb $^{-1}$ and using the maximal allowed value for the mixing angle $\sin\theta_B = 0.3$. We show the number of events for the most relevant channels: $\gamma\gamma t\bar{t}$, $\gamma\gamma b\bar{b}$, $\gamma\gamma jj$, $b\bar{b}b\bar{b}$, $b\bar{b}t\bar{t}$, and $b\bar{b}jj$. The gray region is excluded by the LHC bounds, while the red region is excluded by the bound on the branching ratio of the new Higgs decays. *Figure extracted from Ref. [192].*

4.4 Conclusions

Along this chapter we have studied the main phenomenological features on the minimal gauge theories for baryon number. In the first part, we have presented a detailed study on the cosmological and phenomenological features of the possible DM candidate predicted in these theories, whereas the second part has been devoted to the analysis of possible signals from theories for local baryon number at colliders. Let us briefly expose in a clean way the highlights of the results obtained. In the simplest class of theories where the baryon number is promoted to a local symmetry:

- There is an extra electrically neutral field, $\chi \sim (1, 1, 0, n_\chi)$, predicted by the cancellation of gauge anomalies, which can be stable and hence a good cold DM candidate.
- The mass of the DM candidate is determined by the new symmetry breaking scale; in this case, the scale of baryon number violation.
- The stability of the DM candidate is a natural consequence of the symmetry breaking.
- The masses of the fermions required for anomaly cancellation have an upper bound defined by the new symmetry scale. Among them, the electrically-charged fermions contribute to annihilation of DM into gamma lines.
- An upper bound on the symmetry breaking scale can be found by applying cosmological relic density constraints.

We have found such upper bound to be around the $\mathcal{O}(10)$ TeV scale, what implies that these theories should live somewhere below. Furthermore,

- A light Z_B leptophobic boson, even below the EW scale, can exist in agreement with all experimental bounds and without assuming a very small gauge coupling.

The theoretical power of predicting a viable DM candidate and a source of dynamic baryon number violation, together with the capability of being tested at current or near future experiments make these theories of local baryon number very attractive and turn them into strong candidates for physics beyond the SM.

5.- Leptophilic force

Towards the Neutrino-DM connection.

Chapter based on the work done in 1803.07462 and 1905.06344.

The origin of neutrino masses and the nature of the DM in the Universe are two of the most exciting open problems in particle physics and cosmology, see Chapters 1 and 2 for details. The simplest gauge symmetries we can employ to understand the origin of neutrino masses are $U(1)_{B-L}$ or $U(1)_L$, where B and L stand for baryon and lepton numbers, respectively. As discussed in Chapter 1, there is a deep connection between neutrino masses and lepton number violation. The neutrinos are Majorana fermions when the $B-L$ (or L) symmetry is broken in two units, or they can be Dirac fermions when $B-L$ (or L) is conserved or broken in units different (and greater) than two. In both cases, we can hope to test the mechanism for neutrino masses only if the $B-L$ (or L) violation scale can be reached at current or future colliders. Unfortunately, in a large class of models for Majorana neutrino masses based on the seesaw mechanism [12, 16, 219, 220], the canonical seesaw scale can be very large, $M_{\text{seesaw}} \lesssim 10^{14}$ GeV, which makes the mechanism barely possible to falsify.

In this chapter, we investigate possible connections between the origin of neutrino masses and the properties of DM candidates in simple gauge extensions of the SM based on theories where the lepton number is gauged: local $B-L$ or L symmetries. See Fig. 5.1 for an illustration of this connection. We focus on two main scenarios in the context of $B-L$ theories: (a) Stueckelberg Scenario and (b) Canonical Seesaw Scenario. In the Stueckelberg scenario, the $B-L$ symmetry remains unbroken, the neutrinos are Dirac fermions and the gauge boson acquires mass through the Stueckelberg mechanism. In the Canonical Seesaw scenario the $U(1)_{B-L}$ symmetry is spontaneously broken in

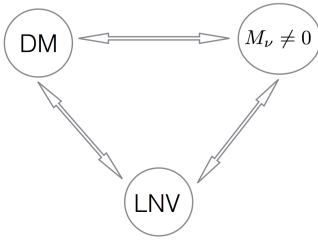


Figure 5.1: Correlation between the origin of neutrino masses, properties of cold DM candidate and lepton number violating (LNV) signatures. *Figure extracted from Ref. [221].*

two units using the Higgs mechanism and the neutrinos are consequently Majorana fermions. In both cases the DM candidate is a vector-like Dirac fermion charged under the $U(1)_{B-L}$ symmetry. For other studies of gauged $B-L$ with a DM candidate see Refs. [222–232], and for scenarios that explore a connection between the origin of neutrino masses and the DM candidate see Refs. [233–238].

We study the simplest theories with gauged lepton number, $U(1)_L$ [168, 169, 171, 239], discussed in Chapter 3, where the existence of a DM candidate is predicted from anomaly cancellation. Models with gauged lepton number have also been studied in Refs. [240–244]. For the simplest local $U(1)_L$, the lepton number is broken in three units and the neutrinos are predicted to be Dirac fermions, while the DM candidate is a Majorana fermion.

In the first part of this chapter, we will study the cosmological constraints on the relic DM density. In the context of these theories, we will show, as we were told in Chapter 4 for $U(1)_B$, that the upper bound on the lepton number violating scale is in the multi-TeV scale. Therefore, one can hope to test these theories for neutrino masses and DM in the near future. If neutrinos are Majorana, the discovery of lepton number violating signatures in low energy experiments or at colliders will be striking signals for NP beyond the SM. In low energy experiments we could discover neutrinoless double beta decay, and at colliders different signatures with same-sign leptons could be seen [245]. If neutrinos are Dirac, we find a strong bound coming from the measurement of the number of effective relativistic neutrino species (N_{eff}) in the early Universe. These discoveries will be crucial to establish the origin of neutrino masses. Our main results suggest that one could be optimistic about the possibility to test the different theories for neutrino masses if there is a simple connection to the properties and origin of DM candidates.

5.1 Unbroken local $U(1)_{B-L}$: Stueckelberg Scenario

The simplest gauge theory where one can understand the origin of neutrino masses is based on local $B-L$. As stated in Chapter 3, anomaly cancellation requires three copies of RH neutrinos. The way lepton number dynamically breaks in this theory, if it ever does, will determine the nature of neutrino masses. In this section, we present the possibility of an unbroken local $B-L$. Consequently, since $U(1)_{B-L}$ is a conserved symmetry, neutrinos will be Dirac particles in this context.

5.1.1 Theoretical framework

The local gauge symmetry $U(1)_{B-L}$ can remain conserved¹ and the associated gauge boson can acquire mass through the Stueckelberg mechanism, as discussed in Chapter 3. Due to the absence of a scalar particle in the $B-L$ sector, it is not possible to write a mass term for a Majorana fermion charged under $U(1)_{B-L}$. Therefore, the DM candidate could be either a scalar $\phi \sim (1, 1, 0, n_\chi)$ or a Dirac fermion with quantum numbers,

$$\chi \sim (1, 1, 0, n_\chi), \quad (5.1)$$

corresponding to the gauge groups $(SU(3)_c, SU(2)_L, U(1)_Y, U(1)_{B-L})$. In the case where the DM is a scalar field, it is not possible to predict an upper bound for the mass of the $B-L$ gauge boson. This is because, through the introduction of a Higgs portal term, $\phi^\dagger \phi H^\dagger H$, the DM candidate can be produced and the Z_{BL} boson can be decoupled. Motivated by the possibility to find an upper bound on the theory and explore its implications, in here we will discuss the scenario where the DM is a Dirac fermion. Unfortunately, χ is not predicted in this theory and we have to include it in order to account for DM. In order to guarantee the stability of the field χ , we should ensure $n_\chi \neq 1$; since such $B-L$ charge allows for χ to mix with the neutrinos and decay. In addition, n_χ cannot be arbitrarily large; perturbativity requires

$$n_\chi g_{BL} < \sqrt{4\pi}, \quad (5.2)$$

¹We remind the reader to the fact that this theory, unlike $U(1)_B$ or $U(1)_L$, is anomaly free (up to the inclusion of three copies of RH neutrinos) so that there is no phenomenological need to break the symmetry since the theory does not predict massless anomalies in this case.

to be satisfied, which comes from the kinetic term of the DM candidate. For a fermion DM candidate singlet under the SM gauge group and charged under the B - L force, the relevant Lagrangian is given by,²

$$\begin{aligned} \mathcal{L} \supset & i\overline{\chi_L}\gamma^\mu D_\mu\chi_L + i\overline{\chi_R}\gamma^\mu D_\mu\chi_R - (Y_\nu\overline{\ell_L}i\sigma_2 H^*\nu_R + M_\chi\overline{\chi_L}\chi_R + \text{h.c.}) \\ & - \frac{1}{2}(M_{Z_{BL}}Z_{BL}^\mu + \partial^\mu\sigma)(M_{Z_{BL}}Z_{BL\mu} + \partial_\mu\sigma), \end{aligned} \quad (5.3)$$

which is invariant under the following gauge transformations,

$$\delta Z_{BL}^\mu = \partial^\mu\lambda(x) \quad \text{and} \quad \delta\sigma = -M_{Z_{BL}}\lambda(x), \quad (5.4)$$

and the σ field decouples from the theory. When the Stueckelberg mechanism is applied to an Abelian gauge group, the theory is renormalizable and unitary. However, for non-Abelian gauge groups, violation of unitarity arises at tree-level in the scattering of longitudinal gauge bosons.

The properties of the DM candidate, $\chi = \chi_L + \chi_R$, are defined by the B - L gauge interaction. The model contains only four free parameters:

$$M_\chi, \quad M_{Z_{BL}}, \quad g_{BL}, \quad \text{and} \quad n_\chi. \quad (5.5)$$

For the rest of our discussion we fix $n_\chi = 1/3$ for simplicity, but the main conclusions can be applied to any other scenario with a different B - L charge.

5.1.2 Cosmological bounds

In this section we discuss the implication of cosmological bounds like the relic abundance $\Omega_\chi h^2 = 0.1200 \pm 0.0012$ [7] measured by Planck and the current and projected bounds on the number of effective d.o.f. N_{eff} given by the Planck satellite mission [7], and CMB Stage-IV [246] experiments, respectively.

²Note that M_χ is a bare mass term in the Lagrangian, not protected by its symmetries.

5.1.2.1 Relic Density

The annihilation channels of our DM candidate are:

$$\bar{\chi}\chi \rightarrow e_i^+ e_i^-, \bar{\nu}_i \nu_i, \bar{u}_i u_i, \bar{d}_i d_i, Z_{BL} Z_{BL},$$

represented explicitly in the Feynman graphs from below:

(5.6)

The annihilation cross section for $\bar{\chi}\chi \rightarrow Z_{BL}^* \rightarrow \bar{f}f$ is given by

$$\sigma_{\bar{\chi}\chi \rightarrow \bar{f}f} = \frac{N_c^f n_f^2 g_{BL}^4 n_\chi^2}{12\pi s} \frac{\sqrt{s - 4M_f^2} (s + 2M_\chi^2) (s + 2M_f^2)}{\sqrt{s - 4M_\chi^2} \left[(s - M_{Z_{BL}}^2)^2 + M_{Z_{BL}}^2 \Gamma_{Z_{BL}}^2 \right]}. \quad (5.7)$$

Here N_c^f is the color multiplicity of the fermion f , i.e. $N_c^f = 1(3)$ for fermions (quarks), with mass M_f , n_f is the $B-L$ charge of the leptons, -1 for leptons and $1/3$ for quarks, s is the square of the center-of-mass energy, and $\Gamma_{Z_{BL}}$ is the total decay width of the Z_{BL} gauge boson, given by

$$\sum_{f_i} \Gamma(Z_{BL} \rightarrow \bar{f}_i f_i) = \sum_{f_i} \frac{g_{BL}^2 N_c^{f_i} n_{f_i}^2}{12\pi M_{Z_{BL}}} \sqrt{1 - \frac{4M_{f_i}^2}{M_{Z_{BL}}^2} (2M_{f_i}^2 + M_{Z_{BL}}^2)}. \quad (5.8)$$

On the other hand, the annihilation cross section for $\bar{\chi}\chi \rightarrow Z_{BL}Z_{BL}$ is given by

$$\sigma(\bar{\chi}\chi \rightarrow Z_{BL}Z_{BL}) = \frac{g_{BL}^4 n_\chi^4 \omega}{32\pi E^2 v} \left[-1 - \frac{(2+z^2)^2}{(2-z^2)^2 - 4v^2} + \frac{6-2z^2+z^4+12v^2+4v^4}{2v\omega(1+v^2+\omega^2)} \ln \left(\frac{1+(v+\omega)^2}{1+(v-\omega)^2} \right) \right], \quad (5.9)$$

where z , v and ω are defined as

$$z = M_{Z_{BL}}/M_\chi, \quad v = p/M_\chi, \quad \text{and} \quad \omega = k/M_\chi, \quad (5.10)$$

being E and p the center-of-mass energy and momentum of the initial particles respectively, $E = \sqrt{s}/2$ and $p = \sqrt{E^2 - M_\chi^2}$, and k the momentum of the final particles, $k = \sqrt{E^2 - M_{Z_{BL}}^2}$.

We note that the annihilation channel into fermions is the dominant one, with a higher contribution from annihilation into leptons due to their larger coupling to Z_{BL} . Since $n_\chi < 1$, the perturbative bound directly applies to the gauge coupling through the kinetic term of the leptons and is given by:

$$g_{BL} < 2\sqrt{\pi}. \quad (5.11)$$

In order to compute numerically the DM relic abundance, $\Omega_\chi h^2$, we use `MicrOMEGAS 5.0.6` [73], implementing the model with the help of `LanHEP 3.2` [201]. We cross-check our results with an independent calculation in `Mathematica`. In Fig. 5.2, we present our results in the M_χ - $M_{Z_{BL}}$ plane for the Stueckelberg scenario. The solid blue line satisfies the correct DM relic abundance $\Omega_\chi h^2 = 0.1200 \pm 0.0012$ [7], while the region shaded in light blue overproduces it. The latter is then ruled out by cosmology unless the thermal history of the Universe is altered. The horizontal red (pink) line corresponds to the LEP [181] (LHC [182]) bound on the mass of the Z_{BL} gauge boson, which were discussed at the end of Chapter 3 (see Fig. 3.4). The left (right) panel corresponds to $g_{BL} = 1.5$ ($g_{BL} = 2$) and $n_\chi = 1/3$. The solid green line shows current experimental bounds from Xenon-1T [205] whereas the purple lines show the projected sensitivity for Xenon-nT [81], which will be discussed in the following subsections.

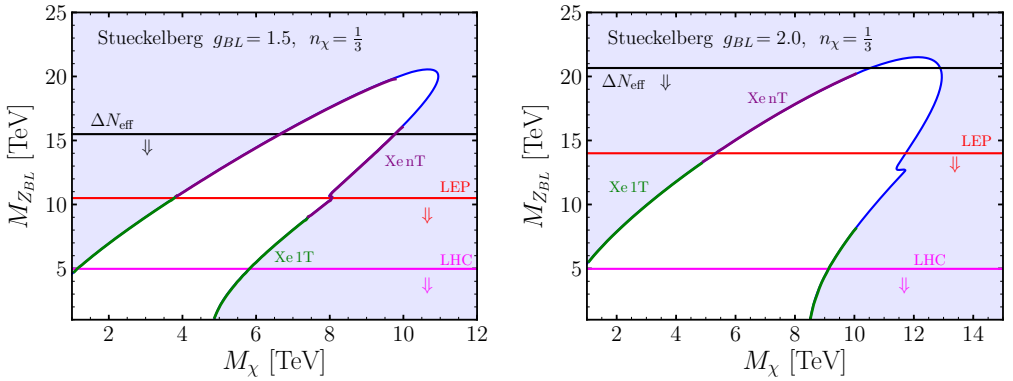


Figure 5.2: Results for the DM relic density in the $(M_\chi, M_{Z_{BL}})$ plane for the Stueckelberg scenario. The solid blue line satisfies the correct DM relic abundance, while the region shaded in light blue overproduces it. For the points that saturate the relic abundance, we mark in green those that are excluded by Xenon-IT [205] and in purple those that will be reached by the Xenon-nT [81] experiment. The horizontal red (pink) line corresponds to the LEP [181] (LHC [182]) bound on the mass of the Z_{BL} gauge boson. The left (right) panel corresponds to $g_{BL} = 1.5$ ($g_{BL} = 2$) and $n_\chi = 1/3$. The bounds from N_{eff} are shown by the horizontal black line. *Figure extracted from Ref. [183].*

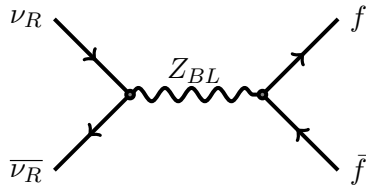
The small feature that can be observed in the right panel at around $M_\chi \approx 12$ TeV corresponds to the region in parameter space where the $\chi\chi \rightarrow Z_{BL}Z_{BL}$ channel also contributes to the relic density.

5.1.2.2 Number of effective relativistic neutrino species (N_{eff})

As discussed in Section 2.1.1.1 from Chapter 2, the RH neutrinos feel the $B-L$ interaction and they could be thermalized with the SM plasma in the early Universe and therefore contribute to N_{eff} , due to their relativistic nature. They can remain in thermal equilibrium with the SM via exchange of the new gauge boson, in this case Z_{BL} , as diagram Diag. 5.13 shows. The cross-section for such annihilation process is given by

$$\sigma_{\bar{\nu}_R \nu_R \rightarrow \bar{f} f} = \frac{g'^4}{12\pi\sqrt{s}} \frac{1}{(s - M_{Z'}^2)^2 + \Gamma_{Z'}^2 M_{Z'}^2} \sum_f N_c^f n_f^2 \sqrt{s - 4M_f^2} (2M_f^2 + s), \quad (5.12)$$

where $Z' \equiv Z_{BL}$ and $g' \equiv g_{BL}$ here.


(5.13)

In this study, we focus on heavy mediators $T_{\nu_R}^{\text{dec}} \ll M_{Z'}$, and hence, we can work in the limit $s \ll M_{Z'}$. Neglecting the fermion masses, the interaction rate, described in Eq. 2.26 from Chapter 2, reads as

$$\Gamma_{\nu_R}(T) = \frac{49\pi^5 T^5}{97200\xi(3)} \left(\frac{g_{BL}}{M_{Z_{BL}}} \right)^4 \sum_f N_c^f n_f^2, \quad (5.14)$$

where the sum is taken over all SM fermions that are in thermal equilibrium at the temperature T . In order to understand the bounds in models where the RH neutrinos are very light, we use the value for N_{eff} derived from the CMB measurement by the Planck satellite mission [7],

$$N_{\text{eff}} = 2.99_{-0.33}^{+0.34} \Rightarrow \Delta N_{\text{eff}} < 0.285, \quad (5.15)$$

adopting the most conservative limit. Moreover, future CMB Stage-IV experiments [246] are expected to improve this measurement to $\Delta N_{\text{eff}} < 0.06$.

In the left panel of Fig. 5.3 we present our results for the decoupling temperature of the RH neutrinos, ν_R , as a function of the ratio $M_{Z_{BL}}/g_{BL}$. In the right panel of Fig. 5.3 we present the prediction for ΔN_{eff} in the context of $U(1)_{B-L}$. To obtain the decoupling temperature we used the relation between the decay rate and the Hubble parameter given in Eq. 2.19 in Chapter 2. As Fig. 5.3 shows, in theories based on local lepton number, the bound coming from Planck is stronger than the collider bound coming from LEP (see Section 3.4 from Chapter 3). Basically, in these theories we find that $M_{Z'}/g' > (9 - 10)$ TeV in order to satisfy the N_{eff} bounds. This has implications for any gauge theory coupled to the SM with very light new particles.

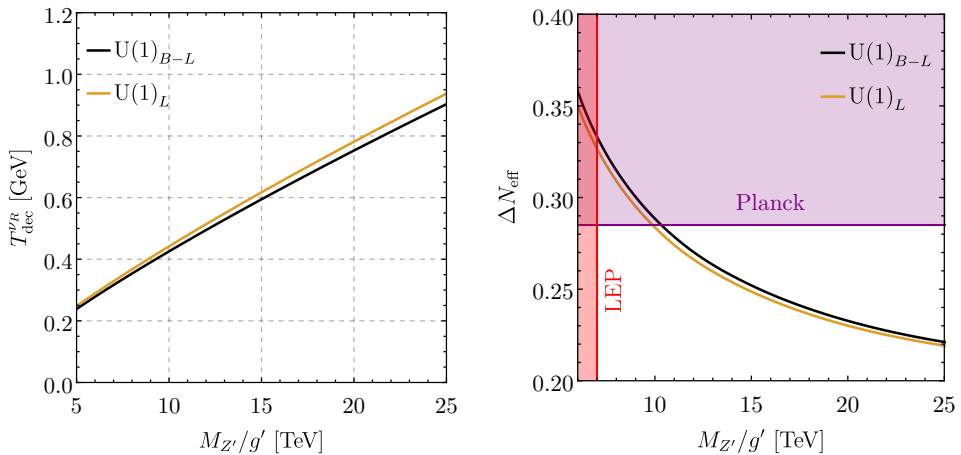


Figure 5.3: *Left panel:* The decoupling temperature of the RH neutrinos ν_R as a function of $M_{Z'}/g'$. *Right panel:* The effective number of extra relativistic species as a function of $M_{Z'}/g'$. The solid black and yellow lines correspond to the prediction for ΔN_{eff} in the scenarios with $U(1)_{B-L}$ and $U(1)_L$, respectively. The region shaded in purple is excluded by the CMB measurement by the Planck satellite mission [7]. For comparison, we show the bound from LEP [181] in red. *Figure extracted from Ref. [183].*

In our case, the bound on ΔN_{eff} corresponds to

$$\Delta N_{\text{eff}} < 0.285 \quad \Rightarrow \quad \frac{M_{Z_{BL}}}{g_{BL}} > 10.33 \text{ TeV}, \quad (5.16)$$

and is given by the black line in Fig. 5.2. Indeed, as the figure shows, this bound is stronger than the LEP bound. As can be seen in the right panel from Fig. 5.2, the upper bound on the gauge coupling for $n_\chi = 1/3$ is $g_{BL} \lesssim 2$, since scenarios with larger values for the gauge coupling are totally excluded by the bounds on N_{eff} .

Therefore, taking into account all cosmological and experimental constraints we find an upper bound on the gauge boson mass, i.e.

$$M_{Z_{BL}} \lesssim 22 \text{ TeV}. \quad (5.17)$$

as shown in Fig. 5.2. In the scenario we have considered, the projected sensitivity of CMB Stage-IV for the measurement of N_{eff} will fully probe this model. However, it

should be noted that the bound coming from ΔN_{eff} can be relaxed by taking the limit $n_\chi \gg 1$, since this would require $g_{BL} \ll 1$ for the DM relic density to be explained. Even though the bounds on N_{eff} may change under the choice of a different n_χ , it can be shown that the upper bound on the B - L scale will not go beyond 100 TeV regardless of the choice of the charge [221]. We will discuss the implications of a different choice for n_χ in the next section. For the case considered here, one can also find an upper bound on the DM mass, i.e. $M_\chi \lesssim 13$ TeV. Then, there is hope to test or rule out this simple theory for neutrino masses and DM in the near future.

5.1.2.3 Phenomenological bounds

DD experiments aim to measure the nuclear recoil from interaction with a DM particle. In this model, the only interaction between DM and the nucleon in atoms occurs via the exchange of a gauge boson,

$$N\chi \rightarrow Z_{BL}^* \rightarrow N\chi.$$

The DD spin-independent cross-section is then given by,

$$\sigma_{\text{SI}} = \frac{m_N^2 M_\chi^2}{\pi(m_N + M_\chi)^2} \frac{n_\chi^2 g_{BL}^4}{M_{Z_{BL}}^4}, \quad (5.18)$$

where m_N corresponds to the nucleon mass. In our case $M_\chi \gg m_N$, and using the collider lower bound from LEP $M_{Z_{BL}}/g_{BL} > 7$ TeV [181] (see Section 3.4 from Chapter 3) one finds an upper bound on the elastic spin-independent nucleon-DM cross section given by

$$\sigma_{\chi N}^{\text{SI}} < 4.54 \times 10^{-44} n_\chi^2 \text{ cm}^2, \quad (5.19)$$

for a given value of n_χ .

In Fig. 5.4, we show the predictions for the DD spin-independent cross-section as a function of the DM mass in the Stueckelberg $U(1)_{B-L}$ scenario. Red points correspond to $g_{BL} = 0 - 0.25$, orange points correspond to $g_{BL} = 0.25 - 0.5$, blue points correspond to $g_{BL} = 0.5 - 0.75$, green points correspond to $g_{BL} = 0.75 - 1.0$, pink points correspond to $g_{BL} = 1.0 - 2.0$ and purple points correspond to $g_{BL} =$

$2.0 - 2\sqrt{\pi}$. The solid black line shows current experimental bounds from Xenon-1T [205], the dashed black line shows the projected sensitivity for Xenon-nT [81] and the dotted black line shows the coherent neutrino scattering limit [83]. In this figure, we also present the bound coming from ΔN_{eff} . As it can be seen, this is a strong bound, and it excludes a large region in parameter space that otherwise could be reached by Xenon-nT. However, some of the points lie below the neutrino floor and hence will escape detection from future DD experiments.

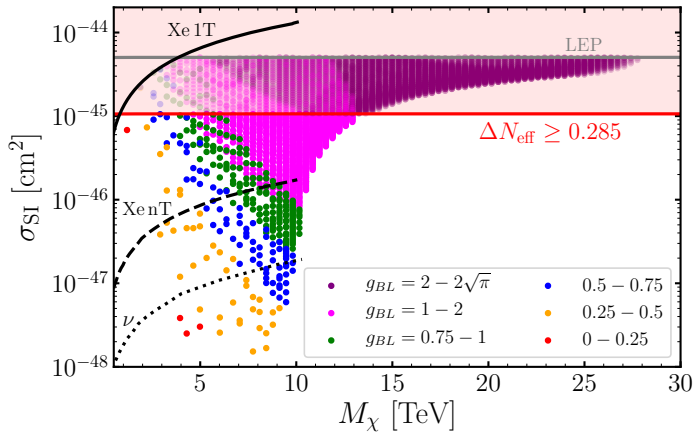


Figure 5.4: Predictions for the DD spin-independent cross-section as a function of the DM mass in the Stueckelberg $U(1)_{B-L}$ scenario with $n_\chi = 1/3$. Points with different colors correspond to different values of the gauge coupling as shown in the legend. All points shown here satisfy the correct relic density $\Omega_\chi h^2 = 0.1200 \pm 0.0036$. The solid black line shows current experimental bounds from Xenon-1T [205], the dashed black line shows the projected sensitivity for Xenon-nT [81], and the dotted black line shows the coherent neutrino scattering limit [83]. The bounds from N_{eff} are shown by a red horizontal line, ruling out the parameter space above this line. *Figure extracted from Ref. [183].*

Notice that local $U(1)_{B-L}$ theories cannot predict gamma lines since they are anomaly-free theories, including the RH neutrinos, and there is no electrically charged field with an axial coupling to the Z_{BL} .

5.2 Broken $U(1)_{B-L}$ in 2 units

Majorana neutrino masses can be generated through the spontaneous breaking of the $B-L$ symmetry in two units, i.e. we introduce a new Higgs with quantum numbers $S_{BL} \sim (1, 1, 0, 2)$. In this section, we will investigate the different DM scenarios in the case where the neutrinos are Majorana particles and their masses are generated through the canonical Type I seesaw. In contrast to the Stueckelberg scenario, these models predict violation of lepton number.

5.2.1 Theoretical framework

The DM can be a Dirac fermion if we add a pair of vector-like fermionic fields, i.e. $\chi_L \sim (1, 1, 0, n_\chi)$ and $\chi_R \sim (1, 1, 0, n_\chi)$, where $n_\chi \neq 1, 3$; in order to avoid mixing with neutrinos and, consequently, the decay of DM. If we allow for non-renormalizable operators, odd values of n_χ will give mixing between the DM candidate and neutrinos, and hence should be forbidden. The Lagrangian in this case is given by,

$$\begin{aligned} \mathcal{L} \supset & i\overline{\chi}_L\gamma^\mu D_\mu\chi_L + i\overline{\chi}_R\gamma^\mu D_\mu\chi_R + (D_\mu S_{BL})^\dagger (D^\mu S_{BL}) \\ & - (Y_\nu\overline{\ell}_L i\sigma_2 H^* \nu_R + y_R \nu_R^T C \nu_R S_{BL} + M_\chi \overline{\chi}_L \chi_R + \text{h.c.}). \end{aligned} \quad (5.20)$$

The covariant derivative for χ is given by $D^\mu\chi_L = \partial^\mu\chi_L + ig_{BL}n_\chi Z_{BL}^\mu\chi_L$, and similarly for χ_R . The scalar potential is analogous to the potential discussed in Eq. 4.1 in Chapter 4, by replacing the scalar singlet S_B charged under $U(1)_B$ by S_{BL} , charged this time under $B-L$. We stress again that, in this scenario, we have chosen the charge for S_{BL} such that a Majorana mass term for the neutrinos is generated after SSB. Therefore, in this context, $B-L$ is violated in two units.³

After SSB, the $B-L$ gauge boson and the RH neutrinos acquire the following masses,

$$M_{Z_{BL}} = 2g_{BL}v_{BL}, \quad \text{and} \quad M_R = \sqrt{2}y_R v_{BL}. \quad (5.21)$$

³If the choice of the scalar charge is a different one, one would end up with Dirac neutrinos and a similar scenario to the one studied in this section with the cosmological constraints from the previous one.

In this theory, the Majorana neutrino masses are generated through the Type I seesaw mechanism, discussed in Chapter 1. In this case, the perturbative bound on the gauge coupling comes from the $S_{BL}^\dagger S_{BL} Z_{BL}^\mu Z_{BL\mu}$ interaction when $n_\chi > 2\sqrt{2}$ and it is therefore given by

$$g_{BL} \leq \sqrt{\frac{\pi}{2}}. \quad (5.22)$$

while for $n_\chi \leq 2\sqrt{2}$, the upper bound on the gauge coupling is given by Eq. 5.2. Henceforth, we set the masses of the three RH neutrinos to the same value M_R without loss of generality. Then, the model contains seven free parameters:

$$M_\chi, \quad M_{Z_{BL}}, \quad M_R, \quad M_{h_2}, \quad \theta_{BL}, \quad g_{BL}, \quad \text{and} \quad n_\chi. \quad (5.23)$$

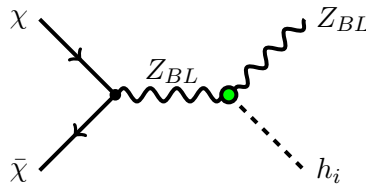
For the rest of this section we fix the DM $B-L$ charge to $n_\chi = 1/3$.

5.2.2 Cosmological bounds

The annihilation channels of our DM candidate in this theory are

$$\bar{\chi}\chi \rightarrow e_i^+ e_i^-, \bar{\nu}_i \nu_i, \bar{u}_i u_i, \bar{d}_i d_i, \bar{N}_i N_i, Z_{BL} Z_{BL}, Z_{BL} h_i,$$

whose explicit Feynman graphs are the ones shown in Diagrams 5.6 plus the extra channel opened because of the $B-L$ SSB, shown below:



$$, \quad (5.24)$$

where $h_{i=1,2}$ are the Higgses present in the theory, related with h and s_{BL} analogously to Eq. 4.9, but with θ_{BL} parametrizing this time the mixing between the scalars.

The cross-section of this annihilation channel is given by

$$\begin{aligned} \sigma_{\bar{\chi}\chi \rightarrow Z_{BL}h_i} &= c_i^2 \frac{g_{BL}^4 n_S^2 n_\chi^2}{48\pi s^2} \left(1 + \frac{2M_\chi^2}{s} \right) \frac{(s^2 + 2s(5M_{Z_{BL}}^2 - M_{h_i}^2) + (M_{Z_{BL}}^2 - M_{h_i}^2)^2)}{(s - M_{Z_{BL}}^2)^2 + \Gamma_{Z_{BL}}^2 M_{Z_{BL}}^2} \\ &\quad \times \sqrt{(s + M_{Z_{BL}}^2 - M_{h_i}^2)^2 - 4M_{Z_{BL}}^2 s} \Big/ \sqrt{1 - \frac{4M_\chi^2}{s}}, \end{aligned} \quad (5.25)$$

where $c_i = (\sin \theta_{BL}, \cos \theta_{BL})$ and n_S is the B - L charge of the S_{BL} Higgs; in our case $n_S = 2$. We note that the annihilation into the SM Higgs is mixing suppressed, indicated by a green vertex in Diag. 5.24. Notice also that this channel will be generically suppressed since kinematically the enhancement caused by the resonance cannot be accessed. Here, neutrinos are Majorana fermions, so that the annihilation cross-section $\bar{\chi}\chi \rightarrow Z_{BL}^* \rightarrow NN$ is slightly modified with respect to Eq. 5.7:

$$\sigma_{\bar{\chi}\chi \rightarrow NN} = \frac{N_c^f n_N^2 g_{BL}^4 n_\chi^2 \sqrt{s - 4M_N^2}}{24\pi s} \frac{(s + 2M_\chi^2)(s - 4M_N^2)}{\sqrt{s - 4M_\chi^2} \left[(s - M_{Z_{BL}}^2)^2 + M_{Z_{BL}}^2 \Gamma_{Z_{BL}}^2 \right]}. \quad (5.26)$$

In Fig. 5.5, we show the numerical results for the branching ratios of the thermal averaged cross-sections for the channels $\bar{\chi}\chi \rightarrow \bar{f}_i f_i$ (solid line), and $\bar{\chi}\chi \rightarrow Z_{BL}Z_{BL}$, $\bar{\chi}\chi \rightarrow Z_{BL}h_2$, and $\bar{\chi}\chi \rightarrow Z_{BL}h_1$ (dashed lines), for different B - L charges. We have used $\cos \theta_{BL} = 0.9$ for the scalar mixing angle, $M_{Z_{BL}} = 3.5$ TeV, $g_{BL} = 0.5$, $M_{h_2} = M_R = 1$ TeV, and we have showed two choices of n_χ for illustration. For low values of the B - L charge, the annihilation channel into two fermions significantly dominates over the other channels. The annihilation into two gauge bosons $\bar{\chi}\chi \rightarrow Z_{BL}Z_{BL}$ can be important when one has large values for the DM B - L charge. However, perturbativity bounds, i.e. Eq. 5.2, constrain this channel in such a way that the annihilation into fermions will always dominate over annihilation into two gauge bosons, regardless of the choice of the B - L charge of the DM candidate. Notice that the DM annihilation into a pair of gauge bosons shown in Eq. 5.9 is proportional to

$$\sigma_{\bar{\chi}\chi \rightarrow Z_{BL}Z_{BL}} \propto (n_\chi g_B)^4 \frac{1}{\Lambda^2} \quad (5.27)$$

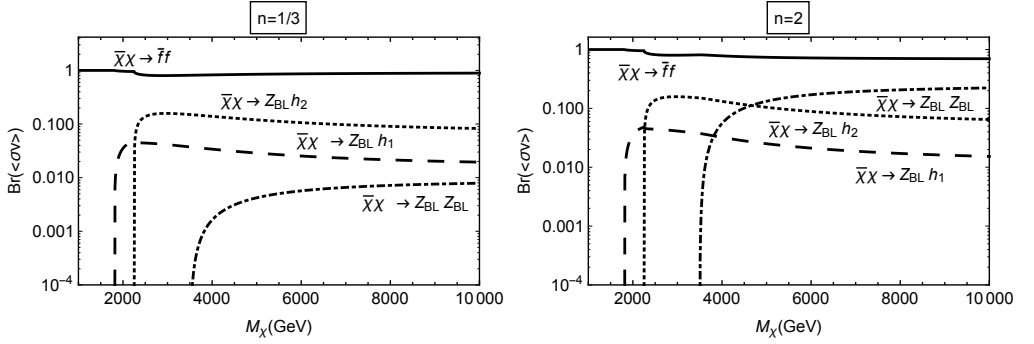


Figure 5.5: Branching ratios of the thermal averaged cross-sections for the channels $\bar{\chi}\chi \rightarrow \bar{f}_i f_i$ (solid line) and $\bar{\chi}\chi \rightarrow Z_{BL} Z_{BL}$, $\bar{\chi}\chi \rightarrow Z_{BL} h_i$ (dashed lines) for different $B-L$ charges. Here we have taken $M_{Z_{BL}} = 3.5$ TeV, $g_{BL} = 0.5$, $\cos \theta_{BL} = 0.9$ for the scalar mixing angle and $M_{h_2} = M_R = 1$ TeV. In the left panel we show the results for $n_\chi = 1/3$, while in the right panel we show the results when $n_\chi = 2$. *Figure extracted from Ref. [221].*

so that it saturates when $n_\chi g_{BL} = 2\sqrt{\pi}$ (see Eq. 5.2). On the other hand, the annihilation into fermions reaches its climax in the resonant region, where Eq. 5.7 behaves as,

$$\sigma_{\bar{\chi}\chi \rightarrow \bar{f}f} \propto \frac{g_{BL}^4 n_\chi^2}{\Gamma_{Z_{BL}}^2} \sim \frac{1}{\Lambda^2} \quad (5.28)$$

since $\Gamma_{Z_{BL}}^2 \propto g_{BL}^4 n_\chi^2$ as well. Then, in the limit of large n_χ , the upper bound of the theory does not exceed a certain absolute value but, due to the constrain in Eq. 5.2, $g_{BL} \ll 1$, i.e. we would be living in a nightmare scenario of no interest under a phenomenological point of view.

In Fig. 5.6, we show the allowed parameter space by DM relic density in the M_χ - $M_{Z_{BL}}$ plane for the maximal value of the gauge coupling when $n_\chi = 1/3$. The solid blue line satisfies the correct DM relic abundance $\Omega_\chi h^2 = 0.1200 \pm 0.0012$, while the region shaded in light blue overproduces it. The horizontal red (pink) line corresponds to the LEP (LHC) bound on the mass of the Z_{BL} gauge boson. We set $M_R = M_{h_2} = 1$ TeV, $g_{BL} = \sqrt{\pi/2}$ and zero scalar mixing angle. In this model, the DM candidate has no Yukawa interaction with S_{BL} , and hence, there is no Higgs portal

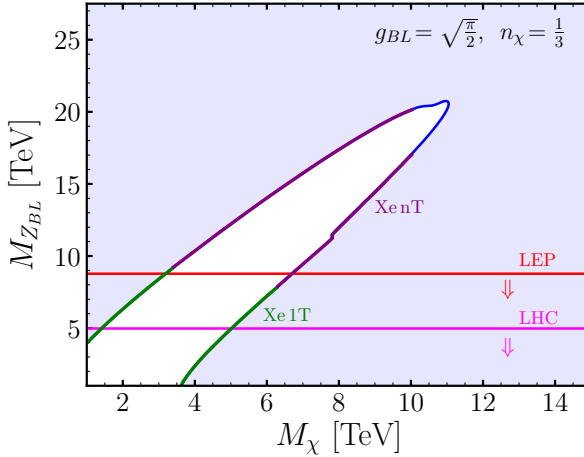


Figure 5.6: Results for the DM relic density in the M_χ - $M_{Z_{BL}}$ plane. The solid blue line satisfies the correct DM relic abundance $\Omega_\chi h^2 = 0.1200 \pm 0.0012$ [7], while the region shaded in light blue overproduces it. For the points that saturate the relic abundance, we mark in green those that are excluded by Xenon-1T [205] and in purple those that will be reached by the Xenon-nT [81] experiment. The horizontal red (pink) line corresponds to the LEP [181] (LHC [182]) bound on the mass of the Z_{BL} gauge boson. We fix $n_\chi = 1/3$, $M_R = M_{h_2} = 1$ TeV, $g_{BL} = \sqrt{\pi/2}$ and $\theta_{BL} = 0$. *Figure extracted from Ref. [183].*

between the DM and the SM fermions. However, a small value for θ_{BL} will only have a small impact on the calculation of the DM relic density.

Having fixed $n_\chi = 1/3$, we perform a random scan on the remaining six parameters in the model. In Fig. 5.7 we present our results, in the left panel we show the points in the $M_\chi - M_{Z_{BL}}$ plane that are in agreement with the measured relic abundance. All points shown satisfy bounds from DD and LEP.

In this model with $n_\chi = 1/3$, we find the following upper bounds on the masses of the B - L gauge boson and the DM candidate

$$M_{Z_{BL}} \lesssim 21 \text{ TeV and } M_\chi \lesssim 11 \text{ TeV.}$$

Clearly, each choice of n_χ , and g_{BL} define a theory which is bounded from above. However, regardless of the value of the B - L charge, and the choice of g_{BL} , we note

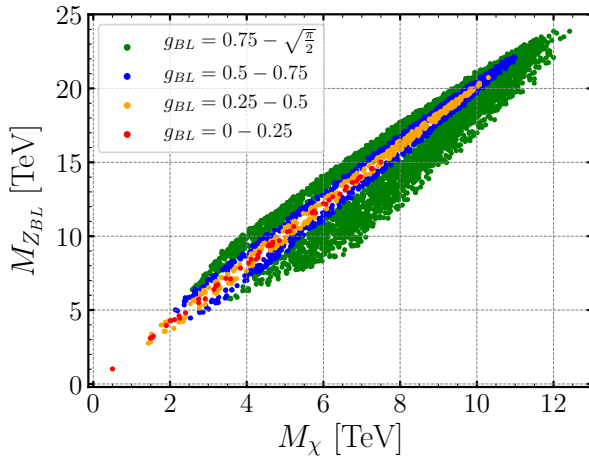


Figure 5.7: Scatter plot of points with $n_{\chi} = 1/3$ in the $M_{Z_{BL}} - M_{\chi}$ plane that are in agreement with the measured relic abundance, $\Omega_{\chi} h^2 = 0.1200 \pm 0.0036$. Points with different colors correspond to different values of the gauge coupling as shown in the legend. All points shown satisfy bounds from DD and LEP [181]. *Figure extracted from Ref. [183].*

that there is an absolute upper bound at the multi-TeV scale for the seesaw scale, as commented before. For completeness of the discussion on the upper bound for the seesaw scale, we would like to mention that the allowed parameter space from Fig. 5.7 is in agreement with partial-wave unitarity of the S-matrix. It is well known that, from a naive model-independent study, partial wave unitarity requires that $M_{\chi} < 340$ TeV [53]. However, in this theory, the partial wave expansion only becomes relevant in regions of the parameter space which are not allowed by cosmology. Therefore, unitarity of the S-matrix does not make any influence on the upper bound for the seesaw scale.

These results are crucial to understand the testability of this theory at colliders. Theories where the $B-L$ gauge symmetry is broken in two units predict Majorana neutrinos through the Type I seesaw mechanism. Unfortunately, as mentioned earlier, the canonical seesaw bound is around 10^{14} GeVs, which is impossible to falsify. However, motivated by the need of explaining the relic abundance in the universe, when including DM, as illustrated in Fig. 5.8, the upper bound on the $B-L$ violation is lowered by about ten orders of magnitude! Therefore, we can hope to test the Type I seesaw mechanism for Majorana neutrinos and this simple theory for DM in the near future.

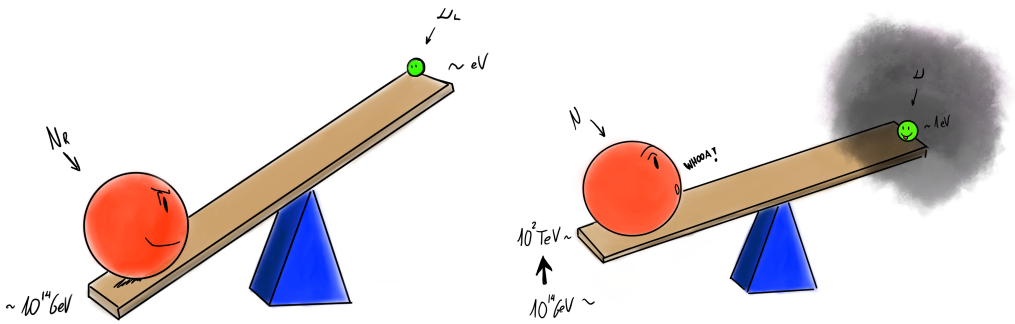


Figure 5.8: Illustration of the effect of including DM in the context of local $B-L$ theories. The bound on the relic abundance indirectly affects the seesaw scale by lowering it about ten orders of magnitude, as discussed along this section.

5.2.3 Phenomenological bounds

The DD spin-independent cross-section, as in the Stueckelberg scenario, is given by Eq. 5.18. In Fig. 5.9, we show the predictions for the DD spin-independent cross-section as a function of the DM mass, for the same points as in Fig. 5.7. Red points correspond to $g_{BL} = 0 - 0.25$, orange points to $g_{BL} = 0.25 - 0.5$, blue points to $g_{BL} = 0.5 - 0.75$ and green points to $g_{BL} = 0.75 - \sqrt{\frac{\pi}{2}}$. The solid black line shows current experimental bounds from Xenon-1T [205], the dashed black line shows the projected sensitivity for Xenon-nT [81] and the dotted black line shows the coherent neutrino scattering limit [83]. Since we know the maximal value for the gauge boson mass, we can show the predictions for the DD cross-section in the full parameter space. As can be seen, the Xenon-nT experiment will be able to probe a large fraction of the parameter space.

5.2.4 Lepton Number Violation at the LHC

The main implication of the results presented in the previous section is that, since the upper bound on the $B-L$ breaking scale is much smaller than the canonical seesaw scale, there is hope to test the existence of a new force associated to $B-L$ and observe lepton number violation at the LHC.

The RH neutrinos can be produced at the LHC through the neutral gauge boson Z_{BL} , i.e. $pp \rightarrow Z_{BL}^* \rightarrow N_i N_i$ or through the Higgses present in the theory [247–251].

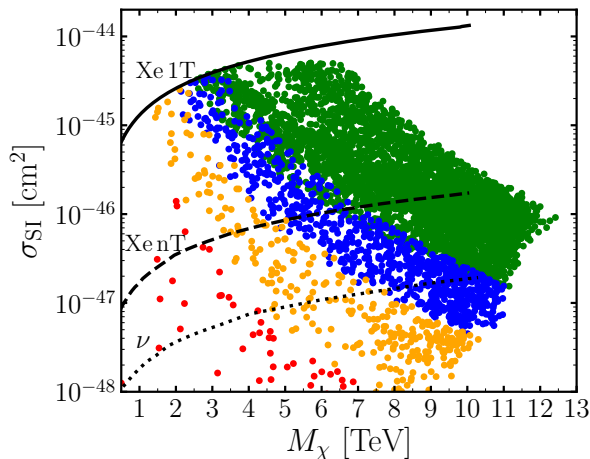


Figure 5.9: Predictions for the DD spin-independent cross-section as a function of the DM mass, for the same points as in Fig. 5.7. We perform a random scan on M_{h_2} and M_R in the range $[0.1 - 20]$ TeV. For the scalar mixing angle we scan over $\sin\theta_{BL} = [0 - 0.3]$, the maximal value corresponds to the LHC bound on the Higgs scalar mixing angle [195]. The solid black line shows current experimental bounds from Xenon-1T [205], the dashed black line shows the projected sensitivity for Xenon-nT [81] and the dotted black line shows the coherent neutrino scattering limit [83]. This figure follows the same color coding as the one used in Fig. 5.7. *Figure extracted from Ref. [183].*

Since the production mechanisms through the Higgses suffer from the dependence on the mixing angle in the Higgs sector, we focus our discussion on the production through the $B-L$ gauge boson, shown in Fig. 5.10.

The RH neutrinos could have the following decays:

$$N_i \rightarrow e_j^\pm W^\mp, \nu_j Z, \nu_j h_1, \nu_j h_2.$$

Therefore, the lepton number violating signatures can be observed when the RH neutrinos decay into charged leptons, and one has the following channels with the same-sign leptons

$$pp \rightarrow Z_{BL}^* \rightarrow N_i N_i \rightarrow e_j^\pm W^\mp e_k^\pm W^\mp \rightarrow e_j^\pm e_k^\pm 4j. \quad (5.29)$$

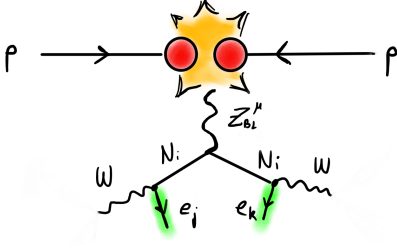


Figure 5.10: Drell-Yan process for $pp \rightarrow Z_{BL}^* \rightarrow N_i N_i$, which violates lepton number in two units. In this example, the RH neutrino N_i decays to $e_j^\pm W^\mp$.

The number of these events is given by

$$N_{e_j^\pm e_k^\pm 4j} = 2 \times \mathcal{L} \times \sigma(pp \rightarrow N_i N_i) \times \text{Br}(N_i \rightarrow e_j^\pm W^\mp) \times \text{Br}(N_i \rightarrow e_k^\pm W^\mp) \times \text{Br}(W \rightarrow jj)^2, \quad (5.30)$$

where \mathcal{L} is the integrated luminosity. Here, the factor two is included to discuss the channels with same-sign leptons without distinguishing the electric charge of the leptons in the final state. In the above expression, the parton level cross section $\sigma(pp \rightarrow Z_{BL}^* \rightarrow N_i N_i)$ for this process is given by

$$\frac{d\sigma}{dt} = \frac{1}{96\pi s(s - 4M_q^2)} \frac{2g_{BL}^4}{9} \frac{\left[(s + t - 2M_{N_i}^2)^2 + (t - 2M_q^2)^2 - 2(M_{N_i}^2 + M_q^2)^2 \right]}{(s - M_{Z_{BL}}^2)^2 + M_{Z_{BL}}^2 \Gamma_{Z_{BL}}^2},$$

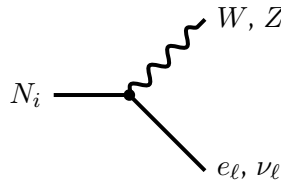
where $t = (p_q - p_N)^2$. The integrated expression reads as

$$\sigma(q\bar{q} \rightarrow Z_{BL}^* \rightarrow N_i N_i) = \frac{g_{BL}^4 (s - 4M_{N_i}^2)(s + 2M_q^2)}{648\pi s \left((s - M_{Z_{BL}}^2)^2 + \Gamma_{Z_{BL}}^2 M_{Z_{BL}}^2 \right)} \sqrt{\frac{s - 4M_{N_i}^2}{s - 4M_q^2}}. \quad (5.31)$$

In the upper-left panel of Fig. 5.11, we show the predictions for the cross section when $\sqrt{s} = 13$ TeV, and for different scenarios consistent with relic density bounds. As in the previous sections, we have chosen $n = 1/3$, and numerical values for M_χ , $M_{Z_{BL}}$, and g_{BL} which satisfy the cosmological and collider bounds. In the upper-right panel, we show the number of events assuming a luminosity $\mathcal{L} = 50 \text{ fb}^{-1}$. We have reviewed the current LHC bounds and unfortunately they cannot exclude the region of the parameter space studied here. A more detailed experimental study will help to

understand the testability of this theory with more luminosity. Similar results are shown in the middle panels of Fig. 5.11, when $\sqrt{s} = 14$ TeV. However, in this case one expects a large number of events for the same-sign leptons for RH neutrino masses below 1 TeV. In the lower panels of Fig. 5.11, we show the predictions for the next generation of proton-proton collider at 100 TeV. In this case one should be able to test most of the parameter space even when the RH neutrinos are in the multi-TeV region. See Ref. [252] for the discovery potential of the 100 TeV collider.

We would like to mention that, in a large part of the parameter space, the right handed neutrino decays can give rise to displaced vertices [251]. This can be understood as follows. The RH neutrino decays in the following way:



$$\Gamma_N \sim |V_{\ell i}|^2 \frac{M_R^3}{\Lambda_{EW}^2}, \quad (5.32)$$

where $|V_{\ell i}|$ encodes the neutrino mixing, which according to the Type I seesaw mechanism (see Chapter 1) is proportional to $|V_{\ell i}|^2 \propto M_\nu/M_R$. Hence,

$$\Gamma_N \propto \frac{M_\nu M_R^2}{\Lambda_{EW}^2} \sim Y_\nu \frac{M_R^2}{\Lambda_{EW}} \Rightarrow \tau_N \propto \frac{\Lambda_{EW}}{Y_\nu M_R^2}. \quad (5.33)$$

Since the seesaw scale has to be at most at the multi-TeV scale $\sim \mathcal{O}(10^2)$ TeV, the Yukawa Dirac Y_ν has to be small in order to reproduce the measured active neutrino masses. A small Y_ν , as shown in Eq. 5.33, enhances the lifetime of the RH neutrinos, which then become long-lived particles. Therefore, as a consequence of having a low seesaw scale, displaced vertices arise as exotic signatures predicted by the model. For instance, when the RH neutrino mass is about 400 GeV, the decay length can be

$$L = (10^{-3} - 10^{-1})\text{mm}.$$

This simple study motivates the search of lepton number violating signatures at the LHC or at future colliders.

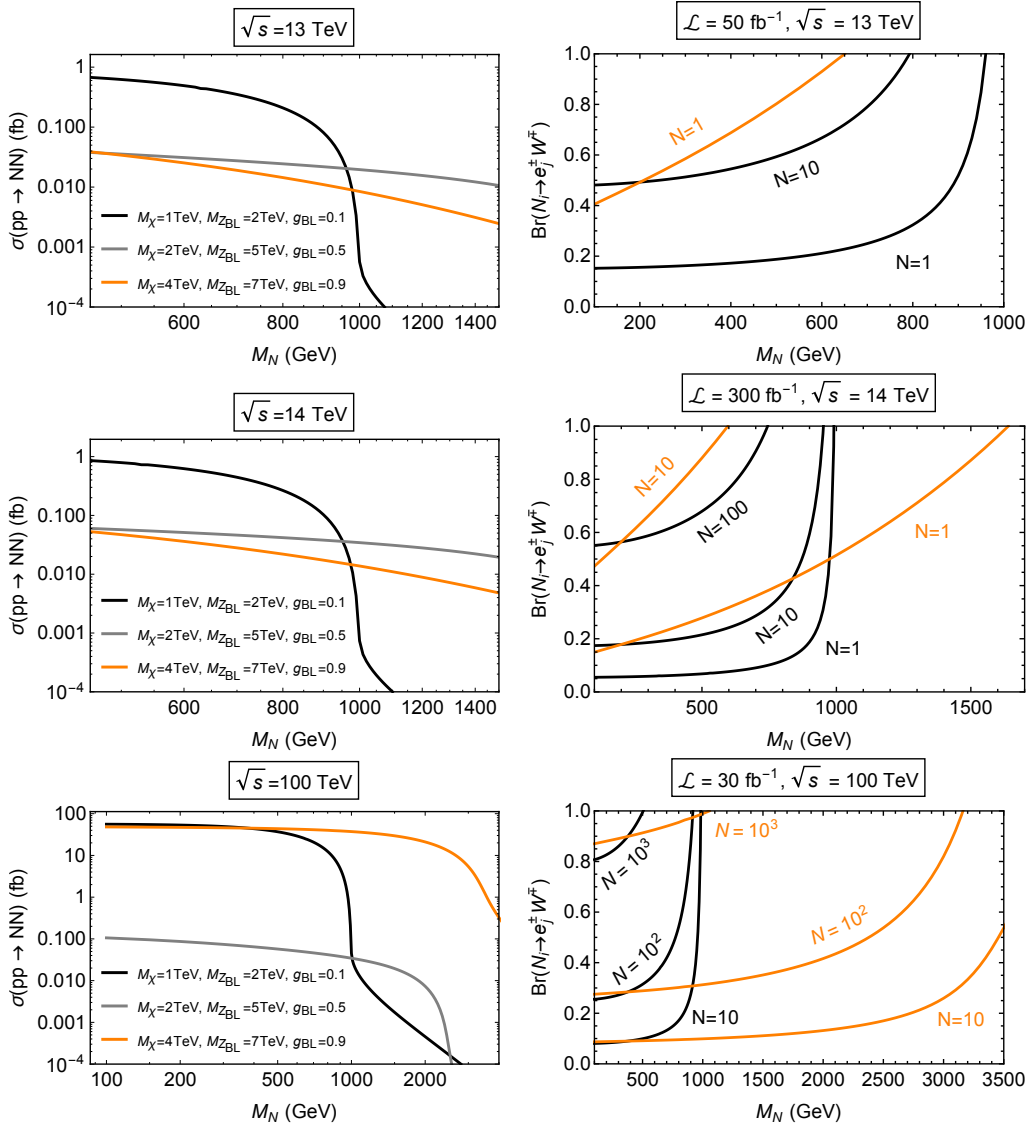


Figure 5.11: On the left panels, production cross section for the RH neutrinos at the LHC for $\sqrt{s} = 13$ TeV (upper panels), $\sqrt{s} = 14$ TeV (middle panels) and $\sqrt{s} = 100$ TeV (lower panels) in different scenarios consistent with the DM relic density. On the right panels, the corresponding expected number of events for the scenarios $M_\chi = 1$ TeV, $M_{Z_{BL}} = 2$ TeV, $g_{BL} = 0.1$ (black), and $M_\chi = 4$ TeV, $M_{Z_{BL}} = 7$ TeV, $g_{BL} = 0.9$ (orange), assuming a luminosity of $\mathcal{L} = 50 \text{ fb}^{-1}$ (upper panel), $\mathcal{L} = 300 \text{ fb}^{-1}$ (middle panel), and $\mathcal{L} = 30 \text{ fb}^{-1}$ (lower panel). *Figure extracted from Ref. [221].*

5.3 Local $U(1)_L$

There are two simple gauge theories based on $U(1)_L$, introduced in Chapter 3, where one predicts the existence of a DM candidate from anomaly cancellation: DFW [169] and FOP [171]. In their context, the DM mass is defined by the $U(1)_L$ symmetry breaking scale and, as we will demonstrate, the scale must be in the multi-TeV scale in order to satisfy the relic density constraints. In the model DFW proposed in Ref. [169], it has been shown that one can cancel the anomalies by adding six new representations to the SM fermionic content plus the three RH neutrinos, and in this context the DM candidate can be either a Dirac or a Majorana, while in the model FOP proposed in Ref. [171] it is shown that the theory can be anomaly-free by adding only four representations and the DM is predicted to be a Majorana fermion. Since the main goal of our study is to investigate the most generic properties of a DM candidate in these theories, we will focus on the Majorana case and show the predictions in the context of a simplified model which describes the most important properties, analogously to the procedure followed in Chapter 4 for the baryon force. Studies where the DM candidate is directly coupled only to leptons have been performed in Refs. [253–260].

5.3.1 Theoretical framework

We consider a simple model for leptophilic Majorana DM which can be obtained in the context of the anomaly-free theories proposed in Refs. [169,171]. In this context, one has the SM leptons and the RH neutrinos,

$$\ell_L \sim (1, 2, -1/2, 1), \quad e_R \sim (1, 1, -1, 1), \quad \nu_R \sim (1, 1, 0, 1),$$

together with the new Higgs needed for SSB, $S_L \sim (1, 1, 0, 3)$, with the leptonic charge fixed by anomaly cancellation, the DM candidate $\chi_L \sim (1, 1, 0, -3/2)$ and other fields needed for anomaly cancellation (anomalons). The explicit extended fermionic sector for the UV completions of this simplified model is shown in Tables 3.1 and 3.2 from Chapter 3, based on the models from Refs. [169,171]. As in Chapter 4, we will assume the limit where the Yukawa couplings in the DFW and FOP Lagrangians, listed in Eq. 3.18 and Eq. 3.17, respectively, are very small.

The relevant Lagrangian for our discussions is given, after SSB, by the simplified Lagrangian obtained in Eq. 4.49 from Chapter 4 identifying $Z_B \rightarrow Z_L$ and $g_B \rightarrow g_L$,

$$\mathcal{L} \supset \frac{3}{4}g_L\bar{\chi}\gamma^\mu\gamma^5\chi Z_\mu^L - g_L\bar{\ell}\gamma^\mu\ell Z_\mu^L - y_i\bar{\chi}\chi h_i - \frac{1}{2}M_\chi\chi^T C\chi, \quad (5.34)$$

where $\ell = \nu_i, e_i$, with $i = 1, 2, 3$, and $\chi = \chi^c$. Note that, this time, only leptons interact with the new mediator and their charge is $+1$. In theories where the DM candidate is predicted by anomaly cancellation, the DM acquires mass through the mechanism of SSB. This connection has phenomenological implications that will be discussed below. The Yukawa couplings in the above equation were derived in Chapter 4 and can be read from Eq. 4.49,

$$y_1 = \frac{M_\chi}{2v_L} \sin \theta_L, \quad \text{and} \quad y_2 = -\frac{M_\chi}{2v_L} \cos \theta_L, \quad (5.35)$$

and the gauge boson mass reads as (analogously to Eq. 4.17 in the context of $U(1)_B$),

$$M_{Z_L} = 3g_L v_L. \quad (5.36)$$

Thus, the gauge boson mass, M_{Z_L} , and the DM mass, M_χ , are defined by the same symmetry breaking scale v_L . This model contains five free parameters:

$$M_\chi, \quad M_{Z_L}, \quad M_{h_2}, \quad \theta_L, \quad \text{and} \quad g_L. \quad (5.37)$$

In this scenario, the DM charge $n_\chi = -3/2$ is predicted by the theory. Note that the charge of the scalar responsible of the spontaneous lepton number violation is also predicted! Therefore, in this context, total lepton number is violated in three units and neutrinos are, consequently, Dirac particles, as discussed in Chapter 1. Hence, similarly to the Stueckelberg scenario from Sec. 5.1, we will expect the cosmological bounds on the number of effective relativistic neutrino species to play an important role here. Those are discussed in the next section.

5.3.2 Cosmological bounds

In this subsection we study the cosmological implications on the theories based on local $U(1)_L$. As in the previous scenarios, the compatibility with the experimental bounds will require the theory to live at most at the multi-TeV scale.

5.3.2.1 Number of effective relativistic neutrino species N_{eff}

In the minimal model with one extra Higgs, the active neutrinos in the SM are predicted to be Dirac fermions. Therefore, as it has been discussed in the subsection 5.1.2.2 from the previous scenario, there is a bound coming from the CMB measurement of N_{eff} . In this case, the cross-section for the thermalization of the RH neutrinos via the Z_L gauge boson is given by Eq. 5.12 with $Z' \equiv Z_L$ and $g' \equiv g_L$.

Fig. 5.3 also presents the prediction for ΔN_{eff} in the context of $U(1)_L$. As the figure shows, for local $U(1)_L$ the CMB measurement gives the following bound,

$$\Delta N_{\text{eff}} < 0.285 \quad \Rightarrow \quad \frac{M_{Z_L}}{g_L} > 9.87 \text{ TeV}. \quad (5.38)$$

Similarly to the Stueckelberg case, it is stronger than the LEP bound and it is shown by the solid purple line in Fig. 5.12. We should stress that by adding a new Higgs scalar with lepton number $L = 2$, a Majorana mass term can be written for ν_R and, if these states are heavy, the bound from N_{eff} would not be relevant.

5.3.2.2 Relic abundance

The annihilation channels for DM in the context of $U(1)_L$ are given by:

$$\chi\chi \rightarrow e_i^+ e_i^-, \bar{\nu}_i \nu_i, Z_L Z_L, Z_L h_i, h_i h_j, WW, ZZ,$$

where $h_i = h_1, h_2$ are the Higgses present in the theory. Their explicit representation in Feynman graphs is shown in Diagrams 4.55-4.59 from Chapter 4 but exchanging the new mediator by Z_L and the quarks by leptons. In this model, as well as in $U(1)_B$ (see Chapter 4), the perturbative bound on the gauge coupling comes from the $S_L^\dagger S_L Z_{L\mu} Z_L^\mu$

coupling and reads as

$$g_L \leq \sqrt{2\pi}/3. \quad (5.39)$$

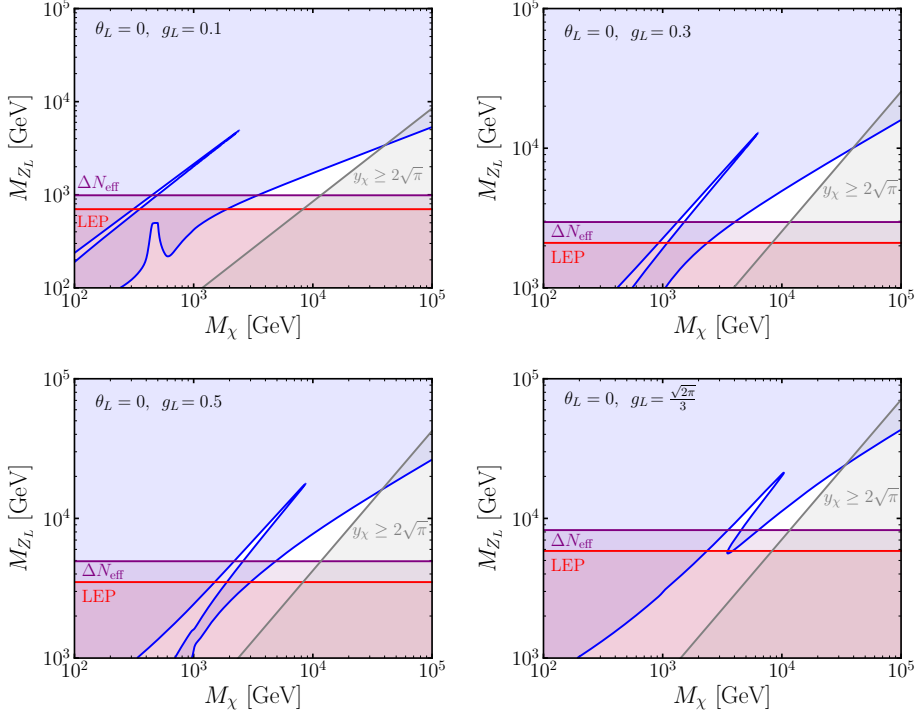


Figure 5.12: Results for the DM relic density in four different scenarios, $g_L = 0.1$ (top-left), $g_L = 0.3$ (top-right), $g_L = 0.5$ (bottom-left) and $g_L = \sqrt{2\pi}/3$ (bottom-right). We take $M_{h_2} = 1$ TeV and no mixing angle. The solid blue line gives the measured DM relic density $\Omega_\chi h^2 = 0.1200 \pm 0.0012$ [7], while the region shaded in blue overproduces it. The region shaded in gray is excluded by the perturbative bound on the Yukawa coupling y_χ . The horizontal red band corresponds to the LEP [181] bound on the $U(1)_L$ gauge boson mass. The bounds from N_{eff} are shown by the purple region and rule out a large fraction of the parameter space. *Figure extracted from Ref. [183].*

In Fig. 5.12, we present our result for the DM relic density and different constraints. The solid blue line saturates the relic abundance, $\Omega_\chi h^2 = 0.1200 \pm 0.0012$ [7], and the region shaded in blue overproduces it.

The four plots have two distinct regions where the correct relic abundance is achieved. One corresponds to the resonance $M_\chi \approx M_{Z_L}/2$ in which annihilation into SM leptons gives the dominant contribution (resonant region). The second one, to the right of the resonance, corresponds to the non-resonant region in which the annihilation channel $\chi\chi \rightarrow Z_L h_2$ gives the dominant contribution to the relic density (*plateau*). The appearance of the non-resonant region arises due to the Yukawa interaction with the scalar h_2 , and hence, new processes contribute to the DM annihilation channels. Particularly, compared to the previous theory $U(1)_{B-L}$, the following new channels contribute to the relic abundance:

We note that the non-resonant region is a special feature of models where the DM gets mass through the SSB of the new force.

The area shaded in gray in Fig. 5.12 shows the excluded parameter space by the perturbative bound on the Yukawa coupling y_χ . This bound gives an upper bound on the DM mass which, due to the connection with M_{Z_L} , translates as an upper bound on the lepton number breaking scale, analogously to the $U(1)_B$ theory (see Eq. 4.54).

In this scenario, the new gauge boson is coupled only to leptons at tree-level, and hence, the LHC bounds given in Fig. 3.4 cannot be applied. Even though the coupling to quarks can be generated at the one-loop level,⁴ the bounds are weaker than the one coming from LEP [181]. The latter are shown by the solid red line.

The upper left panel in Fig. 5.12 corresponds to $g_L = 0.1$. In this case, the bound from ΔN_{eff} requires $M_{Z_L} > 0.99$ TeV and the correct relic abundance can be produced close to the resonance $M_\chi \approx M_{Z_L}/2$ for DM masses $M_\chi \approx 550$ GeV – 2.4 TeV. In the non-resonant regime, the correct relic abundance can be generated for DM

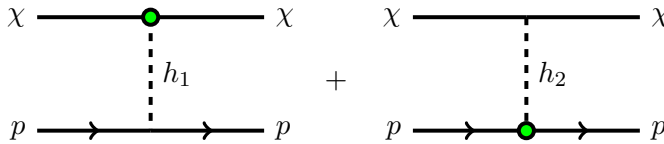
⁴For a study including one-loop effects see [259].

masses $M_\chi \approx 5.4 - 39$ TeV. For larger DM masses, the Yukawa coupling, y_χ , becomes non-perturbative. In the lower right panel of Fig. 5.12, we show our results for the maximal value of g_L allowed by perturbativity, $g_L = \sqrt{2\pi}/3 \approx 0.84$. The bound from ΔN_{eff} requires $M_{Z_L} > 8.25$ TeV. The resonant region that saturates the relic density and satisfies the bounds from LEP and ΔN_{eff} corresponds to $M_\chi \approx 4.6$ GeV – 10.2 TeV, while the non-resonant region works for DM masses $M_\chi \approx 8.9 - 34$ TeV. Above this value, the Yukawa coupling becomes non-perturbative. Therefore, the upper bounds correspond to

$$M_{Z_L} \lesssim 21 \text{ TeV} \quad \text{and} \quad M_\chi \lesssim 34 \text{ TeV}. \quad (5.41)$$

5.3.3 Phenomenological bounds

Regarding DD, the $\chi - N$ interaction can be mediated by Higgs mixing or the exchange of a Z_L . The latter is not coupled to quarks at tree-level, and hence, this process is loop suppressed [259]. Moreover, due to the Majorana nature of DM, there will also be velocity suppression. Hence, we focus on the contribution from Higgs mixing,



$$\chi \text{---} \overset{\bullet}{\text{---}} \text{---} \chi \quad + \quad \chi \text{---} \text{---} \overset{\bullet}{\text{---}} \text{---} \chi \quad (5.42)$$

$p \text{---} \text{---} p \quad \quad \quad p \text{---} \text{---} p$

where the total spin-independent cross-section is given by

$$\sigma_{\chi N}^{\text{SI}}(h_i) = \frac{72G_F}{\sqrt{2}4\pi} \sin^2 \theta_L \cos^2 \theta_L m_N^4 \frac{g_L^2 M_\chi^2}{M_{Z_L}^2} \left(\frac{1}{M_{h_1}^2} - \frac{1}{M_{h_2}^2} \right)^2 f_N^2, \quad (5.43)$$

where m_N corresponds to the nucleon mass, G_F is the Fermi constant, and for the effective Higgs-nucleon-nucleon coupling we take $f_N = 0.3$ [204,261].

In Fig. 5.13, we present our predictions for the spin-independent cross-section as a function of the DM mass in the $U(1)_L$ scenario. We perform a scan over $M_{h_2} = 0.1-20$ TeV and apply the LHC bound on the scalar mixing angle $\sin \theta_L \leq 0.3$ [195]. Green points correspond to $\sin \theta_L = 0 - 0.025$, red points correspond to $\sin \theta_L = 0.025-0.1$, orange points correspond to $\sin \theta_L = 0.1-0.2$, and blue points correspond to $\sin \theta_L =$

0.2-0.3. The solid black line shows current experimental bounds from Xenon-1T [205], the dashed black line shows the projected sensitivity for Xenon-nT [81], and the dotted black line shows the coherent neutrino scattering limit [83].

As illustrated in Fig. 5.13, for DM masses within reach of Xenon-nT, $M_\chi < 10$ TeV, this type of experiments will be able to probe scalar mixing angles $\theta_L > 0.025$, providing a stronger constraint than colliders on the Higgs mixing angle. In this scenario, there is no strong correlation between the ΔN_{eff} and DD bounds because the main contribution to DD is mediated by the Higgses in the theory, while ΔN_{eff} provides a constraint on the ratio M_{Z_L}/g_L .

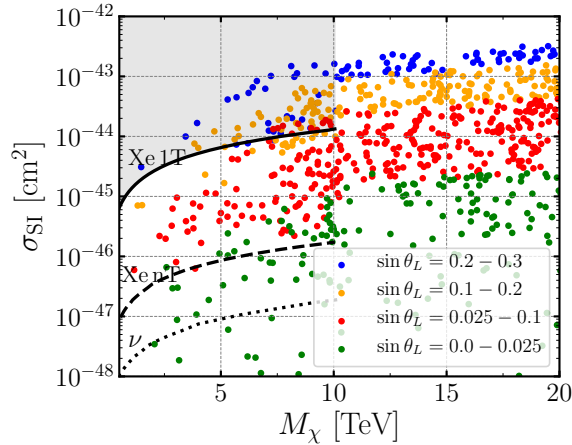


Figure 5.13: Predictions for the DD spin-independent cross-section as a function of the DM mass in the $U(1)_L$ scenario. We scan over $M_{h_2} = 0.1 - 20$ TeV and apply the LHC bound [182] on the mixing angle $\sin \theta_L \leq 0.3$. All points shown here satisfy the relic density $\Omega_\chi h^2 = 0.1200 \pm 0.0036$. The colored points represent different ranges for $\sin \theta_L$, as indicated in the legend. The solid black line shows current experimental bounds from Xenon-1T [205], the dashed black line shows the projected sensitivity for Xenon-nT [81] and the dotted black line shows the neutrino floor [83]. *Figure extracted from Ref. [183].*

5.4 Conclusions

In this chapter, we have investigated possible connections between the origin of neutrino masses and the properties of DM candidates in simple gauge theories based on local $B-L$ or L symmetries. In theories based on $B-L$, the gauge boson mass can be generated through the Stueckelberg or the Higgs mechanism. In the Canonical Seesaw scenario, the $B-L$ symmetry is spontaneously broken in two units via the Higgs mechanism, the neutrinos are Majorana fermions and, in the simplest model, the DM is a Dirac fermion. In the case of anomaly-free gauge theories based on $U(1)_L$, the Higgs mechanism is needed to generate the masses for the new fermions present in the theory for anomaly cancellation. We studied the simplest theories for local lepton number where the existence of a DM candidate is predicted from anomaly cancellation. In this case, the lepton number is broken in three units and the neutrinos are predicted to be Dirac particles, while the DM candidate is a Majorana fermion.

We showed that the cosmological constraint on the relic DM density implies that the upper bound on the symmetry breaking scale in these theories, i.e. the scale for lepton number violation, is in the multi-TeV region. In addition, we demonstrated that in theories where the neutrinos are Dirac, namely, the $B-L$ Stueckelberg scenario and the theory based on $U(1)_L$, the cosmological bound on the effective number of neutrino species, ΔN_{eff} , provides a strong bound in the parameter space of the models. Furthermore, the projected sensitivity to this parameter by the CMB Stage-IV experiments could fully probe the parameter space that also explains DM. In theories where the neutrinos are Majorana, namely $B-L$ broken in two units, the cosmological bound on the lepton number violating scale motivates the search of exotic lepton number violating signals at the LHC and future colliders. These results allow us to be optimistic about the testability of the mechanism for neutrino masses in current and future experiments.

6.- Neutrinos in Grand Unified Theories

Chapter based on the work done in 1604.03377 and 1804.07831.

Grand Unified Theories (GUTs) are well motivated scenarios for a UV completion of the SM. The idea of unification is undeniably attractive. In the context of gauge theories, it has been already proved to occur along the last century. First, electricity and magnetism were unified in the Maxwell equations in 1864 [262], proven to be two faces from the same coin. In the 60's, Glashow [263], Salam [264] and Weinberg [265] unified the electromagnetic and weak interactions in the EW theory. The SM is defined by the tensor product of three different symmetry gauge groups, each of them characterized by the corresponding strength coupling. What if they would be embedded in a single force? By looking at the matter content, we have leptons and quarks, which are fermions with similar patterns of behaviour that differ in their color and hypercharge. What if they come from some common representation where they were treated on an equal footing? Let us look now at the evolution of the strength of the forces conforming the SM, which is represented by their gauge coupling. As Fig. 6.1 shows, where $\alpha_i = g_i^2/4\pi$, when letting those evolve with energy, the three forces point to a common strength around $\Lambda = 10^{14}$ GeV, which is peculiarly close to the canonical seesaw scale for neutrino masses (see Chapter 1) and the experimental bounds on proton decay. This hint on a unified scale at high energies, together with the beauty and predictive power of a theory with a unique gauge coupling, motivated physicists to seek for a unified framework where the SM could be embedded.

The simplest GUT theory where the 15 Weyl d.o.f. of the SM can be embedded is $SU(5)$. *All elementary particle forces (strong, weak, and electromagnetic) are different*

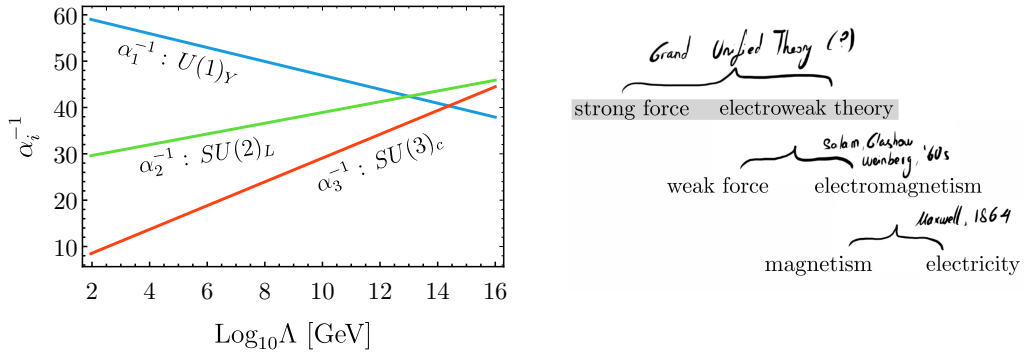


Figure 6.1: On the left, evolution of the SM gauge couplings in the context of the SM particle content. On the right, the steps towards unification in gauge forces are shown.

manifestations of the same fundamental interaction involving a single coupling strength, conjectured Georgi and Glashow in 1974 [266]. In their original minimal theory, quarks and leptons unify in the $\bar{5}$ and 10 representations in an anomaly free way, and the scalar content is composed of the minimal representations needed to break $SU(5)$ down to QED and QCD. Because of the traceless nature of its generators, the charges of the SM fermions are predicted and the theory is anomaly free. Besides, the theory also predicts striking phenomenological signatures such as the decay of the proton, whose lifetime has a lower bound around 10^{32-34} years, what in turn defines a lower bound for the $SU(5)$ scale around $\Lambda_{\text{GUT}} \sim 10^{14-15}$ GeV.¹ Such big scale, to which we will refer as GUT scale, brings us to the hopeless fact that these theories are well beyond the reach of the current accelerators and predict a *great desert* between NP and us. On the other hand, GUTs are so powerful that, although living in such high energy scale, its predictability can be the reason to rule them out, as it is the case of the original $SU(5)$ proposed by Georgi-Glashow ($SU(5)_{\text{GG}}$). The particular reasons that invalidate this theory are enumerated below:

- (i) it does not reproduce the values of the SM gauge couplings at the low scale,
- (ii) it predicts a wrong relation between the down quarks and charged lepton masses,

¹As we will see along this chapter, this lower bound can be relaxed depending on the class of $SU(5)$ theory and its predictive power.

(iii) neutrinos are massless in its context as well as in the SM.

Therefore, one needs to account for the later three aspects in order for the theory to be compatible with experiment, to which we will refer as *realistic*.

Conventionally, there are three ways to tackle problem (i), i.e. to achieve a consistent relation between the charged leptons and down quark masses:

- (a) Include higher-dimensional operators suppressed by the Planck scale [267]. Those allow to correct the relation between the fermion masses, but one has to give up on the renormalizability of the theory.
- (b) Add a new Higgs in the 45_H representation [268]. At the renormalizable level, it is well known that the 45_H contains a second Higgs doublet that couples differently to electrons than down-quarks, what allows to correct their mass relation.
- (c) Add new vector-like fermions [269]. They can correct the mass relation through their mixing with the SM fermions.

To solve both problem (ii) and (iii) in each of the above escenarios, extra representations are needed. In this chapter, we will introduce the $SU(5)_{GG}$ in the first place, we will discuss the possibilities to generate neutrino masses in the context of $SU(5)$, and we will propose two simple realistic $SU(5)$ realizations at the end of this chapter.

6.1 Minimal GUT : $SU(5)$ à la Georgi and Glashow

The 15 Weyl d.o.f. from the SM can be grouped in only two $SU(5)$ representations; the antifundamental and the antisymmetric: ²

$$\bar{5} \sim \underbrace{(1, \bar{2}, -1/2)}_{l_L} \oplus \underbrace{(\bar{3}, 1, 1/3)}_{(d^c)_L}, \quad \text{and} \quad 10 \sim \underbrace{(\bar{3}, 1, -2/3)}_{(u^c)_L} \oplus \underbrace{(3, 2, 1/6)}_{q_L} \oplus \underbrace{(1, 1, 1)}_{(e^c)_L}.$$

²Notice that, unfortunately, $SU(5)$ does not predict the number of families and three copies of the above representations have to be considered as in the SM.

Between brackets we write the explicit decomposition according to the SM quantum numbers. In a matrix form, they can be represented as follows,

$$\bar{5} = \left(\begin{array}{c} d_1^c \\ d_2^c \\ d_3^c \\ e \\ -\nu \end{array} \right)_L \left. \begin{array}{l} \\ \\ \\ \\ \end{array} \right\} \begin{array}{l} SU(3)_c \\ \\ \\ SU(2)_L \end{array} \quad \text{and} \quad 10 = \frac{1}{\sqrt{2}} \left(\begin{array}{ccccc} 0 & u_3^c & -u_2^c & -u^1 & -d^1 \\ -u_3^c & 0 & u_1^c & -u^2 & -d^2 \\ u_2^c & -u_1^c & 0 & -u^3 & -d^3 \\ u^1 & u^2 & u^3 & 0 & e^c \\ d^1 & d^2 & d^3 & -e^c & 0 \end{array} \right)_L \quad (6.1)$$

We note that the first three rows (three columns) can be identified as $SU(3)_c$ indices and the last two rows (two columns), as $SU(2)_L$ indices. The gauge group $SU(5)$ has rank 4, i.e. a total of four diagonal generators:

$$T_3 = \begin{pmatrix} \frac{\lambda_3}{2} & 0 \\ 0 & 0 \end{pmatrix}, \quad T_8 = \begin{pmatrix} \frac{\lambda_8}{2} & 0 \\ 0 & 0 \end{pmatrix}, \quad T_{\sigma_3} = \begin{pmatrix} 0 & 0 \\ 0 & \frac{\sigma_3}{2} \end{pmatrix}, \quad \text{and} \quad T_Y = \frac{1}{2\sqrt{15}} \begin{pmatrix} -2\mathbb{I}_{3 \times 3} & 0 \\ 0 & 3\mathbb{I}_{2 \times 2} \end{pmatrix},$$

as well as the SM, where one can recognize the 2 diagonal generators of $SU(3)_c$ (T_3 and T_8), the diagonal generator of $SU(2)_L$ (T_{σ_3}) and the equivalent to the $U(1)_Y$ generator (T_Y). As the following diagram shows,

$$T_i = \begin{pmatrix} \boxed{} & \cdot & \cdot \\ \cdot & \cdot & \cdot \\ \cdot & \cdot & \cdot \\ \cdot & \cdot & \cdot \\ \cdot & \cdot & \cdot \end{pmatrix}, \quad (6.2)$$

the red block 3×3 corresponds to the $SU(3)_c$ space, while the 2×2 block in blue, to the $SU(2)_L$ indices. The off-diagonal blocks, 3×2 and 2×3 correspond to generators both charged under $SU(2)_L$ and $SU(3)_c$ quantum numbers to which we will refer as leptokuarks (LQ), since they will mediate interactions between leptons and quarks. In the following, we will use block matrices to simplify the explicit expression of the $SU(5)$ representations.

The scalar content of the $SU(5)_{\text{GG}}$ is composed of the minimum amount of scalar representations required for recovering the SM and to trigger the posterior EW SSB:

$$SU(5) \xrightarrow{\text{SSB I}} SU(3)_c \otimes SU(2)_L \otimes U(1)_Y \xrightarrow{\text{SSB II}} SU(3) \otimes U(1)_Q. \quad (6.3)$$

The first breaking step respects the rank of the gauge symmetries. This can be achieved by the adjoint representation of $SU(5)$, i.e. by adding a 24_H :³

$$24_H = \begin{pmatrix} \Sigma_8 & \Sigma_{(3,2)} \\ \Sigma_{(\bar{3},2)} & \Sigma_3 \end{pmatrix} + T_Y \Sigma_0 = \begin{pmatrix} \Sigma_8 - \frac{1}{\sqrt{15}} \Sigma_0 & \Sigma_{(3,2)} \\ \Sigma_{(\bar{3},2)} & \Sigma_3 + \frac{3}{2\sqrt{15}} \Sigma_0 \end{pmatrix}, \quad (6.4)$$

whose components have the following SM quantum numbers,

$$24_H \sim \underbrace{(8, 1, 0)}_{\Sigma_8} \oplus \underbrace{(1, 3, 0)}_{\Sigma_3} \oplus \underbrace{(3, 2, -5/6)}_{\Sigma_{(3,2)}} \oplus \underbrace{(\bar{3}, 2, 5/6)}_{\Sigma_{(\bar{3},2)}} \oplus \underbrace{(1, 1, 0)}_{\Sigma_{24}}. \quad (6.5)$$

The 24_H representation should be broken in the direction of T_Y in order to recover the SM. After SSB, it reads as

$$\langle 24_H \rangle = \frac{v_\Sigma}{2\sqrt{15}} \begin{pmatrix} -2 \mathbb{I}_{3 \times 3} & 0 \\ 0 & 3 \mathbb{I}_{2 \times 2} \end{pmatrix}. \quad (6.6)$$

We note that the LQs do not commute with Σ_0 , while the $SU(3)_c$ and $SU(2)_L$ generators do, so that these local symmetries remain unbroken in the first step.

In the second breaking step, the rank is lowered in two units, and this is achieved by a scalar representation in the fundamental of $SU(5)$, i.e. a 5_H whose $SU(2)_L$ component, H_1 , can be identified with the SM Higgs boson:

$$5_H \sim \underbrace{(1, 2, 1/2)}_{H_1} \oplus \underbrace{(3, 1, -1/3)}_T = \begin{pmatrix} T \\ H_1 \end{pmatrix}. \quad (6.7)$$

³The 24_H is written such that $24_H = 24_H^a T_a$, where T_a are the generators of $SU(5)$. Notice that for Σ_0 the corresponding generator has been explicitly factorized out. Therefore, $\langle \Sigma_0 \rangle = v_\Sigma$.

Taking the above into account, the breaking pattern in Eq. 6.3 can be updated to:

$$SU(5) \xrightarrow{\langle \Sigma_0 \rangle} SU(3)_c \otimes SU(2)_L \otimes U(1)_Y \xrightarrow{\langle H_1 \rangle} SU(3)_c \otimes U(1)_Q. \quad (6.8)$$

Notice that, while in $SU(5)$ the normalization of the hypercharge is well-defined, in the SM it is arbitrary. The generators of a non-abelian gauge group are normalized according to

$$\text{Tr}\{T_a T_b\} = \frac{1}{2} \delta_{ab}, \quad (6.9)$$

so that the normalization of the corresponding non-abelian gauge coupling is unambiguously fixed. In contrast, for abelian groups like $U(1)_Y$, there is freedom in how we define the charge or the gauge coupling. In order to obtain the hypercharges as normalized in the SM, i.e. electric charge of the electron equal to -1 , we will redefine our $U(1)$ gauge coupling (g_1) by imposing $g_Y B = g_1 T_Y$. Since

$$T_Y = \sqrt{\frac{3}{5}} \begin{pmatrix} \frac{1}{3} \mathbb{I}_{3 \times 3} & 0 \\ 0 & -\frac{1}{2} \mathbb{I}_{2 \times 2} \end{pmatrix} = \sqrt{\frac{3}{5}} B \quad \Rightarrow \quad \boxed{g_Y = \sqrt{\frac{3}{5}} g_1}. \quad (6.10)$$

In this way, the hypercharge operator is embedded in $SU(5)$ and enjoys the right normalization $(3/5)\text{Tr}\{B^2\} = 1/2$ in its context. Therefore, once we fix one of the field hypercharges (i.e. $Y(d_L^c) = 1/3$), we can predict all the rest. The same can be applied to the charge operator, which after SSB is given by $Q = T_{\sigma_3} + B = T_{\sigma_3} + \sqrt{3/5} T_Y$. Taking into account the $5^2 - 1 = 24$ generators of $SU(5)$, the gauge content can be classified as:

$$V_{24}^\mu \sim \underbrace{(8, 1, 0)}_{G^\mu} \oplus \underbrace{(1, 3, 0)}_{W^\mu} \oplus \underbrace{(3, 2, -5/6)}_{V_2^{\dagger\mu}} \oplus \underbrace{(\bar{3}, 2, 5/6)}_{V_2^\mu} \oplus \underbrace{(1, 1, 0)}_{B^\mu},$$

which, expressed in a matrix form, reads as

$$V_{24}^\mu = V_{24}^{a\mu} T_a = \begin{pmatrix} G^\mu - \frac{1}{\sqrt{15}} B^\mu & V_2^{\dagger\mu} \\ V_2^\mu & W^\mu + \frac{3}{2\sqrt{15}} B^\mu \end{pmatrix}.$$

In the above expression, the twelve SM generators can be recognized: eight gluons $G_{a=1,\dots,8}^\mu$, the EW bosons $W_{a=1,\dots,3}^\mu$ and the hypercharge operator B^μ in the diagonal. In the off-diagonal blocks we can identify twelve leptiquarks. Those, as we are commenting in the following, will get mass at the GUT scale through the $SU(5)$ SSB.

The relevant terms from the $SU(5)$ Lagrangian for the mass generation of the bosons and fermions in the theory are given by

$$\begin{aligned} \mathcal{L}^{SU(5)} \supset & \underbrace{\text{Tr}\{D_\mu 24_H^\dagger D^\mu 24_H\} + (D_\mu 5_H)^\dagger D^\mu 5_H}_{\text{Gauge boson masses}} + \underbrace{\mathcal{L}_Y}_{\text{Fermion masses}} \\ & + \underbrace{\mu_5^2 5_H^\dagger 5_H - \alpha 5_H^\dagger 5_H \text{Tr}\{24_H^2\} - \beta 5_H^\dagger 24_H^2 5_H}_{\text{Higgs boson masses}}. \end{aligned} \quad (6.11)$$

Once the theory undergoes SSB and both 24_H and 5_H acquire a *vev*, the masses for the vector LQs are given by

$$\text{Tr}\{(D_\mu \langle 24_H \rangle)^\dagger D^\mu \langle 24_H \rangle\} = \frac{5}{6} g_{\text{GUT}}^2 v_\Sigma^2 \text{Tr}\{V_{2\mu}^\dagger V_{2\mu}\} \Rightarrow M_{\text{GUT}} = \sqrt{\frac{5}{6}} g_{\text{GUT}} v_\Sigma. \quad (6.12)$$

Here, we used that the covariant derivative for the adjoint representation of $SU(5)$ reads as $D^\mu 24_H = \partial^\mu 24_H + i g_{\text{GUT}} [V_{24}^\mu, 24_H]$. Notice that the trace over the off-diagonal $SU(5)$ generators has been explicitly written down. The above mass term, i.e. the mass of the LQs, defines the GUT scale $\Lambda_{\text{GUT}} \sim M_{\text{GUT}}$.

On the other hand, the scalar potential defines as well the masses of the Higgs bosons. Of special interest are the masses for the bosons in the 5_H representation, i.e. the masses of the colored triplet and the SM Higgs doublet, which can be inferred from the scalar potential terms from Eq. 6.11 and read as:

$$M_H^2 = -\mu_5^2 + \frac{1}{2} \left(\alpha + \frac{3}{10} \beta \right) v_\Sigma^2, \quad \text{and} \quad M_T^2 = -\mu_5^2 + \frac{1}{2} \left(\alpha + \frac{2}{15} \beta \right) v_\Sigma^2. \quad (6.13)$$

The Higgs doublet should live at the EW scale, what requires a delicate cancellation among the μ_5 and v_Σ terms. Due to the splitting between both boson masses, if such enormous tuning is applied in the M_H^2 in Eq. 6.13, the mass of the triplet will remain at the GUT scale, which is welcome since $T \sim (3, 1, -1/3)$ does mediate proton decay

and, as has been previously mentioned, such bounds are pretty aggressive. This huge splitting in the mass scale of the 5_H representation is known as the doublet-triplet splitting problem, and it constitutes a fine tuning problem of about twelve orders of magnitude that unfortunately fades the beauty of $SU(5)$.

Finally, the Yukawa Lagrangian \mathcal{L}_Y is given by the terms allowed by the gauge symmetry with the particle content described above as an input:

$$-\mathcal{L}_Y = \bar{5} Y_1 10 5_H^* + 10 Y_3 10 5_H \epsilon_5 + \text{h.c.}, \quad (6.14)$$

where, from now on, the implicit notation $R_1 R_2 \equiv R^T C R_2$ will be assumed in the context of GUT theories. After SSB, $\langle 5_H \rangle = v_5 / \sqrt{2}$ and the above Lagrangian generates the following charged fermion masses:

$$M_d = M_e^T = Y_1 \frac{v_5^*}{2}, \quad \text{and} \quad M_u = 2(Y_3 + Y_3^T) \frac{v_5}{\sqrt{2}}. \quad (6.15)$$

where $v_5 = v_0 = 246$ GeV. Here we find the first prediction that invalidates $SU(5)_{\text{GG}}$: charged leptons and down quarks share the same mass matrix at the GUT scale and, unfortunately, when considering the running to the low scale through the corresponding RGE equations, the experimental masses of the SM fermions cannot be achieved in this context. Therefore, we should think about extending the $SU(5)_{\text{GG}}$ to make it realistic.

6.1.1 Unification constraints

The Running Group Evolution (RGE) equations for the gauge couplings of the SM are given by,

$$\frac{1}{\alpha_i(M_Z)} - \frac{1}{\alpha_i(\mu)} = \frac{1}{2\pi} b_i^{\text{SM}} \ln \frac{\mu}{M_Z} + \frac{1}{2\pi} \sum_I b_i^I \Theta(\mu - M_I) \ln \frac{\mu}{M_I}. \quad (6.16)$$

The coefficients b_i in the above expression are determined by the group theory properties of the representation R in a given gauge group, according to

$$b_i = \frac{1}{3} \sum_R S(R) T_i(R) \underbrace{\prod_{j \neq i} \dim_j(R)}_{\text{mult}_i(R)}, \quad (6.17)$$

where $i = 1, 2, 3$. For a given representation R , $S(R) = 1, 2$ and -11 for scalar, chiral fermion and gauge bosons, respectively; $T_i(R)$ is the Dynkin index of R under the gauge group i ; and $\text{mult}_i(R)$ is the multiplicity of R under the rest of the gauge groups in the tensor product, similarly to that introduced in Eq. 3.8. For the SM fields, $b_1^{\text{SM}} = 41/10$, $b_2^{\text{SM}} = -19/6$ and $b_3^{\text{SM}} = -7$ (see Table 6.1). While those are at the EW scale, the new particles I can live in an intermediate scale between $M_Z < M_I < M_{\text{GUT}}$. We also note that in order to write the gauge couplings α_i^{-1} as a function of α_s and α from QCD and QED, respectively, one should take into account the proper normalization:

$$\alpha_1^{-1} \equiv \alpha^{-1} \cos^2 \theta_W \frac{3}{5}, \quad \alpha_2^{-1} \equiv \alpha^{-1} \sin^2 \theta_W, \quad \text{and} \quad \alpha_3^{-1} \equiv \alpha_s^{-1}. \quad (6.18)$$

	$\bar{5}$		10			V_{24}		5_H		24_H	
	l_L	$(d^c)_L$	$(u^c)_L$	q_L	$(e^c)_L$	G_μ	W_μ	H_1	T	Σ_8	Σ_3
b_1	$\frac{3}{5}$	$\frac{2}{5}$	$\frac{8}{5}$	$\frac{1}{5}$	$\frac{6}{5}$	0	0	$\frac{1}{10}$	$\frac{1}{15} r_T$	0	0
b_2	1	0	0	3	0	0	$-\frac{22}{3}$	$\frac{1}{6}$	0	0	$\frac{1}{3} r_{\Sigma_3}$
b_3	0	1	1	2	0	-11	0	0	$\frac{1}{6} r_T$	$\frac{1}{2} r_{\Sigma_8}$	0
B_{12}	$-\frac{4}{5}$	$\frac{2}{15}$	$\frac{8}{15}$	$-\frac{44}{15}$	$-\frac{2}{5}$	0	$\frac{22}{3}$	$-\frac{1}{15}$	$\frac{1}{15} r_T$	0	$-\frac{1}{3} r_{\Sigma_3}$
B_{23}	1	-1	-1	1	0	11	$-\frac{22}{3}$	$\frac{1}{6}$	$-\frac{1}{6} r_T$	$-\frac{1}{2} r_{\Sigma_8}$	$\frac{1}{3} r_{\Sigma_3}$

Table 6.1: Contributions to the B_{ij} coefficients for $SU(5)$.

By the definition itself of a GUT, the different couplings unavoidably unify at the GUT scale because they come from the same force. From Eq. 6.16, knowing that $\alpha_1(M_{\text{GUT}}) = \alpha_2(M_{\text{GUT}}) = \alpha_3(M_{\text{GUT}}) = \alpha_{\text{GUT}}$, and the equivalences from Eq. 6.18, one

can find the following relations among the low scale inputs [270]:

$$\frac{B_{23}}{B_{12}} = \frac{5}{8} \left(\frac{\sin^2 \theta_W(M_Z) - \alpha(M_Z)/\alpha_s(M_Z)}{3/8 - \sin^2 \theta_W(M_Z)} \right) = 0.717, \quad (6.19)$$

$$\ln \frac{M_{GUT}}{M_Z} = \frac{16\pi}{5\alpha(M_Z)} \left(\frac{3/8 - \sin^2 \theta_W(M_Z)}{B_{12}} \right) = \frac{184.95}{B_{12}}, \quad (6.20)$$

where $B_{ij} = B_i - B_j$, being B_i defined as

$$B_i = b_i + \sum_I b_i^I r^I, \quad \text{where } r^I = \frac{\ln(\Lambda_{GUT}/M_I)}{\ln(\Lambda_{GUT}/M_Z)}. \quad (6.21)$$

In the RHS of the conditions from Eq. 6.19 and 6.20, the following experimental values, $\sin^2 \theta_W(M_Z) = 0.23122$, $\alpha(M_Z) = 1/127.955$, and $\alpha_s(M_Z) = 0.1181$ at the M_Z scale [198] have been used. The above expressions are required by unification at the 1-loop level. By taking into account the SM particle content, condition 6.19 gives ≈ 0.53 , far from the desired value. Therefore, in the context of the SM, as Fig. 6.1 shows, unification cannot be achieved.

Let us consider $SU(5)_{GG}$ instead. It contains extra fields with respect to the SM in the representations 5_H and 24_H , which may in principle modify the RGE equations. In Table 6.1, we list the contribution to the running of the gauge couplings of the SM fields plus the extra fields predicted by $SU(5)_{GG}$. Notice that we do not consider the LQ vector bosons because they are at the GUT scale and therefore do not contribute until then,⁴ nor the scalar bosons in the off-diagonal terms of 24_H since they are the GBs responsible for the mass of the vector LQs. Finally, the singlet living in V_{24} and the one living in 24_H are not included because they do not modify the running of the gauge couplings. For $SU(5)_{GG}$, the unification ratio takes the form:

$$\frac{B_{23}^{SU(5)}}{B_{12}^{SU(5)}} = \frac{B_{23}^{SM} + \frac{1}{3}r_{\Sigma_3} - \frac{1}{6}r_T - \frac{1}{2}r_{\Sigma_8}}{B_{12}^{SM} - \frac{1}{3}r_{\Sigma_3} + \frac{1}{15}r_T} \Bigg|_{\text{optimistic}} \lesssim 0.6, \quad (6.22)$$

⁴After Λ_{GUT} they are indeed the responsible fields for making the α_i evolve at once as α_{GUT} .

where the inequality shows that, even adopting the most optimistic scenario (i.e. the values for the splitting between the representations that allow for the largest possible ratio), the proper value in Eq. 6.19 cannot be reached.

And here we have bumped into problem (ii)! It is sometimes found in the literature that *unification cannot be achieved in $SU(5)_{GG}$ so that the theory is ruled out*. The later is an abuse of language; the inability of a GUT theory to satisfy Eq. 6.19 and 6.20 reflects that the experimental values of the SM gauge couplings cannot be reproduced at the low scale regardless of the unification scale we start the running. But of course the gauge couplings unify in $SU(5)$, as well as any other GUT theory!

6.1.2 Proton decay

One of the most exciting predictions of GUT theories based on $SU(5)$ is the decay of the proton. However, we have never seen the proton decaying; actually it is one of the most stable particles in the universe, being the lower bound on its lifetime around 10^{32-34} years. See Fig. 6.2 for a collection of some bounds on proton decay channels. Such prediction has, of course, dramatic implications for the GUT scale.

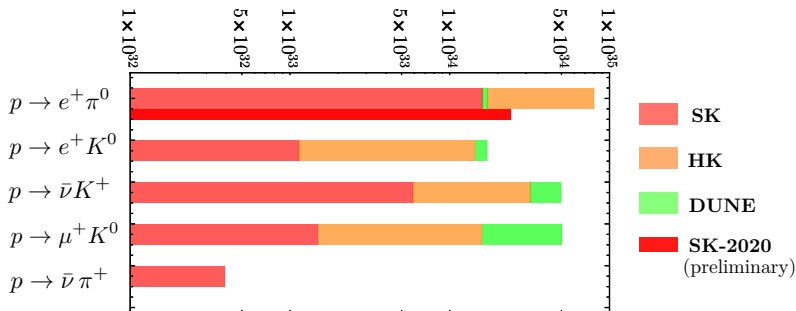


Figure 6.2: Most relevant bounds on proton decay channels by Super-Kamiokande (SK) collaboration (in red), and the respective projected bounds by the Hyper-Kamiokande (HK) collaboration (in orange) and DUNE (in green), extracted from Refs. [158, 271–273]. In darker red we show the preliminary result of Super-K 2020 on the $p \rightarrow \pi^0 e^+$ channel [274].

In order to estimate the proton decay rate, let us present the interactions that can mediate such phenomenon. There are several LQs in this theory that can lead to the decay of the proton, either via a scalar or a vector boson. In the scalar case, one can always escape from the experimental bounds by assuming a small enough Yukawa coupling if there is the freedom to do it. The gauge mediated interactions, however, are clean in the sense that they are mediated by the gauge coupling, which is tightly related to the GUT scale. We will focus only on these interactions since they are the dominant contribution to the $\Delta B = 1$ processes. Let us start from the matter kinetic Lagrangian:

$$\mathcal{L} \supset i\bar{5}^\dagger \gamma^0 \gamma^\mu D_\mu \bar{5} + i\text{Tr}\{10^\dagger \gamma^0 \gamma^\mu D_\mu 10\}, \quad (6.23)$$

where the covariant derivatives depend on the representation on which they act: $D_\mu \bar{5} = \partial_\mu \bar{5} + ig_{\text{GUT}} V_{24\mu}^T \bar{5}$ and $D_\mu 10 = \partial_\mu 10 + ig_{\text{GUT}}(V_{24\mu} 10 + 10V_{24\mu}^T)$. From the above Lagrangian, one obtains the kinetic terms for the SM fermions plus some interacting terms between fermions and gauge bosons included in the covariant derivatives. The non-SM interacting terms involve the V_2^μ LQ. Those are given by,

$$\mathcal{L} \supset \frac{g_{\text{GUT}}}{\sqrt{2}} \left(\underbrace{(\overline{d^c})_L \gamma^\mu V_{2\mu}^T i\sigma_2 \ell_L}_{\text{Kinetic } \bar{5}} + \underbrace{(\overline{u^c})_L V_2^{\mu\dagger} \gamma_\mu q_L - (\overline{e^c})_L \gamma_\mu V_2^{\mu T} i\sigma_2 q_L}_{\text{Kinetic } 10} + \text{h.c.} \right). \quad (6.24)$$

Explicitly expanding over the $SU(2)_L$ components, taking into account that $V_2^\mu = (X^\mu, Y^\mu)^T$ where X and Y have electric charges $4/3$ and $1/3$, respectively, the above Lagrangian can be written as,

$$\begin{aligned} \mathcal{L} \supset \frac{g_{\text{GUT}}}{\sqrt{2}} \left(\underbrace{-\overline{(e^c)}_L Y_\mu \gamma^\mu u_L + \overline{(e^c)}_L X_\mu \gamma^\mu d_L - \overline{(d^c)}_L X_\mu \gamma^\mu e_L + \overline{(d^c)}_L Y_\mu \gamma^\mu \nu_L}_{\text{LQ vertices}} \right. \\ \left. + \underbrace{\overline{(u^c)}_L X_\mu^\dagger \gamma^\mu u_L + \overline{(u^c)}_L Y_\mu^\dagger \gamma^\mu d_L}_{\text{Diquark vertices}} \right) + \text{h.c.} - M_{\text{GUT}}^2 (X_\mu^\dagger X^\mu + Y_\mu^\dagger Y^\mu). \end{aligned} \quad (6.25)$$

As we will see, combination of leptoquark and diquark vertices leads to baryon and lepton violation, although $B-L$ is conserved. Integrating out the X boson, we end up

with the following effective Lagrangian (for more details on integrating out heavy fields see Chapter 8),

$$\mathcal{L}_{\text{eff}}^X \supset \frac{g_{\text{GUT}}^2}{M_{\text{GUT}}^2} \left(\overline{(u^c)_L} \gamma^\mu u_L \overline{(e^c)_L} \gamma_\mu d_L - \overline{(u^c)_L} \gamma_\mu u_L \overline{(d^c)_L} \gamma^\mu e_L + \text{h.c.} \right), \quad (6.26)$$

while, on the other hand, if we integrate out Y , we get instead

$$\mathcal{L}_{\text{eff}}^Y \supset \frac{g_{\text{GUT}}^2}{M_{\text{GUT}}^2} \left(\overline{(e^c)_L} \gamma_\mu u_L \overline{(u^c)_L} \gamma^\mu d_L - \overline{(u^c)_L} \gamma^\mu d_L \overline{(d^c)_L} \gamma_\mu \nu_L + \text{h.c.} \right). \quad (6.27)$$

The first term in the Lagrangian from Eq. 6.27 can be rewritten using the Fierz identities (see Appendix A) in the following way:

$$\overline{(e^c)_L} \gamma_\mu u_L \overline{(u^c)_L} \gamma^\mu d_L \equiv \overline{(u^c)_L} \gamma_\mu u_L \overline{(e^c)_L} \gamma^\mu d_L, \quad (6.28)$$

so that it can be identified with the first interaction from the effective Lagrangian of the X boson. In total, from the above interactions one can recognize three kinds of effective operators contributing to proton decay, listed below:

$$\mathcal{O}_{(e_i^c, d_j^c)}^{\Delta B=1} = \frac{g_{\text{GUT}}^2}{2M_{\text{GUT}}^2} c(e_i^c, d_j^c) \overline{(u_L^c)} \gamma^\mu u_L \overline{(e^c)_{iL}} \gamma_\mu d_{jL}, \quad (6.29)$$

$$\mathcal{O}_{(e_i, d_j^c)}^{\Delta B=1} = \frac{g_{\text{GUT}}^2}{2M_{\text{GUT}}^2} c(e_i, d_j^c) \overline{(u^c)_L} \gamma^\mu u_L \overline{(d^c)_{jL}} \gamma_\mu e_{iL}, \quad (6.30)$$

$$\mathcal{O}_{(\nu_\ell, d_i, d_j^c)}^{\Delta B=1} = \frac{g_{\text{GUT}}^2}{2M_{\text{GUT}}^2} c(\nu_\ell, d_i, d_j^c) \overline{(u^c)_L} \gamma^\mu d_{iL} \overline{(d^c)_{jL}} \gamma_\mu \nu_\ell, \quad (6.31)$$

where some mixing matrices arise when rotating to the mass eigenbasis of the fermions. Those are encoded in the c coefficients [275], defined as ⁵

$$c(e_\alpha^c, d_\beta) = V_1^{11} V_2^{\alpha\beta} + (V_1 V_{UD})^{1\beta} (V_2 V_{UD}^\dagger)^{\alpha 1}, \quad (6.32)$$

$$c(e_\alpha, d_\beta^c) = V_1^{11} V_3^{\beta\alpha}, \quad (6.33)$$

$$c(\nu_\ell, d_\alpha, d_\beta^c) = (V_1 V_{UD})^{1\alpha} (V_3 V_{EN})^{\beta\ell}, \quad (6.34)$$

⁵Notice the two contributions in Eq. 6.32, from the X and Y effective Lagrangians, respectively.

where the V 's are mixing matrices defined as

$$V_1 = U_C^\dagger U, V_2 = E_C^\dagger D, V_3 = D_C^\dagger E, V_{UD} = U^\dagger D \quad \text{and} \quad V_{EN} = E^\dagger N. \quad (6.35)$$

Here, the matrices U , E , D and N define the diagonalization of the Yukawa couplings:

$$U_C^T Y_u U = Y_u^{\text{diag}}, D_C^T Y_d D = Y_d^{\text{diag}}, E_C^T Y_e E = Y_e^{\text{diag}}, \quad \text{and} \quad N^T Y_\nu N = Y_\nu^{\text{diag}}. \quad (6.36)$$

Since $SU(5)$ interactions mediate proton (p) decaying into an anti-lepton ($\bar{\ell}$) and a meson (M), the decay rate of such process can be parametrized as

$$\Gamma_{p \rightarrow M \bar{\ell}} = \frac{m_p}{32\pi} \left(1 - \left(\frac{m_p}{m_M} \right)^2 \right)^2 \left| \sum_i \langle M | \mathcal{O}_i^{\Delta B=1} | p \rangle \right|^2, \quad (6.37)$$

where $\mathcal{O}_i^{\Delta B=1}$ are precisely the operators mediating $\Delta B = 1$ interactions from Eqs. 6.29-6.31. In order to compute the matrix elements, we can get rid of the Lorentz indices from these operators by rewriting them as scalar bilinears:

$$\mathcal{O}_{(e_i^c, d_j)}^{\Delta B=1} = \frac{g_{\text{GUT}}^2}{M_{\text{GUT}}^2} c(e_i^c, d_j) (\bar{u}^c P_R d_j) (\bar{e}_i^c P_L u), \quad (6.38)$$

$$\mathcal{O}_{(e_i, d_j^c)}^{\Delta B=1} = \frac{g_{\text{GUT}}^2}{M_{\text{GUT}}^2} c(e_i, d_j^c) (\bar{u}^c P_L d_j) (\bar{e}_i^c P_R u), \quad (6.39)$$

$$\mathcal{O}_{(\nu_\ell, d_i, d_j^c)}^{\Delta B=1} = \frac{g_{\text{GUT}}^2}{M_{\text{GUT}}^2} c(\nu_\ell, d_i, d_j^c) (\bar{u}^c P_R d_j) (\bar{\nu}^c P_L d_i), \quad (6.40)$$

where the Fierz identities (see Appendix A) have been used again. Plugging in Eq. 6.37 the above operators, we end up with the following expression for the decay rate,

$$\Gamma_{p \rightarrow M \bar{\ell}} = A_{\text{RG}}^2 \frac{\pi m_p}{2} \left(1 - \frac{m_p^2}{m_M^2} \right)^2 \left(\frac{\alpha_{\text{GUT}}}{M_{\text{GUT}}^2} \right)^2 \left| \sum_i c_i \langle M | \bar{\ell}^c (q_1 q_2)_{L/R} q_{3 L/R} | p \rangle \right|^2 \quad (6.41)$$

where inside the matrix element one can recognize the three-quark operator violating baryon number, where $(q_1 q_2)_{L/R} \equiv q_1^T C P_{L/R} q_2$, and the A_{RG} accounts for the running between the GUT scale and $Q \sim 2.3$ GeV, where the hadronic matrix elements are

evaluated:⁶

$$A_{\text{RG}} = \left(\frac{\alpha_3(m_b)}{\alpha_3(M_Z)} \right)^{6/23} \left(\frac{\alpha_3(Q)}{\alpha_3(m_b)} \right)^{6/25} \left(\frac{\alpha_3(M_Z)}{\alpha_3(M_{\text{GUT}})} \right)^{2/7}. \quad (6.42)$$

We can particularize the decay rate in Eq. 6.41 to some specific channels which, as Fig. 6.2 shows, comprise the strongest experimental bounds on proton decay:

$$\Gamma_{p \rightarrow \pi^0 e^+} = \frac{\pi m_p}{2} A_{\text{RG}}^2 \left(\frac{\alpha_{\text{GUT}}}{M_{\text{GUT}}} \right)^4 |V_e \langle \pi^0 | (ud)_L u_R | p \rangle|^2, \quad (6.43)$$

$$\begin{aligned} \Gamma_{p \rightarrow K^+ \bar{\nu}} &= \frac{\pi m_p}{2} \left(1 - \frac{m_{K^+}^2}{m_p^2} \right)^2 A_{\text{RG}}^2 \left(\frac{\alpha_{\text{GUT}}}{M_{\text{GUT}}} \right)^4 \\ &\times \left(|(V_1 V_{UD})^{11} \langle K^+ | (us)_R d_L | p \rangle|^2 + |(V_1 V_{UD})^{12} \langle K^+ | (ud)_{RS} | p \rangle|^2 \right), \end{aligned} \quad (6.44)$$

$$\Gamma_{p \rightarrow \pi^+ \bar{\nu}} = \frac{\pi m_p}{2} A_{\text{RG}}^2 \left(\frac{\alpha_{\text{GUT}}}{M_{\text{GUT}}} \right)^4 |(V_1 V_{UD})^{11} \langle \pi^+ | (du)_R d_L | p \rangle|^2, \quad (6.45)$$

where

$$V_e = \sqrt{\left(|(V_2^{11} + V_{\text{CKM}}^{11} (V_2 V_{\text{CKM}})^{11})|^2 + |V_3^{11}|^2 \right)}, \quad (6.46)$$

and we have explicitly summed over the three neutrino flavours and used that V matrices in Eq. 6.35 are unitary.⁷ For the matrix elements appearing in the above expressions we take as an input the results evaluated via Lattice QCD at the scale Q , given in the recent Ref. [276]:

$$\begin{aligned} \langle \pi^+ | (du)_R d_L | p \rangle &= -0.186 \text{ GeV}^2, & \langle \pi^0 | (ud)_R u_L | p \rangle &= -0.131 \text{ GeV}^2, \\ \langle K^+ | (us)_R d_L | p \rangle &= -0.049 \text{ GeV}^2, & \langle K^+ | (ud)_{RS} | p \rangle &= -0.134 \text{ GeV}^2. \end{aligned} \quad (6.47)$$

Note that, although we could fix $\alpha_{\text{GUT}}/M_{\text{GUT}}^2$ from the unification conditions, we still have some freedom in the fermion mixing matrices V , being the only known one the CKM matrix, $V_{UD} \equiv V_{\text{CKM}}$.

⁶See Ref. [275] for a more details.

⁷We note that, when summing over all possible anti-neutrinos, the crossed terms coming from expanding the modulus squared will disappear due to the orthonormality conditions of the unitary mixing matrices.

In the original $SU(5)_{\text{GG}}$, from Eq. 6.15 we can identify $Y_U \equiv 2(Y_3 + Y_3^T)$, and realize that $Y_U = Y_U^T$ is symmetric. From the spectral theorem it is well-known that a symmetric matrix is diagonalized by an orthonormal matrix, so that the matrix U in Eq. 6.35 is orthonormal up to some complex phase. According to the definition of the mixing matrices in Eq. 6.36, the one that arises from the diagonalization of the up quark mass matrix is therefore,

$$V_1 \equiv U_C^\dagger U = \mathbb{I}e^{i\phi}, \quad (6.48)$$

for theories where the up quark mass matrix is symmetric [275]. This allows us to make a clean prediction for the proton decay channels into antineutrinos, which applying the above result to Eqs. 6.44 and 6.45 read as,

$$\begin{aligned} \Gamma_{p \rightarrow K^+ \bar{\nu}} &= \frac{\pi m_p}{2} \frac{\alpha_{\text{GUT}}^2}{M_{\text{GUT}}^4} \left(1 - \frac{m_{K^+}^2}{m_p^2}\right)^2 A_{\text{RG}}^2 \\ &\times \left(|V_{\text{CKM}}^{11} \langle K^+ | (us)_{RdL} | p \rangle|^2 + |V_{\text{CKM}}^{12} \langle K^+ | (ud)_{RSL} | p \rangle|^2 \right), \end{aligned} \quad (6.49)$$

$$\Gamma_{p \rightarrow \pi^+ \bar{\nu}} = \frac{\pi m_p}{2} \frac{\alpha_{\text{GUT}}^2}{M_{\text{GUT}}^4} A_{\text{RG}}^2 |V_{\text{CKM}}^{11} \langle \pi^+ | (du)_{RdL} | p \rangle|^2, \quad (6.50)$$

which can be further simplified by rewriting them as

$$\Gamma_{p \rightarrow K^+ \bar{\nu}} = \frac{\pi m_p}{2} \frac{\alpha_{\text{GUT}}^2}{M_{\text{GUT}}^4} \left(1 - \frac{m_{K^+}^2}{m_p^2}\right)^2 C_K, \quad (6.51)$$

$$\frac{\Gamma_{p \rightarrow \pi^+ \bar{\nu}}}{\Gamma_{p \rightarrow K^+ \bar{\nu}}} = \frac{C_\pi}{C_K} \left(1 - \frac{m_{K^+}^2}{m_p^2}\right)^{-2} \simeq 20, \quad (6.52)$$

where

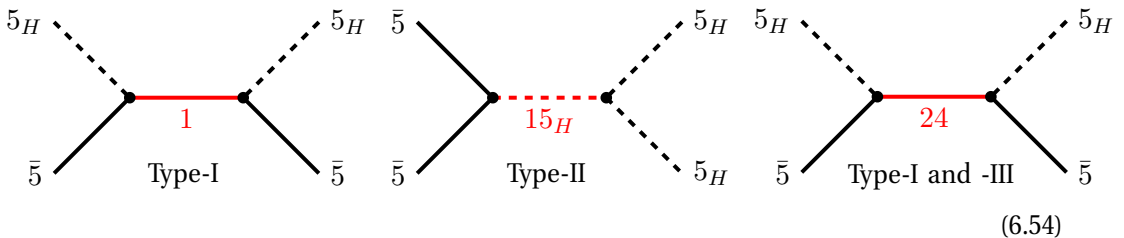
$$\begin{aligned} C_K &= A_{\text{RG}}^2 \left(|V_{\text{CKM}}^{11} \langle K^+ | (us)_{RdL} | p \rangle|^2 + |V_{\text{CKM}}^{12} \langle K^+ | (ud)_{RSL} | p \rangle|^2 \right) \simeq 0.01, \\ C_\pi &= A_{\text{RG}}^2 |V_{\text{CKM}}^{11} \langle \pi^+ | (du)_{RdL} | p \rangle|^2 \simeq 0.1. \end{aligned} \quad (6.53)$$

This is a wonderful prediction from $SU(5)_{GG}$: it can cleanly predict the decay rate of the proton for the decay channels involving antineutrinos. As we will see later, this peculiar prediction is not common in all extensions of $SU(5)_{GG}$: for instance, the introduction of a scalar representation 45_H to correct the relation between the charged fermion masses spoils the symmetric nature of the up-type quark Yukawa coupling.

To close this first part of the chapter, we will comment that $SU(5)_{GG}$, although being the simplest and most predictive GUT ever written, apart from not being able to reproduce the correct charged fermion masses -problem (i)- and the low scale values of the gauge couplings -problem (ii)-, it predicts massless neutrinos since no mass term is allowed by the $SU(5)$ symmetry and the particle content considered in its minimal realization -problem (iii)-, as in the SM. In the next section we present the simplest possibilities to generate neutrino masses in the context of $SU(5)$.

6.2 Mechanisms for neutrino mass generation in $SU(5)$

In this section we discuss the implementation of the three seesaw mechanisms introduced in Chapter 1 in the context of $SU(5)$ (see Diag. 6.54), and two of the simplest 1-loop mechanisms: the colored seesaw and the Zee model.



6.2.1 Type-I seesaw

As discussed in Chapter 1, a Dirac mass term can be generated by adding a fermion singlet under the SM, $(\nu^c)_L \sim 1 \sim (1, 1, 0)$, which can be straightforwardly generalized in $SU(5)$ by adding a 1 fermion representation. The addition of a singlet does not spoil anomaly cancellation of the gauge theory. In addition with the Dirac mass term, we unavoidably have a Majorana mass term too since it is not forbidden by any symmetry.

The relevant Lagrangian in this case is given by,

$$- \mathcal{L}^{\text{Type-I}} \supset Y_\nu^i \bar{5}_i 5_H 1 + \frac{1}{2} M_\nu 1 1 + \text{h.c.} \quad (6.55)$$

The reader may find the above expression familiar; indeed, it corresponds to the Type-I seesaw Lagrangian described in Eq. 1.18 from Chapter 1. The resulting mass matrix for neutrinos is given in Eq. 1.19. Notice, however, that the Yukawa coupling Y_ν in the above Lagrangian is just a vector, as the explicitly written family index indicates, so that the neutrino mass matrix will be rank 1 in this case. Therefore, as pointed out in Chapter 1, in order to generate realistic neutrino masses, at least two copies of $\nu_R \sim 1$ are needed. The implementation of this mechanism with the addition of fermion singlets, in despite of its simplicity, is not attractive from the perspective that the Majorana mass M_ν is a dimensionful parameter, not protected by the gauge symmetry and therefore exposed to any UV effects.

6.2.2 Type-II seesaw

In the context of $SU(5)$, neutrino masses can also be generated through the Type-II seesaw mechanism, introduced in Chapter 1. Such mechanism can be implemented by the addition of a new Higgs representation, the symmetric 15_H . This minimal realistic extension was first proposed in Ref. [277], and further studied in Refs. [278,279]. The 15_H contains the following fields under the SM quantum numbers:

$$15_H = \underbrace{(1, 3, 1)}_{\Delta} \oplus \underbrace{(3, 2, 1/6)}_{\Delta_{(3,2)}} \oplus \underbrace{(6, 1, -2/3)}_{\Delta_S}. \quad (6.56)$$

Inside the 15_H representation, $\Delta \sim (1, 3, 1)$ plays a key role in the implementation of the seesaw mechanism; it can be identified with the scalar triplet with hypercharge 1 needed for the Type-II seesaw (see Eq. 1.21). The Yukawa Lagrangian in the presence of 15_H reads,

$$- \mathcal{L}_Y \supset \bar{5} Y_1 10 15_H + 10 Y_2 10 5_H \epsilon_5 + \bar{5} Y_\Delta \bar{5} 15_H + \text{h.c.}, \quad (6.57)$$

while from the scalar potential of this $SU(5)$ extension we highlight the following terms:

$$V \supset M_\Delta^2 15_H^* 15_H + \left(\tilde{\mu} 5_H^* 5_H^* 15_H + \tilde{\lambda} 5_H^* 5_H^* 24_H 15_H + \text{h.c.} \right). \quad (6.58)$$

The interactions in Eqs. 6.57 and 6.58 lead to the following Lagrangian in the broken phase,

$$-\mathcal{L}_{\text{Type-II}} = M_\Delta^2 \text{Tr}\{\Delta^\dagger \Delta\} + \left(Y_\Delta^{ij} \ell_{iL}^T C i\sigma_2 \Delta \ell_{jL} + (\mu + \lambda v_\Sigma) H_1^T i\sigma_2 \Delta^\dagger H_1 + \text{h.c.} \right), \quad (6.59)$$

where the Type-II seesaw Lagrangian from Eq. 1.22 can be recognized. Once the triplet Δ in 15_H acquires a vev , i.e. $\langle \Delta \rangle = v_\Delta / \sqrt{2}$, the neutrinos get a Majorana mass that, taking into account Eqs. 1.23 and 1.26, can be written as

$$M_\nu^{ij} \sim \sqrt{2} (\mu + \lambda v_\Sigma) Y_\Delta^{ij} \frac{v_0^2}{M_\Delta^2}. \quad (6.60)$$

Note that in order to achieve the scale for neutrino masses observed at experiment, $M_\Delta^2 / (\mu + \lambda v_\Sigma) \sim \mathcal{O}(10^{13-14})$ GeV. Note also that we have written explicitly the family indices in order to point out that, this time, Y_Δ is a matrix that can be up to rank 3. Therefore, in principle, with only one triplet Δ there is enough freedom to reproduce the experimental neutrino masses. The addition of the 15_H is an attractive extension of the $SU(5)_{\text{GG}}$ theory since it has enough potential to recover unification, whose conditions predict the LQ Δ_S to be at the EW scale. Furthermore, although the addition of the 15_H does not modify the charged fermion masses, a consistent relation among them could be achieved by allowing for non-renormalizable interactions.

6.2.3 Type-III seesaw

This mechanism, also described in Chapter 1, is mimicked in $SU(5)$ by adding a fermion representation in the adjoint of $SU(5)$ [27, 28, 280–282]:

$$24 \sim \underbrace{(8, 1, 0)}_{\rho_8} \oplus \underbrace{(1, 3, 0)}_{\rho_3} \oplus \underbrace{(3, 2, -5/6)}_{\rho_{(3,2)}} \oplus \underbrace{(\bar{3}, 2, 5/6)}_{\rho_{(\bar{3},2)}} \oplus \underbrace{(1, 1, 0)}_{\rho_0}, \quad (6.61)$$

which has the following matrix representation,

$$24 = \begin{pmatrix} \rho_8 & \rho_{(3,2)} \\ \rho_{(\bar{3},2)} & \rho_3 \end{pmatrix}_L + T_Y \rho_{0L}.$$

The 24 contains the key ingredient for the Type-III seesaw mechanism: an hyperchargeless $SU(2)_L$ triplet of leptons. To enlarge the matter content by including a real representation is not a problem since, as explained in Chapter 3, such representation does not spoil anomaly cancellation. The relevant interactions for this mechanism are collected below,

$$-\mathcal{L}_{\text{Type-III}} \supset h_1 \bar{5} 24 5_H + M_{24} \text{Tr}\{24^2\} + \lambda \text{Tr}\{24^2 24_H\} + \text{h.c.} \quad (6.62)$$

We note that, in this case, since the 24 also contains a fermion singlet $\rho_0 \sim (1, 1, 0)$, the Type-I seesaw mechanism will inexorably occur together with the Type-III, as illustrated in Diag. 6.63:

$$\begin{array}{c} 5_H \\ \vdots \\ \bullet \\ \vdots \\ \bar{5} \end{array} \begin{array}{c} \bullet \\ \text{---} 24 \text{---} \\ \bullet \\ \vdots \\ \bar{5} \end{array} = \begin{array}{c} H_1 \\ \vdots \\ \bullet \\ \vdots \\ \ell \end{array} \begin{array}{c} \bullet \\ \text{---} (\rho_0)^c \text{---} \\ \bullet \\ \vdots \\ \ell \end{array} \text{Type-I seesaw} + \begin{array}{c} H_1 \\ \vdots \\ \bullet \\ \vdots \\ \ell \end{array} \begin{array}{c} \bullet \\ \text{---} (\rho_3)^c \text{---} \\ \bullet \\ \vdots \\ \ell \end{array} \text{Type-III seesaw} \quad (6.63)$$

After 24_H gets a vev , the above Lagrangian leads to the following interactions,

$$-\mathcal{L}_{\text{Type-III}} \supset \frac{1}{2} M_{\rho_0} \rho_0^T C P_L \rho_0 + M_{\rho_3} \text{Tr}\{\rho_3^T C P_L \rho_3\} + h_1^i \ell_i^T C i \sigma_2 P_L \left(\rho_3 + \frac{3}{2\sqrt{15}} \rho_0 \right) H_1 + \text{h.c.}, \quad (6.64)$$

where $M_{\rho_0} = M_{24} - \lambda v_\Sigma / (2\sqrt{15})$ and $M_{\rho_3} = M_{24} - 3\lambda v_\Sigma / (2\sqrt{15})$. Notice that these interactions reproduce the Type-I and Type-III seesaw Lagrangian from Eqs. 1.18 and 1.28 when identifying $(\rho_0^c)_L \equiv \nu_R$ and $(\rho_3^c)_L \equiv \Sigma_R$, respectively. The neutrino mass matrix

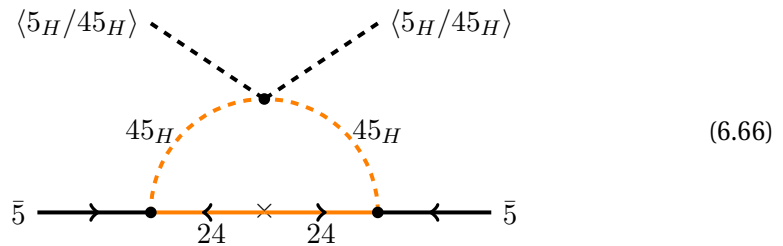
in this context, after EW SSB, is given by,

$$M_\nu^{ij} = \frac{1}{8} \left(\frac{h_1^i h_1^j}{M_{\rho_3}} + \frac{3 h_1^i h_1^j}{5 M_{\rho_0}} \right) v_0^2 = \frac{1}{8} \left(\frac{1}{M_{\rho_3}} + \frac{3}{5} \frac{1}{M_{\rho_0}} \right) v_0^2 h_1^i h_1^j. \quad (6.65)$$

Here we face again the same problem we had when adding a single copy of a singlet or triplet $SU(2)_L$ fermion representations for generating neutrino masses: the rank of the matrix in Eq. 6.65, which is 1, is not enough to generate two non-degenerate neutrino masses as needed. This problem can be fixed in a renormalizable way by adding extra representations that contribute to the neutrino mass matrix in an independent way. However, since those are needed anyway for solving problem (i), this issue can be trivially solved, as we will see in the next section.

6.2.4 Colored seesaw

Notice that, in this case, the Manohar-Wise field $\Phi_1 \sim (8, 2, 1/2)$ needed to participate in the 1-loop graphically presented in Diag. 1.37 from Chapter 1 can be found in 45_H , which also helps to correct the charged fermion masses -problem (i)- and to achieve realistic low scale gauge couplings -problem (ii)-. Together with Φ_1 , we would need a color fermion octet $\rho_8 \sim (8, 1, 0)$ to close the loop; particularly two copies of it in order to predict realistic neutrino masses since, as discussed in Chapter 1, in the presence of a single copy the mass matrix for neutrinos has rank 1.⁸ Notice that, looking at Eq. 6.61, ρ_8 is part of the 24 fermionic representation, which preserves anomaly cancellation (adjoint representation). In the diagram below we show the implementation of this mechanism in $SU(5)$:



⁸In the same manner, one could duplicate the $\Phi_1 \subset 45_H$ instead.

Considering a 45_H together with a 24, we can write down the following terms from the $SU(5)$ Lagrangian,

$$\begin{aligned}
 -\mathcal{L}_{\text{colored}} \supset & Y_\nu \bar{5} 24 45_H + M_{24} \text{Tr}\{24^2\} \\
 & + 45_H 45_H (\lambda_1 5_H^* 5_H^* + \lambda_2 5_H^* 45_H^* + \lambda_3 45_H^* 45_H^*) + \text{h.c.},
 \end{aligned} \tag{6.67}$$

which after the $SU(5)$ breaking lead to a Lagrangian in the form of the relevant interactions for the colored seesaw mechanism described in Eq. 1.36. Therefore, the neutrino mass matrix is given by Eq. 1.38 in the broken phase, where two copies of the adjoint 24 have to be considered to break the degeneracy (or either two copies of 45_H).

6.2.5 Zee mechanism

In Chapter 1, we showed that the implementation of the Zee mechanism requires the participation of a singlet charged scalar running inside the loop as in Diag. 1.31. We remark that, in order to generate Majorana neutrino masses, the lepton number must be violated in the theory. We realized that in $SU(5)$ this mechanism can be implemented by adding the antisymmetric 10_H representation as Diag. 6.68 shows:

$$\tag{6.68}$$

Such representation decomposes in

$$10_H = \underbrace{(1, 1, 1)}_{\delta^+} \oplus \underbrace{(3, 2, 1/6)}_{\delta_{(3,2)}} \oplus \underbrace{(\bar{3}, 1, -2/3)}_{\delta_T}, \tag{6.69}$$

and contains the required charged scalar δ^+ to implement the Zee mechanism. As discussed in Chapter 1, an extra Higgs doublet is needed to break the degeneracy in the neutrino mass matrix. This can be solved either by adding a $5'_H$ or a 45_H . The relevant

interactions at the level of $SU(5)$ read as,

$$\begin{aligned}
 -\mathcal{L}_{\text{Zee}} \supset & \lambda \bar{5} \bar{5} 10_H + \bar{5} (Y_1^* 5_H^* + Y_2^* 45_H^*) 10 \\
 & - \frac{1}{6} \mu 5_H 45_H 10_H^* + \lambda_{24} 5_H 45_H 24_H 10_H^* + \text{h.c.}
 \end{aligned} \tag{6.70}$$

where we have chosen the 45_H to include the second Higgs doublet for convenience (see next section). Once $SU(5)$ is spontaneously broken, the above Lagrangian leads to the interactions in Eq. 1.32.⁹ Finally, the neutrino mass matrix is given by Eq. 1.35.

6.3 Minimal realistic $SU(5)$ theories

In the previous section we have learnt that extra representations should be added to solve the three strikes that rule out $SU(5)_{\text{GG}}$. Now, one could ask: *What is the simplest realistic renormalizable model based on $SU(5)$?*

Starting from problem (i), we mentioned that at the renormalizable level there are two possibilities to generate the correct masses for the charged fermions at the low scale. For each of them, we propose a simple and realistic $SU(5)$ extension.

6.3.1 The Zee- $SU(5)$

In order to render $SU(5)_{\text{GG}}$ realistic, let us add to its particle content a 45_H representation, which contains the following fields:

$$\begin{aligned}
 45_H \sim & \underbrace{(8, 2, 1/2)}_{\Phi_1} \oplus \underbrace{(\bar{6}, 1, -1/3)}_{\Phi_2} \oplus \underbrace{(3, 3, -1/3)}_{\Phi_3} \oplus \underbrace{(\bar{3}, 2, -7/6)}_{\Phi_4} \\
 & \oplus \underbrace{(3, 1, -1/3)}_{\Phi_5} \oplus \underbrace{(\bar{3}, 1, 4/3)}_{\Phi_6} \oplus \underbrace{(1, 2, 1/2)}_{H_2},
 \end{aligned}$$

among which there is a second Higgs doublet, H_2 , that contributes to the fermion masses when it gets a vev . The Yukawa Lagrangian is modified in the presence of the

⁹If there is no discrete symmetry $24_H \rightarrow -24_H$ forbidding the last term in Eq. 6.70, as shown in red in Diag. 6.68, the dimensionful μ parameter from Eq. 1.32 will get an extra contribution proportional to $\lambda_{24} v_\Sigma$.

45_H and reads as,

$$- \mathcal{L}_Y \supset 10 (Y_3 5_H + Y_4 45_H) 10 + \bar{5} (Y_1 5_H^* + Y_2 45_H^*) 10 + \text{h.c.} \quad (6.71)$$

Because of its tensor structure, the 45_H splits the charged lepton and down quark masses once it gets a vev , $\langle 45_H \rangle_1^{15} = \langle 45_H \rangle_2^{25} = \langle 45_H \rangle_3^{35} = v_{45}/\sqrt{2}$ and $\langle 45_H \rangle_4^{45} = -3v_{45}/\sqrt{2}$, in the following way,

$$\begin{aligned} M_u &= \frac{1}{\sqrt{2}} (2 (Y_3 + Y_3^T) v_5 - 4 (Y_4 - Y_4^T) v_{45}), \\ M_e &= \frac{1}{2} (Y_1^T v_5^* - 6Y_2^T v_{45}^*), \\ M_d &= \frac{1}{2} (Y_1 v_5^* + 2Y_2 v_{45}^*), \end{aligned} \quad (6.72)$$

where $\sqrt{v_5^2 + v_{45}^2} = v_0 = 246$ GeV. The above mass matrices enjoy enough freedom to reproduce the correct fermion masses at the low scale. Therefore, with the 45_H , problem (i) is already solved in a renormalizable way.

Regarding problem (ii), let us see what the situation is for the $SU(5)_{GG} + 45_H$. In Table 6.2 we show the B_{ij} coefficients (see Eq. 6.21) for the fields in the 45_H representation.

45_H							
B_{ij}	Φ_1	Φ_2	Φ_3	Φ_4	Φ_5	Φ_6	H_2
B_{12}	$-\frac{8}{15}r_{\Phi_1}$	$\frac{2}{15}r_{\Phi_2}$	$-\frac{9}{5}r_{\Phi_3}$	$\frac{17}{15}r_{\Phi_4}$	$\frac{1}{15}r_{\Phi_5}$	$\frac{16}{15}r_{\Phi_6}$	$-\frac{1}{15}r_{H_2}$
B_{23}	$-\frac{2}{3}r_{\Phi_1}$	$-\frac{5}{6}r_{\Phi_2}$	$\frac{3}{2}r_{\Phi_3}$	$\frac{1}{6}r_{\Phi_4}$	$-\frac{1}{6}r_{\Phi_5}$	$-\frac{1}{6}r_{\Phi_6}$	$\frac{1}{6}r_{H_2}$

Table 6.2: B_{ij} coefficients of the fields in the 45_H . *Table adapted from Ref. [283].*

In the above table we framed in red those scalar LQs participating in the decay of the proton. Note that in the 5_H there is also the colored triplet mediating $\Delta B = 1$ interactions (see Table 6.1). For the scalar LQs, their contribution to proton decay is proportional to a combination of the Yukawa couplings in Eq. 6.71. For instance, the LQ $\Phi_3 \sim (3, 3, -1/3)$ mediates proton decay according to the following effective

dimension-6 interactions that arise after integrating it out,

$$\mathcal{L}_{\text{eff}}^{\Phi_3} \supset \frac{1}{M_{\Phi_3}^2} (\ell_L^T C i\sigma_2 Y_2 q_L) (q_L^T C (Y_4 - Y_4^T) q_L) + \text{h.c.} \quad (6.73)$$

Naively, its contribution to the proton decay width into a neutral pion and a positron is given by

$$\Gamma_p^{\Phi_3} \sim Y_2^2 (Y_4 - Y_4^T)^2 \frac{\Lambda_{\text{QCD}}^5}{M_{\Phi_3}^4}, \quad (6.74)$$

where one can see that either Φ_3 is heavy or the combination of coefficients entering in Eq. 6.74 is suppressed. In our case, as Fig. 6.3 shows, in order to satisfy the unification constraints $M_{\Phi_3} \sim \mathcal{O}(10^8)$ GeVs, so that we need a huge suppression in the above expression to be consistent with proton decay bounds. From Eq. 6.72 one can see that there is enough freedom to be consistent with both proton decay and unification constraints: note that, whereas Y_1 and Y_2 are not constrained since both contributions are needed in order to correct the charged leptons and down quarks mass relations, in M_u one could assume a tiny Y_4 while being consistent with the up quark masses. The later basically implies that

$$M_u \sim 2 \underbrace{(Y_3 + Y_3^T)}_{Y_U} v_5 / \sqrt{2}, \quad (6.75)$$

i.e. the mass matrix for the up quarks should be symmetric as in the original $SU(5)_{\text{GG}}$.

The only field in 24_H which can help for the unification is $\Sigma_3 \sim (1, 3, 0)$, as Table 6.1 shows. As we have seen in Sec. 6.1, even if Σ_3 and H_1 are at the EW scale the constraints in Eqs. 6.19 and 6.20 cannot be satisfied because $B_{23}^{GG}/B_{12}^{GG} \leq 0.6$. Since only the fields with negative contribution to B_{12} and positive contribution to B_{23} can help to achieve unification in agreement with the experiment, the two candidates for helping in the 45_H will be Φ_3 and H_2 . The field Φ_1 helps indirectly by also allowing to increase the GUT scale and consequently suppressing the decay of the proton. In Table 6.2 we have shaded in green the fields from the 45_H that help, and in red those that do not.

In the 5_H , the triplet can also mediate proton decay, but if we assume that Y_4 is small, we cannot skip the proton decay bound this time since

$$\Gamma_p^T \sim Y_1^2 Y_3^2 \frac{m_p^5}{M_T^4}, \quad (6.76)$$

and hence, $M_T \gtrsim 10^{12}$ GeV, and one has the usual doublet-triplet splitting problem in the splitting of the 5_H representation. Now, in the 45_H one has the same fine-tuning problem because the second Higgs H_2 must be light in order to have a large vacuum expectation value needed to correct the fermion masses. As we show in the third panel from Fig. 6.3, with the splitting of the 45_H is enough to satisfy the unification conditions so that we will assume that there is no mass splitting in 24_H , i.e. we will show the unification constraints in the scenarios where less fine-tuning is needed.

As we discussed in Sec. 6.1.2, the dominant contribution to proton decay will come from the vector LQs V_2^μ living in V_{24}^μ . For the strongest bounded channel, $p \rightarrow \pi^0 e^+$, we will assume the most conservative scenario $V_e \sim \sqrt{5}$ (see Eq. 6.46) and for the second most constrained channel, $p \rightarrow K^+ \bar{\nu}$, we will assume that M_u is symmetric (see Eq. 6.75). We show in the left panel from Fig. 6.3 the conservative values for the proton decay lifetime and the experimental bounds at the time of publishing our work, $\tau_p(p \rightarrow \pi^0 e^+) > 1.29 \times 10^{34}$ years [284] from the SK collaboration and the projected bound from the HK experiment as a function of the Manohar-Wise field mass M_{Φ_1} . We have updated the figure by including the preliminary result from the SK collaboration $\tau_p(p \rightarrow \pi^0 e^+) > 2.4 \times 10^{34}$ years [274]. In this way we show that the unification can be realized in agreement with the bounds on the proton decay lifetimes and the fact that the predictions are not far from the reach of the HK experiment, one could hope to test this model in the near future.

In the right panel from Fig. 6.3, assuming unification of the gauge couplings at the one-loop level, we show the allowed values for the masses of the $\Phi_1 \sim (8, 2, 1/2)$ and the unification scale. In this case, we assume that $M_{H_2} = 1$ TeV and the mass of $\Phi_3 \sim (3, 3, -1/3)$ changes from $10^{8.6}$ to $10^{8.9}$ GeV. The green vertical dashed line represents $M_{\Phi_1} \geq 1$ TeV, given by the recent study from Ref. [286], where the authors study from an EFT perspective the possibility to have a light Φ_1 in agreement with all current experimental data. As one can appreciate, the main prediction from the

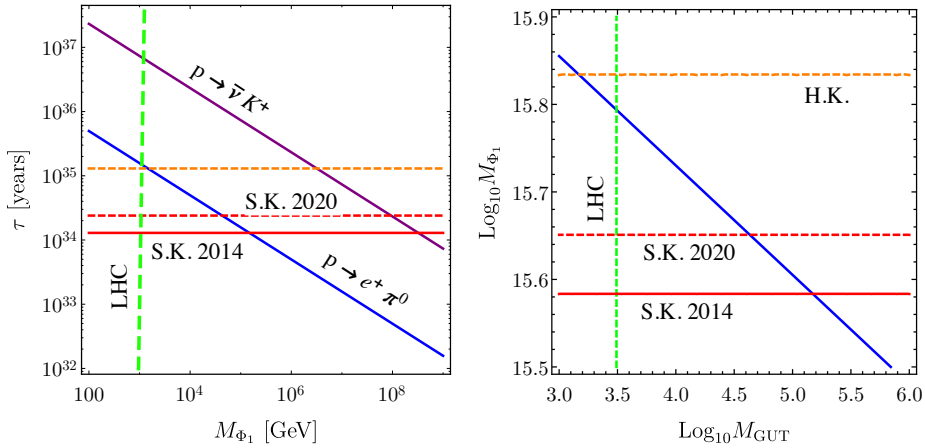


Figure 6.3: On the left panel, predictions for the proton decay lifetimes. The blue line shows the predictions for the decay $p \rightarrow \pi^0 e^+$, while the purple line shows the predictions for the decay $p \rightarrow K^+ \bar{\nu}$. On the right panel, dependence of the scale M_{Φ_1} with M_{GUT} dictated by the unification constrains (blue line). The mass of the Φ_3 (implicit) is in the range $10^{8.6} - 10^{8.9}$ GeV from left to right. In both panels, the horizontal red dashed line shows the current experimental value on proton decay lifetime, $\tau_p(p \rightarrow \pi^0 e^+) > 1.29 \times 10^{34}$ years [284] from the SK collaboration. The orange dashed line shows the projected limit on the proton decay lifetime from the HK collaboration, $\tau_p(p \rightarrow \pi^0 e^+) > 1.3 \times 10^{35}$ years [285]. The green vertical line represents the LHC bound, $M_{\Phi_1} \geq 1$ TeV [286,287], on the colored octet mass. We have assumed $M_{H_2} = 1$ TeV. *Image updated with respect to Ref. [283] with the preliminary bound $\tau_p(p \rightarrow \pi^0 e^+) > 2.4 \times 10^{34}$ years [274].*

unification of the gauge interactions is that the field Φ_1 has to be light and that the model could be tested in the near future in proton decay experiments. In the case when the mass of Φ_1 is close to the TeV scale one could hope to produce it at the LHC. The Yukawa interactions for the field Φ_1 are given by

$$-\mathcal{L}_Y \supset 2(d^c)_L^T C Y_2 \Phi_1^\dagger q_L + 4 q_L^T C (Y_4 - Y_4^T) i \sigma_2 \Phi_1 (u^c)_L + \text{h.c.} \quad (6.77)$$

Notice that one can produce Φ_1 with large cross sections through QCD interactions. The second term in the above equation comes from the interaction $10 \ 10 \ 45_H$. We note that, since the second coupling above is antisymmetric, the decays into two top-quarks

would not be observed. Therefore, one can have exotic signatures such as signals with one top quark and three light jets. We refer the reader to Refs. [288–305] for a study on the phenomenological aspects of the colored octets.

Let us address now problem (iii): neutrino masses. Taking into account the mechanisms introduced in Sec. 6.2, we can classify the different scenarios regarding the number of representations / d.o.f. that we should consider in order to render the GUT realistic without giving up on renormalizability. See Table 6.3 for such classification. The scenarios discussed in Section 6.2 and classified in Table 6.3 can be used as a guide

$Y_e \neq Y_d^T$	$m_\nu \neq 0$	Unification	Extra field content	number of new d.o.f.
45_H	Type-I seesaw	✓	$1(\times 2)$	47
	Type-II seesaw	✓	15_H	60
	Type-III seesaw	✓	24	69
	Zee model	✓	10_H	55
	Colored seesaw	✓	$24(\times 2)$	93

Table 6.3: Possible renormalizable extensions of $SU(5)_{GG}$. By “extra field content” is understood any extra representation apart from the field content of $SU(5)_{GG} + 45_H$.

to define the simplest realistic model. In the Type II- $SU(5)$ case, one has two extra Higgses, 15_H and 45_H [306], or in the Type III- $SU(5)$ scenario, one has 45_H and one extra fermionic 24 representation [281, 307]. We note that, in the later case, there is no need to consider an extra 24 since the 45_H breaks the degeneracy of the neutrino mass matrix. We will explore this scenario in more detail in Chapter 7. Alternatively, the neutrino masses could be generated through Type I seesaw and one would have at least two extra singlets, RH neutrinos, and the extra Higgs 45_H . This scenario can be realistic [308] but one expects naively that the fermionic singlets get mass from above the GUT scale since their masses are not protected by the $SU(5)$ gauge symmetry. We will focus on the second simplest option, highlighted in green, which only requires the addition of the 10_H to the $SU(5)_{GG} + 45_H$. In this way, we show the implementation of the Zee mechanism in a realistic $SU(5)$ GUT.

The 10_H (see Eq. 6.69) contains the field needed for the Zee mechanism, and the only field in there that could help to *achieve unification* is $\delta_{(3,2)} \sim (3, 2, 1/6)$, but it mediates proton decay. Sticking to the less possible fine tuning, we will also assume

there is no mass splitting in the 10_H . Notice that here the 45_H representation plays a threefold role: it corrects the charged lepton and down quark mass relations, brings enough freedom to achieve the proper values of the gauge couplings at the low scale, and allows for a realistic neutrino mass generation via the Zee mechanism.

In Sec. 6.2, we discussed that the mass matrix for the neutrinos in this context is given by Eq. 1.35. One can see from Eq. 6.72 that, since Y_1 and Y_2 cannot be diagonalized simultaneously, the diagonal elements of the neutrino mass matrix are not zero even if λ is antisymmetric. Therefore, the model has enough freedom to be consistent with the experimental values for neutrino masses and mixings. Using the relation between the charged fermion masses and the Yukawa couplings from Eq. 6.72, the neutrino mass matrix from Eq. 1.35 can be written as

$$M_\nu = \lambda M_e \left(c_e M_e^\dagger + 3c_d M_d^* \right) + \left(c_e M_e^* + 3c_d M_d^\dagger \right) M_e^T \lambda^T, \quad (6.78)$$

where the coefficients c_e and c_d , extracted from the loop calculation, are defined as

$$c_e = \frac{(1 - 4 \sin^2 \beta)}{8\pi^2 \sqrt{2} v \sin \beta} \sin 2\theta_+ \ln \left(\frac{m_{h_2^+}^2}{m_{h_1^+}^2} \right), \quad c_d = \frac{\sin 2\theta_+}{8\pi^2 \sqrt{2} v \sin 2\beta} \ln \left(\frac{m_{h_2^+}^2}{m_{h_1^+}^2} \right). \quad (6.79)$$

The relation in Eq. 6.78 is quite interesting because in $SU(5)$ a relation between the neutrino masses and the charged fermion masses is not expected. Notice that the anti-symmetric matrix λ defines this relation and it has only three free parameters. Working in the basis where M_e and M_u are diagonal, using $M_d = D_c^* M_d^{\text{diag}} V_{\text{CKM}}^\dagger$, and neglecting all phases for simplicity, one finds

$$M_\nu = \lambda M_e^{\text{diag}} \left(c_e M_e^{\text{diag}} + 3c_d D_c M_d^{\text{diag}} V_{\text{CKM}}^T \right) + \left(c_e M_e^{\text{diag}} + 3c_d V_{\text{CKM}} M_d^{\text{diag}} D_c^T \right) M_e^{\text{diag}} \lambda^T. \quad (6.80)$$

Here, D_c is the matrix which rotates the d^c quarks (see Eq. 6.36), which has only three parameters in the real case. As one can see the above matrix has enough parameters to reproduce the values for the fermion mixing angles and masses. Notice that, in this model, the ratio between the fermion masses cannot be predicted but one can have a

simple relation between them which can be constrained using the experimental values for fermion masses and mixings.

6.3.2 $SU(5)$ with minimal scalars

In the last subsection, the problem of wrong charged mass relations arising from the $M_E^T = M_D$ prediction has been solved by extending the Higgs sector of the $SU(5)_{\text{GG}}$ with a 45_H representation. However, as mentioned in the introduction of this chapter, such mass relation can also be corrected by adding new vector-like fermions instead. If we stick to the renormalizable level, this possibility is the simplest regarding the amount of new d.o.f. involved. *Can we achieve a realistic GUT based on $SU(5)$ without extending the minimal Higgs sector required by the $SU(5)$ breaking?*

Let us add, in the spirit of the SM, three copies of vector-like fermions in the fundamental and anti-fundamental representations of $SU(5)$. The matter content of this GUT is therefore composed of ¹⁰

$$\bar{5} = \begin{pmatrix} d^c \\ \ell \end{pmatrix}, \quad 10 = \begin{pmatrix} u^c & Q \\ Q & e^c \end{pmatrix}, \quad \bar{5}' = \begin{pmatrix} D^c \\ L \end{pmatrix}, \quad \text{and} \quad 5' = \begin{pmatrix} D \\ L^c \end{pmatrix}. \quad (6.81)$$

These new fermions acquire mass from the following terms in the Lagrangian,

$$- \mathcal{L}_5 \supset M_5 \bar{5}' 5' + \lambda_5 \bar{5}' 24_H 5' + \text{h.c.}, \quad (6.82)$$

which generate the following new fermion masses:

$$M_D = M_5 + \tilde{\lambda}_5 \frac{M_{\text{GUT}}}{\sqrt{\alpha_{\text{GUT}}}}, \quad \text{and} \quad M_L^T = M_5 - \frac{3}{2} \tilde{\lambda}_5 \frac{M_{\text{GUT}}}{\sqrt{\alpha_{\text{GUT}}}},$$

where $\tilde{\lambda}_5 = \lambda_5 / \sqrt{25\pi}$.

Apart from generating the required splitting among the charged leptons and down-type quarks masses, the requirement of the realistic gauge couplings at the low scale still needs to be fulfilled. With three copies in the $5'$ and $\bar{5}'$ is unfortunately not enough, since the impact of these representations in the RGE equations is pretty weak

¹⁰In the following, we assume that all fermions are LH, so that we will not write explicitly their chirality.

(see Table 6.1). Furthermore, neutrinos are still massless in this context. Both problems (ii) and (iii) can be solved by adding the 24 representation (see Eq. 6.62). The relevant terms for the masses of their fields are listed below,

$$-\mathcal{L}_{24} \supset M_{24} \text{Tr}\{24^2\} + \lambda \text{Tr}\{24^2 24_H\} + \text{h.c.}, \quad (6.83)$$

and, after the grand unified symmetry is broken, the mass terms for the fields in the 24 are given by

$$\begin{aligned} -\mathcal{L}_{24} \supset M_{24} \left(\text{Tr}\{\rho_8 \rho_8\} + \text{Tr}\{\rho_3 \rho_3\} + 2\text{Tr}\{\rho_{(\bar{3},2)} \rho_{(3,2)}\} + \frac{1}{2} \rho_0 \rho_0 \right) \\ + v_\Sigma \frac{\lambda}{\sqrt{15}} \left(\text{Tr}\{\rho_8 \rho_8\} - \frac{1}{2} \text{Tr}\{\rho_{(\bar{3},2)} \rho_{(3,2)}\} + \frac{3}{15} \rho_0 \rho_0 - \frac{3}{2} \text{Tr}\{\rho_3 \rho_3\} - 3 \left(\frac{9}{4}\right) \left(\frac{1}{15}\right) \rho \rho \right) + \text{h.c.}, \end{aligned} \quad (6.84)$$

(remember that we are using the simplified notation $\Psi\Psi \equiv \Psi^T C \Psi$ for Yukawa interactions). From the above expression one can read the following masses:

$$\begin{aligned} M_{\rho_8} &= M_{24} + \tilde{\lambda} \frac{M_{\text{GUT}}}{\sqrt{\alpha_{\text{GUT}}}}, & M_{\rho_3} &= M_{24} - \frac{3}{2} \tilde{\lambda} \frac{M_{\text{GUT}}}{\sqrt{\alpha_{\text{GUT}}}}, \\ M_{\rho_{(3,2)}} &= M_{24} - \frac{1}{4} \tilde{\lambda} \frac{M_{\text{GUT}}}{\sqrt{\alpha_{\text{GUT}}}}, & M_{\rho_0} &= M_{24} - \frac{1}{2} \tilde{\lambda} \frac{M_{\text{GUT}}}{\sqrt{\alpha_{\text{GUT}}}}, \end{aligned}$$

where $\tilde{\lambda} = \lambda/\sqrt{25\pi}$ and $M_{\text{GUT}} = \sqrt{5\pi\alpha_{\text{GUT}}/3} v_{24}$. Defining $\hat{m}_{24} = M_{\rho_8}/M_{\rho_3}$, we note the masses in the 24 can be defined as a function of M_{ρ_3} :

$$M_{\rho_8} = \hat{m}_{24} M_{\rho_3}, \quad M_{\rho_0} = \frac{1}{5} (3 + 2 \hat{m}_{24}) M_{\rho_3}, \quad M_{\rho_{(3,2)}} = M_{\rho_{(\bar{3},2)}} = \frac{1}{2} (1 + \hat{m}_{24}) M_{\rho_3},$$

and, in the same spirit as the splitting of the 24, we will write the masses of the new fermions in the $5'$ and $\bar{5}'$ as a function of their splitting

$$M_D = \hat{m}_5 M_L,$$

since this will be useful to later discuss the gauge coupling unification. The masses of the SM fermions are given by the following terms,

$$\begin{aligned}
-\mathcal{L}_f \supset & y_0^i \bar{5}_i 24 5_H + y_1^i \bar{5}'_i 24 5_H + y_2^i 5_H^* 24 5'_i + Y_1 5_H^* \bar{5} 10 \\
& + Y_2 5_H^* \bar{5}' 10 + Y_u 10 10 5_H + M_{\bar{5}5} \bar{5} 5' + \lambda_{\bar{5}5} \bar{5} 24_H 5' + \text{h.c.},
\end{aligned} \tag{6.85}$$

whose relevant interactions for achieving a consistent relation between the masses for charged leptons and down quarks are given by

$$\begin{aligned}
-\mathcal{L} \supset & EM_L E^c + D^c M_D D + M_{\rho_3} \rho_3^+ \rho_3^- + d^c \left(M_{\bar{5}5} + \tilde{\lambda}_{\bar{5}5} \frac{M_{\text{GUT}}}{\sqrt{\alpha_{\text{GUT}}}} \right) D \\
& + e \left(M_{\bar{5}5} - \frac{3}{2} \tilde{\lambda}_{\bar{5}5} \frac{M_{\text{GUT}}}{\sqrt{\alpha_{\text{GUT}}}} \right) E^c + \frac{v_5}{\sqrt{2}} (e Y_1 e^c + d^c Y_1 d + D^c Y_2 d + E Y_2 e^c) \\
& + \frac{v_5}{2} (y_0^i e_i \rho_3^+ + y_1^i E_i \rho_3^+ + y_2^i \rho_3^- E_i^c),
\end{aligned} \tag{6.86}$$

where $\tilde{\lambda}_{\bar{5}5} = \lambda_{\bar{5}5} / \sqrt{15\pi}$. We find the following mass matrix for the down-type quarks:

$$-\mathcal{L} \supset \begin{pmatrix} d^c & D^c \end{pmatrix} \begin{pmatrix} Y_1 \frac{v_5}{\sqrt{2}} & M_{\bar{5}5} + \tilde{\lambda}_{\bar{5}5} \frac{M_{\text{GUT}}}{\sqrt{\alpha_{\text{GUT}}}} \\ Y_2 \frac{v_5}{\sqrt{2}} & M_D \end{pmatrix} \begin{pmatrix} d \\ D \end{pmatrix}, \tag{6.87}$$

where the mixing proportional to $d^c \rho_{(3,2)}$ and $D^c \rho_{(3,2)}$ have been neglected since they enter in the light neutrino mass matrix. In the case of the charged leptons, their mass matrix is given by:

$$-\mathcal{L} \supset \begin{pmatrix} e^c & E^c & \rho_3^+ \end{pmatrix} \begin{pmatrix} Y_1^T \frac{v_5}{\sqrt{2}} & Y_2^T \frac{v_5}{\sqrt{2}} & 0 \\ M_{\bar{5}5}^T - \frac{3}{2} \tilde{\lambda}_{\bar{5}5}^T \frac{M_{\text{GUT}}}{\sqrt{\alpha_{\text{GUT}}}} & M_L^T & \frac{1}{2} y_2 v_5 \\ \frac{1}{2} y_0 v_5 & \frac{1}{2} y_1 v_5 & M_{\rho_3} \end{pmatrix} \begin{pmatrix} e \\ E \\ \rho_3^- \end{pmatrix}. \tag{6.88}$$

The above expressions show that there is enough freedom to have a consistent relation between the masses of the charged leptons and down quarks. We refer the reader to Ref. [309] for a detailed study on the role of $5'$ and $\bar{5}'$ representations in the achievement

of realistic charged fermion masses at the low scale. Therefore, in the context of this theory, problem (i) is already solved.

Regarding (ii), let us study what is the role of the new fermions in the RGEs. The contribution of the new fields to the β -functions is listed in Table 6.4. As it has been

	$\bar{5}' + 5'$		24		
	$L + L^c$	$D + D^c$	ρ_3	ρ_8	$\rho_{(3,2)} + \rho_{(\bar{3},2)}$
B_1	$\frac{6}{5} r_L$	$\frac{4}{5} r_D$	0	0	$\frac{10}{3} r_{32}$
B_2	$2 r_L$	0	$\frac{4}{3} r_3$	0	$2 r_{32}$
B_3	0	$2 r_D$	0	$2 r_8$	$\frac{4}{3} r_{32}$
B_{12}	$-\frac{4}{5} r_L$	$\frac{4}{5} r_D$	$-\frac{4}{3} r_3$	0	$\frac{4}{3} r_{32}$
B_{23}	$2 r_L$	$-2 r_D$	$\frac{4}{3} r_3$	$-2 r_8$	$\frac{2}{3} r_{32}$

Table 6.4: B_{ij} coefficients of the new fields from $SU(5)$ with minimal scalars with respect to $SU(5)_{\text{GG}}$. *Table adapted from Ref. [269].*

previously discussed, the conditions from Eqs. 6.19 and 6.20 must be satisfied in order to reproduce the values of the gauge couplings experimentally measured at the low scale. In the context of this theory, the B_{ij} coefficients, $B_{ij} = B_i - B_j$, entering in the later conditions read as

$$B_{12} = B_{12}^{\text{SM}} - \frac{4}{5} r_5 - \frac{4}{3} r_3 - \frac{1}{3} r_{\Sigma_3} + \frac{4}{3} r_{32}, \quad (6.89)$$

$$B_{23} = B_{23}^{\text{SM}} + 2 r_5 + \frac{4}{3} r_3 + \frac{1}{3} r_{\Sigma_3} - 2 r_8 - \frac{1}{2} r_{\Sigma_8} + \frac{2}{3} r_{32}, \quad (6.90)$$

where $B_{12}^{\text{SM}} = 109/15$, $B_{23}^{\text{SM}} = 23/6$ and $r_5 = r_L - r_D$. We assume that the colored triplet in the 5_H lives at the high scale because it mediates proton decay. We note that r_5 is only a function of the mass splitting \hat{m}_5 , i.e. $r_5 = \ln \hat{m}_5 / (\ln M_{\text{GUT}} - \ln M_Z)$. Since unification is only sensitive to the splitting in mass of the representations, we can eliminate the overall scales and write the above equations in a simple way:

$$B_{12} = B_{12}^{\text{SM}} - \frac{4}{5} r_5 - \frac{1}{3} r_{\Sigma_3} - \frac{4}{3} \frac{\ln\left(\frac{1}{2}(1 + \hat{m}_{24})\right)}{\ln(M_{\text{GUT}}) - \ln(M_Z)},$$

$$B_{23} = B_{23}^{\text{SM}} + 2r_5 + \frac{1}{3}r_{\Sigma_3} + 2\frac{\ln(\hat{m}_{24})}{\ln(M_{\text{GUT}}) - \ln(M_Z)} - \frac{1}{2}r_{\Sigma_8} - \frac{2}{3}\frac{\ln\left(\frac{1}{2}(1 + \hat{m}_{24})\right)}{\ln(M_{\text{GUT}}) - \ln(M_Z)}.$$

Therefore, the relevant parameters for unification are: M_{GUT} , r_{Σ_3} , r_{Σ_8} , \hat{m}_5 and \hat{m}_{24} . In Fig. 6.4 we show in the plane $\text{Log}_{10}M_{\text{GUT}} - \text{Log}_{10}\hat{m}_{24}$ the parameter space where unification takes place, or strictly speaking, where the measured values for the gauge couplings are achieved at the low scale. In the upper panel, we fix $r_{\Sigma_8} = 1$, i.e. we assume the extreme case where the colored octet fermion is at the EW scale, and the mass of the triplet Σ_3 is varied along all its possible mass range. In the bottom panel, we show the other extreme case where Σ_8 is assumed to be at the GUT scale. By showing these two drastic scenarios composing the edges in between the Σ_8 mass can vary, the reader may get an idea about any possible scenario in this theory.

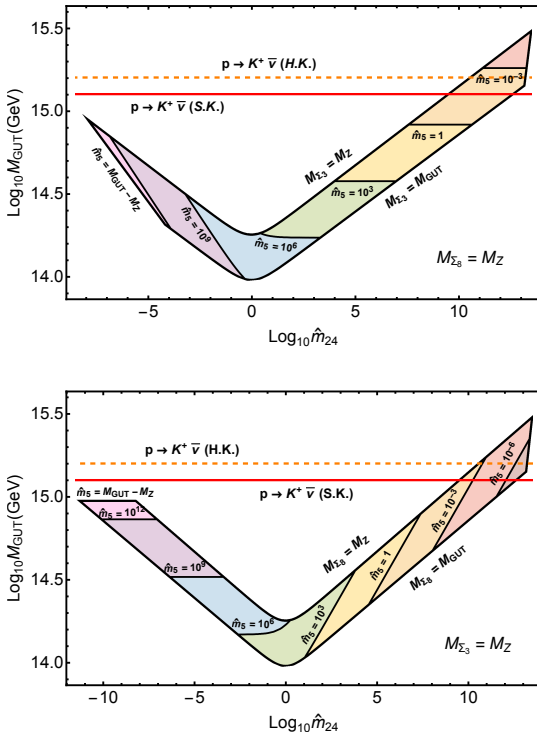


Figure 6.4: Allowed parameter space by the unification of gauge couplings in the plane $\text{Log}_{10}M_{\text{GUT}} - \text{Log}_{10}\hat{m}_{24}$. Every point in the colored area corresponds to a scenario where the gauge couplings unify at the high scale. In the upper panel we show the constraints on the mass spectrum when $M_{\Sigma_8} = M_Z$ changing the mass of Σ_3 between the EW and the GUT scales. In the lower panel we show the same constraints but in the case when $M_{\Sigma_3} = M_Z$, changing the mass of Σ_8 . The red horizontal line corresponds to the current bound on the proton decay lifetime for the channel $p \rightarrow K^+ \bar{\nu}$ [271], while the orange dashed line corresponds to the projected bound from the HK collaboration [273]. *Figure extracted from Ref. [269].*

In Fig. 6.4, the parameter space located above the solid red and dashed orange horizontal lines is excluded because of proton decay constraints. As mentioned in Sec. 6.1.2, the most relevant decay widths for the decay of the proton are the decay channels into charged leptons and antineutrinos, which are given by Eqs. 6.43, 6.44 and 6.45. In there we showed that, as in the previous theory, there is an ambiguity in the prediction of the proton lifetime since the decay width channels depend on some combination of flavour matrices that are, in general, unknown. Particularly, this is the case for the channel $p \rightarrow \pi^0 e^+$, which depends on V_e as Eq. 6.43 shows. To illustrate its effect, we plot in Fig. 6.5 the numerical predictions for some possible values of this matrix, $V_e = 0.1, 0.3$, and 1. As this figure shows, it is not possible to extract a bound

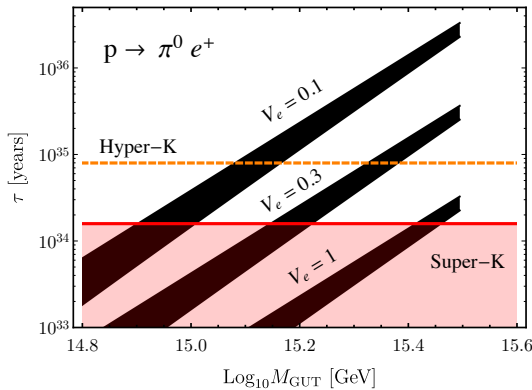


Figure 6.5: Predictions for the proton decay lifetime for the channel $p \rightarrow e^+ \pi^0$ using three different values for the unknown mixing $V_e = V_2^{11} = V_3^{11}$. The red line shows the current proton decay lifetime, i.e. $\tau(p \rightarrow \pi^0 e^+) > 1.6 \times 10^{34}$ years [158]. The orange dashed line shows the projected bound on proton decay lifetime from the HK collaboration, i.e. $\tau(p \rightarrow \pi^0 e^+) > 8 \times 10^{34}$ years [273]. *Figure extracted from Ref. [269].*

from this channel unless some value for V_e is assumed. The width of the band in the above figure represents the possible values that α_{GUT} can acquire given a certain value for M_{GUT} . The later depends on the freedom in the absolute mass scales M_L and M_{ρ_3} from the $5'$ and 24 representations, respectively, to which the unification constraints are not sensitive and, therefore, they can freely vary. In Fig. 6.6 we show this freedom in the GUT coupling as a function of the GUT scale for a given value of the free absolute scales M_{ρ_3} and M_L .

Nevertheless, in the context of this theory, the fact that the up-type quark mass matrix is symmetric, as one can read from Eq. 6.85, allows for a clean prediction of

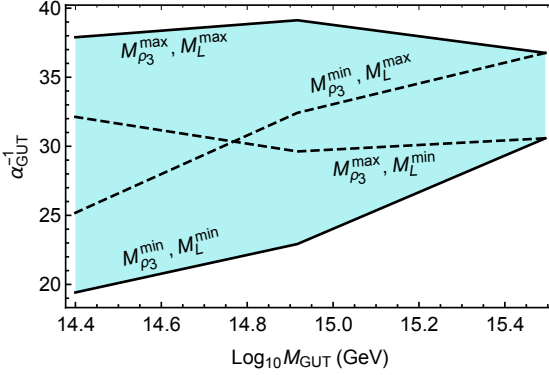


Figure 6.6: Allowed values for the gauge couplings at the GUT scale in agreement with unification for the most interesting scenarios which can be allowed by proton decay. *Figure extracted from Ref. [269].*

the proton decay width for the decay channels into antineutrinos [275], as well as the original $SU(5)_{GG}$ (see discussion in Sec. 6.1.2).

The prediction for the decay width of the proton into antineutrinos is shown in Fig. 6.7. In the left panel we show the prediction for $p \rightarrow K^+ \bar{\nu}$, which enjoys the second strongest bound on the decay of the proton, given by the SK experiment, $\tau(p \rightarrow K^+ \bar{\nu}) > 5.9 \times 10^{33}$ years [271]. The right panel shows the prediction for the $p \rightarrow \pi^+ \bar{\nu}$. As before, the band in these figures represents the possible range of variation of α_{GUT} for a given M_{GUT} . The "cut" on the RHS of the life-time predictions comes from the upper bound on the GUT scale given by the unification conditions, $M_{GUT} \leq 10^{15.5}$ GeV (see Fig. 6.4). We emphasize that, in contrast to other GUT theories where the correction of the fermion mass relations sacrifices the prediction $Y_U = Y_U^T$, we find clean channels which do not depend on any unknown mixing matrix. This allowed us to set an upper bound on the proton decay lifetime, particularly $\tau(p \rightarrow K^+ \bar{\nu}) \lesssim 3.4 \times 10^{35}$ years and $\tau(p \rightarrow \pi^+ \bar{\nu}) \lesssim 1.7 \times 10^{34}$ years, which are striking results in the sense that there is hope to test this theory in future proton decay experiments. In Fig. 6.4, we have shown the parameter space allowed by unification and proton decay constraints as a function of the mass splittings for the fermionic fields living in the 5, 5' and 24 representations, \hat{m}_5 and \hat{m}_{24} , but it is also useful to explicitly show the allowed masses for these fields, as it is done in Fig. 6.8, where we assume the most optimistic case $M_{\Sigma_3} = M_{\Sigma_8} = M_Z$. As this figure shows, the field responsible for the Type-III seesaw mechanism, ρ_3 , has a

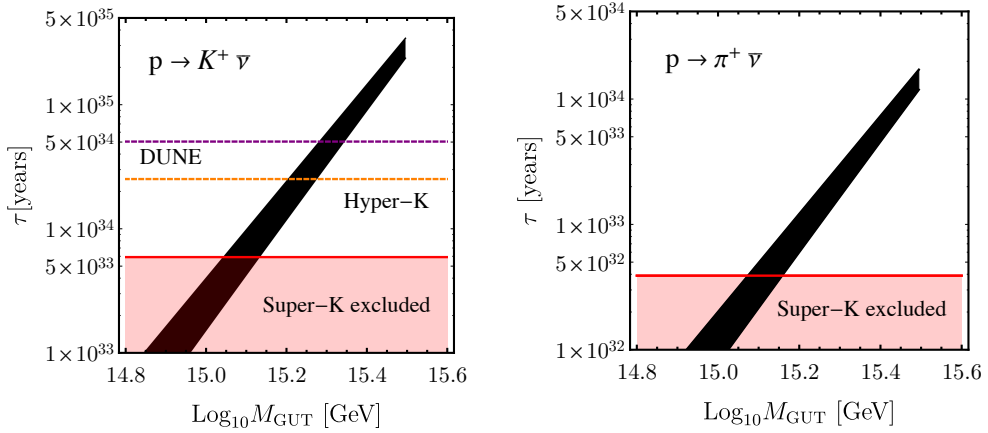


Figure 6.7: Predictions for the proton decay lifetime for the channels $p \rightarrow K^+ \bar{\nu}$ (left panel) and $p \rightarrow \pi^+ \bar{\nu}$ (right panel). The red line corresponds to the current proton decay lifetime for the different channels, i.e. $\tau(p \rightarrow K^+ \bar{\nu}) > 5.9 \times 10^{33}$ years [271] (left panel) and $\tau(p \rightarrow \pi^+ \bar{\nu}) > 3.9 \times 10^{32}$ years [272] (right panel). The orange dashed line on the left panel shows the projected bound on $p \rightarrow K^+ \bar{\nu}$ from the HK collaboration, i.e. $\tau(p \rightarrow K^+ \bar{\nu}) > 2.5 \times 10^{34}$ years [273].

mass at the multi-TeV scale, with an upper bound of $M_{\rho_3} \leq 500$ TeV, which allows the possibility to test the Type-III seesaw mechanism at current or future colliders.

We are left with just one task: to show that it is possible to generate at least two massive neutrinos in the context of this theory. The relevant Lagrangian for the neutrino mass generation reads as,

$$\begin{aligned}
 -\mathcal{L} \supset & \frac{v_5}{2\sqrt{2}} (y_0^i \nu_i + y_1^i N_i - y_2^i N_i^c) (\rho_3 + \xi \rho_0) - NM_L N^c + \frac{1}{2} M_{\rho_0} \rho_0^2 \\
 & + \frac{1}{2} M_{\rho_3} \rho_3^2 - \nu \tilde{M}_{\bar{5}_5} N^c + \text{h.c.},
 \end{aligned} \tag{6.91}$$

where $\xi = 3/\sqrt{15}$, $\tilde{M}_{\bar{5}_5} = M_{\bar{5}_5} - 3\lambda_{\bar{5}_5} M_{\text{GUT}}/(2\sqrt{25\pi\alpha_{\text{GUT}}})$, and v_5 is the vacuum expectation value of the SM Higgs. In this theory there is a well-defined hierarchy among the neutral fermionic sector, imposed by the unification constraints. As Fig. 6.8 shows, the minimum mass splitting in the 24 required by proton decay bounds is nine orders of magnitude, which places ρ_3 near the EW scale, and ρ_0 close to the GUT scale. As also

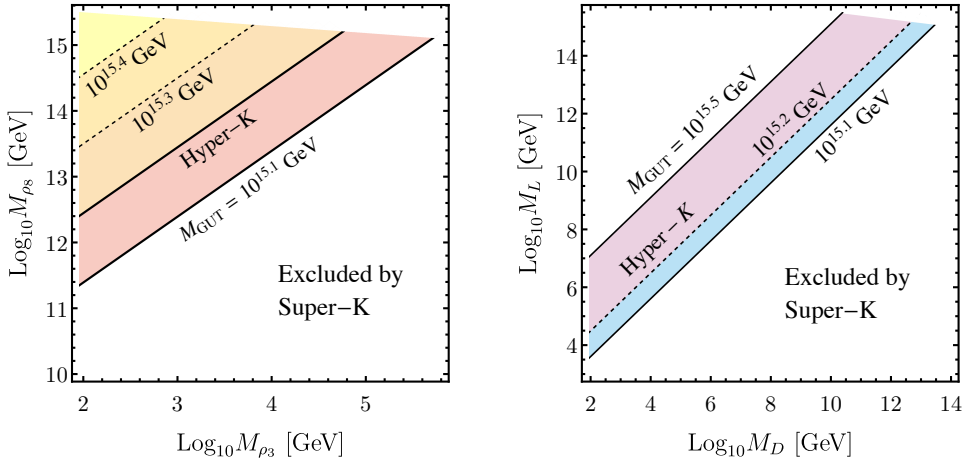


Figure 6.8: Allowed masses of the fields ρ_3 and ρ_8 in agreement with the unification constraints for the most optimistic case: $M_{\Sigma_3} = M_{\Sigma_8} = M_Z$. The white region below the diagonal line is excluded by the bounds on the proton decay lifetime from the SK collaboration [271]. *Figure extracted from Ref. [269].*

shown in this figure, unification conditions grant more freedom for the mass splitting in the 5 and $5'$ representations, and the vector-like fermions could live anywhere in the great desert. The existent gaps between the different scales from the established hierarchy

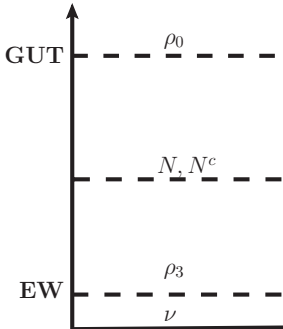


Figure 6.9: Hierarchy of the neutral fermionic fields required by unification and proton decay constraints. *Diagram extracted from Ref. [269].*

in the neutral fermions, which is shown in Fig. 6.9: $M_{\rho_0} \gg M_L \gg M_{\rho_3} \gg M_\nu$, allows for an EFT description at each of the "layers", where one has to take into account the relevant d.o.f. in order to capture correctly the neglected physics in the UV. According

to the ordering fixed by the consistency of the theory, we first integrate out the heaviest neutral field ρ_0 , and its effect on the remaining mass matrix for the N and N^c fields is

$$\begin{pmatrix} N_i & N_i^c \end{pmatrix} \begin{pmatrix} -\frac{1}{4}y_1^i y_1^j \xi^2 v_5^2 / M_{\rho_0} & -M_L^{ij} \\ -M_L^{ji} & -\frac{1}{4}y_2^i y_2^j \xi^2 v_5^2 / M_{\rho_0} \end{pmatrix} \begin{pmatrix} N_j \\ N_j^c \end{pmatrix}, \quad (6.92)$$

where we are neglecting terms of order $\mathcal{O}(M_{\rho_0}^{-2})$, as well as terms order $\mathcal{O}(v_5/M_{\rho_0})$ in front of M_L . The effect of integrating out the ρ_0 is to generate a Majorana mass term for the SM neutrinos, as represented in a schematic way in the following diagram:

$$\begin{array}{c} \longrightarrow \otimes \longleftarrow \\ \nu_i \qquad \nu_j \end{array} = \begin{array}{c} \longrightarrow \times \longleftarrow \otimes \longrightarrow \times \longleftarrow \\ \nu_i \qquad \rho_0 \qquad \nu_j \end{array}, \quad (6.93)$$

where \times symbolises a tree-level interaction between the fermions, \otimes represents a mass term insertion. The N and N^c can be written as a linear combination of the new fields N_1 and N_2 that diagonalize the above mass matrix:

$$N = \cos \theta N_1 + \sin \theta N_2, \quad (6.94)$$

$$N^c = -\sin \theta N_1 + \cos \theta N_2, \quad (6.95)$$

where the mixing angle θ of the rotation is defined as

$$\tan 2\theta = \frac{8M_L^{ij} M_{\rho_0}}{(y_2^i y_2^j - y_1^i y_1^j) \xi^2 v_5^2}. \quad (6.96)$$

We note that, since $M_L M_{\rho_0} \gg v_5^2$, the mixing angle is $\theta \sim \pi/4$, and the masses of the new fields are $\pm M_L$. Note that, since N_1 and N_2 are Majorana fields, we can always rotate our fields by a $e^{i\frac{\pi}{2}}$ phase to define positive masses. According to the mass hierarchy in the neutral fermions, we can integrate N_1 and N_2 out, which leads to the following effective Lagrangian for the light d.o.f.:

$$-\mathcal{L}_{eff}^{\nu, \rho_3} \supset - \left(\xi^2 y_0^i y_0^j \frac{v_5^2}{8M_{\rho_0}} \right) \nu_i \nu_j + \frac{1}{2} M_{\rho_3} \rho_3 \rho_3 + \frac{v_5}{2\sqrt{2}} \nu_i (y_0^i - (y_1^T M_L^{-1} \tilde{M}_{55}^T)^i) \nu_i \rho_3, \quad (6.97)$$

where we do not include terms of order $(M_L M_{\rho_0})^{-1}$ and we neglect corrections to the ρ_3 mass suppressed by M_L . We note that in the limit $\theta \rightarrow \pi/4$, there is no contribution to the light neutrino mass term from the vector-like leptons; however, we point out that they do contribute to the effective coupling between ν and ρ_3 , as it is illustrated in the following diagram, where the reader can clearly see that the integration of the N_i fields has generated an effective vertex for the ρ_3 and ν_i fields, apart from the tree-level interaction:

$$\text{---}\rho_3\text{---}\textcircled{\text{shaded}}\text{---}\nu_i\text{---} = \text{---}\rho_3\text{---}\text{X}\text{---}\nu_i\text{---} + \text{---}\rho_3\text{---}\text{X}\text{---}\textcircled{\text{X}}\text{---}\text{X}\text{---}\nu_i\text{---}. \quad (6.98)$$

Finally, by integrating out the ρ_3 , the final seesaw takes place, and one generates a new contribution to the light neutrinos suppressed by M_{ρ_3} ,

$$\text{---}\nu_i\text{---}\text{X}\text{---}\nu_j\text{---} = \text{---}\nu_i\text{---}\text{X}\text{---}\rho_0\text{---}\text{X}\text{---}\nu_j\text{---} + \text{---}\nu_i\text{---}\textcircled{\text{shaded}}\text{---}\rho_3\text{---}\text{X}\text{---}\textcircled{\text{shaded}}\text{---}\nu_j\text{---}, \quad (6.99)$$

and the mass matrix is given by

$$M_{\nu}^{ij} = \frac{v_5^2}{4} \left(\frac{\xi^2 y_0^i y_0^j}{M_{\rho_0}} + \frac{(y_0^i - (y_1^T M_L^{-1} \tilde{M}_{55}^T)^i)(y_0^j - (y_1^T M_L^{-1} \tilde{M}_{55}^T)^j)}{M_{\rho_3}} \right). \quad (6.100)$$

It should be stressed that the term generated by the integration of the neutral fields in the $5'$ and $\bar{5}'$ representations plays a key role by breaking the degeneracy between the ρ_0 and ρ_3 contributions to the light neutrinos and allows to enlarge the rank of the matrix. We note that with only the contribution of the 24, the model would predict two massless neutrinos; thus, the presence of the $5'$ and $\bar{5}'$ is crucial to guarantee the consistency of the theory with experiment.

6.4 Conclusions

We have discussed the simplest non-supersymmetric theories based on $SU(5)$ and pointed out two simple realistic renormalizable scenarios where one can understand the generation of neutrino masses and predict the proton decay lifetimes of the proton decay channels involving antineutrinos.

On one hand, we have seen that one can extend the scalar sector by a 45_H to correct the charged fermion masses. In that context, the minimal renormalizable theory without gauge singlets corresponds to the case where neutrino masses are generated at the quantum level through the Zee mechanism. In this model one finds a very interesting connection between neutrino masses and the charged fermion masses. In this case the 45_H plays a three-fold role: it corrects the relation between charged lepton and down quark masses, helps towards predicting the correct gauge couplings at the low scale and generates a mass term for the neutrinos through the Zee mechanism.

We have shown the possibility to have the unification of the gauge interactions in agreement with the experiments, also with the help of some fields in the 45_H . In most of the allowed parameter space the colored octet present in the theory is light so that it could give rise to exotic signals at the LHC. We have investigated the predictions for proton decay showing the possibility to test this model at the Super-Kamiokande experiment or at the future Hyper-Kamiokande.

On the other hand, we have also showed that we can have a consistent relation between the charged lepton and down quark masses by extending the $SU(5)_{GG}$ content in three copies of vector-like fermions 5 and $5'$, and the adjoint 24 representation. In this context, one can generate fermion masses consistently with experiment and predict an upper bound on proton decay for the channels with antineutrinos: $\tau(p \rightarrow K^+\bar{\nu}) \lesssim 3.4 \times 10^{35}$ years and $\tau(p \rightarrow \pi^+\bar{\nu}) \lesssim 1.7 \times 10^{34}$ years. The neutrino masses are generated through the Type I and Type III seesaw mechanisms, and we find that the field responsible for the Type III seesaw mechanism must be light, i.e. $M_{\rho_3} \lesssim 500$ TeV.

Both simple theories proposed can be considered as appealing candidates for unification based on $SU(5)$, as they can be tested in current or future proton decay experiments.

7.- Axions in Grand Unified Theories

Chapter based on the work done in 1908.01772 and 1911.05738.

As we mentioned previously in the second part of Chapter 2, after QCD confinement the axion mass is given as a function of the Peccei-Quinn scale f_a ,

$$m_a \sim \frac{m_\pi f_\pi}{f_a}, \quad (7.1)$$

where f_π and m_π are the decay constant and the mass of the pion, respectively. This relation implies that the axion mass can only be predicted in the context where the scale f_a can be computed. As it has been already pointed out, the invisible axion models, although providing a useful approach to realize the Peccei-Quinn mechanism in a realistic way, do not tell us anything about the axion mass. That is because f_a is tied to a singlet scalar whose vev is, in principle, unattached from any given scale, and therefore can be arbitrarily large. As we introduced in Section 2.2, R. Peccei, H. Quinn, S. Weinberg and F. Wilczek [121–124] were the pioneers to predict the axion mass, by linking the PQ scale with the EW scale. Unfortunately, in that case, the axion is too heavy, $m_a \sim \mathcal{O}(\text{eV})$, and the original model is ruled out. Following their idea, in order to propose a realistic SM extension where the strong CP problem and the amount of DM in the universe can be understood, also able to predict the axion mass, we should find a theory with a definite mass scale to which we can attach f_a . Among the motivated BSM theories, Grand Unified Theories are the perfect candidates because the GUT scale can be predicted in their context. See Fig. 7.1 for an illustration.

The connection between the PQ and GUT scales was first pointed out by H. Georgi, S. Glashow and M. Wise in 1982, in Ref. [310]. In there, they propose a global $U(1)_{\text{PQ}}$

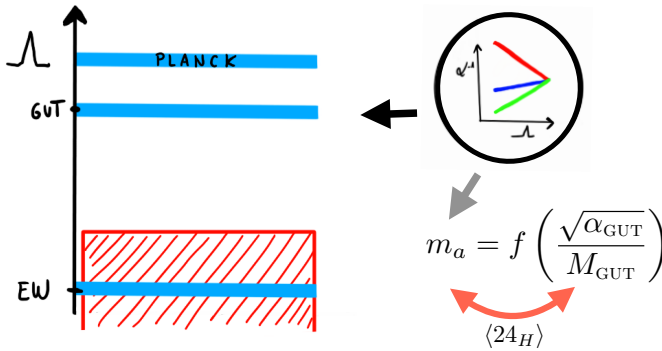


Figure 7.1: By linking the PQ scale with the GUT scale, the axion mass can be predicted in consistency with the experimental bounds. Both scales can be connected through the scalar singlet living in the 24_H representation, responsible from the breaking of both $SU(5)$ and $U(1)_{\text{PQ}}$ symmetries.

on top of the original $SU(5)$ gauge symmetry. In order to predict the PQ scale from unification, the same field that breaks the grand unifying group must simultaneously break the PQ symmetry. This role is played by the 24_H representation, which in the presence of the extra PQ symmetry becomes complex and allows for a CP-odd field constituting its imaginary part, as shown below:

$$24_H \supset \frac{1}{\sqrt{2}} |\Sigma_0| e^{ia(x)/v_\Sigma}. \quad (7.2)$$

Here, v_Σ is the vev of Σ_0 , which is the singlet under the SM quantum numbers that lives in the adjoint representation of $SU(5)$.¹ Moreover, as discussed in Chapter 2, at least a scalar mixing term (DFSZ) or an extra colored fermion (KSVZ) is needed in order to generate the desired $G\tilde{G}$ term. H. Georgi, S. Glashow and M. Wise (GGW) opted for the first possibility and added an extra fundamental representation, $5'_H$ [310], which contains a second Higgs doublet that can mix with both the SM one and the singlet in the 24_H , allowing in this way the successful implementation of the DFSZ mechanism. The relevant Lagrangian for the PQ mechanism in this simple extension of the original

¹See Section 6.1 from Chapter 6 for a brief but more detailed introduction on $SU(5)$.

$SU(5)$ theory is given by

$$-\mathcal{L}_{\text{GGW}}^{SU(5)} \supset \bar{5} Y_5 10 5_H^* + 10 Y_{10} 10 5_H' + \lambda_1 5_H^* 24_H^2 5_H' + \lambda_2 5_H^* 5_H' \text{Tr}\{24_H^2\} + \text{h.c.}, \quad (7.3)$$

whose expression in terms of the relevant SM fields reads as

$$-\mathcal{L}_{\text{GGW}}^{\text{SM}} \supset \bar{d} \frac{Y_5}{\sqrt{2}} H_d^{0*} d + \bar{u} 2(Y_{10} + Y_{10}^T) H_u^0 u + \frac{1}{2} \left(\frac{3}{10} \lambda_1 + \lambda_2 \right) H_d^{0*} H_u^0 \Sigma_0^2 + \text{h.c.} \quad (7.4)$$

In the above equation, the reader can easily identify the canonical two Higgs doublet model from Eq. 2.124, together with the mixing term in the scalar potential from Eq. 2.136 needed for the implementation of the DFSZ mechanism (see Chapter 2). Once the 24_H gets a vev , the vector LQs acquire a mass proportional to it, as explained in Chapter 6, and a topological term $a(x)G\tilde{G}$ is generated in the Lagrangian by rotating the part of the axion living in the Higgs doublets using the PQ symmetry that the quarks enjoy. Unfortunately, in despite of being able to solve the strong CP problem, this simple GUT is ruled out by the same reasons as $SU(5)_{\text{GG}}$: neither the SM gauge couplings -problem (i)- nor the fermion masses -problem (ii)- can be reproduced at the low scale, and neutrinos are predicted massless -problem (iii)- (see Sec. 6.1 from Chapter 6 for details). Therefore, in order to construct the simplest realistic GUT able to host an axion, the aforementioned three points need to be addressed. We will attach ourselves to the renormalizability of the theory, since the presence of non-renormalizable terms would destabilize it. We summarize in Table 7.1 the simplest possibilities to achieve that.

The 45_H contains enough freedom to modify the RGEs and the charged fermion masses with respect to the original $SU(5)_{\text{GG}}$ predictions as we showed in Chapter 6, i.e. to solve problems (i) and (ii) (first and last column from Table 7.1). However, the fact that both 5_H and 45_H representations must couple to the $\bar{5} 10$ term in the same way in order to split M_e and M_d implies that they must carry the same charge under the PQ symmetry. Then, although a mixing term is allowed in the scalar potential by the symmetries of the theory, i.e.

$$V_{SU(5)} \supset \lambda_1 45_H^* 24_H^2 5_H + \lambda_2 45_H^* 5_H \text{Tr}\{24_H^2\} + \text{h.c.}, \quad (7.5)$$

$Y_e \neq Y_d^T$	$M_\nu \neq 0$	PQ	Unification
45_H	1_i	×	✓
	10_H	×	✓
	15_H	×	✓
	24	✓	✓
$5' + \bar{5}'$	1_i	✓	×
	15_H	✓	×
	24	✓	×

Table 7.1: Minimal renormalizable GUTs based on $SU(5)$. The third column indicates whether the PQ symmetry leading to the axion can be implemented. The fourth column indicates whether gauge unification can be achieved. *Table extracted from Ref. [31].*

the 24_H must be a singlet under the global PQ and, therefore, the PQ mechanism cannot be implemented in this case. Nevertheless, still more representations must be included in the theory to account for neutrino masses. As discussed in Chapter 6, Section 6.2, neutrinos could acquire mass by adding a couple of fermion singlets through the Type-I seesaw mechanism. However, the gauge symmetry and field content does not allow for a realistic PQ charges in this case. Neutrino masses could also be generated at the quantum level by adding a 10_H , as we proposed in Sec. 6.3, but no mixing term for the DFSZ implementation (see Sec. 2.2.4.1) is generated in that context. Among possible candidates, the 15_H is interesting because it can generate neutrino masses through the Type-II seesaw mechanism and allows for a mixing term with the SM Higgs and the singlet in the 24_H after SSB via the following term:

$$V_{SU(5)} \supset (\lambda_1 5_H^* + \lambda_2 45_H^*)(\lambda_3 5_H^* + \lambda_4 45_H^*)24_H 15_H + \text{h.c.} \quad (7.6)$$

However, the PQ symmetry defined among the quarks in this case is non-anomalous and, unfortunately, the PQ mechanism does not work.

Let us consider the 24 representation (see Eq. 6.61) instead, which consists of two colorless fields, a singlet ρ_0 and a triplet ρ_3 under $SU(2)_L$, that can generate masses for the neutrinos through the Type-I and Type-III seesaw mechanisms, respectively, and three colored fields, ρ_8 , $\rho_{(3,2)}$ and $\rho_{(\bar{3},2)}$, which can be used to generate the $a(x)G\tilde{G}$

term. The later can be realized by rotating the axion from the Yukawa interaction via these new color fermions *à la* KSVZ (see Sec. 2.2.4.2). The extension of the $SU(5)_{\text{GG}}$ with a 45_H and 24 was proposed in 2010 by P. Fileviez Pérez [281], and constitutes the simplest realistic renormalizable GUT theory where the KSVZ mechanism can be implemented when imposing a global $U(1)_{\text{PQ}}$. This theory will be described in the first section of this chapter.

On the other hand, on top of adding the 45_H to render the GUT realistic, one could further add an extra Higgs doublet *à la* GGW. This $SU(2)_L$ doublet allows for the implementation of the DFSZ mechanism since, in this case, such scalar is not required to correct the charged fermion masses so that it can be charged differently than 5_H or 45_H under PQ. We note that neutrino masses are still not generated in this context and one is forced to add more representations to solve this issue. The extension of the $SU(5)_{\text{GG}}$ with a 45_H and an extra $5'_H$ can be considered, on the other hand, the simplest GUT theory where the strong CP problem is solved via the implementation of the DFSZ mechanism, and it will be addressed in the second part of this chapter.

As it will be shown along this chapter, in the context of GUT theories, the axions turn to be *not that invisible*. For other studies of axions in GUTs see Refs. [312–315]. In Ref. [314] the authors use a non-renormalizable theory where the same higher-dimensional operators, needed to correct the relation between fermion masses and split the particle spectrum, generically could break the PQ symmetry spoiling the predictions for the PQ scale and axion mass.

7.1 KSVZ mechanism in $SU(5)$

The simplest realistic GUT theory in the sense of number of representations able to host an axion is the Adjoint $SU(5)$ [281] $\otimes U(1)_{\text{PQ}}$, composed of the fields from the original $SU(5)_{\text{GG}}$ plus a 45_H and 24 representations. In this theory, the KSVZ mechanism can be implemented if the different representations are charged under the PQ symmetry as follows,

$$\begin{aligned} \bar{5} &\rightarrow e^{-3i\text{PQ}_{10}}\bar{5}, & 10 &\rightarrow e^{+i\text{PQ}_{10}}10, & 5_H &\rightarrow e^{-2i\text{PQ}_{10}}5_H, \\ 24_H &\rightarrow e^{-10i\text{PQ}_{10}}24_H, & 45_H &\rightarrow e^{-2i\text{PQ}_{10}}45_H, & 24 &\rightarrow e^{+5i\text{PQ}_{10}}24, \end{aligned}$$

where the relative PQ charges among all representations are fixed by the consistency of the theory. Under the above charge assignment, the theory enjoys the Yukawa Lagrangian described in Eq. 6.71 from Chapter 6, whose interactions allow for a realistic relation between the charged fermion masses, given by Eq. 6.72 from the same chapter.

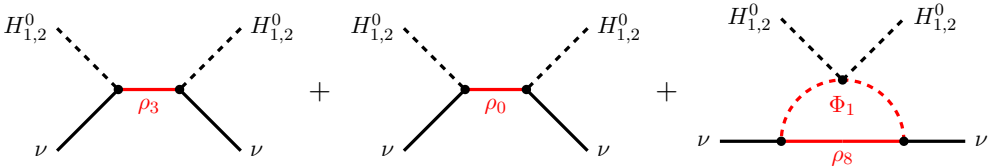
On another hand, neutrino masses are generated through the following interactions,

$$-\mathcal{L} \supset h_1 \bar{5} 24 5_H + h_2 \bar{5} 24 45_H + \lambda \text{Tr} \{24^2 24_H\} + \text{h.c.} \quad (7.7)$$

Note that this Lagrangian is very similar to that in Eq. 6.64 except for two differences: (a) the 24 mass term, $M_{24} \text{Tr}\{24^2\}$, is forbidden by $U(1)_{\text{PQ}}$ in this context, (b) there is a contribution from the 45_H to the neutrino mass matrix analogous to the 5_H that was not considered when discussing the Type-III seesaw mechanism in Sec. 6.2 from Chapter 6. The neutrino mass matrix will be generated from the Type-I, -III seesaws at tree level, and colored seesaw at the radiative level (see Eq. 1.38):

$$M_\nu = M_\nu^{\text{I}} + M_\nu^{\text{III}} + M_\nu^{\text{cs}}. \quad (7.8)$$

The different contributions arise from the following interactions:



The M_ν^{III} in the above equation, given by,

$$(M_\nu^{\text{III}})_{ij} = \frac{1}{8} \left(\frac{(h_1^i v_5 + 3h_2^i v_{45})(h_1^j v_5 + 3h_2^j v_{45})}{M_{\rho_3}} + \frac{3}{5} \frac{(h_1^i v_5 - 5h_2^i v_{45})(h_1^j v_5 - 5h_2^j v_{45})}{M_{\rho_0}} \right), \quad (7.9)$$

is modified with respect to Eq. 6.65 due to the contribution from 45_H ,²

Because of the presence of a single copy of new fermions (only one 24 representation), the Yukawa couplings are vectors so that one of the neutrinos is predicted massless. However, as the diagrams show, the Manohar-Wise $\Phi_1 \sim (8, 2, 1/2) \subset 45_H$ together with the colored octet fermion $\rho_8 \sim (8, 1, 0) \subset 24$ can close a loop carrying color and generate neutrino masses at the radiative level through the colored seesaw (see Diag. 6.66). Note that, although M_ν^{cs} has rank 1 (see Sec. 6.2), together with the contribution of the Type-I and -III seesaws there is enough freedom to embed three massive neutrinos. We refer the reader to Sec. 6.2 from Chapter 6 or, directly to the original Refs. [281,316], for the explicit form of the neutrino mass matrix and other details.

The last term from Eq. 7.7 is the key element for the implementation of the KSVZ mechanism, as it can be recognized from Eq. 2.145. Once the singlet inside the 24_H acquires a non-zero $\nu e \nu$, given by Eq. 6.6, the fermions in the 24 representation acquire a mass and a Yukawa interaction between the axion and the new fermions is generated,³ i.e.

$$\mathcal{L} \supset \frac{\lambda}{\sqrt{15}} v_\Sigma e^{i \frac{\alpha(x)}{v_\Sigma}} \times \left(-\text{Tr}\{\rho_8^T C \rho_8\} + \frac{1}{2} \text{Tr}\{\rho_{(3,2)}^T C \rho_{(3,2)}\} + \frac{3}{2} \text{Tr}\{\rho_3^T C \rho_3\} + \frac{1}{2} \rho_0^T C \rho_0 \right) + \text{h.c.} \quad (7.10)$$

We note that, since the Majorana mass term is forbidden by the PQ symmetry, the masses are only determined by the last term from Eq. 7.7 and therefore the splitting among the different fields from the 24 is fixed. This allows us to write all masses of the fields in the 24 as a function of one of them, for instance the triplet ρ_3 mass,

$$M_{\rho_0} = \frac{1}{3} M_{\rho_3}, \quad M_{\rho_8} = \frac{2}{3} M_{\rho_3}, \quad M_{\rho_{(3,2)}} = M_{\rho_{(\bar{3},2)}} = \frac{1}{6} M_{\rho_3}, \quad (7.11)$$

which can be read off from the above interactions.

²The second Higgs doublet in the 45_H lives in $45_H \alpha^{\beta\gamma} \sim -3\epsilon^{\beta\gamma} H_2^\delta \epsilon_{\alpha\delta}$ and $45_H i^{j\alpha} \supset \delta_i^j H_2^\alpha$, from where the factor 3 and 5 in the H_2 contribution come from with respect to the 5_H case. Note also that for the singlet $\rho_0 \subset 24$, the color indices in the 45_H , in contrast with the term involving ρ_3 , do contribute.

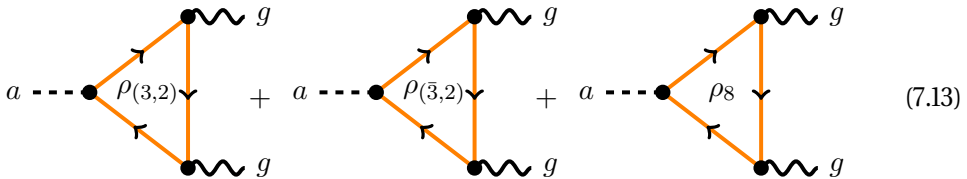
³Notice that this matches the mass terms from Eq. 6.85 with $M_{24} = 0$ and a complex phase.

7.1.1 Implementation of the PQ mechanism

Following the method proposed by Fujikawa [105,106] introduced in Chapter 2, the coupling to gluons can be written as

$$\mathcal{L} \supset \frac{\alpha_3}{8\pi} \frac{a}{v_\Sigma} N G_{\mu\nu}^a \tilde{G}_a^{\mu\nu} \equiv \frac{\alpha_3}{8\pi} \frac{a}{f_a} G_{\mu\nu}^a \tilde{G}_a^{\mu\nu}, \tag{7.12}$$

where N depends on the chiral fields that have been rotated in order to absorb the axion field. In our case, the fields contributing to the generation of the $G\tilde{G}$ -term, listed below,



according to Eq. 2.112 from Chapter 2, generate the following N :

$$N = 2 \times \frac{1}{2} \left(\underbrace{3 \times 1}_{\rho_8} + \underbrace{\frac{1}{2} \times 2}_{\rho(3,2)} + \underbrace{\frac{1}{2} \times 2}_{\rho(3,2)} \right) = 5. \tag{7.14}$$

Hence, the relation between the PQ scale f_a , defined in Eq. 7.12, and the GUT scale, defined in Eq. 6.12, is given by

$$f_a \equiv \frac{v_\Sigma}{N} = \frac{v_\Sigma}{5} = \sqrt{\frac{6}{5\pi\alpha_{\text{GUT}}}} \frac{M_{\text{GUT}}}{10}. \tag{7.15}$$

Therefore, once known the unification scale M_{GUT} , from the above relation it is straightforward to predict the axion mass. Now all we can do is computing the window for the GUT scale predicted by the Adjoint $SU(5)$.

7.1.2 Predicting the GUT scale

In order to predict the axion mass, we need to ask to this specific theory which is the scale where unification can occur. For that, we will take into account the evolution of the SM gauge couplings, which is given by the RGE equations at the 1-loop level described in Eq. 6.16 from Chapter 6.

Besides the b -coefficients from the SM contribution at the EW scale, the rest of the coefficients for the intermediate fields, b_i^I , in this theory are: the colored triplet living in 5_H , the scalars in the 24_H and 45_H , and the fermions in the 24, whose b_i coefficients are given in Tables 6.1, 6.2 and 6.4 from Chapter 6. For achieving the proper values of the gauge couplings at the low scale, the unification constraints described in Eq. 6.19 and 6.20 should be satisfied.

As in the theory $Zee-SU(5)$, only the Φ_1 , Φ_3 and H_2 fields in the 45_H help towards satisfying the unification constraints. For Φ_3 and H_2 , the lighter they are the larger the fraction B_{23}/B_{12} can be. The field Φ_1 helps towards unification indirectly since it gives a negative contribution to B_{12} , which turns into an increase of the GUT scale. The later is needed to be in agreement with proton decay bounds, as we will show in brief. We will assume for simplicity that the rest of the scalars in the 45_H are at the GUT scale and, therefore, do not modify the RGE equations. We will also assume that there is no mass splitting among the fields in the 24_H . Under this perspective, the B_{ij} coefficients are given by

$$B_{ij} = b_{ij}^{\text{SM}} + b_{ij}^{H_2} r_{H_2} + b_{ij}^{\Phi_1} r_{\Phi_1} + b_{ij}^{\Phi_3} r_{\Phi_3} + B_{ij}^{24}, \quad (7.16)$$

where B_{ij}^{24} represents the contribution of the fields in the 24. In this case, because of the presence of the $U(1)_{\text{PQ}}$ symmetry, the Majorana mass term for the 24 is not allowed and, therefore, the mass splitting among the fields in this representation is fixed, as shown in Eq. 7.11. We note that, since unification constraints do not depend on the global mass scale of the fields in a given representation, the contribution of the

24 to the RGE equations is totally fixed. In particular, the B_{ij}^{24} are explicitly given by

$$B_{23}^{24} = -2 \frac{\ln(3/2)}{\ln(M_{\text{GUT}}/M_Z)} + \frac{2}{3} \frac{\ln(6)}{\ln(M_{\text{GUT}}/M_Z)}, \quad (7.17)$$

$$B_{12}^{24} = \frac{4}{3} \frac{\ln(6)}{\ln(M_{\text{GUT}}/M_Z)}. \quad (7.18)$$

Having then as inputs the masses of the M_{H_2} , M_{Φ_1} and M_{Φ_3} , we can use both unification conditions (see Eqs. 6.19 and 6.20) to determine the parameter space where they are satisfied, which we show in Fig. 7.2. In there, the mass of the Φ_3 field is implicitly given by Eqs. 6.20. In the left panel, we show the general parameter space allowed for all possible values of the second Higgs doublet mass, represented with a blue shaded area. However, in the following we will assume that $M_{H_2} = 1$ TeV for our discussions as shown in the right panel; nonetheless, this assumption is quite general in the sense that the mass of a scalar doublet does not have a strong impact in the RGEs, as can be deduced from its b-coefficients (see Table 6.1) and corroborated in Fig. 7.2. By only looking at the parameter space allowed by the unification constraints we obtain a mass window $[2 \times 10^{14} - 10^{16}]$ GeV for the GUT scale when $M_{H_2} = 1$ TeV.⁴ However, not the full range is consistent with experiment. On one hand, there is an upper bound for the GUT scale, which is astonishingly fixed by collider experiments. Note that the Manohar-Wise field, $\Phi_1 \sim (8, 2, 1/2)$, cannot be arbitrarily light since it would get in tension with experimental constraints on new scalars at the low scale. We will use the bound $M_{\Phi_1} > 1$ TeV from Ref. [286], as we did in Chapter 6. This bound translates into an upper bound for the GUT scale: $M_{\text{GUT}} < 5.5 \times 10^{15}$ GeV. On the other hand, it is well-known that proton decay is mainly mediated by the vector LQs of $SU(5)$, whose mass defines the GUT scale. Therefore, the lower bound on the GUT scale window will be given by the experimental bounds coming from proton decay experiments.

Regarding predictions on proton decay, as in the other GUTs we have previously introduced, the most constrained channel, $p \rightarrow \pi^0 e^+$, depends on the unknown parameter V_e defined in Eq. 6.46. In the left panel of Fig. 7.3, we show the predictions of the Adjoint $SU(5)$ for this decay channel as a function of the GUT scale for two different choices of it: $V_e = 0.1$ and $V_e = 1$, where $M_{H_2} = 1$ TeV has been assumed.

⁴When $M_{h_2} = M_{\text{GUT}}$, the allowed range for the GUT scale is $[3.55 \times 10^{14} - 1.41 \times 10^{16}]$ GeV.

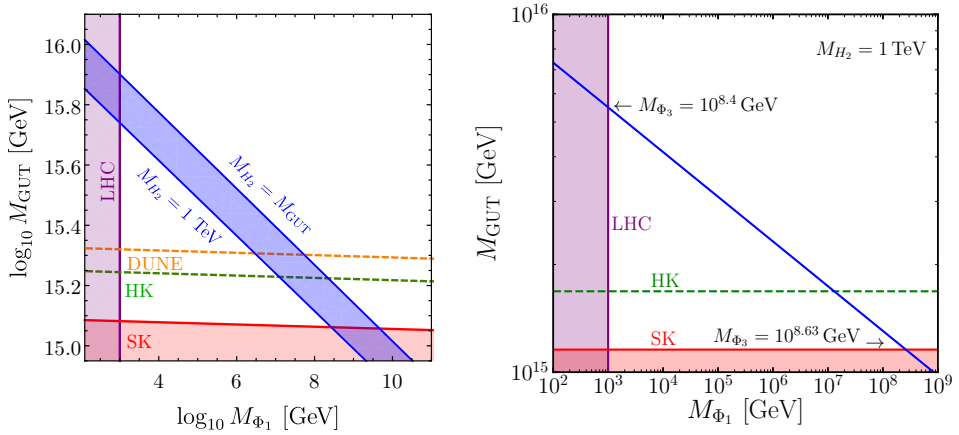


Figure 7.2: *Left Panel:* Predictions for the GUT scale, M_{GUT} , as a function of M_{Φ_1} . We implicitly show in the blue band all possible values that M_{H_2} can take. The purple shaded region shows the current LHC bound on the scalar colored octet $\Phi_1 \sim (8, 2, 1/2)$, $M_{\Phi_1} > 1 \text{ TeV}$ [286]. The region shaded in red shows the current experimental limit on the proton lifetime from the SK collaboration, $\tau(p \rightarrow K^+ \bar{\nu}) > 5.9 \times 10^{33}$ years [271], and the green dashed line shows the projected bound for the HK collaboration, $\tau(p \rightarrow K^+ \bar{\nu}) > 2.5 \times 10^{34}$ years [273]. When applying the bounds from proton lifetime we take the most conservative limit which corresponds to taking $M_{\rho_3} = 10^{15}$ GeV. The mass of the $\Phi_3 \sim (3, 3, -1/3)$ varies between the range $10^{8.4} - 10^{8.63}$ GeV from left to right. *Right Panel:* The results from the left panel are particularized for $M_{H_2} = 1 \text{ TeV}$. *Figure in right panel extracted from Ref. [311].*

The red shaded area shows the parameter space ruled out by the proton decay bound from the SK collaboration [158], while in green and orange the projected bounds from HK [273] and Dune [317], respectively, are shown. We also display shaded in purple the collider lower bound on M_{Φ_1} which determines the upper bound of the GUT scale, as the figure shows. The error of the blue band can be understood as follows. Note that, although unification constraints do not depend on the global mass of the 24 representation, the grand unified coupling α_{GUT} does depend on it. Therefore, for a given GUT scale, one should expect a certain range for the α_{GUT} allowed by the possible values of the global 24 mass, i.e. M_{ρ_3} as we parametrized them in Eq. 7.11. The fields in the 24 must be at the seesaw scale or below in order to generate realistic values for the neutrino masses. The fields ρ_0 and ρ_3 have two body decays and can decay before

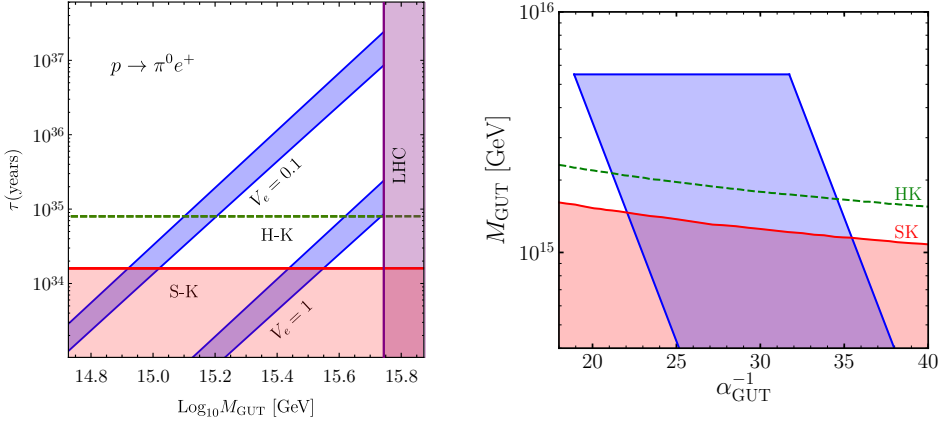


Figure 7.3: *Left Panel:* Predictions for the proton decay lifetime for the channel $p \rightarrow \pi^0 e^+$. The different blue bands show different choices of the magnitude of the unknown mixing matrix V_e . The width of the blue bands is determined by the allowed values of α_{GUT} as we vary $M_{\rho_3} \subset [10^{4.51}, 10^{15}]$ GeV. The red shaded area shows the excluded parameter space by the bound on the proton decay lifetime, $\tau(p \rightarrow \pi^0 e^+) > 1.6 \times 10^{34}$ years [158], from the SK collaboration. The green dashed line shows the projected bound on proton decay lifetime from the HK collaboration, i.e. $\tau(p \rightarrow \pi^0 e^+) > 8 \times 10^{34}$ years [273]. *Right Panel:* Relation between the GUT scale and α_{GUT} . The blue shaded region leads to gauge unification, the width of this band is determined by varying from $M_{\rho_3} = 10^{4.51}$ GeV (left limit determined by the BBN bounds) to $M_{\rho_3} = 10^{15}$ GeV (right limit determined by the perturbative bound on the seesaw scale). Here we use $M_{H_2} = 1$ TeV as in the left panel. *Figure extracted from Ref. [311].*

Big Bang Nucleosynthesis (BBN), while the colored fields ρ_8 , $\rho_{(3,2)}$ and $\rho_{(\bar{3},2)}$ have only three body decays. Since the masses of the all fields in 24 are related, it is enough to understand the limit on M_{ρ_8} . Neglecting all SM fermion masses the decay width for ρ_8 is given by

$$\Gamma(\rho_8) \approx \frac{Y_t^2 \mathcal{O}(1) M_{\rho_8}^5}{48(2\pi)^3 M_T^4}, \quad (7.19)$$

where M_T corresponds to the mass of the scalar triplet inside the 5_H . Here we used the main decay channel defined by the coupling of T to the third generation quarks.

Using that the contribution of ρ_3 to the neutrino masses is given by

$$M_\nu \simeq \frac{\mathcal{O}(1)v_0^2}{M_{\rho_3}}, \quad (7.20)$$

we find that

$$\Gamma(\rho_8) \approx \frac{Y_t^2}{32(2\pi)^3} \frac{M_\nu}{v_0^2} \frac{M_{\rho_8}^6}{M_T^4}. \quad (7.21)$$

In Fig. 7.4 we present the predictions for the ρ_8 lifetime using different M_T masses ($M_T > 10^{12}$ GeV from bounds on the proton lifetime, see Eq. 6.76) and $M_\nu \sim 0.1$ eV (see Eq. 1.10). The region shaded in blue shows the parameter space that leads to $\tau_{\rho_8} > 1$ second and it is excluded by a naive bound coming from BBN. Therefore,

$$10^{4.43} \text{ GeV} < M_{\rho_3} < 10^{15} \text{ GeV}, \quad (7.22)$$

where the upper bound comes from the perturbativity of the Yukawa coupling in Eq. (7.20). The window in Eq. 7.22 will define the error band of α_{GUT} for a given value of the GUT scale, as the right panel of Fig. 7.3 shows.

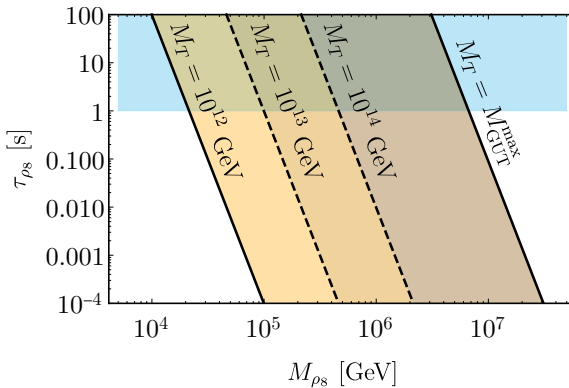


Figure 7.4: Predictions of the ρ_8 lifetime for different M_T masses, we have $M_T > 10^{12}$ GeV from bounds on the proton lifetime. The blue shaded regions shows the predictions for $\tau_{\rho_8} < 1$ second and excluded by a naive bound coming from BBN. *Figure extracted from Ref. [311].*

Unfortunately, the theory can always escape the proton decay bound on $p \rightarrow \pi^0 e^+$ by assuming a small V_e . However, let us look at the second strongest bound on proton decay, which applies to the decay channel $p \rightarrow K^+ \bar{\nu}$. In the Adjoint $SU(5)$, as in the Zee- $SU(5)$ (see Sec. 6.3), we should care about $\Phi_3 \sim (3, 3, -1/3)$. This LQ mediates

proton decay according to the effective dimension-6 interactions Lagrangian shown in Eq. 6.73. In here, as well as in the Zee- $SU(5)$ model, in order to achieve unification $M_{\Phi_3} \sim \mathcal{O}(10^8)$ as Fig. 7.2 shows. Hence, the empirical fact that the theory must be consistent with the proton decay bounds indirectly implies an almost symmetric mass matrix for the up-type quarks since a strong suppression from Y_4 is needed. We refer the reader to Chapter 6 for a detailed explanation. In this context we can make clean predictions for the proton decay into antineutrinos, which are given in Eq. 6.52. The later allows us to determine a lower bound for the GUT scale. In Fig. 7.11 we show the predictions for the proton decay channels $p \rightarrow K^+\bar{\nu}$ and $p \rightarrow \pi^+\bar{\nu}$. This figure shows the same color coding as Fig. 7.3. Taking the later into account, we can conclude

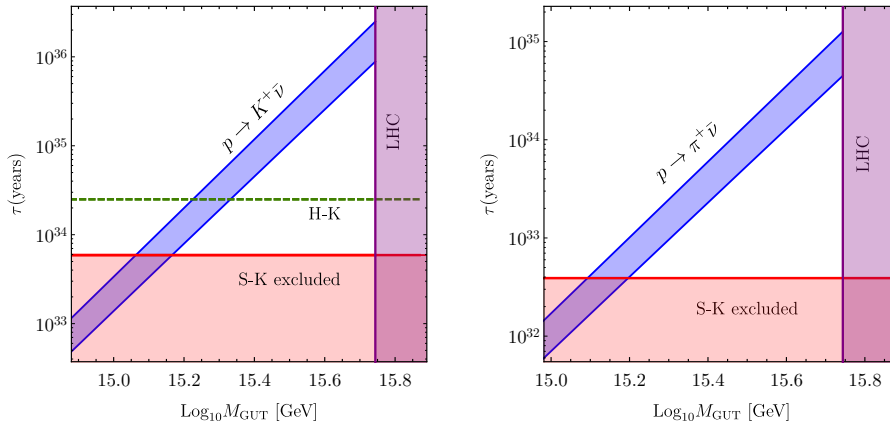


Figure 7.5: Predictions for the proton decay channels $p \rightarrow K^+\bar{\nu}$ and $p \rightarrow \pi^+\bar{\nu}$. The blue bands show the possible range of variation of α_{GUT} , according to $M_{\rho_3} \subset [10^{4.51}, 10^{15}]$ GeV. The red shaded areas show the excluded region by the SK constraints, $\tau(p \rightarrow K^+\bar{\nu}) > 5.9 \times 10^{33}$ years [271] and $\tau(p \rightarrow \pi^+\bar{\nu}) > 3.9 \times 10^{32}$ years [272]. The green dashed line shows the projected bound by the HK collaboration on the $p \rightarrow K^+\bar{\nu}$ channel, $\tau(p \rightarrow K^+\bar{\nu}) > 2.5 \times 10^{34}$ years [273]. *Figure extracted from Ref. [311].*

that the available window for the GUT scale for this Adjoint $SU(5)$ with a global PQ symmetry is

$$M_{\text{GUT}} = [10^{15.06} - 10^{15.74}] \text{ GeV}, \quad (7.23)$$

where we have taken the largest window within the error allowed by the strongest *clean* bound, i.e. that from the $p \rightarrow K^+\bar{\nu}$ channel. The above window is shown in Fig. 7.2, where theory and experimental constraints are all displayed together.⁵

7.1.3 Axion mass and phenomenology

In order to show our numerical results we will use the following relation between m_a and f_a obtained in Refs. [125, 318],

$$m_a = 5.691(51) \times 10^{-6} \text{ eV} \left(\frac{10^{12} \text{ GeV}}{f_a} \right), \quad (7.24)$$

where the authors have computed an improved expression with respect to that in Eq. 2.121 from Chapter 2 by combining NLO results obtained in chiral perturbation theory with recent Lattice QCD results.

As demonstrated in the last subsection, see Eq. 7.23, in Adjoint $SU(5)$ a small range for the GUT scale and α_{GUT} can be predicted. Because the same field is breaking the GUT scale and the PQ symmetry, the GUT scale and the axion mass are connected, as Fig. 7.1 illustrates. This leads to the following prediction for the axion mass:

$$m_a = (2.99 - 13.45) \times 10^{-9} \text{ eV}. \quad (7.25)$$

where we have taken the largest mass range allowed within the uncertainty of α_{GUT} . In Fig. 7.6 we show the predictions for the axion mass as a function of the GUT scale. The blue band shows the parameter space allowed by unification constraints and proton decay. The red (purple) shaded area shows the excluded parameter space by the proton decay bound (LHC bound on M_{Φ_1}). Eq. 7.25 is crucial to understand the testability of this theory at axion experiments because it tells us the specific range for the axion mass where a signal could be expected. In the allowed mass window, an initial misalignment angle of $\theta_i \approx 10^{-2}$ [132–134] must be assumed in order for the axion field to saturate the DM relic abundance $\Omega_{\text{DM}} h^2 = 0.1200 \pm 0.0012$ [7].

⁵In the extreme case $M_{h_2} = M_{\text{GUT}}$, the allowed range for the GUT scale consistent with experimental bounds and unification constraints is given by $10^{15.58} - 10^{16.02}$ GeV.

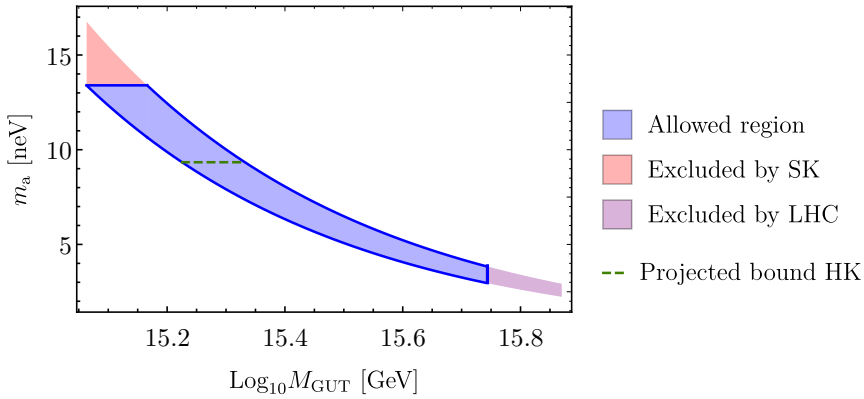
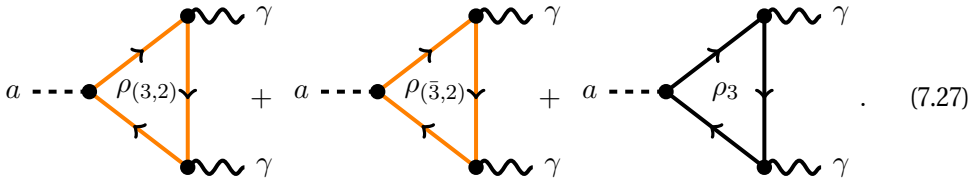


Figure 7.6: Axion mass as a function of the GUT scale. The blue band shows the parameter space allowed by unification constraints and proton decay. The red (purple) shaded area shows the excluded parameter space by the proton decay bounds from SK (LHC bound on M_{Φ_1}). The dashed green line gives the projected sensitivity for HK. *Figure extracted from Ref. [311].*

We proceed to study the phenomenology of the axion in the predicted mass window. The coupling between the axion and photons is given by the red framed term in Eq. 2.153, lead by the effective coupling $g_{a\gamma\gamma}$ given by Eq. 2.123. In this case, $E/N = 8/3$ since we are working with fermions in a complete representation of $SU(5)$. The explicit value for E is given by,

$$E = 2 \times \frac{1}{2} \left(\underbrace{\left(\frac{4}{3}\right)^2 \times 3 + \left(\frac{1}{3}\right)^2 \times 3}_{\rho_{(3,2)}} + \underbrace{\left(\frac{4}{3}\right)^2 \times 3 + \left(\frac{1}{3}\right)^2 \times 3}_{\rho_{(\bar{3},2)}} + \underbrace{1^2 + (-1)^2}_{\rho_3} \right) = \frac{40}{3}, \tag{7.26}$$

where the electrically charged fields participating in the $g_{a\gamma\gamma}$ generation are listed below.



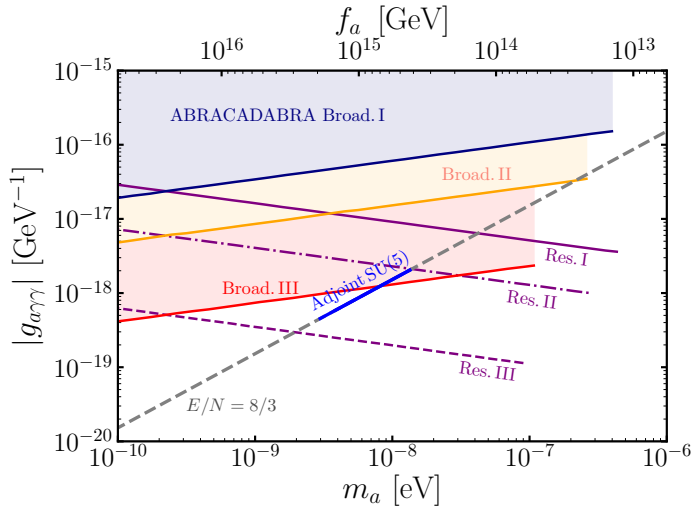


Figure 7.7: The axion-photon coupling versus the axion mass. The blue line corresponds to the axion mass prediction in Adjoint $SU(5)$. The regions shaded in blue, orange and red correspond to the projected sensitivities for Phase I, II and III of the ABRACADABRA experiment [150] using the broadband approach. The purple lines correspond to the projected sensitivities for the three different phases in the resonant approach. *Figure extracted from Ref. [311].*

As described in Chapter 2, the ABRACADABRA experiment [150] is expected to be sensitive to the axion to photon coupling for very light axions, $m_a \lesssim 10^{-6}$ eV. In Fig. 7.7 we present the axion to photon coupling together with the projected reach for ABRACADABRA, as given in Ref. [150]. The regions shaded in different colors correspond to the projected sensitivity for the broadband operating mode, while the purple lines show the ones for the resonant operating mode. The blue solid line corresponds to the prediction in Adjoint $SU(5)$. It is of great interest that the third stage of the broadband mode will be able to probe a portion of this mass range, while the third stage of the resonant operating mode could fully probe the predicted mass window.

At low energies, the axion field has also a coupling to the EDM operator for nucleons, given by the blue framed term in Eq. 2.162, which gives rise to the nucleon EDM [114–117],

$$d_n \equiv g_{aD} a \approx 2.4 \times 10^{-16} \frac{a}{f_a} e \cdot \text{cm}, \quad (7.28)$$

as Eq. 2.114 states. In the presence of an oscillating axion background field, $a(t)$, this interaction generates an oscillating nucleon EDM. Thus, when DM consists of the axion field with $\rho_{\text{DM}} \approx m_a^2 a_0^2/2 \approx 0.4 \text{ GeV/cm}^3$ [149] it could lead to an observable effect on nucleons.

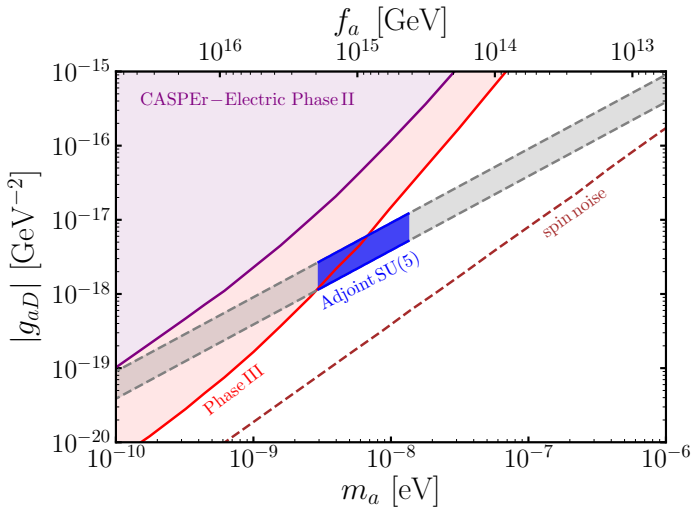


Figure 7.8: The axion coupling to the nucleon EDM versus the axion mass. The blue band is the prediction in Adjoint $SU(5)$. The width of the band corresponds to the theoretical error, as given in [115, 116]. The region shaded in purple and red correspond to the projected sensitivities for Phase II and III of the CASPER-Electric experiment [156]. The brown dashed line shows the ultimate limit from magnetization noise. *Figure extracted from Ref. [311].*

The CASPER-Electric experiment [154] is expected to probe axions with very low masses, $m_a < 10^{-9} \text{ eV}$, which is the region of interest for theories in which the PQ scale has a connection to the GUT or the string scale [319]. See Chapter 2, Sec. 2.2 for more details on the experiment. In Fig. 7.8 we present the predictions for the g_{aD} coupling in the axion mass window predicted by Adjoint $SU(5)$. The region shaded in purple (red) corresponds to the projected sensitivity for Phase II (Phase III) for CASPER-Electric [156], the latter will be able to probe a part of the mass window predicted by Adjoint $SU(5)$. The brown dashed line shows the ultimate limit from magnetization noise. As can be appreciated, these predictions for the axion mass can be probed in the near future.

7.2 DFSZ mechanism in $SU(5)$

The Peccei-Quinn mechanism can be implemented à la Dine, Fischler, Srednicki and Zhitnitsky (DFSZ) [128,129] in GUT theories through a mixing term that connects indirectly the axion with the colored fermions of the theory. It can be implemented in $SU(5)$ enlarging the $SU(5)_{\text{GG}}$ by an extra Higgs in the fundamental representation as Georgi, Glashow and Wise proposed in Ref. [310],

$$5'_H \sim \underbrace{(1, 2, 1/2)}_{H_3} \oplus \underbrace{(3, 1, -1/3)}_{T'}, \quad (7.29)$$

which contains an extra second Higgs doublet, H_3 . However, in order to make the theory realistic, as mentioned in the introduction of this chapter, one needs an extra 45_H to correct the charged fermion masses and predict the observed SM gauge couplings at the low scale. In the context of the scalar sector of this theory, the mixing term between the Higgs doublets and the CP-odd phase in 24_H reads,

$$V \supset 5_H^\dagger 24_H^2 (\lambda_1 5_H + \lambda_2 45_H) + \lambda_3 5_H^\dagger 5_H \text{Tr}\{24_H^2\} + \text{h.c.}, \quad (7.30)$$

which implies that the 5_H and $5'_H$ must transform differently under the PQ symmetry in order for the 24_H to transform non-trivially under $U(1)_{\text{PQ}}$. For the symmetry to be non-anomalous, each of the doublets must couple to a different Yukawa interaction of the original $SU(5)$. Since the fermion mass relation between the charged leptons and down-type quarks must be corrected, the 45_H must couple to the $\bar{5} 10$ interaction in exactly the same way as the 5_H . In this context, the $SU(5) \otimes U(1)_{\text{PQ}}$ theory has the following Yukawa interactions:

$$\mathcal{L}_Y = 10 Y_3 10 5'_H + 10 (Y_1 5_H^* + Y_2 45_H^*) \bar{5} + \text{h.c.}, \quad (7.31)$$

which, together with the scalar potential needed to implement the DFSZ mechanism, fixes the charges of the fields under the global PQ symmetry as follows:

Field	$\bar{5}$	10	$5'_H$	5_H	45_H	24_H
PQ charge	α	β	-2β	$\alpha + \beta$	$\alpha + \beta$	$-(\alpha + 3\beta)/2$

After SSB, the masses for the charged leptons and down quarks are given by Eqs. 6.72, whereas the mass of the up quarks in this context is given by the following expression instead:

$$M_u = \sqrt{2} (Y_3 + Y_3^T) v_{5'}. \quad (7.32)$$

Notice that, in this case, $M_u = M_u^T$, which has strong implications for the proton decay channels with antineutrinos, as we are already familiar with from the previous scenarios. However, this time the symmetric nature of M_u raises from a prediction of the theory rather than from an empirical (phenomenological) need.

Moreover, an extra representation is needed in order to generate masses for the neutrinos. There are several options, each of them leading to different mechanisms. With two copies of a RH neutrino $1_i \equiv \nu_i^c$, singlets under $SU(5)$, the Type-I seesaw mechanism can be implemented (see Sec. 1.2 and Sec. 6.2 for more details). In this case, the PQ would be fixed to $\beta = -2\alpha$ if 1 couples to 5_H , or $\beta = \alpha/2$ if it couples to $5'_H$ instead. The next option regarding simplicity would be the addition of a scalar antisymmetric representation 10_H and implement the Zee mechanism as presented in Sec. 6.3. In this scenario, the relevant Lagrangian for the neutrino mass generation is given by Eq. 6.70, which fixes the PQ charges as follows:

$$\begin{aligned} \bar{5} &\rightarrow e^{i\alpha} \bar{5}, & 10 &\rightarrow e^{-2i\alpha} 10, & 5'_H &\rightarrow e^{4i\alpha} 5'_H, \\ 24_H &\rightarrow e^{5i\alpha/2} 24_H, & 5_H/45_H &\rightarrow e^{-i\alpha} 5_H/45_H, & 10_H &\rightarrow e^{-2i\alpha} 10_H. \end{aligned}$$

See Sec. 6.2 from Chapter 6 for the discussion of other possibilities to generate neutrino masses in this context.

Coming back to the scalar potential responsible for the implementation of the DFSZ mechanism, the interactions in Eq. 7.30 written in terms of the SM fields read as

$$V \supset (m_{12}^2 + \lambda H_1^\dagger H_2) H_1^\dagger H_2 + H_3^\dagger \Sigma_0^2 (\lambda_{a1} H_1 + \lambda_{a2} H_2) + \text{h.c.} \quad (7.33)$$

Following the approach that we introduced in Chapter 2, let us determine *how much* of the axion lives inside each of the scalar representations. After SSB, all neutral fields acquire a vev and the CP-odd component can be written as a function of the two GBs

generated by the spontaneous breaking of two global symmetries of the scalar potential:

$$H_1^0 \supset \frac{v_1}{\sqrt{2}} e^{i a_1/v_1} = \frac{v_1}{\sqrt{2}} e^{i(q \hat{a}_Z + \text{PQ}_1 \hat{a})}, \quad (7.34)$$

$$H_2^0 \supset \frac{v_2}{\sqrt{2}} e^{i a_2/v_2} = \frac{v_2}{\sqrt{2}} e^{i(q \hat{a}_Z + \text{PQ}_2 \hat{a})}, \quad (7.35)$$

$$H_3^0 \supset \frac{v_3}{\sqrt{2}} e^{i a_3/v_3} = \frac{v_3}{\sqrt{2}} e^{i(q \hat{a}_Z + \text{PQ}_3 \hat{a})}, \quad (7.36)$$

$$\Sigma_0 \supset \frac{v_\Sigma}{\sqrt{2}} e^{i a_\Sigma/v_\Sigma} = \frac{v_\Sigma}{\sqrt{2}} e^{i \text{PQ}_\Sigma \hat{a}}. \quad (7.37)$$

where \hat{a} and \hat{a}_Z are the phases of the axion and the EW GB eaten by the Z, respectively. The q factor is the contribution related to the EW quantum numbers and PQ_i parametrizes the presence of the axion in each of the scalar representations. The terms of the scalar potential fix the following conditions for the PQ_i charges:

$$\text{PQ}_1 = \text{PQ}_2, \quad \text{and} \quad \text{PQ}_{1,2} + 2\text{PQ}_\Sigma - \text{PQ}_3 = 0. \quad (7.38)$$

As done explicitly in Chapter 2, linearizing the kinetic terms we end up with two conditions,

$$v_1^2 \text{PQ}_1 + v_2^2 \text{PQ}_2 + v_3^2 \text{PQ}_3 = 0, \quad (7.39)$$

$$v_1^2 \text{PQ}_1^2 + v_2^2 \text{PQ}_2^2 + v_3^2 \text{PQ}_3^2 + v_\Sigma^2 \text{PQ}_\Sigma^2 = n_a^2, \quad (7.40)$$

where the first one is due to the orthogonality of the GBs, and the second one is demanded by the normalization of the kinetic terms, being n_a the normalization factor of the CP-odd phase $\hat{a} \equiv a/n_a$. The above conditions fix the presence of the axion in each of the neutral scalars as follows,

$$H_1^0 \supset \frac{v_1}{\sqrt{2}} e^{i \frac{a}{n}}, \quad H_2^0 \supset \frac{v_2}{\sqrt{2}} e^{i \frac{a}{n}}, \quad H_3^0 \supset \frac{v_3}{\sqrt{2}} e^{-i \left(\frac{v_1^2 + v_2^2}{v_3^2} \right) \frac{a}{n}}, \quad \Sigma_0 \supset \frac{v_\Sigma}{\sqrt{2}} e^{-i \left(\frac{v^2}{2v_3^2} \right) \frac{a}{n}}, \quad (7.41)$$

where $v = \sqrt{v_1^2 + v_2^2 + v_3^2} = 246$ GeV, and

$$n \equiv \frac{n_a}{\text{PQ}_1} = \frac{\sqrt{v_1^2 + v_2^2}}{v_3} v \sqrt{1 + \frac{v_\Sigma^2 v^2}{4v_3^2(v_1^2 + v_2^2)}} \simeq \frac{v^2 v_\Sigma}{2 v_3^2}. \quad (7.42)$$

In the last step from Eq. 7.42, the limit $v_\Sigma \gg v_1, v_2, v_3$ has been taken, which is justified by the fact that M_{GUT} is about 13 orders of magnitude higher than the EW scale. As expected, Eq. 7.42 brings out that the axion lives predominantly in the Σ_0 field.

In the broken phase, the Yukawa Lagrangian from Eq. 7.31 reads as,

$$\mathcal{L}_Y \supset \bar{u}_R M_u u_L e^{-i\left(\frac{v_1^2+v_2^2}{v_3^2}\right)\frac{a}{n}} + \bar{d}_R M_d d_L e^{-i\frac{a}{n}} + \bar{e}_R M_e e_L e^{-i\frac{a}{n}} + \text{h.c.}, \quad (7.43)$$

where, by applying the following PQ rotations,

$$u_{L/R} \rightarrow e^{\pm i\left(\frac{v_1^2+v_2^2}{2v_3^2}\right)\frac{a}{n}} u_{L/R}, \quad d_{L/R} \rightarrow e^{\pm i\frac{a}{2n}} d_{L/R}, \quad \text{and} \quad e_{L/R} \rightarrow e^{\pm i\frac{a}{2n}} e_{L/R}, \quad (7.44)$$

the axion can be reabsorbed from the Yukawa Lagrangian and the following $G\tilde{G}$ term is consequently generated (see Eq. 2.111):

$$\mathcal{L} \supset \frac{\alpha_3}{8\pi} \frac{a}{n} \frac{3v^2}{v_3^2} G_{\mu\nu}^a \tilde{G}_a^{\mu\nu}. \quad (7.45)$$

Comparing the above expression with Eq. 7.12, one can identify the PQ scale as

$$f_a \equiv \frac{v_\Sigma}{N} = \frac{v_3^2}{3v^2} n \simeq \frac{v_\Sigma}{6}. \quad (7.46)$$

Therefore, in order to predict the mass of the axion in the context of this simple GUT theory based on $SU(5)$, the GUT scale needs to be determined. As in the KSVZ- $SU(5)$ scenario described in Sec. 7.1, the GUT scale is fixed by the unification constraints on the gauge couplings and the experimental bounds on proton decay.

7.2.1 Predicting the GUT scale

This scenario is very similar to the Adjoint $SU(5)$ discussed in the previous section because Φ_1 , Φ_3 and $H_2 \subset 45_H$ play the key role in achieving unification.⁶ Here, however, there is an extra Higgs doublet, H_3 , although a significant impact in the RGEs from the fundamental representation of $SU(5)$ is not expected (see Table 6.1). Fig. 7.9

⁶In this case we do not have the fermion fields in the 24 contributing to the RGEs, but we note that their splitting is small and so it is their contribution to the running equations.

displays the parameter space allowed by the unification conditions shown in Eqs. 6.19 and 6.20 in the context of the simplest realistic GUT where the DFSZ mechanism can be implemented. Unification constraints determine M_{GUT} as a function of M_{Φ_1} and the doublet masses M_{H_2} and M_{H_3} , as shown by the blue region in the left panel in Fig. 7.9. We note that, in this case, there is no problem at all in having a light Φ_3 since it does not mediate the decay of the proton because, in this case, the fields in the 45_H do not interact with the 10_{10} in the Yukawa Lagrangian. On the right panel of Fig. 7.9, we show the relation between M_{GUT} and α_{GUT} . As in the left panel, the region shaded in blue satisfies the unification constraints as we vary M_{H_2} and M_{H_3} from 1 TeV to the GUT scale. As in the previous case, the upper bound on the GUT scale is given by the lightest possible value of the Manohar-Wise $\Phi_1 \sim (8, 2, 1/2)$, $M_{\Phi_1} > 1$ TeV [286], shown by a purple line in Fig. 7.9. Elseways, the lower possible GUT scale is fixed by proton decay bounds.

Analogously to the Adjoining $SU(5) \otimes U(1)_{\text{PQ}}$, the most constrained proton decay channel depends on the unknown V_e factor and, unfortunately, cannot set a lower bound for M_{GUT} . See Fig. 7.10 for the prediction on the proton lifetime in this channel under several choices of V_e for illustration. However, for the next strongest bound, $p \rightarrow K^+ \bar{\nu}$, the prediction of the proton decay width for the channels involving anti-neutrinos can be cleanly predicted because $M_u = M_u^T$ in this context. The decay rate, together with that for the $p \rightarrow \pi^+ \bar{\nu}$ channel, are given by Eq. 6.52. As the reader can notice from this equation, the relation between the two decay channels into anti-neutrinos is fixed.

In Fig. 7.11, we present the predictions and correlation for both proton decay channels into antineutrinos. The red shaded area shows the excluded parameter space from SK bounds for both $\tau(p \rightarrow K^+ \bar{\nu}) > 5.9 \times 10^{33}$ years [271] and $\tau(p \rightarrow \pi^+ \bar{\nu}) > 3.9 \times 10^{32}$ years [272]. The projected bounds on the decay channel $p \rightarrow K^+ \bar{\nu}$ from the HK collaboration $\tau(p \rightarrow K^+ \bar{\nu}) > 3.2 \times 10^{34}$ years [320] and the DUNE collaboration $\tau(p \rightarrow K^+ \bar{\nu}) > 5 \times 10^{34}$ years [317] are shown with a green and orange dashed lines, respectively. The purple shaded areas correspond to the parameter space excluded by collider bounds on the colored doublet $M_{\Phi_1} > 1$ TeV [286], where we have assumed the $M_{H_{2,3}} = M_{\text{GUT}}$ in order to account for the largest possible range.

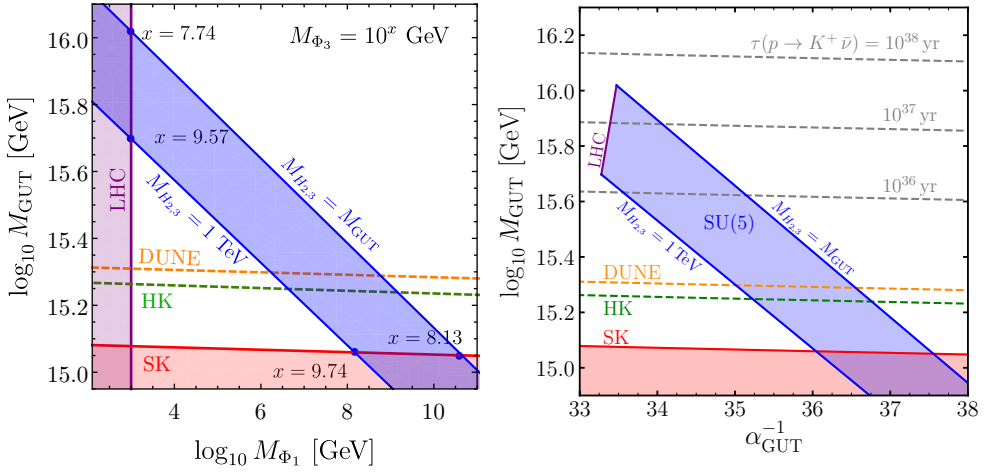


Figure 7.9: Unification constraints in the parameter space. The region shaded in blue satisfies the unification constraints. The red area corresponds to the parameter space ruled out by the SK collaboration $\tau(p \rightarrow K^+\bar{\nu}) > 5.9 \times 10^{33}$ years [271], the green and orange dashed lines show the projected bounds from the HK collaboration $\tau(p \rightarrow K^+\bar{\nu}) > 3.2 \times 10^{34}$ years [320] and the DUNE collaboration $\tau(p \rightarrow K^+\bar{\nu}) > 5 \times 10^{34}$ years [317], respectively. The parameter space excluded by collider bounds on $M_{\Phi_1} > 1$ TeV [286] is colored in purple. *Left Panel:* In blue, prediction of the GUT scale as a function of the $\Phi_1 \sim (8, 2, 1/2)$ mass. *Right Panel:* In blue, prediction of the GUT scale as a function of α_{GUT} . In gray dashed lines we show the sensitivity of different hypothetical decay widths for the $p \rightarrow K^+\bar{\nu}$ channels. In both panels the width of the blue band scans over the possible mass range for the Higgs doublets H_2 and H_3 . *Figure extracted from Ref. [321].*

We note that the theory predicts the upper bound on the proton decay lifetime for the channels with antineutrinos,

$$\tau(p \rightarrow K^+\bar{\nu}) \lesssim 3.5 \times 10^{37} \text{ yr}, \quad \text{and} \quad \tau(p \rightarrow \pi^+\bar{\nu}) \lesssim 1.8 \times 10^{36} \text{ yr}, \quad (7.47)$$

which expose the theory to be tested in current or future proton decay experiments. We emphasize that the peculiar feature $M_u = M_u^T$ from this theory allows us to predict the upper bound of the axion mass window.

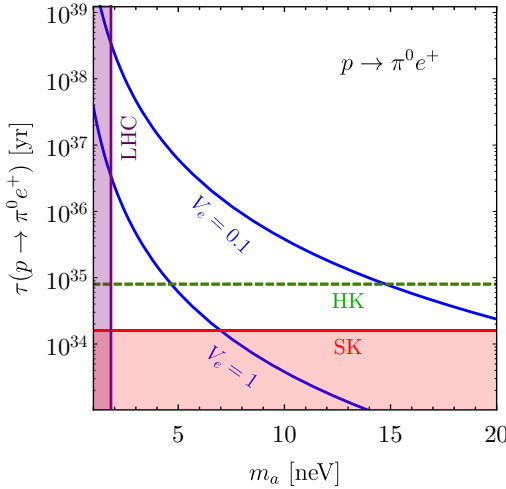


Figure 7.10: Predictions for the proton lifetime from the decay channel $p \rightarrow \pi^0 e^+$. The red area shows the SK constraints, $\tau(p \rightarrow \pi^0 e^+) > 1.6 \times 10^{34}$ years [158], while the green dashed line shows the HK collaboration projected bound, $\tau(p \rightarrow \pi^0 e^+) > 8 \times 10^{34}$ years [273]. The region shaded in purple is ruled out by the collider constraints on the Φ_1 field, $M_{\Phi_1} > 1$ TeV [286]. *Figure extracted from Ref. [321].*

We show the experimental constraints for proton decay in both of the panels in Fig. 7.9 as follows: we show in red the excluded region by the bound on $p \rightarrow K^+ \bar{\nu}$ from the SK collaboration, $\tau(p \rightarrow K^+ \bar{\nu}) > 5.9 \times 10^{33}$ years [271], whereas the projected bound on the same decay from the HK collaboration, $\tau(p \rightarrow K^+ \bar{\nu}) > 3.2 \times 10^{34}$ years [320] and the DUNE collaboration, $\tau(p \rightarrow K^+ \bar{\nu}) > 5 \times 10^{34}$ years [317], are shown with a green and orange dashed lines, respectively. We remind the reader that with the 45_H alone unification can be achieved, as shown in Fig. 7.9, and the splitting in the $5'_H$ helps to increase the parameter space where unification occurs. We find that the allowed window for the GUT scale is given by

$$M_{\text{GUT}} = (1.12 - 10.45) \times 10^{15} \text{ GeV}. \tag{7.48}$$

7.2.2 Axion mass and phenomenology

According to Eq. 7.24, in the context of the f_a obtained in Eq. 7.46, and the relation of the $\langle 24_H \rangle$ with the GUT scale, given by Eq. 6.12, we have that

$$m_a = 5.691(51) \times 10^{-6} \text{ eV} \left(10^{12} \text{ GeV} / \underbrace{\frac{M_{\text{GUT}}}{\sqrt{\alpha_{\text{GUT}}}} \frac{1}{2\sqrt{30\pi}}}}_{f_a} \right). \tag{7.49}$$

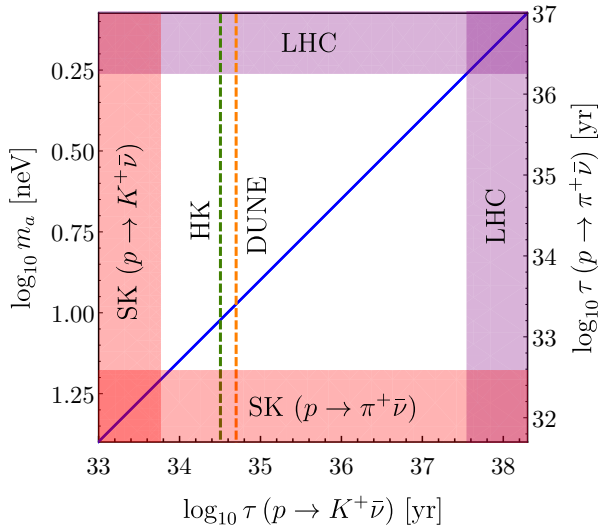


Figure 7.11: Correlation between the proton lifetime prediction for the channels $p \rightarrow K^+ \bar{\nu}$ and $p \rightarrow \pi^+ \bar{\nu}$ with respect to the axion mass. The regions shaded in red show the parameter space excluded by the proton decay bounds from the SK collaboration. The green and orange dashed lines give the projected bounds from the HK collaboration and the DUNE collaboration, respectively. The region shaded in purple is the parameter space ruled out by collider bounds on Φ_1 assuming $M_{H_{2,3}} = M_{\text{GUT}}$. *Figure extracted from Ref. [321].*

We note that the decay width of both channels depends on the ratio $(\alpha_{\text{GUT}}/M_{\text{GUT}}^2)$ in exactly the same way as the expression above, allowing then to relate both observables by

$$m_a \simeq 4.5/\tau^{1/4}(p \rightarrow K^+ \bar{\nu}) \text{ eV}. \quad (7.50)$$

Therefore, if any of these two decay channels is discovered in proton decay experiments one can automatically predict the other channel and the axion mass, as shown in Fig. 7.11. In there, we present the prediction of the axion mass from the lifetime of any of the proton decay channels into antineutrinos. The white region in Fig. 7.11 shows the

available window for the axion mass in this model, which is predicted to be

$$m_a = (1.87 - 16.05) \times 10^{-9} \text{ eV.} \tag{7.51}$$

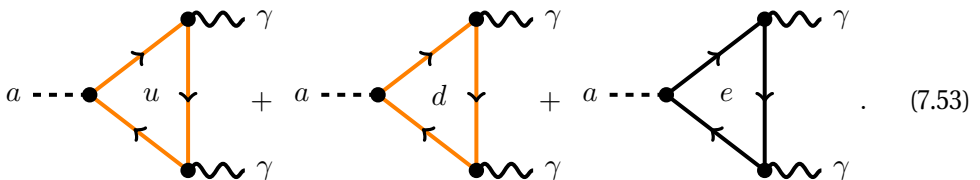
On the other hand, the bounds on the axion mass, which we will present in the following, can constrain the proton decay channels as Eq. 7.50 states. This powerful correlation is an outcome from having a consistent and self-contained theory as a framework. Notice that it relates unambiguously several predictions, what allows to test the theory and make progress if those are successfully noted.

In the following, we study the axion couplings to SM particles in the predicted mass window. We focus on the axion to photon coupling and the interaction between the axion and the EDM of the neutron for which there exist experiments that could probe this scenario. In this work, we consider the case in which the PQ symmetry is broken before inflation and in order to achieve the correct DM relic abundance we assume an initial misalignment angle of $\theta_i \approx 10^{-2}$ [132–134], as in the KSVZ scenario.

The interaction between the axion and photons can be obtained by rotating the axion field from the Yukawa terms of the charged fermions is given by the red framed term in Eq. 2.153, where the effective coupling $g_{a\gamma\gamma}$ is given by Eq. 2.123 with $E/N = 8/3$ as in the KSVZ- $SU(5)$.⁷ In this theory, the fields contributing to the E factor, which is given by,

$$E = 2 \times \frac{v_\Sigma}{n} \left(\underbrace{\left(\frac{1}{3}\right)^2 \times 3 \times 2}_{d_L} + \underbrace{\left(\frac{2}{3}\right)^2 \frac{v_1^2 + v_2^2}{v_3^2} \times 3 \times 2}_{u_L} + \underbrace{(-1)^2 \times 2}_{e_L} \right) \times \underbrace{2}_{L \rightarrow R} = 16 \tag{7.52}$$

are listed below:



⁷This is common when rotating complete representations of $SU(5)$.

We present our results in Fig. 7.12. The solid blue line corresponds to the $g_{a\gamma\gamma}$ coupling in the predicted mass window and we show the projected sensitivities of the ABRACADABRA experiment [150]. The broadband approach in its Phase III, which corresponds to a configuration with magnetic field of 5 T and a volume of 100 m^3 , will be sensitive to a portion of this mass window, as shown by the orange region. This sensitivity takes into account only the irreducible source of noise in the experiment. Phase III of the resonant approach, shown by a purple dotted-dashed line, will be able to cover most of the predicted mass window. The latter assumes that the noise in the SQUID is much smaller than the thermal noise.

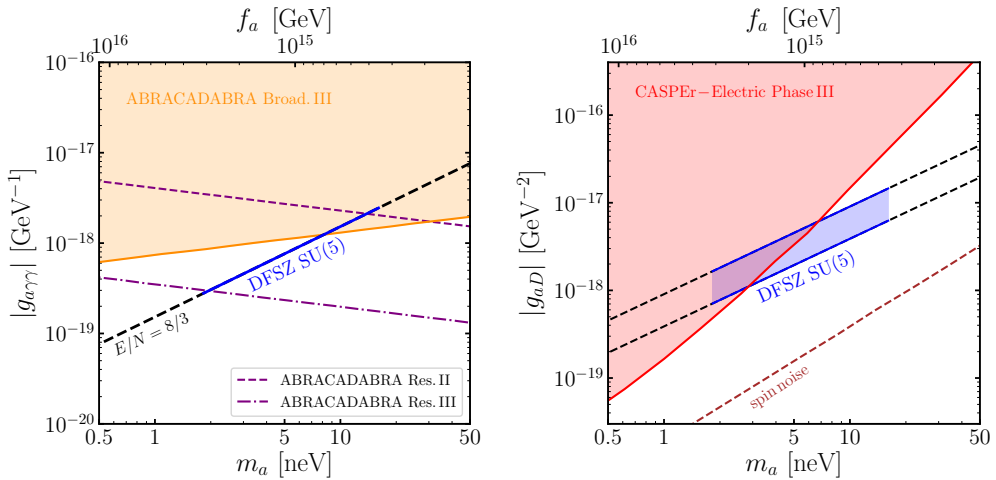


Figure 7.12: *Left panel:* The axion coupling to photons as a function of the axion mass. The blue solid line corresponds to the prediction in the theory considered in this paper. The region shaded in orange gives the projected sensitivity for Phase III of the ABRACADABRA [150] experiment using the broadband approach. The purple dashed (dotted-dashed) line corresponds to Phase II (III) of the resonant approach. *Right panel:* The axion coupling to the neutron EDM as a function of the axion mass. The blue band corresponds to the theoretical error on the g_{aD} coupling [115]. The region shaded in red gives the projected sensitivity to Phase III of the CASPER-Electric [156] experiment. *Figure extracted from Ref. [321].*

The DM axion background field induces an oscillating EDM for the neutron, given by Eq. 7.28 for the f_a predicted in this context. The CASPER-Electric [154,156] experiment

aims to measure this oscillating nEDM and Phase III of this experiment will probe the lower portion of the predicted mass window as shown in Fig. 7.12. Experimental limits have already been found using this search strategy [322]. However, the advanced stage of CASPER-Electric we show in Fig. 7.12 relies on technology that is currently under development. When the projected sensitivities for ABRACADABRA and CASPER-Electric are combined, these experiments will be able to fully probe the mass window in Eq. 7.51. See Chapter 2 for more details on these axion experiments.

One important difference between this scenario and the one studied in Section 7.1 is that here the axion has a tree-level coupling to electrons. However, all the experimental constraints on this coupling are well above the prediction for the QCD axion with mass around 10^{-9} eV. It is important to emphasize that this theory can be fully tested using the predictions for the axion mass and upper bounds on the proton decay lifetimes.

7.3 Conclusions

The QCD axion remains one of the most appealing candidates for the DM in the Universe. We have discussed the implementation of the DFSZ and KSVZ mechanisms in renormalizable grand unified theories based on the gauge symmetry $SU(5)$ since in their context the axion mass can be predicted. In order to connect the GUT scale to the Peccei-Quinn scale we require the same scalar field to break both symmetries. We showed that in the simplest renormalizable models the 5_H and 45_H Higgses must couple in the same way to matter and have the same Peccei-Quinn charge.

In the first part of this chapter, we have shown that the same fermionic field, 24, needed to generate neutrino masses can be used to implement the KSVZ mechanism. The colored and the electrically-charged fields in the 24 generate the couplings of the axion to the gluons and the photons respectively, while the rest of the fields generate neutrino masses through the seesaw mechanism. We have investigated the unification of gauge interactions taking into account the collider and proton decay constraints and we have found that the allowed GUT scale is in a small range which allows to predict the axion mass in the window

$$m_a^{\text{KSVZ}} = (2.9 - 13.5) \times 10^{-9} \text{ eV}.$$

We focused on the scenario where the PQ symmetry is broken before inflation and discussed the predictions for the different axion experiments showing that this theory could be fully tested in the near future by the ABRACADABRA and the CASPER-Electric experiments.

In the second part of the chapter, we presented the minimal realistic renormalizable GUT theory where the DFFZ mechanism can be implemented, following the idea of Wise, Georgi and Glashow. The PQ scale is determined by the GUT scale which predicts the axion mass in the range:

$$m_a^{\text{DFSZ}} \simeq (2 - 16) \times 10^{-9} \text{ eV}.$$

The fact that the mass matrix for up-quarks is symmetric implies that the proton decay channels with antineutrinos is a function of the known mixings at low energy. In the DFSZ-theory (and also in the KSVZ-theory for consistency with proton decay bounds), the upper bounds on the proton decay lifetimes with antineutrinos are given by

$$\tau(p \rightarrow K^+ \bar{\nu}) \lesssim 4 \times 10^{37} \text{ yr}, \quad \text{and} \quad \tau(p \rightarrow \pi^+ \bar{\nu}) \lesssim 2 \times 10^{36} \text{ yr}.$$

These theories are unique due to the fact that they can be fully probed by proton decay experiments such as DUNE or Hyper-Kamiokande and axion experiments such as ABRACADABRA or CASPER.

The theoretical framework studied in this article based on $SU(5) \times U(1)_{\text{PQ}}$ can be considered as appealing theory where it is possible to understand the unification of the SM forces, the origin of neutrino masses, DM, the strong CP problem and the baryon asymmetry through leptogenesis. Furthermore, the lifetime for the proton can be predicted and exotic signatures at colliders are expected.

It should be remarked that the beauty of these theories relies on their capability to predict the axion mass together with some correlations among other observables that arise as a consequence of having a well-defined and consistent theory as a framework.

8.- Effective Field Theories for $b \rightarrow c$ transitions

If the apparent disagreement between the SM predictions for the observables involving $b \rightarrow c$ transitions and their experimental values is further confirmed, these flavour anomalies will become a clear claim for NP affecting the weak sector. Keeping in mind that the SM cannot be the ultimate theory, as we have discussed along this thesis, we should adopt the perspective of an EFT whose Lagrangian can be written as an infinite expansion of operators of all possible dimensions,

$$\mathcal{L}_{\text{SM}}^{\text{eff}} = \mathcal{L}_{\text{SM}}^4 + \sum_{n=5}^{\infty} \frac{C_n}{\Lambda^{n-4}} \mathcal{O}^{(n)}, \quad (8.1)$$

where C_n are dimensionless quantities that parametrize the strength of each operator, called Wilson Coefficients (WCs), and $\mathcal{L}_{\text{SM}}^4$ is the renormalizable SM Lagrangian. In this way, any NP effect can be parametrized as a function of the terms from the above expansion, suppressed by the scale of NP Λ . A semi-leptonic decay such as those based on the transition $b \rightarrow c\tau\bar{\nu}$ can be described by four-fermion operators, so that we will stick to the most general dimension-6 Hamiltonian at the bottom quark mass scale, invariant under $SU(3)_c \otimes U(1)_Q$, involving such fermion currents:

$$\mathcal{H}_{\text{eff}} = \frac{4G_F V_{cb}}{\sqrt{2}} \left(\mathcal{O}_{LL}^V + \sum_{\substack{X=S,V,T \\ A,B=L,R}} C_{AB}^X \mathcal{O}_{AB}^X \right), \quad (8.2)$$

where the operators are classified according to their Lorentz structure and the chirality of the currents composing the operator, as listed below:

$$\begin{aligned}
\mathcal{O}_{AB}^V &\equiv (\bar{c} \gamma^\mu P_A b) (\bar{\tau} \gamma_\mu P_B \nu) , \\
\mathcal{O}_{AB}^S &\equiv (\bar{c} P_A b) (\bar{\tau} P_B \nu) , \\
\mathcal{O}_{AB}^T &\equiv \delta_{AB} (\bar{c} \sigma^{\mu\nu} P_A b) (\bar{\tau} \sigma_{\mu\nu} P_A \nu) .
\end{aligned} \tag{8.3}$$

We note that the tensor operators have two currents with the same chirality. This is a direct consequence of the Dirac-algebra identity $\gamma_5 \sigma^{\mu\nu} = -\frac{i}{2} \varepsilon^{\mu\nu\alpha\beta} \sigma_{\alpha\beta}$, which implies $\sigma_{\mu\nu} \otimes \sigma^{\mu\nu} \gamma_5 = \sigma_{\mu\nu} \gamma_5 \otimes \sigma^{\mu\nu}$ and $\sigma_{\mu\nu} \gamma_5 \otimes \sigma^{\mu\nu} \gamma_5 = \sigma_{\mu\nu} \otimes \sigma^{\mu\nu}$,¹ where \otimes symbolizes the contraction between two fermion currents. See also the Fierz identities in Appendix A. Notice also that the above effective Hamiltonian is built from the SM matter fields plus a RH singlet $\nu_R \sim (1, 1, 0)$. We will consider the existence of light RH sterile neutrinos in order to obtain the most general expressions for our study.

Last thing to remark from Eq. 8.2 is the factorization of the SM contribution from the LH vector current: the normalization of the Hamiltonian in Eq. 8.2 is chosen such that it matches with the contribution from the integration of the W_μ boson. In this way, by setting all WCs to zero the SM is recovered. In other words, any non-zero WC automatically implies NP associated to an UV-mediator whose integration generates at low energies the corresponding non-renormalizable operator.

8.1 New physics behind the $b \rightarrow c$ anomalies

There are in total eleven (tree-level) UV-mediators from different nature (scalars, vector bosons, LQs) that could generate a non-zero WC in the effective Hamiltonian listed in Eq. 8.2. Those can be found by considering all possible tree-level interactions between the fermion fields and a generic new mediator, in this case including the sterile RH neutrino $\nu_R \sim (1, 1, 0)$ as part of the matter content. In Tab. 8.1 the quantum numbers under the SM gauge group of the matter fields, expressed as left-chiral fields, are listed. Let us consider the three point interaction between a couple of fermions, Ψ_L and Φ_L , and the new mediator: $\mathcal{L} \supset \Psi_L^T C A \Phi_L$ for scalar interactions, and $\mathcal{L} \supset \bar{\Psi}_L \gamma_\mu A^\mu \Phi_L$

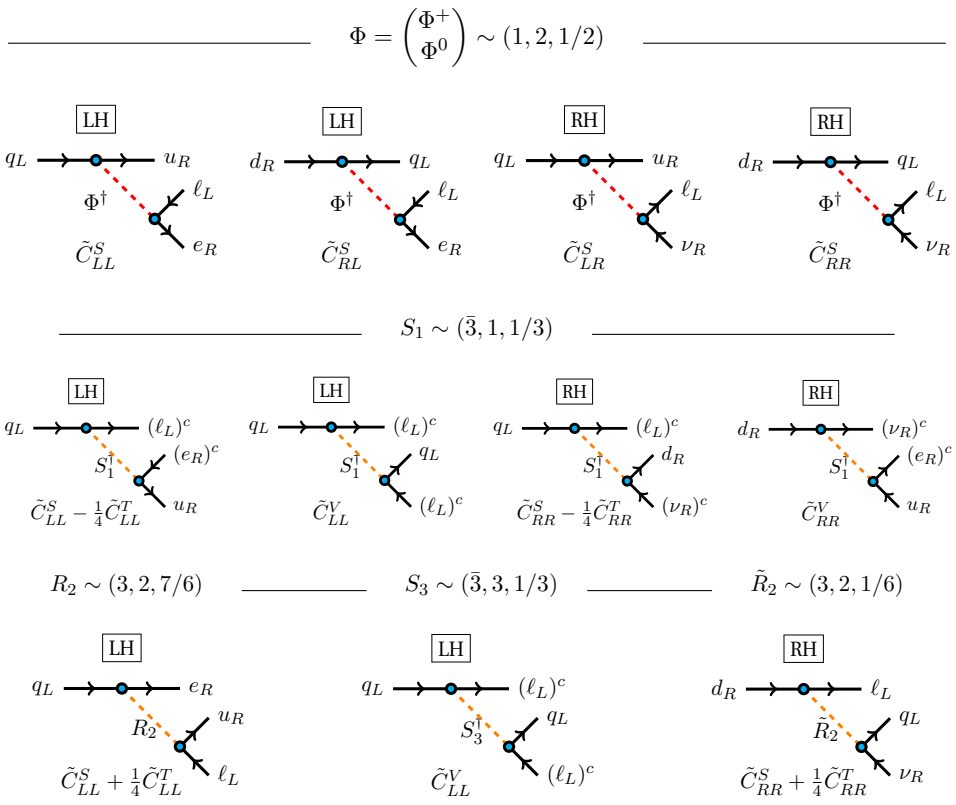
¹We will use the convention $\varepsilon^{0123} = -\varepsilon_{0123} = -1$ along this chapter.

Field	ℓ_L	Q_L	$(u^c)_L$	$(d^c)_L$	$(e^c)_L$	$(\nu^c)_L$
Q.N.	$(1, 2, -1/2)$	$(3, 2, 1/6)$	$(\bar{3}, 1, -2/3)$	$(\bar{3}, 1, 1/3)$	$(1, 1, 1)$	$(1, 1, 0)$

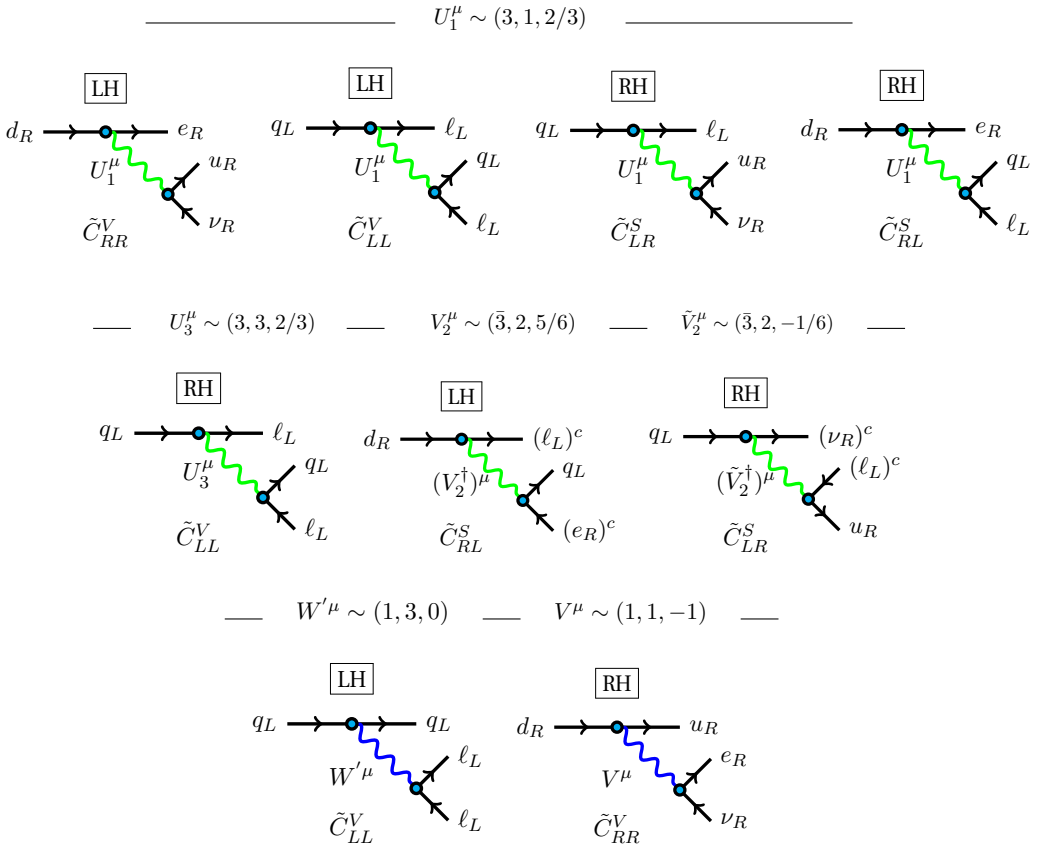
Table 8.1: Quantum numbers of the matter fields potentially involved in the $b \rightarrow c\tau\bar{\nu}$ transitions according to the SM gauge group: $(SU(3)_c, SU(2)_L, U(1)_Y)$.

for spin-1 bosons. By imposing to these vertices Lorentz and gauge invariance, the interactions collected below are allowed, where the fermion lines have been chosen to reproduce the transition $b \rightarrow c\tau\bar{\nu}$.

-Scalar mediators-



-Vector mediators-



The WCs to which the previous diagrams contribute are listed below each interaction. Furthermore, the interactions are also labeled as LH and RH according to the chirality of the leptonic current involved. In the following, we will show explicitly how each of the eleven mediators contributes to the effective Hamiltonian in Eq. 8.2 when integrated out. However, one last thing should be remarked before starting. In the diagrams above, the WCs generated by the possible mediators have been labeled with a tilde. This is because they are different from those appearing in Eq. 8.2 as a consequence of the hierarchy of scales.

The Hamiltonian in Eq. 8.2 describes $b \rightarrow c\tau\bar{\nu}$ transitions in terms of the WCs of an EFT framework defined at the b -quark mass scale. The EFT in this range is

conventionally called Weak Effective Theory (WET) and is composed of the five lightest quarks and the three generations of leptons, and ruled by the $SU(3)_c \otimes U(1)_Q$ gauge symmetry. This is a valid approach assuming – as strongly suggested by all available collider data – that no new d.o.f. exists coupling to this channel with a mass around or below the b quark. However, our goal is to gain insight into the high-energy structure of the theory. To that aim, renormalization-group techniques are used to relate the coefficients entering in the $b \rightarrow c\tau\bar{\nu}$ transitions at the level of the experiment to those relevant at the scale of the potential new high-energy d.o.f.. This process involves several scales and thresholds, as illustrated in Fig. 8.1. Notice that above the EW scale,

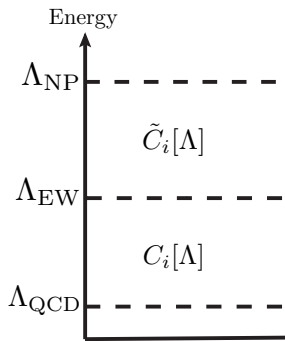


Figure 8.1: Relevant scales for the study of the B anomalies. The dashed lines indicate the thresholds between different EFTs. The WCs $\tilde{C}_i[\Lambda]$ are dimensionless parameters encoding the NP effects, while the $C_i[\Lambda]$ are their transcription at the b -quark scale, taking into account the different EFT frameworks where they are defined and the running effects between them.

the Lagrangian has not undergone SSB and, therefore, the fermionic fields should be expressed in terms of weak eigenstates rather than mass eigenstates. Moreover, the top quark, the EW gauge bosons and the Higgs boson have to be considered as new d.o.f. in the theory. The relevant framework at this scale is the full SM including the RH neutrino, with the addition of the effects of NP. In order to relate the physics at the different scales, one should take into account the gap between the scale where the NP d.o.f. generate the corresponding effective Lagrangian after they are integrated out, and the bottom quark scale where the $b \rightarrow c\tau\bar{\nu}$ transitions take place at experiment. The first EFT should be invariant under the SM gauge group $SU(3)_c \otimes SU(2)_L \otimes U(1)_Y$, while the second one corresponds to the WET. Such energy gap will generate the running of the operators that will determine the relation between the \tilde{C}_i and the WCs appearing in Eq. 8.2. For the first gap ($\Lambda_{\text{QCD}} - \Lambda_{\text{EW}}$), the relation of the WCs in Eq. 8.2 to the coefficients at the EW scale is determined by QCD and is known [323–326]. Finally, one

has to consider the running from Λ_{EW} to Λ_{NP} [327–331]. The corresponding equations can be solved numerically, but also analytically to very good approximation [332].

From the eleven possible mediators generating relevant contributions to the $b \rightarrow c\tau\bar{\nu}$ processes, we will start analyzing the spin-0 fields.

8.1.1 $R_2 \sim (3, 2, 7/6)$ scalar leptoquark

According to the quantum numbers of this scalar LQ, the possible interactions allowed by Lorentz and gauge invariance read as,

$$-\mathcal{L}^{R_2} \supset Y_{eq}(e^c)_L^T C R_2^\dagger q_L + Y_{u\ell}(u^c)_L^T C (i\sigma_2 R_2^*)^\dagger \ell_L + \text{h.c.}, \quad (8.4)$$

which can be written in a perhaps more suitable way,

$$-\mathcal{L}^{R_2} \supset Y_{eq} \bar{e}_R R_2^\dagger q_L + Y_{u\ell} \bar{u}_R (i\sigma_2 R_2^*)^\dagger \ell_L + \text{h.c.}. \quad (8.5)$$

where we used the identity $(\Psi^c)_L = (\Psi_R)^c$ (see Appendix A), The fermion fields u , d , e and ν represent each of the three family members with the same quantum numbers. The Yukawa couplings from Eq. 8.5 are the matrix elements corresponding to the particular u , d -type quarks and the e and ν leptons involved in the transition. Therefore, they will be considered as c-numbers instead of matrices.² R_2 is a doublet under $SU(2)_L$, so that it decomposes in two components split by the isospin, i.e. $R_2 = (R_2^{5/3}, R_2^{2/3})^T$, where the super-index refers to the electric charge of the field. In these terms,

$$-\mathcal{L}^{R_2} \supset Y_{eq} \bar{e}_R (R_2^{5/3*} u_L + R_2^{2/3*} d_L) + Y_{u\ell} \bar{u}_R (R_2^{2/3} \nu_L - R_2^{5/3} e_L) + \text{h.c.}. \quad (8.6)$$

The above Lagrangian explicitly shows that the relevant fields for the $b \rightarrow c\tau\bar{\nu}$ transition is going to be $R_2^{2/3}$. It is reasonable to assume that its mass is heavier than the energy scale where such process takes places. Therefore, by solving the equations of motion,

$$\frac{\delta \mathcal{L}^{R_2}}{\delta R_2^{2/3}} = 0 \quad \Rightarrow \quad R_2^{2/3*} = -\frac{1}{M_{R_2}^2} (Y_{u\ell} \bar{u}_R \nu_L + Y_{eq}^* \bar{d}_L e_R) + \mathcal{O}(M_{R_2}^{-4}), \quad (8.7)$$

²That is why we will use * instead of \dagger , and the coupling will not be affected by the possible transpositions.

where the kinetic term of R_2 has been omitted since it contributes to higher order terms in the heavy mass expansion. Substituting this in Eq. 8.6, we obtain the following effective Lagrangian,

$$\mathcal{L}_{\text{eff}}^{R_2^{2/3}} \supset \frac{Y_{eq} Y_{ul}}{M_{R_2}^2} \overline{u_R} \nu_L \overline{e_R} d_L + \text{h.c.} \quad (8.8)$$

In order to relate the above interactions with the effective Hamiltonian presented in Eq. 8.2, we should reorder the fields by using the proper Fierz identities:³

$$\mathcal{L}_{\text{eff}}^{R_2^{2/3}} = -\frac{Y_{eq} Y_{ul}}{2M_{R_2}^2} \left(\overline{u_R} d_L \overline{e_R} \nu_L + \frac{1}{4} \overline{u_R} \sigma_{\mu\nu} d_L \overline{e_R} \sigma^{\mu\nu} \nu_L \right) + \text{h.c.} \quad (8.9)$$

From the above Lagrangian one can easily identify the non-zero WCs predicted in this context, $\tilde{C}_{LL}^S = 4\tilde{C}_{LL}^T$, which are besides correlated as a consequence of applying the Fierz identities at the scale where $R_2^{2/3}$ is integrated out.

8.1.2 $\tilde{R}_2 \sim (3, 2, 1/6)$ scalar leptoquark

This case is very similar to the previous one; we are also dealing with a scalar LQ, doublet under the $SU(2)_L$ gauge group. The allowed interactions with matter for \tilde{R}_2 are given by

$$-\mathcal{L}^{\tilde{R}_2} \supset Y_{d\ell} (d^c)_L^T C (i\sigma_2 \tilde{R}_2^*)^\dagger \ell_L + Y_{\nu q} (\nu^c)_L^T C \tilde{R}_2^\dagger q_L + \text{h.c.} \quad (8.10)$$

Rewriting the above Lagrangian in terms of the two components of \tilde{R}_2 , i.e. $\tilde{R}_2 = (\tilde{R}_2^{-1/3}, \tilde{R}_2^{2/3})^T$, and also applying the proper charge conjugation relations,

$$-\mathcal{L}^{\tilde{R}_2} \supset Y_{d\ell} \overline{d_R} (\tilde{R}_2^{-1/3} \nu_L - \tilde{R}_2^{2/3} e_L) + Y_{\nu q} \overline{\nu_R} (\tilde{R}_2^{2/3*} u_L + \tilde{R}_2^{-1/3*} d_L) + \text{h.c.}, \quad (8.11)$$

one realizes that the relevant field for our study, i.e. the one that can contribute to $b \rightarrow c \tau \bar{\nu}$, is $\tilde{R}_2^{2/3}$. Proceeding as before, we end up with the following effective Lagrangian:

$$\mathcal{L}_{\text{eff}}^{\tilde{R}_2^{2/3}} = -\frac{Y_{d\ell} Y_{\nu q}}{M_{\tilde{R}_2}^2} (\overline{\nu_R} u_L) (\overline{d_R} e_L) + \text{h.c.} \quad (8.12)$$

³The Fierz identities that are used in this case, and also in most of the following scenarios are listed in Appendix A. This also applies to the charge conjugation properties.

Applying the Fierz identities, one can easily get the convenient form,

$$\mathcal{L}_{\text{eff}}^{\tilde{R}_2^{2/3}} = \frac{Y_{d\ell}^* Y_{\nu q}^*}{2M_{\tilde{R}_2}^2} \left(\overline{u_L} d_R \overline{e_L} \nu_R + \frac{1}{4} \overline{u_L} \sigma^{\mu\nu} d_R \overline{e_L} \sigma_{\mu\nu} \nu_R \right) + \text{h.c.}, \quad (8.13)$$

that allows one to identify the WCs involved.⁴ In this case, $\tilde{C}_{RR}^S = 4\tilde{C}_{RR}^T$, which are related among them by the application of Fierz relations.

8.1.3 $S_1 \sim (\bar{3}, 1, 1/3)$ scalar leptoquark

This case looks in principle simpler since S_1 is an EW singlet, however there are many interactions allowed. The Lagrangian in this case reads as,

$$-\mathcal{L}^{S_1} = Y_{q\ell} \overline{(qL)}^c i\sigma_2 \ell_L S_1 + Y_{eu} \overline{e_R}(u^c)_L S_1^* + Y_{d\nu} \overline{d_R} S_1^* (\nu^c)_L \\ + Y_{ud} \overline{u_R}(d^c)_L S_1 + Y_{qq} \overline{(qL)}^c i\sigma_2 S_1^* qL + \text{h.c.} \quad (8.14)$$

After integrating out S_1 , the relevant interactions for $b \rightarrow c\tau\bar{\nu}$ transitions are given by,

$$\mathcal{L}_{\text{eff}}^{S_1} \supset \frac{1}{M_{S_1}^2} \left(Y_{eu} Y_{q\ell} \overline{e_R}(u^c)_L \overline{(d_L)}^c \nu_L - Y_{d\nu} Y_{q\ell} \overline{d_R}(\nu^c)_L \overline{(u_L)}^c e_L \right. \\ \left. - Y_{q\ell} Y_{q\ell}^* \overline{e_L}(u_L)^c \overline{(d_L)}^c \nu_L + Y_{d\nu} Y_{eu}^* \overline{(u^c)}_L e_R \overline{d_R}(\nu^c)_L \right) + \text{h.c.} \quad (8.15)$$

Note that S_1 mediates proton decay and baryon number conservation would require $Y_{qq} = 0$ (S_1 cannot be too heavy if needed for accounting on the B-anomalies). Doing some gymnastics with the Fierz identities and the properties of the charge conjugate operator, the following effective interaction is derived,

$$\mathcal{L}_{\text{eff}}^{S_1} = - \frac{Y_{eu} Y_{q\ell}}{2M_{S_1}^2} \left(\overline{u_R} d_L \overline{e_R} \nu_L - \frac{1}{4} \overline{u_R} \sigma_{\mu\nu} d_L \overline{e_R} \sigma^{\mu\nu} \nu_L \right) \\ + \frac{Y_{d\nu}^* Y_{q\ell}^*}{2M_{S_1}^2} \left(\overline{u_L} d_R \overline{e_L} \nu_R - \frac{1}{4} \overline{u_L} \sigma_{\mu\nu} d_R \overline{e_L} \sigma^{\mu\nu} \nu_R \right) \\ - \frac{Y_{q\ell} Y_{q\ell}^*}{2M_{S_1}^2} \overline{u_L} \gamma_\mu d_L \overline{e_L} \gamma^\mu \nu_L + \frac{Y_{d\nu}^* Y_{eu}}{2M_{S_1}^2} \overline{u_R} \gamma_\mu d_R \overline{e_R} \gamma^\mu \nu_R + \text{h.c.}, \quad (8.16)$$

⁴We note that the hermitian conjugate in Eq. 8.12 has been used to bring the interactions to the familiar form of the operators in Eq. 8.3.

where the reader can recognize by inspection the generation of the following WCs: $\tilde{C}_{LL}^S = -4\tilde{C}_{LL}^T$, $\tilde{C}_{RR}^S = -4\tilde{C}_{RR}^T$, \tilde{C}_{LL}^V and \tilde{C}_{RR}^V , related as explicitly written down.

8.1.4 $S_3 \sim (\bar{3}, 3, 1/3)$ scalar leptoquark

Here we have an $SU(2)_L$ triplet (as in the previous scenario, this field could contribute to proton decay), whose normalization is fixed by its kinetic term,

$$S_3 = \frac{1}{2} \begin{pmatrix} S_3^{1/3} & \sqrt{2}S_3^{4/3} \\ \sqrt{2}S_3^{-2/3} & -S_3^{1/3} \end{pmatrix}, \quad (8.17)$$

and whose interaction with the matter fields reads

$$-\mathcal{L}^{S_3} \supset Y_{q\ell} \overline{(qL)^c} i\sigma_2 S_3 \ell_L + \text{h.c.} \quad (8.18)$$

The relevant field in this case is clearly $S_3^{1/3}$. Integrating it out, we get

$$\mathcal{L}_{\text{eff}}^{S_3^{1/3}} = \frac{Y_{q\ell}^* Y_{q\ell}}{4M_{S_3}^2} \left(\overline{(d_L)^c} \nu_L \overline{e_L} (u_L)^c \right) + \text{h.c.}, \quad (8.19)$$

which, rewritten in a more familiar way, as we have done in the previous cases,

$$\mathcal{L}_{\text{eff}}^{S_3^{1/3}} = \frac{Y_{q\ell} Y_{q\ell}^*}{8M_{S_3}^2} (\overline{u_L} \gamma_\mu d_L \overline{e_L} \gamma^\mu \nu_L) + \text{h.c.}, \quad (8.20)$$

allows us to identify the contribution to the \tilde{C}_{LL}^V WC.

8.1.5 $\Phi \sim (1, 2, 1/2)$ second Higgs boson

For a Higgs boson, the following interactions are allowed,

$$\begin{aligned} -\mathcal{L}^\Phi &= Y_u^* (u^c)_L^T C (i\sigma_2 \Phi^*)^\dagger q_L + Y_d^* (d^c)_L^T C \Phi^\dagger q_L \\ &\quad + Y_e^* (e^c)_L^T C \Phi^\dagger \ell_L + Y_\nu^* (\nu^c)_L^T C (i\sigma_2 \Phi^*)^\dagger \ell_L + \text{h.c.}, \end{aligned} \quad (8.21)$$

from where one can recognize the familiar Yukawa Lagrangian in the SM. In this case the relevant field is the charged component of the doublet $\Phi = (\Phi^+, \Phi^0)^T$. In terms of

isospin components of $SU(2)_L$, the above Lagrangian reads as,

$$-\mathcal{L}^\Phi \supset Y_u^* \bar{u}_R \Phi^+ d_L + Y_e^* \bar{e}_R \Phi^{++} \nu_L + Y_\nu^* \bar{\nu}_R e_L \Phi^+ + Y_d^* \bar{d}_R u_L \Phi^{++} + \text{h.c.}, \quad (8.22)$$

which leads to the following effective Lagrangian after being integrated out:

$$\begin{aligned} \mathcal{L}_{\text{eff}}^\Phi \supset & \frac{Y_e^* Y_u^*}{M_{\Phi^+}^2} (\bar{u}_R d_L) (\bar{e}_R \nu_L) + \frac{Y_e^* Y_d}{M_{\Phi^+}^2} (\bar{e}_R \nu_L) (\bar{u}_L d_R) \\ & + \frac{Y_\nu^* Y_u^*}{M_\Phi^2} (\bar{u}_R d_L) (\bar{e}_L \nu_R) + \frac{Y_d Y_\nu}{M_\Phi^2} (\bar{e}_L \nu_R) (\bar{u}_L d_R) + \text{h.c.} \end{aligned} \quad (8.23)$$

From the above Lagrangian one can identify the contribution to the \tilde{C}_{LL}^S , \tilde{C}_{RR}^S , \tilde{C}_{LR}^S and \tilde{C}_{RL}^S WCs.

All scalar possibilities have been considered, and now we will start with the vector d.o.f. that can mediate $b \rightarrow c$ transitions.

8.1.6 $U_1^\mu \sim (3, 1, 2/3)$ vector leptoquark

This vector LQ has the following interactions with the matter fields:

$$-\mathcal{L}^{U_1} \supset Y_{ql} \bar{q}_L \gamma_\mu U_1^\mu \ell_L + Y_{de} \bar{d}_R \gamma_\mu U_1^\mu e_R + Y_{uv} \bar{u}_R \gamma_\mu U_1^\mu \nu_R + \text{h.c.} \quad (8.24)$$

Integrating out U_1 , we get the effective interactions listed below,

$$\begin{aligned} \mathcal{L}_{\text{eff}}^{U_1} = & \frac{1}{M_{U_1}^2} (Y_{ql}^* Y_{ql} \bar{\nu}_L \gamma_\mu u_L \bar{d}_L \gamma^\mu e_L + Y_{ql}^* Y_{uv} \bar{e}_L \gamma_\mu d_L \bar{u}_R \gamma^\mu \nu_R \\ & + Y_{ql}^* Y_{de} \bar{\nu}_L \gamma_\mu u_L \bar{d}_R \gamma^\mu e_R + Y_{de}^* Y_{uv} \bar{e}_R \gamma_\mu d_R \bar{u}_R \gamma^\mu \nu_R) + \text{h.c.} \end{aligned} \quad (8.25)$$

Applying Fierz identities, we can rewrite the above Lagrangian as follows:

$$\begin{aligned} \mathcal{L}_{\text{eff}}^{U_1} = & \frac{1}{M_{U_1}^2} (Y_{ql}^* Y_{ql} \bar{u}_L \gamma_\mu d_L \bar{e}_L \gamma^\mu \nu_L - 2Y_{ql}^* Y_{uv} (\bar{u}_R d_L) (\bar{e}_L \nu_R) \\ & - 2Y_{de}^* Y_{ql} \bar{u}_L d_R \bar{e}_R \nu_L + Y_{de}^* Y_{uv} \bar{u}_R \gamma_\mu d_R \bar{e}_R \gamma^\mu \nu_R) + \text{h.c.}, \end{aligned} \quad (8.26)$$

which contributes to the WCs: \tilde{C}_{LL}^V , \tilde{C}_{RR}^V , \tilde{C}_{LR}^S and \tilde{C}_{RL}^S .

8.1.7 $U_3^\mu \sim (3, 3, 2/3)$ vector leptoquark

For the colored and $SU(2)_L$ triplet vector U_3 LQ, the allowed interactions are,

$$-\mathcal{L}^{U_3} \supset g_{q\ell} \bar{q}_L \gamma_\mu U_3^\mu \ell_L + \text{h.c.}, \quad (8.27)$$

which can be written in terms of its EW singlet components as,

$$-\mathcal{L}^{U_3} \supset \frac{g_{q\ell}}{2} \left[(\bar{u}_L U_{3\mu}^{2/3} + \sqrt{2} \bar{d}_L U_{3\mu}^{-1/3}) \gamma^\mu \nu_L + (\sqrt{2} \bar{u}_L U_{3\mu}^{5/3} - \bar{d}_L U_{3\mu}^{2/3}) \gamma^\mu e_L \right] + \text{h.c.} \quad (8.28)$$

Note that this LQ only couples to LH fields. Integrating out the $U_3^{2/3}$ the following interactions are obtained,

$$\mathcal{L}_{\text{eff}}^{U_3^{2/3}} = -\frac{g_{q\ell}^* g_{q\ell}}{4M_{U_3}^2} \bar{u}_L \gamma_\mu d_L \bar{e}_L \gamma^\mu \nu_L + \text{h.c.}, \quad (8.29)$$

which contribute to \tilde{C}_{LL}^V .

8.1.8 $V_2^\mu \sim (\bar{3}, 2, 5/6)$ vector leptoquark

The possible interactions of this LQ with the matter fields are given by,

$$-\mathcal{L}^{V_2} \supset g_{qe} \bar{q}_L i\sigma_2 V_2^{\mu*} \gamma_\mu (e^c)_L + g_{ld} \bar{\ell}_L i\sigma_2 V_2^{\mu*} \gamma_\mu (d^c)_L + g_{qu} \bar{q}_L V_2^\mu \gamma_\mu (u^c)_L + \text{h.c.}, \quad (8.30)$$

which, taking into account that $V_2 = (V_2^{4/3}, V_2^{1/3})^T$, can be rewritten as,

$$\begin{aligned} -\mathcal{L}^{V_2} \supset & g_{qe} (\bar{u}_L V_{2\mu}^{1/3*} \gamma^\mu - \bar{d}_L V_{2\mu}^{4/3*} \gamma^\mu) (e^c)_L + g_{ld} (\bar{\nu}_L V_{2\mu}^{1/3*} \gamma^\mu \\ & - \bar{e}_L V_{2\mu}^{4/3*} \gamma^\mu) (d^c)_L + g_{qu} (\bar{u}_L V_{2\mu}^{4/3} \gamma^\mu + \bar{d}_L V_{2\mu}^{1/3} \gamma^\mu) (u^c)_L + \text{h.c.} \end{aligned} \quad (8.31)$$

This LQ also mediates the decay of the proton, and one has to assume $Y_{qu} = 0$ to avoid the strong experimental bounds on these $\Delta B = 1$ transitions. Integrating out the relevant field for the $b \rightarrow c \tau \bar{\nu}$ transitions, i.e. $V_2^{1/3}$, we have

$$\mathcal{L}_{\text{eff}}^{V_2^{1/3}} = \frac{g_{ld}^* g_{qe}}{M_{V_2}^2} \bar{u}_L \gamma_\mu (e^c)_L \overline{(d^c)_L} \gamma^\mu \nu_L + \text{h.c.} \quad (8.32)$$

Finally, by applying Fierz identities and charge conjugation properties we get to the desired form of the effective Lagrangian,

$$\mathcal{L}_{\text{eff}}^{V_2^{1/3}} = 2 \frac{g_{ld}^* g_{qe}}{M_{\tilde{V}_2}^2} \overline{u}_L d_R \overline{e}_R \nu_L + \text{h.c.}, \quad (8.33)$$

that allows us to identify the solely contribution to the \tilde{C}_{RL}^S WC.

8.1.9 $\tilde{V}_2^\mu \sim (\bar{3}, 2, -1/6)$ vector leptoquark

The interaction Lagrangian for this LQ is given by,

$$-\mathcal{L}^{\tilde{V}_2} \supset g_{\ell u} \overline{\ell}_L i \sigma_2 \tilde{V}_2^{\mu*} \gamma_\mu (u^c)_L + g_{q\nu} \overline{q}_L i \sigma_2 \tilde{V}_2^{\mu*} \gamma_\mu (\nu^c)_L + g_{qd} \overline{q}_L \tilde{V}_2^\mu \gamma_\mu (d^c)_L + \text{h.c.}, \quad (8.34)$$

which can be written in terms of the EW components as,

$$\begin{aligned} -\mathcal{L}^{\tilde{V}_2} \supset & g_{\ell u} (\overline{\nu}_L \tilde{V}_{2\mu}^{-2/3*} - \overline{e}_L \tilde{V}_{2\mu}^{1/3*}) \gamma^\mu (u^c)_L + g_{q\nu} (\overline{u}_L \tilde{V}_{2\mu}^{-2/3*} \\ & - \overline{d}_L \tilde{V}_{2\mu}^{1/3*}) \gamma^\mu (\nu^c)_L + g_{qd} (\overline{u}_L \tilde{V}_{2\mu}^{1/3} + \overline{d}_L \tilde{V}_{2\mu}^{-2/3}) \gamma^\mu (d^c)_L + \text{h.c.}, \end{aligned} \quad (8.35)$$

where we have taken into account that $\tilde{V}_2 = (\tilde{V}_2^{1/3}, \tilde{V}_2^{-2/3})^T$. Now, by integrating out the field able to contribute in $b \rightarrow c \tau \bar{\nu}$, i.e. $\tilde{V}_2^{1/3}$, and only taking into account those interactions that are relevant for this process, the effective Lagrangian generated reads as

$$\mathcal{L}_{\text{eff}}^{\tilde{V}_2^{1/3}} \supset \frac{g_{\ell u} g_{q\nu}^*}{M_{\tilde{V}_2}^2} \overline{e}_L \gamma^\mu (u^c)_L \overline{(\nu^c)_L} \gamma_\mu d_L + \text{h.c.} \quad (8.36)$$

Rearranging those terms by playing with the Fierz identities and charge conjugation properties, we end up with the following effective Lagrangian,

$$\mathcal{L}_{\text{eff}}^{\tilde{V}_2^{1/3}} \supset 2 \frac{g_{\ell u} g_{q\nu}^*}{M_{\tilde{V}_2}^2} \overline{u}_R d_L \overline{e}_L \nu_R + \text{h.c.}, \quad (8.37)$$

where we can identify the contribution to the \tilde{C}_{LR}^S WC.

8.1.10 $W'^{\mu} \sim (1, 3, 0)$ vector boson

This scenario might be more familiar to us, because of the EW W_{μ} gauge boson. The interaction Lagrangian is given by,

$$-\mathcal{L}^{W'} \supset g_q \bar{q}_L W'^{\mu} \gamma_{\mu} q_L + g_{\ell} \bar{\ell}_L W'^{\mu} \gamma_{\mu} \ell_L, \quad (8.38)$$

which, expanded in terms of its $SU(2)_L$ components, reads as

$$-\mathcal{L}^{W'} \supset \frac{g_q}{\sqrt{2}} (\bar{d}_L W'^{-}_{\mu} \gamma^{\mu} u_L + \text{h.c.}) + \frac{g_{\ell}}{\sqrt{2}} (\bar{e}_L W'^{-}_{\mu} \gamma^{\mu} \nu_L + \text{h.c.}). \quad (8.39)$$

Integrating W'^{-} out we directly obtain an effective Lagrangian in the desired form,

$$\mathcal{L}_{\text{eff}}^{W'^{-}} \supset \frac{g_{\ell} g_q}{2M_{W'}^2} (\bar{u}_L d_L \bar{e}_L \nu_L + \text{h.c.}), \quad (8.40)$$

so that immediately we can recognize the contribution to the \tilde{C}_{LL}^V WC.

8.1.11 $V^{\mu} \sim (1, 1, -1)$ vector boson

This $SU(2)_L$ and $SU(3)_c$ singlet, only charged under $U(1)_Y$, has the following allowed interactions with matter:

$$-\mathcal{L}^V \supset g_{ud} \overline{(u^c)_L} \gamma_{\mu} (d^c)_L V^{\mu} + g_{\nu e} \overline{(\nu^c)_L} \gamma_{\mu} (e^c)_L V^{\mu} + \text{h.c.} \quad (8.41)$$

By using the properties of the charge conjugate operator, the previous Lagrangian can be rewritten as

$$-\mathcal{L}^V \supset g_{ud} \bar{d}_R \gamma_{\mu} u_R V^{\mu} + g_{\nu e} \bar{e}_R \gamma_{\mu} \nu_R V^{\mu} + \text{h.c.} \quad (8.42)$$

After integrating out V , the following effective Lagrangian is obtained,

$$\mathcal{L}_{\text{eff}}^V = \frac{g_{ud}^* g_{\nu e}}{M_V^2} \bar{u}_R \gamma_{\mu} d_R \bar{e}_R \gamma^{\mu} \nu_R + \text{h.c.}, \quad (8.43)$$

which allows the identification of \tilde{C}_{RR}^V as the contribution of this mediator.

We are now aware of all possibilities that could be responsible of the so-called flavour anomalies, i.e. all fields that can contribute to the $b \rightarrow c\tau\bar{\nu}$ processes. We note that, although there is for instance no direct contribution to the tensor operator from any of the mediators, a non-zero tensor WC can be generated by the running from the NP scale down to the relevant scale for these transitions.

The next step would be to control how the NP effects, encoded in the WCs, enter in the $b \rightarrow c\tau\bar{\nu}$ transitions. The latter can be easily tackled from an EFT perspective.

8.2 Leptonic transitions

Let us start from the leptonic decay of a pseudoscalar meson (i.e. $J^P \equiv 0^-$) into a pair of leptons. For simplicity and posterior interest, we will specify the calculation to the process $B_c \rightarrow \tau\bar{\nu}$. Starting from the hadronic part, parity tells us that only the axial and pseudoscalar operators of our effective Hamiltonian (see Eq. 8.2) will contribute to this amplitude. Lorentz invariance determines the structure of the outcomes of the transition matrices. In summary, both possible transitions can be parametrized as follows by symmetries; first, the axial transition,

$$\langle 0 | \bar{b} \gamma_\mu \gamma_5 c | B_c(p_B) \rangle = i p_{B\mu} f_{B_c}, \quad (8.44)$$

where m_B is the mass of the meson B_c , $p_{B\mu}$ is its four-momentum, and f_{B_c} is the parameter that encodes the non-perturbativity nature of the transition. The pseudoscalar transitions can be derived from Eq. 8.44 by applying the axial Ward identity, therefore getting,

$$\langle 0 | \bar{b} \gamma_5 c | B_c(p_B) \rangle = -i \frac{m_{B_c}^2 f_{B_c}}{m_c + m_b}. \quad (8.45)$$

The amplitude of the $B_c \rightarrow \tau\bar{\nu}$ process shown in Fig. 8.2a and 8.2b ⁵ for the process with the LH neutrino in the final state is given by,

⁵Note that, since we are neglecting the neutrino mass, RH and LH neutrino channels do not interfere.

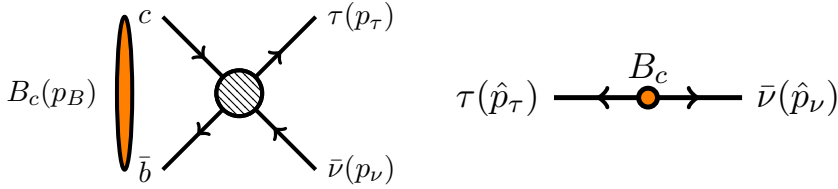


Figure 8.2: On the left panel, the leptonic decay of the B_c meson, $B_c(p_B) \rightarrow \tau(p_\tau)\bar{\nu}(p_\nu)$. On the right panel, the same decay from the τ - $\bar{\nu}$ (or B_c) rest-frame.

$$\mathcal{M} = \sqrt{2}G_F V_{bc} f_{B_c} \bar{u}(p_\tau) \left((C_{RL}^S - C_{LL}^S) \frac{m_{B_c}^2}{m_c + m_b} + (1 + C_{RL}^V - C_{LL}^V) \gamma^\mu p_{B\mu} \right) P_L v(p_\nu). \quad (8.46)$$

Similarly, the amplitude for the process involving a final RH neutrino,

$$\mathcal{M} = \sqrt{2}G_F V_{bc} f_{B_c} \bar{u}(p_\tau) \left((C_{RR}^S - C_{LR}^S) \frac{m_{B_c}^2}{m_c + m_b} + (C_{RR}^V - C_{LR}^V) \gamma^\mu p_{B\mu} \right) P_R v(p_\nu). \quad (8.47)$$

Hence, computing the squared amplitude of each channel, averaging among the spins and helicities, and summing both contributions independently we get the total amplitude of the process. The decay width is generically given by

$$\Gamma(B \rightarrow 1 + \dots + N) = \frac{1}{2M_B} \int dQ_N |\bar{\mathcal{M}}_{B \rightarrow 1 + \dots + N}|^2, \quad (8.48)$$

for a N-body decay, where the N-body phase space is defined as

$$dQ_N = (2\pi)^4 \int \prod_{i=1}^N \frac{d^3 p_i}{(2\pi)^3 2E_i} \delta \left(p_B - \sum_{j=1}^N p_j \right). \quad (8.49)$$

Particularly, for a two body decay, it is given by

$$dQ_2(\hat{p}_\ell, \hat{p}_\nu) = \frac{1}{(2\pi)^2} \frac{|\hat{p}_\ell|}{4m_{ij}} d\cos\theta_\ell d\phi, \quad (8.50)$$

where $m_{ij}^2 = (p_i + p_j)^2 = s$ and \hat{p}_i are the momenta in the center-of-mass frame.

Applying Eq. 8.48 we can compute for our scenario the following branching ratio,

$$\mathcal{B}(B_c \rightarrow \tau \bar{\nu}) = \tau_{B_c} \frac{m_{B_c} m_\tau^2 f_{B_c}^2 G_F^2 |V_{cb}|^2}{8\pi} \left(1 - \frac{m_\tau^2}{m_{B_c}^2}\right)^2 \times \quad (8.51)$$

$$\left(\left| 1 + C_{LL}^V - C_{RL}^V + \frac{m_{B_c}^2/m_\tau}{(m_b + m_c)} (C_{RL}^S - C_{LL}^S) \right|^2 + \left| C_{RR}^V - C_{LR}^V + \frac{m_{B_c}^2/m_\tau}{(m_b + m_c)} (C_{LR}^S - C_{RR}^S) \right|^2 \right),$$

where the decay width has been normalized by the total decay width of the B_c : $\tau_{B_c}^{-1}$.

8.3 Semileptonic transitions: The helicity formalism.

In this section we will be dealing with a pseudoscalar meson B decaying into another meson M . To compute the transition $B(p_B) \rightarrow M(p_M, \lambda_M) \ell(p_\ell, \lambda_\ell) \bar{\nu}(p_\nu, \lambda_\nu)$, where $\lambda_{M,\ell,\nu}$ refers to the helicity of the meson, the charged lepton and the neutrino, respectively, we will appeal to the helicity amplitude formalism, which allows the factorization of the amplitude in an hadronic and a leptonic pieces via a virtual gauge boson V_μ^* acting as a mediator,

$$B(p_B) \rightarrow M(p_M, \lambda_M) V_\mu^*(q, \lambda) \rightarrow M(p_M, \lambda_M) \ell(p_\ell, \lambda_\ell) \bar{\nu}(p_\nu, \lambda_\nu), \quad (8.52)$$

where q is the four-momentum carried by the the virtual mediator, i.e. $q^2 \equiv (p_B + p_M)^2 = (p_\tau + p_{\bar{\nu}})^2$, and $\lambda (= 0, \pm 1, t)$ its helicity. Figure 8.3 represents the semileptonic decay mediated by the virtual boson. In the B rest-frame, the kinematics of the decay can be described by the four-momenta carried by the B -meson (p_B^μ), the M -meson (p_M^μ), and the virtual boson (q^μ), which are given by

$$p_B^\mu = \begin{pmatrix} m_B \\ 0 \\ 0 \\ 0 \end{pmatrix}, \quad p_M^\mu = \begin{pmatrix} E_M \\ 0 \\ 0 \\ |\vec{q}| \end{pmatrix}, \quad q^\mu \equiv p_B^\mu - p_M^\mu = \begin{pmatrix} q_0 \\ 0 \\ 0 \\ -|\vec{q}| \end{pmatrix}, \quad (8.53)$$

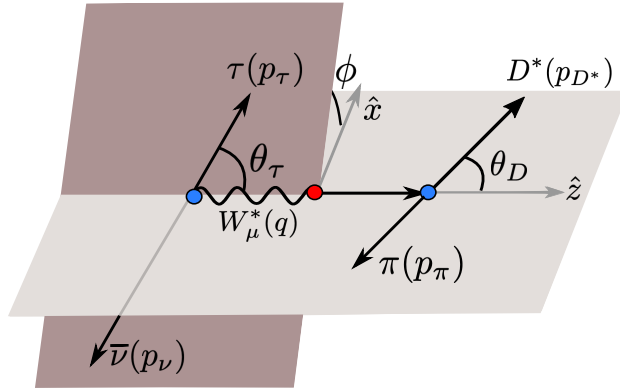


Figure 8.3: Visual representation of the relevant kinematical variables. In addition to the lepton-pair invariant-mass squared $q^2 = (p_\tau - p_{\bar{\nu}})^2$, we use as kinematic variables the three angles ϕ , θ_ℓ and θ_D , which are defined as follows. Taking as positive z -axis the direction of the D^* momentum in the B rest-frame, θ_τ and θ_D are the polar angles of the τ and the final D meson in the $\tau\bar{\nu}$ and $D\pi$ rest frames, respectively. The azimuth ϕ is the angle between the decay planes formed by $\tau\bar{\nu}$ and $D\pi$. *Figure extracted from Ref. [333].*

where

$$|\vec{q}| = \frac{\sqrt{\lambda_M(q^2)}}{2m_B}, \quad q_0 = \frac{m_B^2 - m_M^2 + q^2}{2m_B}, \quad E_M = \frac{m_B^2 + m_M^2 - q^2}{2m_B}, \quad (8.54)$$

being $\lambda_M(q^2)$ the Källén function, defined as

$$\lambda_M(q^2) \equiv \lambda(m_B^2, m_M^2, q^2) = m_B^4 + m_M^4 + q^4 - 2m_B^2 m_M^2 - 2m_M^2 q^2 - 2m_B^2 q^2. \quad (8.55)$$

The Hamiltonian presented in Eq. 8.2 can be rewritten as

$$\mathcal{H}_{\text{eff}} = \frac{G_F}{\sqrt{2}} V_{cb} \sum_X (J_h^\mu J_{\ell\mu}^X + J_h J_\ell^X + J_h^{\mu\nu} J_{\ell\mu\nu}^X), \quad (8.56)$$

where we have grouped the fermion currents in the Hamiltonian, factorized in their hadronic J_h and leptonic J_ℓ parts, according to their Lorentz structure. We note that the chiral projector in the hadronic currents has been explicitly expanded, and that

those currents contain the information on the WCs. The different NP components of the above Hamiltonian contribute to the amplitude for the decay $B \rightarrow M(\lambda_M)\ell(\lambda_\ell)\bar{\nu}_X$ as follows,

$$\begin{aligned} \mathcal{M}[B \rightarrow M(\lambda_M)\ell(\lambda_\ell)\bar{\nu}_{X=L,R}] &= \\ &= \frac{G_F}{\sqrt{2}} V_{cb} (\langle M|J_h^\mu|\bar{B}\rangle\langle\ell\bar{\nu}|J_{\ell\mu}^X|0\rangle + \langle M|J_h|\bar{B}\rangle\langle\ell\bar{\nu}|J_\ell^X|0\rangle + \langle M|J_h^{\mu\nu}|\bar{B}\rangle\langle\ell\bar{\nu}|J_{\ell\mu\nu}^X|0\rangle) \end{aligned} \quad (8.57)$$

Let us factorize the hadronic and leptonic currents above by letting the polarization vectors $\epsilon_\mu(\lambda)$ of the virtual V_μ^* boson play their role, which are defined in the B rest-frame as

$$\epsilon^\mu(\pm) = \frac{1}{\sqrt{2}} \begin{pmatrix} 0 \\ \mp 1 \\ i \\ 0 \end{pmatrix}, \quad \epsilon^\mu(0) = \frac{1}{\sqrt{q^2}} \begin{pmatrix} |\vec{q}| \\ 0 \\ 0 \\ -q_0 \end{pmatrix}, \quad \text{and} \quad \epsilon^\mu(t) = \frac{1}{\sqrt{q^2}} \begin{pmatrix} q_0 \\ 0 \\ 0 \\ -|\vec{q}| \end{pmatrix}. \quad (8.58)$$

Inserting the completeness relation of the polarization vectors of the off-shell vector boson in each of the amplitudes, i.e.

$$\sum_\lambda \delta_\lambda \epsilon_\mu^*(\lambda) \epsilon_\nu(\lambda) = g_{\mu\nu} \quad \text{with} \quad \delta_0 = \delta_\pm = -\delta_t = -1, \quad (8.59)$$

the amplitude in Eq. 8.58 can be decomposed according to their Lorentz indices in the following factorization of hadronic and leptonic tensors:

$$\begin{aligned} \mathcal{M}[B \rightarrow M(\lambda_M)\ell(\lambda_\ell)\bar{\nu}_{X=L,R}] &\equiv (G_F/\sqrt{2}) V_{cb} \mathcal{M}_{L,R}^{\lambda_M,\lambda_\ell} \\ &= (G_F/\sqrt{2}) V_{cb} \sum_{Y=L,R} \left\{ (\delta_{YL}\delta_{XL} + C_{YX}^V) \sum_\lambda \delta_\lambda H_{V_Y,\lambda}^{\lambda_M} L_{V_{\mp A},\lambda}^{\lambda_\ell,X} \right. \\ &\quad \left. + C_{YX}^S H_{S_Y}^{\lambda_M} L_{S_{\mp P}}^{\lambda_\ell,X} + C_{YX}^T \sum_{\lambda,\lambda'} \delta_\lambda \delta_{\lambda'} H_{T_Y,\lambda\lambda'}^{\lambda_M} L_{T_{\mp T5},\lambda\lambda'}^{\lambda_\ell,X} \right\}. \end{aligned} \quad (8.60)$$

The hadronic helicities from the above expression are defined as follows,

$$H_{V_{LR}^M, \lambda}^{\lambda} \equiv \epsilon_{\mu}^*(\lambda) \langle M | \bar{c} \gamma^{\mu} (2P_{LR}) b | \bar{B} \rangle, \quad (8.61)$$

$$H_{S_{LR}^M}^{\lambda} \equiv \langle M | \bar{c} (2P_{LR}) b | \bar{B} \rangle, \quad (8.62)$$

$$H_{T_{LR}^M, \lambda\lambda'}^{\lambda} \equiv i \epsilon_{\mu}^*(\lambda) \epsilon_{\nu}^*(\lambda') \langle M | \bar{c} \sigma^{\mu\nu} (2P_{LR}) b | \bar{B} \rangle, \quad (8.63)$$

where the hadronic currents have been expanded. On the other hand, the leptonic helicities read as,⁶

$$L_{V_{\mp A}^{\lambda, X}}^{\lambda, X} \equiv \epsilon_{\mu}(\lambda) \langle \ell(\lambda_{\ell}) \bar{\nu} | \bar{\tau} \gamma^{\mu} (2P_L) \nu | 0 \rangle, \quad (8.64)$$

$$L_{S_{\mp P}^{\lambda, X}}^{\lambda, X} \equiv \langle \ell(\lambda_{\ell}) \bar{\nu} | \bar{\tau} (2P_L) \nu | 0 \rangle, \quad (8.65)$$

$$L_{T_{\mp T5}^{\lambda, X}}^{\lambda, X} \equiv -i \epsilon_{\mu}(\lambda) \epsilon_{\nu}(\lambda') \langle \ell(\lambda_{\ell}) \bar{\nu} | \bar{\tau} \sigma^{\mu\nu} (2P_L) \nu | 0 \rangle. \quad (8.66)$$

Because of the possibility of having NP in $b \rightarrow c$ transitions suggested by the experimental evidence,⁷ particularly involving only the third generation of leptons, the two upcoming subsections of this chapter are devoted to the cases $M = D, D^*$, and the charged lepton will be identified as the tau lepton, i.e. $\ell \rightarrow \tau$. The procedure followed here, although particularized to $D^{(*)}$ is also valid for any pseudoscalar decaying into a pseudoscalar meson $J^P = 0^-$ or vector meson $J^P = 1^-$, addressed in the first and second upcoming subsections, respectively. Both processes, however, have their leptonic part in common, so that they share the leptonic contribution to the amplitude. To tackle it, it is convenient to express the polarization vectors of the virtual gauge boson in the V^* rest-frame, where they simply read as

$$\epsilon^{\mu}(\pm) = \mp \frac{1}{\sqrt{2}} \begin{pmatrix} 0 \\ 1 \\ \mp i \\ 0 \end{pmatrix}, \quad \epsilon^{\mu}(0) = \begin{pmatrix} 0 \\ 0 \\ 0 \\ -1 \end{pmatrix}, \quad \epsilon^{\mu}(t) = \frac{1}{\sqrt{q^2}} q^{\mu} = \begin{pmatrix} 1 \\ 0 \\ 0 \\ 0 \end{pmatrix}, \quad (8.67)$$

⁶We did not specify the helicity of the neutrino since, as it will be shown later, it is fixed by the chirality of the leptonic current.

⁷The reader is referred to Chapter 9 for details on the flavour anomalies found in $b \rightarrow c$ transitions.

This can be achieved by boosting the polarization vectors in the B rest-frame, shown in Eq. 8.58, to the V^* rest-frame, with the following boost:

$$\Lambda(\omega) = \begin{pmatrix} \cosh \omega & 0 & 0 & \sinh \omega \\ 0 & 1 & 0 & 0 \\ 0 & 0 & 1 & 0 \\ \sinh \omega & 0 & 0 & \cosh \omega \end{pmatrix}, \quad (8.68)$$

where $\cosh \omega = (1 - v_{V^*}^2/c^2)^{-1/2} = q_0/\sqrt{q^2}$, and v_{V^*} is the relative motion between both frames.

Fig. 8.3 also shows the perspective from the V^* rest-frame, where we can define the polar angle θ_τ as the angle of τ in the $\tau\text{-}\bar{\nu}$ rest-frame. In there, the four-momenta of the leptons and that of the virtual gauge boson read as

$$p_\tau^\mu = \begin{pmatrix} E_\tau \\ p_\tau \sin \theta_\tau \\ 0 \\ p_\tau \cos \theta_\tau \end{pmatrix}, \quad p_\nu^\mu = p_\nu \begin{pmatrix} 1 \\ -\sin \theta_\tau \\ 0 \\ -\cos \theta_\tau \end{pmatrix}, \quad \text{and} \quad q^\mu = \begin{pmatrix} \sqrt{q^2} \\ 0 \\ 0 \\ -|\vec{q}| \end{pmatrix}, \quad (8.69)$$

being

$$p_\tau = p_\nu = \frac{q^2 - m_\tau^2}{2\sqrt{q^2}}, \quad E_\tau = \frac{q^2 + m_\tau^2}{2\sqrt{q^2}}. \quad (8.70)$$

The leptonic matrix elements from Eq. 8.64-8.66 can be computed as

$$\langle \tau(\lambda_\tau) \bar{\nu} | J_{\tau X}^\mu | 0 \rangle \equiv \langle \tau(\lambda_\tau) \bar{\nu} | \bar{\tau} \gamma^\mu (2P_X) \nu | 0 \rangle = \bar{u}(p_\tau, \lambda_\tau) \gamma^\mu (2P_X) v(p_\nu, \lambda_X), \quad (8.71)$$

where P_X refers to the chirality projectors $X = L, R$, and the helicity of the antineutrino, because of their massless nature, is fixed by the projector: $\lambda_\nu = +1/2$ for a LH antineutrino and $\lambda_\nu = -1/2$ for a RH antineutrino. The matrix element in Eq. 8.71 also applies to currents with different number of Lorentz indices, i.e. J and $J^{\mu\nu}$. The four-spinors in the chiral representation for a particle with helicity λ_τ and an antiparticle with helicity $-\lambda_\tau$, respectively, defined in Eq. 2.47 from Chapter 2 give us

in this case:

$$u(p_\tau, \lambda_\tau) = \begin{pmatrix} \sqrt{E_\tau - 2\lambda_\tau p_\tau} \chi_{\lambda_\tau} \\ \sqrt{E_\tau + 2\lambda_\tau p_\tau} \chi_{\lambda_\tau} \end{pmatrix}, \quad \text{and} \quad v(p_\tau, \lambda_\tau) = \begin{pmatrix} -\sqrt{E_\tau + 2\lambda_\tau p_\tau} \chi_{-\lambda_\tau} \\ \sqrt{E_\tau - 2\lambda_\tau p_\tau} \chi_{-\lambda_\tau} \end{pmatrix}, \quad (8.72)$$

where $\chi(\lambda_\tau)$ are the helicity eigenspinors, given by

$$\chi_{+\frac{1}{2}} = \begin{pmatrix} \cos \frac{\theta_\tau}{2} \\ \sin \frac{\theta_\tau}{2} e^{i\phi} \end{pmatrix}, \quad \text{and} \quad \chi_{-\frac{1}{2}} = \begin{pmatrix} -\sin \frac{\theta_\tau}{2} e^{-i\phi} \\ \cos \frac{\theta_\tau}{2} \end{pmatrix}, \quad (8.73)$$

and the Dirac matrices in this representation are given in Eq. 2.49 from Chapter 2. The azimuth ϕ is the angle between the decay planes formed by $\tau\bar{\nu}$ and $D\pi$ (see Fig. 8.3).

Now, all material needed for computing the leptonic helicities is on the table. By making the contraction $L_{V-A,\lambda}^{\lambda_\tau X} \equiv \epsilon_\mu(\lambda) \langle \bar{\tau}(\lambda_\tau) \bar{\nu} | J_{\ell X}^\mu | 0 \rangle$ we obtain the following leptonic vector helicity amplitudes:

$$\begin{aligned} L_{V-A,+}^{+,L} &= \sqrt{2} m_\tau \beta_\tau \sin \theta_\tau e^{-2i\phi}, & L_{V+A,+}^{-,R} &= \sqrt{2} m_\tau \beta_\tau \sin \theta_\tau, \\ L_{V-A,-}^{+,L} &= -\sqrt{2} m_\tau \beta_\tau \sin \theta_\tau, & L_{V+A,-}^{-,R} &= -\sqrt{2} m_\tau \beta_\tau \sin \theta_\tau e^{2i\phi}, \\ L_{V-A,0}^{+,L} &= 2 m_\tau \beta_\tau \cos \theta_\tau e^{-i\phi}, & L_{V+A,0}^{-,R} &= 2 m_\tau \beta_\tau \cos \theta_\tau e^{i\phi}, \\ L_{V-A,t}^{+,L} &= -2 m_\tau \beta_\tau e^{-i\phi}, & L_{V+A,t}^{-,R} &= -2 m_\tau \beta_\tau e^{i\phi}, \\ L_{V-A,\pm}^{-,L} &= \sqrt{2q^2} \beta_\tau (1 \pm \cos \theta_\tau) e^{\mp i\phi}, & L_{V+A,\pm}^{+,R} &= \sqrt{2q^2} \beta_\tau (1 \mp \cos \theta_\tau) e^{\mp i\phi}, \\ L_{V-A,0}^{-,L} &= -2\sqrt{q^2} \beta_\tau \sin \theta_\tau, & L_{V+A,0}^{+,R} &= 2\sqrt{q^2} \beta_\tau \sin \theta_\tau, \\ L_{V-A,t}^{-,L} &= 0, & L_{V+A,t}^{+,R} &= 0. \end{aligned}$$

while the scalar ones, $L_{S-P}^{\lambda_\tau X} \equiv \langle \tau(\lambda_\tau) \bar{\nu} | J_{\ell X} | 0 \rangle$, are given by

$$\begin{aligned} L_{S-P}^{+,L} &= -2\sqrt{q^2} \beta_\tau e^{-i\phi}, & L_{S+P}^{-,R} &= -2\sqrt{q^2} \beta_\tau e^{i\phi}, \\ L_{S-P}^{-,L} &= 0, & L_{S+P}^{+,R} &= 0, \end{aligned} \quad (8.74)$$

and finally, by computing $L_{T^-T_5, \lambda\lambda'}^{\lambda_\tau X} \equiv \epsilon_\mu(\lambda)\epsilon_\nu(\lambda')\langle\tau(\lambda_\tau)\bar{\nu}|J_{\ell X}^{\mu\nu}|0\rangle$, the following tensor leptonic helicity amplitudes are obtained:

$$\begin{aligned}
L_{T^-T_5, +0}^{+,L} &= \sqrt{2q^2} \beta_\tau s\theta_\tau e^{-2i\phi}, & L_{T^+T_5, +0}^{-,R} &= -\sqrt{2q^2} \beta_\tau s\theta_\tau, \\
L_{T^-T_5, -0}^{+,L} &= \sqrt{2q^2} \beta_\tau s\theta_\tau, & L_{T^+T_5, -0}^{-,R} &= -\sqrt{2q^2} \beta_\tau s\theta_\tau e^{2i\phi}, \\
L_{T^-T_5, +-}^{+,L} &= 2\sqrt{q^2} \beta_\tau c\theta_\tau e^{-i\phi}, & L_{T^+T_5, +-}^{-,R} &= -2\sqrt{q^2} \beta_\tau c\theta_\tau e^{i\phi}, \\
L_{T^-T_5, 0t}^{+,L} &= -2\sqrt{q^2} \beta_\tau c\theta_\tau e^{-i\phi}, & L_{T^+T_5, 0t}^{-,R} &= -2\sqrt{q^2} \beta_\tau c\theta_\tau e^{i\phi}, \\
L_{T^-T_5, +t}^{+,L} &= -\sqrt{2q^2} \beta_\tau s\theta_\tau e^{-2i\phi}, & L_{T^+T_5, +t}^{-,R} &= -\sqrt{2q^2} \beta_\tau s\theta_\tau, \\
L_{T^-T_5, -t}^{+,L} &= \sqrt{2q^2} \beta_\tau s\theta_\tau, & L_{T^+T_5, -t}^{-,R} &= \sqrt{2q^2} \beta_\tau s\theta_\tau e^{2i\phi}. \\
L_{T^-T_5, \pm 0}^{-,L} &= \pm\sqrt{2} m_\tau \beta_\tau (1 \pm c\theta_\tau) e^{\mp i\phi}, & L_{T^+T_5, \pm 0}^{+,R} &= \mp\sqrt{2} m_\tau \beta_\tau (1 \mp c\theta_\tau) e^{\mp i\phi}, \\
L_{T^-T_5, +-}^{-,L} &= -L_{T^-T_5, 0t}^{-,L} = -2m_\tau \beta_\tau s\theta_\tau, & L_{T^+T_5, +-}^{+,R} &= L_{T^+T_5, 0t}^{+,R} = -2m_\tau \beta_\tau s\theta_\tau, \\
L_{T^-T_5, \pm t}^{-,L} &= -\sqrt{2} m_\tau \beta_\tau (1 \pm c\theta_\tau) e^{\mp i\phi}, & L_{T^+T_5, \pm t}^{+,R} &= -\sqrt{2} m_\tau \beta_\tau (1 \mp c\theta_\tau) e^{\mp i\phi}.
\end{aligned} \tag{8.75}$$

where $c\theta_\tau(s\theta_\tau)$ refer to $\cos\theta_\tau(\sin\theta_\tau)$. The hadronic part depends on the meson we are dealing with. A pseudoscalar meson $J^P = 0^-$, D for instance, has a single helicity state, corresponding to the 0 helicity state. Therefore, we will omit the label of the meson helicity in that case, in order to distinguish it from the 0 helicity state of the vector meson $J^P = 1^-$, D^* for instance, whose helicity states are $\lambda_{D^*} = -1, 0, 1$.

8.3.1 $B \rightarrow D\tau\bar{\nu}$

Let us parametrize the hadronic matrix elements exploiting their Lorentz structure. Lorentz invariance and parity impose the axial and pseudoscalar matrix elements to vanish, so that observables involving $B \rightarrow D$ transitions will be only sensitive to the vector combination $C_{LX}^V + C_{RX}^V$, scalar combination $C_{LX}^S + C_{RX}^S$ and tensor WCs. On the other hand, they also demand a certain structure for the hadronic matrix elements, which can be factorized in kinematical variables and pure hadronic inputs named as form factors, as follows:

$$\langle D|\bar{c}\gamma_\mu b|\bar{B}\rangle = \left[(p_B + p_D)_\mu - \frac{m_B^2 - m_D^2}{q^2} q_\mu \right] F_1(q^2) + q_\mu \frac{m_B^2 - m_D^2}{q^2} F_0(q^2),$$

$$\begin{aligned}
\langle D|\bar{c}b|\bar{B}\rangle &= \frac{m_B^2 - m_D^2}{m_b - m_c} F_0(q^2), \\
\langle D|\bar{c}\sigma_{\mu\nu}b|\bar{B}\rangle &= -i(p_{B\mu}p_{D\nu} - p_{D\mu}p_{B\nu}) \frac{2F_T(q^2)}{m_B + m_D}, \\
\langle D|\bar{c}\sigma_{\mu\nu}\gamma_5b|\bar{B}\rangle &= -\epsilon_{\mu\nu\alpha\beta}p_B^\alpha p_D^\beta \frac{2F_T(q^2)}{m_B + m_D}.
\end{aligned} \tag{8.76}$$

The form factors $F_0(q^2)$, $F_1(q^2)$ and $F_T(q^2)$ appearing in the D matrix elements are described in the last section of this chapter.

Contracting these hadronic matrix elements with the polarization vectors of the virtual boson according to Eq. 8.60, the following hadronic helicity amplitudes are obtained:

$$\begin{aligned}
H_{V,0}(q^2) &\equiv H_{V_L,0}(q^2) = H_{V_R,0}(q^2) = \sqrt{\frac{\lambda_D(q^2)}{q^2}} F_1(q^2), \\
H_{V,t}(q^2) &\equiv H_{V_L,t}(q^2) = H_{V_R,t}(q^2) = \frac{m_B^2 - m_D^2}{\sqrt{q^2}} F_0(q^2), \\
H_S(q^2) &\equiv H_{S_L}(q^2) = H_{S_R}(q^2) \simeq \frac{m_B^2 - m_D^2}{m_b - m_c} F_0(q^2), \\
H_T(q^2) &\equiv H_{T_{L+-}} = H_{T_{L0t}} = -H_{T_{R+-}} = H_{T_{R0t}} = -\frac{\sqrt{\lambda_D(q^2)}}{m_B + m_D} F_T(q^2).
\end{aligned} \tag{8.77}$$

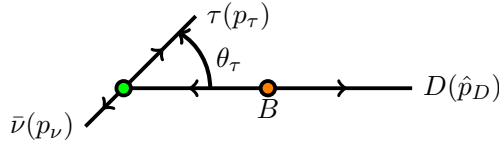
Finally, following Eq. 8.60, the reduced amplitudes, decomposed in helicity states and lepton chiralities for the $B \rightarrow D\tau\bar{\nu}$ process are obtained:

$$\begin{aligned}
\mathcal{M}_L^{+\frac{1}{2}} &= -2\sqrt{q^2} \beta_\tau e^{-i\phi} \left\{ \frac{m_\tau}{\sqrt{q^2}} [\tilde{\mathcal{A}}_t^L + \cos\theta_\tau \tilde{\mathcal{A}}_0^L] + \tilde{\mathcal{A}}_S^L - 2 \cos\theta_\tau \tilde{\mathcal{A}}_T^L \right\}, \\
\mathcal{M}_L^{-\frac{1}{2}} &= 2\sqrt{q^2} \beta_\tau \sin\theta_\tau \left\{ \tilde{\mathcal{A}}_0^L - \frac{2m_\tau}{\sqrt{q^2}} \tilde{\mathcal{A}}_T^L \right\}, \\
\mathcal{M}_R^{+\frac{1}{2}} &= -2\sqrt{q^2} \beta_\tau \sin\theta_\tau \left\{ \tilde{\mathcal{A}}_0^R - \frac{2m_\tau}{\sqrt{q^2}} \tilde{\mathcal{A}}_T^R \right\}, \\
\mathcal{M}_R^{-\frac{1}{2}} &= -2\sqrt{q^2} \beta_\tau e^{i\phi} \left\{ \frac{m_\tau}{\sqrt{q^2}} [\tilde{\mathcal{A}}_t^R + \cos\theta_\tau \tilde{\mathcal{A}}_0^R] + \tilde{\mathcal{A}}_S^R - 2 \cos\theta_\tau \tilde{\mathcal{A}}_T^R \right\}
\end{aligned} \tag{8.78}$$

where the transversity amplitudes $\tilde{\mathcal{A}}$ are combinations of WCs and hadronic helicity amplitudes, as listed below:

$$\begin{aligned}
 \tilde{\mathcal{A}}_0^L &= (1 + C_{LL}^V + C_{RL}^V) H_{V,0}, & \tilde{\mathcal{A}}_0^R &= (C_{LR}^V + C_{RR}^V) H_{V,0}, \\
 \tilde{\mathcal{A}}_t^L &= (1 + C_{LL}^V + C_{RL}^V) H_{V,t}, & \tilde{\mathcal{A}}_t^R &= (C_{LR}^V + C_{RR}^V) H_{V,t}, \\
 \tilde{\mathcal{A}}_S^L &= (C_{RL}^S + C_{LL}^S) H_S, & \tilde{\mathcal{A}}_S^R &= (C_{RR}^S + C_{LR}^S) H_S, \\
 \tilde{\mathcal{A}}_T^L &= 2 C_{LL}^S H_T, & \tilde{\mathcal{A}}_T^R &= 2 C_{RR}^S H_T.
 \end{aligned} \tag{8.79}$$

To compute the three body decay, which is illustrated in the following diagram from the B rest-frame perspective:



we can reduce dQ_3 given in Eq. 8.49 to the following factorization:

$$dQ_3 = \frac{dq^2}{2\pi} dQ_2(p_D, q) dQ_2(\hat{p}_\tau, \hat{p}_\nu) = \frac{1}{16} \frac{1}{(2\pi)^3} \frac{|\vec{q}|}{m_B} \left(1 - \frac{m_\tau^2}{q^2}\right) dq^2 d\cos\theta_\tau. \tag{8.80}$$

Applying this result to Eq. 8.48 we obtain the differential distribution of the decay $B \rightarrow D\tau\bar{\nu}$,

$$\frac{d\Gamma(B \rightarrow D\tau\bar{\nu})}{dq^2 d\cos\theta_\tau} = \frac{3}{4} \mathcal{N}_D(q^2) \{J_0(q^2) + J_1(q^2) \cos\theta_\tau + J_2(q^2) \cos^2\theta_\tau\}, \tag{8.81}$$

with the normalization $\mathcal{N}_D^{(*)}(q^2)$, which will be also applicable to the D^* decay mode, given by

$$\mathcal{N}_D^{(*)}(q^2) \equiv \frac{G_F^2 V_{cb}^2}{192 m_B^3 \pi^3} q^2 \lambda_{D^{(*)}}^{1/2}(q^2) \left(1 - \frac{m_\tau^2}{q^2}\right)^2. \tag{8.82}$$

The coefficient functions of the different angular dependences are given by

$$J_0(q^2) = \left| \tilde{\mathcal{A}}_0^L - \frac{2m_\tau}{\sqrt{q^2}} \tilde{\mathcal{A}}_T^L \right|^2 + \frac{m_\tau^2}{q^2} \left| \tilde{\mathcal{A}}_t^L + \frac{\sqrt{q^2}}{m_\tau} \tilde{\mathcal{A}}_S^L \right|^2 + (\text{L} \rightarrow \text{R}),$$

$$\begin{aligned}
J_1(q^2) &= \frac{2m_\tau^2}{q^2} \operatorname{Re} \left[\left(\tilde{\mathcal{A}}_0^L - \frac{2\sqrt{q^2}}{m_\tau} \tilde{\mathcal{A}}_T^L \right) \left(\tilde{\mathcal{A}}_t^{L*} + \frac{\sqrt{q^2}}{m_\tau} \tilde{\mathcal{A}}_S^{L*} \right) \right] + (\text{L} \rightarrow \text{R}), \\
J_2(q^2) &= - \left(1 - \frac{m_\tau^2}{q^2} \right) \left(|\tilde{\mathcal{A}}_0^L|^2 - 4 |\tilde{\mathcal{A}}_t^L|^2 \right) + (\text{L} \rightarrow \text{R}). \tag{8.83}
\end{aligned}$$

The linear term in the θ_τ distribution given in Eq. 8.81 can be accessed via the forward-backward asymmetry, traditionally defined as

$$\mathcal{A}_{FB}^D = \frac{1}{d\Gamma/dq^2} \left[\int_0^1 - \int_{-1}^0 \right] d \cos \theta_\tau \frac{d^2\Gamma}{dq^2 d \cos \theta_\tau} = \frac{1}{2} \frac{J_1(q^2)}{J_0(q^2) + \frac{1}{3} J_3(q^2)}. \tag{8.84}$$

Finally, integrating Eq. 8.81 over $\cos \theta_\tau$, one obtains the q^2 differential distribution [334], where the dependence on the WCs has been explicitly shown:

$$\begin{aligned}
\frac{d\Gamma}{dq^2}(B \rightarrow D\tau\bar{\nu}) = & \mathcal{N}_D(q^2) \left\{ \left(|1 + C_{LL}^V + C_{RL}^V|^2 + |C_{LR}^V + C_{RR}^V|^2 \right) \left[(H_{V,0})^2 \left(\frac{m_\tau^2}{2q^2} + 1 \right) + \frac{3m_\tau^2}{2q^2} (H_{V,t})^2 \right] \right. \\
& + \frac{3}{2} (H_S)^2 \left(|C_{RL}^S + C_{LL}^S|^2 + |C_{RR}^S + C_{LR}^S|^2 \right) + 8 \left(|C_{LL}^T|^2 + |C_{RR}^T|^2 \right) (H_T)^2 \left(1 + \frac{2m_\tau^2}{q^2} \right) \\
& + 3 \operatorname{Re} \left[(1 + C_{LL}^V + C_{RL}^V) (C_{RL}^S + C_{LL}^S)^* + (C_{LR}^V + C_{RR}^V) (C_{RR}^S + C_{LR}^S)^* \right] \frac{m_\tau}{\sqrt{q^2}} H_S H_{V,t} \\
& \left. - 12 \operatorname{Re} \left[(1 + C_{LL}^V + C_{RL}^V) C_{LL}^{T*} + (C_{RR}^V + C_{LR}^V) C_{RR}^{T*} \right] \frac{m_\tau}{\sqrt{q^2}} H_T H_{V,0} \right\}. \tag{8.85}
\end{aligned}$$

8.3.2 $B \rightarrow D^* \tau \bar{\nu}$

For the process $B \rightarrow D^* \tau \bar{\nu}$, exploiting Lorentz invariance and parity, the hadronic matrix elements can be parametrized as

$$\begin{aligned}
\langle D^* | \bar{c} \gamma_\mu b | \bar{B} \rangle &= -i \epsilon_{\mu\nu\rho\sigma} \epsilon^{\nu*}(\lambda_M) p_B^\rho p_{D^*}^\sigma \frac{2V(q^2)}{m_B + m_{D^*}} \\
\langle D^* | \bar{c} \gamma_\mu \gamma_5 b | \bar{B} \rangle &= (m_B + m_{D^*}) A_1(q^2) \left(\epsilon_\mu^*(\lambda_M) - q_\mu \frac{(\epsilon^*(\lambda_M) \cdot q)}{q^2} \right) \\
&\quad + q_\mu (\epsilon^*(\lambda_M) \cdot q) \frac{2m_{D^*}}{q^2} A_0(q^2)
\end{aligned}$$

$$\begin{aligned}
& -\frac{\epsilon^*(\lambda_M) \cdot q}{m_B + m_{D^*}} A_2(q^2) \left((p_B + p_{D^*})_\mu - q_\mu \frac{m_B^2 - m_{D^*}^2}{q^2} \right), \\
\langle D^* | \bar{c} \gamma_5 b | \bar{B} \rangle &= -(\epsilon^*(\lambda_M) \cdot q) \frac{2m_{D^*}}{m_b + m_c} A_0(q^2), \\
\langle D^* | \bar{c} \sigma_{\mu\nu} b | \bar{B} \rangle &= \epsilon_{\mu\nu\rho\sigma} \left\{ -\epsilon^{\rho*}(\lambda_M) (p_B + p_{D^*})^\sigma T_1(q^2) \right. \\
&+ 2 \frac{(\epsilon^*(\lambda_M) \cdot q)}{q^2} p_B^\rho p_{D^*}^\sigma \left(T_1(q^2) - T_2(q^2) - \frac{q^2}{m_B^2 - m_{D^*}^2} T_3(q^2) \right) \\
&\left. + \epsilon^{*\rho}(\lambda_M) q^\sigma \frac{m_B^2 - m_{D^*}^2}{q^2} (T_1(q^2) - T_2(q^2)) \right\}, \tag{8.86}
\end{aligned}$$

where the form factors $A_0(q^2)$, $A_1(q^2)$, $A_2(q^2)$, $V(q^2)$, $T_1(q^2)$, $T_2(q^2)$ and $T_3(q^2)$ are defined in the last section of this chapter. Notice that the contribution of the scalar current proportional to $(C_{LX}^S + C_{RX}^S)$ is absent because of parity constraints. In this case, performing the contraction with the polarization vectors of the virtual vector boson in the B rest-frame as Eq. 8.60 dictates, the next hadronic helicity amplitudes are obtained:

$$\begin{aligned}
H_{V,\pm}(q^2) &\equiv H_{V_L,\pm}^\pm(q^2) = -H_{V_R,\mp}^\mp(q^2) \\
&= (m_B + m_{D^*}) A_1(q^2) \mp \frac{\sqrt{\lambda_{D^*}(q^2)}}{m_B + m_{D^*}} V(q^2), \\
H_{V,0}(q^2) &\equiv H_{V_L,0}^0(q^2) = -H_{V_R,0}^0(q^2) \\
&= \frac{m_B + m_{D^*}}{2m_{D^*} \sqrt{q^2}} \left[-(m_B^2 - m_{D^*}^2 - q^2) A_1(q^2) + \frac{\lambda_{D^*}(q^2)}{(m_B + m_{D^*})^2} A_2(q^2) \right], \\
H_{V,t}(q^2) &\equiv H_{V_L,t}^0(q^2) = -H_{V_R,t}^0(q^2) = -\sqrt{\frac{\lambda_{D^*}(q^2)}{q^2}} A_0(q^2), \\
H_S(q^2) &\equiv H_{S_R}^0(q^2) = -H_{S_L}^0(q^2) \simeq -\frac{\sqrt{\lambda_{D^*}(q^2)}}{m_b + m_c} A_0(q^2), \\
H_{T,0}(q^2) &\equiv H_{T_L 0t}^0(q^2) = H_{T_L +}^0(q^2) = -H_{T_R 0t}^0(q^2) = H_{T_R +}^0(q^2) \\
&= \frac{1}{2m_{D^*}} \left[-(m_B^2 + 3m_{D^*}^2 - q^2) T_2(q^2) + \frac{\lambda_{D^*}(q^2)}{m_B^2 - m_{D^*}^2} T_3(q^2) \right], \\
H_{T\pm}(q^2) &\equiv H_{T_L \pm 0}^\pm(q^2) = \pm H_{T_L \pm t}^\pm(q^2) = \mp H_{T_R \mp t}^\mp(q^2) = -H_{T_R \mp 0}^\mp(q^2) \\
&= \frac{1}{\sqrt{q^2}} \left[\pm(m_B^2 - m_{D^*}^2) T_2(q^2) + \sqrt{\lambda_{D^*}} T_1(q^2) \right]. \tag{8.87}
\end{aligned}$$

Those, contracted with the leptonic part of the amplitude according to Eq. 8.60, give rise to the following reduced amplitudes involving LH neutrinos:

$$\begin{aligned}
\mathcal{M}_L^{+1,+\frac{1}{2}} &= -\sqrt{q^2} \beta_\tau \sin \theta_\tau e^{-2i\phi} \left\{ \frac{m_\tau}{\sqrt{q^2}} (\mathcal{A}_\parallel^L + \mathcal{A}_\perp^L) - 2(\mathcal{A}_{T\parallel}^L + \mathcal{A}_{T\perp}^L) \right\}, \\
\mathcal{M}_L^{+1,-\frac{1}{2}} &= -\sqrt{q^2} \beta_\tau (1 + \cos \theta_\tau) e^{-i\phi} \left\{ \mathcal{A}_\parallel^L + \mathcal{A}_\perp^L - \frac{2m_\tau}{\sqrt{q^2}} (\mathcal{A}_{T\parallel}^L + \mathcal{A}_{T\perp}^L) \right\}, \\
\mathcal{M}_L^{0,+\frac{1}{2}} &= -2m_\tau \beta_\tau e^{-i\phi} \left\{ \mathcal{A}_{tP}^L + \cos \theta_\tau \left[\mathcal{A}_0^L - \frac{2\sqrt{q^2}}{m_\tau} \mathcal{A}_{T0}^L \right] \right\}, \\
\mathcal{M}_L^{0,-\frac{1}{2}} &= 2\sqrt{q^2} \beta_\tau \sin \theta_\tau \left[\mathcal{A}_0^L - \frac{2m_\tau}{\sqrt{q^2}} \mathcal{A}_{T0}^L \right], \\
\mathcal{M}_L^{-1,+\frac{1}{2}} &= \sqrt{q^2} \beta_\tau \sin \theta_\tau \left\{ \frac{m_\tau}{\sqrt{q^2}} (\mathcal{A}_\parallel^L - \mathcal{A}_\perp^L) - 2(\mathcal{A}_{T\parallel}^L - \mathcal{A}_{T\perp}^L) \right\}, \\
\mathcal{M}_L^{-1,-\frac{1}{2}} &= -\sqrt{q^2} \beta_\tau (1 - \cos \theta_\tau) e^{i\phi} \left\{ \mathcal{A}_\parallel^L - \mathcal{A}_\perp^L - 2 \frac{m_\tau}{\sqrt{q^2}} (\mathcal{A}_{T\parallel}^L - \mathcal{A}_{T\perp}^L) \right\}, \quad (8.88)
\end{aligned}$$

whereas those involving RH neutrinos are given by

$$\begin{aligned}
\mathcal{M}_R^{+1,+\frac{1}{2}} &= -\sqrt{q^2} \beta_\tau (1 - \cos \theta_\tau) e^{-i\phi} \left\{ \mathcal{A}_\parallel^R + \mathcal{A}_\perp^R - 2 \frac{m_\tau}{\sqrt{q^2}} (\mathcal{A}_{T\parallel}^R + \mathcal{A}_{T\perp}^R) \right\}, \\
\mathcal{M}_R^{+1,-\frac{1}{2}} &= -\sqrt{q^2} \beta_\tau \sin \theta_\tau \left\{ \frac{m_\tau}{\sqrt{q^2}} (\mathcal{A}_\parallel^R + \mathcal{A}_\perp^R) - 2(\mathcal{A}_{T\parallel}^R + \mathcal{A}_{T\perp}^R) \right\}, \\
\mathcal{M}_R^{0,+\frac{1}{2}} &= -2\sqrt{q^2} \beta_\tau \sin \theta_\tau \left[\mathcal{A}_0^R - \frac{2m_\tau}{\sqrt{q^2}} \mathcal{A}_{T0}^R \right], \\
\mathcal{M}_R^{0,-\frac{1}{2}} &= -2m_\tau \beta_\tau e^{i\phi} \left\{ \mathcal{A}_{tP}^R + \cos \theta_\tau \left[\mathcal{A}_0^R - \frac{2\sqrt{q^2}}{m_\tau} \mathcal{A}_{T0}^R \right] \right\}, \\
\mathcal{M}_R^{-1,+\frac{1}{2}} &= -\sqrt{q^2} \beta_\tau (1 + \cos \theta_\tau) e^{i\phi} \left\{ \mathcal{A}_\parallel^R - \mathcal{A}_\perp^R - 2 \frac{m_\tau}{\sqrt{q^2}} (\mathcal{A}_{T\parallel}^R - \mathcal{A}_{T\perp}^R) \right\}, \\
\mathcal{M}_R^{-1,-\frac{1}{2}} &= \sqrt{q^2} \beta_\tau \sin \theta_\tau e^{2i\phi} \left\{ \frac{m_\tau}{\sqrt{q^2}} (\mathcal{A}_\parallel^R - \mathcal{A}_\perp^R) - 2(\mathcal{A}_{T\parallel}^R - \mathcal{A}_{T\perp}^R) \right\}. \quad (8.89)
\end{aligned}$$

In the above expressions, the $\mathcal{A}_\lambda^{L,R}$ denote the transversity amplitudes, which are the projections of the total decay amplitude into the explicit polarization basis. The contribution from the RH neutrino transitions to the angular coefficients is equivalent to that from the LH neutrino ones, i.e. ($L \rightarrow R$), up to a sign that depends on the relation between RH and LH leptonic transversity amplitudes. In the SM, the decay $B \rightarrow D^* \tau \bar{\nu}$ can be described by a total of four transversity amplitudes that correspond to one longitudinal (\mathcal{A}_0) and two transverse ($\mathcal{A}_{\perp,\parallel}$) directions, and a time-like component (\mathcal{A}_t) for the virtual vector boson decaying into the $\tau \bar{\nu}$ pair. However, with the inclusion of RH neutrinos, we must distinguish the left and right chiralities of the leptonic current; thus, we get in total eight amplitudes: $\mathcal{A}_{0,\perp,\parallel,t}^{L,R}$. Now, in presence of the NP operators given in Eq. 8.3, the (axial)vector contributions can be incorporated in the above mentioned eight transversity amplitudes, modified by the presence of the new WCs. Nevertheless, the (pseudo)scalar and tensor operators induce eight further amplitudes (four for each neutrino chirality): two (pseudo)scalar amplitudes $\mathcal{A}_P^{L,R}$ and six tensor transversities $\mathcal{A}_{T0,T\perp,T\parallel}^{L,R}$. Thus, with the most general dimension-6 Hamiltonian in Eq. 8.2, the decay $B \rightarrow D^*(\rightarrow D\pi)\tau\bar{\nu}$ can be described by a total of sixteen transversity amplitudes, which are defined as:

$$\begin{aligned}
\mathcal{A}_0^L &= H_{V,0} (1 + C_{LL}^V - C_{RL}^V), \\
\mathcal{A}_{\parallel}^L &= (H_{V,+} + H_{V,-}) (1 + C_{LL}^V - C_{RL}^V)/\sqrt{2}, \\
\mathcal{A}_{\perp}^L &= (H_{V,+} - H_{V,-}) (1 + C_{LL}^V + C_{RL}^V)/\sqrt{2}, \\
\mathcal{A}_t^L &= H_{V,t} (1 + C_{LL}^V - C_{RL}^V), \\
\mathcal{A}_P^L &= H_S (C_{RL}^S - C_{LL}^S), \\
\mathcal{A}_{T0}^L &= 2H_{T,0} C_{LL}^T, \\
\mathcal{A}_{T\parallel}^L &= \sqrt{2} (H_{T,+} - H_{T,-}) C_{LL}^T, \\
\mathcal{A}_{T\perp}^{L,R} &= \sqrt{2} (H_{T,+} + H_{T,-}) C_{LL}^{T,R}, \\
\mathcal{A}_0^R &= H_{V,0} (C_{LR}^V - C_{RR}^V), \\
\mathcal{A}_{\parallel}^R &= (H_{V,+} + H_{V,-}) (C_{LR}^V - C_{RR}^V)/\sqrt{2},
\end{aligned}$$

$$\begin{aligned}
\mathcal{A}_{\perp}^R &= (H_{V,+} - H_{V,-}) (C_{LR}^V + C_{RR}^V)/\sqrt{2}, \\
\mathcal{A}_t^R &= H_{V,t}(C_{LR}^V - C_{RR}^V), \\
\mathcal{A}_P^R &= H_S(C_{RR}^S - C_{LR}^S), \\
\mathcal{A}_{T0}^R &= -2H_{T,0}C_{RR}^T, \\
\mathcal{A}_{T\parallel}^R &= -\sqrt{2}(H_{T,+} - H_{T,-})C_{RR}^T,
\end{aligned} \tag{8.90}$$

which are combinations of the WCs and the hadronic helicities. Here, the abbreviated form $\mathcal{A}_{tP}^{L,R}$ has been introduced to allow for more compact expressions.

$$\mathcal{A}_{tP}^{L,R} = \left(\mathcal{A}_t^{L,R} + \frac{\sqrt{q^2}}{m_{\tau}} \mathcal{A}_P^{L,R} \right). \tag{8.91}$$

To compute the full four-body decay amplitude $B \rightarrow D^* \tau \bar{\nu} \rightarrow (D\pi) \tau \bar{\nu}$, we need to describe the propagation and the decay of the vector boson D^* to the $D\pi$ final state. The $D^* \rightarrow D\pi$ amplitude can be parametrized in the form

$$\mathcal{M}_{D^* \rightarrow D\pi}^{\lambda_{D^*}} = g_{D^*D\pi} \varepsilon_{\mu}(\lambda_{D^*}) p_D^{\mu}, \tag{8.92}$$

with an effective coupling $g_{D^*D\pi}$ that can be determined from the total decay width,

$$\Gamma(D^* \rightarrow D\pi) = C \frac{\lambda^{3/2}(m_{D^*}^2, m_D^2, m_{\pi}^2)}{192\pi m_{D^*}^5} |g_{D^*D\pi}|^2, \tag{8.93}$$

where $C = 1, \frac{1}{2}$ for a final π^{\pm}, π^0 , respectively. The dependence of the effective amplitude 8.92 on the momentum and polarization vectors fixes the angular structure of the three possible helicity amplitudes:

$$\mathcal{M}_{D^* \rightarrow D\pi}^0 = -g_{D^*D\pi} |\vec{p}_D| \cos \theta_D \quad \text{and} \quad \mathcal{M}_{D^* \rightarrow D\pi}^{\pm 1} = \pm \frac{1}{\sqrt{2}} g_{D^*D\pi} |\vec{p}_D| \sin \theta_D,$$

with $|\vec{p}_D| = \lambda^{1/2}(m_{D^*}^2, m_D^2, m_{\pi}^2)/(2m_{D^*})$ being the three-momentum of the D meson in the D^* rest-frame.

The propagation of the D^* can be described through a Breit-Wigner function. Since the decay width of the D^* is much smaller than its mass, we can use the narrow-width approximation,

$$\frac{1}{(m_{D\pi}^2 - m_{D^*}^2)^2 + m_{D^*}^2 \Gamma_{D^*}^2} \xrightarrow{\Gamma_{D^*} \ll m_{D^*}} \frac{\pi}{m_{D^*} \Gamma_{D^*}} \delta(m_{D\pi}^2 - m_{D^*}^2), \quad (8.94)$$

and write the decay probability of the process $B \rightarrow (D\pi) \tau \bar{\nu}$ in the form

$$|\mathcal{M}[B \rightarrow (D\pi) \tau(\lambda_\tau) \nu_X]|^2 = \frac{1}{2} G_F^2 |V_{cb}|^2 \frac{\pi}{m_{D^*} \Gamma_{D^*}} \times \delta(m_{D\pi}^2 - m_{D^*}^2) \left| \sum_{\lambda_{D^*}} \mathcal{M}_X^{\lambda_{D^*}, \lambda_\tau} \mathcal{M}_{D^* \rightarrow D\pi}^{\lambda_{D^*}} \right|^2, \quad (8.95)$$

where $\mathcal{M}_X^{\lambda_{D^*}, \lambda_\tau}$ are the reduced amplitudes defined in Eqs. 8.88 and 8.89. Notice that the dependence on $g_{D^* D\pi}$ cancels out from this expression.

The four-body angular distribution can be computed in a similar way as in the $B \rightarrow D\tau\bar{\nu}$ case, but now taking into account that B decays into four fields. As before, the four-body phase-space can be reduced to a product of two body phase spaces,

$$dQ_4 = \frac{dq^2}{2\pi} \frac{dm_{D\pi}^2}{2\pi} dQ_2(p_{D\pi}, q) dQ_2(\hat{p}_D, \hat{p}_{D\pi}) dQ_2(\hat{p}_\tau, \hat{p}_\nu), \quad (8.96)$$

where $\hat{p}_{D\pi} = -\vec{q}$, \hat{p}_D and \hat{p}_τ are defined in the B , $D\pi$ and $\tau\bar{\nu}$ rest-frames, respectively, and are given by

$$|\hat{p}_{D\pi}| = \frac{\sqrt{\lambda(m_B^2, m_{D\pi}^2, q^2)}}{2m_B}, \quad |\hat{p}_D| = \frac{\sqrt{\lambda(m_{D\pi}^2, m_D^2, m_\pi^2)}}{2m_{D\pi}}, \quad |\hat{p}_\tau| = \frac{q^2 - m_\tau^2}{2\sqrt{q^2}}. \quad (8.97)$$

Here, the angle θ_D is defined, taking as positive z -axis the direction of the D^* momentum in the B rest-frame, as the polar angle of the final D meson in the $D\pi$ rest-frame. See Fig. 8.3 for a visual representation of this angle.

The differential decay distribution of the transition process $B(p_B) \rightarrow D^*(p_{D^*}) \tau(p_\tau) \bar{\nu}(p_{\bar{\nu}})$, with $D^*(p_{D^*}) \rightarrow D(p_D) \pi(p_\pi)$ on the mass shell, can be

expressed in the form [335]:

$$\begin{aligned}
 \frac{d^4\Gamma(B \rightarrow D^* \tau \bar{\nu})}{dq^2 d \cos \theta_\tau d \cos \theta_D d\phi} &= \frac{9}{64\pi} \mathcal{N}_{D^*}(q^2) \mathcal{B}(D^* \rightarrow D\pi) \\
 &\times \left\{ I_1^s \sin^2 \theta_D + I_1^c \cos^2 \theta_D \right. \\
 &\quad + (I_2^s \sin^2 \theta_D + I_2^c \cos^2 \theta_D) \cos 2\theta_\tau \\
 &\quad + (I_3 \cos 2\phi + I_9 \sin 2\phi) \sin^2 \theta_D \sin^2 \theta_\tau \\
 &\quad + (I_4 \cos \phi + I_8 \sin \phi) \sin 2\theta_D \sin 2\theta_\tau \\
 &\quad + (I_5 \cos \phi + I_7 \sin \phi) \sin 2\theta_D \sin \theta_\tau \\
 &\quad \left. + (I_6^s \sin^2 \theta_D + I_6^c \cos^2 \theta_D) \cos \theta_\tau \right\}. \quad (8.98)
 \end{aligned}$$

The interferences among the unobservable helicity amplitudes of the intermediate D^* meson generate the different dependences on θ_D appearing in the above expression. As Eq. 8.98 shows, the vector meson D^* in the final state provides additional observables compared to the previous case. The angular coefficients I_i 's are functions of q^2 that encode both short- and long-distance physics contributions. They can be written in terms of the hadronic form factors as,

$$\begin{aligned}
 I_1^c &= 2 \left(1 + \frac{m_\tau^2}{q^2} \right) \left(|\mathcal{A}_0^L|^2 + 4 |\mathcal{A}_{T0}^L|^2 \right) - \frac{16m_\tau}{\sqrt{q^2}} \operatorname{Re}\{\mathcal{A}_0^L \mathcal{A}_{T0}^{L*}\} + \frac{4m_\tau^2}{q^2} |\mathcal{A}_{tP}^L|^2 + (\text{L} \rightarrow \text{R}), \\
 I_1^s &= \frac{1}{2} \left(3 + \frac{m_\tau^2}{q^2} \right) \left(|\mathcal{A}_\perp^L|^2 + |\mathcal{A}_\parallel^L|^2 \right) + 2 \left(1 + \frac{3m_\tau^2}{q^2} \right) \left(|\mathcal{A}_{T\perp}^L|^2 + |\mathcal{A}_{T\parallel}^L|^2 \right) \\
 &\quad - 8 \frac{m_\tau}{\sqrt{q^2}} \operatorname{Re}\{\mathcal{A}_\perp^L \mathcal{A}_{T\perp}^{L*} + \mathcal{A}_\parallel^L \mathcal{A}_{T\parallel}^{L*}\} + (\text{L} \rightarrow \text{R}), \\
 I_2^c &= -2 \left(1 - \frac{m_\tau^2}{q^2} \right) \left(|\mathcal{A}_0^L|^2 - 4 |\mathcal{A}_{T0}^L|^2 + (\text{L} \rightarrow \text{R}) \right), \\
 I_2^s &= \frac{1}{2} \left(1 - \frac{m_\tau^2}{q^2} \right) \left(|\mathcal{A}_\perp^L|^2 + |\mathcal{A}_\parallel^L|^2 - 4 (|\mathcal{A}_{T\perp}^L|^2 + |\mathcal{A}_{T\parallel}^L|^2) + (\text{L} \rightarrow \text{R}) \right), \\
 I_3 &= \left(1 - \frac{m_\tau^2}{q^2} \right) \left(|\mathcal{A}_\perp^L|^2 - |\mathcal{A}_\parallel^L|^2 - 4 (|\mathcal{A}_{T\perp}^L|^2 - |\mathcal{A}_{T\parallel}^L|^2) + (\text{L} \rightarrow \text{R}) \right), \\
 I_4 &= \sqrt{2} \left(1 - \frac{m_\tau^2}{q^2} \right) \operatorname{Re}\{\mathcal{A}_0^L \mathcal{A}_\parallel^{L*} - 4 \mathcal{A}_{T0}^L \mathcal{A}_{T\parallel}^{L*} + (\text{L} \rightarrow \text{R})\},
 \end{aligned}$$

$$\begin{aligned}
I_5 &= 2\sqrt{2} \left[\text{Re}\{(\mathcal{A}_0^L - 2 \frac{m_\tau}{\sqrt{q^2}} \mathcal{A}_{T0}^L) (\mathcal{A}_\perp^{L*} - 2 \frac{m_\tau}{\sqrt{q^2}} \mathcal{A}_{T\perp}^{L*}) - (\text{L} \rightarrow \text{R})\} \right. \\
&\quad \left. - \frac{m_\tau^2}{q^2} \text{Re}\{A_{tP}^{L*} (\mathcal{A}_\parallel^L - 2 \frac{\sqrt{q^2}}{m_\tau} \mathcal{A}_{T\parallel}^L) + (\text{L} \rightarrow \text{R})\} \right], \\
I_6^c &= \frac{8m_\tau^2}{q^2} \text{Re}\{A_{tP}^{L*} (\mathcal{A}_0^L - 2 \frac{\sqrt{q^2}}{m_\tau} \mathcal{A}_{T0}^L) + (\text{L} \rightarrow \text{R})\}, \\
I_6^s &= 4 \text{Re}\{(\mathcal{A}_\parallel^L - 2 \frac{m_\tau}{\sqrt{q^2}} \mathcal{A}_{T\parallel}^L) (\mathcal{A}_\perp^{L*} - 2 \frac{m_\tau}{\sqrt{q^2}} \mathcal{A}_{T\perp}^{L*}) - (\text{L} \rightarrow \text{R})\}, \\
I_7 &= -2\sqrt{2} \left[\text{Im}\{(\mathcal{A}_0^L - 2 \frac{m_\tau}{\sqrt{q^2}} \mathcal{A}_{T0}^L) (\mathcal{A}_\parallel^{L*} - 2 \frac{m_\tau}{\sqrt{q^2}} \mathcal{A}_{T\parallel}^{L*}) - (\text{L} \rightarrow \text{R})\} \right. \\
&\quad \left. + \frac{m_\tau^2}{q^2} \text{Im}\{A_{tP}^{L*} (\mathcal{A}_\perp^L - 2 \frac{\sqrt{q^2}}{m_\tau} \mathcal{A}_{T\perp}^L) + (\text{L} \rightarrow \text{R})\} \right], \\
I_8 &= \sqrt{2} \left(1 - \frac{m_\tau^2}{q^2} \right) \text{Im}\{\mathcal{A}_0^{L*} \mathcal{A}_\perp^L - 4 \mathcal{A}_{T0}^{L*} \mathcal{A}_{T\perp}^L + (\text{L} \rightarrow \text{R})\}, \\
I_9 &= 2 \left(1 - \frac{m_\tau^2}{q^2} \right) \text{Im}\{\mathcal{A}_\parallel^L \mathcal{A}_\perp^{L*} - 4 \mathcal{A}_{T\parallel}^L \mathcal{A}_{T\perp}^{L*} + (\text{L} \rightarrow \text{R})\}. \tag{8.99}
\end{aligned}$$

The angular analysis of a four-body final state, namely $B \rightarrow D^*(\rightarrow D\pi)\tau\bar{\nu}$, further allows us to construct a multitude of observables that can be extracted from data [335-342].

Measuring this four-dimensional distribution is obviously a major experimental challenge, since the subsequent τ decay involves one ($\tau \rightarrow \nu_\tau + \text{hadrons}$) or two ($\tau \rightarrow \nu_\tau \ell \bar{\nu}_\ell$) additional neutrinos, making difficult to reconstruct the τ direction. However, one can study different angular observables by properly integrating one variable or a set of them.

Performing the angular integrations in Eq. 8.98, one easily obtains the differential distribution with respect to q^2 , given by

$$\frac{d\Gamma}{dq^2} \equiv \Gamma_f = \frac{1}{4} \mathcal{N}_{D^*} \mathcal{B}(D^* \rightarrow D\pi) (3I_1^c + 6I_1^s - I_2^c - 2I_2^s), \tag{8.100}$$

which written explicitly in terms of the different WCs takes the following form:

$$\begin{aligned}
\frac{d\Gamma(B \rightarrow D^* \tau \bar{\nu})}{dq^2} &= \mathcal{N}_{D^*}(q^2) \mathcal{B}(D^* \rightarrow D\pi) \\
&\times \left\{ \left(|1 + C_{LL}^V|^2 + |C_{RL}^V|^2 + |C_{LR}^V|^2 + |C_{RR}^V|^2 \right) \left(1 + \frac{m_\tau^2}{2q^2} \right) (H_{V,+}^2 + H_{V,-}^2) \right. \\
&+ \left(|1 + C_{LL}^V - C_{RL}^V|^2 + |C_{LR}^V - C_{RR}^V|^2 \right) \left[\left(1 + \frac{m_\tau^2}{2q^2} \right) H_{V,0}^2 + \frac{3}{2} \frac{m_\tau^2}{q^2} H_{V,t}^2 \right] \\
&- 4 \operatorname{Re} \left[(1 + C_{LL}^V) C_{RL}^{V*} + C_{LR}^V C_{RR}^{V*} \right] \left(1 + \frac{m_\tau^2}{2q^2} \right) H_{V,+} H_{V,-} \\
&+ \frac{3}{2} \left(|C_{RL}^S - C_{LL}^S|^2 + |C_{RR}^S - C_{LR}^S|^2 \right) H_S^2 \\
&+ 8 \left(|C_{LL}^T|^2 + |C_{RR}^T|^2 \right) \left(1 + \frac{2m_\tau^2}{q^2} \right) (H_{T,+}^2 + H_{T,-}^2 + H_{T,0}^2) \\
&+ 3 \operatorname{Re} \left\{ (1 + C_{LL}^V - C_{LR}^V) (C_{RL}^{S*} - C_{LL}^{S*}) + (C_{LR}^V - C_{RR}^V) (C_{RR}^{S*} - C_{LR}^{S*}) \right\} \frac{m_\tau}{\sqrt{q^2}} H_S H_{V,t} \\
&- 12 \operatorname{Re} \left[(1 + C_{LL}^V) C_{LL}^{T*} + C_{RR}^V C_{RR}^{T*} \right] \frac{m_\tau}{\sqrt{q^2}} (H_{T,0} H_{V,0} + H_{T,+} H_{V,+} - H_{T,-} H_{V,-}) \\
&+ 12 \operatorname{Re} \left[C_{RL}^V C_{LL}^{T*} + C_{LR}^V C_{RR}^{T*} \right] \frac{m_\tau}{\sqrt{q^2}} (H_{T,0} H_{V,0} + H_{T,+} H_{V,-} - H_{T,-} H_{V,+}) \left. \right\}. \quad (8.101)
\end{aligned}$$

Differential distributions with respect to a single angle, which can be obtained by integrating two angles at a time, are also of special interest. These are

$$\begin{aligned}
\frac{d^2\Gamma}{dq^2 d \cos \theta_\ell} &= \frac{3}{8} \mathcal{N}_{D^*} \mathcal{B}(D^* \rightarrow D\pi) \\
&\left[(I_1^c + 2I_1^s - I_2^c - 2I_2^s) + (I_6^c + 2I_6^s) \cos \theta_\ell + (2I_2^c + 4I_2^s) \cos^2 \theta_\ell \right] \quad (8.102)
\end{aligned}$$

$$\begin{aligned}
\frac{d^2\Gamma}{dq^2 d \cos \theta_D} &= \frac{3}{8} \mathcal{N}_{D^*} \mathcal{B}(D^* \rightarrow D\pi) \left[(3I_1^s - I_2^s) + (3I_1^c - I_2^c - 3I_1^s + I_2^s) \cos^2 \theta_D \right] \\
&= \frac{3}{4} \Gamma_f \left[F_T^{D^*} \sin^2 \theta_D + 2 F_L^{D^*} \cos^2 \theta_D \right] \quad (8.103)
\end{aligned}$$

$$\begin{aligned}
\frac{d^2\Gamma}{dq^2 d\phi} &= \frac{1}{8\pi} \mathcal{N}_{D^*} \mathcal{B}(D^* \rightarrow D\pi) \left[(3I_1^c + 6I_1^s - I_2^c - 2I_2^s) + 4I_3 \cos 2\phi + 4I_9 \sin 2\phi \right] \\
&= \frac{1}{2\pi} \Gamma_f \left[1 + A_3 \cos 2\phi + A_9 \sin 2\phi \right]. \quad (8.104)
\end{aligned}$$

In the following we define several observables constructed from the coefficients of various angular dependences. The distribution with respect to $\cos \theta_D$ in Eq. 8.103 provides the longitudinal and transverse polarization fractions for the D^* meson, defined as [335, 338]

$$F_L^{D^*} = \frac{3I_1^c - I_2^c}{3I_1^c + 6I_1^s - I_2^c - 2I_2^s}, \quad \text{and} \quad F_T^{D^*} = \frac{2(3I_1^s - I_2^s)}{3I_1^c + 6I_1^s - I_2^c - 2I_2^s}, \quad (8.105)$$

which satisfy that $F_L^{D^*} + F_T^{D^*} = 1$. The angular coefficients I_3 and I_9 can simply be extracted by measuring the terms proportional to $\cos 2\phi$ and $\sin 2\phi$ in Eq. (8.104),

$$A_3 = \frac{I_3^N}{\Gamma_f}, \quad \text{and} \quad A_9 = \frac{I_9^N}{\Gamma_f}, \quad (8.106)$$

respectively, where $I_i^N \equiv \mathcal{N}_{D^*} \mathcal{B}(D^* \rightarrow D\pi) I_i$. Furthermore, we define several asymmetries starting with the well-known forward-backward asymmetry, defined as

$$A_{FB}^{D^*} = \frac{1}{\Gamma_f} \left[\int_0^1 - \int_{-1}^0 \right] d \cos \theta_\ell \frac{d^2 \Gamma}{dq^2 d \cos \theta_\ell}. \quad (8.107)$$

The coefficients I_4 and I_5 in Eq. (8.98) can be extracted with the two angular asymmetries:

$$\begin{aligned} A_4 &= \frac{1}{\Gamma_f} \left[\int_{-\frac{\pi}{2}}^{\frac{\pi}{2}} - \int_{\frac{\pi}{2}}^{\frac{3\pi}{2}} \right] d\phi \left[\int_0^1 - \int_{-1}^0 \right] d \cos \theta_D \left[\int_0^1 - \int_{-1}^0 \right] d \cos \theta_\ell \frac{d^4 \Gamma}{dq^2 d \cos \theta_\ell d \cos \theta_D d\phi}, \\ A_5 &= \frac{1}{\Gamma_f} \left[\int_{-\frac{\pi}{2}}^{\frac{\pi}{2}} - \int_{\frac{\pi}{2}}^{\frac{3\pi}{2}} \right] d\phi \left[\int_0^1 - \int_{-1}^0 \right] d \cos \theta_D \int_{-1}^1 d \cos \theta_\ell \frac{d^4 \Gamma}{dq^2 d \cos \theta_\ell d \cos \theta_D d\phi}. \end{aligned} \quad (8.108)$$

One can further define the following two observables,

$$A_7 = \frac{1}{\Gamma_f} \left[\int_0^\pi - \int_\pi^{2\pi} \right] d\phi \left[\int_0^1 - \int_{-1}^0 \right] d \cos \theta_D \int_{-1}^1 d \cos \theta_\ell \frac{d^4 \Gamma}{dq^2 d \cos \theta_\ell d \cos \theta_D d\phi}, \quad (8.109)$$

$$A_8 = \frac{1}{\Gamma_f} \left[\int_0^\pi - \int_\pi^{2\pi} \right] d\phi \left[\int_0^1 - \int_{-1}^0 \right] d \cos \theta_D \left[\int_0^1 - \int_{-1}^0 \right] d \cos \theta_\ell \frac{d^4 \Gamma}{dq^2 d \cos \theta_\ell d \cos \theta_D d\phi},$$

which are non-vanishing only if NP induces a complex contribution to the amplitude. This holds true for the coefficient A_9 as well. These asymmetries are simply related to the angular coefficients I_i^N as follows:

$$A_4 = \frac{2}{\pi} \frac{I_4^N}{\Gamma_f}, \quad A_5 = \frac{3}{4} \frac{I_5^N}{\Gamma_f}, \quad \mathcal{A}_{FB}^{D^*} = \frac{3}{8} \frac{I_6^{cN} + 2I_6^{sN}}{\Gamma_f}, \quad A_7 = \frac{3}{4} \frac{I_7^N}{\Gamma_f}, \quad A_8 = \frac{2}{\pi} \frac{I_8^N}{\Gamma_f}.$$

Finally, the total branching ratio can be decomposed in terms of the τ polarization, giving rise to another observable: the lepton polarization asymmetry, defined as

$$\mathcal{P}_\tau^{D^{(*)}} = \frac{d\Gamma_{\lambda_\tau=1/2}/dq^2 - d\Gamma_{\lambda_\tau=-1/2}/dq^2}{\Gamma_f}, \quad (8.110)$$

whose definition is also applicable in the context of the decay $B \rightarrow D\tau\bar{\nu}$.

Notice that the above quantities are functions of q^2 . We define the q^2 -integrated observables, labeled with a bar, as follows,

$$\bar{\mathcal{O}} \equiv \frac{1}{\Gamma} \int_{q_{\min}^2}^{q_{\max}^2} dq^2 \mathcal{O}[q^2] \Gamma_f[q^2], \quad (8.111)$$

where Γ is the total decay width.

8.4 Hadronic Form Factors

This final section is devoted to the form factors (FF) parametrizing the hadronic part of the $B \rightarrow D^{(*)}$ transitions. The determination of these FF requires non perturbative methods. Lattice QCD (LQCD) calculations provide information at zero-recoil (maximal q^2), and even lately non-zero recoil calculations of the FF have been released for $B \rightarrow D$. At low q^2 , information on the FF can be extracted through QCD light-cone sum rules (LCSR). To extrapolate the FF from zero-recoil along the whole q^2 range, a certain parametrization must be used. There are two main approaches followed in the literature: The Boyd-Grinstein-Lebed (BGL) [343–345] is a model independent parametrisation that uses QCD dispersion relations, analyticity, unitarity and crossing-symmetry to parametrize the FF. On the other hand, the

Caprini-Lellouch-Neubert (CLN) parametrization [346] exploits Heavy Quark Effective Field Theory (HQEFT) [347, 348] to parametrize the FF. Recently, the community has been intensively debating about the most adequate way to parametrise the relevant hadronic FF due to the relevance of hadronic uncertainties in the determination of $|V_{cb}|$ [349–356], and it has been suggested that the accuracy of the usually adopted CLN parametrisation [346] has been probably overestimated at the current experimental precision. However, for studying the anomalies in $b \rightarrow c$ transitions, such precision is of less relevance since we are mostly dealing with ratios, reducing the overall FF sensitivity. For our study, we parametrize the FF following a Heavy Quark Expansion beyond the original CLN parametrization as it will be described in the following. In the heavy quark limit all FF either vanish or reduce to a common functional form, the Isgur-Wise function $\xi(q^2)$ [357]. Thus, it is convenient to factor out $\xi(q^2)$ by defining [353]

$$\hat{h}(q^2) = h(q^2)/\xi(q^2). \quad (8.112)$$

The leading Isgur-Wise function can be more conveniently expressed in terms of the kinematical parameters

$$\omega(q^2) = \frac{m_B^2 + m_{D^{(*)}}^2 - q^2}{2m_B m_{D^{(*)}}} \quad \text{and} \quad z(q^2) = \frac{\sqrt{\omega(q^2) + 1} - \sqrt{2}}{\sqrt{\omega(q^2) + 1} + \sqrt{2}}. \quad (8.113)$$

The variable $\omega(q^2)$ is the inner product of the B and $D^{(*)}$ velocities, so that $\omega = 1$ corresponds to the zero-recoil point, $q_{\max}^2 = (m_B - m_{D^{(*)}})^2$, where $\xi(q_{\max}^2) = 1$. Although q^2 in semileptonic B decays ranges from m_τ^2 to $(m_B - m_{D^{(*)}})^2$, the FF can be continued analytically in the q^2 complex plane [350]. However, they have a cut at $q^2 = (m_B + m_{D^{(*)}})^2$. The conformal mapping $z(q^2)$ encodes in a very efficient way the analyticity properties of the FF, transforming the cut in the q^2 plane into the boundary of the circle $|z| < 1$ [358], so that a perturbative expansion in powers of $z(q^2)$ has an optimized convergence. See Fig. 8.4 for an illustration. In this case, the origin of the circle generated by the conformal transformation in Eq. 8.113 is chosen at the point of maximum recoil $\omega = 1$. In the original CLN parametrization, the Isgur-Wise function is expanded up to z^2 and its slope and curvature parameters are constrained by spin-symmetry relations, whereas in here, we let them to be independent parameters.

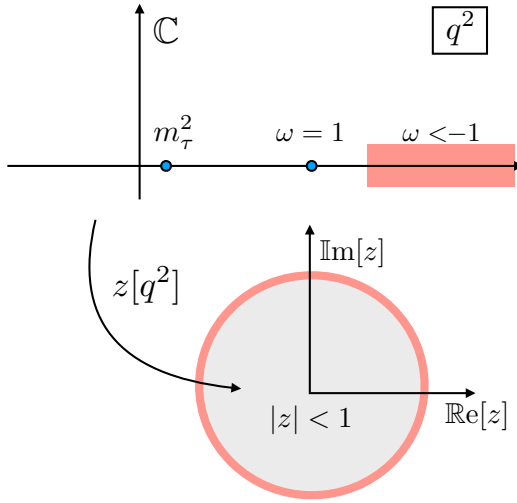


Figure 8.4: Conformal mapping of the q^2 complex plane to a unit disk. The cut in the q^2 plane is mapped to the boundary of the disk $|z| = 1$. The origin $z = 0$ corresponds to the point of maximum q^2 , i.e. $\omega = 1$.

Besides, as recently Refs. [359,360] have pointed out the phenomenological necessity to include orders higher than z^2 in this expansion, we will consider the $\xi(q^2)$ up to $\mathcal{O}(z^4)$ corrections,

$$\begin{aligned}\xi(q^2) &= 1 - \rho^2 [\omega(q^2) - 1] + c [\omega(q^2) - 1]^2 + d [\omega(q^2) - 1]^3 + \mathcal{O}([\omega - 1]^4) \\ &= 1 - 8\rho^2 z(q^2) + (64c - 16\rho^2) z^2(q^2) + (256c - 24\rho^2 + 512d) z^3(q^2) + \mathcal{O}(z^4),\end{aligned}\quad (8.114)$$

described through the parameters ρ^2 , c and d , which are assumed to be independent.

The functions $\hat{h}(q^2)$ introduce corrections of order $\Lambda_{\text{QCD}}/m_{b,c}$ parametrized by the subleading Isgur-Wise functions $\chi_{2,3}(\omega)$, $\eta(\omega)$. Furthermore, we include $\Lambda_{\text{QCD}}/m_c^2$ corrections to those functions $\hat{h}(q^2)$ that are protected, because of Luke's theorem, from $1/m_{c,b}$ corrections, i.e. those that do not vanish at zero recoil:

$$\begin{aligned}h_i(1) &= 1 + \mathcal{O}(1/m_{c/b}^2) & i = +, V, A_1, A_3, S, P, T \text{ and } T_1 \\ h_i(1) &= \mathcal{O}(1/m_c, 1/m_b) & i = -, A_2, T_2 \text{ and } T_3.\end{aligned}$$

The $1/m_c^2$ corrections are introduced by the subleading $l_{1,2}(\omega)$ functions, via the parameters $\{l_1(1), l_2(1)\}$, respectively. These functions also include the corrections of order α_s .

The FF appearing in the D matrix elements, following HQEFT, can be parametrized as

$$\begin{aligned} F_1(q^2) &= \frac{1}{2\sqrt{m_B m_D}} \left[(m_B + m_D) h_+(q^2) - (m_B - m_D) h_-(q^2) \right], \\ F_0(q^2) &= \frac{1}{2\sqrt{m_B m_D}} \left[\frac{(m_B + m_D)^2 - q^2}{m_B + m_D} h_+(q^2) - \frac{(m_B - m_D)^2 - q^2}{m_B - m_D} h_-(q^2) \right], \\ F_T(q^2) &= \frac{m_B + m_D}{2\sqrt{m_B m_D}} h_T(q^2), \end{aligned} \quad (8.115)$$

while the D^* helicity amplitudes, for the $B \rightarrow D^*$ amplitude, involve the functions

$$\begin{aligned} V(q^2) &= \frac{m_B + m_{D^*}}{2\sqrt{m_B m_{D^*}}} h_V(q^2), \\ A_1(q^2) &= \frac{(m_B + m_{D^*})^2 - q^2}{2\sqrt{m_B m_{D^*}}(m_B + m_{D^*})} h_{A_1}(q^2), \\ A_2(q^2) &= \frac{m_B + m_{D^*}}{2\sqrt{m_B m_{D^*}}} \left[h_{A_3}(q^2) + \frac{m_{D^*}}{m_B} h_{A_2}(q^2) \right], \\ A_0(q^2) &= \frac{1}{2\sqrt{m_B m_{D^*}}} \left[\frac{(m_B + m_{D^*})^2 - q^2}{2m_{D^*}} h_{A_1}(q^2) - \frac{m_B^2 - m_{D^*}^2 + q^2}{2m_B} h_{A_2}(q^2) \right. \\ &\quad \left. - \frac{m_B^2 - m_{D^*}^2 - q^2}{2m_{D^*}} h_{A_3}(q^2) \right], \\ T_1(q^2) &= \frac{1}{2\sqrt{m_B m_{D^*}}} \left[(m_B + m_{D^*}) h_{T_1}(q^2) - (m_B - m_{D^*}) h_{T_2}(q^2) \right], \\ T_2(q^2) &= \frac{1}{2\sqrt{m_B m_{D^*}}} \left[\frac{(m_B + m_{D^*})^2 - q^2}{m_B + m_{D^*}} h_{T_1}(q^2) - \frac{(m_B - m_{D^*})^2 - q^2}{m_B - m_{D^*}} h_{T_2}(q^2) \right], \\ T_3(q^2) &= \frac{1}{2\sqrt{m_B m_{D^*}}} \left[(m_B - m_{D^*}) h_{T_1}(q^2) \right. \\ &\quad \left. - (m_B + m_{D^*}) h_{T_2}(q^2) - 2 \frac{m_B^2 - m_{D^*}^2}{m_B} h_{T_3}(q^2) \right]. \end{aligned} \quad (8.116)$$

We refer the reader to Ref. [353,359] for the explicit expressions of the \hat{h} as a function of the parameters described above. Notice that the main difference to the latter article is the introduction of the z^3 term in the leading Isgur-Wise function, that renders the fit compatible with the extrapolation of the recent LQCD data [349,361] to large recoil.

9.- Global fit to $b \rightarrow c$ transitions

Chapter based on the work done in 1904.09311 and 2004.06726.

Signals of lepton flavour universality violation have been appearing since the last decade in the flavour sector, attractively suggesting NP. They have been observed in the B -meson semileptonic decays to particles involving the second generation of quarks, what enters in the scope of the B-factories: BaBar, Belle and the LHCb experiment. The certainty that the SM cannot be the ultimate theory, the lack of NP signals in the recent years, together with the possibility to explore such phenomena at the current experiments make understandable the great attention that these discrepancies have caught from a *thirsty* scientific community. Particularly interesting are the anomalies related to $b \rightarrow c$ transitions; in there, the effect of NP competes with the SM contribution coming from a charged W boson exchange, which tells us that the NP is rather light or strongly coupled to the SM. In this context, it is convenient to study the ratios

$$\mathcal{R}_{D^{(*)}} \equiv \frac{\mathcal{B}(B \rightarrow D^{(*)} \tau \bar{\nu})}{\mathcal{B}(B \rightarrow D^{(*)} \ell \bar{\nu})}, \quad (9.1)$$

where $\ell = e, \mu$ refers to the light lepton modes. Those are particularly clean observables since the leading hadronic uncertainties, as well as the controversial $|V_{cb}|$ component of the CKM matrix are factorized out. Fig. 9.1 shows the different experimental measurements of these ratios that have been published since 2012 by several experimental collaborations. These results lead to the following world average,

$$\mathcal{R}_D^{\text{ave}} = 0.340 \pm 0.027 \pm 0.013, \quad \text{and} \quad \mathcal{R}_{D^*}^{\text{ave}} = 0.295 \pm 0.011 \pm 0.008, \quad (9.2)$$

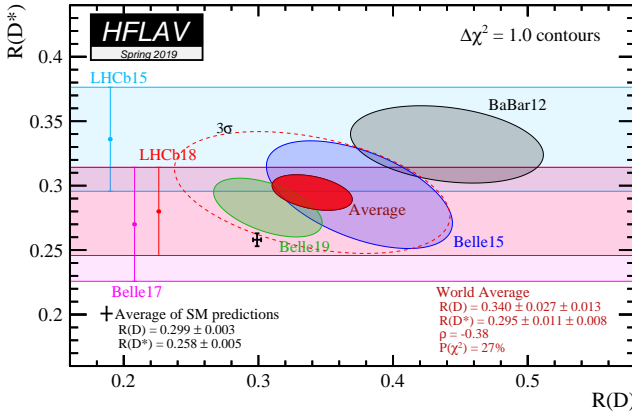


Figure 9.1: Measurements on the $\mathcal{R}_{D^{(*)}}$ ratios up to Spring 2019, together with the averaged value from the SM predictions and the world average from HFLAV. Image extracted from Ref. [362].

performed by the Heavy Flavour Averaging Group (HFLAV) [362], with -0.38 correlation, also shown in Fig. 9.1 in a red ellipse. The HFLAV averaged results deviate at the 3.1σ level from the arithmetic average of the SM predictions [350, 352, 353, 356] quoted by HFLAV: $\mathcal{R}^{\text{SM}} = 0.299 \pm 0.003$ (1.4σ) and $\mathcal{R}_{D^*}^{\text{SM}} = 0.258 \pm 0.005$ (2.5σ) [362]. Using the more updated FF [359], introduced in Sec. 8.4 from the previous chapter and further discussed in this chapter, we get

$$\mathcal{R}_D^{\text{SM}} = 0.302 \pm 0.004, \quad \text{and} \quad \mathcal{R}_{D^*}^{\text{SM}} = 0.258^{+0.006}_{-0.005}, \quad (9.3)$$

which slightly increases the tension to 3.2σ . The climax of these discrepancies was reached a few years ago, after both Belle [363, 364] and the LHCb [365] collaborations updated their analysis and the discrepancies added up to 4.0σ from the SM predictions [366]. This tension, however, was relaxed with the subsequent measurements, being the cherry on top the most recent measurement by Belle [367], released in Moriond 2019, which reported a value closer to the SM prediction (only 2.1σ from it), that softened the claim of physics beyond the SM.

Anomalies have also been observed in other observables involving $b \rightarrow c$ transitions. The recent measurement of the longitudinal polarization of the D^{*-} meson in $B^0 \rightarrow D^{*-} \tau^+ \bar{\nu}$ reported by Belle,

$$\bar{F}_L^{D^*} = 0.60 \pm 0.08 \pm 0.04, \quad (9.4)$$

differs from its SM prediction by 1.6σ [368]. Besides, the recent LHCb measurement [369] of the $B_c \rightarrow J/\Psi$ ratio,

$$\mathcal{R}_{J/\psi} \equiv \frac{\mathcal{B}(B_c \rightarrow J/\psi \tau \bar{\nu}_\tau)}{\mathcal{B}(B_c \rightarrow J/\psi \mu \bar{\nu}_\mu)} = 0.71 \pm 0.17 \pm 0.18, \quad (9.5)$$

also deviates from the SM predictions $\mathcal{R}_{J/\psi}^{SM} \approx 0.25\text{--}0.28$ [370–381] in the same direction as its predecessors. There is also the measurement of the τ -polarisation of the $B \rightarrow D^*$ semileptonic decay from Belle [382],

$$\bar{P}_\tau^{D^*} = -0.38 \pm 0.51_{-0.16}^{+0.21}, \quad (9.6)$$

which is still compatible with the SM prediction but could also allow for modifications within its large uncertainties.

In summary, there is experimental evidence of deviations from the SM predictions in some observables involving $b \rightarrow c$ transitions, which curiously seem to point to a common direction. This tension, if further confirmed and stretched, could be crucial to gain a better insight into the laws describing nature, and thus it needs to be understood.

In this chapter, we present a general study to $b \rightarrow c$ transitions from an EFT bottom-up perspective by performing a global fit to the most general dimension-6 Hamiltonian and all available experimental data on such processes.¹ We take as our starting point the most general effective Hamiltonian describing $b \rightarrow c$ semileptonic transitions, i.e. Eq. 8.2 from Chapter 8, up to four well-motivated assumptions that we name in the following:

- **NP only enters in the third generation of leptons.**

This assumption is motivated by the absence of experimental evidence of deviations from the SM in tree-level transitions involving light leptons. We refer to the phenomenological analysis of $b \rightarrow c(e, \mu)\bar{\nu}_{(e, \mu)}$ transitions made in Ref. [359] which constrains potential effects to be negligible in the present context.

¹A caveat must be done here regarding the experimental measurements taken as inputs of the fit. The ratios $\mathcal{R}_{D^{(*)}}$ have been updated along the writing of the two references on which this chapter is based. The experimental values used in each fit will be specified, being all of them in the last fit that we have presented the most updated values at the time of writing this thesis.

- **The C_{RL}^V WC is lepton-flavour universal.**

This statement can be derived [383–385] by assuming the Standard Model Effective Field Theory (SMEFT) [386, 387], which is the appropriate effective theory in the presence of a sizeable energy gap above the EW scale under the condition of a linear EW symmetry breaking. The fact that no new states beyond the SM have been found so far up to an energy scale of approximately 1 TeV, and that measurements of the Higgs couplings are all consistent with the SM expectations support this scenario. In this context, taking into account our first assumption, we take $C_{RL}^V = 0$, which will therefore reduce the d.o.f. of our fit. As we will see later in this chapter, when the assumption of linear breaking is relaxed, a non-universal C_{RL}^V coefficient can be generated [385].

- **Only LH neutrinos are considered.**

In the EFT framework used to parametrize the semileptonic decays based on $b \rightarrow c$ transitions, we do not consider the possibility of having light RH neutrinos. We stick to the matter content of the SM.

- **All WCs are CP-conserving and, therefore, real.**

The later has been assumed for convenience since, as will be commented later, the quality of the fit results was not significantly improved by relaxing this assumption whereas, by halving the number of WCs to fit, numerous degenerated minima were avoided. We refer the reader to the following references, Ref. [388–392], where possible CP-violating contributions have been studied.

Along this chapter our study gains generality as we relax some of the above assumptions. In this way, we get a better understanding of their particular effect on the results of the global fit. The first part of the chapter is devoted to the study of $b \rightarrow c$ transitions under the four assumptions just mentioned, while in the second and third part, the second and third assumptions are relaxed, respectively. Conclusions are drawn at the end.

9.1 Global fit to $b \rightarrow c$ transitions: SMEFT

Let us remind the starting point of the upcoming study: the most general dimension-6 Hamiltonian built from the SM matter content respecting Lorentz invariance, the gauge symmetry at the bottom quark scale, i.e. $SU(3)_c \otimes U(1)_Q$, and the four assumptions listed before,

$$\mathcal{H}_{\text{eff}}^{b \rightarrow c \tau \bar{\nu}} = \frac{4G_F}{\sqrt{2}} V_{cb} [(1 + C_{LL}^V) \mathcal{O}_{LL}^V + C_{LR}^S \mathcal{O}_{RL}^S + C_{LL}^S \mathcal{O}_{LL}^S + C_{LL}^T \mathcal{O}_{LL}^T] + \text{h.c.}, \quad (9.7)$$

where the operators are defined according to their chirality, indicated by the chiral projector $P_{X=L,R}$ acting on the quark current,²

$$\mathcal{O}_{LL}^V = (\bar{c} \gamma^\mu P_L b) (\bar{\tau} \gamma_\mu \nu_L), \quad \mathcal{O}_{XL}^S = (\bar{c} P_X b) (\bar{\tau} \nu_L), \quad \mathcal{O}_{LL}^T = (\bar{c} \sigma^{\mu\nu} P_L b) (\bar{\tau} \sigma_{\mu\nu} \nu_L),$$

and the WCs in the above Hamiltonian are parametrizing any NP signal, in such a way that we can recover the SM by setting all of them to zero.

9.1.1 Fit independent analysis

The first step towards the understanding of these phenomena is to study in a totally fit-independent way the dependence of the currently accessible observables, i.e. $\mathcal{R}_{D^{(*)}}$, $\bar{P}_\tau^{D^*}$ and $\bar{F}_L^{D^*}$, on the individual WCs. Such dependence is shown in Fig. 9.2. We abstain from including the J/ψ observable in our study because the hadronic uncertainties are not at the same level as for the observables related to $B \rightarrow D^{(*)}$ transitions and the experimental error is large. As Fig. 9.2 shows, a positive vector WC C_{LL}^V would help shifting the predictions of the ratios $\mathcal{R}_{D^{(*)}}$ closer to their experimental values. Since the C_{LL}^V enters in the EFT in the same way as the contribution from the W gauge boson, we will refer to a non-zero C_{LL}^V as a *global modification* of the SM. Fig. 9.3, which reflects the correlation between the ratio observables \mathcal{R}_D and \mathcal{R}_{D^*} , corroborates that an enhancement of the SM contribution would be enough to achieve the consistency between theory and experiment in the context of these observables. In spite of this, special attention must be drawn to the recently measured longitudinal

²We note that, since there are not RH neutrinos in the theory, the lepton currents have a fixed chirality.

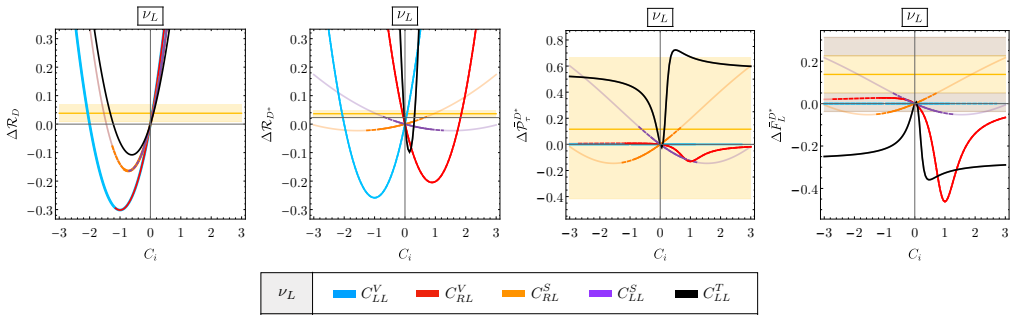


Figure 9.2: Individual contributions of the WCs involving LH neutrinos. The solid (dashed) lines show the parameter space allowed by the constraint $\mathcal{B}(B_c \rightarrow \tau \nu) < 10\%$ (30%), whereas the fainter lines show the predictions without taking into account this constraint. *Figure extracted from Ref. [393].*

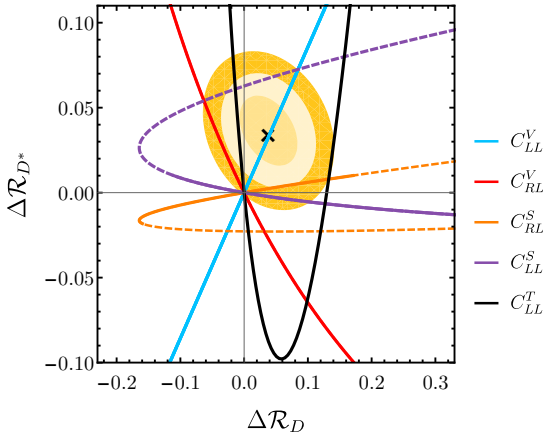


Figure 9.3: Correlation between $\Delta \mathcal{R}_D$ and $\Delta \mathcal{R}_{D^*}$ as a function of the WCs. The experimental central value is denoted by a black cross and the 1σ , 2σ and 3σ uncertainties by yellow rings. *Figure extracted from Ref. [393].*

polarization $\bar{F}_L^{D^*}$ since neither a shift of C_{LL}^V , nor any other individual contribution of WCs, would help to improve the theoretical prediction with respect to its experimental value. The reader may notice that scalar WCs C_{RL}^S and C_{LL}^S could be good candidates when positive and negative contributions, respectively, are achieved. Unfortunately, these possibilities are forbidden by the indirect constraint on the branching ratio of the

leptonic decay:

$$\begin{aligned} \mathcal{B}(B_c \rightarrow \tau \bar{\nu}_\tau) &= \tau_{B_c} \frac{m_{B_c} m_\tau^2 f_{B_c}^2 G_F^2 |V_{cb}|^2}{8\pi} \left(1 - \frac{m_\tau^2}{m_{B_c}^2}\right)^2 \\ &\times \left| 1 + C_{LL}^V - C_{RL}^V + \frac{m_{B_c}^2}{m_\tau(m_b + m_c)} (C_{RL}^S - C_{LL}^S) \right|^2, \quad (9.8) \end{aligned}$$

which was computed in Chapter 8 (see Eq. 8.52). Although there is no explicit measurement of this quantity, and it is not expected to be measured in the foreseeable future, this decay has been indirectly constrained by the total lifetime of the B_c meson [388, 394, 395], giving an upper bound of 30 – 40%. A more stringent 10% bound can be obtained from LEP data at the Z peak as recently pointed out by the authors of Ref. [396], which might become even stronger if the full L3 data is included in the analysis [397]. The later bound has been used lately in the literature, sometimes even pushed down to 5%. However, there are some caveats that must be taken into account: (a) It assumes the probability of a b quark hadronising into a B_c meson to be the same at LEP (e^+e^-), the Tevatron ($p\bar{p}$) and LHCb (pp), which exhibit very different transverse momenta. This is known to be a bad approximation in the case of b -baryons, see Ref. [398]. (b) It makes use of the SM theoretical prediction for $\mathcal{B}(B_c \rightarrow J/\Psi \tau \bar{\nu})$. See Ref. [391] for a more detailed discussion.

It is remarkable that the above constraint restricts two particular combinations of WCs, the so-called axial $C_A \equiv C_{RL}^V - (1 + C_{LL}^V)$ and pseudoscalar $C_P \equiv C_{RL}^S - C_{LL}^S$ combinations. Note that under the assumption of $C_{RL}^V = 0$, the axial and vector coefficients match. Conveniently, the pattern of dependences in Eq. 9.8 is also found in the observables involving the D^* meson. The later are also sensitive to the tensor WC, which is however absent in the leptonic B_c decay. The common set of WCs describing $B_c \rightarrow \tau \bar{\nu}$ and the D^* observables allows us to extend our fit-independent study by looking at the simultaneous effect of several WCs. In this way, we can get a more realistic overview since the later approach, although providing a fair intuition of their main effect on the observables, is hiding possible interferences and correlations among the different WCs.

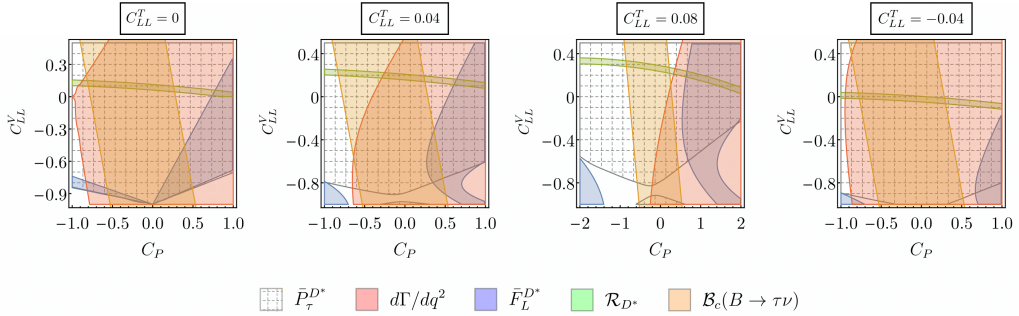


Figure 9.4: Allowed regions at 1σ from $F_L^{D^*}$ (blue), \mathcal{R}_{D^*} (green), $\mathcal{P}_\tau^{D^*}$ (gray grid) and the q^2 distribution of $\Gamma(B \rightarrow D^* \tau \bar{\nu}_\tau)$ (red), together with the region satisfying the bound $\mathcal{B}(B_c \rightarrow \tau \bar{\nu}) < 10\%$ (orange). *Figure extracted from Ref. [393].*

Fig. 9.4 shows the region for the WCs entering in $B \rightarrow D^*$ observables we consider, i.e. \mathcal{R}_{D^*} , $\bar{P}_\tau^{D^*}$ and $\bar{F}_L^{D^*}$, allowed by their experimental values within the 1σ level. The permitted phase-space is represented in the $C_{LL}^V - C_P$ plane for different values of C_{LL}^T . As the figure shows, there is no overlapping region at 1σ , as the study of individual WCs was already suggesting. In fact, the 1σ range for $F_L^{D^*}$ cannot be reached by any combination of NP parameters in this setup, when only imposing $\mathcal{B}(B_c \rightarrow \tau \bar{\nu}) \leq 10\%$ or even 30% , and at the same time requiring a positive shift in \mathcal{R}_{D^*} . Agreement can presently be achieved, however, at the 2σ level. A confirmation of the present central value with higher precision could indicate inconsistency between experimental data and the theoretical assumptions made in our approach, since no kind of NP can apparently resolve the tension at 1σ .

9.1.2 Global Fit

Let us now contrast the previous ideas with the information obtained from a global fit. In this subsection, we will first provide some details about the fit structure, then the results of the global fit will be presented, together with the predictions for some observables in their context. The results obtained will be interpreted at the end.

9.1.2.1 Fit structure

In order to seek for the most favourable scenarios given the available experimental data, one can minimize the so-called *Chi square* function, which is built from the differences between the theoretical predictions (f_{th}) and their experimental values (f_{exp}):

$$\chi^2(y_i) = F^T(y_i) V^{-1} F(y_i), \quad F(y_i) = f_{\text{th}}(y_i) - f_{\text{exp}}, \quad V_{ij} = \rho_{ij} \sigma_i \sigma_j, \quad (9.9)$$

where the matrix V contains the information about the uncertainties (σ_i for the observable i), and the correlation (ρ_{ij}) between the quantities (i and j), and the y_i are the free inputs we are fitting, that in our case correspond to the four WCs $\{C_{LL}^V, C_{RL}^S, C_{LL}^S, C_{LL}^T\}$, and the ten FF parameters $\{\rho^2, c, d, \chi_2(1), \chi_2'(1), \chi_3'(1), \eta(1), \eta'(1), l_1(1), l_2(1)\}$, described in Section 8.4 from Chapter 8. The uncertainty of a parameter y_i is determined as the shift Δy_i in that parameter where the minimization of $\chi^2|_{y_i=y_i^{\text{min}}+\Delta y_i}$, varying all remaining parameters in the vicinity of the minimum, leads to an increase of $\Delta\chi^2 = 1$.

Our χ^2 splits in four parts which are uncorrelated between each other. Those are:

$$\chi^2 = \underbrace{\chi_{R_{D^{(*)}}}^2 + \chi_{d\Gamma/dq^2}^2 + \chi_{FP^*}^2}_{\chi_{\text{exp}}^2} + \underbrace{\chi_{\text{FF}}^2}_{\chi_{\text{theo}}^2}. \quad (9.10)$$

They can be classified in two main groups: χ_{exp}^2 and χ_{theo}^2 . The later contains the information on the hadronic FF. As explained in the last section of Chapter 8, the FF can be described by ten parameters (listed above) following a HQEFT approach beyond the CLN parametrization [346], including corrections of order α_s , $\Lambda_{\text{QCD}}/m_{b,c}$ and partly $\Lambda_{\text{QCD}}^2/m_c^2$, mostly following Refs. [353, 359]. Those ten parameters are fitted to the inputs from LQCD [349, 361, 399, 400], LCSR [401] and QCD sum rules [402–404] (see Ref. [359] for details). Their fitted values are given in Table 9.1, while the corresponding correlation matrix is listed in Table II from Ref. [393]. In this sense, such fit renders the FF independent of the NP scenario considered, since it does not rely on experimental data. Thus, in our χ^2 , the FF will be treated as pseudo-observables with the model-independent fitted values listed in Table 9.1 as “experimental” inputs. In this way, we are taking into account the propagation of the error associated to these

ρ^2	c	d	$\chi_2(1)$	$\chi'_2(1)$
1.32 ± 0.06	1.20 ± 0.12	-0.84 ± 0.17	-0.058 ± 0.020	0.001 ± 0.020
$\chi'_3(1)$	$\eta(1)$	$\eta'(1)$	$l_1(1)$	$l_2(1)$
0.036 ± 0.020	0.355 ± 0.040	-0.03 ± 0.11	0.14 ± 0.23	2.00 ± 0.30

Table 9.1: Inputs used to determine the FF in the HQET parametrization as in [353]. The first three parameters determine the leading Isgur-Wise function, while the last seven enter in the $1/m_{c,b}$ and $1/m_c^2$ corrections. *Table adapted from Ref. [393].*

quantities.

On the other hand, the χ_{exp}^2 splits in three parts, corresponding to the three class of observables we use in our analysis:

- **The ratios $\mathcal{R}_{D^{(*)}}$**

As mentioned at the beginning of this chapter, BaBar, Belle and LHCb have published different experimental measurements for $R_{D^{(*)}}$. We use in the fit the results averaged by the HFLAV collaboration [398]. Because the analysis we present in this part of the chapter was performed along 2019, at first we used in the global fit the averaged results:

$$\mathcal{R}_D^{\text{avg}} = 0.407 \pm 0.039 \pm 0.024, \quad \text{and} \quad \mathcal{R}_{D^*}^{\text{avg}} = 0.306 \pm 0.013 \pm 0.007,$$

with a correlation of -20% , what did not include the most recent measurement from Belle [405]. When we were about to publish our analysis, a preliminar result was released in Moriond 2019 [406], which slightly shifted the average towards the SM predictions. When being aware of this information, we repeated the global fit including the new average, so that the effect of the latest measurement is tangible by contrasting the results from both fits.

As mentioned above, these ratios are advantageous both theoretically and experimentally, as they allow for the cancellation of uncertainties, specifically the CKM factors and leading FF uncertainties on the theoretical side.

- **Differential distributions of the decay rates $\Gamma(B \rightarrow D^{(*)} \tau \bar{\nu})$**

Belle and BaBar have also released data on the measured q^2 distributions for $B \rightarrow D^{(*)} \tau \bar{\nu}$ [363, 407], which provide complementary information on $b \rightarrow c$ transitions that has not been exploited in the literature, with the exception of Refs. [388, 408–410]. The reported binned values are listed in Table 9 from Ref. [393].

Since the global normalizations of these distributions are already implicitly included in $\mathcal{R}_{D^{(*)}}$, they are not independent d.o.f. in the fit. This can be taken into account either by introducing a free normalization factor for the distributions as in Ref. [388] or by normalizing the differential binned distributions in the following way:

$$\tilde{\Gamma}(B \rightarrow D^{(*)} \tau \bar{\nu})_{\text{bin}} \equiv \frac{\Gamma(B \rightarrow D^{(*)} \tau \bar{\nu})_{\text{bin}}}{\sum_{\text{all bins}} \Gamma(B \rightarrow D^{(*)} \tau \bar{\nu})_{\text{bin}}}, \quad (9.11)$$

which keeps the information about the shape of the distribution, independently of the global normalization. The treatment of systematic uncertainties and correlations follows Ref. [388]. The expressions for the semileptonic $B \rightarrow D^{(*)} \tau \bar{\nu}$ differential distributions are given in Eqs. 8.85 and 8.100 from Chapter 8.

- **The longitudinal polarization fraction $\bar{F}_L^{D^*}$**

A measurement of the D^* longitudinal polarization fraction, defined in Eq. 8.105 from Chapter 8, has been recently announced by the Belle collaboration [368]. Being normalized to the total rate, this observable also enjoys the advantages of the other ratios. To study the implications of this measurement, we perform one fit including $\bar{F}_L^{D^*}$ and one without it.

Besides the semi-leptonic processes included in the fit, as commented earlier, the pure leptonic decay $B_c \rightarrow \tau \bar{\nu}$ is crucial in determining the direction of potential NP effects. In our fits, we will compare the results obtained when imposing the upper bounds 10% and 30% on the later branching ratio. These bounds are implemented in the χ^2 as a Heaviside Theta function, whose contribution is zero for parameter combinations where these limits are obeyed and infinity for those where they are not.

9.1.2.2 Fit results

Let us start discussing the SM scenario, which corresponds to all the WCs set to zero. In this context,

$$\chi_{\text{SM}}^2/\text{d.o.f.} = 65.5/57, \quad (9.12)$$

where the denominator indicates the number of d.o.f. considered in the fit. It corresponds to a naive confidence level (C.L.) of $\sim 20\%$. We note that the limit from the B_c lifetime is irrelevant in the SM fit. The *apparent* good quality of the fit, i.e. $\chi_{\text{SM}}^2/\text{d.o.f.} < 1$, might be surprising in comparison with the discrepancy claimed in the $\mathcal{R}_{D^{(*)}}$ measurements. In fact, the normalized value of the χ^2 is misleading as an indicator of the quality of the fit. The reason is that the systematic uncertainties added to the $d\Gamma/dq^2$ distributions are chosen to be maximally conservative, so that the corresponding χ^2 contribution is reduced. For instance, the contribution from the q^2 -distributions is $\chi_{\text{SM},d\Gamma}^2 \sim 43$ for, again naively, 54 d.o.f., which illustrates such phenomenon. Considering instead the contribution from $\mathcal{R}_{D^{(*)}}$, indeed we do reproduce the well-known puzzle, i.e. we obtain $\chi_{\text{SM},\mathcal{R}_{D^{(*)}}}^2 = 22.6$ for 2 d.o.f., corresponding to a 4.4σ tension. These observations imply that also NP scenarios should not be judged simply by their absolute χ^2 vs. d.o.f., but by the relative improvement of their χ^2 with respect to the one obtained in the SM as an indicator of their *quality*.

Considering the four relevant WCs in Eq. 9.7 and not including $\bar{F}_L^{D^*}$ as an input, the global fit gives a total of three minima, described in Table 9.2: a global minimum with $\chi_{\text{Min } 1}^2 = 34.1$ for 53 d.o.f.; and two local minima, with $\chi_{\text{Min } 2}^2 = 37.5$ and $\chi_{\text{Min } 3}^2 = 58.6$, being the later highly disfavoured by the differential distributions in q^2 . The local minima are not very deep, resulting in complications in the determination of the uncertainties for the WCs at these points. We mark with a symbol \dagger such uncertainties that, before reaching the $\Delta\chi^2 = 1$, fall into another minimum.

Since the WCs enter each observable bilinearly, there is a degeneracy between a set of WCs and a mirror minimum with

$$C_{LL}^{V'} = -2 - C_{LL}^V \text{ }^3, \quad \text{and} \quad C_i' = -C_i, \quad \text{for} \quad C_i = C_{RL}^S, C_{LL}^S, C_{LL}^T. \quad (9.13)$$

³Notice that the coefficient of the LH vector operator is $(1 + C_{LL}^V)$.

	Min 1	Min 2	Min 3	Min 1	Min 2	Min 3
$\mathcal{B}(B_c \rightarrow \tau \bar{\nu})$	10%			30%		
$\chi^2_{\min}/\text{d.o.f.}$	34.1/53	37.5/53	58.6/53	33.8/53	36.6/53	58.4/53
C_{LL}^V	$0.17^{+0.13}_{-0.14}$	$0.41^{+0.05}_{-0.06}$	$-0.57^{+0.23}_{-0.24}$	$0.19^{+0.13}_{-0.17}$	$0.42^{+0.06}_{-0.06}$	$-0.54^{+0.23}_{-0.24}$
C_{RL}^S	$-0.39^{+0.38}_{-0.15}$	$-1.15^{+0.18}_{-0.08}$	$0.06^{+0.59}_{-0.19}$	$-0.56^{+0.49}_{-0.17}$	$-1.33^{+0.25}_{-0.08}$	$-0.14^{+0.69}_{-0.18}$
C_{LL}^S	$0.36^{+0.11}_{-0.35}$	$-0.34^{+0.12}_{-0.19}$	$0.64^{+0.13}_{-0.49}$	$0.54^{+0.10}_{-0.46}$	$-0.16^{+0.13}_{-0.22}$	$0.81^{+0.12}_{-0.58}$
C_{LL}^T	$0.01^{+0.06}_{-0.05}$	$0.12^{+0.04}_{-0.04}$	$0.32^{+0.02}_{-0.03}$	$0.01^{+0.07}_{-0.05}$	$0.12^{+0.04}_{-0.04}$	$0.32^{+0.02}_{-0.03}$

Table 9.2: NP parameters for the minima obtained from the χ^2 minimization and 1σ uncertainties. There are, in addition, three corresponding sign-flipped minima, as indicated in Eq. 9.13. In the first three columns, the constraint $\mathcal{B}(B_c \rightarrow \tau \bar{\nu}) \leq 10\%$ has been applied, whereas in the last three columns, such constraint has been relaxed to 30% . *Table from Ref. [393].*

Actually, this discrete degeneracy is just a remnant of the continuous rephasing invariance that the complex WCs enjoy in the context of the observables entering in the fit. Since the two sets of WCs give the same χ^2 and the same predictions, in the following we will only discuss one of them, particularly the scenario with smaller $|C_{LL}^V|$.

When adding the longitudinal polarization to the global fit, the overall structure for the best two minima remains, although the available parameter space for the NP parameters is slightly reduced. Nevertheless, strikingly, the less favoured local minimum disappears. The results for the NP parameters at the minima obtained when including \bar{F}_L^{D*} , which will be referred under the label “b”, can be found in Table 9.3.

	Min 1b	Min 2b	Min 1b	Min 2b
$\mathcal{B}(B_c \rightarrow \tau \bar{\nu})$	10%		30%	
$\chi^2_{\min}/\text{d.o.f.}$	37.6/54	42.1/54	37.6/54	42.0/54
C_{LL}^V	$0.14^{+0.14}_{-0.12}$	$0.41^{+0.05}_{-0.05}$	$0.14^{+0.14}_{-0.14}$	$0.40^{+0.06}_{-0.07}$
C_{RL}^S	$0.09^{+0.14}_{-0.52}$	$-1.15^{+0.18}_{-0.09}$	$0.09^{+0.33}_{-0.56}$	$-1.34^{+0.57}_{-0.08}$
C_{LL}^S	$-0.09^{+0.52}_{-0.11}$	$-0.34^{+0.13}_{-0.19}$	$-0.09^{+0.68}_{-0.21}$	$-0.18^{+0.13}_{-0.57}$
C_{LL}^T	$0.02^{+0.05}_{-0.05}$	$0.12^{+0.04}_{-0.04}$	$0.02^{+0.05}_{-0.05}$	$0.11^{+0.03}_{-0.04}$

Table 9.3: NP parameters for the minima obtained from the χ^2 minimization including \bar{F}_L^{D*} and their 1σ uncertainties. There are, in addition, the corresponding sign-flipped minima, as indicated in Eq. 9.13. *Table from Ref. [393].*

Graphically, the results of the fit for the scenarios with and without $\bar{F}_L^{D^*}$ are represented in Fig. 9.5. In both cases the FF parameters reproduce their input distributions up to very small shifts; that is why we do not report them in the following.

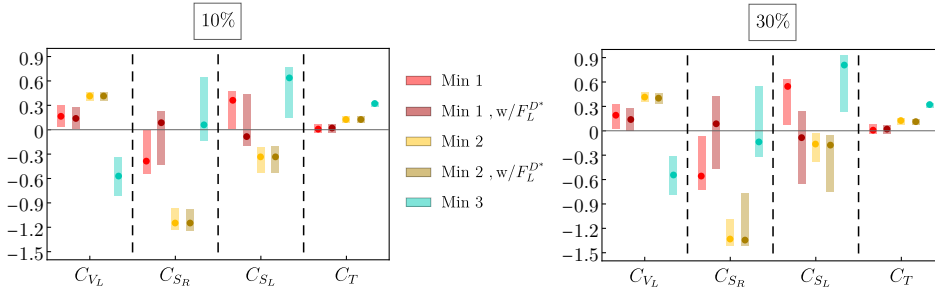


Figure 9.5: WCs for the minima obtained in the global fit with and without including the $\bar{F}_L^{D^*}$ polarization. On the left (right) panel, $\mathcal{B}(B_c \rightarrow \tau\bar{\nu}) < 10\%$ (30%). See Tables 9.2 and 9.3 for their explicit values. *Figure extracted from Ref. [393].*

There are important correlations between the NP parameters obtained from the fit, which are illustrated in the two-dimensional plots from Fig. 9.6 for the different scenarios: with and without $\bar{F}_L^{D^*}$ and for 10% and 30% upper bounds on $\mathcal{B}(B_c \rightarrow \tau\bar{\nu})$. The contours shown in that figure are relative to the global minimum. We note that the distributions for, especially, the scalar parameters are highly non-gaussian. This asymmetry can be understood from the way that the upper limit on $\mathcal{B}(B_c \rightarrow \tau\bar{\nu})$ is implemented in the fit. In addition, since only their sum and difference enter in $B \rightarrow D$ and $B \rightarrow D^*$ decays, respectively, these parameters are furthermore highly correlated. The non-gaussianity is also a consequence from the fact that the first two minima overlap to some extent.

As we commented before, we used the HFLAV average for the ratios $\mathcal{R}_{D^{(*)}}$ from Eq. 9.11 as input for our fit. Including the new average shown in Eq. 9.2 instead, we found again qualitatively similar solutions to the previous case, as the comparison of the numerical results in Tables 9.3 and 9.4 reflects. In the later, the results from the fit including the new HFLAV average are shown. For simplicity, we present only the solutions with $\mathcal{B}(B_c \rightarrow \tau\bar{\nu}) < 10\%$; increasing this limit results again essentially in larger ranges for especially the scalar WCs, although the new global minimum now *does* saturate this limit, so also the central values change.

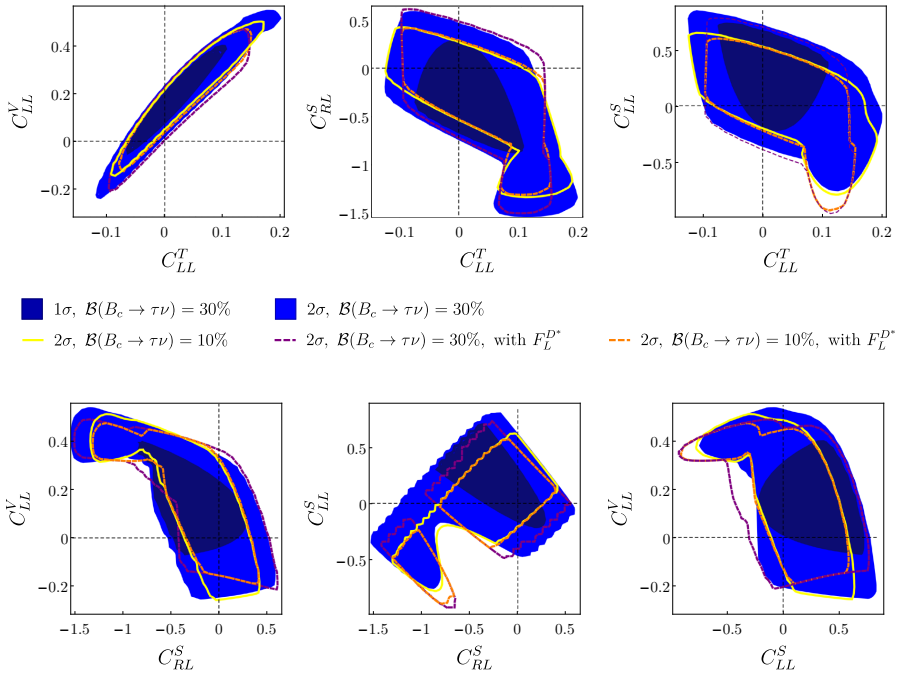


Figure 9.6: Allowed regions for all possible combinations of two WCs for different scenarios: Blue areas (lighter 95% and darker 68% C.L.) show the minima without \bar{F}_L^{D*} and with $\mathcal{B}(B_c \rightarrow \tau\bar{\nu}) \leq 30\%$. The yellow lines display how the 95% C.L. bounds change when $\mathcal{B}(B_c \rightarrow \tau\bar{\nu}) \leq 10\%$. The dashed lines show the effect of adding the observable \bar{F}_L^{D*} for both $\mathcal{B}(B_c \rightarrow \tau\bar{\nu}) \leq 30\%$ (purple) and for $\leq 10\%$ (orange). *Figure extracted from Ref. [393].*

	Min 1b	Min 2b
$\chi_{\min}^2/\text{d.o.f.}$	37.4/54	40.1/54
C_{LL}^V	$0.09^{+0.13}_{-0.11}$	$0.35^{+0.04}_{-0.07}$
C_{RL}^S	$0.14^{+0.06}_{-0.67}$	$-1.27^{+0.66}_{-0.07}$
C_{LL}^S	$-0.20^{+0.58}_{-0.03}$	$-0.30^{+0.12}_{-0.51}$
C_{LL}^T	$0.007^{+0.046}_{-0.044}$	$0.091^{+0.029}_{-0.030}$

Table 9.4: Minima and 1σ uncertainties obtained from the global χ^2 minimization, including the (at that time preliminary) Moriond-19 result measured by Belle on the $\mathcal{R}_{D^{(*)}}$ ratios [406] and the \bar{F}_L^{D*} polarization [368], using $\mathcal{B}(B_c \rightarrow \pi\nu) < 10\%$. There are, in addition, the corresponding sign-flipped minima, as indicated in Eq. 9.13. *Table from Ref. [393].*

9.1.3 Predictions

In Fig. 9.7 the predictions for the ratios $\mathcal{R}_{D^{(*)}}$ in the context of the scenarios studied in the previous section at their different minima are represented. In blue, the SM prediction is shown, while the experimental central value of the ratios and its uncertainty are shown in a gray solid line and bands of the same color, respectively.

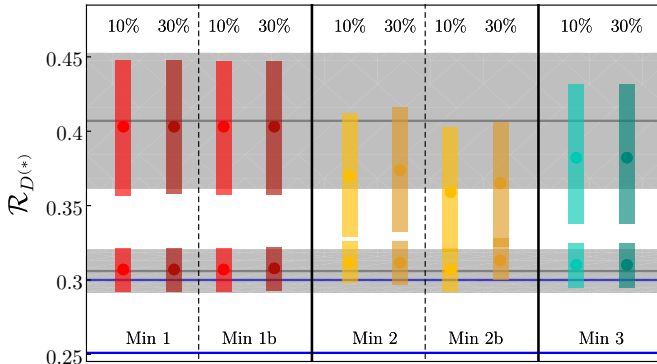


Figure 9.7: Predictions for \mathcal{R}_D (higher numerical values) and \mathcal{R}_{D^*} (lower numerical values) for the minima obtained in the fit, both with and without including $\bar{F}_L^{D^*}$, with $\mathcal{B}(B_c \rightarrow \tau \bar{\nu}) \leq 10\%$ and $\leq 30\%$. The experimental values are represented by the horizontal black lines, with their corresponding uncertainties (grey bands). The blue lines show the SM predictions, $\mathcal{R}_D = 0.300^{+0.005}_{-0.004}$ (upper blue line) and $\mathcal{R}_{D^*} = 0.251^{+0.004}_{-0.003}$ (lower blue line). *Figure extracted from Ref. [393].*

The predictions for the integrated angular observables within their 1σ uncertainty are displayed in Fig. 9.8. In red bars we show the predictions for $\bar{F}_L^{D^*}$. Notice that, although being included in the scenarios “b” of the fit, still the $\bar{F}_L^{D^*}$ predictions are not compatible with experiment within 1σ ; however, they are closer to the experimental value as one would expect. In yellow, we show the predictions for $\bar{\mathcal{P}}_\tau^{D^*}$, defined in Eq. 8.110, whose experimental value was not included in the fit due to its large uncertainties. Indeed, as the figure shows, all predictions of $\mathcal{P}_\tau^{D^*}$ are compatible with the experimental value at less than 1σ . To complete our study, we also show the predictions for other accessible observables that have not been measured yet, such as the forward-backward asymmetries $\bar{\mathcal{A}}_{FB}^D$ (purple) and $\bar{\mathcal{A}}_{FB}^{D^*}$ (green), defined in Eq. 8.84

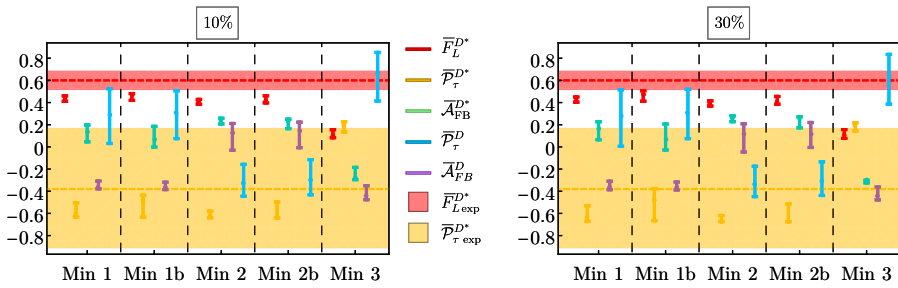


Figure 9.8: Predictions of the integrated observables for the different minima without (Min 1, Min 2 and Min 3) and with (Min 1b, Min 2b) the inclusion of \bar{F}_L^{D*} in the fit. The shaded areas show the experimental results at 1σ where applicable. On the left (right) panel, a bound of $\mathcal{B}(B_c \rightarrow \tau\bar{\nu}) \leq 10\%$ (30%) has been applied. *Figure extracted from Ref. [393].*

and 8.110 from Chapter 8, respectively; and the τ polarization for the D meson, \bar{P}_τ^D (blue), described in Eq. 8.110 from the same chapter.

For completion, the integrated angular observables obtained when updating the fit to include the last Belle measurement on the ratios $\mathcal{R}_{D^{(*)}}$ released in Moriond-19 are also shown in Fig. 9.9.

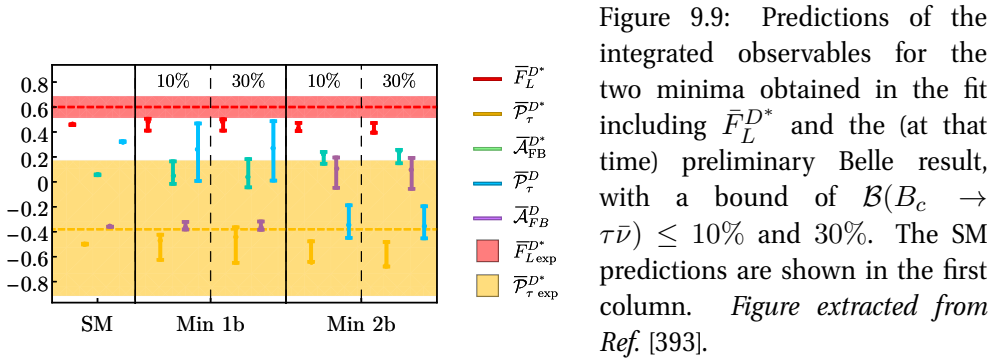


Figure 9.9: Predictions of the integrated observables for the two minima obtained in the fit including \bar{F}_L^{D*} and the (at that time) preliminary Belle result, with a bound of $\mathcal{B}(B_c \rightarrow \tau\bar{\nu}) \leq 10\%$ and 30% . The SM predictions are shown in the first column. *Figure extracted from Ref. [393].*

To close this section, we show the q^2 dependence of the angular observables at the 1σ level in the context of the global (red) and local (yellow) minima obtained when including the \bar{F}_L^{D*} measurement and the Moriond-19 \bar{F} measurement of the ratios in the

fit, assuming the more conservative upper bound of 30% for $\mathcal{B}(B_c \rightarrow \tau \bar{\nu})$. In blue, the SM prediction is shown.

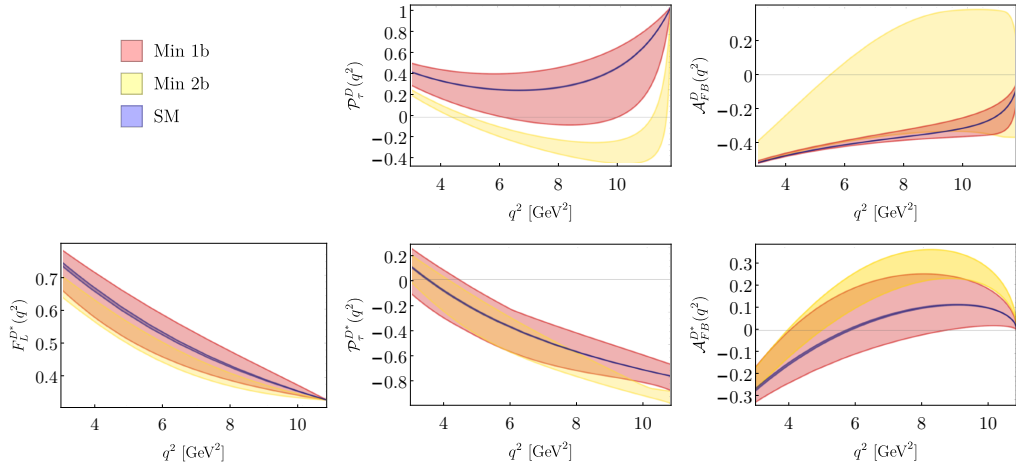


Figure 9.10: Predictions and 1σ uncertainty on the q^2 dependence of the $B \rightarrow D^{(*)}\tau\bar{\nu}$ observables, for the solutions of the fit including the Moriond-19 result and $\bar{F}_L^{D^*}$. An upper bound of $\mathcal{B}(B_c \rightarrow \tau\bar{\nu}) \leq 30\%$ has been adopted. The predictions of Min 1b, Min 2b and the SM are represented by a red, yellow and blue band, respectively. *Figure extracted from Ref. [393].*

9.1.4 Interpretation of the results

Let us analyze the results obtained so far. From those not including $\bar{F}_L^{D^*}$, the following information can be extracted:

- The reduction of the global χ^2 by 31.4 (31.7) for 4 NP parameters implies a strong preference of NP compared to the SM, taking the present data set at face value and $\mathcal{B}(B_c \rightarrow \tau\bar{\nu}) \leq 10\%$ (30%).
- There is no absolute preference of a single WC in the sense that for the global minimum each individual WC is compatible with zero within at most 1.1σ .
- On the other hand, considering scenarios with only a single WC present, there is a clear preference for C_{LL}^V : removing the other three WCs increases χ^2 only

by 1.4, corresponding to 0.14σ . Hence, Min 1 is well compatible with a global modification of the SM, that is, C_{LL}^V being the only non-zero coefficient.

- The other two minima are numerically further away from the SM; instead of a single dominant contribution, there are several sizeable WCs whose contributions partly cancel each other in some observables. These minima also imply different values for the fitted observables: Min 2 corresponds to a slightly worse fit for both, $\mathcal{R}_{D^{(*)}}$ and their q^2 distributions, while Min 3 fits $\mathcal{R}_{D^{(*)}}$ perfectly, but is essentially already excluded by the (rather coarse) measurements of the distributions available.
- All minima saturate the constraint $\mathcal{B}(B_c \rightarrow \tau\bar{\nu}) \leq 10\%$ (30%). Relaxing the upper bound allows for a larger splitting between the two scalar WCs, and the contribution of the scalar operators gets enlarged. This constraint is consequently the main argument at low energies disfavouring a solution with only scalar coefficients. Any such solution would require a lower value for \mathcal{R}_{D^*} by about 2σ .
- Having solutions with relevant contributions from all WCs illustrates the importance of taking into account scalar and tensor operators in the fit.
- The fit results for the FF parameters reproduce their input values displayed in Table 9.1 up to tiny shifts. This implies that the uncertainties of the experimental data with tauonic final states are large compared to the hadronic uncertainties. Differently stated, while the ranges obtained for the NP parameters are obtained in fits varying all FF parameters simultaneously with the NP ones, they are essentially determined by the experimental uncertainties at the moment.
- Generalizing the fit to complex WCs does not improve the minimal χ^2 value, but opens up a continuum of solutions. Hence, complex WCs can explain the anomalies as well as real ones, but they do not offer any clear advantages regarding the fit quality, so they have not been considered here for simplicity. It should be mentioned, however, that in specific models the option of complex WCs can open up qualitatively new solutions, as for example the model proposed in Ref. [389], where only the coefficients C_{LL}^S, C_{LL}^T ($C_{LL}^S \sim C_{LL}^T$)

are present, *requiring* a non-vanishing imaginary part in order to accommodate the experimental data. This fact implies correlations with new observables like electric dipole moments, which can then be used to differentiate this model from solutions allowing for real coefficients [411].

- As discussed above, for each minimum given in Table 9.2 there is a degenerate solution, see Eq. 9.13.

Including the recent measurement of the longitudinal polarization \bar{F}_L^{D*} in the global fit, the above statements hold up to the following differences:

- Still there is no clear preference for a single WC. In this context, the central values for the scalar coefficients are smaller for the global minimum, such that the bound from the B_c lifetime is not saturated even in the 10% case. As a consequence, the minimum does not change when allowing for larger values of $\mathcal{B}(B_c \rightarrow \tau \bar{\nu})$; only the allowed parameter ranges increase.
- The second local minimum (previously referred to as Min 3) disappears.

Finally, considering the updated average of the ratios $\mathcal{R}_{D^{(*)}}$ released in Moriond 2019, we observe that again all individual coefficients are roughly compatible with zero at 1σ . C_{LL}^V alone also still provides an excellent fit to all the data, now with a smaller central value of ~ 0.08 . Interestingly, the fit with only C_{LL}^T is improved by the new results, although this does not correspond to any concrete UV complete scenarios.

It is not straightforward to compare our fit with the results from other analyses in the literature, because we are including the information from the q^2 distributions that has been ignored in most of the previous fits, as commented earlier. Besides that, some works include additional observables such as $\mathcal{R}_{J/\psi}$ or slightly different bounds on $\mathcal{B}(B_c \rightarrow \tau \bar{\nu})$. Nevertheless, comparing the findings of previous fits with our results is quite enlightening since it illustrates the relevance of the additional observables we are considering. Generic fits to the $\mathcal{R}_{D^{(*)}}$ world averages in Eq. (9.11), with the effective Hamiltonian of Eq. 9.7 [331, 337, 353, 359, 388, 390, 391, 395, 409, 410, 412–430], have shown the existence of many possible solutions, some of them involving only one or two WCs. Including the $\mathcal{B}(B_c \rightarrow \tau \bar{\nu})$ upper bound reduces the number of allowed possibilities,

but several different scenarios remain still consistent with the data. These solutions can be easily reproduced when the q^2 distributions are dropped from our fit. However, most of them lead to differential distributions in clear conflict with the BaBar and Belle measurements. While a sizeable NP contribution to some WC can easily generate the needed enhancement of the $B \rightarrow D^{(*)} \tau \bar{\nu}$ rates, it tends to distort the shape of the differential distributions in a way than can no-longer accommodate the data, similarly to what happens for Min 3. Once the full experimental information on $\mathcal{R}_{D^{(*)}}$ (rates and binned distributions) is taken into account, the χ^2 minimization only gives the three solutions shown in Table 9.2, and when including $\bar{F}_L^{D^*}$ in the fit, the number of solutions is further reduced to two.

Looking at the collection of results obtained in the global fit and reminding us what we have learnt from the fit-independent analysis, we can conclude that NP is strongly preferred compared to the SM. In contrast, for the global minimum, each individual WC is compatible with zero at 1σ ; ⁴. Hence, there is no preferred direction for NP that could explain the so-called flavour anomalies for $b \rightarrow c$ transitions. In addition, under the assumptions that C_{RL}^V is flavour universal and there are no RH neutrinos, it is not possible to find agreement between all experimental measurements at 1σ regardless of the form of the UV theory behind. This potential incompatibility would suggest one of several possibilities:

- 1) One of our theoretical assumptions is incorrect and the SMEFT cannot be applied at the EW scale. This could happen if one or several of the following cases apply: (a) There is an insufficient gap between the EW and the NP scale, i.e., there are new d.o.f. close enough to the EW scale to invalidate an EFT approach. (b) The EW symmetry breaking is non-linear, changing also the character of the observed Higgs-like particle. In that case C_{RL}^V could contribute to the fitted observables, because it would no-longer be necessarily flavour universal. (c) There are additional light d.o.f. like RH neutrinos [431–433], yielding additional operators.

⁴This apparent contradiction can be understood by looking at Fig. 9.6 there are strong correlations among the WCs. For instance, as the panel in the left-up corner shows, it is not possible to set both the vector and tensor WCs to zero simultaneously.

Note that we also assumed the semi-leptonic decays with light leptons to be free from NP. However, the corresponding constraints are so strong that even relaxing this assumption would not significantly change our analysis [359].

- 2) An unidentified or underestimated systematic uncertainty in one or several of the experimental measurements.

In any case, the upcoming experimental studies of not only the LHCb collaboration, but also the Belle II experiment, which started to take data, will hopefully resolve this question soon.

9.2 Global fit to $b \rightarrow c$: Including C_{RL}^V

We will first explore the possibility that the EW symmetry breaking is not linearly realized, i.e. C_{RL}^V is not flavour universal so that it could modify the predictions for the $b \rightarrow c$ observables. The aim of relaxing this initial assumption we made in the previous fit is to study whether this allows us to find agreement among all experimental measurements in the context of a consistent theoretical framework.

Going back to the fit-independent analysis of the D^* observables, we find that, in this case, overlap between all observables at 1σ can be found. This is illustrated in Fig. 9.11, for different benchmark values of C_{LL}^V and C_{LL}^T , in the C_{RL}^V - C_P plane.

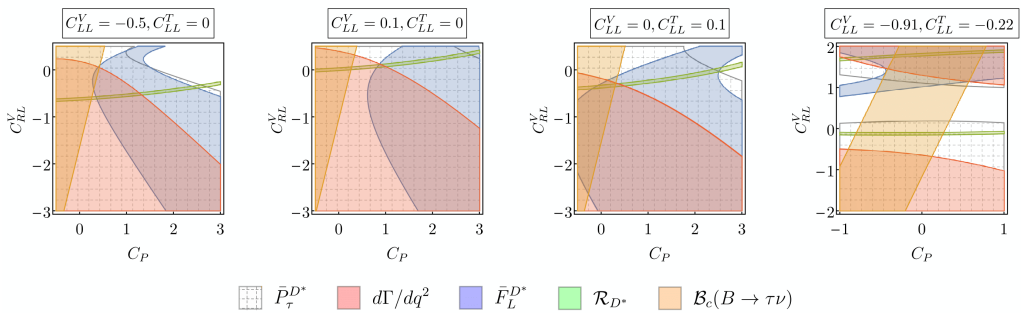


Figure 9.11: Allowed regions at 1σ from $\bar{F}_L^{D^*}$ (blue), \mathcal{R}_{D^*} (green), $\bar{\mathcal{P}}_{\tau}^{D^*}$ (gray grid) and the q^2 distribution of $\Gamma(B \rightarrow D^* \tau \bar{\nu})$ (red), together with the region satisfying the bound $\mathcal{B}(B_c \rightarrow \tau \bar{\nu}) < 10\%$ (orange), with $C_{RL}^V \neq 0$.

In this case, the fit has an extra d.o.f. with respect to the previous one, C_{RL}^V , and the number of minima is doubled (plus their sign-flipped counterparts), as shown in Fig. 9.12. The \bar{F}_L^{D*} measurement has been included in this fit. These four minima, together with the value of the NP parameters in their context, are numerically listed in Table 9.5.

	Min 4	Min 5	Min 6	Min 7
$\chi_{\min}^2/\text{d.o.f.}$	32.5/53	33.3/53	37.6/53	38.9/53
C_{LL}^V	$-0.91^{+0.10}_{-0.09}$	$-0.85^{+0.20}_{-0.10}$	$0.14^{+0.14}_{-0.12}$	$0.35^{+0.08}_{-0.08}$
C_{RL}^V	$1.89^{+0.19}_{-0.22}$	$-1.58^{+0.23}_{-0.22}$	$0.02^{+0.21}_{-0.24}$	$0.34^{+0.18}_{-0.18}$
C_{RL}^S	$-0.44^{+0.12}_{-0.45}$	$-0.33^{+0.52}_{-0.16}$	$0.10^{+0.15}_{-0.59}$	$-0.68^{+0.54}_{-0.14}$
C_{LL}^S	$-1.34^{+0.49}_{-0.12}$	$0.56^{+0.23}_{-0.54}$	$-0.12^{+0.65}_{-0.15}$	$-0.92^{+0.58}_{-0.11}$
C_{LL}^T	$-0.22^{+0.10}_{-0.11}$	$0.19^{+0.10}_{-0.10}$	$0.01^{+0.09}_{-0.07}$	$-0.02^{+0.08}_{-0.07}$

Table 9.5: Minima with their 1σ uncertainties obtained from the global χ^2 minimization, including \bar{F}_L^{D*} and $\mathcal{B}(B_c \rightarrow \tau \bar{\nu}) < 10\%$ in the fit while allowing for $C_{RL}^V \neq 0$. There are, in addition, the corresponding sign-flipped minima, as indicated in Eq. 9.13. *Table from Ref. [393].*

The doubling of minima can be understood qualitatively in the following way: $B \rightarrow D$ is dominated by the combination of WCs corresponding to the vector coupling $C_V \equiv 1 + C_{LL}^V + C_{RL}^V$, while $B \rightarrow D^*$ is dominated by the axial-vector coupling $C_A \equiv C_{RL}^V - (1 + C_{LL}^V)$. Their rates are correspondingly roughly given by $|C_{V,A}|^2$. For $C_{RL}^V = 0$ we have $C_V = -C_A$, and the only remaining discrete symmetry is the \mathcal{Z}_2 symmetry in the WCs, the second solution being eliminated by our choice $C_{LL}^V > -1$. With a finite coefficient C_{RL}^V , these two solutions become four ($\{C_A = \pm|C_A|, C_V = \pm|C_V|\}$), since now $|C_A| \neq |C_V|$; two of those are again eliminated by our choice for C_{LL}^V , leaving two solutions per minimum with $C_{RL}^V = 0$. This degeneracy is broken by interference terms, notably $\text{Re}(C_A C_V^*)$ in $B \rightarrow D^*$, but also the interference with scalar and tensor operators. Nevertheless, this approximate degeneracy explains the doubling of solutions for finite C_{RL}^V .

Comparing these minima with the ones previously obtained, listed in Table 9.3, we find that the previous global minimum, Min 1b, remains a solution of this more

general fit, now called Min 6. Furthermore, Min 1b doubles into an extra local minimum in this case, which enjoys a significant contribution from C_{RL}^V that compensates the change in C_{LL}^V with respect to Min 1b results. The new global minimum, called Min 4, and the close-lying Min 5 improve the agreement of the fit with the data significantly. However, in these scenarios, the SM coefficient is almost completely cancelled and its effect replaced by several NP contributions. These are hence fine-tuned scenarios, and should be taken with a grain of salt.

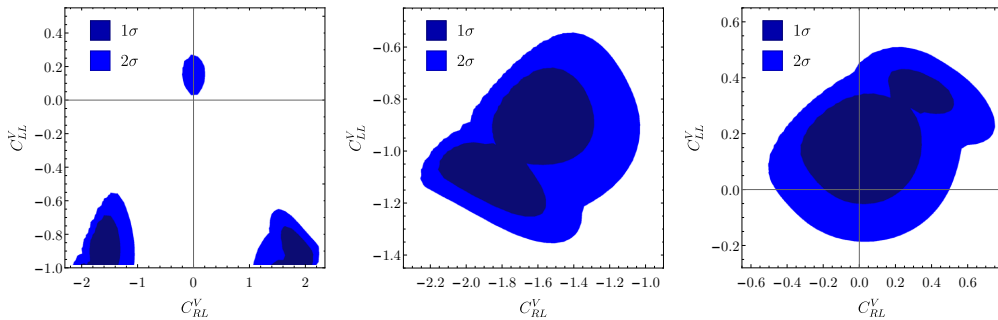


Figure 9.12: Allowed regions in the $C_{RL}^V - C_{LL}^V$ plane, for the global fit including \bar{F}_L^{D*} , restricting $\mathcal{B}(B_c \rightarrow \tau \bar{\nu}) \leq 10\%$. Lighter and darker blue areas show regions with 95% and 68% CL, respectively. Left: All four minima shown in the chosen parameter convention with $C_{LL}^V > -1$, relative to the global minimum. Center: the two minima with $C_{LL}^V \sim -1$, without restricting $C_{LL}^V > -1$, see text. Right: the two minima with $|C_{RL,LL}^V| < 1$, relative to Min 6. *Figure extracted from Ref. [393].*

In accordance with the above reduction for χ_{\min}^2 , and looking at the fourth panel of Fig. 9.11 where the result of the global minimum Min 4 has been assumed for the fixed WCs, we observe that, in this case, it is possible to have an overlap of all the bands. However, it is still not possible to reach the central value for the longitudinal polarization fraction, and as mentioned above, one should be aware that this scenario corresponds to a fine-tuned combination of parameters.

9.3 Global fit to $b \rightarrow c$: Including ν_R

From the previous section we have realized that, by allowing for a non-flavour universal C_{RL}^V , although consistency between theory and experiment can be found at the 1σ level, the fit proposes scenarios that, even fine-tuned, would not be able to provide a satisfactory answer if the statistics is improved and the central value does not change.

At this stage, there is only one assumption left that we could relax; let us assume that light RH neutrinos can play a role in our EFT. This statement is well-motivated by the fact that neutrinos have a tiny mass which, as we have already discussed several times along this thesis, cannot be explained within the SM matter content. A RH d.o.f. could provide mass to the $SU(2)_L$ neutrino that the SM contains. Even though the origin of this mass, the nature of neutrinos and their embedding in a UV-completion of the SM remain as big question marks, as discussed in Chapter 1, we will assume the existence of a $\nu_R \sim (1, 1, 0)$, a sterile neutrino, affecting our EFT at low energies. The RH singlet comprises the simplest ingredient for neutrino masses and it is further motivated by consistent gauge theories involving the lepton number (see Chapters 3 and 5). In the literature, light RH neutrinos have been suggested as a possible way to evade the current phenomenological constraints on the EFT operators containing ν_L fields, see Refs. [334, 340, 415, 431–444]. Besides, the existing limits from the neutrino sector do not constrain significantly the scale of ν_R operators beyond what is probed in $b \rightarrow c\tau\bar{\nu}$ transitions. In order not to disrupt the measured $B \rightarrow D^{(*)}\tau\bar{\nu}$ invariant mass distributions, we will assume light RH neutrinos, $m_{\nu_R} \lesssim \mathcal{O}(100)$ MeV, which is also consistent with other cosmological and astrophysical limits. Although this neutrino mass range is not specially motivated with respect to other mass scales, it is motivated by our aim: to study whether light RH neutrino could modify our conclusions about the anomalies so far.

If neutrino masses are neglected, the two chiralities do not interfere and, therefore, the decay probability becomes an incoherent sum of the LH and RH neutrino contributions:

$$\Gamma(B \rightarrow c\tau\bar{\nu}) = \Gamma(B \rightarrow c\tau\bar{\nu}_L) + \Gamma(B \rightarrow c\tau\bar{\nu}_R) \quad (9.14)$$

By extending the SM matter content to an extra RH singlet, new interactions unavoidably appear. In this context, the number of WCs of the effective Hamiltonian is doubled. In Chapter 8, in Eq. 8.2, the most general Hamiltonian describing the relevant interactions for $b \rightarrow c\tau\bar{\nu}$ transitions was introduced, and it will be the basis of the study presented in this section.

9.3.1 Fit-independent analysis

As we previously did for the LH coefficients, let us study the effect of the WCs involved in the RH neutrino lepton currents on the observables we are interested in. In Fig. 9.13, the dependence of the observables on the individual RH neutrino WCs is displayed, together with their experimental values within their 1σ uncertainty, shaded with a yellow band.

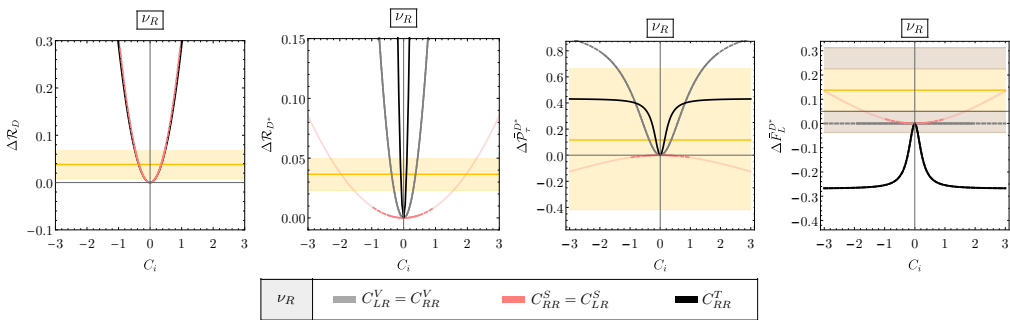


Figure 9.13: Individual contributions of the WCs involving RH neutrinos. The solid (dashed) lines show the parameter space allowed by the constraint $\mathcal{B}(B_c \rightarrow \tau\bar{\nu}) < 10\%$ (30%), whereas the fainter lines show the predictions without taking into account this constraint. *Figure extracted from Ref. [333].*

As the reader can see, because of the absence of the W contribution in the RH sector, the expressions for the D and D^* observables enjoy explicitly more symmetry than before. For instance, in Fig. 9.13, we can see how the effect of vector and scalar WCs is degenerated when switched on individually. Comparing the contributions of the RH neutrino WCs with the LH ones, shown in Fig. 9.2, both behave similarly in the sense that vector WCs, as Fig. 9.14 also shows, constitute a perfect remedy for the discrepancies in the ratios $\mathcal{R}_{D^{(*)}}$ but for $\bar{F}_L^{D^*}$, in contrast, the prediction deviates even

more from its experimental value. Scalar contributions would also help towards lowering the tension of these observables but they are strongly constrained by the $\mathcal{B}(B_c \rightarrow \tau \bar{\nu})$ decay, similarly to the scenario with LH neutrinos. That is why we should in general expect a better agreement between theory and experiment when such bound is relaxed, although as we will see this is not always the case. So far, from the contributions of

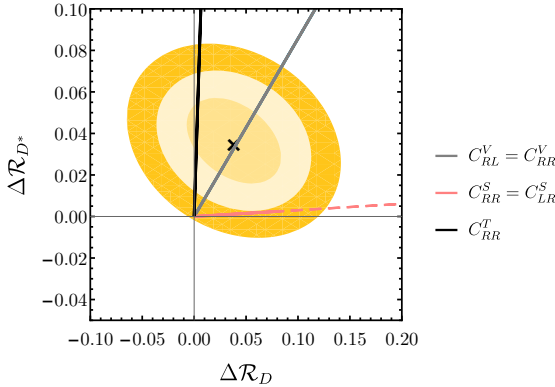


Figure 9.14: Correlation between $\Delta\mathcal{R}_D$ and $\Delta\mathcal{R}_{D^*}$, where the dependence on the individual RH neutrino WCs is displayed according to the legend. The experimental central value is denoted by a black cross, whereas in yellow bands we show the 1-, 2- and 3- σ uncertainties.

individual RH neutrino WCs, one can conclude that no agreement can be found at 1σ , likewise the previous case. Apparently, even doubling the number of free parameters in our EFT, the experimental value for $\bar{F}_L^{D^*}$ together with the $B_c \rightarrow \tau \bar{\nu}$ decay keep theory and experiment from being compatible at the 1σ level. Notice that such incompatibility disappears when the $\bar{F}_L^{D^*}$ measurement is taken at 2σ , as Fig. 9.13 shows in brown bands. Let us study whether the interferences between several WCs, as well as the addition of both LH and RH contributions help towards achieving a consistent scenario for the charged current flavour anomalies.

9.3.2 Global Fit

For the global fit we follow the same procedure obeyed when only considering LH leptonic currents with the following differences:

- We updated the average of the ratios to the numbers published by HFLAV in summer 2019 [362],

$$\mathcal{R}_D^{\text{ave}} = 0.340 \pm 0.027 \pm 0.013 \quad \text{and} \quad \mathcal{R}_{D^*}^{\text{ave}} = 0.295 \pm 0.011 \pm 0.008. \quad (9.15)$$

- In spite of its big uncertainties, $\bar{\mathcal{P}}_\tau^{D^*}$ was included this time in the fit. The reason is that in this case the number of free variables is doubled and this constrain helped to stabilize the fit.

9.3.2.1 Standard Model

First of all, let us look at the SM scenario in this context. Very similar to the previous case, up to the above modifications, by setting all the WCs to zero the χ^2 for the SM, with now 59 d.o.f., is given by

$$\chi_{\text{SM}}^2/\text{d.o.f.} = 52.87/59, \quad (9.16)$$

corresponding to a 69.95% probability (p-value, defined below). As in the previous case, we should take the normalized χ^2 with a grain of salt, since we know that the inclusion of multiple inputs with large uncertainties, in our case the differential q^2 distributions of the semileptonic decays, reduce considerably the absolute χ^2 value and can lead to misleading conclusions. The overestimation of the quality of the fit can be understood, in exactly the same way as we argued in the first section of this chapter, by looking at the split contributions of the fit inputs. Considering only the contribution of the q^2 distributions we find that $\chi_{\text{SM}}^2(q^2 \text{ distributions})/\text{d.o.f.} = 36.77/56$, while $\chi_{\text{SM}}^2(\mathcal{R}_{D^{(*)}}, \bar{F}_L^{D^*}, \bar{\mathcal{P}}_\tau^{D^*})/\text{d.o.f.} = 16.1/4$, corresponding to a 2.98σ tension for the later. Taking into account only the χ^2 value of $\mathcal{R}_{D^{(*)}}$ we obtain 13.36 for 2 d.o.f., recovering the well-known 3.2σ tension. As a *fair* indicator of the fit quality, let us define the SM-pull, which is a statistical measure that quantifies the goodness of the fit. It is defined as the probability in units of σ corresponding to the difference $\Delta\chi_i^2 \equiv \chi_{\text{SM}}^2 - \chi_i^2$, assuming that $\Delta\chi_i^2$ follows a χ^2 distributed function with $\Delta n_i \equiv n_{\text{SM}} - n_i$ d.o.f., where the label i refers to the i th scenario. The translation from probability to σ s is done by associating such probability to the one corresponding to a *Pull* number of standard deviations in a normal distribution with Δn_i d.o.f.,⁵ i.e. [423,445]

$$\text{Pull}_{\text{SM}} \equiv \text{prob}(\Delta\chi_i^2, \Delta n_i)[\sigma] = \sqrt{2} \text{Erf}^{-1}[\text{CDF}(\Delta\chi_i^2, \Delta n_i)], \quad (9.17)$$

⁵A probability of (68.3%, 95.5%, 99.7%) equals to (1σ , 2σ , 3σ), respectively.

All: C_{LL}^V + All RH neutrino WCs								
Min.	Br	$\chi^2/\text{d.o.f.}$	C_{LL}^V	C_{LR}^V	C_{RR}^V	C_{RR}^S	C_{LR}^S	C_{RR}^T
All[1]	10%	37.26/53	$-0.36^{+0.34}_{-0.64^\dagger}$	$1.10^{+0.46}_{-0.50}$	$0.031^{+0.14}_{-0.17}$	$-0.03^{+0.18}_{-0.60}$	$-0.29^{+0.31}_{-0.53}$	$-0.105^{+0.066}_{-0.084}$
	30%	36.42/53	$-0.50^{+0.41}_{-0.49^\dagger}$	$1.34^{+0.25}_{-0.60}$	$0.204^{+0.298}_{-0.020}$	$-0.22^{+0.27^\dagger}_{-0.27}$	$-0.92^{+0.22^\dagger}_{-0.15}$	$-0.123^{+0.069}_{-0.077}$
All[2]	10%	38.86/53	$-0.13^{+0.10}_{-0.82}$	$-0.09^{+0.29}_{-0.27}$	$-0.69^{+0.64^\dagger}_{-0.44}$	$0.34^{+0.37}_{-0.56^\dagger}$	$-0.030^{+0.74}_{-0.18^\dagger}$	$-0.006^{+0.239^\dagger}_{-0.082}$
	30%	38.54/53	$-0.15^{+0.21}_{-0.86}$	$-0.15^{+0.31^\dagger}_{-0.17^\dagger}$	$-0.69^{+0.70}_{-0.42}$	$0.59^{+0.38^\dagger}_{-0.41}$	$-0.24^{+0.61}_{-0.13^\dagger}$	$0.007^{+0.114}_{-0.087}$

Table 9.6: NP parameters for the Scenario "All", described in the text.

where $\text{CDF}(\Delta\chi_i^2, \Delta n_i) \equiv 1 - p(\Delta\chi_i^2, \Delta n_i)$ is the χ^2 -cumulative distribution function evaluated at $\Delta\chi_i^2$ for Δn_i d.o.f.. The probability is given by the p -value, which also characterizes the goodness of the fit, defined as

$$p(\chi_{\min}^2, n) \equiv \int_{\chi_{\min}^2}^{\infty} dz \chi^2(z, n), \quad (9.18)$$

where $\chi^2(z, n)$ is the χ^2 probability distribution function with n d.o.f..

9.3.2.2 General cases

As previously mentioned, by adding RH neutrinos, the set of operators increases from 5 to 10. The large number of free parameters makes it difficult to perform a global fit to the full basis of operators. Let us cleverly use the information extracted from the previous fits for this multitudinous case.

Since the best scenario involving LH currents was a global modification of the SM, i.e. a positive C_{LL}^V contribution, being the rest of LH neutrino WCs compatible with zero, let us only consider C_{LL}^V together with all RH neutrino WCs in this new fit. We will label this scenario as "All". The results of the fit in this context are listed in Table 9.6. Imposing the bound $\mathcal{B}(B_c \rightarrow \tau\bar{\nu})$, two minima are found. By shifting the WCs up to 1.2σ , the global minimum becomes compatible with a solution in which the only non-vanishing WCs are C_{LR}^V and C_{RR}^T . As Fig. 9.13 shows, both C_{LR}^V and C_{RR}^T help to reproduce the experimental value of $\mathcal{R}_D, \mathcal{R}_{D^*}$ and $\bar{\mathcal{P}}_\tau^{D^*}$. For $\bar{F}_L^{D^*}$ it is a combination of several operators that helps. In the local minimum, the dominant contribution comes from C_{RR}^V . Since both minima saturate the $\mathcal{B}(B_c \rightarrow \tau\bar{\nu}) \leq 10\%$ constraint, we relaxed

it to 30% and found, as expected, that the value of the $\chi^2/\text{d.o.f.}$ slightly improves in this case, whereas the scalar WCs are further away from the SM limit.

In both cases one can see that most of the WCs have large uncertainties. This can be understood from the fact that a large set of variables to fit allow for larger correlations among them, which in turn allows wider ranges for the WCs considered. The global and local minima have in fact quite close values of $\chi^2/\text{d.o.f.}$, and the χ^2 distribution in the region between them is rather flat. Thus, when evaluating their 1σ variations, one minimum falls often into the other one, as indicated by the \dagger symbol.

One can also wonder which would be the most preferred scenario by the experimental data when NP only affects the currents involving a RH neutrino. We refer to this scenario as “ ν_R ”, and their results are shown in Table 9.7. Here, C_{LL}^V is switched off so that one would expect C_{LR}^V and C_{RR}^T to dominate again in the fit. Indeed, by shifting all the WCs within their 1σ uncertainties, the global minimum is

ν_R : All RH neutrino WCs							
Min.	Br.	χ^2	C_{LR}^V	C_{RR}^V	C_{RR}^S	C_{LR}^S	C_{RR}^T
$\nu_R[1]$	10%	38.54/54	$0.52_{-0.16}^{+0.13}$	$0.06_{-0.22}^{+0.15}$	$0.04_{-0.66}^{+0.35}$	$-0.35_{-0.16}^{+0.72}$	$-0.057_{-0.058}^{+0.080}$
	30%	38.33/54	$0.47_{-0.20}^{+0.16}$	$0.10_{-0.23}^{+0.21}$	$0.28_{-0.97}^{+0.24}$	$-0.59_{-0.17}^{+0.80}$	$-0.054_{-0.058}^{+0.081}$
$\nu_R[2]$	10%	39.05/54	$0.07_{-0.30\dagger}^{+0.30}$	$0.42_{-0.21}^{+0.11}$	$-0.32_{-0.21}^{+0.74}$	$0.10_{-0.68}^{+0.20\dagger}$	$0.004_{-0.088}^{+0.080}$
	30%	38.80/54	0.12 ± 0.30	$0.38_{-0.20}^{+0.13}$	$-0.57_{-0.28}^{+0.57\dagger}$	$0.33_{-0.48\dagger}^{+0.20\dagger}$	$-0.006_{-0.091}^{+0.081}$

Table 9.7: NP parameters for the Scenario “ ν_R ”, described in the text.

compatible with a solution in which the only non-zero coefficient is C_{LR}^V . In that sense, C_{LR}^V plays a similar role as the C_{LL}^V in the previous scenario, which acted modifying the SM contribution. In the local minimum, the main contributions to the observables are coming from C_{RR}^V . By relaxing the $\mathcal{B}(B_c \rightarrow \tau\bar{\nu})$ bound up to 30%, as one could already expect, the χ^2 slightly improves.

9.3.3 Scenarios involving all possible UV-mediators

Let us now focus on the different motivated scenarios presented in the first section of Chapter 8. Those arise by integrating out each of the single NP mediators that could contribute to the $b \rightarrow c\tau\bar{\nu}$ transitions involving RH leptonic currents. By doing that,

there are six scenarios to consider where only small subsets of operators at the m_b scale are generated, so that the number of free parameters to fit is considerably reduced. As we showed in Chapter 8, in some cases, when integrating out the UV mediator, LH neutrino WCs are also unavoidably generated. For these scenarios we will consider both the solely RH contribution together with the more general case where both RH and LH neutrino WCs participate. In the context of these particular scenarios, one, two or four WCs are generated, being the rest zero. This allows us to have a better control on the numerics of the fit and even study in a fit-independent way the different scenarios, allowing for a global and better overview of the situation.

From what we learnt in Chapter 8 about the possible UV mediators, V^μ , \tilde{R}_2 and \tilde{V}^μ do not contribute to any LH operator. We will refer to those as *genuine* RH scenarios. In the scenarios involving \tilde{R}_2 and S_1 , where scalar and tensor couplings arise at the NP scale, the renormalization-group running between $\Lambda_{\text{NP}} \sim 1$ TeV and the scale m_b generates the factor $r \approx 2$. Except the scenario involving \tilde{V}_2^μ , the rest of them have been also studied at Ref. [433].

Within each scenario we will perform a standard χ^2 fit to the data. There are 60 experimental d.o.f., 4 corresponding to $\mathcal{R}_{D^{(*)}}$, $\bar{F}_L^{D^*}$ and $\bar{\mathcal{P}}_\tau^{D^*}$, and 56 to the binned q^2 distributions. Therefore, the number of d.o.f. of our fits is $60 - N_{\text{WC}} - 1 = 59 - N_{\text{WC}}$, where N_{WC} is the number of WCs entering in the fit. All solutions resulting from our fits will present up to three *flipped* minima with degenerate χ^2 values. The first flipped minimum is obtained by reversing the sign of the LH neutrino WCs while keeping the RH neutrino WCs untouched:

$$C_{LL}^{V'} = -2 - C_{LL}^V, \quad C_{iL}^{X'} = -C_{iL}^X, \quad C_{iR}^{X'} = C_{iR}^X, \quad (9.19)$$

for $X = S, V, T$ and $i = L, R$, except for C_{LL}^V . The second flipped minimum is obtained reversing only the RH coefficients,

$$C_{iL}^{X'} = C_{iL}^X, \quad C_{iR}^{X'} = -C_{iR}^X, \quad (9.20)$$

for $X = S, V, T$ and $i = L, R$, and the last one flipping both left and right WCs,

$$C_{LL}^{V'} = -2 - C_{LL}^V, \quad C_{iL}^{X'} = -C_{iL}^X, \quad C_{iR}^{X'} = -C_{iR}^X, \quad (9.21)$$

for $X = S, V, T$ and $i = L, R$, except for C_{LL}^V . From now on, we will only discuss the closest minimum to the SM scenario.

In Fig. 9.15, the first row represents the parameter space allowed by the different measurements within their 1σ of the observables considered in the fit in the RH neutrino WCs plane. In here, LH neutrino WCs are switched off. In the second row, the same predictions are displayed but this time fixing the LH neutrino WCs to their central values of the minimum obtained in the fit (see Table 9.8). In the last row, we show the *genuine* scenarios which only depend on a single RH neutrino WC.

As one can see from this figure, there is no overlap at the 1σ level between all observables, regardless of the values taken by the WCs. When considering the experimental value of $F_L^{D^*}$ at 2σ , agreement can be found in most of them, but in the scenario involving the second Higgs doublet, where the compatibility is spoiled by the bound on the $\mathcal{B}(B_c \rightarrow \tau \bar{\nu})$ decay.

Spin 0							
$\tilde{R}_2 \sim (3, 2, 1/6): C_{RR}^S = 4rC_{RR}^T$							
Scen.	Min.	Br.	$\chi^2/\text{d.o.f.}$	C_{RR}^T			
\tilde{R}_2	-	10%	44.20/58	$0.054^{+0.009}_{-0.011}$			
$\Phi \sim (1, 2, 1/2)$							
Scen.	Min.	Br.	$\chi^2/\text{d.o.f.}$	C_{RR}^S	C_{LR}^S	C_{RL}^S	C_{LL}^S
Φ	$\Phi[1]$	10%	49.93/57	$0.46^{+0.05}_{-0.18}$	$-0.06^{+0.19}_{-0.07}$	-	-
		30%	44.49/57	$0.297^{+0.074}_{-0.096}$	$-0.673^{+0.091}_{-0.053}$	-	-
	$\Phi[2]$	10%	49.93/57	$0.06^{+0.07}_{-0.19}$	$-0.46^{+0.18}_{-0.05}$	-	-
		30%	44.49/57	$0.673^{+0.053}_{-0.091}$	$-0.297^{+0.096}_{-0.074}$	-	-
$\Phi + \text{LH}$	-	10%	43.56/55	0.0 ± 0.3	0.0 ± 0.3	$0.21^{+0.03}_{-0.11}$	$-0.11^{+0.07}_{-0.08}$
		30%	40.03/55	0.00 ± 0.45	0.00 ± 0.45	$0.407^{+0.032}_{-0.137}$	$-0.329^{+0.146}_{-0.080}$
$S_1 \sim (\bar{3}, 1, 1/3): C_{RR}^S = -4rC_{RR}^T \text{ and } C_{LL}^S = -4rC_{LL}^T$							
Scen.	Min.	Br.	$\chi^2/\text{d.o.f.}$	C_{RR}^V	C_{RR}^T	C_{LL}^V	C_{LL}^T
S_1	-	10%	39.21/57	$0.422^{+0.071}_{-0.126}$	$0.022^{+0.032}_{-0.037}$	-	-
$S_1 + \text{LH}$	-	10%	39.06/55	$0.367^{+0.68}_{-1.41\dagger}$	$0.004^{+0.048}_{-0.055\dagger}$	$0.034^{+0.11}_{-0.70}$	$0.010^{+0.037}_{-0.041}$
Spin 1							
$U_1^\mu \sim (3, 1, 2/3)$							
Scen.	Min.	Br.	$\chi^2/\text{d.o.f.}$	C_{RR}^V	C_{LR}^S	C_{LL}^V	C_{RL}^S
U_1^μ	-	10%	39.39/57	$0.39^{+0.07}_{-0.08}$	$-0.1^{+0.2}_{-0.5}$	-	-
$U_1^\mu + \text{LH}$	-	10%	39.37/55	$0.38^{+0.60}_{-1.40}$	$-0.01^{+0.56}_{-0.54}$	$0.007^{+0.10}_{-0.65}$	$-0.03^{+0.07}_{-0.45}$
$\tilde{V}_2^\mu \sim (\bar{3}, 2, -1/6)$							
Scen.	Min.	Br.	$\chi^2/\text{d.o.f.}$	C_{LR}^S			
\tilde{V}_2^μ	-	10%	47.32/57	$0.418^{+0.097}_{-0.125}$			
$\tilde{V}^\mu \sim (1, 1-, 1)$							
Scen.	Min.	Br.	$\chi^2/\text{d.o.f.}$	C_{RR}^V			
V^μ	-	10%	39.50/58	$0.370^{+0.051}_{-0.059}$			

Table 9.8: NP parameters for all scenarios considered, together with their χ^2 .

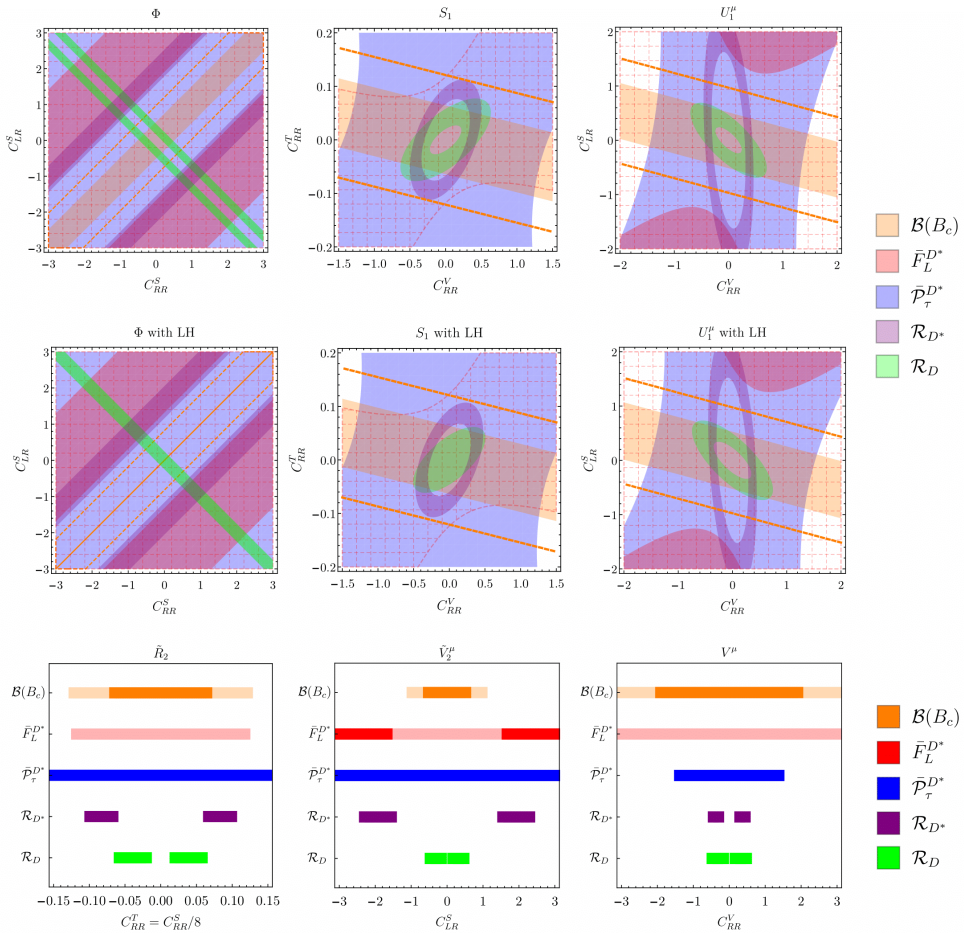


Figure 9.15: Fit-independent plots for the UV-motivated scenarios displaying the regions allowed at 1σ . On the first row, only the RH neutrino WCs shown are switched on, whereas on the second row the corresponding LH neutrino WCs are fixed to their best-fit values. In the third row we show the genuine scenarios for RH neutrino currents. The dashed orange line shows the more relaxed bound $\mathcal{B}(B_c \rightarrow \tau \bar{\nu}) \leq 30\%$, and the red grid shows the parameter space consistent with the experimental measurement of $\bar{F}_L^{D^*}$ at 2σ . *Figure extracted from Ref. [333].*

In order to parametrize the quality of the scenarios, the Pull with respect to the SM is computed, together with the p-value, defined in Eqs. 9.17 and 9.18. Both are shown in Fig. 9.16.

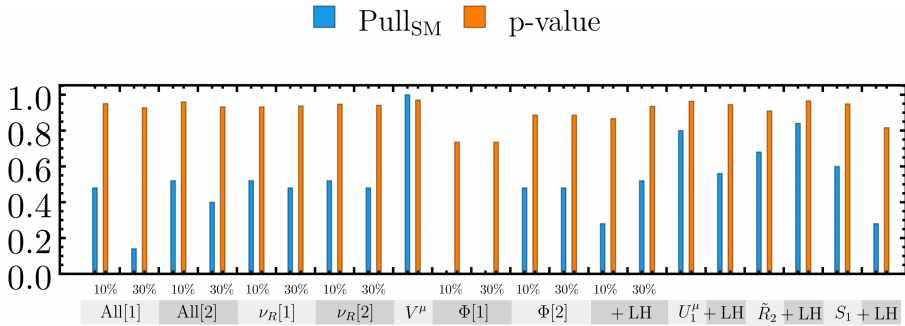


Figure 9.16: Pull and p-value of the different scenarios discussed.

Fig. 9.17 also includes the pull applied to the different pieces of the χ^2 , namely $\chi^2[\mathcal{R}_{D^{(*)}}]$ the ratios contribution, $\chi^2[d\Gamma/dq^2]$ the contribution from the q^2 -differential distributions, and $\chi^2[\text{Pol}]$ the contribution from the integrated polarization observables $\bar{\mathcal{P}}_\tau^{D^*}$ and $\bar{F}_L^{D^*}$, in order to quantify how preferred the scenarios are regarding these particular class of observables. Negative bars in this figure indicate that the corresponding χ^2 scenario is worse than the SM one, representing a disfavorable case.

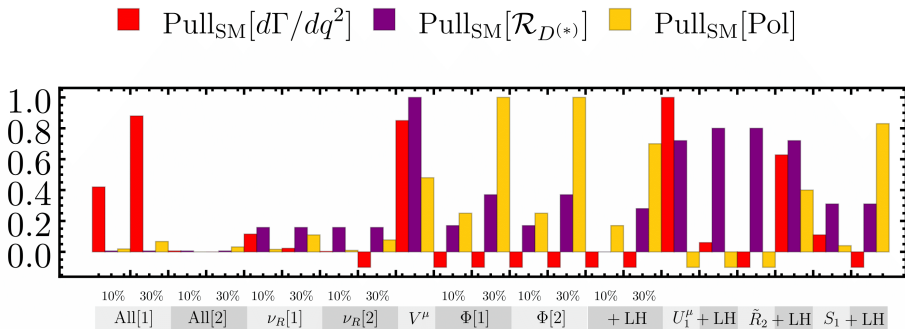


Figure 9.17: Specific pulls regarding the different contributions to the χ^2 from the q^2 -differential distributions, the integrated polarization observables, and the ratios.

9.3.4 Predictions

Given the results obtained by the global fit, let us analyze what are the predictions of the observables we can access at experiment.

The predicted values of the different observables within each fitted scenario are given in Fig. 9.18 and in Table 9.9, where the numerical predictions are marked either with a green tick (✓) if they agree with the experimental value at 1σ or with a red cross (✗) if they do not. All minima are in agreement with all experimental observables at the 2σ level.

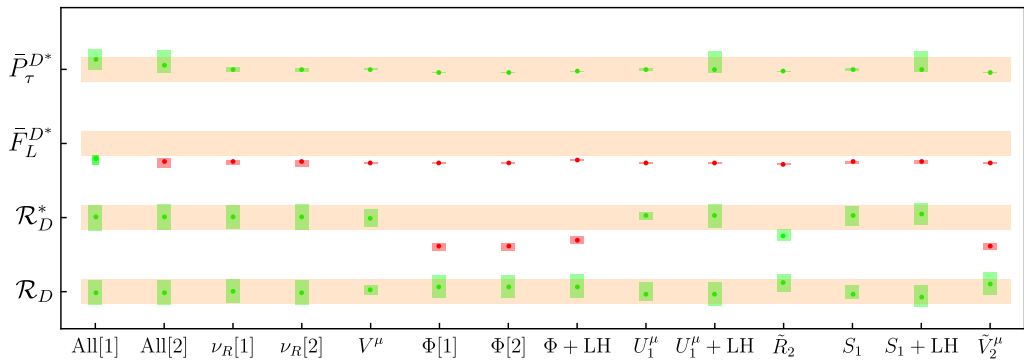


Figure 9.18: Predictions for the fitted observables, normalized to their measured values, with their 1σ experimental uncertainties shown as orange bands. For these predictions $\mathcal{B}(B_c \rightarrow \tau \bar{\nu}) \leq 10\%$ is taken. The green and red regions indicate the predictions arising from each NP scenario that are in agreement or not with the experimental value, respectively, at the 1σ level. The labels within brackets specify the minimum within a given scenario. The numerical values of these predictions are listed in Table 9.9. *Figure adapted from Ref. [333].*

As discussed in Chapter 8, the three-body differential distribution in $B \rightarrow D\tau\bar{\nu}$ and the full four-body angular analysis of $B \rightarrow D^*\tau\bar{\nu} \rightarrow (D\pi)\tau\bar{\nu}$ provide a multitude of observables that could be experimentally accessible. The presence of neutrinos in the final state makes the measurement troublesome, compared to the case of well-known neutral-current transitions like $B \rightarrow K^*\mu\bar{\mu}$. Nevertheless, measuring the distribution of the secondary τ decay, some information on the angular coefficients J_i and I_i , defined in Eqs. 8.81 and 8.98, could be obtained in the near future. As it can be seen from their explicit analytic expressions in Eqs. 8.83 and 8.99, these q^2 -dependent functions can

be very sensitive to the NP WCs present in the theory. In this section, we provide the predictions of such observables in some relevant NP scenarios considered in this work.

Fig. 9.19 shows the predictions for the forward-backward asymmetries $\mathcal{A}_{FB}^{D^{(*)}}$ defined in Eqs. 8.84 and (8.107), the lepton polarization asymmetries of Eq. 8.110 and the longitudinal D^* polarization $F_L^{D^*}$ defined in Eq. 8.105, as functions of q^2 . For simplicity we have illustrated the four NP scenarios with largest pulls with respect to the SM. Notice that the scenario coming from the V_μ integration, which contains the single WC C_{RR}^V , will always give the same predictions as the SM scenario for the forward-backward asymmetries, $\bar{F}_L^{D^*}(q^2)$ and the angular coefficients $\bar{I}_i(q^2)$. Therefore, this scenario is only included in the τ polarization asymmetries. Error bands in these plots correspond only to the uncertainties arising from the fitted WCs. These uncertainties have been obtained by minimizing the χ^2 , imposing $O_i = O_{i,\min} + \Delta O_{i,\min}$, and taking the value of the observable O_i for which $\chi^2 = \chi_{\min}^2 + 1$. Other smaller errors such as FF parameters or additional inputs are not taken into account. Therefore the SM predictions, plotted as dotted black lines, do not present any uncertainties.

From these plots, we can see that scenarios with a larger number of WCs also have larger uncertainties (Scenario *All*), as expected. The forward-backward asymmetry \mathcal{A}_{FB}^D could be useful to distinguish the scenario generated by \tilde{R}_2 from the SM, but the large uncertainties make difficult to discriminate it from other scenarios or to differentiate the SM from scenarios coming from U_1^μ , V^μ and S_1 . A precise measurement of $\mathcal{A}_{FB}^{D^*}$ would allow to distinguish Scenario *All* and the Scenario \tilde{R}_2 from the rest of NP scenarios, which partly overlap with the SM prediction. A similar situation occurs for $\bar{F}_L^{D^*}$, where clear differences manifest at low values of q^2 while the different scenarios considered tend to overlap at high q^2 . The τ polarizations $\mathcal{P}_\tau^{D^{(*)}}$ are useful to distinguish Scenario V_μ from the SM, since these are the only observables that are sensitive to a single shift in C_{RR}^V . Moreover, in Scenario *All*, \mathcal{P}_τ^D and $\mathcal{P}_\tau^{D^*}$ exhibit a quite different dependence on q^2 compared to the other scenarios, which could be exploited to distinguish it at low q^2 values. In the high q^2 region, $\mathcal{P}_\tau^{D^*}$ also allows to discriminate Scenario *All* from the other possibilities.

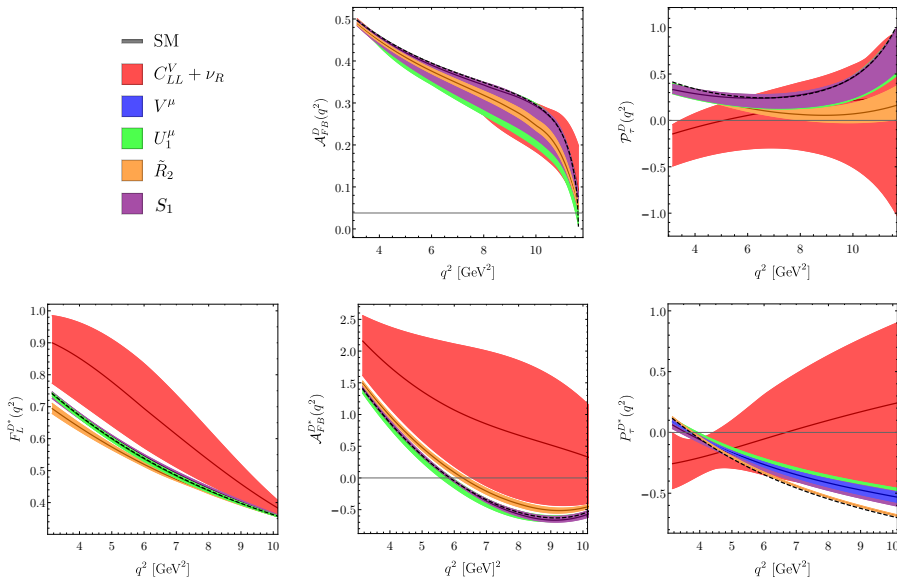


Figure 9.19: Dependence on q^2 of $\mathcal{A}_{FB}^{D(*)}$, $\mathcal{P}_\tau^{D(*)}$ and F_L^{D*} , for the best-fit scenarios. Figure extracted from Ref. [333].

In Fig. 9.20 we plot the $B \rightarrow D^* \tau \bar{\nu}$ angular coefficients, as functions of q^2 , normalized by the decay width, i.e.

$$\bar{I}_i(q^2) = \frac{\mathcal{N}_{D^*}(q^2) I_i(q^2)}{\Gamma_f(q^2)} \quad (9.22)$$

where the angular coefficients $I_i(q^2)$ are given in Eq. 8.99 from Chapter 8. The CP-odd quantities I_7 , I_8 and I_9 are identically zero in our case, because we have only considered real WCs in our fits. It is interesting to notice that despite the large uncertainties, Scenario *All* can be easily distinguished from the SM predictions and from other minima (for instance looking at \bar{I}_{1s} or \bar{I}_5). However, being able to distinguish other scenarios would be more complicated, unless the current errors on the WCs are sizable reduced. There is always an overlap between the SM predictions, Scenario S_1 and Scenario U_1^μ . The scenario coming from \tilde{R}_2 is close to the ones generated by U_1^μ , S_1 and the SM

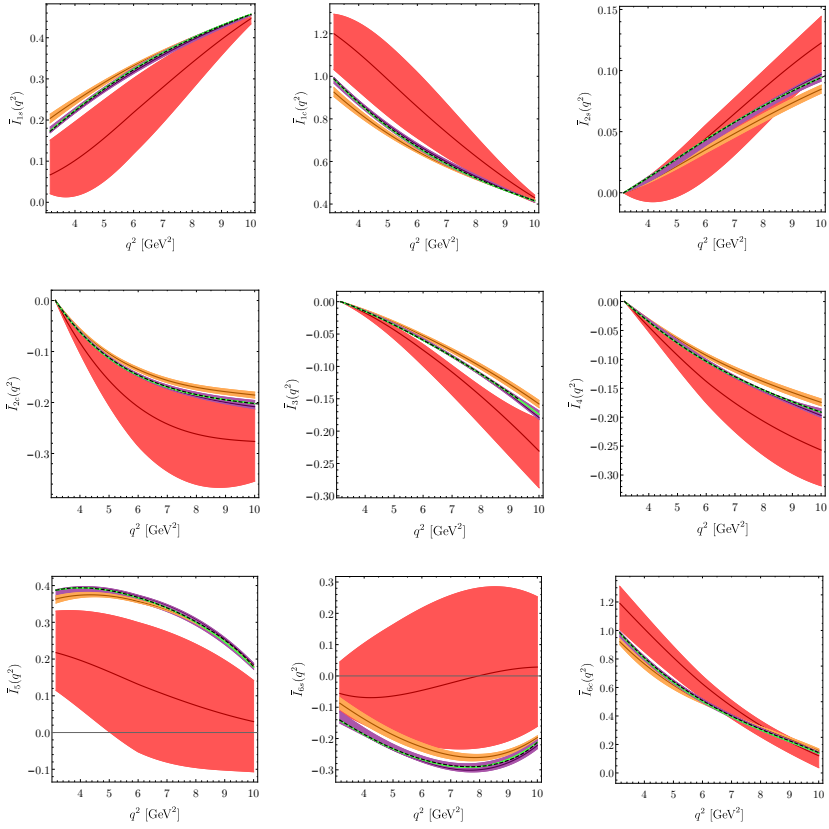


Figure 9.20: \bar{I}_i (see Eq. 9.22) for different scenarios. Same colour legend as in Fig. 9.19. *Figure extracted from Ref. [333].*

predictions, but it is still possible to distinguish it looking at low (\bar{I}_{1s} , \bar{I}_5) or high (\bar{I}_{2s} , \bar{I}_{2c} , \bar{I}_3 and \bar{I}_4) q^2 values.

Scenario	$\mathcal{B}(B_c \rightarrow \tau \bar{\nu})$	\mathcal{R}_D	\mathcal{R}_{D^*}	$\bar{P}_L^{D^*}$	$\bar{P}_\tau^{D^*}$
Experiment	-	$0.340 \pm 0.027 \pm 0.013$	$0.295 \pm 0.011 \pm 0.008$	$0.60 \pm 0.08 \pm 0.04$	$-0.38 \pm 0.51_{-0.16}^{+0.21}$
All[1]	10%	0.339 ± 0.030 ✓	0.295 ± 0.014 ✓	$0.494_{-0.045}^{+0.025}$ ✓	$0.06_{-0.45}^{+0.43}$ ✓
	30%	0.338 ± 0.030 ✓	0.295 ± 0.014 ✓	$0.510_{-0.043}^{+0.014}$ ✓	$0.08_{-0.46}^{+0.32}$ ✓
All[2]	10%	0.338 ± 0.030 ✓	0.296 ± 0.014 ✓	$0.472_{-0.044}^{+0.023}$ ✗	$-0.20_{-0.30}^{+0.67}$ ✓
	30%	0.338 ± 0.030 ✓	0.296 ± 0.014 ✓	$0.488_{-0.050}^{+0.032}$ ✓	$-0.24_{-0.28}^{+0.64}$ ✓
$\nu_R[1]$	10%	$0.341_{-0.028}^{+0.029}$ ✓	0.296 ± 0.013 ✓	$0.474_{-0.024}^{+0.010}$ ✗	$-0.42_{-0.07}^{+0.13}$ ✓
	30%	$0.341_{-0.028}^{+0.029}$ ✓	0.296 ± 0.013 ✓	$0.489_{-0.048}^{+0.011}$ ✗	$-0.47_{-0.05}^{+0.15}$ ✓
$\nu_R[2]$	10%	0.339 ± 0.030 ✓	0.296 ± 0.014 ✓	$0.471_{-0.033}^{+0.012}$ ✗	$-0.401_{-0.064}^{+0.094}$ ✓
	30%	0.340 ± 0.030 ✓	0.295 ± 0.014 ✓	$0.484_{-0.045}^{+0.015}$ ✗	$-0.45_{-0.07}^{+0.13}$ ✓
V^μ	2.5%	0.343 ± 0.012 ✓	0.294 ± 0.010 ✓	0.462 ± 0.004 ✗	$-0.377_{-0.033}^{+0.031}$ ✓
$\Phi[1]$	10%	$0.353_{-0.027}^{+0.028}$ ✓	$0.2638_{-0.0049}^{+0.0034}$ ✗	$0.4662_{-0.0057}^{+0.0039}$ ✗	$-0.5028_{-0.0035}^{+0.0051}$ ✓
	30%	$0.348_{-0.027}^{+0.028}$ ✓	$0.2699_{-0.0058}^{+0.0032}$ ✗	$0.4792_{-0.0064}^{+0.0041}$ ✗	$-0.5144_{-0.0032}^{+0.0056}$ ✓
$\Phi[2]$	10%	$0.353_{-0.027}^{+0.028}$ ✓	$0.2638_{-0.0049}^{+0.0034}$ ✗	$0.4662_{-0.0057}^{+0.0039}$ ✗	$-0.5028_{-0.0034}^{+0.0051}$ ✓
	30%	$0.348_{-0.027}^{+0.028}$ ✓	$0.2699_{-0.0058}^{+0.0032}$ ✗	$0.4792_{-0.0064}^{+0.0041}$ ✗	$-0.5144_{-0.0032}^{+0.0056}$ ✓
$\Phi + \text{LH}$	10%	0.353 ± 0.028 ✓	$0.2708_{-0.0052}^{+0.0032}$ ✗	$0.4815_{-0.0068}^{+0.0041}$ ✗	$-0.442_{-0.026}^{+0.005}$ ✓
	30%	0.340 ± 0.028 ✓	$0.2866_{-0.0081}^{+0.0030}$ ✓	$0.5125_{-0.0126}^{+0.0044}$ ✓	$-0.356_{-0.066}^{+0.006}$ ✓
U_1^μ	2.2%	$0.335_{-0.017}^{+0.027}$ ✓	$0.2966_{-0.0042}^{+0.0043}$ ✓	$0.4611_{-0.0070}^{+0.0056}$ ✗	$-0.364_{-0.050}^{+0.048}$ ✓
$U_1^\mu + \text{LH}$	2.0%	0.334 ± 0.029 ✓	0.297 ± 0.013 ✓	$0.4609_{-0.0083}^{+0.0059}$ ✗	$-0.38_{-0.16}^{+0.77}$ ✓
\tilde{R}_2	7.6%	$0.361_{-0.021}^{+0.022}$ ✓	$0.2748_{-0.0059}^{+0.0066}$ ✓	0.4522 ± 0.0050 ✗	$-0.4800_{-0.0076}^{+0.0078}$ ✓
S_1	4.6%	$0.335_{-0.011}^{+0.021}$ ✓	0.297 ± 0.011 ✓	$0.468_{-0.011}^{+0.007}$ ✗	$-0.377_{-0.058}^{+0.033}$ ✓
$S_1 + \text{LH}$	4.3%	$0.328_{-0.025}^{+0.026}$ ✓	0.299 ± 0.012 ✓	$0.471_{-0.013}^{+0.014}$ ✗	$-0.38_{-0.12}^{+0.77}$ ✓
\tilde{V}_2^μ	7.3%	$0.359_{-0.027}^{+0.028}$ ✓	0.2629 ± 0.0036 ✗	0.4644 ± 0.0043 ✗	-0.5012 ± 0.0039 ✓

Table 9.9: Predictions for the fitted observables in the different minima, and their experimental values. *Table adapted from Ref. [333].*

9.3.5 Interpretation of the results

From the last section, together with the results of the fit collected in Tables 9.6, 9.7 and 9.8, the following conclusions can be extracted:

- In general, it is difficult to reproduce the experimental value of the longitudinal D^* polarization within its 1σ range. From Fig. 9.18 and Table 9.9 we can see that

the only solutions reproducing all the experimental values (marked with a ✓) are the scenario *All* with either a 10% (Min[1]) or a 30% (Min[1] and Min[2]) upper limit on $\mathcal{B}(B_c \rightarrow \tau \bar{\nu})$, and the scenario Φ with LH neutrino WCs with a 30%.

- All solutions exhibit pulls between 1.2 and 3.7 with respect to the SM fit, showing a clear preference for NP contributions.
- The largest pull with respect to the SM fit is obtained in the scenario with V_μ , which only contributes to the C_{RR}^V coefficient. Notice that C_{RR}^V plays a similar role than C_{LL}^V in the observables involving $b \rightarrow c$ transitions. Therefore, the preference of the fit for this scenario can be easily understood, since a SM-like modification was the best fit solution in absence of RH neutrinos [393].
- Scenarios generated by Φ , \tilde{R}_2 and \tilde{V}_2 , involving only scalar (and tensor) operators, have the largest χ^2 value. As Table 9.9 and Fig. 9.18 show, scenarios with Φ and \tilde{V}_2 fail badly reproducing the experimental value of \mathcal{R}_{D^*} .
- Scenarios generated by Φ , \tilde{R}_2 , \tilde{V}_2 and Min[2] from Scenario ν_R , are disfavoured by the q^2 differential distributions of the $B \rightarrow D^{(*)}$ decay with respect to the SM, as the corresponding Pull_{SM} in Fig. 9.17 shows.
- Those solutions further away from the SM (larger pulls) present higher p -values, as Fig 9.16 shows.
- In scenarios with several operators, the best fits correspond to solutions where all WCs but one are compatible with zero. The non-zero WC is typically C_{RR}^V (Scenarios U_1^μ and S_1).
- When scenarios with and without LH neutrino operators are compared, the fit indicates a preference for solutions with all LH neutrino WCs compatible with zero within 1σ .

9.4 Conclusions

In this chapter we presented a global fit to $b \rightarrow c$ transitions taking the available experimental information at face value. As a theoretical framework we adopted an EFT

approach based on the most general Hamiltonian relevant for such processes under the assumptions that NP enters only in the third generation of leptons, that there is a sizeable gap between NP and the EW scale, that the EW symmetry breaking is linearly realized, and that there are no light RH neutrinos entering in our EFT study. We also assumed that the WCs are real, although we relaxed this assumption and did not find an improved description of the data. In contrast to the previous works, we considered the q^2 distributions measured by Belle and BaBar on the $B \rightarrow D^{(*)}\tau\bar{\nu}$ decays.

We observed that the preferred scenario for the global fit can be interpreted as a global modification of the SM; that is, none of the fitted WCs are required to be non-zero for the global minimum. However, a strong improvement in the χ^2 is found for such minimum with respect to the SM scenario. The later can be understood by taking into account the large correlations between the WCs. Taking also into account the model-independent results obtained when studying the individual contributions of the WCs, together with the scenario for the D^* observables, we observe that $\bar{F}_L^{D^*}$ cannot be accommodated within 1σ for any combination of WCs. In other words, if the central values of the experimental measurements were sharpened, no NP would be able to explain such discrepancies. The later would force us to conclude that either the current experimental values are not the ultimate ones and they will eventually approach the SM predictions with more statistics, or that one of our initial assumptions is not correct.

To disentangle this dilemma, regarding the first possibility, we should still wait for more statistics and data. The second option, however, can be further explored, what motivated us to relax some of the initial assumptions. First, we considered a non-zero C_{RL}^V in our fit, i.e. we allowed for a non-linear breaking of the EW symmetry. However, although having an extra d.o.f., the scenarios consistent with all the experimental measurements at 1σ are very fine tuned.

Given the circumstances, we decided to relax one more assumption and include a light RH neutrino in our EFT, expecting that more d.o.f. could allow for a successful fit to the given experimental data. For the RH case, the best scenario involves vector coefficients, likewise the previous case. Among all scenarios analysed, the vector boson V^μ seems to be the preferred option, in terms of the pulls from the SM hypothesis. The next two possibilities are the scalar leptoquark S_1 and the vector leptoquark U_1^μ , switching on the RH neutrino couplings only, which can also provide good agreement

to the data. However, it is important to note that none of these three possibilities can generate values of the longitudinal D^* polarization within its current 1σ experimental range; they can only reach agreement with the $\bar{F}_L^{D^*}$ measurement at the 2σ level. Interestingly, the $\bar{F}_L^{D^*}$ data can only be explained at 1σ in very few cases, namely, with all RH neutrino operators plus the SM-like contribution, i.e. Scenario *All*, or with a scalar boson Φ , switching on both ν_L and ν_R operators and with a relaxed upper limit of 30% on $\mathcal{B}(B_c \rightarrow \tau\bar{\nu})$. However, these scenarios are not the best choices in explaining the $\mathcal{R}_{D^{(*)}}$ measurements in terms of pulls. Nevertheless, they do reduce the $\mathcal{R}_{D^{(*)}}$ deviation significantly, and bear very important information about simultaneous agreement of all observables considered in this work. Due to the large uncertainty of the current $\mathcal{P}_\tau^{D^*}$ measurement, all scenarios are compatible (within $\pm 1\sigma$) with it. The \mathcal{R}_D measurement is also easily accommodated in all the NP scenarios that have been analysed. Measurements of additional observables such as polarizations and angular distributions could help to disentangle the dynamical origin of the current anomalies. In particular, we have displayed the information contained in the three-body and four-body angular distributions of $B \rightarrow D\tau\bar{\nu}$ and $B \rightarrow D^*(\rightarrow D\pi)\tau\bar{\nu}$, respectively, and their sensitivity to the different NP scenarios analysed. The experimental measurement of these distributions is of course very challenging because of the presence of undetected neutrinos, and one would need to further analyse the decay products of the τ in order to recover the accessible information.

Said that, and before closing this chapter, some ideas must be stressed. In this work we analyzed the NP parameter space able to explain the current anomalies in $b \rightarrow c\tau\bar{\nu}$ data, i.e. disregarding the possibility that these anomalies could originate in underestimated systematic uncertainties or statistical fluctuations. As we are all aware, this field is highly dynamical and probably the particular numeric results of the global fits performed here become at some point obsolete. However, this statement does not extend to the main results of this chapter and its preceding Chapter 8. The study about how NP enters in $b \rightarrow c$ transitions can be applied to constrain any NP d.o.f. affecting such processes. Besides, this material can be easily generalized and therefore applied to other semileptonic decays involving pseudoscalar to pseudoscalar mesons, or pseudoscalar to vector mesons.

Final remarks

These pages have been added after the thesis was submitted, and have not been evaluated (and are not pretended to be). However, after the suggestion of some members of the committee about including some final conclusions, I decided to rather add some personal thoughts about the results of the thesis and make a global overview. Along these four years of exploring beyond the Standard Model territories, my impression is that is hard to find something simpler and more elegant than the SM we already have to complete our knowledge and still be consistent with experimental data. It seems that, the more precision and energy range we gain experimentally (more powerful spyglasses we construct), the further the awaited new physics is pushed away from us. That is also the impression I get when looking at arXiv every morning. But it should be there, somewhere! There is undeniably evidence for its existence, and this is indeed a motivation for the whole community to look for it. But where to look?

The evidence of new physics (the neutrino oscillations, the matter excess in the evolution of the universe, the existence of dark matter and dark energy, the strong CP problem, maybe the flavour B anomalies) teaches us a lesson: we should not think anymore about the SM as a renormalizable and complete theory, but as the lowest terms of an infinite tower of higher dimensional operators suppressed by subsequent powers of the scale where new physics becomes relevant. Effective Field Theories are a magnificent tool to figure out information about the new land everyone is searching for, but it is as useful as dangerous. It is based on the degrees of freedom available at our energies (on the material from our home) and follows at least the forces we are familiar with, although it might respect a larger set of symmetries that we are not aware of.

The least suppressed and therefore first effect in the EFT expansion that we are supposed to notice are processes violating the lepton number in two units, for instance, Majorana neutrino masses. Are neutrino masses a prediction of such expansion? That was recently pointed out by Steven Weinberg during one of his talks.⁶ It is not a bijection, but the observation of neutrino oscillations is indeed an encouraging argument in favour of it. Next dimension of operators predict baryon number violation, particularly the decay of the proton. Those dangerous interactions would be compatible with experiment if the scale of new physics is about 10^{15} GeV, also known as the GUT scale. Grand unified theories are beautiful candidates to bet on. The evolution of couplings points there, so does the canonical Type-I seesaw mechanism, the mass of the axion would fit nicely in such scales too... I personally like these theories because of their simplicity which translates into a powerful ability for launching predictions. Without thinking on it twice, they would be the natural bet when contrasting the EFT expansion built from the symmetries in the SM with experiment. However, it is hard (at least for me) to admit that the relevant scale for new physics is that far from our energy reach...

Those were my thoughts before I fell in love with local baryon number. I consider myself very fortunate for having worked in motivated models able to produce testable predictions along my PhD, and I have fallen in love with any single work I was involved in with my collaborators. However, once my supervisor Pavel asked me, *Clara, if you had to make a choice, what theory from those you've worked in would you bet on?* It took me three seconds to answer: local baryon number. The fact that by promoting a symmetry in the Lagrangian that we are already very familiar with, baryon number, to a local symmetry and sticking to the simplest matter content to making it consistent with gauge invariance, a Majorana dark matter candidate is naturally predicted is priceless. The fact that the need of a mass term for the anomalous forces $U(1)_B$ to be spontaneously broken in three units and allows one to understand how baryon number can be dynamically violated. We may not be observing the proton decay because it is highly suppressed by a huge scale that we will never reach in our lifetimes, but because it is actually forbidden. Local $U(1)_B$ forbids the decay of the proton at any order in theory of perturbations. Let us now allow the DM to annihilate to the SM content

⁶This was his talk on September 29 2020 at the *All Things EFT* seminar.

or the new scalar in the theory, and surprise! We find that cosmological observations force the scale of baryon number violation to be, at most, a few TeVs. Is this a problem with collider searches? Double surprise, there is full of room for a new mediator with a reasonable large gauge coupling to be discovered at our LHC. The new Higgs has exotic properties and our current experiments have enough potential to discover it. I mean, what else do we need to fall in love with such theory?

I previously qualified the EFTs as a useful and a dangerous tool, a double-edged sword. It allows you to infer elegantly and very smartly information from the distant new physics, and in my view it is a very proper way to proceed towards the unknown. However, once you fit your EFT to a certain set of new physics data, how can you proof which is the new land completing the SM lying behind it? I will rephrase here some thoughts pointed out by Goran Senjanović at a recent conference ⁷ about the value of having a complete and self-consistent theory as a candidate. Such frameworks, like $SU(5)$ or $U(1)_{B,L}$, make correlated predictions about different observables, which allow these theories to be tested or falsified. In this way, we can make progress towards dismantle the next theory completing the SM.

New physics might be terribly ugly, hidden in some complicated theory with tens of representations and a large tensor product of special unitary groups spontaneously breaking to others, we do not know. I honestly hope that we find new physics in a shiny island that overwhelms us with its beauty and simplicity. On the meanwhile, I am convinced we should try harder, learn more from what the SM and the experimental data we have can teach us from abroad, because undoubtedly what we are observing is impregnated with the new physics footprints.

⁷The conference was the Snowmass workshop on 9th July 2020.

A.- Fierz and charge conjugation identities

A.1 Fierz identities involving chiral fermions

$$\begin{aligned} (\overline{\Psi}_L^1 \Psi_R^2)(\overline{\Psi}_L^3 \Psi_R^4) &= -\frac{1}{2}(\overline{\Psi}_L^1 \Psi_R^4)(\overline{\Psi}_L^3 \Psi_R^2) \\ &\quad -\frac{1}{8}(\overline{\Psi}_L^1 \sigma_{\mu\nu} \Psi_R^4)(\overline{\Psi}_L^3 \sigma^{\mu\nu} \Psi_R^2) \end{aligned} \quad (\text{A.1})$$

$$(\overline{\Psi}_{L(R)}^1 \Psi_{R(L)}^2)(\overline{\Psi}_{R(L)}^3 \Psi_{L(R)}^4) = -\frac{1}{2}(\overline{\Psi}_{L(R)}^1 \gamma_\mu \Psi_{L(R)}^4)(\overline{\Psi}_{R(L)}^3 \gamma^\mu \Psi_{R(L)}^2) \quad (\text{A.2})$$

$$(\overline{\Psi}_L^1 \gamma_\mu \Psi_L^2)(\overline{\Psi}_R^3 \gamma^\mu \Psi_R^4) = -2(\overline{\Psi}_L^1 \Psi_R^4)(\overline{\Psi}_R^3 \Psi_L^2) \quad (\text{A.3})$$

$$(\overline{\Psi}_{L(R)}^1 \gamma_\mu \Psi_{L(R)}^2)(\overline{\Psi}_{L(R)}^3 \gamma^\mu \Psi_{L(R)}^4) = (\overline{\Psi}_{L(R)}^1 \gamma_\mu \Psi_{L(R)}^4)(\overline{\Psi}_{L(R)}^3 \gamma^\mu \Psi_{L(R)}^2) \quad (\text{A.4})$$

$$\begin{aligned} (\overline{\Psi}_L^1 \sigma_{\mu\nu} \Psi_R^2)(\overline{\Psi}_L^3 \sigma^{\mu\nu} \Psi_R^4) &= -6(\overline{\Psi}_L^1 \Psi_R^4)(\overline{\Psi}_L^3 \Psi_R^2) \\ &\quad +\frac{1}{2}(\overline{\Psi}_L^1 \sigma_{\mu\nu} \Psi_R^2)(\overline{\Psi}_L^3 \sigma^{\mu\nu} \Psi_R^4) \end{aligned} \quad (\text{A.5})$$

$$(\overline{\Psi}_L^1 \sigma_{\mu\nu} \Psi_R^2)(\overline{\Psi}_R^3 \sigma^{\mu\nu} \Psi_L^4) = 0 \quad (\text{A.6})$$

A.2 Charge conjugation identities

Taking into account the properties listed below of the charge conjugation operator,

$$C = i\gamma_0\gamma_2 \text{ (in Dirac representation only), } C^\dagger = C^{-1} = C^T = -C, \quad C^T \gamma_\mu C = -\gamma_\mu^T,$$

which acts on a fermion as $\Psi^c \equiv C\bar{\Psi}^T$, the following identities can be derived:

- i $\overline{\Psi}^C P_L \phi^C = \bar{\phi} P_L \Psi,$
- ii $\overline{\Psi}^C \gamma_\mu P_L \phi^C = -\bar{\phi} \gamma_\mu P_R \Psi,$
- iii $\overline{\Psi}^C \sigma_{\mu\nu} P_L \phi^C = -\bar{\phi} P_L \sigma_{\mu\nu} \Psi.$

B.- Gamma lines

B.1 Cross Sections for the Gamma Lines

For relevant interactions for the DM annihilation into gamma lines, which can be written as

$$\mathcal{L} \supset -g' \bar{f} \left(n_V^f \gamma^\mu + n_A^f \gamma^\mu \gamma^5 \right) f Z'_\mu - \frac{e}{\sin \theta_W \cos \theta_W} \bar{f} \left(g_V^f \gamma^\mu + g_A^f \gamma^\mu \gamma^5 \right) f Z_\mu, \quad (\text{B.1})$$

where f are the charged fermions of the theory interacting with Z' . The annihilation cross section for the different annihilation channels mediated by the new gauge boson Z' are given by:

- **Cross section for the $\chi\chi \rightarrow \gamma\gamma$ annihilation.**

$$\begin{aligned} \sigma v_{\chi\chi \rightarrow \gamma\gamma} &= \frac{\alpha^2 (g')^4 n_\chi^2 M_\chi^2}{\pi^3 M_{Z'}^4} \frac{(4M_\chi^2 - M_{Z'}^2)^2}{(4M_\chi^2 - M_{Z'}^2)^2 + \Gamma_{Z'}^2 M_{Z'}^2} \left| \sum_f N_c^f n_A^f Q_f^2 (2M_f^2 C_0^\gamma + 1) \right|^2, \\ &\stackrel{\text{A.C.}}{=} \frac{\alpha^2 (g')^4 n_\chi^2 M_\chi^2}{\pi^3 M_{Z'}^4} \frac{(4M_\chi^2 - M_{Z'}^2)^2}{(4M_\chi^2 - M_{Z'}^2)^2 + \Gamma_{Z'}^2 M_{Z'}^2} \left| \sum_f N_c^f n_A^f Q_f^2 M_f^2 C_0^\gamma \right|^2. \quad (\text{B.2}) \end{aligned}$$

- **Cross section for the $\chi\chi \rightarrow \gamma Z$ annihilation:**

$$\begin{aligned} \sigma v_{\chi\chi \rightarrow \gamma Z} &= \frac{\alpha^2 (g')^4 n_\chi^2}{32\pi^3 \sin^2 2\theta_W} \frac{(4M_\chi^2 - M_{Z'}^2)^3}{(4M_\chi^2 - M_{Z'}^2)^2 + \Gamma_{Z'}^2 M_{Z'}^2} \frac{(M_{Z'}^2 - 4M_\chi^2)^2}{M_\chi^4 M_{Z'}^4} \quad (\text{B.3}) \\ &\times \left| \sum_f N_c^f Q_f \left(n_V^f g_A^f + n_A^f g_V^f (2M_f^2 C_0^Z + 1) \right) \right|^2 \end{aligned}$$

$$\stackrel{A.C.}{=} \frac{\alpha^2 (g')^4 n_\chi^2}{32\pi^3 \sin^2 2\theta_W} \frac{(4M_\chi^2 - M_{Z'}^2)^3}{(4M_\chi^2 - M_{Z'}^2)^2 + \Gamma_{Z'}^2 M_{Z'}^2} \frac{(M_{Z'}^2 - 4M_\chi^2)^2}{M_\chi^4 M_{Z'}^4} \times \left| \sum_f N_c^f Q_f n_A^f g_V^f 2M_f^2 C_0^Z \right|^2. \quad (B.4)$$

• **Cross section for the $\chi\chi \rightarrow \gamma h$ annihilation:**

$$\sigma_{\chi\chi \rightarrow \gamma h} = v^2 \frac{(g')^4 n_\chi^2 \alpha}{768\pi^4 M_\chi^2} \frac{4M_\chi^2 - M_h^2}{(4M_\chi^2 - M_{Z'}^2)^2 + \Gamma_{Z'}^2 M_{Z'}^2} \times \left| \sum_f N_c^f g_S^f n_V^f M_f Q_f \left(\frac{8M_\chi^2}{4M_\chi^2 - M_h^2} (\Lambda_\chi^f - \Lambda_h^f) + 2 + (4M_\chi^2 - M_h^2 + 4M_f^2) C_0^h \right) \right|^2 \quad (B.5)$$

where the *A.C.* indicates that the anomaly cancellation conditions have been applied (see Chapter 2). Here, $\alpha = e^2/4\pi$, $C_0^A = C_0(0, M_A^2, s; M_f, M_f, M_f)$ is the Passarino-Veltman loop function as defined in Ref. [446] and n_χ is the dark matter charge under $U(1)_\chi$, and Z' the corresponding mediator. In order to predict the cross-sections for these quantum mechanical processes we need to use the interactions of the new fields required for anomaly cancellation.

B.2 Final State Radiation

The amplitude squared of the processes contributing to the final state radiation can be written as an expansion on the velocity,

$$|\mathcal{M}|_{\text{FSR}}^2 = \frac{M_q^2}{M_{Z_B}^2} A + v^2 B + \mathcal{O}(v^4), \quad (B.6)$$

where A and B coefficients are given by

$$A = 12\pi \alpha (g')^4 Q_q^2 (M_{Z'}^2 - 4M_\chi^2)^2 \frac{(E_q + E_\gamma - M_\chi)^2 (2(E_q - M_\chi)(E_q + E_\gamma - M_\chi) - 3M_q^2)}{M_{Z'}^2 (E_q - M_\chi)^2 (E_q + E_\gamma - M_\chi)^2 ((4M_\chi^2 - M_{Z'}^2)^2 + \Gamma_{Z'}^2 M_{Z'}^2)}, \quad (B.7)$$

$$B = 12\pi \alpha (g')^4 M_\chi^2 Q_q^2 \times \frac{(2E_q M_\chi (E_\gamma^2 - 3E_\gamma M_\chi + 2M_\chi^2) - 2E_q^4 - 2E_q^3 (E_\gamma - 2M_\chi) - E_q^2 (E_\gamma^2 - 6E_\gamma M_\chi + 6M_\chi^2) - 2M_\chi^2 (E_\gamma - M_\chi)^2)}{M_{Z_B}^2 (E_q + E_\gamma - M_\chi)^2 ((4M_\chi^2 - M_{Z'}^2)^2 + \Gamma_{Z'}^2 M_{Z'}^2)}. \quad (B.8)$$

Bibliography

- [1] R. Davis, D. S. Harmer and K. C. Hoffman, *Search for neutrinos from the sun*, *Phys. Rev. Lett.* **20** (1968) 1205.
- [2] SUPER-KAMIOKANDE collaboration, *Evidence for oscillation of atmospheric neutrinos*, *Phys. Rev. Lett.* **81** (1998) 1562 [hep-ex/9807003].
- [3] SNO collaboration, *Measurement of the rate of $\nu_e + d \rightarrow p + p + e^-$ interactions produced by 8B solar neutrinos at the Sudbury Neutrino Observatory*, *Phys. Rev. Lett.* **87** (2001) 071301 [nucl-ex/0106015].
- [4] KAMLAND collaboration, *First results from KamLAND: Evidence for reactor anti-neutrino disappearance*, *Phys. Rev. Lett.* **90** (2003) 021802 [hep-ex/0212021].
- [5] K2K collaboration, *Indications of neutrino oscillation in a 250 km long baseline experiment*, *Phys. Rev. Lett.* **90** (2003) 041801 [hep-ex/0212007].
- [6] KATRIN collaboration, *Improved Upper Limit on the Neutrino Mass from a Direct Kinematic Method by KATRIN*, *Phys. Rev. Lett.* **123** (2019) 221802 [1909.06048].
- [7] PLANCK collaboration, *Planck 2018 results. VI. Cosmological parameters*, 1807.06209.
- [8] I. Esteban, M. Gonzalez-Garcia, M. Maltoni, T. Schwetz and A. Zhou, *The fate of hints: updated global analysis of three-flavor neutrino oscillations*, 2007.14792.
- [9] P. de Salas, D. Forero, S. Gariazzo, P. Martínez-Miravé, O. Mena, C. Ternes et al., *2020 Global reassessment of the neutrino oscillation picture*, 2006.11237.

- [10] S. Weinberg, *Baryon and Lepton Nonconserving Processes*, *Phys. Rev. Lett.* **43** (1979) 1566.
- [11] C. Miralles Vila, *Naturalness and the Hierarchy Problem in the Type I and Type II See-saw Models*, Ph.D. thesis, Heidelberg U., 2016.
- [12] P. Minkowski, $\mu \rightarrow e\gamma$ at a Rate of One Out of 10^9 Muon Decays?, *Phys. Lett. B* **67** (1977) 421.
- [13] O. Sawada and A. Sugamoto, eds., in *Proceedings: Workshop on the Unified Theories and the Baryon Number in the Universe: Tsukuba, Japan, February 13-14, 1979*, (Tsukuba, Japan), Natl.Lab.High Energy Phys., 1979.
- [14] M. Levy, J. Basdevant, D. Speiser, J. Weyers, R. Gastmans and M. Jacob, eds., in *QUARKS AND LEPTONS. PROCEEDINGS, SUMMER INSTITUTE, CARGESE, FRANCE, JULY 9-29, 1979*, vol. 61, 1980. 10.1007/978-1-4684-7197-7.
- [15] P. R. M. Gell-Mann and R. Slansky, in *Supergravity*, eds. P. van Nieuwenhuizen et al. (North-Holland, 1979).
- [16] R. N. Mohapatra and G. Senjanovic, *Neutrino Mass and Spontaneous Parity Nonconservation*, *Phys. Rev. Lett.* **44** (1980) 912.
- [17] W. Konetschny and W. Kummer, *Nonconservation of Total Lepton Number with Scalar Bosons*, *Phys. Lett. B* **70** (1977) 433.
- [18] T. Cheng and L.-F. Li, *Neutrino Masses, Mixings and Oscillations in $SU(2) \times U(1)$ Models of Electroweak Interactions*, *Phys. Rev. D* **22** (1980) 2860.
- [19] J. Schechter and J. Valle, *Neutrino Masses in $SU(2) \times U(1)$ Theories*, *Phys. Rev. D* **22** (1980) 2227.
- [20] G. Gelmini and M. Roncadelli, *Left-Handed Neutrino Mass Scale and Spontaneously Broken Lepton Number*, *Phys. Lett. B* **99** (1981) 411.
- [21] PARTICLE DATA GROUP collaboration, *Review of Particle Physics*, *PTEP* **2020** (2020) 083C01.

- [22] P. Fileviez Perez, T. Han, G.-Y. Huang, T. Li and K. Wang, *Testing a Neutrino Mass Generation Mechanism at the LHC*, *Phys. Rev. D* **78** (2008) 071301 [0803.3450].
- [23] J. Garayoa and T. Schwetz, *Neutrino mass hierarchy and Majorana CP phases within the Higgs triplet model at the LHC*, *JHEP* **03** (2008) 009 [0712.1453].
- [24] A. Akeroyd, M. Aoki and H. Sugiyama, *Probing Majorana Phases and Neutrino Mass Spectrum in the Higgs Triplet Model at the CERN LHC*, *Phys. Rev. D* **77** (2008) 075010 [0712.4019].
- [25] F. del Aguila and J. Aguilar-Saavedra, *Distinguishing seesaw models at LHC with multi-lepton signals*, *Nucl. Phys. B* **813** (2009) 22 [0808.2468].
- [26] R. Foot, H. Lew, X. He and G. C. Joshi, *Seesaw Neutrino Masses Induced by a Triplet of Leptons*, *Z. Phys. C* **44** (1989) 441.
- [27] E. Ma, *Pathways to naturally small neutrino masses*, *Phys. Rev. Lett.* **81** (1998) 1171 [hep-ph/9805219].
- [28] B. Bajc, M. Nemevsek and G. Senjanovic, *Probing seesaw at LHC*, *Phys. Rev. D* **76** (2007) 055011 [hep-ph/0703080].
- [29] P. Fileviez Perez, *Type III Seesaw and Left-Right Symmetry*, *JHEP* **03** (2009) 142 [0809.1202].
- [30] T. Hambye, Y. Lin, A. Notari, M. Papucci and A. Strumia, *Constraints on neutrino masses from leptogenesis models*, *Nucl. Phys. B* **695** (2004) 169 [hep-ph/0312203].
- [31] R. Franceschini, T. Hambye and A. Strumia, *Type-III see-saw at LHC*, *Phys. Rev. D* **78** (2008) 033002 [0805.1613].
- [32] A. Arhrib, B. Bajc, D. K. Ghosh, T. Han, G.-Y. Huang, I. Puljak et al., *Collider Signatures for Heavy Lepton Triplet in Type I+III Seesaw*, *Phys. Rev. D* **82** (2010) 053004 [0904.2390].
- [33] T. Li and X.-G. He, *Neutrino Masses and Heavy Triplet Leptons at the LHC: Testability of Type III Seesaw*, *Phys. Rev. D* **80** (2009) 093003 [0907.4193].

- [34] A. Zee, *A Theory of Lepton Number Violation, Neutrino Majorana Mass, and Oscillation*, *Phys. Lett. B* **93** (1980) 389.
- [35] L. Wolfenstein, *A Theoretical Pattern for Neutrino Oscillations*, *Nucl. Phys. B* **175** (1980) 93.
- [36] A. Y. Smirnov and M. Tanimoto, *Is Zee model the model of neutrino masses?*, *Phys. Rev. D* **55** (1997) 1665 [hep-ph/9604370].
- [37] X.-G. He, *Is the Zee model neutrino mass matrix ruled out?*, *Eur. Phys. J. C* **34** (2004) 371 [hep-ph/0307172].
- [38] X.-G. He and S. K. Majee, *Implications of Recent Data on Neutrino Mixing and Lepton Flavour Violating Decays for the Zee Model*, *JHEP* **03** (2012) 023 [1111.2293].
- [39] P. Fileviez Perez and M. B. Wise, *On the Origin of Neutrino Masses*, *Phys. Rev. D* **80** (2009) 053006 [0906.2950].
- [40] V. C. Rubin and J. Ford, W.Kent, *Rotation of the Andromeda Nebula from a Spectroscopic Survey of Emission Regions*, *Astrophys. J.* **159** (1970) 379.
- [41] J. H. Oort, *The Force Exerted by the Stellar System in the Direction Perpendicular to the Galactic Plane and Some Related Problems*, *Bull. Astron. Inst. Netherlands* **6** (1932) 249.
- [42] F. Zwicky, *Die Rotverschiebung von extragalaktischen Nebeln*, *Helv. Phys. Acta* **6** (1933) 110.
- [43] W. R. Roberts, M.S., *Rotation curve and geometry of M31 at large galactocentric distances*, *Astrophysical Journal* **201(2)** 327.
- [44] V. Rubin, N. Thonnard and J. Ford, W.K., *Rotational properties of 21 SC galaxies with a large range of luminosities and radii, from NGC 4605 ($R = 4\text{ kpc}$) to UGC 2885 ($R = 122\text{ kpc}$)*, *Astrophys. J.* **238** (1980) 471.

- [45] M. Persic, P. Salucci and F. Stel, *The Universal rotation curve of spiral galaxies: I. The Dark matter connection*, *Mon. Not. Roy. Astron. Soc.* **281** (1996) 27 [astro-ph/9506004].
- [46] M. Lisanti, M. Moschella, N. J. Outmezguine and O. Slone, *Testing Dark Matter and Modifications to Gravity using Local Milky Way Observables*, *Phys. Rev. D* **100** (2019) 083009 [1812.08169].
- [47] C. Skordis, D. Mota, P. Ferreira and C. Boehm, *Large Scale Structure in Bekenstein's theory of relativistic Modified Newtonian Dynamics*, *Phys. Rev. Lett.* **96** (2006) 011301 [astro-ph/0505519].
- [48] J. Zuntz, T. Zlosnik, F. Bourliot, P. Ferreira and G. Starkman, *Vector field models of modified gravity and the dark sector*, *Phys. Rev. D* **81** (2010) 104015 [1002.0849].
- [49] T. Lin, *Dark matter models and direct detection*, *PoS* **333** (2019) 009 [1904.07915].
- [50] W. Hu, R. Barkana and A. Gruzinov, *Cold and fuzzy dark matter*, *Phys. Rev. Lett.* **85** (2000) 1158 [astro-ph/0003365].
- [51] S. Horiuchi, P. J. Humphrey, J. Onorbe, K. N. Abazajian, M. Kaplinghat and S. Garrison-Kimmel, *Sterile neutrino dark matter bounds from galaxies of the Local Group*, *Phys. Rev. D* **89** (2014) 025017 [1311.0282].
- [52] B. W. Lee and S. Weinberg, *Cosmological Lower Bound on Heavy Neutrino Masses*, *Phys. Rev. Lett.* **39** (1977) 165.
- [53] K. Griest and M. Kamionkowski, *Unitarity Limits on the Mass and Radius of Dark Matter Particles*, *Phys. Rev. Lett.* **64** (1990) 615.
- [54] E. W. Kolb and M. S. Turner, *The Early Universe*, vol. 69. 1990.
- [55] S. Borsanyi et al., *Calculation of the axion mass based on high-temperature lattice quantum chromodynamics*, *Nature* **539** (2016) 69 [1606.07494].
- [56] K. Enqvist, K. Kainulainen and V. Semikoz, *Neutrino annihilation in hot plasma*, *Nucl. Phys.* **B374** (1992) 392.

- [57] P. F. de Salas and S. Pastor, *Relic neutrino decoupling with flavour oscillations revisited*, *JCAP* **1607** (2016) 051 [1606.06986].
- [58] V. Barger, P. Langacker and H.-S. Lee, *Primordial nucleosynthesis constraints on Z' properties*, *Phys. Rev.* **D67** (2003) 075009 [hep-ph/0302066].
- [59] J. Hamann, S. Hannestad, G. G. Raffelt and Y. Y. Y. Wong, *Sterile neutrinos with eV masses in cosmology: How disfavoured exactly?*, *JCAP* **1109** (2011) 034 [1108.4136].
- [60] L. A. Anchordoqui and H. Goldberg, *Neutrino cosmology after WMAP 7-Year data and LHC first Z' bounds*, *Phys. Rev. Lett.* **108** (2012) 081805 [1111.7264].
- [61] S. Hannestad, I. Tamborra and T. Tram, *Thermalisation of light sterile neutrinos in the early universe*, *JCAP* **1207** (2012) 025 [1204.5861].
- [62] A. Solaguren-Beascoa and M. C. Gonzalez-Garcia, *Dark Radiation Confronting LHC in Z' Models*, *Phys. Lett.* **B719** (2013) 121 [1210.6350].
- [63] L. A. Anchordoqui, H. Goldberg and G. Steigman, *Right-Handed Neutrinos as the Dark Radiation: Status and Forecasts for the LHC*, *Phys. Lett.* **B718** (2013) 1162 [1211.0186].
- [64] C. M. Ho and R. J. Scherrer, *Limits on MeV Dark Matter from the Effective Number of Neutrinos*, *Phys. Rev.* **D87** (2013) 023505 [1208.4347].
- [65] C. Brust, D. E. Kaplan and M. T. Walters, *New Light Species and the CMB*, *JHEP* **12** (2013) 058 [1303.5379].
- [66] C. Boehm, M. J. Dolan and C. McCabe, *A Lower Bound on the Mass of Cold Thermal Dark Matter from Planck*, *JCAP* **1308** (2013) 041 [1303.6270].
- [67] P. Fileviez Perez and S. Spinner, *Supersymmetry at the LHC and The Theory of R -parity*, *Phys. Lett.* **B728** (2014) 489 [1308.0524].
- [68] M. Escudero, *Neutrino decoupling beyond the Standard Model: CMB constraints on the Dark Matter mass with a fast and precise N_{eff} evaluation*, *JCAP* **1902** (2019) 007 [1812.05605].

- [69] D. Cadamuro, S. Hannestad, G. Raffelt and J. Redondo, *Cosmological bounds on sub-MeV mass axions*, *JCAP* **1102** (2011) 003 [1011.3694].
- [70] A. Salvio, A. Strumia and W. Xue, *Thermal axion production*, *JCAP* **1401** (2014) 011 [1310.6982].
- [71] M. Kawasaki, M. Yamada and T. T. Yanagida, *Observable dark radiation from a cosmologically safe QCD axion*, *Phys. Rev.* **D91** (2015) 125018 [1504.04126].
- [72] D. Baumann, D. Green and B. Wallisch, *New Target for Cosmic Axion Searches*, *Phys. Rev. Lett.* **117** (2016) 171301 [1604.08614].
- [73] G. Bélanger, F. Boudjema, A. Goudelis, A. Pukhov and B. Zaldivar, *micrOMEGAs5.0 : Freeze-in*, *Comput. Phys. Commun.* **231** (2018) 173 [1801.03509].
- [74] M. Drees, F. Hajkarim and E. R. Schmitz, *The Effects of QCD Equation of State on the Relic Density of WIMP Dark Matter*, *JCAP* **06** (2015) 025 [1503.03513].
- [75] P. Gondolo and G. Gelmini, *Cosmic abundances of stable particles: Improved analysis*, *Nucl. Phys. B* **360** (1991) 145.
- [76] A. Berlin, D. Hooper and S. D. McDermott, *Simplified Dark Matter Models for the Galactic Center Gamma-Ray Excess*, *Phys. Rev. D* **89** (2014) 115022 [1404.0022].
- [77] M. W. Goodman and E. Witten, *Detectability of Certain Dark Matter Candidates*, *Phys. Rev. D* **31** (1985) 3059.
- [78] LUX COLLABORATION collaboration, *Results from a search for dark matter in the complete lux exposure*, *Phys. Rev. Lett.* **118** (2017) 021303.
- [79] DARKSIDE COLLABORATION collaboration, *Low-mass dark matter search with the darkside-50 experiment*, *Phys. Rev. Lett.* **121** (2018) 081307.
- [80] PANDA-X-II COLLABORATION collaboration, *Dark matter results from 54-ton-day exposure of pandax-ii experiment*, *Phys. Rev. Lett.* **119** (2017) 181302.
- [81] XENON collaboration, *Physics reach of the XENONIT dark matter experiment*, *JCAP* **04** (2016) 027 [1512.07501].

- [82] XENON COLLABORATION 7 collaboration, *Dark matter search results from a one ton-year exposure of xenon1t*, *Phys. Rev. Lett.* **121** (2018) 111302.
- [83] J. Billard, L. Strigari and E. Figueroa-Feliciano, *Implication of neutrino backgrounds on the reach of next generation dark matter direct detection experiments*, *Phys. Rev. D* **89** (2014) 023524 [1307.5458].
- [84] M. Schumann, *Direct Detection of WIMP Dark Matter: Concepts and Status*, *J. Phys. G* **46** (2019) 103003 [1903.03026].
- [85] G. Jungman, M. Kamionkowski and K. Griest, *Supersymmetric dark matter*, *Phys. Rept.* **267** (1996) 195 [hep-ph/9506380].
- [86] P. Fileviez Pérez and C. Murgui, *Gamma Lines from the Hidden Sector*, *Phys. Rev. D* **100** (2019) 123007 [1901.10483].
- [87] FERMI-LAT collaboration, *Updated search for spectral lines from Galactic dark matter interactions with pass 8 data from the Fermi Large Area Telescope*, *Phys. Rev. D* **91** (2015) 122002 [1506.00013].
- [88] FERMI-LAT collaboration, *Search for Gamma-ray Spectral Lines with the Fermi Large Area Telescope and Dark Matter Implications*, *Phys. Rev. D* **88** (2013) 082002 [1305.5597].
- [89] M. Gustafsson, E. Lundstrom, L. Bergstrom and J. Edsjo, *Significant Gamma Lines from Inert Higgs Dark Matter*, *Phys. Rev. Lett.* **99** (2007) 041301 [astro-ph/0703512].
- [90] C. Garcia-Cely, M. Gustafsson and A. Ibarra, *Probing the Inert Doublet Dark Matter Model with Cherenkov Telescopes*, *JCAP* **02** (2016) 043 [1512.02801].
- [91] M. Duerr, P. Fileviez Pérez and J. Smirnov, *Gamma-Ray Excess and the Minimal Dark Matter Model*, *JHEP* **06** (2016) 008 [1510.07562].
- [92] M. Duerr, P. Fileviez Pérez and J. Smirnov, *Scalar Dark Matter: Direct vs. Indirect Detection*, *JHEP* **06** (2016) 152 [1509.04282].

- [93] C. Jackson, G. Servant, G. Shaughnessy, T. M. Tait and M. Taoso, *Gamma-ray lines and One-Loop Continuum from s-channel Dark Matter Annihilations*, *JCAP* **07** (2013) 021 [1302.1802].
- [94] C. Jackson, G. Servant, G. Shaughnessy, T. M. Tait and M. Taoso, *Higgs in Space!*, *JCAP* **04** (2010) 004 [0912.0004].
- [95] L. Bergstrom and P. Ullio, *Full one loop calculation of neutralino annihilation into two photons*, *Nucl. Phys. B* **504** (1997) 27 [hep-ph/9706232].
- [96] L. Bergstrom, T. Bringmann, M. Eriksson and M. Gustafsson, *Gamma rays from heavy neutralino dark matter*, *Phys. Rev. Lett.* **95** (2005) 241301 [hep-ph/0507229].
- [97] M. Cirelli, T. Hambye, P. Panci, F. Sala and M. Taoso, *Gamma ray tests of Minimal Dark Matter*, *JCAP* **10** (2015) 026 [1507.05519].
- [98] C. Garcia-Cely, A. Ibarra, A. S. Lamperstorfer and M. H. G. Tytgat, *Gamma-rays from Heavy Minimal Dark Matter*, *JCAP* **10** (2015) 058 [1507.05536].
- [99] M. Duerr, P. Fileviez Perez and J. Smirnov, *Gamma Lines from Majorana Dark Matter*, *Phys. Rev. D* **93** (2016) 023509 [1508.01425].
- [100] L. Bergstrom, T. Bringmann, M. Eriksson and M. Gustafsson, *Two photon annihilation of Kaluza-Klein dark matter*, *JCAP* **04** (2005) 004 [hep-ph/0412001].
- [101] L. Bergstrom, T. Bringmann, M. Eriksson and M. Gustafsson, *Gamma rays from Kaluza-Klein dark matter*, *Phys. Rev. Lett.* **94** (2005) 131301 [astro-ph/0410359].
- [102] J. Bell and R. Jackiw, *A PCAC puzzle: $\pi^0 \rightarrow \gamma\gamma$ in the σ model*, *Nuovo Cim. A* **60** (1969) 47.
- [103] S. Weinberg, *The U(1) Problem*, *Phys. Rev. D* **11** (1975) 3583.
- [104] H. R. Pagels, *Some Remarks on the U(1)-a Problem of Quantum Chromodynamics*, *Phys. Rev. D* **13** (1976) 343.
- [105] K. Fujikawa, *Path Integral Measure for Gauge Invariant Fermion Theories*, *Phys. Rev. Lett.* **42** (1979) 1195.

- [106] K. Fujikawa, *Path Integral for Gauge Theories with Fermions*, *Phys. Rev.* **D21** (1980) 2848.
- [107] A. M. Polyakov, *Compact Gauge Fields and the Infrared Catastrophe*, *Phys. Lett. B* **59** (1975) 82.
- [108] A. Belavin, A. M. Polyakov, A. Schwartz and Y. Tyupkin, *Pseudoparticle Solutions of the Yang-Mills Equations*, *Phys. Lett. B* **59** (1975) 85.
- [109] P. Fileviez Perez and H. H. Patel, *The Electroweak Vacuum Angle*, *Phys. Lett. B* **732** (2014) 241 [1402.6340].
- [110] G. 't Hooft, *Computation of the Quantum Effects Due to a Four-Dimensional Pseudoparticle*, *Phys. Rev. D* **14** (1976) 3432.
- [111] G. 't Hooft, *Symmetry Breaking Through Bell-Jackiw Anomalies*, *Phys. Rev. Lett.* **37** (1976) 8.
- [112] R. Jackiw and C. Rebbi, *Vacuum Periodicity in a Yang-Mills Quantum Theory*, *Phys. Rev. Lett.* **37** (1976) 172.
- [113] J. Callan, Curtis G., R. Dashen and D. J. Gross, *The Structure of the Gauge Theory Vacuum*, *Phys. Lett. B* **63** (1976) 334.
- [114] R. J. Crewther, P. Di Vecchia, G. Veneziano and E. Witten, *Chiral Estimate of the Electric Dipole Moment of the Neutron in Quantum Chromodynamics*, *Phys. Lett.* **88B** (1979) 123.
- [115] M. Pospelov and A. Ritz, *Theta vacua, QCD sum rules, and the neutron electric dipole moment*, *Nucl. Phys.* **B573** (2000) 177 [hep-ph/9908508].
- [116] T. Chupp, P. Fierlinger, M. Ramsey-Musolf and J. Singh, *Electric dipole moments of atoms, molecules, nuclei, and particles*, *Rev. Mod. Phys.* **91** (2019) 015001 [1710.02504].
- [117] P. W. Graham and S. Rajendran, *New Observables for Direct Detection of Axion Dark Matter*, *Phys. Rev.* **D88** (2013) 035023 [1306.6088].

- [118] A. Hook, *TASI Lectures on the Strong CP Problem and Axions*, PoS **TASI2018** (2019) 004 [1812.02669].
- [119] A. Pich, *Chiral perturbation theory*, *Rept. Prog. Phys.* **58** (1995) 563 [hep-ph/9502366].
- [120] H. Leutwyler, *The Ratios of the light quark masses*, *Phys. Lett. B* **378** (1996) 313 [hep-ph/9602366].
- [121] R. Peccei and H. R. Quinn, *CP Conservation in the Presence of Instantons*, *Phys. Rev. Lett.* **38** (1977) 1440.
- [122] R. Peccei and H. R. Quinn, *Constraints Imposed by CP Conservation in the Presence of Instantons*, *Phys. Rev. D* **16** (1977) 1791.
- [123] S. Weinberg, *A New Light Boson?*, *Phys. Rev. Lett.* **40** (1978) 223.
- [124] F. Wilczek, *Problem of Strong P and T Invariance in the Presence of Instantons*, *Phys. Rev. Lett.* **40** (1978) 279.
- [125] G. Grilli di Cortona, E. Hardy, J. Pardo Vega and G. Villadoro, *The QCD axion, precisely*, *JHEP* **01** (2016) 034 [1511.02867].
- [126] I. Antoniadis and T. N. Truong, *Lower Bound for Branching Ratio of $K^+ \rightarrow \pi^+$ Axion and Nonexistence of Peccei-Quinn Axion*, *Phys. Lett. B* **109** (1982) 67.
- [127] E787 collaboration, *Search for the decay $K^+ \rightarrow \pi^+ \nu \bar{\nu}$ in the momentum region $P(\pi)$ less than 195-MeV/c*, *Phys. Lett. B* **537** (2002) 211 [hep-ex/0201037].
- [128] M. Dine, W. Fischler and M. Srednicki, *A Simple Solution to the Strong CP Problem with a Harmless Axion*, *Phys. Lett.* **104B** (1981) 199.
- [129] A. R. Zhitnitsky, *On Possible Suppression of the Axion Hadron Interactions. (In Russian)*, *Sov. J. Nucl. Phys.* **31** (1980) 260.
- [130] J. E. Kim, *Weak Interaction Singlet and Strong CP Invariance*, *Phys. Rev. Lett.* **43** (1979) 103.

- [131] M. A. Shifman, A. I. Vainshtein and V. I. Zakharov, *Can Confinement Ensure Natural CP Invariance of Strong Interactions?*, *Nucl. Phys.* **B166** (1980) 493.
- [132] J. Preskill, M. B. Wise and F. Wilczek, *Cosmology of the Invisible Axion*, *Phys. Lett. B* **120** (1983) 127.
- [133] L. F. Abbott and P. Sikivie, *A Cosmological Bound on the Invisible Axion*, *Phys. Lett.* **B120** (1983) 133.
- [134] M. Dine and W. Fischler, *The Not So Harmless Axion*, *Phys. Lett.* **B120** (1983) 137.
- [135] P. Sikivie, *Experimental Tests of the Invisible Axion*, *Phys. Rev. Lett.* **51** (1983) 1415.
- [136] D. M. Lazarus, G. C. Smith, R. Cameron, A. C. Melissinos, G. Ruoso, Y. K. Semertzidis et al., *Search for solar axions*, *Phys. Rev. Lett.* **69** (1992) 2333.
- [137] S. Moriyama, M. Minowa, T. Namba, Y. Inoue, Y. Takasu and A. Yamamoto, *Direct search for solar axions by using strong magnetic field and x-ray detectors*, *Phys. Lett. B* **434** (1998) 147 [hep-ex/9805026].
- [138] Y. Inoue, T. Namba, S. Moriyama, M. Minowa, Y. Takasu, T. Horiuchi et al., *Search for sub-electronvolt solar axions using coherent conversion of axions into photons in magnetic field and gas helium*, *Phys. Lett. B* **536** (2002) 18 [astro-ph/0204388].
- [139] Y. Inoue, Y. Akimoto, R. Ohta, T. Mizumoto, A. Yamamoto and M. Minowa, *Search for solar axions with mass around 1 eV using coherent conversion of axions into photons*, *Phys. Lett. B* **668** (2008) 93 [0806.2230].
- [140] K. Zioutas et al., *A Decommissioned LHC model magnet as an axion telescope*, *Nucl. Instrum. Meth. A* **425** (1999) 480 [astro-ph/9801176].
- [141] S. DePanfilis, A. C. Melissinos, B. E. Moskowitz, J. T. Rogers, Y. K. Semertzidis, W. U. Wuensch et al., *Limits on the abundance and coupling of cosmic axions at $4.5 < m_a < 5.0 \mu\text{eV}$* , *Phys. Rev. Lett.* **59** (1987) 839.
- [142] W. U. Wuensch, S. De Panfilis-Wuensch, Y. K. Semertzidis, J. T. Rogers, A. C. Melissinos, H. J. Halama et al., *Results of a laboratory search for cosmic axions and other weakly coupled light particles*, *Phys. Rev. D* **40** (1989) 3153.

- [143] C. Hagmann, P. Sikivie, N. S. Sullivan and D. B. Tanner, *Results from a search for cosmic axions*, *Phys. Rev. D* **42** (1990) 1297.
- [144] I. G. Irastorza and J. Redondo, *New experimental approaches in the search for axion-like particles*, *Prog. Part. Nucl. Phys.* **102** (2018) 89 [1801.08127].
- [145] P. W. Graham, I. G. Irastorza, S. K. Lamoreaux, A. Lindner and K. A. van Bibber, *Experimental Searches for the Axion and Axion-Like Particles*, *Ann. Rev. Nucl. Part. Sci.* **65** (2015) 485 [1602.00039].
- [146] E. W. Lentz, T. R. Quinn, L. J. Rosenberg and M. J. Tremmel, *A New Signal Model for Axion Cavity Searches from N-Body Simulations*, *Astrophys. J.* **845** (2017) 121 [1703.06937].
- [147] L. Bergstrom, P. Ullio and J. H. Buckley, *Observability of gamma-rays from dark matter neutralino annihilations in the Milky Way halo*, *Astropart. Phys.* **9** (1998) 137 [astro-ph/9712318].
- [148] Y. Sofue and V. Rubin, *Rotation curves of spiral galaxies*, *Ann. Rev. Astron. Astrophys.* **39** (2001) 137 [astro-ph/0010594].
- [149] R. Catena and P. Ullio, *A novel determination of the local dark matter density*, *JCAP* **1008** (2010) 004 [0907.0018].
- [150] Y. Kahn, B. R. Safdi and J. Thaler, *Broadband and Resonant Approaches to Axion Dark Matter Detection*, *Phys. Rev. Lett.* **117** (2016) 141801 [1602.01086].
- [151] J. W. Foster, N. L. Rodd and B. R. Safdi, *Revealing the Dark Matter Halo with Axion Direct Detection*, *Phys. Rev. D* **97** (2018) 123006 [1711.10489].
- [152] J. L. Ouellet et al., *First Results from ABRACADABRA-10 cm: A Search for Sub- μeV Axion Dark Matter*, *Phys. Rev. Lett.* **122** (2019) 121802 [1810.12257].
- [153] J. L. Ouellet et al., *Design and implementation of the ABRACADABRA-10 cm axion dark matter search*, *Phys. Rev. D* **99** (2019) 052012 [1901.10652].

- [154] D. Budker, P. W. Graham, M. Ledbetter, S. Rajendran and A. Sushkov, *Proposal for a Cosmic Axion Spin Precession Experiment (CASPER)*, *Phys. Rev.* **X4** (2014) 021030 [1306.6089].
- [155] A. Garcon et al., *The Cosmic Axion Spin Precession Experiment (CASPER): a dark-matter search with nuclear magnetic resonance*, 1707.05312.
- [156] D. F. Jackson Kimball et al., *Overview of the Cosmic Axion Spin Precession Experiment (CASPER)*, 1711.08999.
- [157] A. Sakharov, *Violation of CP Invariance, C asymmetry, and baryon asymmetry of the universe*, *Sov. Phys. Usp.* **34** (1991) 392.
- [158] SUPER-KAMIOKANDE collaboration, *Search for proton decay via $p \rightarrow e^+ \pi^0$ and $p \rightarrow \mu^+ \pi^0$ in 0.31 megaton-years exposure of the Super-Kamiokande water Cherenkov detector*, *Phys. Rev.* **D95** (2017) 012004 [1610.03597].
- [159] S. R. Elliott and P. Vogel, *Double beta decay*, *Ann. Rev. Nucl. Part. Sci.* **52** (2002) 115 [hep-ph/0202264].
- [160] P. Nath and P. Fileviez Perez, *Proton stability in grand unified theories, in strings and in branes*, *Phys. Rept.* **441** (2007) 191 [hep-ph/0601023].
- [161] A. Pais, *Remark on baryon conservation*, *Phys. Rev. D* **8** (1973) 1844.
- [162] S. Rajpoot, *GAUGE SYMMETRIES OF ELECTROWEAK INTERACTIONS*, *Int. J. Theor. Phys.* **27** (1988) 689.
- [163] R. Foot, G. C. Joshi and H. Lew, *Gauged Baryon and Lepton Numbers*, *Phys. Rev. D* **40** (1989) 2487.
- [164] C. D. Carone and H. Murayama, *Realistic models with a light U(1) gauge boson coupled to baryon number*, *Phys. Rev. D* **52** (1995) 484 [hep-ph/9501220].
- [165] H. Georgi and S. L. Glashow, *Decays of a leptophobic gauge boson*, *Phys. Lett. B* **387** (1996) 341 [hep-ph/9607202].

- [166] P. Fileviez Perez and M. B. Wise, *Baryon and lepton number as local gauge symmetries*, *Phys. Rev.* **D82** (2010) 011901 [1002.1754].
- [167] T. R. Dulaney, P. Fileviez Perez and M. B. Wise, *Dark Matter, Baryon Asymmetry, and Spontaneous B and L Breaking*, *Phys. Rev. D* **83** (2011) 023520 [1005.0617].
- [168] P. Fileviez Perez and M. B. Wise, *Breaking Local Baryon and Lepton Number at the TeV Scale*, *JHEP* **08** (2011) 068 [1106.0343].
- [169] M. Duerr, P. Fileviez Perez and M. B. Wise, *Gauge Theory for Baryon and Lepton Numbers with Leptoquarks*, *Phys. Rev. Lett.* **110** (2013) 231801 [1304.0576].
- [170] M. Duerr and P. Fileviez Perez, *Baryonic Dark Matter*, *Phys. Lett. B* **732** (2014) 101 [1309.3970].
- [171] P. Fileviez Perez, S. Ohmer and H. H. Patel, *Minimal Theory for Lepto-Baryons*, *Phys. Lett.* **B735** (2014) 283 [1403.8029].
- [172] S. Ohmer and H. H. Patel, *Leptobaryons as Majorana Dark Matter*, *Phys. Rev. D* **92** (2015) 055020 [1506.00954].
- [173] S. L. Adler, *Axial vector vertex in spinor electrodynamics*, *Phys. Rev.* **177** (1969) 2426.
- [174] S. L. Adler and W. A. Bardeen, *Absence of higher order corrections in the anomalous axial vector divergence equation*, *Phys. Rev.* **182** (1969) 1517.
- [175] W. A. Bardeen, *Anomalous Ward identities in spinor field theories*, *Phys. Rev.* **184** (1969) 1848.
- [176] S. Weinberg, *Physical Processes in a Convergent Theory of the Weak and Electromagnetic Interactions*, *Phys. Rev. Lett.* **27** (1971) 1688.
- [177] K. Ishiwata and M. B. Wise, *Higgs Properties and Fourth Generation Leptons*, *Phys. Rev. D* **84** (2011) 055025 [1107.1490].
- [178] H. Ruegg and M. Ruiz-Altaba, *The Stueckelberg field*, *Int. J. Mod. Phys. A* **19** (2004) 3265 [hep-th/0304245].

- [179] D. Feldman, P. Fileviez Perez and P. Nath, *R-parity Conservation via the Stueckelberg Mechanism: LHC and Dark Matter Signals*, *JHEP* **01** (2012) 038 [1109.2901].
- [180] P. Fileviez Perez, *New Paradigm for Baryon and Lepton Number Violation*, *Phys. Rept.* **597** (2015) 1 [1501.01886].
- [181] S. Alioli, M. Farina, D. Pappadopulo and J. T. Ruderman, *Catching a New Force by the Tail*, *Phys. Rev. Lett.* **120** (2018) 101801 [1712.02347].
- [182] ATLAS collaboration, *Search for new high-mass phenomena in the dilepton final state using 36 fb of proton-proton collision data at 13 TeV with the ATLAS detector*, *JHEP* **10** (2017) 182 [1707.02424].
- [183] P. Fileviez Pérez, C. Murgui and A. D. Plascencia, *Neutrino-Dark Matter Connections in Gauge Theories*, *Phys. Rev. D* **100** (2019) 035041 [1905.06344].
- [184] CMS collaboration, *Search for narrow resonances in dijet final states at $\sqrt{s} = 8$ TeV with the novel CMS technique of data scouting*, *Phys. Rev. Lett.* **117** (2016) 031802 [1604.08907].
- [185] CMS collaboration, *Search for narrow resonances in the b-tagged dijet mass spectrum in proton-proton collisions at $\sqrt{s} = 8$ TeV*, *Phys. Rev. Lett.* **120** (2018) 201801 [1802.06149].
- [186] CMS collaboration, *Search for Low-Mass Quark-Antiquark Resonances Produced in Association with a Photon at $\sqrt{s} = 13$ TeV*, *Phys. Rev. Lett.* **123** (2019) 231803 [1905.10331].
- [187] CMS collaboration, *Search for low mass vector resonances decaying into quark-antiquark pairs in proton-proton collisions at $\sqrt{s} = 13$ TeV*, *Phys. Rev.* **D100** (2019) 112007 [1909.04114].
- [188] CMS collaboration, *Search for narrow and broad dijet resonances in proton-proton collisions at $\sqrt{s} = 13$ TeV and constraints on dark matter mediators and other new particles*, *JHEP* **08** (2018) 130 [1806.00843].

- [189] CMS collaboration, *Search for dijet resonances using events with three jets in proton-proton collisions at $\sqrt{s} = 13$ TeV*, 1911.03761.
- [190] ATLAS collaboration, *Search for low-mass dijet resonances using trigger-level jets with the ATLAS detector in pp collisions at $\sqrt{s} = 13$ TeV*, *Phys. Rev. Lett.* **121** (2018) 081801 [1804.03496].
- [191] P. Fileviez Perez, E. Goliias, R.-H. Li and C. Murgui, *Leptophobic Dark Matter and the Baryon Number Violation Scale*, *Phys. Rev.* **D99** (2019) 035009 [1810.06646].
- [192] P. Fileviez Perez, E. Goliias, C. Murgui and A. D. Plascencia, *The Higgs and Leptophobic Force at the LHC*, *JHEP* **20** (2020) 087 [2003.09426].
- [193] M. Duerr and P. Fileviez Perez, *Theory for Baryon Number and Dark Matter at the LHC*, *Phys. Rev.* **D91** (2015) 095001 [1409.8165].
- [194] M. Duerr, P. Fileviez Perez and J. Smirnov, *Baryonic Higgs at the LHC*, *JHEP* **09** (2017) 093 [1704.03811].
- [195] A. Ilnicka, T. Robens and T. Stefaniak, *Constraining Extended Scalar Sectors at the LHC and beyond*, *Mod. Phys. Lett.* **A33** (2018) 1830007 [1803.03594].
- [196] K. S. Babu, C. F. Kolda and J. March-Russell, *Implications of generalized $Z - Z'$ -prime mixing*, *Phys. Rev.* **D57** (1998) 6788 [hep-ph/9710441].
- [197] A. Hook, E. Izaguirre and J. G. Wacker, *Model Independent Bounds on Kinetic Mixing*, *Adv. High Energy Phys.* **2011** (2011) 859762 [1006.0973].
- [198] PARTICLE DATA GROUP collaboration, *Review of Particle Physics*, *Phys. Rev.* **D98** (2018) 030001.
- [199] CMS collaboration, *Search for a narrow resonance decaying to a pair of muons in proton-proton collisions at 13 TeV*, .
- [200] LHCb collaboration, *Search for Dark Photons Produced in 13 TeV pp Collisions*, *Phys. Rev. Lett.* **120** (2018) 061801 [1710.02867].

- [201] A. Semenov, *LanHEP — A package for automatic generation of Feynman rules from the Lagrangian. Version 3.2*, *Comput. Phys. Commun.* **201** (2016) 167 [1412.5016].
- [202] PLANCK collaboration, *Planck 2015 results. XIII. Cosmological parameters*, *Astron. Astrophys.* **594** (2016) A13 [1502.01589].
- [203] P. Fileviez Perez, E. Goliás, R.-H. Li, C. Murgui and A. D. Plascencia, *Anomaly-free dark matter models*, *Phys. Rev.* **D100** (2019) 015017 [1904.01017].
- [204] M. Hoferichter, P. Klos, J. Menéndez and A. Schwenk, *Improved limits for Higgs-portal dark matter from LHC searches*, *Phys. Rev. Lett.* **119** (2017) 181803 [1708.02245].
- [205] XENON collaboration, *First Dark Matter Search Results from the XENONIT Experiment*, *Phys. Rev. Lett.* **119** (2017) 181301 [1705.06655].
- [206] XENON collaboration, *Dark Matter Search Results from a One Ton-Year Exposure of XENONIT*, *Phys. Rev. Lett.* **121** (2018) 111302 [1805.12562].
- [207] H.E.S.S. collaboration, *Search for Photon-Lineline Signatures from Dark Matter Annihilations with H.E.S.S.*, *Phys. Rev. Lett.* **110** (2013) 041301 [1301.1173].
- [208] CTA CONSORTIUM collaboration, B. S. Acharya et al., *Science with the Cherenkov Telescope Array*. WSP, 2018, 10.1142/10986, [1709.07997].
- [209] M. Cepeda et al., *Report from Working Group 2, CERN Yellow Rep. Monogr.* **7** (2019) 221 [1902.00134].
- [210] A. Alloul, N. D. Christensen, C. Degrande, C. Duhr and B. Fuks, *FeynRules 2.0 - A complete toolbox for tree-level phenomenology*, *Comput. Phys. Commun.* **185** (2014) 2250 [1310.1921].
- [211] J. Alwall, R. Frederix, S. Frixione, V. Hirschi, F. Maltoni, O. Mattelaer et al., *The automated computation of tree-level and next-to-leading order differential cross sections, and their matching to parton shower simulations*, *JHEP* **07** (2014) 079 [1405.0301].

- [212] A. D. Martin, W. J. Stirling, R. S. Thorne and G. Watt, *Parton distributions for the LHC*, *Eur. Phys. J.* **C63** (2009) 189 [0901.0002].
- [213] ATLAS, CMS collaboration, *Measurements of the Higgs boson production and decay rates and constraints on its couplings from a combined ATLAS and CMS analysis of the LHC pp collision data at $\sqrt{s} = 7$ and 8 TeV*, *JHEP* **08** (2016) 045 [1606.02266].
- [214] LHC HIGGS CROSS SECTION WORKING GROUP collaboration, *Handbook of LHC Higgs Cross Sections: 4. Deciphering the Nature of the Higgs Sector*, 1610.07922.
- [215] G. Apollinari, I. Béjar Alonso, O. Brüning, P. Fessia, M. Lamont, L. Rossi et al., *High-Luminosity Large Hadron Collider (HL-LHC)*, *CERN Yellow Rep. Monogr.* **4** (2017) 1.
- [216] ATLAS collaboration, *Observation of $H \rightarrow b\bar{b}$ decays and VH production with the ATLAS detector*, *Phys. Lett. B* **786** (2018) 59 [1808.08238].
- [217] CMS collaboration, *Evidence for the Higgs boson decay to a bottom quark–antiquark pair*, *Phys. Lett. B* **780** (2018) 501 [1709.07497].
- [218] J. M. Butterworth, A. R. Davison, M. Rubin and G. P. Salam, *Jet substructure as a new Higgs search channel at the LHC*, *AIP Conf. Proc.* **1078** (2009) 189 [0809.2530].
- [219] M. Gell-Mann, P. Ramond and R. Slansky, *Complex Spinors and Unified Theories*, *Conf. Proc.* **C790927** (1979) 315 [1306.4669].
- [220] T. Yanagida, *Horizontal gauge symmetry and masses of neutrinos*, *Conf. Proc.* **C7902131** (1979) 95.
- [221] P. Fileviez Pérez and C. Murgui, *Dark Matter and The Seesaw Scale*, *Phys. Rev.* **D98** (2018) 055008 [1803.07462].
- [222] N. Okada and O. Seto, *Higgs portal dark matter in the minimal gauged $U(1)_{B-L}$ model*, *Phys. Rev.* **D82** (2010) 023507 [1002.2525].
- [223] T. Basak and T. Mondal, *Constraining Minimal $U(1)_{B-L}$ model from Dark Matter Observations*, *Phys. Rev.* **D89** (2014) 063527 [1308.0023].

- [224] S. Kanemura, T. Matsui and H. Sugiyama, *Neutrino mass and dark matter from gauged $U(1)_{B-L}$ breaking*, *Phys. Rev.* **D90** (2014) 013001 [1405.1935].
- [225] M. Duerr, P. Fileviez Perez and J. Smirnov, *Simplified Dirac Dark Matter Models and Gamma-Ray Lines*, *Phys. Rev.* **D92** (2015) 083521 [1506.05107].
- [226] E. Ma, N. Pollard, R. Srivastava and M. Zakeri, *Gauge $B - L$ Model with Residual Z_3 Symmetry*, *Phys. Lett.* **B750** (2015) 135 [1507.03943].
- [227] W. Wang and Z.-L. Han, *Radiative linear seesaw model, dark matter, and $U(1)_{B-L}$* , *Phys. Rev.* **D92** (2015) 095001 [1508.00706].
- [228] N. Okada and S. Okada, *Z'_{BL} portal dark matter and LHC Run-2 results*, *Phys. Rev.* **D93** (2016) 075003 [1601.07526].
- [229] K. Kaneta, Z. Kang and H.-S. Lee, *Right-handed neutrino dark matter under the $B - L$ gauge interaction*, *JHEP* **02** (2017) 031 [1606.09317].
- [230] V. De Romeri, E. Fernandez-Martinez, J. Gehrlein, P. A. N. Machado and V. Niro, *Dark Matter and the elusive Z' in a dynamical Inverse Seesaw scenario*, *JHEP* **10** (2017) 169 [1707.08606].
- [231] S. Okada, *Z' Portal Dark Matter in the Minimal $B - L$ Model*, *Adv. High Energy Phys.* **2018** (2018) 5340935 [1803.06793].
- [232] M. Escudero, S. J. Witte and N. Rius, *The dispirited case of gauged $U(1)_{B-L}$ dark matter*, *JHEP* **08** (2018) 190 [1806.02823].
- [233] E. Ma, *Verifiable radiative seesaw mechanism of neutrino mass and dark matter*, *Phys. Rev.* **D73** (2006) 077301 [hep-ph/0601225].
- [234] C. Boehm, Y. Farzan, T. Hambye, S. Palomares-Ruiz and S. Pascoli, *Is it possible to explain neutrino masses with scalar dark matter?*, *Phys. Rev.* **D77** (2008) 043516 [hep-ph/0612228].
- [235] Y. Farzan, S. Pascoli and M. A. Schmidt, *AMEND: A model explaining neutrino masses and dark matter testable at the LHC and MEG*, *JHEP* **10** (2010) 111 [1005.5323].

- [236] B. Batell, T. Han and B. Shams Es Haghi, *Indirect Detection of Neutrino Portal Dark Matter*, *Phys. Rev.* **D97** (2018) 095020 [1704.08708].
- [237] B. Batell, T. Han, D. McKeen and B. Shams Es Haghi, *Thermal Dark Matter Through the Dirac Neutrino Portal*, *Phys. Rev.* **D97** (2018) 075016 [1709.07001].
- [238] M. Blennow, E. Fernandez-Martinez, A. Olivares-Del Campo, S. Pascoli, S. Rosauero-Alcaraz and A. V. Titov, *Neutrino Portals to Dark Matter*, *Eur. Phys. J.* **C79** (2019) 555 [1903.00006].
- [239] P. Schwaller, T. M. P. Tait and R. Vega-Morales, *Dark Matter and Vectorlike Leptons from Gauged Lepton Number*, *Phys. Rev.* **D88** (2013) 035001 [1305.1108].
- [240] W. Chao, *Pure Leptonic Gauge Symmetry, Neutrino Masses and Dark Matter*, *Phys. Lett.* **B695** (2011) 157 [1005.1024].
- [241] A. Aranda, E. Jiménez and C. A. Vaquera-Araujo, *Electroweak phase transition in a model with gauged lepton number*, *JHEP* **01** (2015) 070 [1410.7508].
- [242] B. Fornal, Y. Shirman, T. M. P. Tait and J. R. West, *Asymmetric dark matter and baryogenesis from $SU(2)_\ell$* , *Phys. Rev.* **D96** (2017) 035001 [1703.00199].
- [243] W.-F. Chang and J. N. Ng, *Study of Gauged Lepton Symmetry Signatures at Colliders*, *Phys. Rev.* **D98** (2018) 035015 [1805.10382].
- [244] W.-F. Chang and J. N. Ng, *Alternative Perspective on Gauged Lepton Number and Implications for Collider Physics*, *Phys. Rev.* **D99** (2019) 075025 [1808.08188].
- [245] Y. Cai, T. Han, T. Li and R. Ruiz, *Lepton Number Violation: Seesaw Models and Their Collider Tests*, *Front. in Phys.* **6** (2018) 40 [1711.02180].
- [246] CMB-S4 collaboration, *CMB-S4 Science Book, First Edition*, 1610.02743.
- [247] L. Basso, A. Belyaev, S. Moretti and C. H. Shepherd-Themistocleous, *Phenomenology of the minimal B-L extension of the Standard model: Z' and neutrinos*, *Phys. Rev. D* **80** (2009) 055030 [0812.4313].

- [248] K. Huitu, S. Khalil, H. Okada and S. K. Rai, *Signatures for right-handed neutrinos at the Large Hadron Collider*, *Phys. Rev. Lett.* **101** (2008) 181802 [0803.2799].
- [249] J. Aguilar-Saavedra, *Heavy lepton pair production at LHC: Model discrimination with multi-lepton signals*, *Nucl. Phys. B* **828** (2010) 289 [0905.2221].
- [250] E. Accomando, L. Delle Rose, S. Moretti, E. Olaiya and C. H. Shepherd-Themistocleous, *Extra Higgs boson and Z' as portals to signatures of heavy neutrinos at the LHC*, *JHEP* **02** (2018) 109 [1708.03650].
- [251] P. Fileviez Perez, T. Han and T. Li, *Testability of Type I Seesaw at the CERN LHC: Revealing the Existence of the B-L Symmetry*, *Phys. Rev. D* **80** (2009) 073015 [0907.4186].
- [252] N. Arkani-Hamed, T. Han, M. Mangano and L.-T. Wang, *Physics opportunities of a 100 TeV proton-proton collider*, *Phys. Rept.* **652** (2016) 1 [1511.06495].
- [253] P. J. Fox and E. Poppitz, *Leptophilic Dark Matter*, *Phys. Rev.* **D79** (2009) 083528 [0811.0399].
- [254] J. Kopp, V. Niro, T. Schwetz and J. Zupan, *DAMA/LIBRA and leptonically interacting Dark Matter*, *Phys. Rev.* **D80** (2009) 083502 [0907.3159].
- [255] N. F. Bell, Y. Cai, R. K. Leane and A. D. Medina, *Leptophilic dark matter with Z' interactions*, *Phys. Rev.* **D90** (2014) 035027 [1407.3001].
- [256] A. Freitas and S. Westhoff, *Leptophilic Dark Matter in Lepton Interactions at LEP and ILC*, *JHEP* **10** (2014) 116 [1408.1959].
- [257] F. del Aguila, M. Chala, J. Santiago and Y. Yamamoto, *Collider limits on leptophilic interactions*, *JHEP* **03** (2015) 059 [1411.7394].
- [258] N. Chen, J. Wang and X.-P. Wang, *The leptophilic dark matter with Z' interaction: from indirect searches to future e^+e^- collider searches*, 1501.04486.
- [259] F. D'Eramo, B. J. Kavanagh and P. Panci, *Probing Leptophilic Dark Sectors with Hadronic Processes*, *Phys. Lett.* **B771** (2017) 339 [1702.00016].

- [260] E. Madge and P. Schwaller, *Leptophilic dark matter from gauged lepton number: Phenomenology and gravitational wave signatures*, *JHEP* **02** (2019) 048 [1809.09110].
- [261] J. M. Alarcon, J. Martin Camalich and J. A. Oller, *The chiral representation of the πN scattering amplitude and the pion-nucleon sigma term*, *Phys. Rev.* **D85** (2012) 051503 [1110.3797].
- [262] J. C. Maxwell, *A dynamical theory of the electromagnetic field*, *Philosophical Transactions of the Royal Society of London* **155** (1865) 459.
- [263] S. Glashow, *Partial Symmetries of Weak Interactions*, *Nucl. Phys.* **22** (1961) 579.
- [264] A. Salam and J. C. Ward, *Electromagnetic and weak interactions*, *Phys. Lett.* **13** (1964) 168.
- [265] S. Weinberg, *A Model of Leptons*, *Phys. Rev. Lett.* **19** (1967) 1264.
- [266] H. Georgi and S. Glashow, *Unity of All Elementary Particle Forces*, *Phys. Rev. Lett.* **32** (1974) 438.
- [267] J. R. Ellis and M. K. Gaillard, *Fermion Masses and Higgs Representations in SU(5)*, *Phys. Lett. B* **88** (1979) 315.
- [268] H. Georgi and C. Jarlskog, *A New Lepton - Quark Mass Relation in a Unified Theory*, *Phys. Lett. B* **86** (1979) 297.
- [269] P. Fileviez Pérez, A. Gross and C. Murgui, *Seesaw scale, unification, and proton decay*, *Phys. Rev. D* **98** (2018) 035032 [1804.07831].
- [270] A. Givon, L. J. Hall and U. Sarid, *SU(5) unification revisited*, *Phys. Lett.* **B271** (1991) 138.
- [271] SUPER-KAMIOKANDE collaboration, *Search for proton decay via $p \rightarrow \bar{\nu} K^+$ using 260 kiloton-year data of Super-Kamiokande*, *Phys. Rev.* **D90** (2014) 072005 [1408.1195].
- [272] SUPER-KAMIOKANDE collaboration, *Search for Nucleon Decay via $n \rightarrow \bar{\nu} \pi^0$ and $p \rightarrow \bar{\nu} \pi^+$ in Super-Kamiokande*, *Phys. Rev. Lett.* **113** (2014) 121802 [1305.4391].

- [273] HYPER-KAMIOKANDE PROTO collaboration, *The Hyper-Kamiokande Experiment*, in *Proceedings, Prospects in Neutrino Physics (NuPhys2016): London, UK, December 12-14, 2016*, 2017, 1705.00306.
- [274] E. Kearns, *Proton decay (experiments)*, *Talk given at BLV2020* (2020) .
- [275] P. Fileviez Perez, *Fermion mixings versus $d = 6$ proton decay*, *Phys. Lett. B* **595** (2004) 476 [hep-ph/0403286].
- [276] Y. Aoki, T. Izubuchi, E. Shintani and A. Soni, *Improved lattice computation of proton decay matrix elements*, *Phys. Rev. D* **96** (2017) 014506 [1705.01338].
- [277] I. Dorsner and P. Fileviez Perez, *Unification without supersymmetry: Neutrino mass, proton decay and light leptiquarks*, *Nucl. Phys. B* **723** (2005) 53 [hep-ph/0504276].
- [278] I. Dorsner, P. Fileviez Perez and R. Gonzalez Felipe, *Phenomenological and cosmological aspects of a minimal GUT scenario*, *Nucl. Phys. B* **747** (2006) 312 [hep-ph/0512068].
- [279] I. Dorsner, P. Fileviez Perez and G. Rodrigo, *Fermion masses and the UV cutoff of the minimal realistic $SU(5)$* , *Phys. Rev. D* **75** (2007) 125007 [hep-ph/0607208].
- [280] B. Bajc and G. Senjanovic, *Seesaw at LHC*, *JHEP* **08** (2007) 014 [hep-ph/0612029].
- [281] P. Fileviez Perez, *Renormalizable adjoint $SU(5)$* , *Phys. Lett. B* **654** (2007) 189 [hep-ph/0702287].
- [282] I. Dorsner and P. Fileviez Perez, *Upper Bound on the Mass of the Type III Seesaw Triplet in an $SU(5)$ Model*, *JHEP* **06** (2007) 029 [hep-ph/0612216].
- [283] P. Fileviez Perez and C. Murgui, *Renormalizable $SU(5)$ Unification*, *Phys. Rev. D* **94** (2016) 075014 [1604.03377].
- [284] SUPER-KAMIOKANDE collaboration, *Search for Nucleon Decay into Charged Anti-lepton plus Meson in Super-Kamiokande I and II*, *Phys. Rev. D* **85** (2012) 112001 [1203.4030].

- [285] M. Miura, *Plans and prospects for the Hyper-Kamiokande detector, talk given at BLV2013* (2013) .
- [286] V. Miralles and A. Pich, *LHC bounds on colored scalars*, *Phys. Rev. D* **100** (2019) 115042 [1910.07947].
- [287] A. Hayreter and G. Valencia, *LHC constraints on color octet scalars*, *Phys. Rev. D* **96** (2017) 035004 [1703.04164].
- [288] A. V. Manohar and M. B. Wise, *Flavor changing neutral currents, an extended scalar sector, and the Higgs production rate at the CERN LHC*, *Phys. Rev. D* **74** (2006) 035009 [hep-ph/0606172].
- [289] M. I. Gresham and M. B. Wise, *Color octet scalar production at the LHC*, *Phys. Rev. D* **76** (2007) 075003 [0706.0909].
- [290] M. Gerbush, T. J. Khoo, D. J. Phalen, A. Pierce and D. Tucker-Smith, *Color-octet scalars at the CERN LHC*, *Phys. Rev. D* **77** (2008) 095003 [0710.3133].
- [291] A. Idilbi, C. Kim and T. Mehen, *Factorization and resummation for single color-octet scalar production at the LHC*, *Phys. Rev. D* **79** (2009) 114016 [0903.3668].
- [292] C. Kim and T. Mehen, *Octetonium at the LHC*, *Nucl. Phys. B Proc. Suppl.* **200-202** (2010) 179 [0909.5695].
- [293] J. M. Arnold, M. Pospelov, M. Trott and M. B. Wise, *Scalar Representations and Minimal Flavor Violation*, *JHEP* **01** (2010) 073 [0911.2225].
- [294] I. Dorsner, S. Fajfer, J. F. Kamenik and N. Kosnik, *Light colored scalars from grand unification and the forward-backward asymmetry in t t -bar production*, *Phys. Rev. D* **81** (2010) 055009 [0912.0972].
- [295] S. Ham, S.-A. Shim and S. Oh, *Electroweak phase transition in an extension of the standard model with scalar color octet*, *Phys. Rev. D* **81** (2010) 055015 [1002.0237].
- [296] R. Boughezal and F. Petriello, *Color-octet scalar effects on Higgs boson production in gluon fusion*, *Phys. Rev. D* **81** (2010) 114033 [1003.2046].

- [297] A. Idilbi, C. Kim and T. Mehen, *Pair Production of Color-Octet Scalars at the LHC*, *Phys. Rev. D* **82** (2010) 075017 [1007.0865].
- [298] J. M. Arnold and B. Fornal, *Color octet scalars and high p_T four-jet events at LHC*, *Phys. Rev. D* **85** (2012) 055020 [1112.0003].
- [299] S. Bertolini, L. Di Luzio and M. Malinsky, *Light color octet scalars in the minimal $SO(10)$ grand unification*, *Phys. Rev. D* **87** (2013) 085020 [1302.3401].
- [300] J. Cao, P. Wan, J. M. Yang and J. Zhu, *The SM extension with color-octet scalars: diphoton enhancement and global fit of LHC Higgs data*, *JHEP* **08** (2013) 009 [1303.2426].
- [301] X.-G. He, H. Phoon, Y. Tang and G. Valencia, *Unitarity and vacuum stability constraints on the couplings of color octet scalars*, *JHEP* **05** (2013) 026 [1303.4848].
- [302] S. Khalil, S. Salem and M. Allam, *$SU(5)$ Octet Scalar at the LHC*, *Phys. Rev. D* **89** (2014) 095011 [1401.1482].
- [303] S. Fajfer and J. O. Eeg, *Colored scalars and the neutron electric dipole moment*, *Phys. Rev. D* **89** (2014) 095030 [1401.2275].
- [304] P. Fileviez Perez, R. Gavin, T. McElmurry and F. Petriello, *Grand Unification and Light Color-Octet Scalars at the LHC*, *Phys. Rev. D* **78** (2008) 115017 [0809.2106].
- [305] T. Han, I. Lewis and Z. Liu, *Colored Resonant Signals at the LHC: Largest Rate and Simplest Topology*, *JHEP* **12** (2010) 085 [1010.4309].
- [306] I. Dorsner and I. Mocioiu, *Predictions from type II see-saw mechanism in $SU(5)$* , *Nucl. Phys. B* **796** (2008) 123 [0708.3332].
- [307] P. Fileviez Perez, H. Iminniyaz and G. Rodrigo, *Proton Stability, Dark Matter and Light Color Octet Scalars in Adjoint $SU(5)$ Unification*, *Phys. Rev. D* **78** (2008) 015013 [0803.4156].
- [308] I. Dorsner and P. Fileviez Perez, *Unification versus proton decay in $SU(5)$* , *Phys. Lett. B* **642** (2006) 248 [hep-ph/0606062].

- [309] I. Dorsner, S. Fajfer and I. Mustac, *Light vector-like fermions in a minimal SU(5) setup*, *Phys. Rev. D* **89** (2014) 115004 [1401.6870].
- [310] M. B. Wise, H. Georgi and S. L. Glashow, *SU(5) and the Invisible Axion*, *Phys. Rev. Lett.* **47** (1981) 402.
- [311] P. Fileviez Pérez, C. Murgui and A. D. Plascencia, *The QCD Axion and Unification*, *JHEP* **11** (2019) 093 [1908.01772].
- [312] R. T. Co, F. D'Eramo and L. J. Hall, *Supersymmetric axion grand unified theories and their predictions*, *Phys. Rev.* **D94** (2016) 075001 [1603.04439].
- [313] S. M. Boucenna and Q. Shafi, *Axion inflation, proton decay, and leptogenesis in $SU(5) \times U(1)_{PQ}$* , *Phys. Rev.* **D97** (2018) 075012 [1712.06526].
- [314] L. Di Luzio, A. Ringwald and C. Tamarit, *Axion mass prediction from minimal grand unification*, *Phys. Rev.* **D98** (2018) 095011 [1807.09769].
- [315] A. Ernst, A. Ringwald and C. Tamarit, *Axion Predictions in $SO(10) \times U(1)_{PQ}$ Models*, *JHEP* **02** (2018) 103 [1801.04906].
- [316] D. Emmanuel-Costa, C. Simoes and M. Tortola, *The minimal adjoint-SU(5) \times Z_4 GUT model*, *JHEP* **10** (2013) 054 [1303.5699].
- [317] DUNE collaboration, *Long-Baseline Neutrino Facility (LBNF) and Deep Underground Neutrino Experiment (DUNE)*, 1512.06148.
- [318] M. Gorghetto and G. Villadoro, *Topological Susceptibility and QCD Axion Mass: QED and NNLO corrections*, *JHEP* **03** (2019) 033 [1812.01008].
- [319] P. Svrcek and E. Witten, *Axions In String Theory*, *JHEP* **06** (2006) 051 [hep-th/0605206].
- [320] HYPER-KAMIOKANDE collaboration, *Hyper-Kamiokande Design Report*, 1805.04163.
- [321] P. Fileviez Pérez, C. Murgui and A. D. Plascencia, *Axion Dark Matter, Proton Decay and Unification*, *JHEP* **01** (2020) 091 [1911.05738].

- [322] C. Abel et al., *Search for Axionlike Dark Matter through Nuclear Spin Precession in Electric and Magnetic Fields*, *Phys. Rev.* **X7** (2017) 041034 [1708.06367].
- [323] G. Buchalla, A. J. Buras and M. E. Lautenbacher, *Weak decays beyond leading logarithms*, *Rev. Mod. Phys.* **68** (1996) 1125 [hep-ph/9512380].
- [324] J. Aebischer, M. Fael, C. Greub and J. Virto, *B physics Beyond the Standard Model at One Loop: Complete Renormalization Group Evolution below the Electroweak Scale*, *JHEP* **09** (2017) 158 [1704.06639].
- [325] E. E. Jenkins, A. V. Manohar and P. Stoffer, *Low-Energy Effective Field Theory below the Electroweak Scale: Operators and Matching*, *JHEP* **03** (2018) 016 [1709.04486].
- [326] E. E. Jenkins, A. V. Manohar and P. Stoffer, *Low-Energy Effective Field Theory below the Electroweak Scale: Anomalous Dimensions*, *JHEP* **01** (2018) 084 [1711.05270].
- [327] E. E. Jenkins, A. V. Manohar and M. Trott, *Renormalization Group Evolution of the Standard Model Dimension Six Operators I: Formalism and lambda Dependence*, *JHEP* **10** (2013) 087 [1308.2627].
- [328] E. E. Jenkins, A. V. Manohar and M. Trott, *Renormalization Group Evolution of the Standard Model Dimension Six Operators II: Yukawa Dependence*, *JHEP* **01** (2014) 035 [1310.4838].
- [329] R. Alonso, E. E. Jenkins, A. V. Manohar and M. Trott, *Renormalization Group Evolution of the Standard Model Dimension Six Operators III: Gauge Coupling Dependence and Phenomenology*, *JHEP* **04** (2014) 159 [1312.2014].
- [330] M. González-Alonso, J. Martin Camalich and K. Mimouni, *Renormalization-group evolution of new physics contributions to (semi)leptonic meson decays*, *Phys. Lett.* **B772** (2017) 777 [1706.00410].
- [331] Q.-Y. Hu, X.-Q. Li and Y.-D. Yang, *$b \rightarrow c\tau\nu$ transitions in the standard model effective field theory*, *Eur. Phys. J.* **C79** (2019) 264 [1810.04939].

- [332] A. J. Buras and M. Jung, *Analytic inclusion of the scale dependence of the anomalous dimension matrix in Standard Model Effective Theory*, *JHEP* **06** (2018) 067 [1804.05852].
- [333] R. Mandal, C. Murgui, A. Peñuelas and A. Pich, *The role of right-handed neutrinos in $b \rightarrow c\tau\bar{\nu}$ anomalies*, 2004.06726.
- [334] P. Asadi, M. R. Buckley and D. Shih, *Asymmetry Observables and the Origin of $R_{D^{(*)}}$ Anomalies*, *Phys. Rev.* **D99** (2019) 035015 [1810.06597].
- [335] Bečirević, Damir and Fedele, Marco and Nišandžić, Ivan and Tayduganov, Andrey, *Lepton Flavor Universality tests through angular observables of $\bar{B} \rightarrow D^{(*)}\ell\bar{\nu}$ decay modes*, 1907.02257.
- [336] M. Duraisamy and A. Datta, *The Full $B \rightarrow D^*\tau^-\bar{\nu}_\tau$ Angular Distribution and CP violating Triple Products*, *JHEP* **09** (2013) 059 [1302.7031].
- [337] M. Duraisamy, P. Sharma and A. Datta, *Azimuthal $B \rightarrow D^*\tau^-\bar{\nu}_\tau$ angular distribution with tensor operators*, *Phys. Rev.* **D90** (2014) 074013 [1405.3719].
- [338] D. Becirevic, S. Fajfer, I. Nisandzic and A. Tayduganov, *Angular distributions of $\bar{B} \rightarrow D^{(*)}\ell\bar{\nu}_\ell$ decays and search of New Physics*, *Nucl. Phys. B* **946** (2019) 114707 [1602.03030].
- [339] R. Alonso, A. Kobach and J. Martin Camalich, *New physics in the kinematic distributions of $\bar{B} \rightarrow D^{(*)}\tau^-(\rightarrow \ell^-\bar{\nu}_\ell\nu_\tau)\bar{\nu}_\tau$* , *Phys. Rev. D* **94** (2016) 094021 [1602.07671].
- [340] Z. Ligeti, M. Papucci and D. J. Robinson, *New Physics in the Visible Final States of $B \rightarrow D^{(*)}\tau\nu$* , *JHEP* **01** (2017) 083 [1610.02045].
- [341] D. Hill, M. John, W. Ke and A. Poluektov, *Model-independent method for measuring the angular coefficients of $B^0 \rightarrow D^{*-}\tau^+\nu_\tau$ decays*, *JHEP* **11** (2019) 133 [1908.04643].
- [342] J. Aebischer, T. Kuhr and K. Lieret, *Clustering of $\bar{B} \rightarrow D^{(*)}\tau^-\bar{\nu}_\tau$ kinematic distributions with ClusterKinG*, *JHEP* **04** (2020) 007 [1909.11088].

- [343] C. Boyd, B. Grinstein and R. F. Lebed, *Constraints on form-factors for exclusive semileptonic heavy to light meson decays*, *Phys. Rev. Lett.* **74** (1995) 4603 [hep-ph/9412324].
- [344] C. Boyd, B. Grinstein and R. F. Lebed, *Model independent determinations of anti- $B \rightarrow D$ (lepton), D^* (lepton) anti-neutrino form-factors*, *Nucl. Phys. B* **461** (1996) 493 [hep-ph/9508211].
- [345] C. Boyd, B. Grinstein and R. F. Lebed, *Precision corrections to dispersive bounds on form-factors*, *Phys. Rev. D* **56** (1997) 6895 [hep-ph/9705252].
- [346] I. Caprini, L. Lellouch and M. Neubert, *Dispersive bounds on the shape of $\bar{B} \rightarrow D^{(*)} \ell \bar{\nu}$ form-factors*, *Nucl. Phys.* **B530** (1998) 153 [hep-ph/9712417].
- [347] M. Neubert, *Heavy quark symmetry*, *Phys. Rept.* **245** (1994) 259 [hep-ph/9306320].
- [348] A. V. Manohar and M. B. Wise, *Heavy quark physics*, *Camb. Monogr. Part. Phys. Nucl. Phys. Cosmol.* **10** (2000) 1.
- [349] MILC collaboration, *$B \rightarrow D\tau\nu$ form factors at nonzero recoil and $|V_{cb}|$ from 2+1-flavor lattice QCD*, *Phys. Rev.* **D92** (2015) 034506 [1503.07237].
- [350] D. Bigi and P. Gambino, *Revisiting $B \rightarrow D\ell\nu$* , *Phys. Rev. D* **94** (2016) 094008 [1606.08030].
- [351] D. Bigi, P. Gambino and S. Schacht, *A fresh look at the determination of $|V_{cb}|$ from $B \rightarrow D^*\ell\nu$* , *Phys. Lett.* **B769** (2017) 441 [1703.06124].
- [352] D. Bigi, P. Gambino and S. Schacht, *$R(D^*)$, $|V_{cb}|$, and the Heavy Quark Symmetry relations between form factors*, *JHEP* **11** (2017) 061 [1707.09509].
- [353] F. U. Bernlochner, Z. Ligeti, M. Papucci and D. J. Robinson, *Combined analysis of semileptonic B decays to D and D^* : $R(D^{(*)})$, $|V_{cb}|$, and new physics*, *Phys. Rev.* **D95** (2017) 115008 [1703.05330].
- [354] F. U. Bernlochner, Z. Ligeti, M. Papucci and D. J. Robinson, *Tensions and correlations in $|V_{cb}|$ determinations*, *Phys. Rev.* **D96** (2017) 091503 [1708.07134].

- [355] B. Grinstein and A. Kobach, *Model-Independent Extraction of $|V_{cb}|$ from $\bar{B} \rightarrow D^* \ell \bar{\nu}$* , *Phys. Lett.* **B771** (2017) 359 [1703.08170].
- [356] S. Jaiswal, S. Nandi and S. K. Patra, *Extraction of $|V_{cb}|$ from $B \rightarrow D^{(*)} \ell \nu_\ell$ and the Standard Model predictions of $R(D^{(*)})$* , *JHEP* **12** (2017) 060 [1707.09977].
- [357] N. Isgur and M. B. Wise, *WEAK TRANSITION FORM-FACTORS BETWEEN HEAVY MESONS*, *Phys. Lett.* **B237** (1990) 527.
- [358] C. Bourrely, B. Machtet and E. de Rafael, *Semileptonic Decays of Pseudoscalar Particles ($M \rightarrow M' \ell \nu_\ell$) and Short Distance Behavior of Quantum Chromodynamics*, *Nucl. Phys.* **B189** (1981) 157.
- [359] M. Jung and D. M. Straub, *Constraining new physics in $b \rightarrow c \ell \nu$ transitions*, *JHEP* **01** (2019) 009 [1801.01112].
- [360] M. Bordone, M. Jung and D. van Dyk, *Theory determination of $\bar{B} \rightarrow D^{(*)} \ell^- \bar{\nu}$ form factors at $\mathcal{O}(1/m_c^2)$* , *Eur. Phys. J. C* **80** (2020) 74 [1908.09398].
- [361] HPQCD collaboration, *$B \rightarrow D \ell \nu$ form factors at nonzero recoil and extraction of $|V_{cb}|$* , *Phys. Rev.* **D92** (2015) 054510 [1505.03925].
- [362] HFLAV collaboration, *Averages of b -hadron, c -hadron, and τ -lepton properties as of 2018*, 1909.12524.
- [363] BELLE collaboration, *Measurement of the branching ratio of $\bar{B} \rightarrow D^{(*)} \tau^- \bar{\nu}_\tau$ relative to $\bar{B} \rightarrow D^{(*)} \ell^- \bar{\nu}_\ell$ decays with hadronic tagging at Belle*, *Phys. Rev. D* **92** (2015) 072014 [1507.03233].
- [364] BELLE collaboration, *Measurement of the branching ratio of $\bar{B}^0 \rightarrow D^{*+} \tau^- \bar{\nu}_\tau$ relative to $\bar{B}^0 \rightarrow D^{*+} \ell^- \bar{\nu}_\ell$ decays with a semileptonic tagging method*, in *51st Rencontres de Moriond on EW Interactions and Unified Theories*, 3, 2016, 1603.06711.
- [365] LHCb collaboration, *Measurement of the ratio of branching fractions $\mathcal{B}(\bar{B}^0 \rightarrow D^{*+} \tau^- \bar{\nu}_\tau) / \mathcal{B}(\bar{B}^0 \rightarrow D^{*+} \mu^- \bar{\nu}_\mu)$* , *Phys. Rev. Lett.* **115** (2015) 111803 [1506.08614].

- [366] HFLAV WEB PAGE collaboration, <https://hflav.web.cern.ch>, .
- [367] BELLE collaboration, *Measurement of $\mathcal{R}(D)$ and $\mathcal{R}(D^*)$ with a semileptonic tagging method*, 1904.08794.
- [368] BELLE collaboration, *Measurement of the D^{*-} polarization in the decay $B^0 \rightarrow D^{*-} \tau^+ \nu_\tau$* , 1903.03102.
- [369] LHCb collaboration, *Measurement of the ratio of branching fractions $\mathcal{B}(B_c^+ \rightarrow J/\psi \tau^+ \nu_\tau)/\mathcal{B}(B_c^+ \rightarrow J/\psi \mu^+ \nu_\mu)$* , *Phys. Rev. Lett.* **120** (2018) 121801 [1711.05623].
- [370] A. Yu. Anisimov, I. M. Narodetsky, C. Semay and B. Silvestre-Brac, *The B_c meson lifetime in the light front constituent quark model*, *Phys. Lett.* **B452** (1999) 129 [hep-ph/9812514].
- [371] V. V. Kiselev, *Exclusive decays and lifetime of B_c meson in QCD sum rules*, hep-ph/0211021.
- [372] M. A. Ivanov, J. G. Korner and P. Santorelli, *Exclusive semileptonic and nonleptonic decays of the B_c meson*, *Phys. Rev.* **D73** (2006) 054024 [hep-ph/0602050].
- [373] E. Hernandez, J. Nieves and J. M. Verde-Velasco, *Study of exclusive semileptonic and non-leptonic decays of B_c - in a nonrelativistic quark model*, *Phys. Rev.* **D74** (2006) 074008 [hep-ph/0607150].
- [374] T. Huang and F. Zuo, *Semileptonic B_c decays and charmonium distribution amplitude*, *Eur. Phys. J.* **C51** (2007) 833 [hep-ph/0702147].
- [375] W. Wang, Y.-L. Shen and C.-D. Lu, *Covariant Light-Front Approach for B_c transition form factors*, *Phys. Rev.* **D79** (2009) 054012 [0811.3748].
- [376] A. Issadykov and M. A. Ivanov, *The decays $B_c \rightarrow J/\psi + \bar{\ell} \nu_\ell$ and $B_c \rightarrow J/\psi + \pi(K)$ in covariant confined quark model*, *Phys. Lett.* **B783** (2018) 178 [1804.00472].
- [377] W.-F. Wang, Y.-Y. Fan and Z.-J. Xiao, *Semileptonic decays $B_c \rightarrow (\eta_c, J/\Psi) l \nu$ in the perturbative QCD approach*, *Chin. Phys.* **C37** (2013) 093102 [1212.5903].

- [378] X.-Q. Hu, S.-P. Jin and Z.-J. Xiao, *Semileptonic decays $B_c \rightarrow (\eta_c, J/\psi)l\bar{\nu}_l$ in the "PQCD + Lattice" approach*, 1904.07530.
- [379] D. Leljak, B. Melic and M. Patra, *On lepton flavour universality in semileptonic $B_c \rightarrow \eta_c, J/\psi$ decays*, 1901.08368.
- [380] K. Azizi, Y. Sarac and H. Sundu, *Lepton flavour universality violation in semileptonic tree level weak transitions*, 1904.08267.
- [381] C.-T. Tran, M. A. Ivanov, J. G. Körner and P. Santorelli, *Implications of new physics in the decays $B_c \rightarrow (J/\psi, \eta_c)\tau\nu$* , *Phys. Rev.* **D97** (2018) 054014 [1801.06927].
- [382] BELLE collaboration, *Measurement of the τ lepton polarization and $R(D^*)$ in the decay $\bar{B} \rightarrow D^*\tau^-\bar{\nu}_\tau$ with one-prong hadronic τ decays at Belle*, *Phys. Rev. D* **97** (2018) 012004 [1709.00129].
- [383] V. Cirigliano, J. Jenkins and M. Gonzalez-Alonso, *Semileptonic decays of light quarks beyond the Standard Model*, *Nucl. Phys.* **B830** (2010) 95 [0908.1754].
- [384] R. Alonso, B. Grinstein and J. Martin Camalich, *$SU(2) \times U(1)$ gauge invariance and the shape of new physics in rare B decays*, *Phys. Rev. Lett.* **113** (2014) 241802 [1407.7044].
- [385] O. Catà and M. Jung, *Signatures of a nonstandard Higgs boson from flavor physics*, *Phys. Rev.* **D92** (2015) 055018 [1505.05804].
- [386] W. Buchmuller and D. Wyler, *Effective Lagrangian Analysis of New Interactions and Flavor Conservation*, *Nucl. Phys.* **B268** (1986) 621.
- [387] B. Grzadkowski, M. Iskrzynski, M. Misiak and J. Rosiek, *Dimension-Six Terms in the Standard Model Lagrangian*, *JHEP* **10** (2010) 085 [1008.4884].
- [388] A. Celis, M. Jung, X.-Q. Li and A. Pich, *Scalar contributions to $b \rightarrow c(u)\tau\nu$ transitions*, *Phys. Lett.* **B771** (2017) 168 [1612.07757].
- [389] D. Bečirević, I. Doršner, S. Fajfer, N. Košnik, D. A. Faroughy and O. Sumensari, *Scalar leptoquarks from grand unified theories to accommodate the B -physics anomalies*, *Phys. Rev.* **D98** (2018) 055003 [1806.05689].

- [390] S. Bhattacharya, S. Nandi and S. Kumar Patra, *b* → *c*τν_τ Decays: a catalogue to compare, constrain, and correlate new physics effects, *Eur. Phys. J.* **C79** (2019) 268 [1805.08222].
- [391] M. Blanke, A. Crivellin, S. de Boer, M. Moscati, U. Nierste, I. Nišandžić et al., *Impact of polarization observables and B_c → τν on new physics explanations of the b → cτν anomaly*, 1811.09603.
- [392] B. Bhattacharya, A. Datta, S. Kamali and D. London, *CP Violation in B̄⁰ → D*⁺μ⁻ν̄_μ*, 1903.02567.
- [393] C. Murgui, A. Peñuelas, M. Jung and A. Pich, *Global fit to b → cτν transitions*, *JHEP* **09** (2019) 103 [1904.09311].
- [394] M. Beneke and G. Buchalla, *The B_c Meson Lifetime*, *Phys. Rev.* **D53** (1996) 4991 [hep-ph/9601249].
- [395] R. Alonso, B. Grinstein and J. Martin Camalich, *Lifetime of B_c⁻ Constrains Explanations for Anomalies in B → D^(*)τν*, *Phys. Rev. Lett.* **118** (2017) 081802 [1611.06676].
- [396] A. G. Akeroyd and C.-H. Chen, *Constraint on the branching ratio of B_c → τν̄ from LEP1 and consequences for R(D^(*)) anomaly*, *Phys. Rev.* **D96** (2017) 075011 [1708.04072].
- [397] L3 collaboration, *Measurement of D_s → τ⁻ν_τ and a new limit for B⁻ → τ⁻ν_τ*, *Phys. Lett.* **B396** (1997) 327.
- [398] HFLAV collaboration, *Averages of b-hadron, c-hadron, and τ-lepton properties as of summer 2016, and online update at <https://lhflav.web.cern.ch/>*, *Eur. Phys. J.* **C77** (2017) 895 [1612.07233].
- [399] FERMILAB LATTICE, MILC collaboration, *Update of |V_{cb}| from the B̄ → D*ℓν̄ form factor at zero recoil with three-flavor lattice QCD*, *Phys. Rev.* **D89** (2014) 114504 [1403.0635].

- [400] HPQCD collaboration, *Lattice QCD calculation of the $B_{(s)} \rightarrow D_{(s)}^* \ell \nu$ form factors at zero recoil and implications for $|V_{cb}|$* , *Phys. Rev.* **D97** (2018) 054502 [1711.11013].
- [401] S. Faller, A. Khodjamirian, C. Klein and T. Mannel, *$B \rightarrow D^{(*)}$ Form Factors from QCD Light-Cone Sum Rules*, *Eur. Phys. J.* **C60** (2009) 603 [0809.0222].
- [402] M. Neubert, Z. Ligeti and Y. Nir, *QCD sum rule analysis of the subleading Isgur-Wise form-factor $\chi_2(v \cdot v')$* , *Phys. Lett.* **B301** (1993) 101 [hep-ph/9209271].
- [403] M. Neubert, Z. Ligeti and Y. Nir, *The Subleading Isgur-Wise form-factor $\chi_3(v \cdot v')$ to order α_s in QCD sum rules*, *Phys. Rev.* **D47** (1993) 5060 [hep-ph/9212266].
- [404] Z. Ligeti, Y. Nir and M. Neubert, *The Subleading Isgur-Wise form-factor $\xi_3(v \cdot v')$ and its implications for the decays $\bar{B} \rightarrow D^* \ell \bar{\nu}$* , *Phys. Rev.* **D49** (1994) 1302 [hep-ph/9305304].
- [405] BELLE collaboration, *Measurement of $R(D)$ and $R(D^*)$ with a semileptonic tagging method*, 1904.08794.
- [406] G. Caria, "Measurement of $R(D)$ and $R(D^*)$ with a semileptonic tag at Belle." 2019.
- [407] BABAR collaboration, *Evidence for an excess of $\bar{B} \rightarrow D^{(*)} \tau^- \bar{\nu}_\tau$ decays*, *Phys. Rev. Lett.* **109** (2012) 101802 [1205.5442].
- [408] Y. Sakaki, M. Tanaka, A. Tayduganov and R. Watanabe, *Probing New Physics with q^2 distributions in $\bar{B} \rightarrow D^{(*)} \tau \bar{\nu}$* , *Phys. Rev.* **D91** (2015) 114028 [1412.3761].
- [409] M. Freytsis, Z. Ligeti and J. T. Ruderman, *Flavor models for $\bar{B} \rightarrow D^{(*)} \tau \bar{\nu}$* , *Phys. Rev.* **D92** (2015) 054018 [1506.08896].
- [410] S. Bhattacharya, S. Nandi and S. K. Patra, *Looking for possible new physics in $B \rightarrow D^{(*)} \tau \nu_\tau$ in light of recent data*, *Phys. Rev.* **D95** (2017) 075012 [1611.04605].
- [411] W. Dekens, J. de Vries, M. Jung and K. K. Vos, *The phenomenology of electric dipole moments in models of scalar leptoquarks*, *JHEP* **01** (2019) 069 [1809.09114].

- [412] A. Celis, M. Jung, X.-Q. Li and A. Pich, *Sensitivity to charged scalars in $B \rightarrow D^{(*)} \tau \nu_\tau$ and $B \rightarrow \tau \nu_\tau$ decays*, *JHEP* **01** (2013) 054 [1210.8443].
- [413] A. Datta, M. Duraisamy and D. Ghosh, *Diagnosing New Physics in $b \rightarrow c \tau \nu_\tau$ decays in the light of the recent BaBar result*, *Phys. Rev.* **D86** (2012) 034027 [1206.3760].
- [414] M. Duraisamy and A. Datta, *The Full $B \rightarrow D^* \tau^- \bar{\nu}_\tau$ Angular Distribution and CP violating Triple Products*, *JHEP* **09** (2013) 059 [1302.7031].
- [415] R. Dutta, A. Bhol and A. K. Giri, *Effective theory approach to new physics in $b \rightarrow u$ and $b \rightarrow c$ leptonic and semileptonic decays*, *Phys. Rev.* **D88** (2013) 114023 [1307.6653].
- [416] Y. Sakaki, M. Tanaka, A. Tayduganov and R. Watanabe, *Testing leptoquark models in $\bar{B} \rightarrow D^{(*)} \tau \bar{\nu}$* , *Phys. Rev.* **D88** (2013) 094012 [1309.0301].
- [417] R. Alonso, B. Grinstein and J. Martin Camalich, *Lepton universality violation and lepton flavor conservation in B -meson decays*, *JHEP* **10** (2015) 184 [1505.05164].
- [418] D. Boubaa, S. Khalil and S. Moretti, *Resolving the $\bar{B} \rightarrow D \tau \nu$ and $\bar{B} \rightarrow D^* \tau \nu_\tau$ puzzle in the MSSM*, 1604.03416.
- [419] D. Bardhan, P. Byakti and D. Ghosh, *A closer look at the R_D and R_{D^*} anomalies*, *JHEP* **01** (2017) 125 [1610.03038].
- [420] D. Choudhury, A. Kundu, S. Nandi and S. K. Patra, *Unified resolution of the $R(D)$ and $R(D^*)$ anomalies and the lepton flavor violating decay $h \rightarrow \mu \tau$* , *Phys. Rev.* **D95** (2017) 035021 [1612.03517].
- [421] A. K. Alok, D. Kumar, S. Kumbhakar and S. U. Sankar, *D^* polarization as a probe to discriminate new physics in $\bar{B} \rightarrow D^* \tau \bar{\nu}$* , *Phys. Rev.* **D95** (2017) 115038 [1606.03164].
- [422] A. K. Alok, D. Kumar, J. Kumar, S. Kumbhakar and S. U. Sankar, *New physics solutions for R_D and R_{D^*}* , *JHEP* **09** (2018) 152 [1710.04127].

- [423] B. Capdevila, A. Crivellin, S. Descotes-Genon, L. Hofer and J. Matias, *Searching for New Physics with $b \rightarrow s\tau^+\tau^-$ processes*, *Phys. Rev. Lett.* **120** (2018) 181802 [1712.01919].
- [424] W. Altmannshofer, P. Bhupal Dev and A. Soni, *$R_{D^{(*)}}$ anomaly: A possible hint for natural supersymmetry with R -parity violation*, *Phys. Rev.* **D96** (2017) 095010 [1704.06659].
- [425] D. Buttazzo, A. Greljo, G. Isidori and D. Marzocca, *B -physics anomalies: a guide to combined explanations*, *JHEP* **11** (2017) 044 [1706.07808].
- [426] Y. Cai, J. Gargalionis, M. A. Schmidt and R. R. Volkas, *Reconsidering the One Leptoquark solution: flavor anomalies and neutrino mass*, *JHEP* **10** (2017) 047 [1704.05849].
- [427] A. Crivellin, D. Müller and T. Ota, *Simultaneous explanation of $R(D^{(*)})$ and $b \rightarrow s\mu^+\mu^-$: the last scalar leptoquarks standing*, *JHEP* **09** (2017) 040 [1703.09226].
- [428] A. Biswas, D. K. Ghosh, A. Shaw and S. K. Patra, *$b \rightarrow c\ell\nu$ anomalies in light of extended scalar sectors*, 1801.03375.
- [429] A. Azatov, D. Bardhan, D. Ghosh, F. Sgarlata and E. Venturini, *Anatomy of $b \rightarrow c\tau\nu$ anomalies*, *JHEP* **11** (2018) 187 [1805.03209].
- [430] A. Angelescu, D. Bečirević, D. A. Faroughy and O. Sumensari, *Closing the window on single leptoquark solutions to the B -physics anomalies*, *JHEP* **10** (2018) 183 [1808.08179].
- [431] P. Asadi, M. R. Buckley and D. Shih, *It's all right(-handed neutrinos): a new W' model for the $R_{D^{(*)}}$ anomaly*, *JHEP* **09** (2018) 010 [1804.04135].
- [432] A. Greljo, D. J. Robinson, B. Shakya and J. Zupan, *$R(D^{(*)})$ from W' and right-handed neutrinos*, *JHEP* **09** (2018) 169 [1804.04642].
- [433] D. J. Robinson, B. Shakya and J. Zupan, *Right-handed Neutrinos and $R(D^{(*)})$* , *JHEP* **02** (2019) 119 [1807.04753].

- [434] A. Azatov, D. Barducci, D. Ghosh, D. Marzocca and L. Ubaldi, *Combined explanations of B-physics anomalies: the sterile neutrino solution*, *JHEP* **10** (2018) 092 [1807.10745].
- [435] J. Heeck and D. Teresi, *Pati-Salam explanations of the B-meson anomalies*, *JHEP* **12** (2018) 103 [1808.07492].
- [436] K. S. Babu, B. Dutta and R. N. Mohapatra, *A theory of $R(D^*, D)$ anomaly with right-handed currents*, *JHEP* **01** (2019) 168 [1811.04496].
- [437] D. Bardhan and D. Ghosh, *B -meson charged current anomalies: The post-Moriond 2019 status*, *Phys. Rev.* **D100** (2019) 011701 [1904.10432].
- [438] R.-X. Shi, L.-S. Geng, B. Grinstein, S. Jäger and J. Martin Camalich, *Revisiting the new-physics interpretation of the $b \rightarrow c\tau\nu$ data*, *JHEP* **12** (2019) 065 [1905.08498].
- [439] J. D. Gómez, N. Quintero and E. Rojas, *Charged current $b \rightarrow c\tau\bar{\nu}_\tau$ anomalies in a general W' boson scenario*, *Phys. Rev.* **D100** (2019) 093003 [1907.08357].
- [440] R. Dutta and A. Bhol, *$B_c \rightarrow (J/\psi, \eta_c)\tau\nu$ semileptonic decays within the standard model and beyond*, *Phys. Rev.* **D96** (2017) 076001 [1701.08598].
- [441] R. Dutta, *Exploring R_D, R_{D^*} and $R_{J/\Psi}$ anomalies*, 1710.00351.
- [442] R. Dutta and A. Bhol, *$b \rightarrow (c, u), \tau\nu$ leptonic and semileptonic decays within an effective field theory approach*, *Phys. Rev. D* **96** (2017) 036012 [1611.00231].
- [443] D. Bečirević, S. Fajfer, N. Košnik and O. Sumensari, *Leptoquark model to explain the B-physics anomalies, R_K and R_D* , *Phys. Rev.* **D94** (2016) 115021 [1608.08501].
- [444] J. M. Cline, *Scalar doublet models confront τ and b anomalies*, *Phys. Rev. D* **93** (2016) 075017 [1512.02210].
- [445] B. Capdevila, U. Laa and G. Valencia, *Anatomy of a six-parameter fit to the $b \rightarrow s\ell^+\ell^-$ anomalies*, *Eur. Phys. J. C* **79** (2019) 462 [1811.10793].
- [446] H. H. Patel, *Package-X: A Mathematica package for the analytic calculation of one-loop integrals*, *Comput. Phys. Commun.* **197** (2015) 276 [1503.01469].

Resum

El Model Estàndard és la teoria que utilitzem per a descriure el món subatòmic de les partícules. Consta de tres famílies de 15 camps Weyl que interaccionen entre ells seguint un patró marcat per les forces de la cromodinàmica quàntica (QCD), representada per la simetria $SU(3)_c$, i la interacció feble, representada per $SU(2)_L \otimes U(1)_Y$, on els nombres quàntics de l'última corresponen a la hipercàrrega. Després que el Higgs, camp que necessitem per donar-li massa als fermions de la teoria, adquireix un valor d'expectació, la simetria es trenca espontàniament, donant pas a l'electrodinàmica quàntica (QED), mentre que QCD roman inalterada. Hui en dia és la millor teoria que la comunitat científica disposa, ja que pot explicar un alt percentatge dels fenòmens que ocorren a la natura a nivell microscòpic. No obstant això, aquesta teoria té també els seus punts febles; certes evidències experimentals queden fora del seu abast, així com aspectes *estètics* als quals no se'ls pot atorgar una explicació satisfactòria. L'objectiu d'aquesta tesi és esbrinar aquells terrenys desconeguts mitjançant extensions del Model Estàndard que permeten entendre l'existència simultània d'aquests al context d'un marc teòric ben definit. Els models teòrics que proposem permeten una perspectiva més completa de la natura i, a més de ser compatibles amb els experiments, són simples des d'un punt de vista minimalista, capaços de donar prediccions, quotes per als paràmetres o correlacions entre observables. Sobretot, destaquen per ser falsables, és a dir, amb prediccions que estan a l'abast dels experiments que disposem en l'actualitat o d'aquells que es plantegen construir en un futur pròxim. A continuació, enumerem alguns dels fets experimentals, junt amb altres fets d'una índole més estètica, que posen en evidència les limitacions del Model Estàndard:

- **Els neutrins tenen massa.** Les simetries locals i el contingut de partícules del Model Estàndard no permeten que els neutrins siguin massius. No obstant això, experimentalment s'han observat oscil·lacions al sabor dels neutrins, fet que implica que almenys dues generacions de neutrins han de tindre una massa no-degenerada. A més, aquestes masses són, sorprenentment, de l'ordre de l'eV, és a dir, un milió de voltes més menudes que la massa de l'electró. Aquestes partícules són les úniques transparents sota les forces del Model Estàndard, i segons com prenen la massa podem classificar la seua natura com Majorana o Dirac, la qual està íntimament lligada a la violació del número leptònic. Si aquest últim es trenca en dues unitats, els neutrins seran Majorana, mentre que si el número leptònic es conserva o es trenca en un número d'unitats major que dos, els neutrins seran Dirac. Si són Majorana, hi ha tres tipus de mecanismes a nivell arbre que permeten generar un terme de massa per als neutrins: els mecanismes de balancí del tipus I, II i III; encara que també existeixen alternatives a nivell quàntic que generen un terme de massa comptant amb la supressió natural dels bucles, com el mecanisme de Zee o el del balancí amb color. Al Capítol 1 hem presentat una breu introducció a la física de neutrins parlant amb detall el que s'ha comentat en aquest paràgraf.
- **Asimetria de matèria respecte a l'antimatèria.** El Model Estàndard no pot explicar l'excés de matèria respecte a l'antimatèria del nostre univers. D'acord amb A. Sakharov, tres condicions s'han d'acomplir per tal de donar lloc a aquesta asimetria, essent una d'elles la violació del número bariònic.
- **Un 25% del nostre univers està compost de matèria fosca.** La velocitat de rotació galàctica, entre altres observacions cosmològiques, manifesta l'existència d'un excés de matèria respecte a l'observada (i esperada) a l'aurèola de les galàxies. L'adjectiu "fosca" ve del fet que, malgrat manifestar interaccions gravitatòries, no sembla interaccionar electromagnèticament, és a dir, és matèria que "està" però que no veiem. De la llarga llista de candidats de matèria fosca, en aquesta tesi ens hem centrat en les partícules massives d'interacció feble (WIMPs) i axions. Ambdós candidats s'han presentat al Capítol 2 d'aquesta tesi. Les primeres són atractives per la seua familiaritat: disposem de la mecànica quàntica de camps, un marc teòric definit per tractar amb interaccions entre partícules, el qual podem aplicar tant a les partícules del Model Estàndard

com a qualsevol partícula hipotètica i de comportament semblant a les anteriors que puga fer de candidata de matèria fosca. Curiosament, entre un ordre de massa del GeV-TeV, aquest tipus de partícules prediuen l'abundància de densitat relíquia estimada experimentalment. Els axions, d'altra banda, són candidats de matèria fosca altament no-tèrmics. A l'inici de l'evolució de l'univers, aquestes partícules no tenien massa, ja que els efectes dels instantons, responsables de donar-li-la, estaven fortament suprimits. Aleshores, s'esperaria un desaligament inicial arbitrari respecte a l'angle zero de l'amplitud del camp axiònic. A temperatures pròximes a la massa del protó, l'axió adquireix massa i comença a oscil·lar cap al centre del potencial, és a dir, cap al valor fixat per la dinàmica de QCD: el de zero violació de CP. La densitat d'energia dissipada a aquestes oscil·lacions es comporta com matèria no-relativista sota l'evolució de l'univers, la qual contribueix a la densitat relíquia i podria explicar la seua existència. No obstant això, a part del seu potencial com candidats de matèria fosca, els axions van nàixer com una solució atractiva al problema fort de CP.

- **Problema fort de CP.** Teòricament, QCD prediu violació de CP proporcional a una fase provinent de dos orígens diferents al seu Lagrangiana. Sorprenentment, a l'experiment no s'ha observat aquest fenomen i els límits experimentals ens diuen que dita fase hauria de ser l'ordre de 10^{-10} . Dit en altres paraules, QCD sembla preservar sense cap mena d'explicació la simetria CP, fet que es coneix com el problema fort de CP. Aquesta tensió entre el que u esperaria teòricament i l'experiment, conseqüència del caràcter anòmal de les transformacions quirals en presència d'una teoria no-abeliana amb una estructura del buit no trivial, es pot solucionar afegint una partícula pseudoescalar que, mitjançant una simetria al Lagrangiana que es comporte com la quiral en presència de fermions no-massius, permeta compensar, de manera natural (per la mateixa dinàmica de QCD), la contribució de la fase responsable de la violació de CP als observables on participa. La simetria que genera aquestes partícules s'anomena Peccei-Quinn (PQ), i aquestes partícules s'anomenen axions. Aquests són bosons pseudo-Goldstone a causa de la seua xicoteta massa generada per efectes instantònics, la qual és inversament proporcional a l'escala PQ. Els axions s'han presentat a aquesta tesi a la segona part del Capítol 2. El mecanisme original enllaça, mitjançant un model de dos doblets de Higgs i la imposició d'una simetria global PQ, l'escala en què es trenca la simetria PQ amb

l'escala electrofeble, la qual no és prou *pesada* per suprimir les interaccions entre l'axió i la matèria del Model Estàndard i és la raó per què aquest model està descartat. Es van proposar alternatives realístiques de la implementació d'aquest mecanisme sota el nom de models d'axions invisibles, els quals eviten els límits experimentals mitjançant el desacoblament de l'escala PQ amb l'electrofeble, amb la introducció d'un escalar transparent (singlet) a les forces del Model Estàndard, podent ser aquesta escala PQ arbitràriament gran. Segons com aquest desacoblament s'implemente, podem distingir dos tipus de mecanismes: el mecanisme DFSZ, on aquest singlet escalar que conté l'axió suprimit per l'escala arbitràriament gran interactua amb els quarks indirectament a partir d'un terme de mescla amb els dos dobles de Higgs al potencial escalar, i el mecanisme KSVZ, on l'escalar en aquest cas no actua a nivell arbre amb els quarks del Model Estàndard, sinó amb nous fermions de color la redefinició dels quals permet, d'igual manera, la resolució del problema fort de CP. La contrapartida és que, en principi, aquests models no permeten predir la massa de l'axió (ja que no prediuen l'escala PQ), donant peu a desenes d'ordres de magnitud a l'espectre de masses on buscar-los.

- **Què ens poden contar les simetries accidentals del Model Estàndard?** Al Lagrangia del Model Estàndard, a conseqüència de les simetries locals que imposem i donat el seu contingut de camps, apareixen inesperadament simetries globals relacionades amb el número leptònic (L) i bariònic (B) de les partícules, les quals es coneixen com a simetries accidentals, ja que emergeixen *per accident* a la teoria. Ja hem vist que el número leptònic està intrínsecament relacionat amb la natura dels neutrins. El número bariònic està relacionat amb el decaïment del protó entre altres, el qual està fortament acotat pels resultats experimentals i que, juntament amb la no-observació d'oscil·lacions de neutrons, la no-observació del fenomen de decaïment doble beta, o altres fenòmens de transició del número bariònic i leptònic, sembla suggerir que aquests es conserven, almenys de forma pertorbativa, a la natura. Com a excepció de l'anterior estan els instantons (efectes no-pertorbatius) els quals medien processos altament suprimitos a temperatures baixes de trencament de número bariònic i leptònic en tres unitats. No obstant això, sabem que el Model Estàndard no pot ser la teoria definitiva, i si expressem qualsevol teoria de nova física des del punt de vista de

l'escala baixa a partir d'una expansió efectiva d'operadors, res ens garanteix a priori que aquestes simetries vagen a ser respectades en presència d'aquests nous operadors no-renormalitzables. I si la raó per què el protó no decau és perquè no pot fer-ho? I si aquestes simetries accidentals són el remanent d'una versió local que ha sigut trencada (o encara continua vigent) a una certa escala? Abans hem comentat que un dels ingredients necessaris per a explicar l'asimetria de matèria-antimatèria és la violació del número bariònic. Com mostrem al Capítol 3, la cancel·lació d'anomalies a les teories més senzilles on el número leptònic i/o bariònic són promoguts a simetries locals prediu que aquest s'ha de trencar en tres unitats, predient com a conseqüència l'estabilitat del protó a tots els ordres en teoria de perturbacions. A més, aquestes teories també prediuen un candidat de matèria fosca del tipus WIMP, el qual interacciona amb les partícules del Model Estàndard mitjançant el bosó abelià associat a la nova força. Aquesta última predicció és també conseqüència de la cancel·lació d'anomalies, és a dir, de la pròpia consistència de la teoria, i la seua estabilitat està garantida per la simetria remanent després de la ruptura espontània del número leptònic i/o bariònic. Al Capítol 4 mostrem que el límit cosmològic de la densitat relíquia es tradueix en una quota superior per a l'escala de violació del número leptònic i/o bariònic de l'ordre dels 20 TeVs. L'últim implica que aquestes teories han de viure per davall d'eixa escala, pel que podem aspirar a accedir-hi, si no ara, en un futur pròxim. En el cas del número bariònic local, els límits experimentals permeten que aquest trencament espontani de simetria ocorregui a una escala sorprenentment baixa sense haver-hi de desacoplar la teoria sota l'elecció d'un acoplament de nova força excessivament menut. El darrer ens dóna esperança de detectar un bosó leptofòbic als col·lisionadors de partícules, junt amb el Higgs necessari per a trencar espontàniament el número bariònic (en el cas del número leptònic els límits experimentals són més severs a escales baixes). I per remarcar la bellesa d'aquestes teories, direm que disposen de nous fermions també predits per la cancel·lació d'anomalies que gaudeixen d'una interacció axial amb el nou bosó. Aquest fet, junt amb la possibilitat de tindre un candidat de matèria fosca del tipus Majorana predit de forma natural en aquest tipus de teories, permet l'observació de línies de fotons, que són senyals genuïnes de la matèria fosca, l'observació de les quals permetria conèixer la massa d'aquesta, com expliquem al Capítol 2. En el cas que promoguem el número leptònic a simetria local, com mostrem al Capítol 5, la

cancel·lació d'anomalies prediu l'existència de tres neutrins de quiralitat dextrogira, de manera que automàticament podem formar un terme de massa Dirac al Lagrangià a través de la interacció amb el Higgs, igual que la resta de fermions del Model Estàndard. En el cas del número leptònic local pur, com que aquest es trenca en tres unitats, els neutrins són partícules de Dirac. L'existència de partícules lleugeres com els nous neutrins han de ser consistents amb la cosmologia: aquests interaccionen mitjançant el bosó de la força leptònica amb la resta de matèria, de manera que en algun punt de l'evolució de l'univers, segons la seua ràtio d'interacció, es poden haver desacoblat de la resta del bany tèrmic, contribuint aleshores a la densitat d'energia. Aquesta hipotètica contribució es quantifica amb el paràmetre N_{eff} i, a partir de les mesures cosmològiques, es trasllada en límits sobre la massa del nou bosó. A les teories que presentem que involucren número leptònic total, mostrem que el paràmetre de fases de la teoria podria ser falsejat per les projeccions dels futurs límits en N_{eff} . Un poc divers és el cas en què promoguem a simetria local la combinació $B-L$. En aquest escenari, a part dels tres neutrins de quiralitat dextrogira que poden adquirir massa a través del mecanisme de Higgs, cap altre camp es necessita per cancel·lar anomalies. Com que $B-L$ és una teoria abeliana, existeix la possibilitat que mai s'haja trencat, ja que el bosó corresponent pot adquirir massa a partir del mecanisme de Stuckelberg. En aquest context, els neutrins serien partícules Dirac i els límits cosmològics de N_{eff} aplicarien també, igual que en el cas que $B-L$ es trenque en una unitat superior a dos. Tanmateix, si la simetria es trenca espontàniament en dues unitats, els neutrins serien Majorana, i la seua massa estaria relacionada amb l'escala de violació del número leptònic. El mecanisme del balancí de tipus I posa una quota superior a l'escala d'aquesta massa de l'ordre de 10^{14} GeV, la qual queda prou lluny de l'abast dels nostres experiments. En aquest cas, malgrat que la teoria no prediu de forma natural un candidat de matèria fosca, si el considerem mitjançant l'addició d'un parell de camps fermionics singlets sota el Model Estàndard (de natura vectorial), la pròpia consistència de la teoria fixa una quota superior on podria viure i l'escala del balancí es redueix almenys uns nou ordres de magnitud, cosa que ens dóna la possibilitat de detectar als experiments actuals senyals de violació leptònica i la fenomenologia típica d'un mecanisme de balancí que ocorre a escales baixes, com per exemple vèrtex desplaçats.

- **Per què hi ha tres forces diferents? Les tres semblen convergir a energies altes...**
Açò últim suggereix un origen comú d'aquestes a una escala que anomenarem escala de gran unificació. Les teories de gran unificació (GUTs) ofereixen una perspectiva molt atractiva i un poder predictiu admirable, malgrat viure usualment a escales altes i malauradament inaccessibles experimentalment. La teoria més senzilla on el Model Estàndard es pot incloure és $SU(5)$, la qual prediu, entre altres coses, el decaïment del protó, fet que obliga a l'escala GUT a viure per damunt dels 10^{15} GeVs donada l'agressivitat dels límits experimentals. Aquesta teoria es capaç d'agrupar els 15 camps Weyl del Model Estàndard en sols dues representacions i explica la quantització de les càrregues elèctriques dels camps del Model Estàndard. Malgrat la seua senzillesa, el model original està descartat pel seu poder predictiu, particularment per les següents raons: no pot predir relacions realistes entre les masses dels fermions (prediu la mateixa matriu de massa per als leptons carregats que per als quarks tipus baix a l'escala de GUT, la qual cosa no permet reproduir els valors experimentals a l'escala baixa); tampoc és capaç de predir els valors correctes dels acoblaments de les forces del Model Estàndard a baixes energies, ni massa per als neutrins. A aquesta tesi, concretament al Capítol 6, proposem dues de les alternatives renormalitzables més simples que permeten la resolució dels tres problemes anteriorment mencionats. En una d'elles, *Zee- $SU(5)$* , les masses dels fermions carregats i l'evolució dels acoblaments per tal que unifiquen a l'escala GUT s'ha aconseguit amb la introducció de la representació escalar 45_H , la qual també participa, junt amb el singlet carregat de la representació 10_H , a la generació a nivell bucle de la massa dels neutrins mitjançant el mecanisme de Zee. Aquesta teoria prediu l'existència d'un doblet de Higgs amb color (a la representació adjunta de $SU(3)_c$) lleuger, amb una quota superior d'uns 10^5 GeV. Per una altra banda, proposem una GUT basada en $SU(5)$ que, a part del contingut original, conté tres generacions més de fermions de natura vector en la fonamental i antifonamental de $SU(5)$, 5 i $\bar{5}$, i una representació 24 fermiònica, sense ampliar el contingut escalar de la teoria original i de manera consistent amb la cancel·lació d'anomalies. Els nous fermions en la 5 i $\bar{5}$ permeten assolir masses realistes per als fermions carregats del Model Estàndard mitjançant l'efecte de mescla amb aquests. Per altra banda, el mecanisme de balanç de tipus I i III permet generar massa per a dues generacions de neutrins, a partir dels nous camps sense color de la 24. També mostrem que aquesta

teoria disposa d'escenaris consistents amb les condicions d'unificació. La teoria prediu un neutrí sense massa, un triplet fermiònic per sota els 500 TeVs (responsable de generar la massa dels neutrins a partir del mecanisme de balanç de tipus III), i una quota superior per als canals de decaïment del protó que involucren antineutrins d'uns $\tau(p \rightarrow K^+ \bar{\nu}) \lesssim 3.4 \times 10^{35}$ anys i $\tau(p \rightarrow \pi^+ \bar{\nu}) \lesssim 1.7 \times 10^{34}$ anys, els quals romanen prop de les projeccions d'experiments com DUNE, Super- i Hyper-Kamiokande. La possibilitat de predir una quota superior per al decaïment del protó és conseqüència que en aquest model la massa dels quarks amunt és simètrica, ja que no ha fet falta afegir una representació escalar extra per corregir les masses dels fermions carregats.

A més, una de les qualitats d'aquestes teories és la capacitat de predir la seua escala: els límits experimentals sobre el decaïment del protó junt amb els límits de col·lisionadors de partícules (que indirectament actuen sobre l'escala de GUT imposant una quota inferior sobre la massa del Higgs de color que viu a la 45_H , peça clau per satisfer les condicions d'unificació), permeten fixar una finestra concreta per l'escala de GUT. Si aprofitem aquesta qualitat i afegim una simetria PQ a $SU(5)$ podem predir la massa de l'axió! La teoria $SU(5) \otimes U(1)_{PQ}$ permet enllacar els models d'axió-invisible amb l'escala de GUT mitjançant el singlet escalar que viu a la 24_H , responsable, per una banda, de definir l'escala GUT, i per altra, la massa de l'axió. Al Capítol 7 proposem la teoria basada en $SU(5)$ més senzilla que prediu la massa de l'axió a través del mecanisme KSVZ, y la corresponent amb el DFSZ. Al context d'aquestes teories, l'axió resulta no ser tan "invisible", ja que les prediccions per a la seua massa es troben a l'abast d'experiments d'axions com ABRACADABRA i CASPER. Les prediccions per a la massa de l'axió són $m_a^{KSVZ} \simeq (2.9 - 13.5) \times 10^{-9}$ eV, i $m_a^{DFSZ} \simeq (2 - 16) \times 10^{-9}$ eV, al context del mecanisme KSVZ i DFSZ, respectivament.

Altrament (i en particular d'una manera més clara a la teoria que implementa el mecanisme DFSZ), la teoria prediu una forta correlació entre el decaïment del protó i la massa de l'axió, de manera que els experiments de decaïment del protó actuarien en aquest context com experiments de recerca d'axions. Per tant, experiments com Super-Kamiokande, Hyper-Kamiokande o DUNE s'afegirien a la llista d'"ulls" capaços de veure els axions predits a aquestes teories. A més, aquestes prediccions permeten correlacions sòlides entre la vida mitjana del protó, la massa de l'axió i la seua interacció

amb els fotons i els nucleons. Les quotes per al decaïment del protó predites al context d'aquestes teories en canals que involucren als antineutrins són: $\tau(p \rightarrow K^+\bar{\nu}) \lesssim 4 \times 10^{37}$ anys, i $\tau(p \rightarrow \pi^+\bar{\nu}) \lesssim 2 \times 10^{36}$ anys.

Aquestes dues propostes basades en $SU(5)$ es poden considerar teories atractives on és possible entendre la unificació de les forces del Model Estàndard, l'origen de la massa dels neutrins, la matèria fosca, el problema fort de CP, i es podria entendre l'asimetria matèria - antimatèria a través del mecanisme de leptogènesis.

- **Anomalies relacionades en sabor!** Recentment, experiments que estudien transicions semileptòniques de b a c han suggerit la violació universal del número leptònic en una direcció comú, la qual cosa entra en conflicte amb les prediccions del Model Estàndard. Al Capítol 9 presentem un ajust global a transicions b a c tenint en compte les dades experimentals disponibles hui en dia i partint del Hamiltonià de dimensió-6 més general sota les següents assumpcions: la nova física entra solament en la tercera generació de leptons, hi ha una finestra energètica suficientment gran entre l'escala electrofeble i la nova física que assegura la validesa de la teoria efectiva del Model Estàndard, no hi ha graus de llibertat lleugers a part dels del Model Estàndard (particularment, no considerem un neutrí de quiralitat dextrogira de massa menuda), i assumim que els coeficients de Wilson del nostre Hamiltonià són reals. Al Capítol 8 presentem el marc teòric de teories efectives que ens permet inferir informació del tipus de nova física a partir de les simetries i graus de llibertat a l'escala baixa. A l'ajust incloem els valors experimentals dels quocients \mathcal{R}_D i \mathcal{R}_{D^*} (disponibles al 2017), així com les distribucions en moment transferit, q^2 . Els primers són observables molt nets a causa de les cancel·lacions que la seua definició de quocient gaudeix, mentre que les segones són interessants perquè no han sigut considerades en la gran majoria de referències a la literatura i observem que juguen un paper clau en reduir el número de solucions de l'ajust global. També considerem l'efecte de la recent mesura sobre la polarització longitudinal $F_L^{D^*}$ anunciada per Belle a una segona versió de l'ajust, la qual cosa ens permet quantificar el seu impacte mitjançant la comparació dels resultats d'ambdós. Observem als resultats que l'ajust, malgrat preferir configuracions de nova física respecte al Model Estàndard, no es decanta per una direcció de nova física preferent, observació que s'accentuà quan vam actualitzar els quocients $\mathcal{R}(D^{(*)})$ amb la nova mesura de

Belle. Si ajustem els coeficients de Wilson per separat, la solució preferida és, no obstant, la del coeficient vectorial, el qual és proporcional a la contribució del Model Estàndard. A més, no es pot trobar un escenari consistent amb totes les mesures experimentals considerant 1σ d'incertesa a les últimes, independentment de la nova física que es considere. Açò ens motivà a relaxar les nostres assumpcions inicials per tal de veure si es podia assolir un panorama consistent amb una teoria més general. La consideració de coeficients de Wilson complexes no suposa una millora notable a la qualitat de l'ajust, mentre que sí que implica un augment quantitatiu al número de solucions, la qual cosa complica considerablement l'anàlisi. Permetent que el trencament de la simetria electrofeble siga no-lineal implica la presència d'un coeficient de Wilson extra al nostre ajust. Aquesta llibertat afegida permet aconseguir escenaris on els diferents observables són compatibles, però a costa d'uns paràmetres de nova física altament sincronitzats. Si relaxem una altra de les nostres hipòtesis inicials i considerem neutrins lleugers de quiralitat dextrogira, el nombre de coeficients de Wilson a ajustar es dobla. A aquest últim ajust, també vam incloure el valor experimental de la polarització del tau, P_{τ}^{D*} , ja que, malgrat la seua gran incertesa, permet reduir la nova llibertat introduïda a l'ajust. A més, hem particularitzat els resultats per a diferents escenaris motivats per l'ajust previ i pels possibles camps de nova física que poden mediar interaccions rellevants per a les transicions b a c, tant en neutrins de quiralitat dextrogira com levogira. Malgrat doblar el número de coeficients de Wilson a ajustar, continuem observant una certa discrepància entre les prediccions dels diferents observables que participen en l'ajust tenint en compte 1σ de la seua incertesa, la qual només es resol en un parell d'escenaris molt particulars. Concloem que per a comprovar si la discrepància és d'origen teòric (amb les implicacions corresponents al relaxar cadascuna de les assumpcions) o experimental (implicant l'última que les pròximes mesures dels observables involucrant transicions semileptòniques b a c s'aproximaran eventualment a la predicció del Model Estàndard) necessitem més estadística.

Al llarg d'aquesta tesi s'han presentat teories motivades pel fet de donar múltiple resposta als problemes oberts del Model Estàndard. Hem explorat la interconnexió de diferents camps dins la física de partícules, sempre buscant el marc més senzill que pot descriure de manera satisfactòria ambdós i explotar les conseqüències de les

connexions entre aquests. Les extensions del Model Estàndard que hem proposat a aquesta tesi tenen en comú la seua capacitat predictiva: la seua estructura ben definida i completa permet llançar prediccions correlacionades entre els seus observables que, per una banda, exposen la teoria a ser falsada per l'experiment en un futur pròxim, i per altra, permeten progressar cap a una teoria que complete el Model Estàndard.

Acknowledgments

En primer lloc, el meu agraïment més sincer als meus dos directors de tesi: Pavel Fileviez Pérez i Toni Pich. Toni, moltíssimes gràcies pel teu suport, els teus consells i tot allò que m'has ensenyat, especialment a utilitzar la intuïció per a analitzar qualsevol problema i el meravellós poder de les simetries per estalviar-se maldecaps. Gràcies per donar-me la llibertat de treballar en qualsevol tema que m'interessara, per la teua paciència, pels teus ànims, per les conferències i escoles que tan bons records em porten i que hi han omplit aquest PhD de motivació, discussions interessants, i algunes escapades a montanyes de 3 km amb molt de gel. Pavel, aprendí contigo el modelo estándar en Heidelberg, en el máster me enseñaste las fantásticas tierras que hay más allá, y en este doctorado hemos hecho un viaje maravilloso, aprendiendo muchísimo, enfrentándonos a nuevos retos con ganas e ilusión. Esa emoción en el estómago cuando estamos cerca de conquistar una idea, la espontaneidad de nuestras discusiones de física por teléfono, en un tren, una tarde en un café... Gracias por enseñarme todo lo que he querido aprender y más, por empujarme siempre a lo máximo, por hacer de padre cuando estoy lejos de mi familia y llenar mi doctorado de momentos tan especiales. Thanks also to Mark Wise, for his honest advice, his support and for those discussions covering the $x \rightarrow \infty$ blackboards that made the time fly (and the wonderful meals afterwards). Thanks Mark for sharing with me a little of your admirable perspective to tackle challenges.

M'agradaria agrair a la beca La Caixa-Severo Ochoa el suport econòmic durant aquests anys i les oportunitats que m'ha donat de fer estades i assistir a conferències. I would also like to thank the members of the committee of my thesis: Gino Isidori, Verónica Sanz, Géraldine Servant, Thomas Hambye, Germán Rodrigo and Alberto Casas.

Thanks for your patience, your implication and your fruitful comments on the thesis. Quería agradecer también a Joannis Papavassiliou por todo su apoyo.

Durante esta etapa académica, no he podido encontrar mejor apoyo que el de mis *hermanos mayores* de la física: Fabrizio Rompineve, Javi Fuentes y Miguel Escudero. Ellos, a parte de darme momentos muy bonitos y una buena lista de aventuras, me han guiado en este doctorado dándome ánimos y transmitiéndome su amor por la física. Fabri, por tus consejos, tu preocupación y por tu don de sacarme siempre una sonrisa; Javi, por tu apoyo y compañía, por contagiarme esa motivación tuya infinita; Miguel, por cuidarme, por tus ánimos constantes, por esa corriente de pasión que transmites por lo que haces. ¡Muchísimas gracias a los tres!

De manera molt especial, vull agrair a Ana Peñuelas, la meua companya de viatge i batalles, tot el que ha fet i significat per a mi en aquesta etapa. Ana, des del moment zero em vas acollir a l'Ific com una més, integrant-me amb la resta de PhDs, al grup, a la vida en València. Sempre que he tingut el mínim problema (des d'aranyes al despatx, robatoris de bicis, pèrdues de memòria a les 3 del matí, despatx bloquejat, dubtes de física o rallades de la vida) he acudit a tu sense sentir-me malament, perquè sent que em vols ajudar de veritat. Per haver sigut la meua companya de física, de risas i plors, i de moments tan guais que guardaré amb molt de carinyo. Gràcies per tindre tanta paciència amb mí i per estar sempre ahí!

Agradecer también a mis compañeros de comidas, de muchos *cafeses* y *cerves*, de noches en *el Kurdo*, *el Terra*, o *el Olegari*, por llenar mis cuatro años aquí de buenos momentos y muchas risas. Especialmente a los *Garchers*; mil gracias por aguantar mis locuras (*for the honour of Grayskull!*) y darme tanto amor. Gràcies als *Pisiers*, qui han entrat ben fort en l'última etapa, per animar-me en aquest final de tesi i pels moments tan guais (ruta pobles, nits de OT, tardeos...). Thanks also to the *LHCPheno* group members, to those who are now and those who already left. Y a mis compis de despacho-nevera, Miguel y Pablo, por su buen humor, su simpatía y su paciencia con mis 10^3 olvidos de llaves y mis continuas negaciones a ir a la cafe a merendar. I would also like to acknowledge the Cleveland crew! Special thanks to Alexis, for all his support and the nice discussions we shared. Es muy divertido hacer física contigo. Thanks to Ruihao and Elliot; it is always a pleasure to do physics and eat tacos with you. And of course to my two dear *sisters*, Klaountia and Shamreen, for the orchestra nights, beers,

shopping days and all the cooking. You guys made me don't miss Valencia too much when being there! I would also like to thank Femke, for the nice time we had at *Les Houches* and other conferences, and for letting me know that *Ggggroningen* exists.

Gracias a mi Juli, quien supe desde conocerlo en el TAE que se convertiría en uno de mis mejores amigos. Gracias por tu apoyo, tu agradable compañía, por tu don de convertir lo más cotidiano en una aventura. Gràcies a Ana Montaner, per trencar amb escapades (una de les quals acabaria sent el viatge més emocionant que mai he fet) la meua rutina. Gràcies per mostrar-me la teua motivació contagiosa. Gràcies als meravellosos membres del club *Rack*! Per tots els viatges, dies *Rack*, skypes i el vostre suport incondicional. M'encanta que hàgem crescut junts, i que continuem fent-ho, i cada volta sent una família més gran! Entre ellos, Sonia, gracias por animarme estos cuatro años con los miércoles de anime y cenas japos. Tu creatividad sin limites y tu motivación han sido siempre una fuente de inspiración. Gràcies també a les peludes i corrinxeres, pels viatges i celebracions; sobretot per la vostra paciència amb este caos de persona, pel vostre suport i per fer-me riure tant. I d'una manera especial, agrair a Clarita, la meua *amica geniale*, el meu *entangled state*, amb qui m'haguera encantat compartir aquests anys d'aprenentatge (queda pendent el Miralles-Murgui, encara que ningú s'enrecorde del pobre Schröeder). Malgrat els quilòmetres que ens separen, sempre et tinc molt present. Basti i tu sou la meua medicina.

Per acabar, volia donar-li les gràcies als membres de *Villacousin*: Paula, Carmen i Joan, per haver complit el meu somni de viure junts i haver fet del segon de doctorat un any tan especial. La felicitat de tornar a casa i trobar-me amb les vostres risses, les ganes de fer locures improvisades, els desdjunis eternals, la vostra paciència amb els meus *punts*, la sensació d'estar tan a gust... és indescriptible. I amb un carinyo infinit als membres del pisi: Martí, Iker, Silvia i Ana. Mil gràcies pel vostre suport sense límits, per tot el vostre amor, per tot el que m'heu ensenyat i fet créixer com a persona. Sou la meua segona família i no puc sentir-me més afortunada d'haver compartit aquests dos anys plens de moments preciosos amb vosaltres (incloent una quarantena de tres mesos). Gràcies també al meu *bichito* Emmy, també coneguda com la Dr. Noether, a qui malgrat haver-me trencat l'ordinador i introduït algún *typo* a la tesi no puc voler més.

I persupostíssim, a la meua família, a la qui no existeixen paraules per agrair tot el que han fet per mi. Als meus tios i cosins, pel vostre ànim i confiança constants.

Als meus *uelos*, per l'esforç de seguir el que faig i tots els noms d'on vaig i torne, i per mostrar-me el vostre orgull. Als meus germans, Joan i Maria, els qui més m'han *aguantat en modo mineral* (i mencionar la casa de Joan en Benidorm on m'he refugiat i escrit bona part d'aquesta tesi). Gràcies per tots els moments, pels nostres viatges, complicitats, jocs i locures. Sou els que més em sabeu animar i com fer-ho, i lo més bonico que tinc. I als meus pares, Visan i Juanjo, per la seua paciència, suport i amor infinits. Gràcies per haver-nos animat, des de que tenim consciència, a despertar la nostra curiositat i crear amb llibertat, sense barreres. A vosaltres, i amb molt de carinyo a la *uela* Visan, va dedicada aquesta tesi.